AD NUMBER
AD387190
CLASSIFICATION CHANGES
TO: **UNCLASSIFIED**
FROM: **CONFIDENTIAL**
LIMITATION CHANGES
TO: **Approved for public release; distribution is unlimited. Document partially illegible.**
FROM: **Distribution authorized to U.S. Gov't. agencies and their contractors; Administrative/Operational Use; JAN 1968. Other requests shall be referred to Air Force Rocket Propulsion Laboratory, Edwards AFB, CA 93523. Document partially illegible.**
AUTHORITY
AFRPL ltr dtd 15 Mar 1971; AFRPL ltr dtd 5 Feb 1986

SECURITY MARKING

The classified or limited status of this report applies to each page, unless otherwise marked.
Separate page printouts MUST be marked accordingly.

THIS DOCUMENT CONTAINS INFORMATION AFFECTING THE NATIONAL DEFENSE OF THE UNITED STATES WITHIN THE MEANING OF THE ESPIONAGE LAWS, TITLE 18, U.S.C., SECTIONS 793 AND 794. THE TRANSMISSION OR THE REVELATION OF ITS CONTENTS IN ANY MANNER TO AN UNAUTHORIZED PERSON IS PROHIBITED BY LAW.

NOTICE: When government or other drawings, specifications or other data are used for any purpose other than in connection with a definitely related government procurement operation, the U. S. Government thereby incurs no responsibility, nor any obligation whatsoever; and the fact that the Government may have formulated, furnished, or in any way supplied the said drawings, specifications, or other data is not to be regarded by implication or otherwise as in any manner licensing the holder or any other person or corporation, or conveying any rights or permission to manufacture, use or sell any patented invention that may in any way be related thereto.

AFRPL-TR-67-280

(Unclassified Title)

FINAL REPORT ADVANCED CRYOGENIC ROCKET ENGINE PROGRAM, AEROSPIKE NOZZLE CONCEPT VOLUME II

F. B. Lary
Rocketdyne
A Division of North American Rockwell Corporation
6633 Canoga Ave.
Canoga Park, California

Technical Report AFRPL-TR-67-280

January 1968

Group 4
Downgraded at 3-Year Intervals
Declassified After 12 Years

In addition to security requirements which must be met, this document is subject to special export controls and each transmittal to foreign governments or foreign nationals may be made only with prior approval of AFRPL (RPPR/STINFO), Edwards, California, 93523.

Air Force Rocket Propulsion Laboratory
Air Force Systems Command
United States Air Force
Edwards Air Force Base, California

When U.S. Government drawings, specifications, or other data are used for any purpose other than a definitely related Government procurement operation whatsoever, and the fact that the Government may have formulated, furnished or in any way supplied the said drawings, specification, or other data, is not to be regarded by implication or otherwise, or in any manner licensing the holder or any other person or corporation, or conveying any rights or permission to manufacture, use, or sell any patented invention that may in any way be related thereto.

In addition to security requirements which must be met, this document is subject to special export controls and each transmittal to foreign governments or foreign nationals may be made only with prior approval of AFRPL (RPPR/STINFO), Edwards, California, 93523.

This material contains information affecting the national defense of the United States within the meaning of the espionage laws, Title 18 U.S.C., Sections 793 and 794, the transmission of revelation of which in any manner to an unauthorized person is prohibited by law.

ERRATA

1. Page 28, paragraph 2, line 4 (Unclassified)
2. Page 28, paragraph 3, line 25 (Confidential)
3. Page 94, paragraph 3, line 9 (Confidential)
4. Page 197, paragraph 2, line 10 (Confidential)
5. Page 197, paragraph 3, line 21 (Confidential)
6. Page 213, paragraph 4, line 13 (Confidential)
7. Page 287, Figure 125 (Confidential)
8. Page 379, paragraph 1, line 1 (Confidential)
9. Page 442, paragraph 2, line 14 (Confidential)
10. Page 549, line 31, title (Confidential)
11. Page 642, paragraph 3, line 12 (Confidential)
12. Page 642, paragraph 4, line 21 (Unclassified)
13. Page 765, paragraph 5, line 21 (Confidential)
14. Page 809, Figure 370 (Confidential)
15. Page 866, paragraph 2, line 9 (Confidential)

AFRPL-TR-67-280

(Unclassified Title)

FINAL REPORT, ADVANCED CRYOGENIC ROCKET ENGINE PROGRAM, AEROSPIKE NOZZLE CONCEPT

(VOLUME II)

F. B. Lary
Rocketdyne,
A Division of North American Rockwell Corporation
6633 Canoga Ave.
Canoga Park, California

Technical Report AFRPL-TR-67-280

January 1968

Group 4
Downgraded at 3-Year Intervals
Declassified After 12 Years

Air Force Rocket Propulsion Laboratory
Air Force Systems Command
United States Air Force
Edwards Air Force Base, California

FOREWORD

This report presents the work accomplished on Phase I of the Advanced Cryogenic Rocket Engine Program, Aerospike Nozzle Concept under Air Force Contract AF04(611)-11399. The work reported herein was conducted by Rocketdyne, A Division of North American Rockwell Corporation, 6633 Canoga Avenue, Canoga Park, California, under the Technical direction of Capt. Vernon L. Mahugh, Project Engineer, Air Force Rocket Propulsion Laboratory, Edwards, California. This report covers the contract period 1 March 1966 through 21 October 1967.

A portion of the design and tooling effort in Task II represents a joint effort with the Advanced Engineering Program, System and Dynamic Investigation (Aerospike), Contract NAS8-19.

Classified information has been extracted from documents listed under References.

This report, submitted January 1968, has been assigned Rocketdyne Report No. R-7168, Volumes I and II.

This technical report has been reviewed and is approved.

Vernon L. Mahugh
Capt, USAF
Project Engineer
Air Force Rocket Propulsion Laboratory

Ernie D. Braunschweig
Capt, USAF
Program Manager
Air Force Rocket Propulsion Laboratory

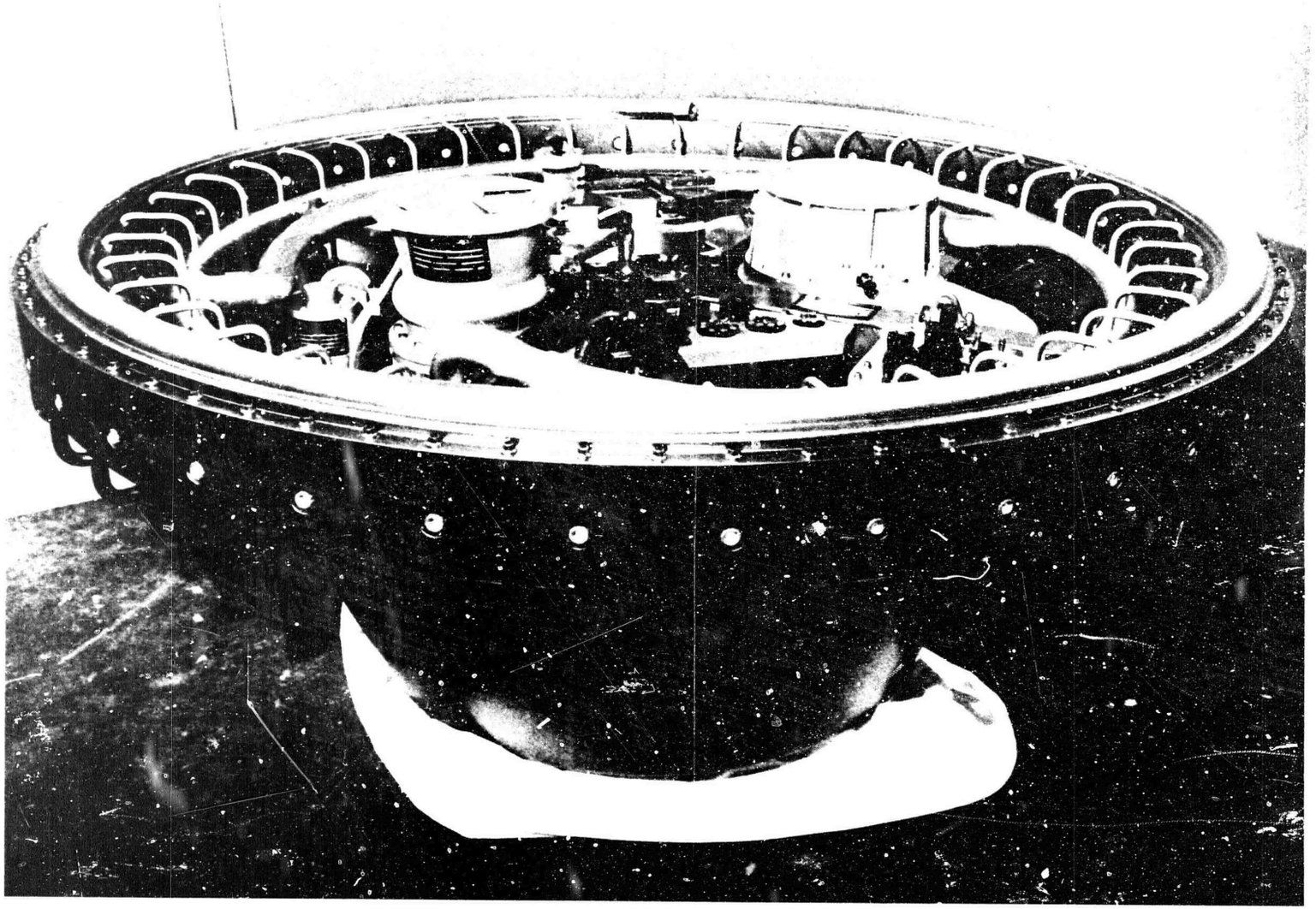

Frontispiece. Aerospike Flight Engine Mockup

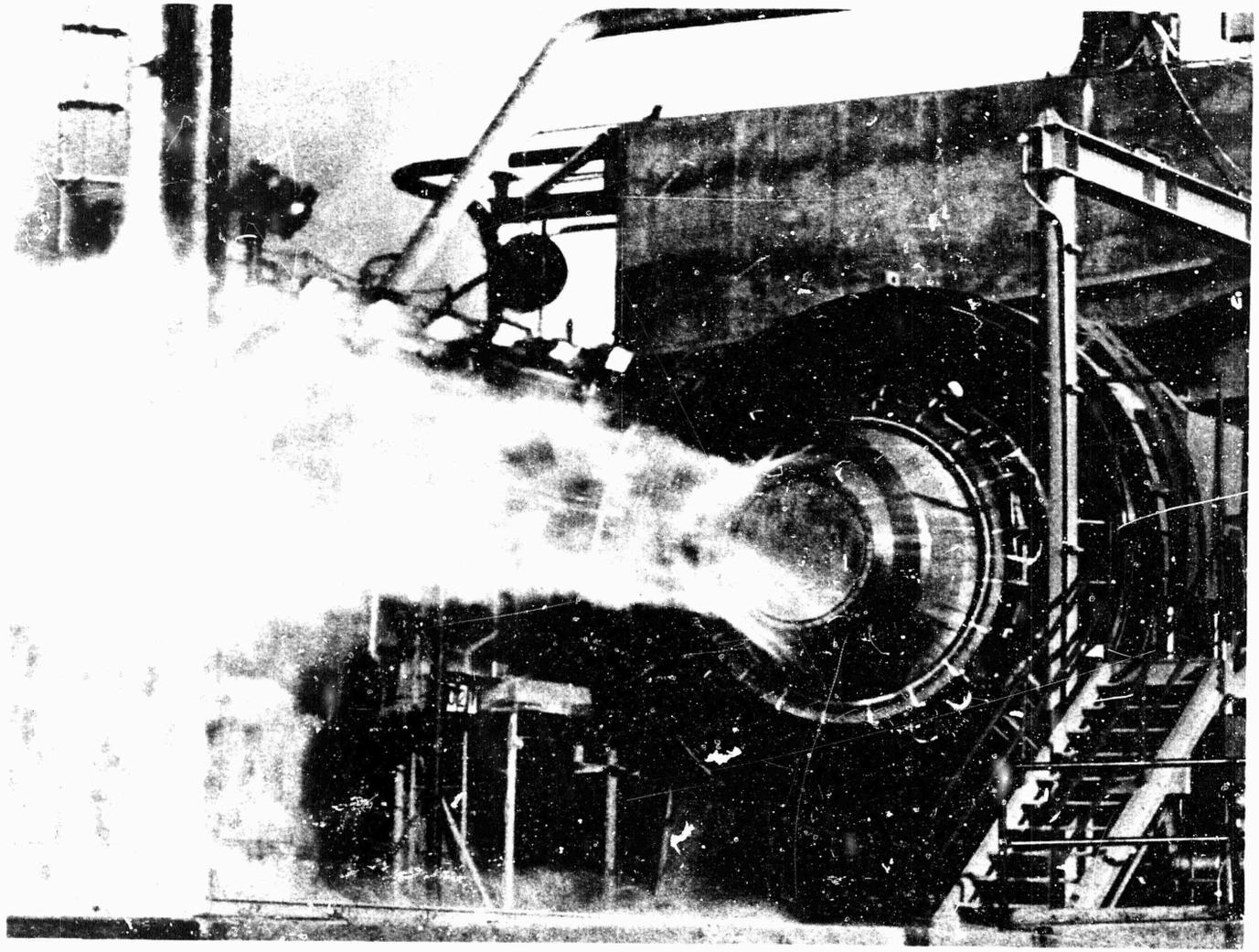

1XW24-9/29/67-R1*

Frontispiece: 250K Tube-Wall Test and Firing
at Nevada Field Laboratory

ABSTRACT

(U) Technical results obtained at the completion of the contract effort are described for the Advanced Cryogenic Rocket Engine Program, Aerospike. This program includes analysis and preliminary design of an advanced rocket engine using an aerospike nozzle and experimental evaluation of critical technology related to the aerospike concept. Component and system features, physical arrangements, design parameters and details, operational characteristics, and performance have been established for an optimum demonstrator engine. Studies were made of application of a flight engine to certain vehicles. Experimental injector performance investigations and experimental cooling investigations on segment chambers were conducted, producing the target combustion performance. Various materials were studied for long life of thrust chamber cooling passages and the target life was demonstrated. Full-scale, cooled thrust chambers were fabricated and tested for overall combustor and nozzle performance demonstrations. Injector failure limited these tests; however, nozzle and combustor performance were as predicted when not influenced by excess leakage. Structural and cooling evaluations were conducted on a segment embodying essential elements of the Demonstrator chamber design.

CONTENTS

Volume I

Introduction 1

Summary 5

Module Design 5

Application Study 26

Fabrication and Test 28

Conclusions and Recommendations 57

Task I, Design and Analysis 61

Demonstrator Module Design 61

Flight Module Design 362

Application Study 382

Volume II

Task II: Fabrication and Test 393

Injector Performance Investigation 393

Thrust Chamber Cooling Investigation 462

Thrust Chamber-Nozzle Demonstration 579

Segment Structural Evaluation 779

Appendix I

Performance Calculation Technique for the ADP Film-Cooled Segment Tests 859

Appendix II

Hot-Gas Tapoff Calculations 870

Appendix III

Heat Transfer Data Reduction for Water-Cooled Segments 874

Appendix IV

Tube-to-Body Cavity Vent Provision 878

Appendix V

System Performance Sample Calculations 881

Appendix VI

Instrumentation Nomenclature 891

Appendix VII

Flowrate Calculation Methods 894

Appendix VIII

Chamber Start Sequence 897

Appendix IX

Altitude Compensation 903

References 907

ILLUSTRATIONS

Frontispiece. Aerospike Flight Engine Mockup iii

Frontispiece. 250K Tube-Wall Test and Firing at Nevada Field Laboratory iv

1. Demonstrator Module Schematic 7

2A. Demonstrator Module Layout 11

2B. Demonstrator Module Layout 12

3. Engine Accessibility 8

4. 250K Thrust Chamber Demonstrator Module 15

5. Regenerative-Coolant Flow Circuit 16

6. Demonstrator Engine Fuel Turbopump 19

7. Demonstrator Engine Oxidizer Turbopump 22

8. Demonstrator Engine Throttling and Mixture Ratio Control . . 24

9. 60-Degree LO_2 Impinging Triplet With Fuel Post Extended and Both Chamfered and Nonchamfered LO_2 Strips 32

10. Triplet Injector Performance in the 2.5K Segment Thrust Chamber 33

11. Combustion Efficiency vs Cyclic Test Number Nickel Tube-Wall Segment Cycling Tests 34

12. 250K Performance Compared to 2.5K Performance 35

13. 250K Candidate Triplet With Fuel Post 36

14. Injector After First Brazo Cycle 37

15. 250K Tube-Wall Thrust Chamber C_v Performance vs Pressure Ratio 40

16. Experimental Heat Pressure 41

17. 250K Tube-Wall Thrust Chamber Specific Impulse vs Pressure Ratio 42

18. Experimental Heat Flux Distribution From 2.5K Water-Cooled Segment Test 43

19. Throat Heat Flux vs Chamber Pressure 45

20. Contoured Tube Overall Heat Transfer Characteristics . . . 46

21. Experimental H_2 Coolant Heat Transfer Results for 250K Experimental Tubes Relative to Theoretical Straight Smooth Tube Heat Transfer Coefficient 47

22. Low-Cycle Fatigue Characteristics (Nickel 200) 48
23. Completed 250K Tube Wall Outer Body 55
24. Completed 250K Tube Wall Inner Body 56
25A. Demonstrator Module Layout 68
25B. Demonstrator Module Layout 69
26. Demonstrator Module Schematic 70
27. Demonstrator Engine 76
28. Demonstrator Engine I_s vs Altitude 80
29. Demonstrator Engine Throttling Performance 82
30. Engine Vacuum Start Transients 83
31. Engine Sea Level Start Transients 86
32. Engine Cutoff Transients 88
33. Tapoff Throttle Valve ΔP vs Flowrate 91
34. Oxidizer Turbine Throttle Valve ΔP vs Flowrate 92
35. Variation of η_{c^*} With Mixture Ratio 98
36. Variation of Throat Chamber Mixture Ratio With Engine Mixture Ratio 98
37. Demonstrator Engine I_s vs Altitude 100
38. Demonstrator Engine Throttling Performance 101
39. Nozzle Geometric Efficiency vs Mixture Ratio 102
40. Variation of Base Pressure With Flowrate at Vacuum Conditions 104
41. Variation of Engine Vacuum I_s With Secondary Flowrate at Vacuum Conditions 104
42. Tapoff Gas MR vs Hydrogen Inlet Temperature 105
43. 2.5K Segment Tapoff Temperature vs Chamber Pressure . . . 105
44. Delivered Performance Calculation Procedure 106
45. Vacuum Specific Impulse vs Chamber Pressure, Effect of Turbine Inlet Temperature 108
46. Vacuum Specific Impulse vs Chamber Pressure, Effect of Turbopump Efficiencies 108
47. Engine Sensitivity With Turbomachinery Parameters 108
48. Start Model, HGI Flow Transient 110
49. HGI Oxidizer Pressure Regulator Requirements 112
50. Aerospike Cycle Comparison 115
51. Candidate Engine Control Points 120

52. Dynamic Performance Path for an Open-Loop Control System . 125
53. Operating Envelope Comparisons 127
54. Comparison of Effect of Mixture Ratio on Performance Index . 128
55A. System and Subsystem Schematic 133
55B. System and Subsystem Schematic 134
56A. Thrust System Layout 136
56B. Thrust System Layout 137
57. Aerospike Engine Thrust Load Diagram 138
58. Thrust Structure Candidates 141
59. Titanium Thrust Structure Weight vs Depth of Truss Structure 142
60. Gimbal Height and Thrust Structure Space Limitation Diagram 144
61. Increase in Dynamic Envelope Requirement With Gimbal Center Elevation Above Position Where $R_{static} = R_{dynamic}$ . . . 144
62. Proposed Adjustable Pump Mounting Concept 147
63. Propellant Feed Subsystem Layout 149
64A. Demonstrator Module Turbine Drive Subsystem 153
64B. Demonstrator Module Turbine Drive Subsystem 154
65A. Demonstrator Module Ignition Hot-Gas Subsystem 156
65B. Demonstrator Module Ignition Hot-Gas Subsystem 157
66. Engine Accessibility 159
67. 250K Thrust Chamber Demonstrator Module 163
68. Demonstrator Engine Thrust Chamber Assembly 164
69. Demonstrator Module Thrust Chamber Segmented Titanium Structural Shell 169
70. Regenerative-Coolant Flow Circuit 170
71. Application, Machining, and Plug Insertion 174
72. Double-Expansion Shroud Nozzle Design Schematic 178
73. Sea Level Inner Body Wall Pressure Profile 180
74. Full-Length Shroud Pressure Profile 182
75. Sea Level and Altitude Nozzle Pressure Profile 183
76. Combustor Body Loads Due to Thrust and Pressure 185
77. Shear Strength vs Temperature HT 424 Film Adhesive . . . 187
78. Throat Deflections for Center Compartment at Several Chamber Pressures 188

79. Experimental Heat Flux Distribution From 2.5K Water-Cooled Segment Tests 191
80. Throat Heat Flux vs Chamber Pressure 192
81. Effect of Mixture Ratio on Throat Peak Heat Flux With O_2/H_2 Propellants 193
82. Effect of Mixture Ratio on Coolant Mass Velocity and Flow Area Requirements O_2/H_2, 1500 P_c, Constant Combustion Gas Flowrate 0.008 Inch 347 CRES Tube, T_{wg} = 1600 F 195
83. Contoured Tube Overall Heat Input Characteristics . . . 196
84. Design Coolant-Side Curvature Enhancement Factor 198
85. Coolant-Side Roughness Enhancement Factor 199
86. Gas-Wall Temperature vs Coolant Curvature Enhancement . . 200
87. 250K Demonstrator Heat Flux Profiles 203
88. Demonstrator Engine Inner Body, 0.012-Inch Nickel 200 Tube . 204
89. 250K Demonstrator Inner Body Coolant Mass Velocity and Total Pressure Profiles 205
90. 250K Demonstrator Hydrogen Temperature Profile, Inner Body 207
91. 250K Demonstrator Outer Body 208
92. 250K Demonstrator Outer-Body Coolant Total Pressure and Mass Velocity Profiles 209
93. H_2 Injection Temperature vs Chamber Pressure 211
94. Bulk Temperature (R) of Hydrogen in Coolant Tubes vs MR . . 212
95. Hydrogen Velocity Head as a Function of Mass Flux for Transfer Passage Design 214
96. Coolant Passage Area vs Flowrate for Selected Mass Flux . . 215
97. Conventional Inconel 718 Structural Concept, 250K Aerospike Thrust Chamber Demonstrator Module 216
98. Demonstrator Chamber Study 217
99. Demonstrator Chamber, Pressure Diffusion-Bonded Titanium . 218
100. Structural Tie Concepts 221
101. 250K Flow Circuits 223
102A. 250K Demonstrator Engine Injector Assembly 225
102B. 250K Demonstrator Engine Injector Assembly 226
103. Axial Bolted Injector Design Concepts 233

104. Integral Baffle Injector 236
105. 25% Demonstrator Module Porous Base Closure Assembly . . 238
106. Base Closure Temperatures, Phase I Solid Wall 240
107. Flat Plate Base Closure 241
108. Oblate Spheroidal Membrane Base Closure 241
109. Head and Efficiency vs Flow 247
110. Candidate Preinducer Configurations 250
111. Fuel Turbine Weight and Flowrate Tradeoffs 255
112. Mark 39 Turbine Disc Profiles 257
113. First-Stage Fuel Turbine Disc Stress vs Radius 258
114. Second-Stage Fuel Turbine Disc Stress vs Radius 259
115 Third-Stage Fuel Turbine Disc Stress vs Radius 260
116. Allowable Operating Speed vs Disc Center Thickness . . . 262
117. Summary of Springrates for Pinned-Pinned Struts 264
118. Summary of Springrates for Fixed-Fixed Struts 265
119. Demonstrator Engine Fuel Turbopump 267
120. Mark 39-F Turbine Gas Path Sketch 272
121. Mark 39 Fuel Pump Performance Map 278
122. Volute Mockup 280
123. Minimum Required Impeller Vane Thickness 284
124. Fuel Impeller Representative Backplate Stress Distribution 286
125. Allowable Separating Load vs Temperature for Fuel Impeller Through Bolts 287
126. Balance Piston Backplate 289
127. Turbine Estimated Performance, Three-Stage Version . . . 291
128. Third-Stage Turbine Blade Interference Diagram 294
129. LF_2 Turbopump Critical Speed vs Bearing Spring Rate . . 298
130. Turbopump First Critical Speed Mode Shape 299
131. Oxidizer Turbine Disc Sizing. 302
132. First-Stage Oxidizer Turbine Disc Stress vs Radius . . . 303
133. Second-Stage Oxidizer Turbine Disc Stress vs Radius . . 304
134. Third-Stage Oxidizer Turbine Disc Stress vs Radius . . . 305
135. Mark 39-0 Turbine Third Stage Disc Preliminary Sizing Disc With Hole 306

136A. Demonstrator Engine Oxidizer Turbopump 308
136B. Demonstrator Engine Oxidizer Turbopump 309
137. Turbine Gas Path Sketch 313
138. Mark 30 Oxidizer Pump Performance Map 318
139. Oxidizer Impeller Stress vs Radius 320
140. Mark 30-0 Turbine Estimated Performance, Tapoff Cycle, Parallel Operation, Three-Stage Version 322
141. LO_2 Third-Stage Turbine Rotor Blade Interference Diagram Blade Machined Integral 324
142. Critical Speed vs Bearing Spring Rate for Mainshaft . . 326
143. Critical Speeds of LO_2 Inducer 327
144. Turbopump First Critical Speed Mode Shape 329
145. Functional Diagram, Demonstrator Module Performance Controls 331
146. Performance Controls System Block Diagram 335
147. Throttle Valve Position Transfer Function 336
148. Demonstrator Module Response Chamber Pressure as a Function of Tapoff Throttle Valve Area at Constant Oxidizer Turbine Throttle Valve Area 337
149. Demonstrator Module Response Mixture Ratio as a Function of Oxidizer Turbine Throttle Valve Area at Constant Tapoff Throttle Valve Area 338
150. Control System Block Diagram 340
151. Effect of Pump and Turbine Curves on Open-Loop Mixture Ratio Control System 343
152. Main Oxidizer Propellant Valve Layout 350
153. Main Fuel Propellant Valve Layout 351
154A. Hot-Gas Tapoff Throttle Valve Assembly 356
154B. Hot-Gas Tapoff Throttle Valve Assembly 357
155. Tapoff Throttle Valve Pressure Drop Requirements . . . 359
156. Tapoff Throttle Valve Relative Resistance 359
157. Oxidizer Turbine Throttle Valve Pressure Drop Requirements. 362
158. Oxidizer Turbine Throttle Valve Relative Resistance . . . 362
159A. 250K Flight Engine 364
159B. 250K Flight Engine 364
160. Specific Impulse vs Diameter 373

161. Effect of Engine Diameter on Nozzle Area Ratio 374
162. Engine Length vs Engine Diameter 374
163. Application Study Parameters for Optimum and Common Modules (Six Cases), MR = 6 386
164. Area Ratio for Optimum and Common Modules, Six Cases . . 388
165. 60-Degree LO_2 Impinging Triplet With Fuel Post Extended and Both Chamfered and Nonchamfered LO_2 Strips 398
166. LO_2 Fan Injector Pattern (With Fuel Post) 400
168. Reversed Pattern, 60-Degree Fuel on LO_2 Fan 402
169. Staggered Triplet Injector (No. 1-1A) 403
170. Reversed LO_2 Fan (No. 1-2A) 404
171. 60-Degree Triplet With Fuel Post (No. 1-3A to 1-3B) . . . 405
172. 60-Degree LO_2 Triplet With Fuel Post (No. 1-4A to 1-4B) 406
173. 60-Degree Triplet With Fuel Post (No. 2-1A to 2-1G) . . . 407
174. 60-Degree Triplet With Fuel Post (No. 2-2A) 408
175. 60-Degree LO_2 Triplet With Fuel Post (No. 2-3A) 409
176. LO_2 Fan With Fuel Post (No. 3-2A to 3-2B) 410
177. Reversed LO_2 Fan With Fuel Impinging at 80 Degrees (No. 4-1A to 4-1B) 411
178. Triplet With LO_2 Impinging at 60 Degrees (No. 4-2A to 4-2G) 412
179. Showerhead Injector (No. 5-1A) 413
180. 250K Candidate Triplet With Fuel Post (No. 6-1A to 6-1D) 414
181. 60-Degree LO_2 Triplet Injector (No. 6-2A) 415
182A. 2.5K Segment Injector Body, Oxidizer Feed System . . . 417
182B. 2.5K Segment Injector Body, Oxidizer Feed System . . . 418
183. 2.5K Solid-Wall Thrust Chamber 421
184. 2.5K Segment Injector Modified to Duplicate the Repair Made to the 250K Injector 429
185. Influence Coefficient to Account for Effect of Frictional Drag on Thrust 434

186. Throat Area Decrease vs Chamber Pressure for 2.5K Copper Nozzle 436
187. Divergence Correction for 2500-Pound-Thrust Chamber . . . 439
188. Triplet Injector Performance in the 2.5K Segment Thrust Chamber 441
189. Effect of Chamber Pressure 446
190. Measured Hot-Gas Tapoff Characteristics (2.5K Chamber) . . 447
191. Simulated 250K Hot-Gas Tapoff Ports in 250K Thrust Chamber 449
192A. Gas Tapoff Configuration for Tests 088 Through 092 . . . 450
192B. Gas Tapoff Configuration for Tests 093 Through 099 . . . 451
193. 2.5K Segment Tapoff Temperature vs Chamber Pressure . . . 453
194. 2.5K Film-Cooled, Solid-Wall Segment Coolant Passage Location 454
195. Variation in Heat Transfer Rates into Passage Immediately Upstream of Throat 456
196. Variation in Local Heat Fluxes During 2.5K Water Cooled Segment Firings (Tests No. 79 and 80) 458
197. Comparison of Q/A for Triplet and Fan Injectors 460
198. Initially Predicted Gas-Side Wall Temperature, Heat Flux, Curvature Enhancement, and Mass Velocity Profiles for 2.5K Experimental Segment (O_2/H_2, P_c = 1500 psia, MR = 6.0, W_{ct} = 0.956 lb/sec) 466
199. 2.5K Tube-Wall Segment Design 468
200A. 2.5K Nickel Tube-Wall Segment in Process Fabrication . . 473
200B. 2.5K Nickel Tube-Wall Segment in Process Fabrication . . 474
200C. 2.5K Nickel Tube-Wall Segment in Process Fabrication . . 475
200D. 2.5K Nickel Tube-Wall Segment in Process Fabrication . . 476
200E. 2.5K Nickel Tube-Wall Segment in Process Fabrication . . 477
201. Injector End 2.5K Repaired Nickel Segment After Cleaning and Machining Upper Coolant Wall 484

202. Repaired 2.5K Nickel Tube-Wall Temperature Simulation of 250K Demonstrator 485
203. Cycling Test Instrumentation and Flow Circuit Schematic Nickel Tube-Wall Segment 488
204. Segment Thrust Chamber Mounted on CTL-3 489
205. Typical Chamber Pressure Trace During 2.5K Tube-Wall Segment Mainstage Cycling Program 490
206. 2.5K Nickel Tube-Wall Segment Posttest 243 504
207. 2.5K Injector Unit 4-4, After 229 Cycles 506
208. Typical Tube Tester Thermal Fatigue Crack (347 CRES Specimen After 300 Cycles at 70 to 1100 F) 507
209. Thrust Chamber Tube Tester (High Pressure) 508
210. Typical Throat Cooling Requirements for 2.5K Contour Wall LO_2/H_2 Thrust Chamber 514
211. Typical Throat Cooling Requirements for 2.5K Contour Tube-Wall LO_2/H_2 Thrust Chamber 515
212. Gas Side Wall Temperature for 2.5K Contour Tube Thrust Chamber 517
213. Throat Heat Flux for LO_2/H_2 With Gas Side Wall Temperature of 1450 F at Chamber Pressure of 1500 psia 518
214. Maximum Outside Tube Diameter at Throat 518
215. Cooling Limit Results for OFHC Copper 519
216. Cooling Limits for Nickel 200 520
217. Contoured Tube Overall Heat Transfer Characteristics (2.5K Copper and Repaired Nickel Segments) 522
218. Material Selection Program 525
219. Comparison of OFHC Copper Tube Grain Size in the Annealed Condition and After Simulated Braze Cycle 535
220. Comparison of Beryllium-Copper Grain Size Prior to Brazing and After Brazing 536

221. Comparison of Nickel 270 Tube Grain Size in the Annealed Condition and After Simulated Furnace Braze Cycle 537
222. Comparison of Nickel 200 Tube Grain Size in the Annealed Condition and After Simulated Furnace Braze Cycle 538
223. Axial Load, Strain Cycle for a Thrust Chamber Tube . . . 543
224. Mechanical Strain at Elevated Temperatures, Test Results on Brazed Nickel 200 544
225. Mechanical Strain at Elevated Temperatures, Test Results of Candidate Materials 545
226. 2.5K Copper Tube-Wall Overall Heat Transfer Characteristics 550
227. 2.5K Copper Tube-Wall Thrust Chamber Heat Transfer Distribution 551
228. Effect of Chamber Pressure on Tube Life, 2.5K Segment . . 555
229. Throat Tube Gas-Wall Temperatures Nickel Tube-Wall Segment Cycling Tests 557
230. Low Cycle Fatigue Characteristics, Nickel 200 560
231. Order of Appearance of Tube Microcracks and Splits Nickel Tube-Wall Segment Cycling Tests 562
232. Combustion Efficiency vs Cyclic Test Number Nickel Tube-Wall Segment Cycling Tests 564
233. Nickel Tube-Wall Segment Throat Condition After Cycle 315 566
234. Nickel Tube-Wall Segment Throat Condition After Cycle 315 (Side B) 567
235. Hot-Gas Crowns of Two Tubes at the Throat 568
236. Longitudinal Section of Tube A28. The Section Is Not Exactly on the Axis, so That It Falsely Indicates a Tapering Tube Crown Height 569

237. Cross Section of "A" High in the Combustion Zone, Where There Was Moderate Damage From Impingement . . . 571
238. Tube B43, With Microhardness Readings in Diamond Pyramid Hardness Numbers 572
239. 2.5K Nickel Tube-Wall Segment 573
240. Effect of Wall Temperature on Tube Fatigue Life Demonstrator Module 576
241. Effect of Chamber Pressure on Tube Fatigue Life Demonstrator Module 577
242. 250K Solid-Wall Thrust Chamber Body Assembly 582
243. Chamber Locations of Pulse Gun Ports 587
244. Pulse Gun 588
245. Maximum Gas-Side Wall Temperature vs Time for 250K Solid-Wall, Film-Cooled Chamber 590
246. Wall Temperature Distribution in Throat of Water Film-Cooled Solid-Wall Chamber After 0.72 Second 591
247. Predicted vs Measured Conductivity Solid-Wall Outer Body 593
248. Inner-Body Solid-Wall Assembly 595
249. Outer Solid-Wall No. 1 596
250. 250K Solid-Wall Inner and Outer Bodies in Assembly Fixture 597
251A. 250K Tubular Thrust Chamber Inner-Wall Assembly 599
251B. 250K Tubular Thrust Chamber Inner-Wall Assembly 600
252. 250K Tubular Thrust Chamber, Outer-Wall Assembly 601
253. r Tube, Aerospike Thrust Chamber 603
254. Outer Thrust Chamber Tube 604
255. Nozzle Contour 606
256. Shroud Length Comparison 607
257. Performance vs Shroud Length 608
258. Shroud and Spike Pressure Profiles 610
259. Expansion and Compression Waves in Aerodynamic Spike Nozzle Flow Field Analysis 611

260. Sea Level Centerbody Spike Wall Pressure Profiles . . . 613

261. Theoretical and Experimental Heat Transfer Coefficients, 250K Experimental Thrust Chamber Breadboard Engine, O_2/H_2, MR = 6.0, P_c = 1500 psia, Vacuum Operation . . . 614

262. Simplified Curved Gaseous Hydrogen Heat Transfer Test Section (66-1) 617

263. Comparison of Film Coefficient Enhancement Factor Used for Design With Experimental Results 618

264. Heat Transfer Results for Inner-Body Coolant Tube; Ratio of Flame-Side Surface to Predicted Straight Tube Heat Transfer Coefficients 619

265. Heat Transfer Results for Outer-Body Coolant Tube; Ratio of Flame-Side Surface to Predicted Straight Tube Heat Transfer Coefficients 620

266. Effect of Tube Tolerances and Coolant Mass Velocity on Gas Wall Temperature 623

267. Forces Acting on Inner Body 625

268. Forces Acting on Outer Body 626

269. Forces Acting on Injector 627

270. Transient Wall Temperature Profile 628

271. 250K Tube-Wall Inner-Body After Rough Machining 630

272. 250K Tube Wall Inner Body Machined for Braze Assembly . . 631

273 250K Cooling Tube Pressure Forming 633

274. Inner and Outer Thrust Chamber Tubes 634

275. Stacking of Tubes for 250K Tube-Wall Thrust Chamber . . . 635

276. Thrust Chamber Tube Calibration Console 638

277. Thermochromistic Indication of Braze Bond; Outer Body, Tube Wall 641

278. Completed 250K Tube Wall Outer Body 643

279. Completed 250K Tube Wall Inner Body 644

280A. 250K Injector Body 646

280a. 250K Injector Body 647
281. Injector Baffle Configurations 649
282. Hypergol Tube 649
283. Hot-Gas System 650
284. 250K Candidate Triplet with Fuel Post (No. 6-1A to 6-1D) 651
285. Injector After First Braze Cycle 657
286. Realloying of Slotted Injector Strips 658
287. Hot-Gas Ignition and Tapoff Manifold 660
288. 250K Uncooled Nozzle Extension 662
289. Base Closure Showing Perforated Plate 664
290. 250K Uncooled Nozzle Extension with Perforated Base Closure Installed 665
291. 250K Thrust Mount 666
292. Solid-Wall Thrust Chamber Assembly 668
293. Solid-Wall Assembly 669
294. Oxidizer Manifold Center Plenum and Diffuser Section . . 670
295. 250K Tube-Wall Inner and Outer Bodies During Assembly . . 674
296. Completed 250K Tube Wall Thrust Chamber Assembly 675
297. High-Pressure Facility, D-2 677
298. Thrust-Measuring System 678
299. Liquid Oxygen Sample System Schematic 680
300. Aerospike Thrust Chamber Handling Equipment 681
301. 250K Solid-Wall Operation in Nevada Field Laboratory Test Stand Under Different Test Conditions 683
302. Injector Condition Posttest 006 687
303. Uncooled Chamber Posttest 006 688
304. Injector Strip Repair Posttest 006 690
305. Erosion of Baffle Edges and One Tapoff Port 691
306. Erosion of Strip Adjacent to Baffles 693
307. Erosion Pattern of Solid-Wall Innerbody, 124.5-Degree Location 695

308. Erosion Pattern of Solid-Wall Outer Body 696
309. 250K Solid-Wall Thrust Chamber Throat Gap Variation, Posttest 004 697
310. Tube-Wall Thrust Chamber Mounted on Reno Test Stand . . . 700
311. Tube-Wall Thrust Chamber Operation 701
312. Overall View of Injector 704
313. Injector Damage (Inner), 085 to 105 Degrees 705
314. Two Compartments of Chamber Posttest 025 706
315. Failed Tube With Slag Deposition at Injector Ring, Outer Body 709
316. Failed Tube With Slag Deposition in Shroud, Outer Body 709
317. Undamaged Tube at Injector Ring, Outer Body 710
318. Tube at Throat, Outer Body With Incipient Melted Surface 710
319. Failed Tube in Combustion Zone, Inner Body Caused by Hot-Gas Erosion 713
320. Tube-to-Body Crack Location No. 1 Inner Body 713
321. Fractured Tube Walls Showing Multiplane Topography Typical of Reverse-Bending Fatigue 714
322A. Test 025 Mainstage Operation 715
322B. Test 025 Mainstage Operation 716
323. Test Events During Test 025 718
324. Test 025 Failure Mode Sequence 719
325. Photo of Facility Damage Within Altitude Capsule 720
326. Major Tapoff Passage Erosion at Areas of Major Injector Damage 722
327. Hot-Gas Circulation Path in Injector Gap 724
328. Chamber Erosion Caused by Strip End Oxidizer Leak . . . 725
329. Cross-Sectional View of Injector Installation in Tube-Wall Thrust Chamber 726

330. No. 2 Tube-Wall Modified Start Sequence 728
331. Posttest 027 Injector Baffle Condition 729
332. Chamber Inner-Body Posttest 027 731
333. View of Injector Face Showing Two Compartments 732
334. Exposed Baffle Coolant Passages 733
335. Exposed Coolant Passages 734
336. Eroded Baffles 736
337. Aerodynamic Spike Performance, Altitude Compensation 738
338. Tube-Wall Thrust Chamber C_T Performance vs Pressure Ratio 739
339. Theoretical Optimum Thrust Coefficient, Effects of Water 740
340. Minimum Model Nozzle Performance Test Results 742
341. Experimental Base Pressure 743
342. Wall Pressure Profile for Aerospike Utilizing LO_2/GH_2 with H_2O in Equilibrium 745
343. Wall Pressure Profiles 746
344. Combustion Performance, Comparison of Two Different Method Results 748
345. 250K Tube-Wall Thrust Chamber Specific Impulse vs Pressure Ratio 753
346. Throat Gas Variation During Mainstage of Test 028 . . . 755
347. 250K Outer Body Throat Predicted Cooling Requirements . . 757
348. 250K Outer Body Predicted Throat Cooling Requirements . . 758
349. 250K Predicted Coolant Discharge Temperature Outer Body O_2/H_2 759
350. Chamber Pressure for Test 006 761
351. Chamber Pressure for Test 017 762
352. Test 028 Chamber Pressure Trace 764
353. No. 2 LOX Manifold Photocon Traces, Mainstage 766

354A. Sonics for Tube-Wall Aerospike Chamber 767
354B. Sonics for Tube-Wall Aerospike Chamber 768
354C. Sonics for Tube-Wall Aerospike Chamber 769
354D. Sonics for Tube-Wall Aerospike Chamber 770
355. Orientation of Streak Camera 772
356. Streak Photography Results, Test 28 773
357A. Section Through Chamber at Structural Baffle, 20K Demonstration Segment 784
357B Section Through Chamber Between Structrual Baffles, 20K Demonstration Segment 785
358. 20K Chamber Segment Maximum Baffle Temperature Distribution 787
359. Hydrogen Mass Velocity Requirements vs Gas Wall Temperature (0.070-Inch Copper Wall) 788
360. 20K Segment Flow Schematic 791
361. Perspective View of the 20K Segment Thrust Chamber . . . 792
362. 20K End Plate Assembly 795
363. 20K Baffle Seat Subassembly, Before Brazing 796
364. 20K Baffle Seat Subassembly Complete 797
365. 20K Tube Wall Subassembly Before Brazing 801
366. 20K Tube Wall Subassembly in Brazing Fixture 802
367. 20K Tube Wall Subassembly Complete 803
368. 20K Tube Wall Subassembly, Structure Side 804
369. 20K Thrust Chamber Braze Assembly 807
370. 20K Baffle Assembly 809
371. 20K Titanium Structure, Outside 812
372. 20K Titanium Structure, Tube-Side 813
373. 20K Titanium Side with Verafilm 815
374. 20K Chamber with Verafilm Applied 816
375. 20K Thrust Chamber With Baffles Installed 818
376. 20K Structural Segment Assembly 819
377. 20K Injector Unit No. 2 Baffle Recess Erosion 820

378. 20K Thrust Chamber Braze Assembly, Gap at Tube-to-End Plate Joint 825
379. Damage to Titanium Structure 827
380. 20K Thrust Chamber With Convex Bulges 828
381. 20K Segment Strain Gage Results, Baffle Bolts 834
382. Lower Baffle Bolt Load Diagram 835
383. 20K Segment Strain Gage Results Horizontal Ribs 837
384. 20K Segment Vertical Ribs 838
385. 20K Throat Gap Measurements 840
386. Thrust Chamber Structure Analytical Model 841
387. 20K Injector Unit No. 2 845
388. 20K Total Heat Flux to Tubes 846
389. 20K c* Efficiency vs Chamber Pressure 847
390. 20K Total Heat Flux 848
391. 20K Tube Bundle Total $\Delta P \times \bar{\rho}$ vs Flowrate 852
392. Injector LO_2 Strip Thermocouple Installation 853
393. Damage to 20K Injector Baffle Recess Cavity 856
394. Posttest View of Adhesive Used in the Structural Segment 857
395. Combustion Temperature for LO_2/LH_2 at a Chamber Pressure of 600 psia 871
396. Combustion Products Molecular Weight for LO_2/LH_2 at a Pressure of 600 psia 872
397. Tube Vent Technique 879
398. Solid-Wall and Tubular Thrust Chamber Boss Nomenclature 892
399. Flow Diagram, Tube-Wall Thrust Chamber 895
400. Typical Solid-Wall Test Sequence 899
401. 250K Tube-Wall Start and Shutdown Sequence, Test No. 025 900
402. 250K Tube-Wall Step Start Sequence 901
403. CTF Ignition System Schematic 902
404. Aerospike Flow Field Model 904

TABLES

1. Engine Characteristics 2
2A. Demonstrator Module Operating Characteristics 9
2B. Demonstrator Module Operating Characteristics 10
3. Thrust Chamber Design Parameters 14
4. Summary of Fuel Turbopump Design Characteristics 18
5. Summary of Oxidizer Turbopump Design Characteristics 20
6. Phase I Demonstration Requirements and Accomplishments, Task II Fabrication and Test Items 29
7. Tube-Wall Thrust Chamber Performance Data Summary 39
8. Thermal Fatigue Tube Tester Results on Nickel 200 49
9. Demonstrator Module Design Requirements 62
10A. Demonstrator Module Operating Characteristics 78
10B. Demonstrator Module Operating Characteristics 79
11. Hot-Gas System Pressure Schedule 90
12. Tapoff Throttle Valve Requirements 91
13. Oxidizer Turbine Throttle Valve Requirements 92
14. Liquid-Oxidizer Propellant Feed Pressure Schedule 93
15. Liquid-Fuel Propellant Feed Pressure Schedule 93
16. Independent Variable 3σ Variations 95
17. Predicted Maximum Parameter Variations 96
18. HGI Oxidizer Pressure Regulator Data 113
19. Comparison of Significant Engine Parameters at Steady State 122
20. Thrust vs Mixture Ratio Comparison 126
21. Relative Ranking of Candidate Thrust Structure Designs . . . 145
22. Summary of Demonstrator Module Weights 161
23. Thrust Chamber Assembly Design Requirements 162
24. Thrust Chamber Design Parameters 166

25. Design Comparison Study 219
26. Injector Design Parameters 224
27. Design Requirements--Injector 228
28. Turbopump Design Conditions 244
29. Turbine Gas Properties 245
30. Liquid Hydrogen Pump Parameters at Design Point, Mixture Ratio = 6 245
31. Turbopump Comparison 249
32. Mark 30-7 Turbine Disk Data 261
33. Aft Bearing Support 266
34. Design Parameters and Fuel Preinducer Off-Design Operating Conditions 269
35. Fuel Pump Impeller Design Parameters 270
36. LH_2 Turbopump Bearing Design Requirements 273
37. Liquid Hydrogen Turbopump Seal Design Requirements 275
38. Geometry and Maximum Allowable TIP Velocities 281
39. Two-Stage Impeller Weight Comparison 283
40. LH_2 Turbine Blade Stresses 293
41. Oxidizer Turbopump Design Conditions 300
42. Oxidizer Preinducer 310
43. Oxidizer Centrifugal Pump Stage Geometry 312
44. Oxidizer Bearing Design Requirements 315
45. Oxidizer Seal Package Design Requirements 317
46. LO_2 Turbine Blade Stresses 323
47. Main Propellant Valve Trade Study Summary 348
48. Main Propellant Valve Pressure Loss Summary 349
49. Hot-Gas Valve Trade Study Summary 354
50. Comparison of Turbopump Efficiencies for Demonstrator Module and Target Efficiencies for Flight Module 369
51. Flight Module Operating Characteristics 371
52. Flight Engine Parametric Design Parameters 372
53. Summary Comparison of Demonstrator and Flight Engine Weights 380

54. Summary Explanation of Differences Between Demonstrator and Flight Engine Weights 381
55. Interface Location 382
56. Performance Index Optimization Results of the 250K Common Module 384
57. Performance Index Optimization Results of the 350K Common Module 385
58. 250K Modules 389
59. 350K Modules 390
60. Summary of 2.5K Water-Cooled Thrust Chamber Performance Tests 425
61. Summary of 2.5K Film-Cooled Thrust Chamber Performance 426
62. 2.5K Water-Cooled Thrust Chamber Gas Tapoff Study 427
63. Influence Coefficient Summary 440
64. Thrust Chamber Performance Summary for Film-Cooled Tests . . 445
65. Braze Alloy Remelt Temperature 480
66. 2.5K Copper Tube-Wall Segment Performance Data 482
67. Summary of 2.5K Segment Cycle Tests 491
68A. Comparison of 2.5K Segment Cycle Tests To Demonstrator Module 492
68B. Comparison of 2.5K Segment Cycle Tests To Demonstrator Module 493
68C. Comparison of 2.5K Segment Cycle Tests To Demonstrator Module 494
68D. Comparison of 2.5K Segment Cycle Tests To Demonstrator Module 495
68E. Comparison of 2.5K Segment Cycle Tests To Demonstrator Module 496
68F. Comparison of 2.5K Segment Cycle Tests To Demonstrator Module 497

68G. Comparison of 2.5K Segment Cycle Tests To Demonstrator Module 498
68H. Comparison of 2.5K Segment Cycle Tests To Demonstrator Module 499
68I. Comparison of 2.5K Segment Cycle Tests To Demonstrator Module 500
68J. Comparison of 2.5K Segment Cycle Tests To Demonstrator Module 501
68K. Comparison of 2.5K Segment Cycle Tests To Demonstrator Module 502
68L. Comparison of 2.5K Segment Cycle Tests To Demonstrator Module 503
69. Thermal Fatigue Tube Tester Results on Nickel 200 512
70. Summary of Results, Plastic Strain Analysis 529
71. Candidate Materials for Thrust Chamber Usage 531
72. Summary of Results, Material Property Literature Survey 532
73. Summary of Results, Material Property Literature Survey 534
74. Brazing Feasibility Tests, Nickel 200, 270, and Beryllium Copper 540
75. Mechanical Strain at Elevated Temperature Fatigue Tests, Summary of Test Conditions 542
76. Factors Affecting Selection of 20K-Segment Tube Material 547
77. Factors Affecting Selection of Long-Range Tube Materials 548
78. Comparison of Operating Conditions 2.5K Copper Tube-Wall and 250K Demonstrator 552
79. Comparison of 250K Demonstrator and 2.5K Segment Cooling and Life Parameters 558

80. Tube Tolerance 636
81. GN_2 Flow Variation Due to Tube Tolerance 636
82. Flow Group Identification 639
83. 205K Solid-Wall Test Program:
Summary of Mainstage Tests 685
84. 250K Tube-Wall Test Program Summary of Mainstage Tests. . . 698
85. Tube-Wall Thrust Chamber Performance Data Summary 750
86. Baffle Seat Assembly Fabrication History 799
87. Tube Wall Assembly Braze Cycle Results 805
88. RL000104X Baffle Assembly Fabrication History. 810
89. Results of 20K Segment Mainstage and Ignition Tests. . . . 823
90. 20K/250K Primary Simulation Parameters 824
91. Comparison of 20K and 250K Thrust Chambers. 830
92. Recapitulation of Weight Difference:
20K and 250K Thrust Chambers 832
93. 20K Results Summary 843
94. Stability Summary, 20K Segment. 850
95. 20K LO_2 Strip Temperature Data. 854

NOMENCLATURE

Symbol	Parameter	Units
A	area	$in.^2$
A*	aerodynamic threat area	$in.^2$
A_t	geometric throat area	$in.^2$
A_{otv}	oxidizer turbine throttle valve area	$in.^2$
A_{ttv}	tapoff throttle valve area	$in.^2$
C	turbine nozzle isentropic gas velocity	ft/sec
C_F	thrust coefficient	—
C_p	specific heat at constant pressure	Btu/lbm-R
C_T	overall nozzle efficiency	—
C_v	primary nozzle velocity coefficient	—
DN	bore diameter x speed	mm x rev/min
E	modules of elasticity	psi
F	thrust	lbf
F_{tu}	ultimate tensile strength	psi
F_{ty}	tensile yield strength	psi
G_c	coolant mass velocity	$lbm/in.^2$-sec
GPM	fluid flowrate	gal/min
GH_2	gaseous hydrogen	—
GN_2	gaseous nitrogen	—
GO_2, GOX	gaseous oxygen	—
HGI	hot-gas-ignition	—
I_s	specific impulse	lbf/sec/lbm
K	one thousand	(as noted)

Symbol	Parameter	Units
LH_2	liquid hydrogen	—
LO_2, LOX	liquid oxygen	—
MFV	main fuel valve	—
MR	mixture ratio, oxidizer-to-fuel	$(lbm)_o/(lbm)_f$
N, rpm	rotational speed	rev/min
N_{cy}	number of cycles to fatigue failure	—
NPSH	net positive suction head	feet
N_{NU}	Nusselt number	—
N_{PR}	Prandtl number	—
N_{RE}	Reynolds number	—
N_{ST}	Staton number	—
OFHC	oxygen-free-high-conductivity	—
P	pressure	psia
P_c	nozzle throat stagnation pressure	psia
P_D	pump discharge	--
Q	volumetric flowrate	(as noted)
Q/A	local heat flux	$Btu/in.^2-sec$
$R_{dynamic}$	module dynamic envelop radius	in.
T	temperature	R, (as noted)
U	blade speed	ft/sec
c*	characteristic velocity	ft/sec
fps	--	ft/sec
g	gravitational constant (32.2)	$lbm-ft/lbf-sec^2$
h_g	gas-side heat transfer coefficient	$Btu/in.^2-sec-R$

Symbol	Parameter	Units
k	spring rate	lbf/in.
scfm	standard flowrate	ft^3/min
t	wall thickness	inches
$\dot{w}$	mass flowrate	Btu/sec
α	coefficient of thermal expansion	in./in.-R
γ	specific heat ratio	—
ϵ	nozzle expansion area ratio	—
ϵ_R	surface roughness	microinches
η	efficiency	—
η_{Po}	injector-end stagnation pressure/ nozzle throat stagnation pressure	—
η_T	friction influence coefficient	—
θ^*	throat flow angle	degree
μ	Poisson's ratio	—
ρ	density	lbm/ft^3
σ	standard deviation	—
σ_{hyd}	hydraulic stress	psi
σ_y	yield strength	psi
τ	ratio of secondary-to-primary flow	(by weight)
φ_c	coolant curvature heat transfer enhancement factor	—
φ_E	coolant entrance heat transfer enhancement factor	—
φ_ϵ	coolant roughness heat transfer enhancement factor	—

Subscripts

B	bulk temperature
D	discharge
Ref	reference
Reg	regulator
a, amb	ambient
b	base
c	chamber
d	drag
e	exit
f	fuel
g	geometric
k	kinetic
o	oxidizer
p	primary
s	secondary
t	total flow
v, vac	cacuum
w	wall
cc	combustion chamber
ct	coolant
eng	engine
fc	film coolant
gg	gas generator
ie	injector end

Subscripts

inj	injector
pf	potential flow
tc	thrust chamber
to	tapoff
wc, wl	coolant-side-wall
wg	gas-side-wall
$\bar{}$(bar)	average
$'$(prime)	flight system

NOMENCLATURE

CONTENTS

Task II: Fabrication and Test 393
Injector Performance Investigation (2.5K Solid-Wall Segments) . 393
Objectives and Requirements 393
Summary of Work Accomplished. 394
Description of Hardware and Fabrication 395
Candidate Patterns 397
Testing. 423
Analysis of Results. 428
Problem Areas and Solutions 459
Thrust Chamber Cooling Investigation (2.5K Tube-Wall Segments) . 462
Objectives and Requirements 462
Summary of Work Accomplished. 463
Description of Hardware and Fabrication 464
Fabrication 469
Testing. 478
Analysis of Results. 513
Problem Areas and Solutions 578
Thrust Chamber-Nozzle Demonstration 579
Objectives and Requirements 579
Summary of Work Accomplished. 580
Description of Hardware and Fabrication 583
Testing. 676
Analysis of Results. 735
Problem Areas and Solutions 775
Segment Structural Evaluation 779
Objectives and Requirements 779
Summary of Work Accomplished. 780
Description of Hardware and Fabrication 782
Testing. 821
Analysis of Results. 830
Problem Areas and Solutions 851

TASK II: FABRICATION AND TEST

INJECTOR PERFORMANCE INVESTIGATION (2.5K SOLID-WALL SEGMENTS)

Objectives and Requirements

(C) The requirements of this subtask were to evaluate promising injector designs in solid-wall 2.5K chamber segments and select the injector configuration to be used in the 2.5K and 20K tube-wall segments and in the full-scale (250K) workhorse thrust chambers. The selected injector was to have demonstrated stable, high-performance combustion over a mixture ratio range from 5:1 to 7:1 and throttled operation (100 to 200 percent). During these segment tests, the dimensions of the combustion chamber also were to be varied to evaluate the effects on combustion efficiency. In this manner, the selection of chamber dimensions, made during the design and analysis effort, was to be confirmed.

(C) The 2.5K segment injector investigation effort was designed to utilize the segmentation potential of the aerospike thrust chamber for the development of candidate injector patterns for the 250K injector. The experimental objectives of this task were: (1) selecting an injector design that delivers characteristic velocity efficiency in excess of 0.96 over the operating range, (2) determining thrust chamber heat transfer characteristics, (3) developing a gas tapoff system that yields gases suitable for use as a turbine working fluid, (4) evaluating injector durability, (5) determining injector stability, and (6) developing injector patterns that would lend themselves to fabrication of the 250K injector. The segment approach provided the capability for rapid turnaround time when major injector changes were being made, and provided a much larger amount of data within the planned program than had originally been anticipated.

(C) Previous effort and analysis indicated that durability at 1500-psi chamber pressure would be a major problem. The performance problem would

manifest itself primarily in the low chamber pressure regions. Heat transfer in annular combustors has been shown to be primarily a function of chamber contour; however, injector effects on throat heat transfer have been experienced and were expected on this effort. Fabricability of the selected patterns restricted the choice of candidate injectors to those that could be readily produced for the 250K injector.

(C) Stability of the patterns also was considered to be important; however, it was recognized that the 2.5K segments, representing approximately one-half of a 250K compartment, will probably not support any acoustic modes, the nearest mode being the first longitudinal at approximately 5500 cps, however. The possibility of low-frequency buzzing could not be discounted, however.

Summary of Work Accomplished

(C) A total of 128 tests was made during this phase of the program, and 31 injector modifications were utilized in the testing. Tests were conducted at chamber pressures ranging from 274 to 1614 psia and mixture ratios from 3.90 to 9.71. Three injection patterns, the triplet, LO_2 fan, and reverse flow, were utilized in 123 tests. All three patterns exhibited high performance, i.e., characteristic velocity efficiency in excess of 95 percent of theoretical shifting equilibrium characteristic velocity. On the basis of these tests, the triplet injection pattern was selected as the 250K candidate injector because this pattern yielded high characteristic velocity efficiency over the chamber pressure range of 500 to 1500 psia, and for mixture ratios from 4.5 to 7.5, it exhibited good durability and was not subject to combustion instability.

(C) Feasibility of hot-gas tapoff was demonstrated, and it was shown that the tapoff was fuel rich by observing the drop in tapoff gas temperature when ambient temperature fuel was added to the tapoff gas downstream of the thrust chamber tapoff ports. Tapoff temperatures ranged from 1400 to 1600 F over the chamber pressure range of 400 to 1500 psia.

(C) Heat transfer data were obtained up to 900 psia chamber pressure by the calorimetric method. The data obtained between 300 and 900 psia were extrapolated to 1500 psia, and the predicted peak throat heat flux at 1500 psia was 58 Btu/in.^{2}-sec.

(U) The bulk of the 2.5K segment testing was accomplished by using a hypergol ignition system. The majority of tests utilized ClF_3, but a few tests were made using triethylaluminum-triethylboron(TEA-TEB). In addition, hot-gas ignition tests were accomplished.

(U) All the objectives of the 2.5K segment thrust chamber testing portion of the aerospike program were successfully met or exceeded. The segment testing was useful in that small-scale hardware which could be fabricated at a reasonably low cost was used, and the segment was ideal for achieving rapid turnaround time for testing so that many injector modifications could be tested.

(U) Results from the segment tests were directly applicable to the design and fabrication of the 250K injector. Factors that were applied were: (1) utilization of small injection strips as building blocks for the 250K injector, (2) the triplet injection pattern was fixed on the basis of results from segment tests, (3) tapoff geometry and injection strip modification at the tapoff point was directly applied, and (4) fuel bias was established in the segment tests.

Description of Hardware and Fabrication

(U) Theoretical Basis and Background for Injector Designs. The injector segment work conducted under Contract NAS8-19 provided the background for the injector designs advanced to the aerospike effort. The results of that program showed that the attainment of high performance with LO_2 and H_2

propellants in short, toroidal chambers was solely dependent on achieving maximum atomization through use of the potential energy of both the LO_2 and the H_2. The best performing injector of that study was a LO_2 fan pattern. In this design, the LO_2 impinged on itself as a doublet on both sides of a series of hydrogen orifices. Primary atomization was accomplished through this process. The atomized LO_2 fans were then further atomized through passing into the path of the hydrogen gas.

(U) Theoretical analysis shows that the same effect of a self-impinging doublet can be attained through control of the liquid jet length before impingement. For a given jet momentum, the jet has a length at which surface instabilities will appear which lead to atomization. This characteristic was designed into the basic triplet element.

(U) Theoretical analysis shows that the primary atomization produces mean drop sizes on the order of 150 microns. Secondary atomization by the hydrogen under proper impingement produces mean drop sizes on the order of 50 microns. However, the attainment of this small drop size requires careful control of the hydrogen jet dynamics. Cold-flow studies revealed that the jet dissipates rapidly and, if the point of LO_2 impingement is too far away, the H_2 escapes around the combustion field. If the jet is too close to the point of impingement, the H_2 spreads the LO_2 fans (or jets) apart and never mixes. Best atomization occurs when the H_2 jet to LO_2 impingement distance is approximately 2 to 4 jet diameters. This results in an impingement distance of approximately 0.150 inch. This is the distance designed into the injectors. The use of this distance and matching the ΔP to peak performance has resulted in a nominal 1-1/2- to 2-percent improvement over the performance results obtained in the NAS8-19 program.

(C) The NAS8-19 program was conducted at approximately 650-psia chamber pressure, and no injector heat transfer problem was encountered. It was expected that injector heat transfer at 1500-psia chamber pressure might be a major problem because of the high recirculation potential of the GH_2/LO_2 designs. Jet dynamic calculations show that as much as 83 percent

of the total propellant flow through the injector will be recirculated at 1500-psia chamber pressure for the proposed injector designs. Such high recirculation provides an added basis for high performance but, also, it presents a potential face heat transfer problem. The basic approaches to the face heat transfer problem considered were: (1) use of a raised fuel post to prevent face gas recirculation and, also, control impingement distance, and (2) use of a face pattern with predominant hydrogen face cooling. The basic triplet patterns use the raised face, while the reverse-flow pattern provides for maximum hydrogen face cooling.

(C) Thermochemical calculations on the LO_2 drops show that below approximately 1100 psi, the drops actually exist as liquid droplets throughout their consumption. Above 1100 psi, the drops rapidly rise to and exceed their critical temperature. Because of the high contraction ratio of the aerospike engine, combustion-induced turbulence (along with GH_2 jet turbulence) is high and persists. This turbulence above 1100 psi results in rapid eddy diffusive mixing of the LO_2 vapor and, therefore, once fine atomization is achieved, near theoretical performance can be expected.

Candidate Patterns.

(C) 60-Degree LO_2 Impinging Triplet Pattern. The basic triplet pattern consists of a showerhead fuel stream (from a raised fuel strip) impinging on a 60-degree LO_2 doublet (Fig. 165). The purpose of the raised fuel post is to place the fuel stream exit point close to the point of LO_2 impingement to obtain good primary propellant atomization. The post also acts to prevent recirculation from causing high face heat transfer.

(U) The injector strips are oriented perpendicular to the chamber circumference with eight propellant elements per strip. Modifications to the

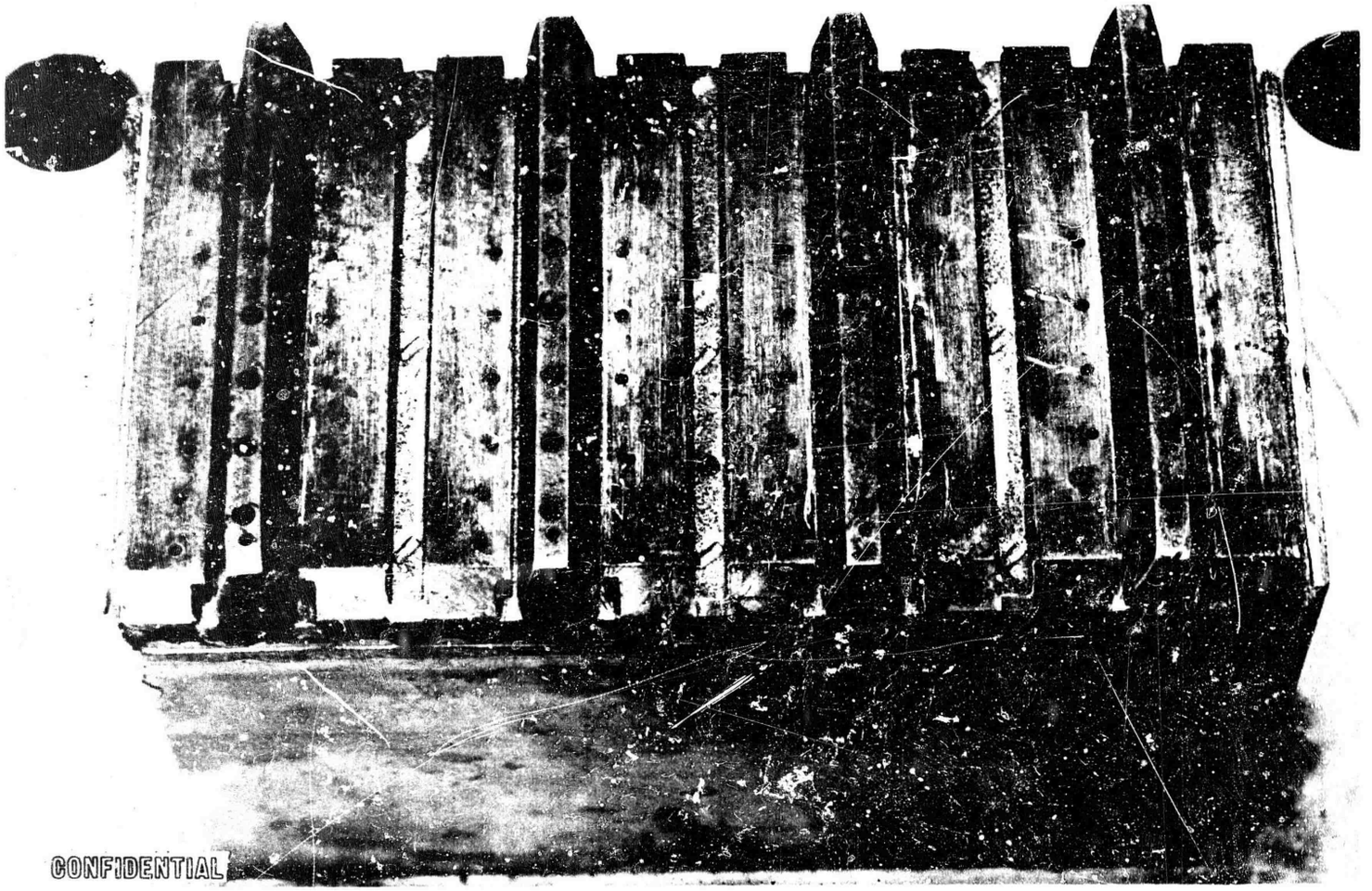

5AA34-S/24/66-S1A

Figure 165. 60-Degree LO_2 Impinging Triplet With Fuel Post Extended and Both Chamfered and Nonchamfered LO_2 Strips

CONFIDENTIAL

basic triplet pattern consisted of:

1. Addition of fuel bias at fuel strip ends (incorporated into 250K injector pattern)
2. Extending raised fuel strips to chamber wall (square ends); incorporated into 250K injector pattern
3. Beveling LO_2 strip ends (found to be unnecessary with square-end fuel strips)
4. Introduction of fuel bias along sides of injector
5. Enlarging fuel orifices to lower injection pressure drop (found to be unnecessary)

(C) LO_2 Fan Pattern With Fuel Post. The LO_2 fan pattern with a raised fuel strip also was considered as a candidate for the 250K injector pattern. Satisfactory performance and durability were demonstrated with this pattern; however, the chamber throat heat flux was found to be slightly higher with the LO_2 fan pattern than with the triplet. The hot-gas tapoff temperature was considerably lower than the tapoff temperature using the triplet injector pattern.

(C) An element of the LO_2 fan pattern consists of two pairs of LO_2 doublets forming doublet fans impinging at 60 degrees above a raised fuel strip (Fig. 166). Four showerhead fuel streams were directed at the line of impingement of the doublet fans. Each set of strips contained six propellant elements.

(U) Modification of the basic pattern consisted of enlarging the fuel orifices and providing fuel bias of the main orifices at the fuel strip ends.

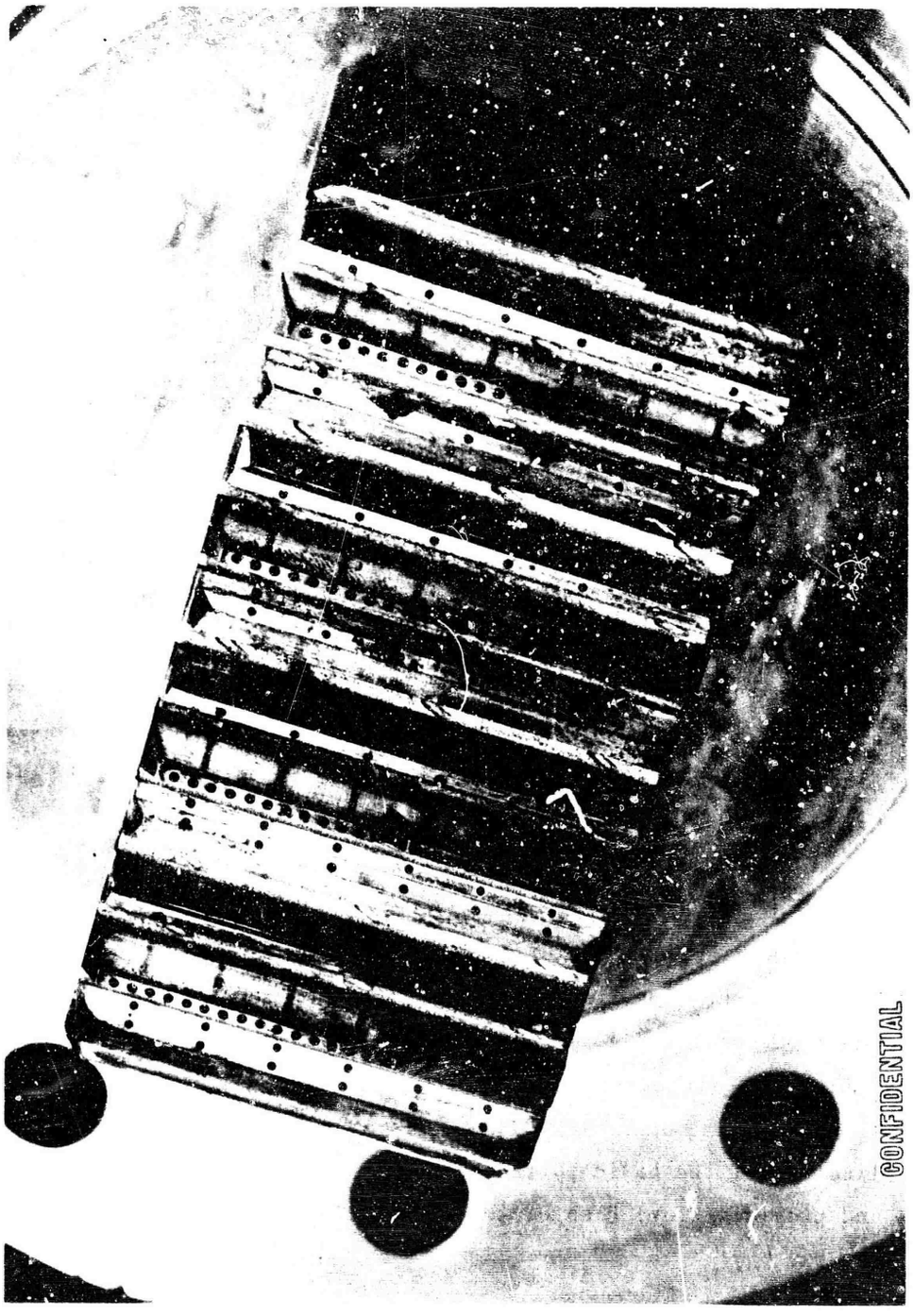

5AA35-7/13/66-S1A

Figure 166. LO_2 Fan Injector Pattern (With Fuel Post)

(C) The LO_2 fan pattern with the raised fuel strip was an improved version of the LO_2 fan concept tested during the first quarter which featured 90-degree LO_2 impinging fans and no raised fuel strip. Severe burning of the LO_2 strips was sustained in these tests.

(C) Reversed Pattern. The reversed pattern (Fig.168) was so named to indicate that the point of introduction of propellants was reversed from that of the other patterns tested (fuel on the outside and LO_2 in the center of an element of the reversed pattern). The reversed pattern element consisted of a LO_2 fan (formed by a LO_2 doublet) impinging on an 80-degree impinging fuel doublet. The pattern was placed on a flat face injector.

(U) Modification of the basic pattern consisted of enlarging the fuel orifices to lower the injection pressure drop.

(U) Erosion of the strip ends was sustained during high chamber pressure tests, and the face appeared to be overheating to the point of being marginal.

(U) Injector Modifications. There were three basic injection patterns tested, i.e., triplet, LO_2 fan, and reversed pattern. These injector patterns were subjected to various minor modifications to achieve adequate fuel bias and optimum gas tapoff properties. A complete description of all injectors tested, and the respective modifications, is presented in Fig. 169 through 181.

(U) The injector identification numbers were planned to describe certain aspects of the injector. For example, the injector number 1-1A has the following meaning: the first number identifies the injector body as body number 1; the first number after the dash describes the injection strip and was changed when a major strip modification was made so that injectors

LXV43-5/19/66-81D

Figure 168. Reversed Pattern, 60-Degree Fuel on LO_2 Fan

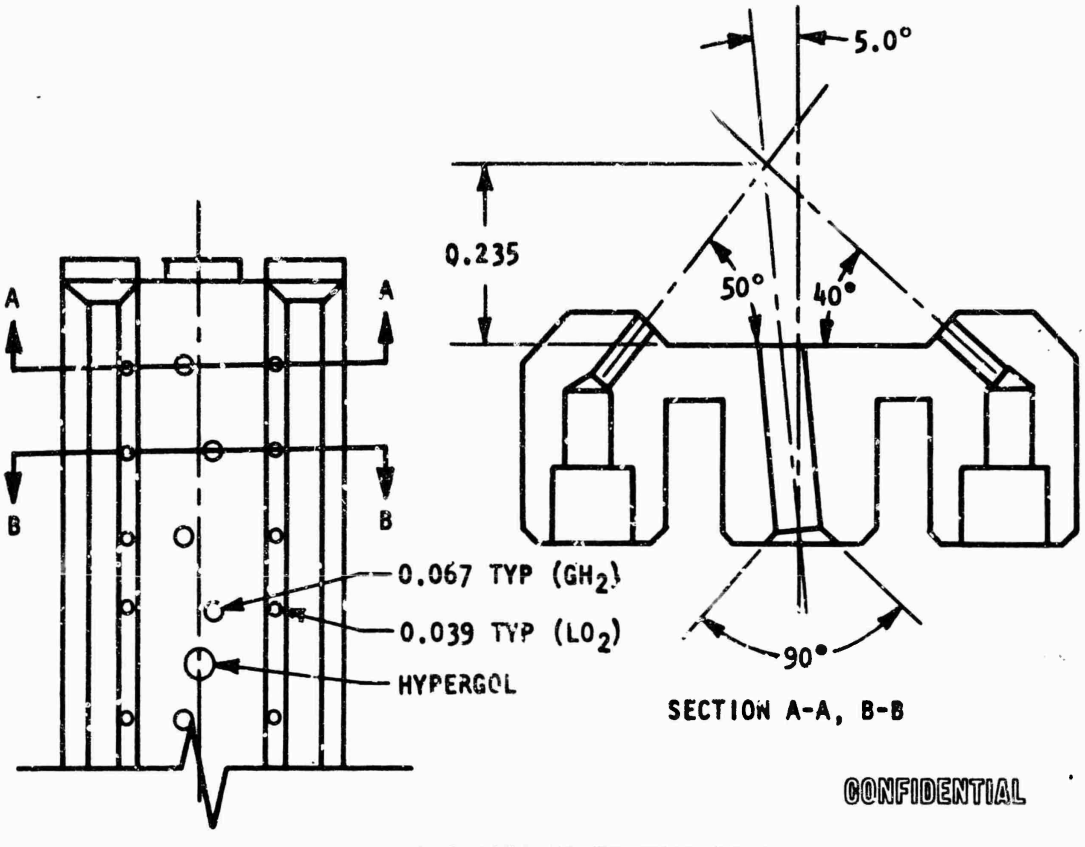

NO MODIFICATIONS TO THIS DESIGN

Figure 169. Staggered Triplet Injector (No. 1-1A)

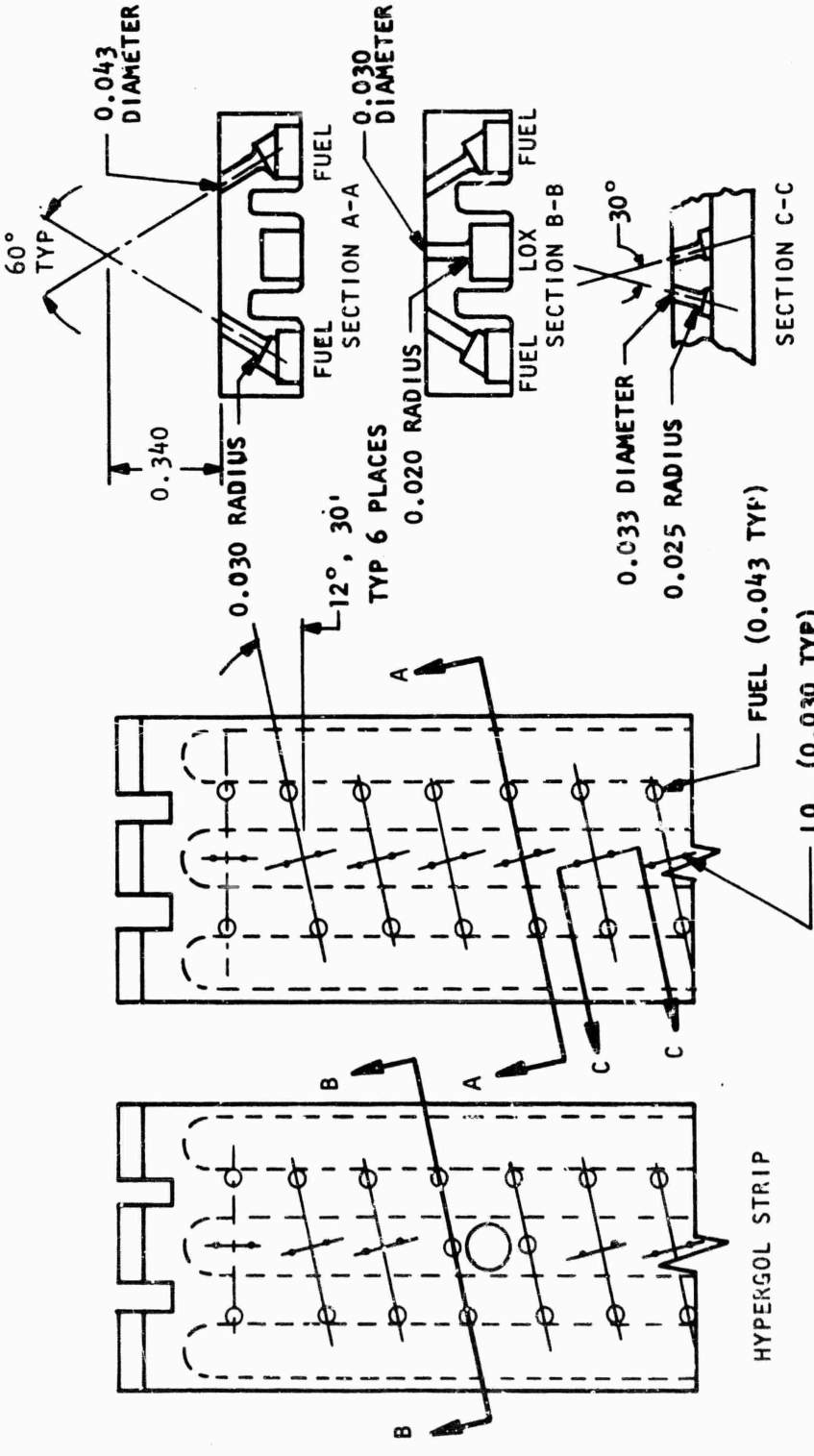

Figure 170. Reversed LO_2 Fan (No. 1-2A)

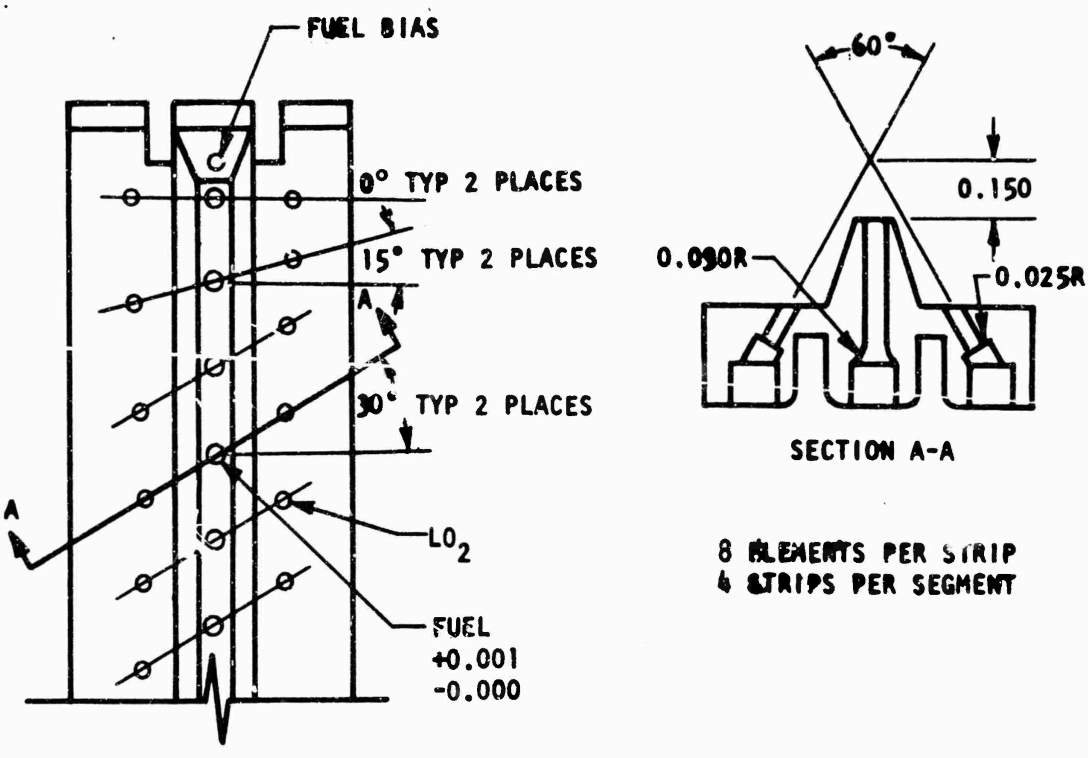

CONFIDENTIAL

MODIFICATION DASH NO.	LO_2 ORIFICE		FUEL ORIFICE		MIXTURE RATIO BIAS		
	DIAMETER	TOTAL AREA	DIAMETER	TOTAL AREA	LO_2 DIAMETER	GH_2 DIAMETER	NO. OF ELEMENTS
-3A	0.033	0.0547	0.065	0.106			
-3B	0.033	0.0547	0.065	0.112		0.031	8

Figure 171. 60-Degree Triplet With Fuel Post (No. 1-3A to 1-3B)

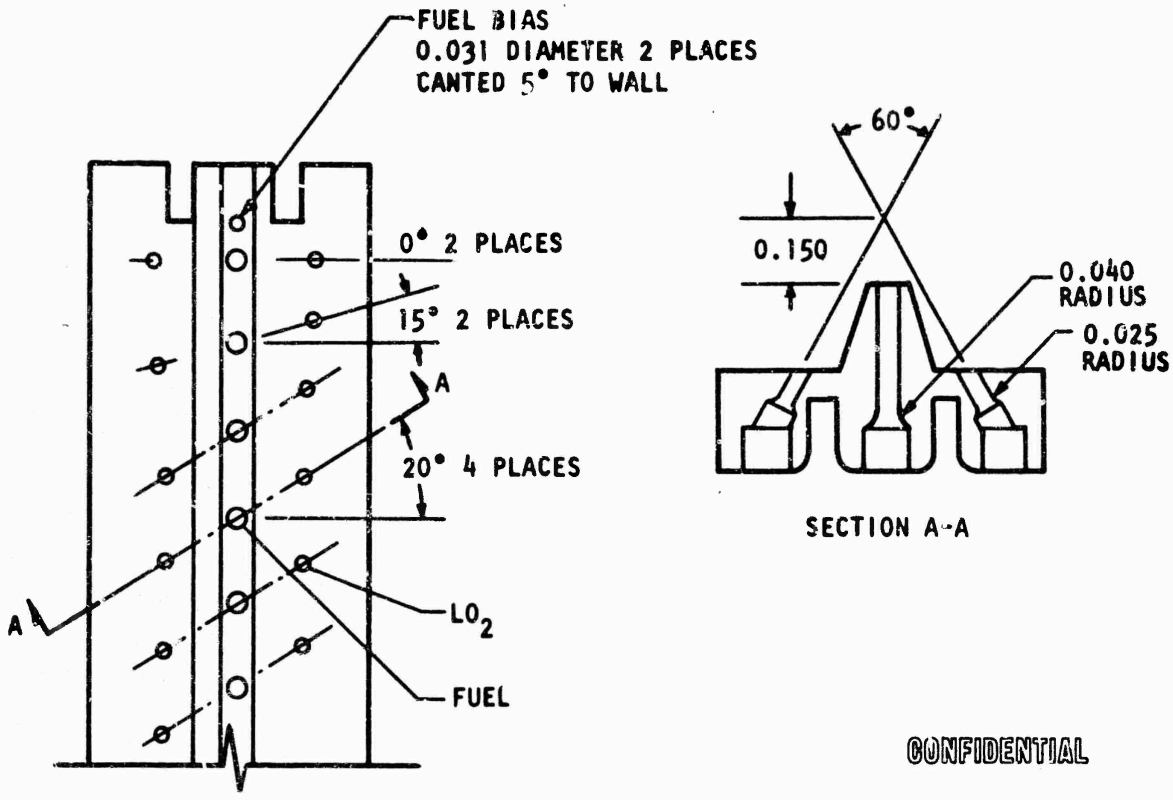

MODIFICATION DASH NO.	LO_2 ORIFICE		FUEL ORIFICE		MIXTURE RATIO BIAS		
	DIAMETER	TOTAL AREA	DIAMETER	TOTAL AREA	LO_2 DIAMETER	GH_2 DIAMETER	NO. OF ELEMENTS
-4A	0.033	0.0547	0.065	0.112		0.031	8
-4B	0.030	0.0547	0.070			0.031	

Figure 172. 60-Degree LO_2 Triplet With Fuel Post (No. 1-4A to 1-4B)

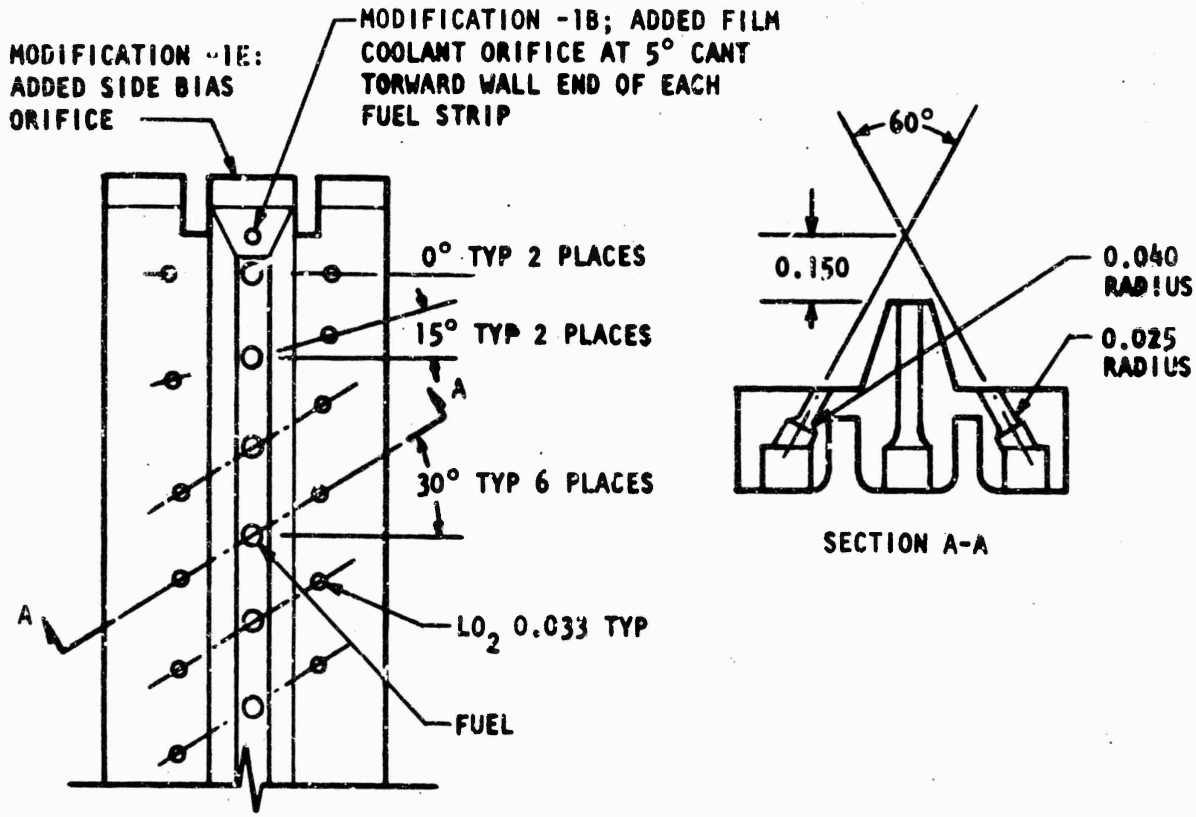

CONFIDENTIAL

MODIFICATION DASH NO.	LO_2 ORIFICE		FUEL ORIFICE		MIXTURE RATIO BIAS			FUEL FILM COOLANT
	DIAMETER	TOTAL AREA	DIAMETER	TOTAL AREA	LO_2 DIAMETER	GH_2 DIAMETER	NO. OF ELEMENTS	
-1A	0.033	0.0547	0.059	0.087				NONE
-1B	0.033	0.0547	0.066	0.118				0.031
-1C	0.033	0.0547	0.066	0.1205				0.042
-1D	0.033	0.0547	0.070	0.134				0.042
-1E	0.033	0.0547	0.070	0.142		0.055	8 (SIDE)	
-1F	0.033	0.547	0.070	0.123		—	—	
-1G	0.033	0.547	0.070	0.155		0.0995	8 (END)	

Figure 173. 60-Degree Triplet With Fuel Post (No. 2-1A to 2-1G)

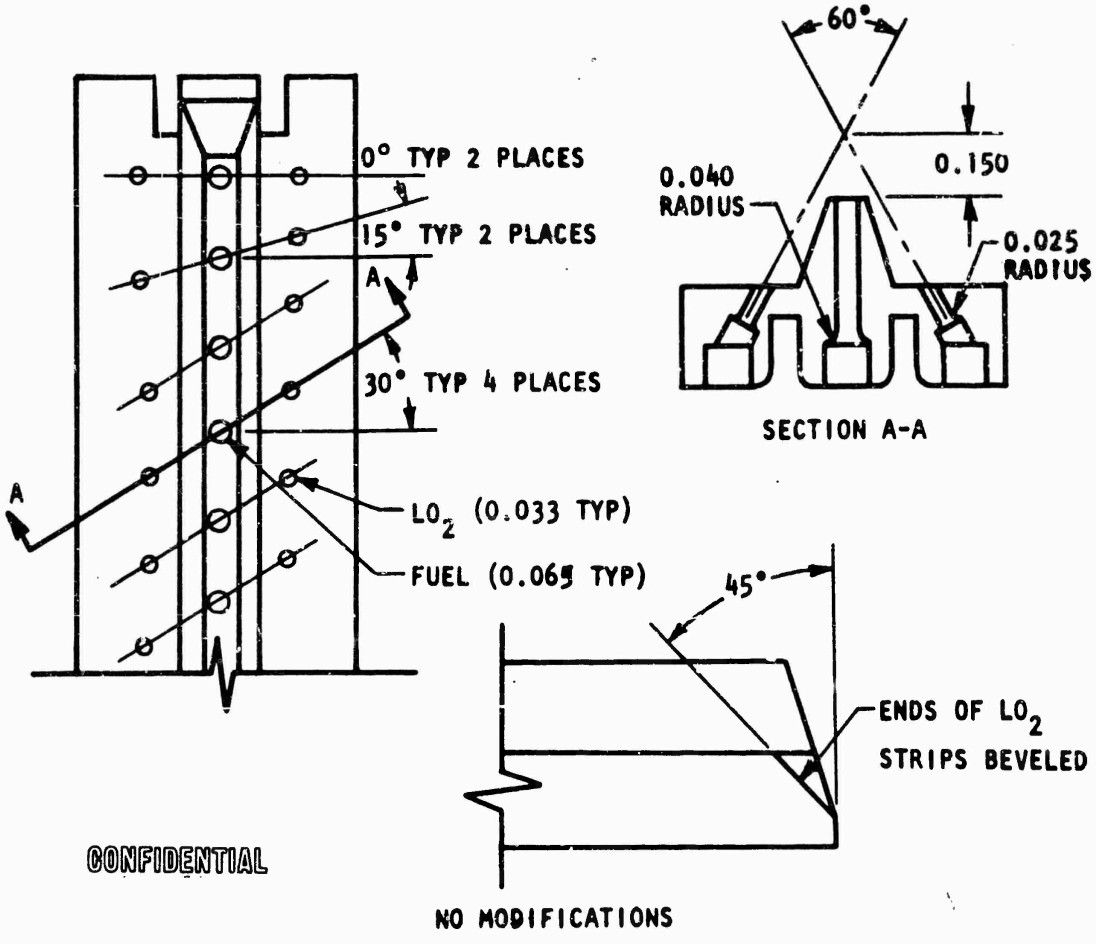

Figure 174. 60-Degree Triplet With Fuel Post (No. 2-2A)

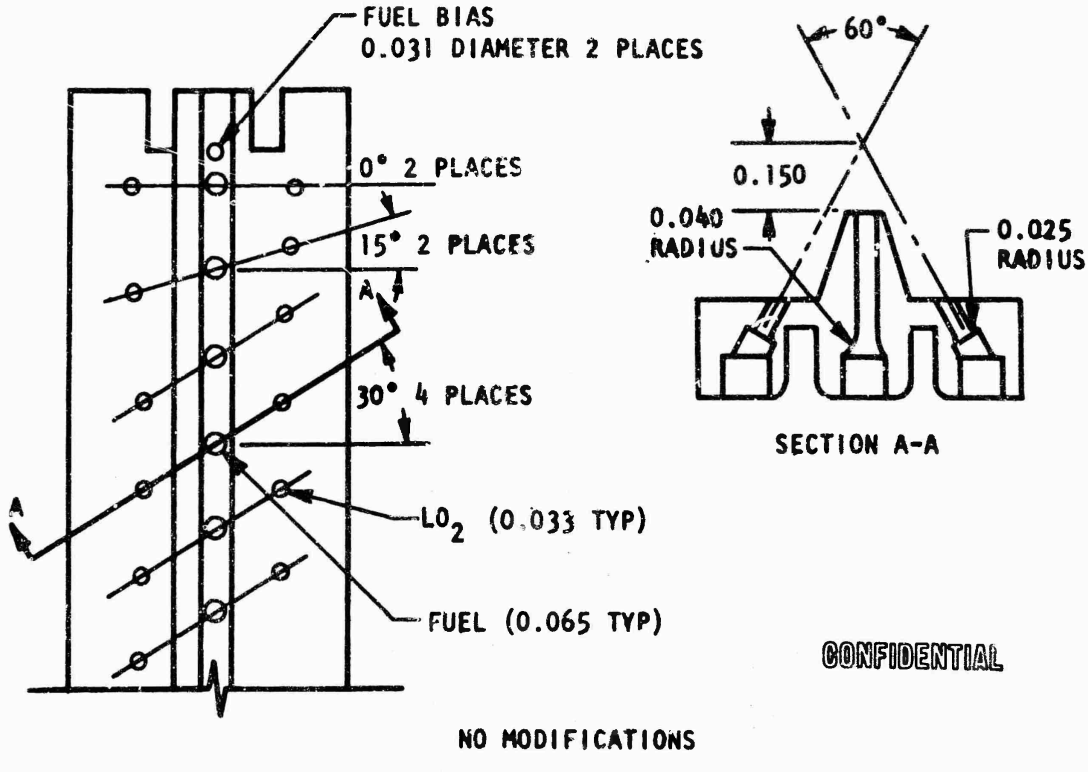

Figure 175. 60-Degree LO_2 Triplet With Fuel Post (No. 2-3A)

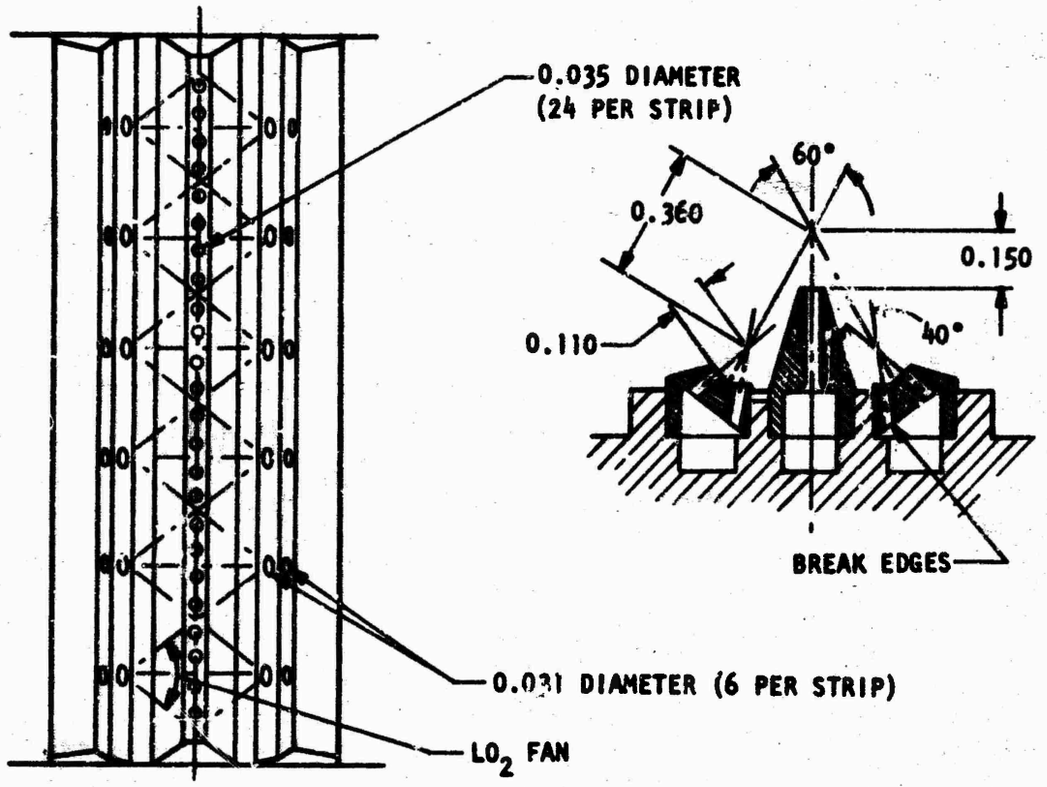

CONFIDENTIAL

MODIFICATION DASH NO.	LO_2 ORIFICE		FUEL ORIFICE	
	DIAMETER	TOTAL AREA	DIAMETER	TOTAL AREA
2A	0.031	0.0724	0.035	0.0924
2B	0.031	0.0724	0.0465	

Figure 176. LO_2 Fan With Fuel Post (No. 3-2A to 3-2B)

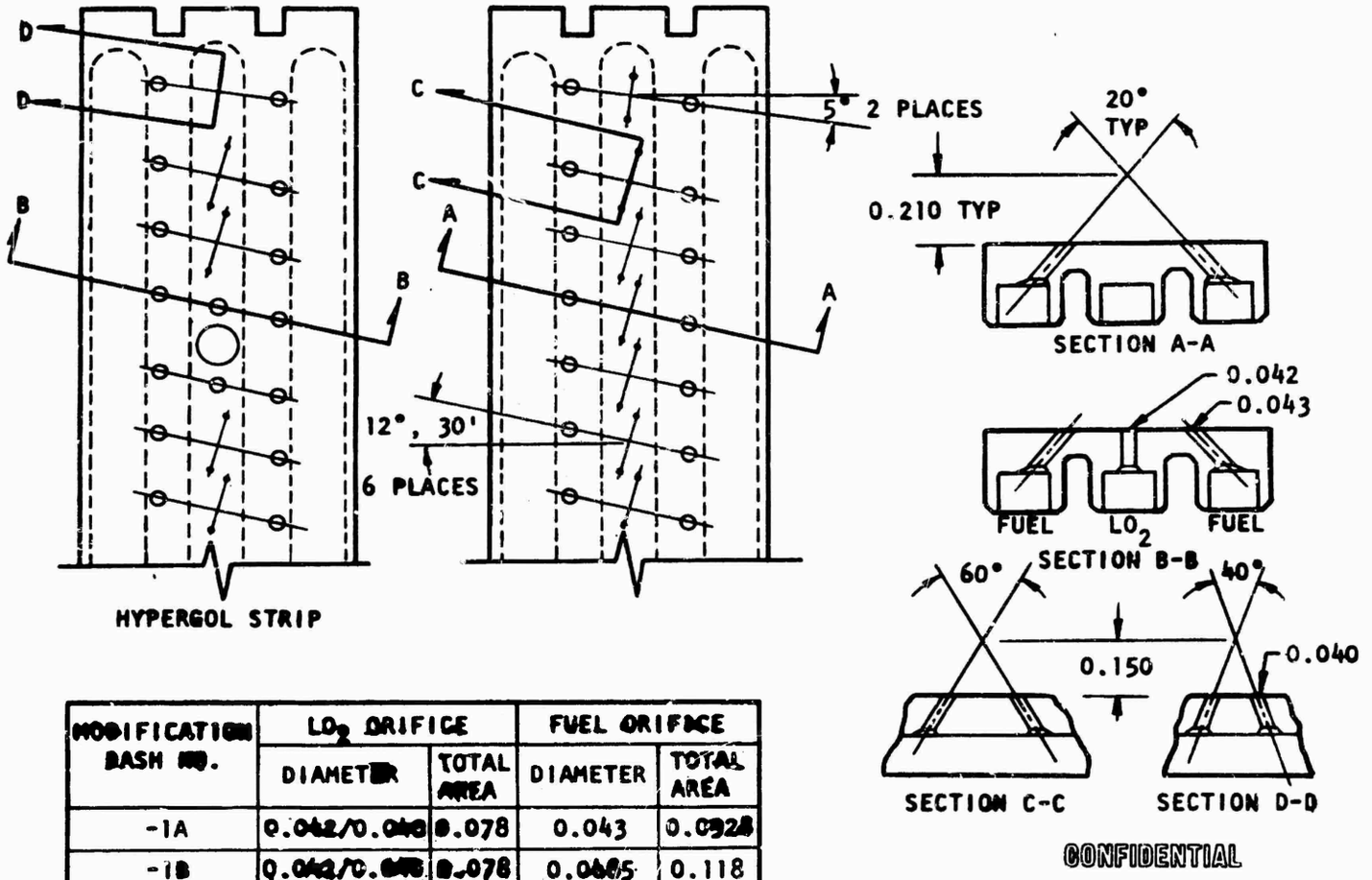

MODIFICATION DASH NO.	LO_2 ORIFICE		FUEL ORIFICE	
	DIAMETER	TOTAL AREA	DIAMETER	TOTAL AREA
-1A	0.042/0.040	0.078	0.043	0.0928
-1B	0.042/0.040	0.078	0.0805	0.118

Figure 177. Reversed LO_2 Fan With Fuel Impinging at 80 Degrees (No. 4-1A to 4-1B)

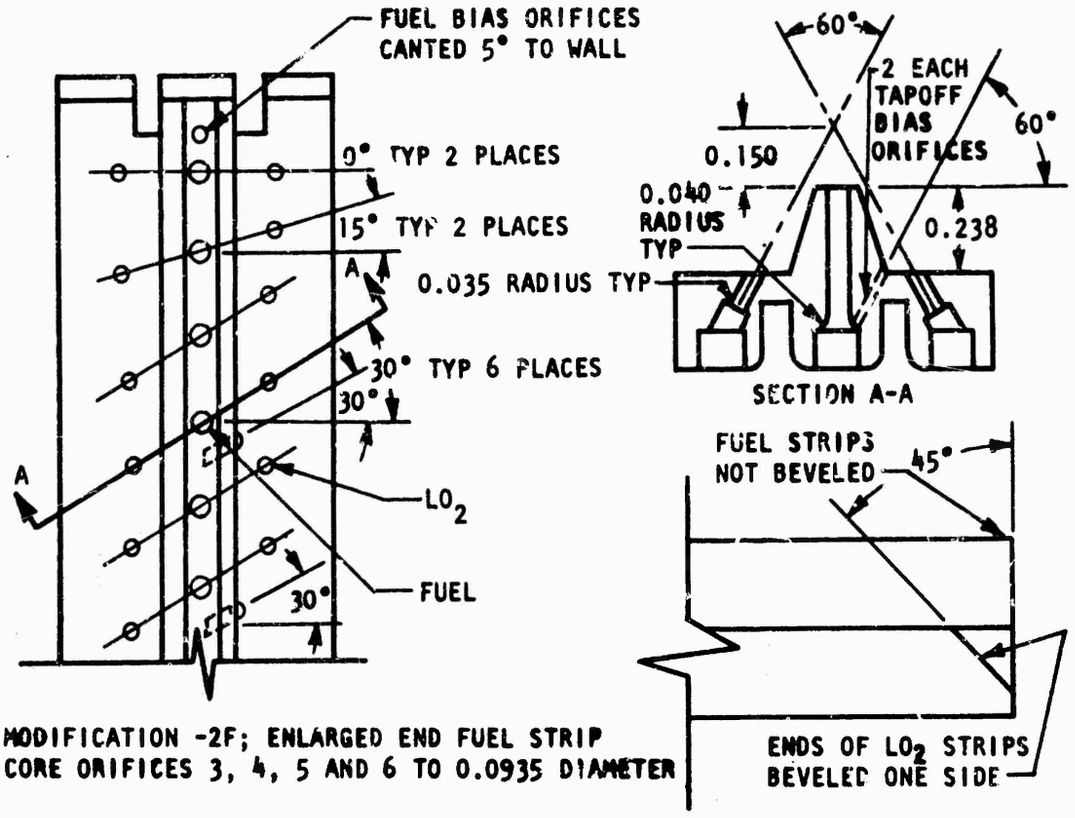

MODIFICATION -2F; ENLARGED END FUEL STRIP
CORE ORIFICES 3, 4, 5 AND 6 TO 0.0935 DIAMETER

CONFIDENTIAL

MODIFICATION DASH NO.	LO_2 ORIFICE		FUEL ORIFICE		MIXTURE RATIO BIAS			TAPOFF BIAS
	DIAMETER	TOTAL AREA	DIAMETER	TOTAL AREA	LO_2 DIAMETER	GH_2 DIAMETER	NO. OF ELEMENTS	
-2A	0.033	0.0547	0.065	0.112		0.031	8	
-2B	0.033	0.0547	0.065	0.114		0.031	8	0.032
-2C	0.033	0.0547	0.065	0.119		0.031	8	0.067
-2D	0.033	0.0547	0.065	0.121		0.031	8	0.076
-2E	0.033	0.0547	0.065	0.124		0.031	8	0.089
-2F	0.033	0.0547	0.065/ 0.095	0.133	-	0.031	8	0.089
-2G	0.033	0.0513	0.065	0.126	PLUGGED 4 ORIFICES	0.031	8	

Figure 178. Triplet With LO_2 Impinging at 60 Degrees (No. 4-2A to 4-2G)

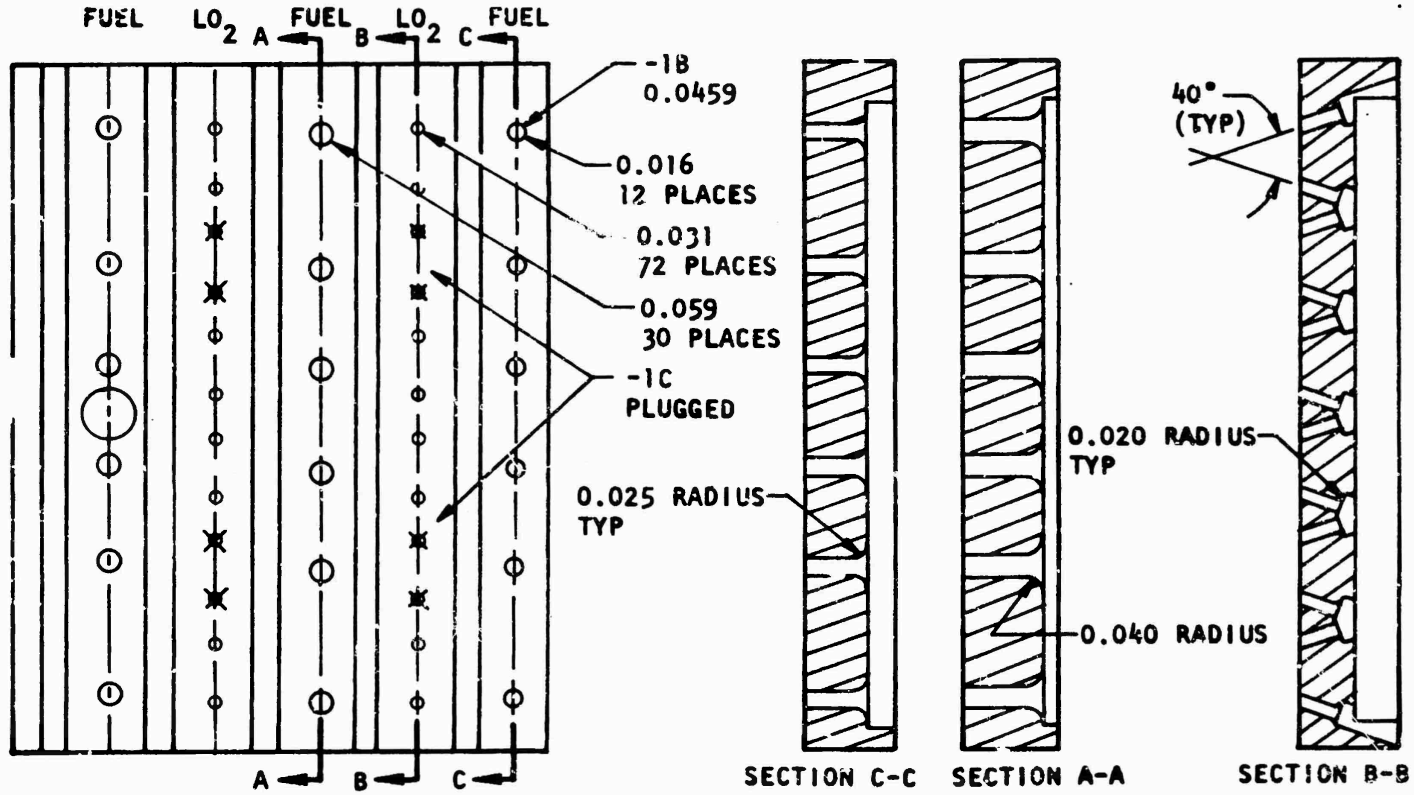

MODIFICATION DASH NO.	LO_2 ORIFICE		FUEL ORIFICE	
	DIAMETER	TOTAL AREA	DIAMETER	TOTAL AREA
-1A	0.031	0.0543	0.059/0.036	0.0942
-1B	0.031	0.0543	0.059/0.0469	0.103
-1C	0.031	0.0362	0.059/0.0469	0.103

CONFIDENTIAL

Figure 179. Showerhead Injector (No. 5-1A)

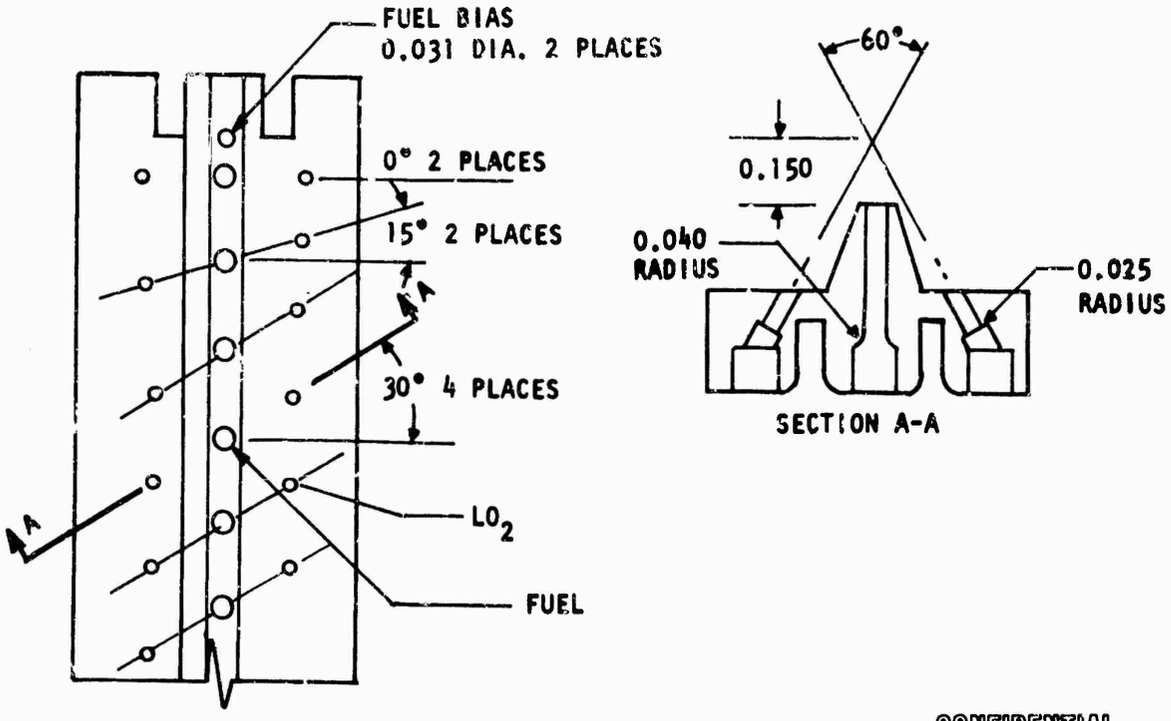

CONFIDENTIAL

MODIFICATION DASH NO.	LO_2 ORIFICE		FUEL ORIFICE		MIXTURE RATIO BIAS			TAPOFF BIAS (FUEL)
	DIAMETER	TOTAL AREA	DIAMETER	TOTAL AREA	LO_2 DIAMETER	GH_2 DIAMETER	NO. OF ELEMENTS	
-1A	0.0368	0.0682	0.070	0.1307		0.031	8	
-1B	61 EA/0.0368	0.0650	0.070	0.1307		0.031	8	
-1C	61 EA/0.0368	0.0650	0.070	0.1384		0.031	8	2 EA/0.070
-1D	61 EA/0.0368	0.0650	0.070	0.1444		0.031	8	2 EA/0.0935

Figure 180. 250K Candidate Triplet With Fuel Post (No. 6-1A to 6-1D)

CONFIDENTIAL

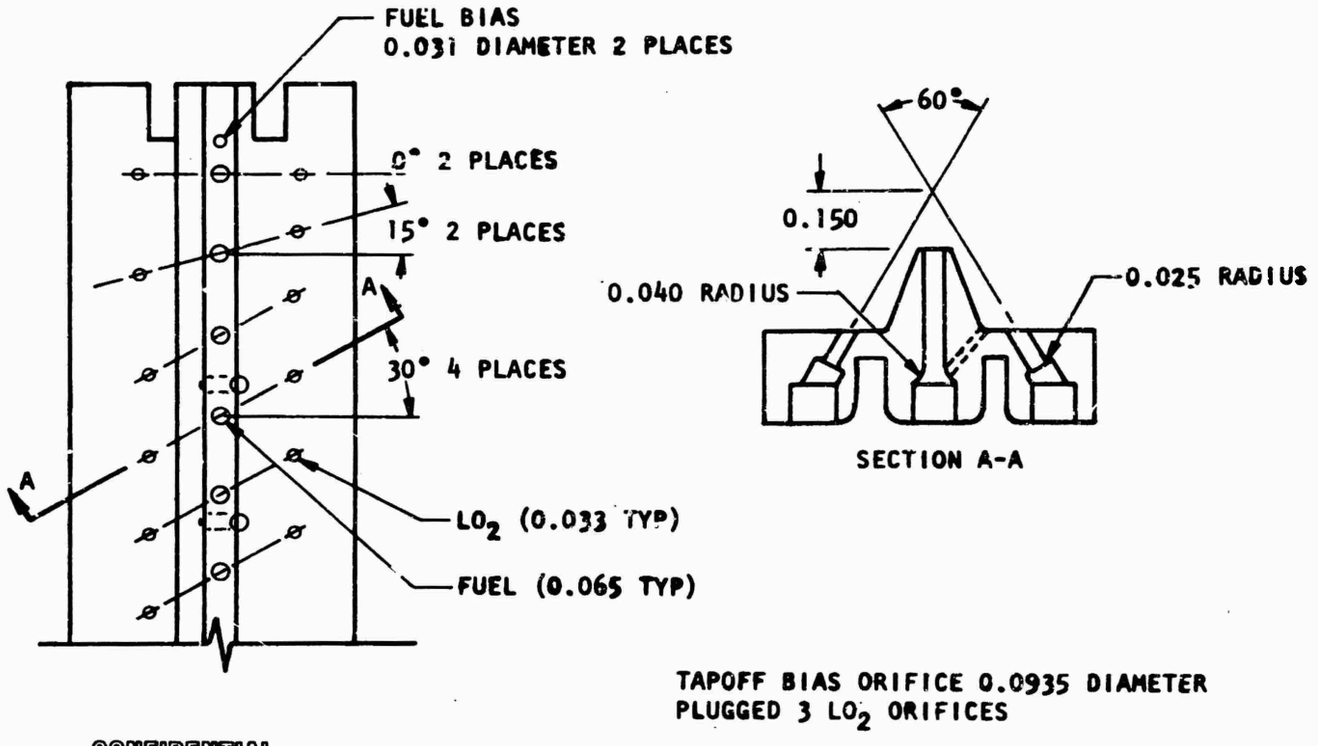

Figure 181. 60-Degree LO_2 Tripiet Injector (No. 6-2A)

1-1A and 1-2A used the same body, but the injection strip was substantially changed in going from 1-1A to 1-2A; and finally, the letter after the numbers represents the minor modifications to the injection strip. Letter A is used for the first strip configuration, but if injection holes are enlarged or some other such modification is made, then the number would become, for example, 1-2B. Comparison of Fig.170 and 171 illustrates the nomenclature in a graphic manner. The 1-2A injector is shown in Fig.170, the 1-3B injector is shown in Fig.171. The change from -2 to -3 was dictated by the change of reversing the flow pattern, and the change from A to B, by the addition of fuel bias orifices in the latter case.

(U) 2.5K Segment Injector Design. The body used for the 2.5K injectors was designed to simulate critical braze fabrication processes to be used on the 250K injectors, and to provide a tool capable of being refurbished repeatedly. Figure 182 illustrates the design employed.

(U) The injector body is designed as a one-piece unit containing provision for accepting and distributing oxidizer and fuel propellants, introducing hypergolic ignition fluids, and measuring propellant manifold and injector end chamber pressures. The body accepts propellants from two facility connections, one each for oxidizer and fuel, and distributes them to four injection strips, each containing eight impinging triplet patterns (two oxidizer on one fuel).

(C) Oxidizer is introduced into the body at the aft end (opposite the 2.0- x 3.7-inch face) through a 1.0-inch port. Two cross-drilled, stepped holes, located perpendicular to and intersecting the inlet

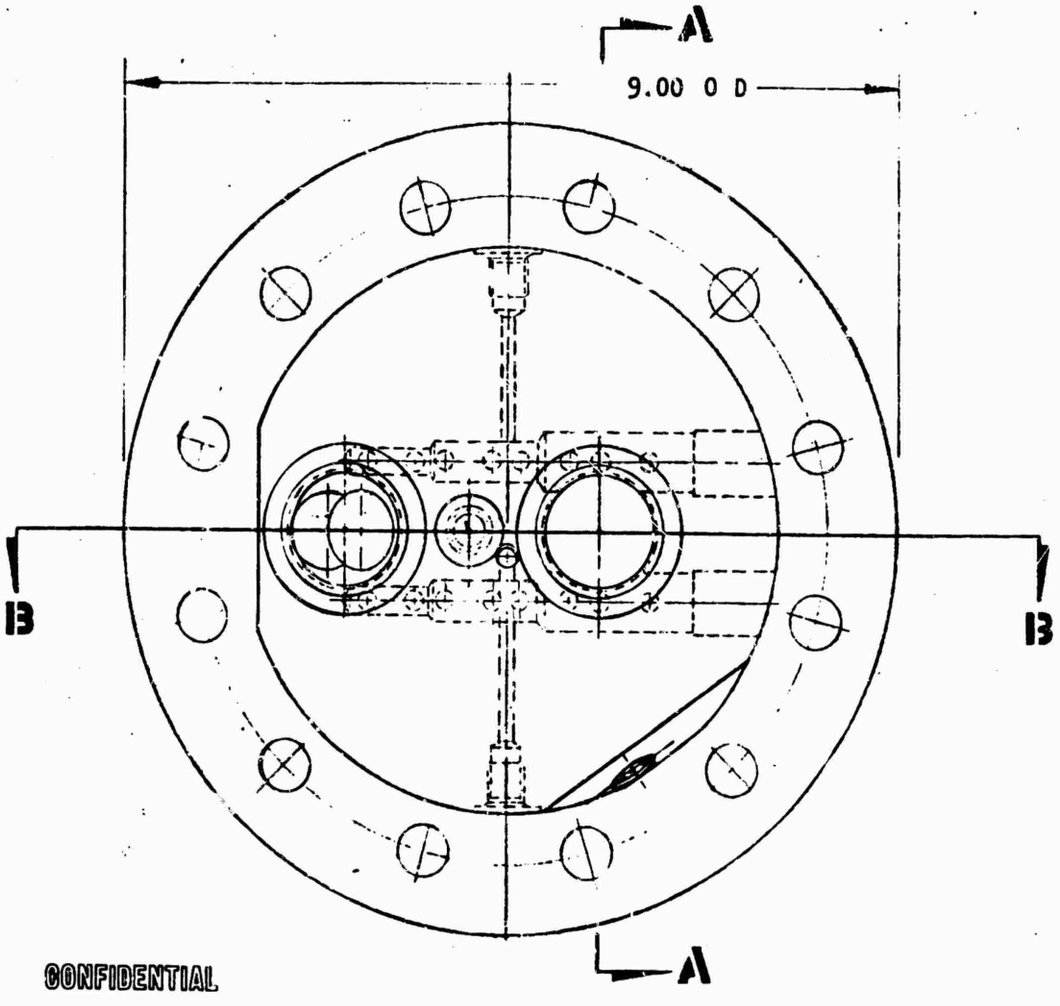

Figure 182A. 2.5K Segment Injector Body,
Oxidizer Feed System

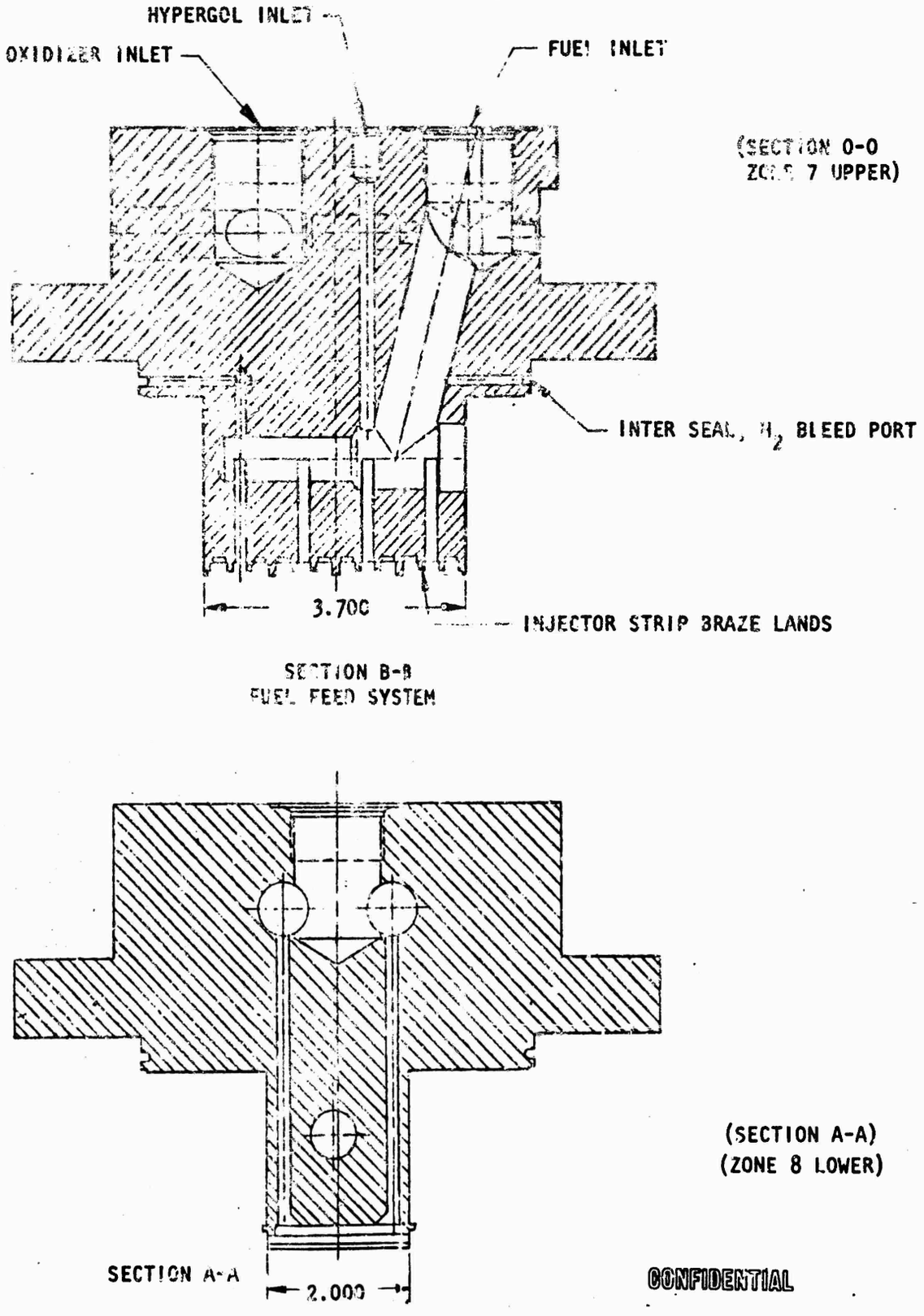

Figure 182B. 2.5K Segment Injector Body, Oxidizer Feed System

port, distribute the LO_2 across the 3.7-inch body dimension. Eight axial holes, 0.161-inch diameter, connect each of the cross-drilled passages to the ends of cavities, providing manifolding behind the eight oxidizer strips on the brazed assembly.

(U) Sealing of the cross-drilled holes is accomplished by plugs brazed into the body concurrently with the strips.

(U) Hydrogen propellant is introduced into the body adjacent to the oxidizer inlet through a similar port. Distribution is affected by a canted axial hole connecting a single, stepped, cross-drilled hole. Four axial slots connect this hole and provide the manifolds behind the four fuel strips installed on the brazed assembly. As with the oxidizer, the fuel cross-drilled hole is sealed with a braze plug.

(U) Installation of the four injector strips is accomplished by braze of the strip into body lands machined on the face. Thirteen such lands provide vertical shear interface for the strips, affording structural integrity against manifold pressures and thermal gradients. The distance between each land is machined to exacting tolerances, ±0.001 inch, to insure structurally sound and leak-tight braze joints.

(U) Provision for introduction of hypergol injector fluid is made through an axial hole, entrance to which is located between oxidizer and fuel inlets via a 0.25-inch port, and exiting into the second fuel cavity feeding a fuel strip. A hypergol tube for conveying fluid is attached at the inlet, sealed by a K seal, and exits through a hole in the face of the second fuel strip.

(U) Ports enable mounting of instrumentation for measurement of propelland manifold pressures. Injector end chamber pressure measurements are made through a similar port exiting at the injector face through a 0.060-inch-diameter hole in a land between strips.

(U) Provision for attaching the injector solid- or tube-wall 2.5K chamber bodies is afforded by 12 holes through the body flange. Sealing is accomplished by a primary metallic O-ring and a secondary flexitallic gasket. These are spaced so that hydrogen bled from the manifolding is contained between them, and leakage of either primary or secondary seals vents hydrogen either overboard or into the chamber. In this way, hot-gas leak potential is eliminated.

(U) Fabrication of 2.5K Injectors. The 2.5K injector consisted of two basic pieces: (1) the body which served as part of the propellant manifold feed system and provided the lands to which the injection strips were brazed, and (2) the injection strips which were drilled to give the desired propellant impingement pattern. Utilization of this strip technique permitted great versatility and simplified injector fabrication. In addition, strips that were identical to those that would be used in the 250K injector could be fabricated and tested in the 2.5K test hardware. Four injectors had been made available for the 2.5K evaluation efforts from an in-house effort. A total of four patterns was started through evaluation (Fig.169,170,171, and176). These patterns are all basically triplet patterns.

(U) 2.5K Water-Cooled Segments. The water-cooled 2.5K solid-wall segment provided a versatile tool to obtain injector performance data over run durations long enough to stabilize propellant flowrates, as well as pressure, temperature, and thrust measurements. The chamber is made up of segments (chamber spacers and nozzle) to allow variable combustion length evaluations with selected injectors. The chamber also provided the capability of obtaining detailed local heat flux measurements through calorimetric measurements on the cooling passages. A section of the chamber assembly is shown in Fig. 183.

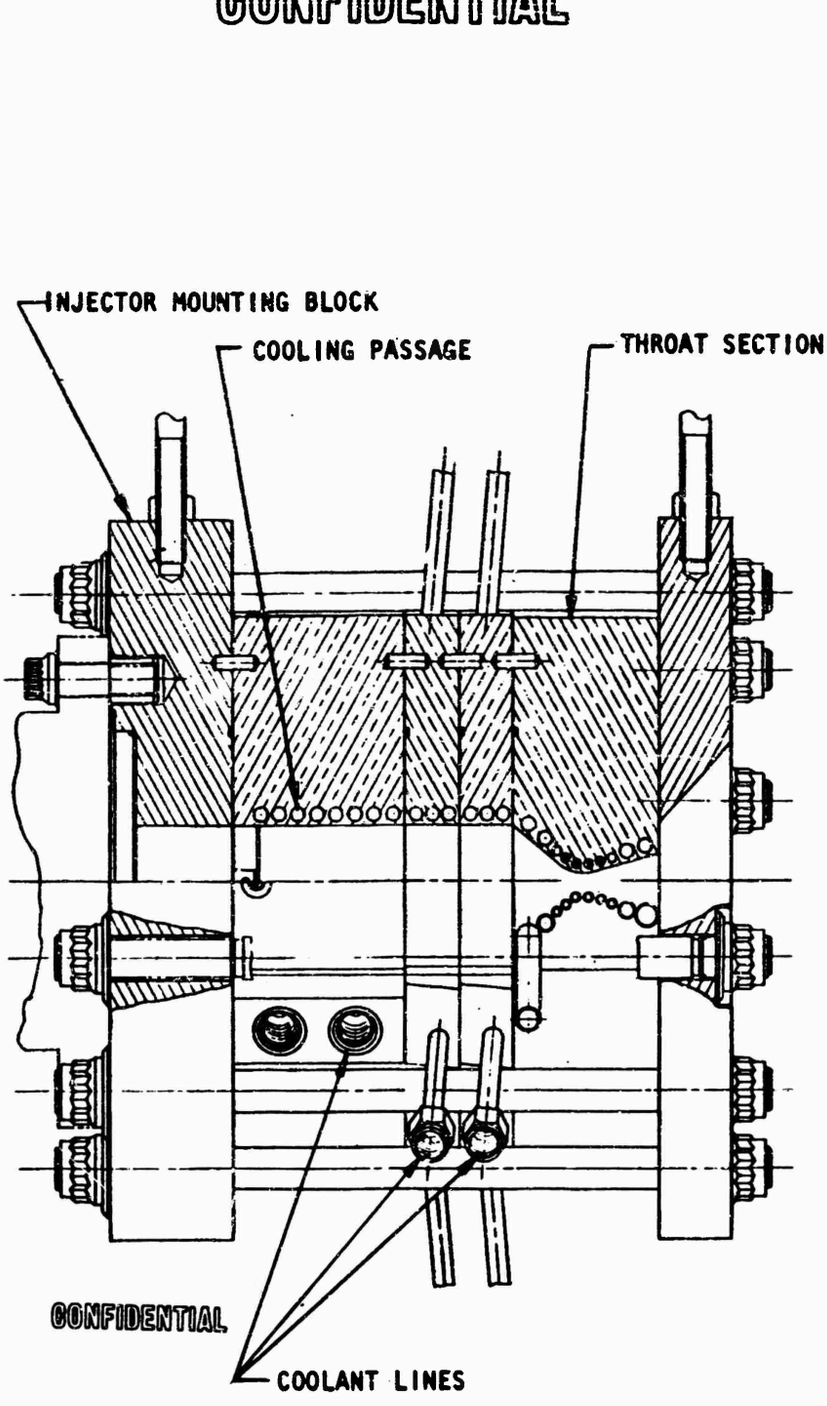

Figure 183. 2.5K Solid-Wall Thrust Chamber

(C) The chamber assembly consists of four copper sections, forming the body of the chamber. Chamber operating parameters were:

Thrust, pounds	=	2500
Chamber Pressure, psia	=	300 to 1500
Mixture Ratio	=	5.0 to 7.0

(U) The copper water-cooled sections of the chamber were internally machined to define the chamber cross section when stacked together. The No. 1 copper block, the forward body assembly, and the two following spacers defined the combustion zone of the chamber. The above-mentioned blocks contain coolant passages which cover all four walls of the combustion zone in circuits normal to the chamber (Fig. 183). The remaining copper section forms the throat and nozzle. The nozzle employs 15-degree divergent half angles with an area ratio of 3.60. The low area ratio value was chosen for full nozzle flow (underexpanded) over all chamber pressure values.

(U) The higher heat flux regions of the throat section utilize coolant passages with bent 321 CRES ribbon flow swirlers to improve heat transfer coefficient coolant side values. The balance of the throat section was cooled passages without swirlers. The part was designed to be capable of incorporating H_2 gas film cooling on all surfaces in the event this modification is required for certain test conditions.

(C) A heat transfer analysis of the 2.5K water-cooled chamber was conducted, with particular emphasis being placed on the drilled holes in the throat region. The analysis was based on a copper chamber with a minimum "reach" (distance from coolant wall to gas wall) of 0.070 inch and a maximum reach of approximately 0.10 inch. Both water and hydrogen cooling were considered. Using water cooling at 1500 psi pressure and 65 F temperature, the coolant wall temperature under nucleate boiling conditions would be

about 600 F. Under these conditions, the required water velocity would be about 200 ft/sec, including a 50-percent factor of safety over the burnout velocity. The corresponding gas wall temperatures are 1350 and 1560 F for the minimum and maximum reach, respectively.

Testing

(C) Method of Evaluation. Evaluations were conducted in the basic 6-inch-long by 2-1/8-inch-wide segment hardware previously described. When the safe operating heat flux limit of the water-cooled segment (40 Btu/in.^{2}-sec) was approached, auxiliary hydrogen film cooling was provided in the combustion chamber convergent section to facilitate duration runs at high pressures.

(C) The method of approach to injector evaluation was to begin with low chamber pressure performance tests and heat transfer tests, followed by high pressure runs (1500 psia) in uncooled hardware for 250 milliseconds to evaluate injector face durability. Surviving candidates were then run through additional performance runs over the range of operation, and heat transfer data were acquired. Buzzing evaluation was made on its spontaneous appearance anywhere in the pressure range of operation.

(U) Instrumentation provided highly accurate determination of thrust, chamber pressure, and propellant flowrates. Precision studies of these measurements are included in the Analysis of Results section. Thermocouples and coolant flowmeters for measurement of heat flux at the various stations down the chamber were provided. These could be (and were) shifted during the test series for more detailed study of heat flux at one location.

(U) On the tests which were to be examined for possible combustion instability or oscillations, the following instrumentation was provided: AC radiometers, streak photographs of the flame, accelerometers, Fastax

cameras, and normal Taber pressure transducers. On tests on which gas tapoff was evaluated, special provisions for determination of gas properties were made, as described in the Analysis of Results section.

(U) Performance data at high chamber pressures were obtained in two manners: (1) with film cooling flowing, and results corrected analytically as described, and (2) by turning off the film coolant.

(U) Evaluation Series. A total of 128 tests was conducted on eleven different injectors with a total of 31 modifications. The details of each test are delineated in Tables 60 through 62. Tests are grouped by: (1) water-cooled tests for performance and heat transfer data, (2) film-cooled tests for high chamber pressure performance and durability data, and (3) tests for gas tapoff data, as well as performance and heat transfer. The approach to test conduct and handling of the data is discussed fully in the Analysis of Results section for each evaluation.

(C) Testing Support For the 250K Testing. A 2.5K segment injector was modified to simulate the 250K injector hand-repair made at the Nevada Field Laboratory (this repair is described more fully in the section dealing with the 250K) and tested to evaluate the effectiveness of this repair. Modification of the 2.5K segment injector essentially duplicated the 250K injector repair with 0.065 inch of tungsten inert gas (TIG) braze (50-percent Au; 50-percent Ni braze alloy) replacing the top of two adjacent OFHC copper oxidizer strips. Also, the modification consisted of drilling seven fuel holes in each of the two bordering fuel strips, as done on the 250K injector, to provide fuel cooling to the two brazed-over oxidizer strips.

cameras, and normal Taber pressure transducers. On tests on which gas tapoff was evaluated, special provisions for determination of gas properties were made, as described in the Analysis of Results section.

(U) Performance data at high chamber pressures were obtained in two manners: (1) with film cooling flowing, and results corrected analytically as described, and (2) by turning off the film coolant.

(U) Evaluation Series. A total of 128 tests was conducted, on eleven different injectors with a total of 31 modifications. The details of each test are delineated in Tables 60 through 62. Tests are grouped by: (1) water-cooled tests for performance and heat transfer data, (2) film-cooled tests for high chamber pressure performance and durability data, and (3) tests for gas tapoff data, as well as performance and heat transfer. The approach to test conduct and handling of the data is discussed fully in the Analysis of Results section for each evaluation.

(C) Testing Support For the 250K Testing. A 2.5K segment injector was modified to simulate the 250K injector hand-repair made at the Nevada Field Laboratory (this repair is described more fully in the section dealing with the 250K) and tested to evaluate the effectiveness of this repair. Modification of the 2.5K segment injector essentially duplicated the 250K injector repair with 0.065 inch of tungsten inert gas (TIG) braze (50-percent Au; 50-percent Ni braze alloy) replacing the top of two adjacent OFHC copper oxidizer strips. Also, the modification consisted of drilling seven fuel holes in each of the two bordering fuel strips, as done on the 250K injector, to provide fuel cooling to the two brazed-over oxidizer strips.

CONFIDENTIAL

TABLE 60

(C) SUMMARY OF 2.5K WATER-COOLED THRUST CH

Test No.	Test Date, 1966	Injector S/N	Test Duration, seconds	Ambient Pressure, psia	A_t, sq in.	Thrust, pounds	Temperatures			Pressures						Flowrates			
							Oxid Inlet F	Fuel Inlet, F	Film Coolant, F	Oxidizer Inlet, psia	Fuel Inlet, psia	Film Coolant, psia	Throat Stagnation Pressure, P_c psia	Fuel Injection ΔP, psi	Oxidizer Injection, ΔP, psi	Oxidizer, lb/sec	Fuel, lb/sec	Film Coolant, lb/sec	W lb
027	5-21	2-1A	3.7	13.30	0.990	937		70		674	894		641	253	33	2.251	0.387		2.
028	5-21	2-1A	3.9			1415		71		1104	1319		971	348	133	3.500	0.538		4.
029	5-21	2-1A	3.7			420		71		315	460		306	154	9	1.020	0.202		1.
031	5-27	4-1A	0.4			1850		78					1564						8.
032	5-31	1-2A	0.4			1850		78					1614						6.
033	6-6	2-1B	4.3		0.980	896		91		669	754		630	124	39	2.177	0.368		2.
034	6-6	2-1B	4.3			1377		98		1092	1143		974	169	118	3.415	0.531		3.
035	6-6	2-1B	4.0			430		2		333	393		325	68	8	1.140	0.200		1.
036	6-6	4-1A	4.3			1710							1189						4.
037 Through 045 (No data available, nozzle throat eroded)																			
046	6-16	2-1D	4.3			446				348	400		334	66	14	1.189	0.20[illegible]		1.
047	6-16	2-1D	4.4			955				735	803		680	123	55	2.364	0.389		2.
048	6-16	2-1D	4.3			933				719	789		665	124	54	2.307	0.389		2.
049	6-16	2-1D	4.3			920				712	786		658	128	54	2.263	0.391		2.
050	6-21	2-1E	4.2		0.965	425				341	389		326	63	15	1.110	0.205		1.
051	6-21	2-1E	4.3			909				708	774		653	121	55	2.207	0.395		2.
052	6-21	2-1E	4.2			911				711	781		658	123	53	2.234	0.397		2.
053	6-22	2-1E	4.3			418				330	379		318	61	12	1.055	0.199		1.
054	6-22	2-1F	4.3			672				525	579		495	84	30	1.680	0.290		1.
055	6-22	2-1E	4.3			898				706	770		634	116	52	2.280	0.386		2.
056 Through 071 (No data, injector strip-to-land separation, buzz induced [illegible] failure)																			
072	7-5	1-3A	4.0		0.950	745				602	677		549	128	53	1.981	0.290		2.
073	7-5	1-3A	4.3			1062				874	1013		779	234	95	2.632	0.462		3.
074	7-5	1-3A	4.3			1057				861	1018		773	245	88	2.461	0.479		2.
075	7-6	1-3A (No data, nozzle throat eroded)																	
076	7-8	1-3B	4.4			870				698	808		634	174	64	2.140	0.380		2.
077	7-8	1-3B	4.4			886				712	819		647	172	65	2.239	0.381		2.
078	7-8	1-3B	4.4			846				679	795		621	174	58	2.109	0.377		2.
079	7-12	1-3B	14.3		0.940	1079		100		870	973		779	194	91	2.639	0.435		3.
080	7-12	1-3B	14.3		0.940	1061		101		849	951		766	185	83	2.631	0.424		3.
081	7-13	3-2A	0.4		OP	1900							1514						6.
082	7-15	3-2A	12.7		0.940	1111		93		842	1065		805	260	37	2.401	0.422		3.
192 Through 194 (No data, facility malfunction)																			
195	10-20	6-1A	3.6		0.970	444		72		359	413		347	66	12	1.115	0.235		1.
196	10-20	6-1A	3.8		0.970	444		73		356	412		344	68	12	1.082	0.236		1.

TABLE 60

-COOLED THRUST CHAMBER PERFORMANCE TESTS

Flowrates				Injector* Mixture Ratio, o/f	Based on P_c						Nozzle Area Ratio	Oxidizer-to-Fuel Momentum Ratio	Oxidizer Injection Velocity, ft/sec	Fuel Injection Velocity, ft/sec	Throat Peak Heat Flux, Btu/in.^{2}-sec	Comments
Oxidizer, lb/sec	Fuel, lb/sec	Film Coolant, lb/sec	$\dot{W}_T$, lb/sec		c*, ft/sec	C_F	I_s, seconds	η_{c*}	η_{C_F}	η_{I_s}						
2.251	0.387		2.638	5.81	7635	1.477	367	0.989	1.017	1.006	3.5:1	0.1832	84	2664	30.1	
3.500	0.538		4.038	6.50	7537	1.472	362	0.998	0.995	0.993		0.3368	130	2509	51.5	IR&D funded
1.020	0.202		1.223	5.04	7750	1.386	356	0.989	1.024	1.013		0.0681	38	2812	14.4	
			6.123	9.71		1.195								2195		Injector erosion
			6.859	7.78		1.158								2193		Bomb test
2.177	0.368		2.545	5.91	7695	1.451	364	1.000	1.001	1.001		0.2322	82	2087	25.8	
3.416	0.531		3.947	6.43	7662	1.443	361	1.012	0.974	0.986		0.4128	127	1978	42.7	
1.140	0.200		1.340	5.69	7531	1.350	332	0.979	0.978	0.975		0.1152	43	2123	13.7	
			4.956	6.38		1.468								2540		Coolant leak into thrust chamber
1.189	0.206		1.394	5.79	7373	1.363	331	0.963	0.992	0.555		0.1428	46	1864	13.2	
2.364	0.389		2.753	6.07	7666	1.433	359	1.002	0.985	0.987		0.3050	90	1791	33.1	
2.367	0.389		2.749	5.94	7657	1.432	358	0.996	0.986	0.982		0.2799	86	1825	35.2	
2.263	0.391		2.653	5.80	7679	1.427	359	0.995	0.985	0.980		0.2704	86	1814	34.8	
1.110	0.205		1.304	5.38	7633	1.351	337	0.980	0.984	0.964		0.1275	42	1772	11.9	
2.207	0.395		2.599	5.60	7879	1.443	362	0.988	0.995	0.983		0.2679	83	1741	23.2	
2.234	0.397		2.631	5.63	7644	1.435	358	0.984	0.989	0.973		0.2704	84	1749	25.7	
1.055	0.199		1.254	5.31	7756	1.362	345	0.994	0.991	0.985		0.1199	40	1771	12.5	
1.680	0.290		1.970	5.79	7665	1.407	353	0.994	0.987	0.981		0.2150	63	1696	21.1	
2.280	0.386		2.666	5.90	7525	1.423	349	0.977	0.979	0.956		0.2907	85	1725	27.4	
1.981	0.290		2.270	6.84	7270	1.428	339	0.979	0.991	0.970		0.2449	74	2067	33.8	
2.632	0.462		3.096	5.70	7585	1.435	355	0.977	0.982	0.959		0.2435	99	2317	45.0	
2.461	0.479		2.942	5.15	7958	1.439	372	1.005	0.984	0.989		0.1983	93	2415	41.9	
2.140	0.380		2.522	5.64	7567	1.444	357	0.975	0.998	0.973		0.2102	81	2173	24.1	
2.239	0.381		2.622	5.88	7477	1.441	350	0.969	0.989	0.958		0.2298	84	2149	28.9	
2.109	0.377		2.488	5.59	7527	1.434	352	0.967	0.992	0.959		0.2002	79	2205	29.6	
2.659	0.435		3.094	6.11	7500	1.474	361	0.980	1.006	0.986		0.2924	100	2089	26.8	
2.631	0.424		3.055	6.21	7484	1.474	359	0.982	1.004	0.986		0.2932	98	2075	32.9	
			6.614	7.63										2342		Uncooled hardware
2.401	0.422		3.172	6.52	7570	1.468	409	1.004	1.099	1.103		0.1940	69	2319	35.3	
1.115	0.235		1.350	4.74	7887	1.319	340	0.990	0.957	0.947		0.0797	35	2082		
1.082	0.236		1.318	4.58	8001	1.331	349	0.999	0.970	0.969		0.0771	35	2078		

2

CONFIDENTIAL

TABLE 61

(C) SUMMARY OF 2.5K FILM-COOLED THRUST CHAMBER E

Test No.	Test Date, 1966	Injector S/N	Test Duration, seconds	Ambient Pressure, psia	A_t, sq in.	Thrust, pounds	Temperatures			Pressures						Flowrates				Mixture Ratios		c*, ft/sec	
							Oxidizer, Inlet, F	Fuel Inlet, F	Film Coolant, F	Oxidizer Inlet, psia	Fuel Inlet, psia	Film Coolant, psia	Throat Stagnation Pressure, P_c psia	Fuel Injection ΔP, psi	Oxidizer Injection, ΔP, psi	Oxidizer, lb/sec	Fuel, lb/sec	Film Coolant, lb/sec	$\dot{W}_T$, lb/sec	Injector o/f	Overall o/f		
100	8-2	1-3B		13.80																			
101	8-2	1-3C	3.4		0.950	982		90		775	907		720	187	55	2.149	0.407		2.556	5.28			1
102	8-2	1-3B	3.5			1385		88		1105	1281		1004	277	101	2.828	0.573		3.401	4.94			1
103	8-2	1-3B	3.5			1617		87		1319	1484		1169	315	150	3.4023	0.659		4.052	5.16			1
104	8-3	1-3B	3.6			1902		102		1574	1673		1364	309	210	3.9968	0.687		4.684	5.81			1
105	8-5	1-3B	3.3			2105		101		1787	1782		1494	288	293	4.860	1.141	0.438	6.001	6.89	4.26	7363	1
106	8-5	3-2A	3.2			2130		90		1719	1946		1505	441	214	5.005	1.147	0.443	6.152	7.07	4.36	7286	1
107	8-9	4-1B	3.3			2151		98		1667	1755		1504	251	163	5.388	1.066	0.400	6.454	8.05	5.05	6938	1
108	8-9	4-1B	3.7			1022		97		781	914		741	173	40	2.499	0.563	0.159	3.062	6.19	4.44	6952	1
109	8-9	5-1A	4.4			527		88		418	519		385	134	33	1.332	0.364	0.132	1.696	5.74	3.66	7015	1
110	8-9	5-1A	0.8			2176		86		1890	1821		1491	330	405	5.030	1.105	0.454	6.135	6.87	4.55	7148	1
111	8-12	3-2A	4.9		0.970	390		94		300	468		294	174	6	0.944	0.345	0.135	1.289	4.55	2.74	7839	1
112	8-12	3-2A	4.8			406		93		312	439		304	135	8	1.047	0.322	0.133	1.369	5.54	3.25	7562	1
113	8-12	3-2A	4.6			1378		94		1027	1306		969	337	58	3.146	0.756	0.258	3.902	6.08	4.16	7491	1
114	8-12	3-2A	3.4			1340		94		1002	1277		946	331	56	3.126	0.640	0.128	3.766	6.11	4.88	7561	1
115	8-12	3-2A	3.4			2308		90		1799	1963		1562	401	237	5.697	1.065	0.365	6.762	8.13	5.35		1
116	8-17	2-2A	2.1			540		81					411							6.14			1
117	8-19	3-2A	3.9		0.925	860		99		665	913		639	274	26	1.996	0.589	0.199	2.583	5.12	3.39		1
118	8-19	3-2A	3.9			874		93		681	842		640	192	31	2.288	0.523	0.194	2.811	6.93	4.37		1
119	8-19	3-2A	4.5			411		87		326	471		324	147	2	0.888	0.375	0.147	1.263	3.90	2.37		1
120	8-19	3-2A	4.5			398		85		320	423		317	106	3	0.886	0.327	0.150	1.213	5.03	2.71	7714	1
121	8-23	3-2B	3.5			787		102		693	809		666	143	27	1.952	0.574	0.202	2.526	5.24	3.40	7503	1
122	8-23	3-2B	2.9			1012		100		1123	1224		1046	178	77	3.055	0.918	0.385	3.973	5.72	3.32	7567	
123	8-24	4-2A	3.9			838		103		674	778		633	145	41	1.805	0.524	0.172	2.329	5.12	3.44	7923	1
124	8-24	4-2A	3.8			810		98		656	764		614	150	42	1.654	0.560	0.206	2.214	4.68	2.95	8026	1
125	8-24	4-2A	2.7			1354		97		1108	1205		1005	201	103	2.774	0.918	0.402	3.692	5.39	3.02	7824	1
126	8-24	4-2A	2.0			1782		93		1521	1626		1320	306	201	3.720	1.167	0.445	4.887	5.16	3.19	7941	1
127	8-24	4-2A	2.6			2032		91		1772	1757		1492	265	280	4.528	1.143	0.437	5.671	6.39	3.96	7620	1
128	8-26	4-2A																					
129	8-26	4-2A	1.7		0.935	1231		99		1045	1173		982	191	63				3.426	5.39			1
130	8-26	3-2B	1.7		0.935	1020		88		815	932		762	170	53				2.999	5.88			1
197	10-20	6-1A	3.9		0.970	1316		77		1011	1113		950	163	61	2.652	0.579		3.231	4.58			1
198	10-24	6-1A	4.2			2208		92		1776	1747		1548	199	228	5.044	1.107	0.271	6.151	6.04	4.56	7640	1
199	10-24	6-1A	4.2			1341		95		1040	1094		959	135	81	3.0627	0.795	0.251	3.858	5.64	3.86	7511	1

TABLE 61

4-COOLED THRUST CHAMBER PERFORMANCE

Flowrates			Mixture Ratios											Based on P_c				
, lb/sec	Film Coolant, lb/sec	$\dot{W}_T$, lb/sec	Injector o/f	Overall o/f	c^*, ft/sec	C_F	I_s, seconds	η_{C_F}	η_{I_s}	Nozzle Area Ratio	Oxidizer-to-Fuel Momentum Ratio	Oxidizer Injection Velocity, ft/sec	Fuel Injection Velocity, ft/sec	η_{c^*} (By Heat Balance)	η_{c^*} (After Film Coolant Shutoff)	η_{c^*} (With Film Coolant Flowing)	Throat Peak Heat Flux, Btu/in.^{2}-sec	Comments
										3.5:1								
2		2.556	5.28			1.436					0.2043	80	2067				7.6	
5		3.401	4.94			1.452					0.2490	106	2104				14.2	Coolant water leaked into chamber
9		4.052	5.16			1.456					0.3100	126	2095				16.4	
7		4.684	5.81			1.468					0.4427	149	1955					Nozzle throat eroded
1	0.438	6.001	6.89	4.26	7363	1.483	339				0.6752	180	1837	0.985			20.0	
7	0.443	6.152	7.07	4.36	7286	1.490	337				0.4645	141	2146	0.981			23.2	
5	0.400	6.434	8.05	5.05	6958	1.505	324				0.6947	142	1646	0.965		0.884	26.4	
3	0.159	3.062	6.19	4.44	6952	1.452	313				0.2179	68	1929	0.913	0.907	0.870	30.6	
4	0.132	1.696	5.74	3.66	7915	1.441	314				0.1182	52	2526	0.912	0.896	0.820	20.7	
9	0.454	6.135	6.87	4.55	7148	1.536	341				0.6032	192	2188	0.955		0.892	20.7	IR&D funded
9	0.135	1.289	4.55	2.74	7839	1.363	333				0.0437	28	2931	0.979	0.969	0.959	17.4	
2	0.133	1.369	5.54	3.23	7562	1.377	323				0.0676	32	2621		0.977		19.4	
5	0.238	3.902	6.08	4.16	7431	1.466	341				0.2329	91	2377	0.977		0.939		
0	0.128	3.766	6.11	4.88	7561	1.460	343				0.2261	89	2404	0.988		0.958		
7	0.365	6.762	8.13	5.35		1.523					0.6228	159	2075					Nozzle throat eroded
			6.14			1.354							2100				22.1	Igniter malfunction
2	0.199	2.583	5.12	3.39		1.455					0.1121	58	2650	0.957	0.977	0.944	31.6	
3	0.194	2.811	6.93	4.37		1.454					0.2010	65	2240	0.986	0.991	0.959	34.7	
3	0.147	1.263	3.90	2.37		1.371					0.0363	25	2677	0.944	0.984	0.916	16.4	
7	0.150	1.213	5.03	2.71	7714	1.357	325				0.0533	25	2358	0.979	0.974	0.925	17.5	
0	0.202	2.526	5.24	3.40	7503	1.440	336				0.2138	59	1445	0 953	0.976	0.933	30.8	
8	0.385	5.973	5.72	3.32	7567						0.4193	99	1350	0.973		0.936	38.3	
8	0.172	2.329	5.12	3.44	7923	1.431	352				0.1741	71	2086	1.004	0.990		28.3	
8	0.206	2.214	4.68	2.95	8026	1.426	355				0.1470	67	2130	1.002	0.997		27.0	
2	0.402	3.492	5.39	3.02	7824	1.457	334				0.2964	107	1946	0 998			35.8	
2	0.445	4.887	5.16	3.19	7941	1.439	360				0.3596	145	2080	1.002			36.8	
8	0.437	5.671	6.39	3.96	7620	1.472	348				0.5955	171	1835	1.002			40.8	Sequence malfunction
		3.426	5.39			1.340							2082		0.984			
		2.999	5.88			1.432							1447		0.975			
9		3.231	4.59			1.428					0.1928	81	1923					Film-coolant instrumentation error
7	0.271	6.151	6.04	4.36	7640	1.470	349				0.5068	152	1811	0.991				
9	0.251	3.858	5.64	3.85	7511	1.442	336				0.2826	93	1855	0.963				

CONFIDENTIAL

2

CONFIDENTIAL

TABLE 62

(C) 2.5K WATER-COOLED THRUST CHAMBER GAS T

Test No.	Test Date, 1966	Injector S/N	Test Duration, seconds	Ambient Pressure, psia	A_t, sq in.	Thrust, pounds	Temperatures			Pressures						Flowrates					Mixture Ratio	
							Oxidizer Inlet, F	Fuel Inlet, F	Film Coolant, F	Oxidizer Inlet, psia	Fuel Inlet, psia	Film Coolant, psia	Throat Stagnation Pressure, psia	Fuel Injection ΔP, psi	LOX Injection ΔP, psi	Oxidizer, lb/sec	Fuel, lb/sec	Film Coolant, lb/sec	Tapoff (Total), lb/sec	$\dot{w}_T$, lb/sec	Injector, o/f	Overall o/f
083	7-18	1-3B	1.2	13.80	0.940	360	-272	99			384		274	118		0.980	0.200			1.180	4.61	
084	7-18		0.8			369					381		285	146		1.147	0.272			1.419	5.96	
085	7-18		1.4			400				321	349		304	95	17	1.236	0.261			1.497	6.16	
086	7-18		1.4			572		93		466	600		440	160	28	1.561	0.299			1.860	5.22	
087	7-18		1.2			822		94		675	784		615	169	56	2.160	0.374			2.534	5.78	
088	7-21		1.3			410		95		349	410		317	93	32	1.173	0.200			1.373	5.87	
089	7-21		1.7			830		95		679	802		609	193	70	2.093	0.394			2.489	5.32	
090	7-22		1.5			547		95		449	539		412	127	37	1.481	0.268			1.683	5.45	
091	7-22		1.7			505		97		415	515		387	128	28	1.380	0.254			1.574	5.20	
092	7-22		1.8			679		99		551	662		506	156	45	1.787	0.317			2.104	5.63	
093	7-27		1.3			764		89		772	880		685	195	87	2.363	0.414			2.777	5.72	
094	7-27		1.4			929		89		764	920		678	242	86	2.284	0.460			2.744	4.96	
095	7-27		1.3		0.950	957		87		792	859		688	171	104	2.528	0.388			2.916	6.52	
096	7-27		1.4		0.950	924		87		755	868		668	200	87	2.400	0.418			2.818	5.74	
097	7-29		1.8		0.880	866		77		782	899		705	194	77	2.168	0.325			2.493	5.19	
098	7-29		1.8			856		77		779	937		698	239	81	2.104	0.461			2.565	4.52	
099	7-29		1.9			892		77		814	867		709	196	105	2.385	0.380			2.765	6.28	
133	8-31	4-2A	2.2		0.925	401		71		334	445		326	119	8	1.072	0.237			1.308	4.53	
134	8-31		2.5			411		71		338	450		330	120	8	1.095	0.236			1.330	4.60	
135	8-31		1.8			470		71					333			1.190	0.187			1.379	6.41	
136	9-31		2.4			1261		74		1031	1226		969	257	62	2.979	0.500			3.479	4.97	
137	8-31		2.6			1264		72		1066	1140		988	152	72	3.281	0.500			3.791	6.58	
138	9-1	4-2B	1.7			460		74					324			0.937	0.214			1.370	5.33	
139	9-1	4-2B	1.6			1239		64		1030	1191		966	225	64	3.052	0.584			3.636	5.23	
140	9-6	4-2C	1.9			490		74					334			1.171	0.211			1.382	5.52	
141	9-6	4-2D	2.0			372		77		329	392		319	73	10	1.019	0.209			1.228	4.80	
142	9-6	4-2E	1.6			373		77		322	387		315	72	7	0.935	0.210			1.145	4.45	
143	9-6	4-2E						67								5.513	0.207					
144	9-6	4-2F	1.8			448		71		343	374		326	48	17	1.150	0.208			1.387	5.68	
169	9-25	4-2G	1.5			442		71					324							1.[illegible]	4.14	
170	9-26		1.3			413		71		346	391		341	50	5	1.042	0.192			1.234	5.43	
171	9-26		1.3			461		73		385	420		378	42	7	1.1726	0.377	0.188	0.022	1.550	6.21	3.20
172	9-26		1.3			813		77		668	739		645	94	23	1.877	0.663	0.315	0.039	2.540	5.39	2.93
173	9-26		1.2			1100		76		925	941		871	70	54	2.651	0.838	0.442	0.053	3.489	6.70	3.29
174	9-26		1.3			487		83		403	431		397	34	6	1.265	0.368	0.187	0.230	1.633	6.98	3.54
175	9-28	4-2G	1.3		0.925	377		83			366		316	50		0.960	0.389	0.207	0.018	1.349	5.27	2.52
176	9-28		2.3			377		84			364		316	48		0.910	0.394	0.210	0.018	1.304	5.07	2.36
177	9-28		2.3			378	-286	85		318	368		316	52	2	0.917	0.791	0.212	0.018	1.308	5.09	2.38
178	9-28		2.4			390	-287	83		325	371		321	50	4	0.952	0.376	0.199	0.019	1.328	5.35	2.59
179	9-28		2.4			385	-289	82		322	369		315	54	7	1.122	0.188	0.000	0.018	1.310	6.27	6.31
180	9-28		1.1			2005	-298	82		1724	1763		1581	182	143	4.582	1.696	0.918	0.094	6.278	5.90	2.78
181	9-30		0.7			1377	-286	74		1124	1323		1068	255	56	2.749	1.419	1.109	0.060	4.168	3.95	1.97
182	9-30		1.0			1657	-266	76		1399	1529		1308	221	91	3.507	1.595	1.064	0.071	5.102	6.60	2.23
183	9-30		1.0			1662	-281	79		1515	1710		1416	294	99	3.824	1.747	0.878	0.076	5.571	4.40	2.21
184	10-3		1.5			402	-282	64		338	462		335	127	3	0.895	0.420	0.297	0.018	1.315	7.29	2.16
185	10-3		2.2			390	-272	65		334	476		330	146	4	0.820	0.129			0.949	6.36	
200	10-26	6-1B	1.4		0.980	371	-285	67		306	374		292	82	14	0.962	0.238			1.200	4.05	
201	10-26	6-1C	1.6			387		72			371		299	72		1.008	0.235			1.243	4.28	
202	10-26	6-1D	1.5			366	-259	77		307	360		288	72	19	0.976	0.236			1.212	4.13	
203	10-26	6-1D	1.6			1235	-266	63		978	1011		868	143	110	3.220	0.559			3.349	5.94	
204	10-26	6-1D	1.6			1876	-271	85		1565	1469		1285	184	280	5.218	0.745			5.963	7.00	

TABLE 62

ED THRUST CHAMBER GAS TAPOFF SUMMARY

Flowrates			Mixture Ratio		Based on P_c					Nozzle Area Ratio	Oxidizer-to-Fuel Momentum Ratio	Oxidizer Injection Velocity, ft/sec	Fuel Injection Velocity, ft/sec	Tapoff Temperature °F	Throat Peak Heat Flux, Btu/in.^{2}-sec	Comments
Film Coolant, lb/sec	Tapoff (Total), lb/sec	$\dot{w}_T$, lb/sec	Injector, o/f	Overall, o/f	c^*, ft/sec	C_F	I_s, seconds	η_{c^*}	η_{I_s}							
		1.128	4.61			1.398				3.5:1	0.0678	38	2582			
		1.459	5.96			1.377									13.1	Data unstable, no tapoff temperatures or pressures
		1.437	6.16			1.400									13.2	
		1.860	5.22			1.383					0.1275	59	2446		22.8	No tapoff temperatures or pressures
		2.534	5.78			1.422					0.2129	82	2226		30.5	
		1.573	5.87			1.376							2269		13.5	No tapoff temperatures, tapoff temperatures decayed during
		2.489	5.32			1.450					0.1812	80	2348		30.5	No tapoff pressure, tapoff temperature out of instrument ra
		1.685	5.45			1.412							2290		19.6	No tapoff pressure, tapoff temperature decayed
		1.574	5.28			1.388					0.1124	51	2359		19.6	
		2.104	5.63			1.428					0.1702	69	2282		25.2	No tapoff pressure
		2.773	5.72			1.497					0.2427	93	2192		28.8	
		2.744	4.96			1.438							2427		32.7	
		2.956	6.32			1.464					0.3144	99	2053		35.3	Tapoff temperatures out of instrument range, no tapoff pressure
		2.918	5.74			1.458							2253		33.8	
		2.595	5.16			1.395					0.1996	84	2146		14.2	
		2.565	4.32			1.394					0.1597	82	2320		13.1	
		2.765	6.28			1.430					0.3062	94	1928		14.2	
		1.305	4.53			1.330					0.0752	41	2468			Excessively low tapoff temperatures
		1.730	4.60			1.346					0.0789	42	2249			
		1.579	6.41			1.526						45				
		3.579	4.97			1.407					0.2523	113	2226			
		3.791	6.58			1.383					0.4399	124	1855			
		1.570	5.43			1.534						36				
		3.696	5.23			1.387					0.2926	118	2109			Tapoff temperatures greater than 2300 F
		1.382	5.32			1.586						45				
		1.228	4.88			1.261					0.0934	41	2142			
		1.143	4.45			1.280					0.0795	38	2126			
												243				
		1.587	5.66			1.485					0.1596	47	1913			Tapoff temperatures out of instrument range
		1.124	4.14			1.475										
		1.254	5.43			1.309					0.1280	42	1782			
0.188	0.022	1.550		3.20	7302	1.318	299	0.976			0.0931	48	3201	1185		
0.315	0.039	2.540	5.39	2.95	7546	1.363	320	0.980			0.1229	76	3332	1116		
0.442	0.053	3.489	6.70	3.29	7271	1.365	308	0.992			0.2267	108	3192	947		
0.187	0.230	1.633	6.98	3.54	7081	1.326	288	0.971			0.1166	51	3052	1294		
0.207	0.018	1.349	5.27	2.52	6900	1.290	276	0.893					3971	1282		
0.210	0.018	1.304	5.07	2.36	7258	1.290	291	0.926					4655	1265		
0.212	0.018	1.308	5.09	2.38	7066	1.295	284	0.909			0.0471	37	3999	1295		
0.199	0.019	1.328	5.35	2.59	7579	1.314	301	0.958			0.0538	38	3779	1427		
0.500	0.018	1.510	6.27	6.51	7147	1.321	295	0.950			0.1473	45	1915	1326		
0.918	0.094	6.278	5.90	2.78	7172	1.371	305	0.940			0.2834	177	3685	1570		
1.109	0.060	4.168	5.95	1.97	8717	1.394	377	0.824			0.1015	110	4289	2014		
1.064	0.071	5.102	6.60	2.23	7368	1.370	313	0.991			0.2379	146	4050	1760		
0.878	0.076	5.571	4.40	2.21	7778	1.376	332	0.962			0.1648	154	4112	2010		
0.297	0.018	1.315	7.29	2.16	7400	1.297	298	1.040			0.0704	36	3725	1915		
		0.949	6.36			1.278					0.1882	34	1149			Injector rotated 180 degrees, tapoff thermocouple destroye
		1.200	4.05			1.296					0.0525	31	2391			Oxidizer-rich tapoff
		1.243	4.28			1.321							2218			Oxidizer-rich tapoff
		1.212	4.13			1.297					0.0629	34	2231			Fuel-rich tapoff
		3.849	5.94			1.432					0.3526	110	1853			
		5.965	7.00			1.490					0.6945	170	1714			

2

(C) Seven hot-firing tests were then performed with this injector to evaluate the face-cooling capability of this modified strip. Maximum duration was 3 seconds at 600 psia and maximum chamber pressure was 1500 psia for 0.400 second. No apparent damage resulting from any of these tests. A postfiring view of the injector is shown in Fig. 184.

(C) A 1-second checkout test was conducted in the 2.5K segment hardware on segment injector S/N 6-7A, which incorporated two strips which were hand-brazed into the body. This modification was used to replace the TIG braze repair made at the Nevada Field Laboratory and was accomplished after completion of the solid-wall tests. The test was conducted at 1450-psia chamber pressure and 5.0 mixture ratio. Post-test inspection revealed no damage.

Analysis of Results

(U) Injector Performance Data. One of the major program objectives was injector performance. The parameter which is proportional to combustion performance, and therefore proportional to injector performance, is characteristic velocity. Experimental values of characteristic velocity were obtained by two calculations, therefore, good agreement between the two calculated results provided a measure of confidence in the results. Specifically, characteristic velocity was calculated from measured chamber pressure and from measured thrust.

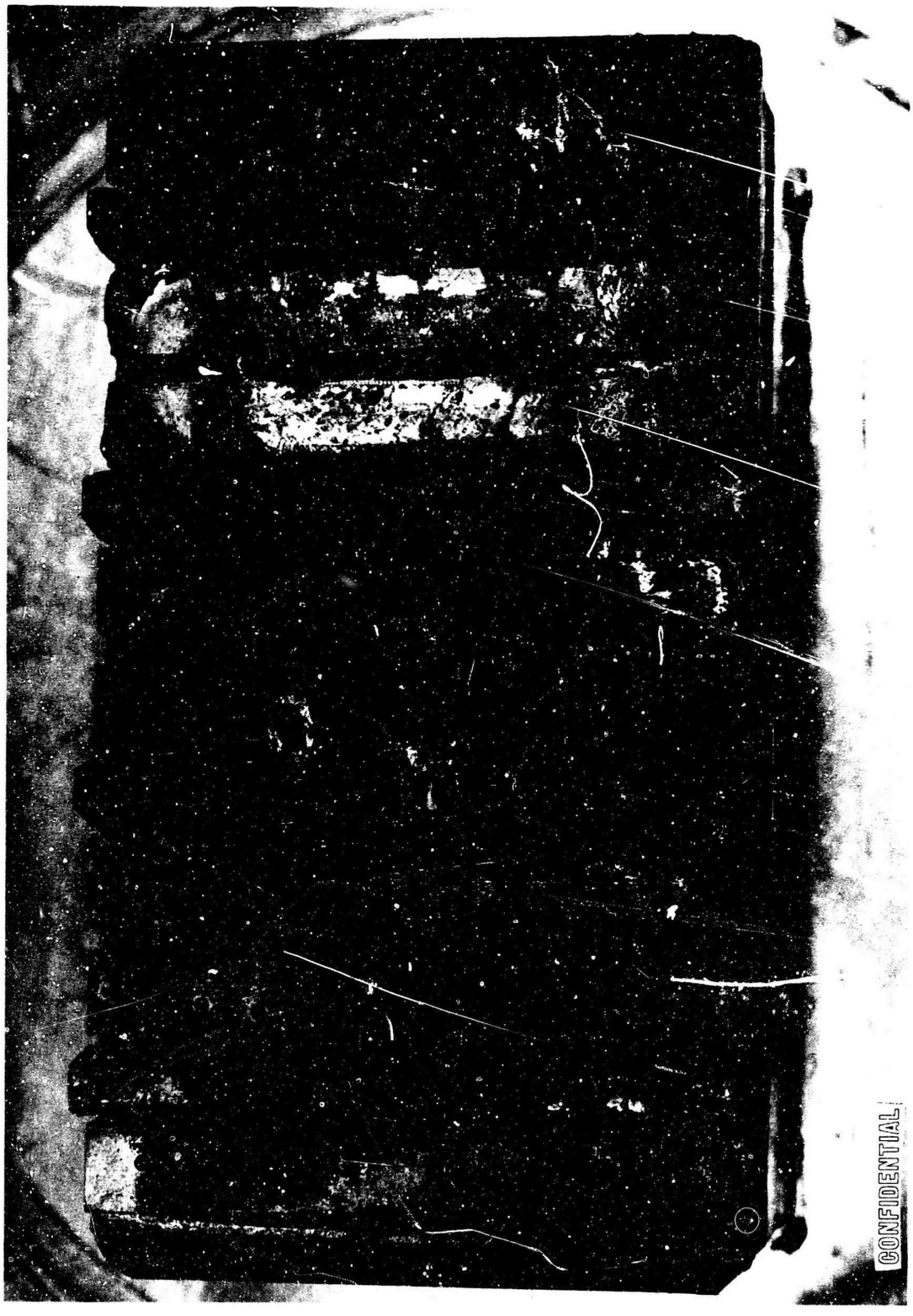

5AA36-4/10/67-S1B

Figure 184. 2.5K Segment Injector Modified to Duplicate the Repair Made to the 250K Injector

(U) The calculation of characteristic velocity from chamber pressure was accomplished by use of

$$c^* = \frac{P_c A_t g}{\dot{w}} \eta_2 \qquad (1)$$

where

P_c = nozzle throat stagnation pressure

A_t = physical nozzle throat area

g = 32.2 lbm-ft/lbf-sec^2

$\dot{w}$ = total propellant flowrate

η_2 = factor to account for performance decrease due to heat transfer, friction, nozzle discharge coefficient, and change in throat area due to thermal effects.

(U) Characteristic velocity was calculated from measured thrust by using the following expression:

$$c^* = \frac{\left[\frac{F}{\dot{w}}\right]}{\left[C_{F_{vac}} - \frac{P_a}{P_c}\epsilon\right]} \eta_1 \qquad (2)$$

where

F = thrust (measured)

$\dot{w}$ = total propellant flowrate (calculated)

$C_{F_{vac}}$ = vacuum nozzle thrust coefficient (theoretical)

η = factor to account for thrust decrease resulting from friction, heat transfer, and nozzle divergence

P_a = local ambient pressure

ϵ = expansion area ratio

P_c = nozzle throat stagnation pressure

(U) It has been shown (Ref. 7) that characteristic velocity as calculated from Eq. 1 and 2 will agree to within 1 percent in a well-managed experiment.

(U) Precision. Achievement of precise performance values is directly dependent upon the instrumentation precision. An analysis was made to determine the instrumentation precision that would be required for attainment of 0.5-percent precision (standard deviation) in experimental performance. Sensitivity analysis techniques (Ref. 8) were applied to fuel flowrate, total flowrate, mixture ratio, specific impulse, and characteristic velocity.

(U) Values of measurement precision were assumed on the basis of past experience with the instrumentation in the test area. Precision values of 1.0 percent in pressure, 1.5 percent in temperature, 0.5 percent in thrust, and 0.25 percent in oxidizer flowrate were taken to be representative of experimentally achievable values. Utilization of the aforementioned precision values in a sensitivity analysis showed that the resultant precision in fuel flowrate, mixture ratio, specific impulse, and characteristic velocity from thrust would be 1.06, 0.06, 0.55, and 0.60 percent, respectively. A similar analysis conducted to determine the standard deviation in characteristic velocity calculated from chamber pressure showed that the precision in characteristic velocity would be 1.08 percent.

(U) Based upon these results, calibration precisions of 0.5 percent in thrust, 0.25 percent in oxidizer flowrate, and 1.0 percent in pressure at

the 95-percent confidence level was specified so that achievement of precise thrust chamber performance was assured.

(U) Monitoring Techniques. Instrument calibrations were monitored to ensure that the forementioned precision levels were achieved. This was accomplished by use of the Rocketdyne Random Walk measurement analysis program. In this analysis program, it was assumed that the input/output ratio for a sensor at a particular input level performs a random walk in time which has a normal distribution and variance. It assumed also that there was a random measurement error in the observed data which was independent of the random walk and which was also normally distributed. The output from this analysis program included a decision, based upon the calculated coefficient of variation and a prescribed precision limit, as to whether the sensor should be used as is, recalibrated immediately, or discarded.

(U) The use of the Beckman system in conjunction with the IBM 7094 system ensured accurate and rapid data reduction with the option of selecting more than one time slice during a test for reduction. The Beckman system is an on-line digital data acquisition system that records test data on magnetic tape. These data on magnetic tape are retrieved by the IBM 7094 system and data are then presented in engineering units. The data reduction program computed specific impulse and characteristic velocity from thrust and chamber pressure.

(U) Performance Data Analysis. Because the purpose of evaluating characteristic velocity efficiency was to compare various injection patterns such that the most efficient would be selected for the 250K injector, those physical effects that cause thrust chamber performance to deviate from ideal theoretical performance must be properly taken into account during data analysis. These effects were calculated and properly combined to obtain the values for η_1 and η_2 in Eq. 1 and 2 . These various effects were taken into account as follows.

(U) Stagnation Pressure Loss. Measured injector end static pressure was adjusted for stagnation pressure by using the Rayleigh criterion (Ref. 9) which is a function of contraction ratio, specific heat ratio, and nozzle entrance Mach number. The stagnation pressure loss factor was

$$\eta_{Po} = 0.9953$$

(U) Friction. A potential flow and boundary-layer analysis was used to obtain the skin friction coefficient from which the frictional drag force was computed. The integral momentum boundary-layer equation, in conjunction with a skin friction correlation (Ref. 10) was used to evaluate the frictional drag. The friction influence coefficient was given by:

$$\eta_{\tau} = 1.0135$$

(U) The dependence of η_{τ} on chamber pressure and mixture ratio is shown in Fig.185.

(U) Heat Transfer. In a water-cooled thrust chamber, the heat transferred to the coolant water is lost and not available for conversion to directed velocity. This heat loss results in a reduction of combustion gas temperature and, consequently, the delivered performance is less than the ideal thermodynamic performance. The influence of heat loss on performance was calculated by using a modified theoretical thermodynamic propellant performance program that accounts for heat transfer in the energy balance. A heat flux profile typical of the experimentally determined heat flux profile was employed. The performance calculations with heat loss are made incrementally so that the effect of spatially distributed heat transfer on the flow field properties is calculated and, thereby, the effect of heat loss on performance is calculated. These heat loss influence

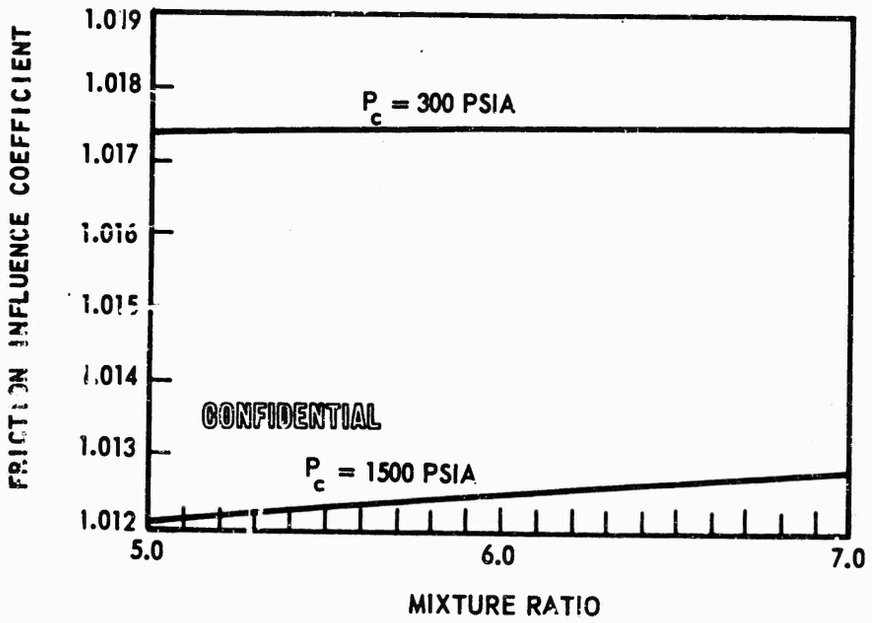

Figure 185. Influence Coefficient to Account for Effect of Frictional Drag on Thrust

coefficients are:

$$\bar{\eta}_{H.L.}(c^*) = 1.0078 \quad (5)$$

and

$$\bar{\eta}_{H.L.}(F) = 1.0095 \quad (6)$$

(U) Nozzle Throat Area Change. Nozzle throat area during a test is different from the nozzle throat area before or after a test. During a test, there are pressure loads acting on the internal nozzle surface upon which thermal effects due to the increased wall temperature (as the result of heat flux) are superimposed. In the 2.5K water-cooled thrust chamber, the hardware is sufficiently massive so that the effect of internal pressure loads is negligibly small compared to the thermal effects. Due to the heat flux, the nozzle throat area is less than in the cool pretest condition. The influence coefficient for nozzle throat area change due to thermal effects is shown in Fig. 186 and the nominal value is:

$$\bar{\eta}_{TH}(A_t) \quad 0.980 \quad (7)$$

(C) The value given in Eq. 7 is based on an elastic-plastic strain analysis which showed that the average value of 0.980 when applied at all chamber pressures between 300 and 1500 psia (Fig. 186) yields less than a 1 percent difference over the chamber pressure range which is less than the error in calculating c* from test data.

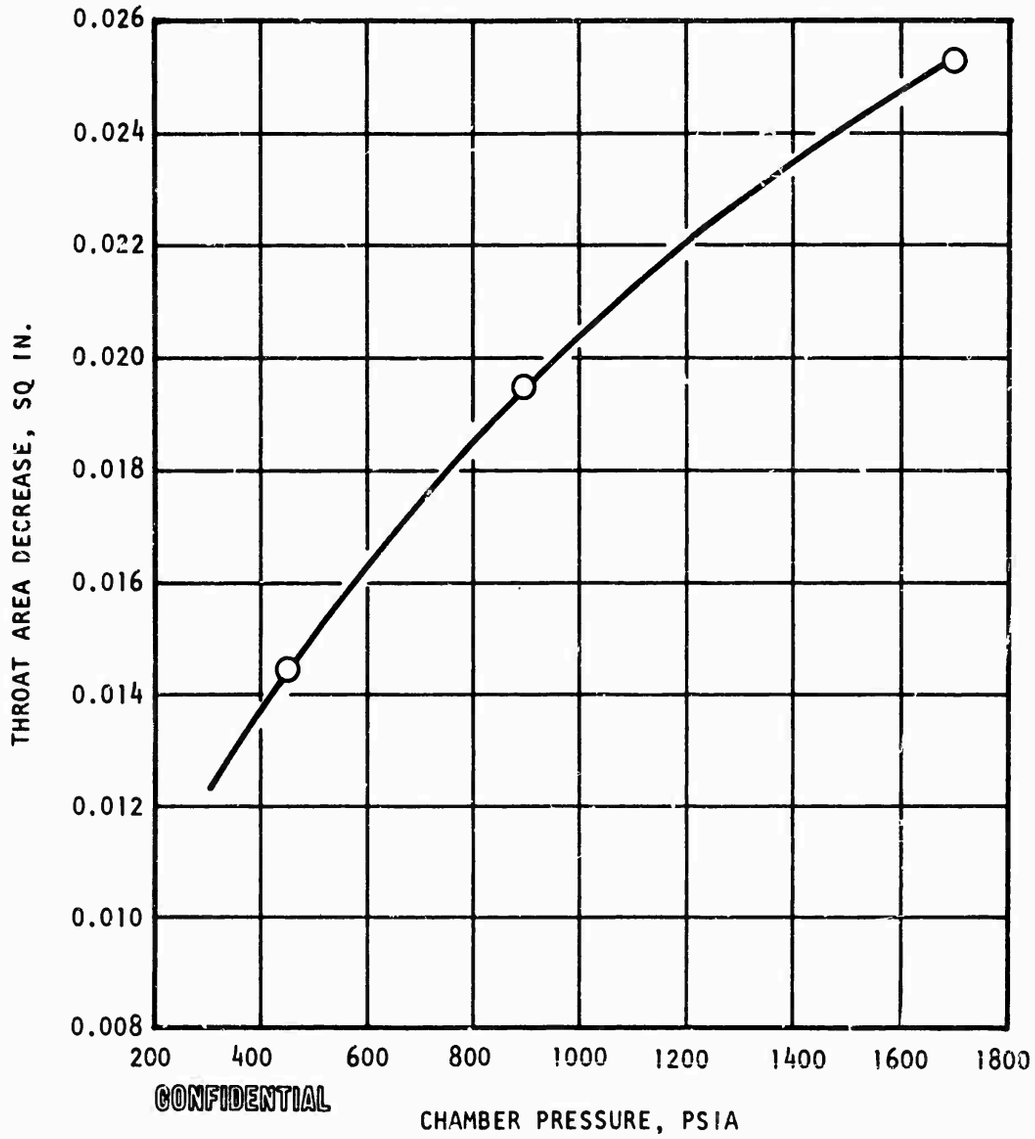

Figure 186. Throat Area Decrease vs Chamber Pressure for 2.5K Copper Nozzle

(U) Nozzle Divergence. Nozzle divergence losses were evaluated by comparing two-dimensional axisymmetric thrust coefficient with the ideal one-dimensional nozzle thrust coefficient. The two-dimensional nozzle thrust coefficient was computed by a method of characteristics analysis which utilizes variable flow field properties and the internal contour of the nozzle used on the thrust chamber. By definition, the thrust coefficient is given by:

$$C_F = \frac{F}{P_o A_t} \tag{8}$$

where

C_F = thrust coefficient

F = thrust

P_o = nozzle throat stagnation pressure

A_t = nozzle throat area

It should be noted that this definition applies to one-dimensional as well as to two-dimensional flow. Because the axial component of thrust is less for two-dimensional diverging flow than for ideal one-dimensional flow, the two-dimensional thrust coefficient is less than the ideal one-dimensional thrust coefficient and this difference is the nozzle divergence loss. This may be seen as follows:

$$\Delta C_F = C_F\ (1\text{-D}) - C_F\ (2\text{-D}) \tag{8a}$$

where

ΔC_F = thrust coefficient difference

$C_F\ (1\text{-D})$ = one-dimensional thrust coefficient

$C_F\ (2\text{-D})$ = two-dimensional thrust coefficient

Utilizing Eq. 8 in Eq. 8a yields

$$\Delta C_F = \left(\frac{F}{P_o A_t}\right)_{(1\text{-}D)} - \left(\frac{F}{P_o A_t}\right)_{(2\text{-}D)} \tag{8b}$$

where the subscripts 1-D and 2-D refer to one-dimensional and two-dimensional, respectively. For the same nozzle throat stagnation pressure and throat area, Eq. 8b shows that the thrust loss due to two-dimensional flow is:

$$\Delta C_F = \Delta F \tag{9}$$

where ΔF is the difference between the one-dimensional and the two-dimensional thrust. This then is the divergence loss and has a numerical value of:

$$\bar{\eta}_{DIV} = 1.0110 \tag{10}$$

(U) Nozzle divergence loss dependence on chamber pressure and mixture ratio is shown in Fig. 187.

(U) Non-One-Dimensional Flow. In the linearized theory of transonic flow, the mass flow crossing the throat section is always found to be less than the critical flow corresponding to one-dimensional conditions. The ratio of the two-dimensional mass flow to the one-dimensional mass flow is the nozzle discharge coefficient. The nozzle discharge coefficient is:

$$\eta_{CD} = 0.997 \tag{11}$$

(U) These influence coefficients and the resultant average value for the influence coefficient are summarized in Table 63.

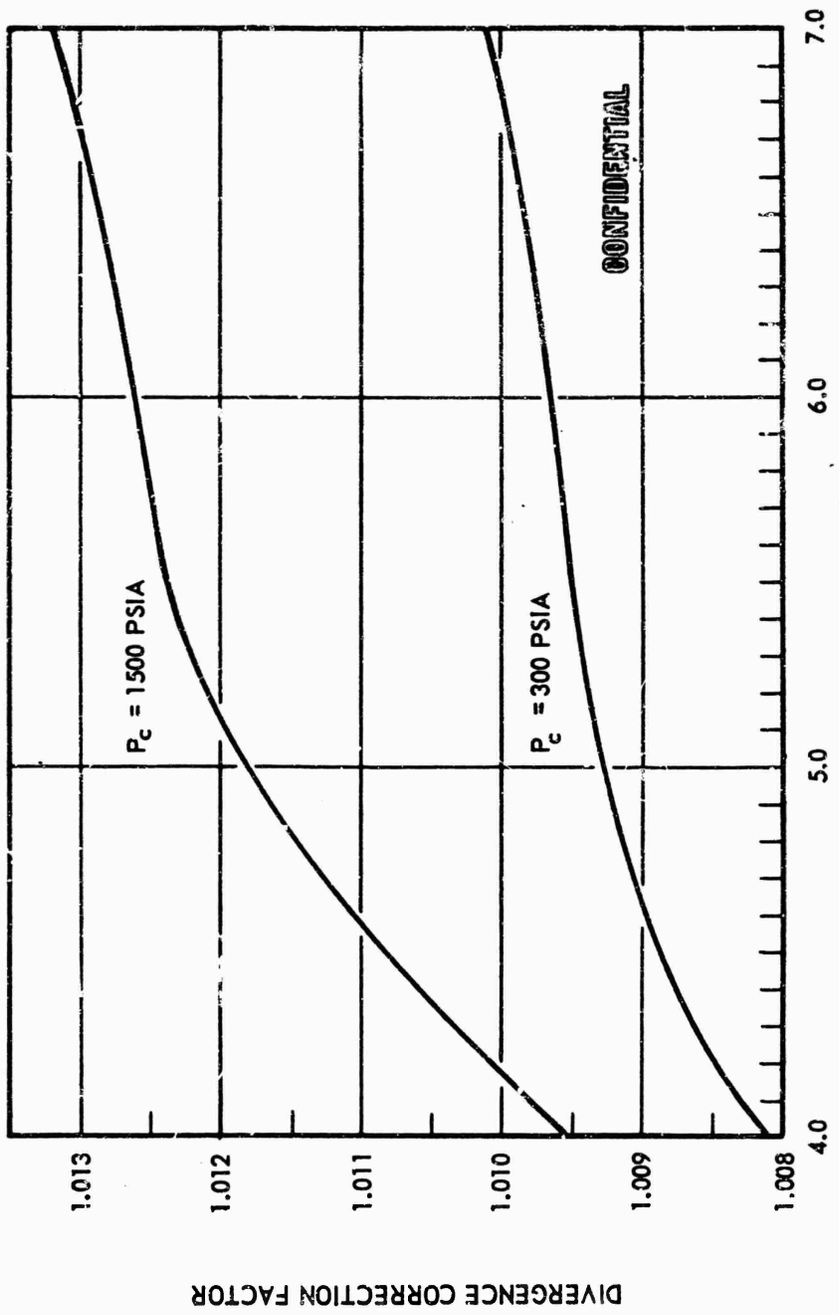

Figure 187. Divergence Correction for 2500-Pound-Thrust Chamber

TABLE 63

(C) INFLUENCE COEFFICIENT SUMMARY

Physical Effect	Influence on Experimental	
	Characteristic Velocity	Specific Impulse
Heat Loss	1.0078	1.0095
Friction		1.0135
Nozzle Divergence		1.0110
Nozzle Discharge Coefficient	0.9970	
Throat Shrinkage	0.9800	
Stagnation Pressure Loss	0.9953	
Resultant Average Value	0.9801	1.0344

(U) Selected Pattern. The triplet pattern was selected for the injectors as shown in Fig. 180. The 25OK injector is baffled into 40 compartments; each compartment contains seven injector strips.

(C) The above-described pattern and injector configuration were selected based on several considerations. Among these considerations were:

1. High performance was demonstrated in segment testing (η_{c*} above 97 percent at chamber pressure of 300 psia and above 98 percent at chamber pressure of 1500 psia) as shown in Fig.188.
2. Little sensitivity to mixture ratio was observed over chamber pressure operating range.
3. Excellent durability was demonstrated over entire operating range.

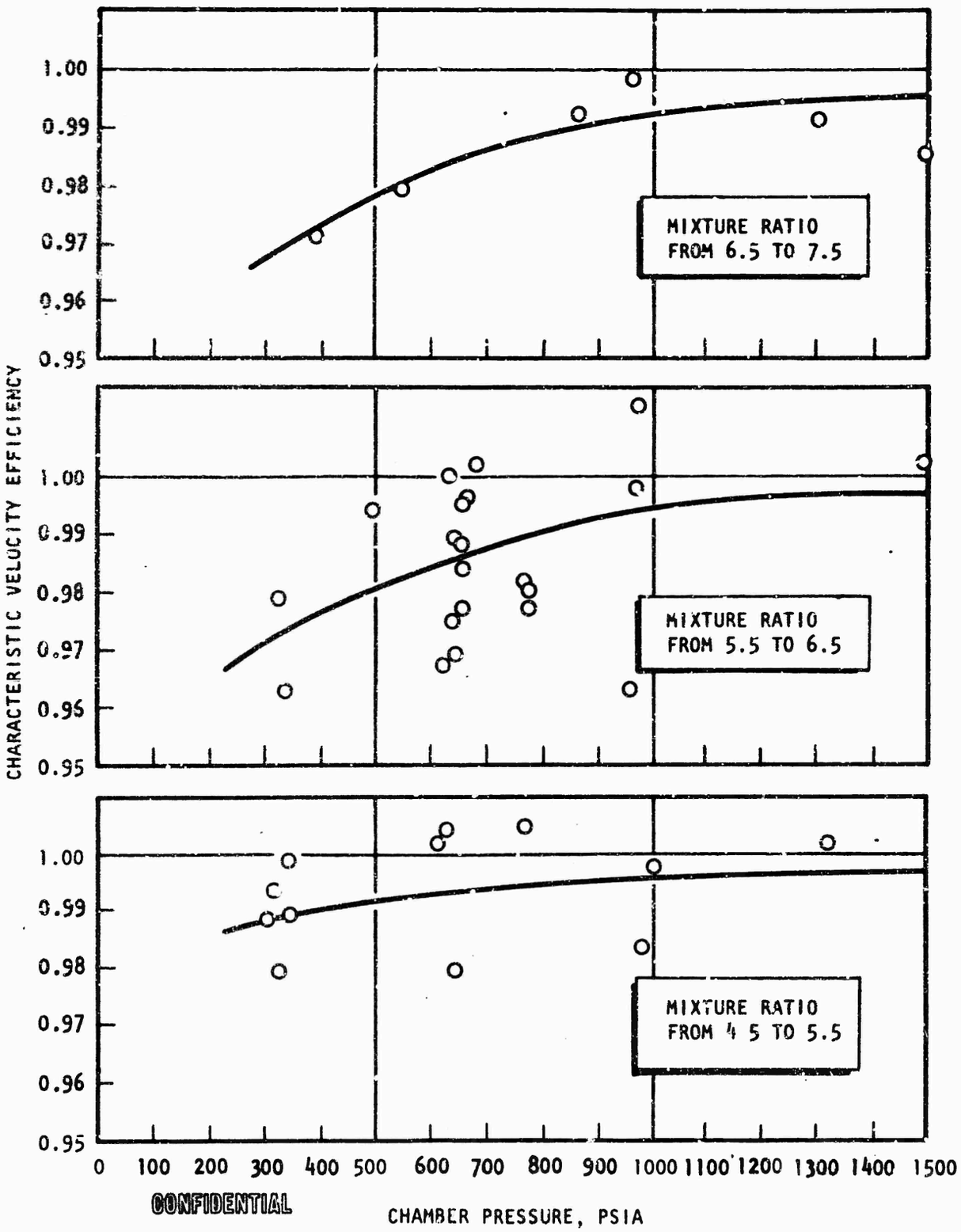

Figure 188. Triplet Injector Performance in the 2.5K Segment Thrust Chamber

4. No spontaneous combustion instability was encountered during segment testing. Several bomb tests were also conducted to verify stability characteristics; no adverse stability effects were observed.

5. Excellent injector hydraulic characteristics were demonstrated over operating range; i.e., no hydraulic flip.

6. Strip configuration lends itself to modification for tapoff bias.

7. Hot-gas ignition has been demonstrated in segment testing.

8. Simplicity of strip machining is achieved because all strips are essentially identical.

9. Strip concept permits individual strip calibration for uniform injector mixture ratio and flowrate.

(U) It should be noted that other injection patterns tested failed to exhibit all of the necessary qualities for achievement of program objectives. The reverse flow pattern had acceptable durability and stability but was slightly lower in performance than the 60 degree triplet. Buzz-type instability was encountered with the LO_2 flow pattern, thereby eliminating this pattern as a possible candidate injector.

(U) The performance of the selected pattern, and minor variations of it, is summarized on Fig.188. The effects of mixture ratio are more clearly shown for the experimental data obtained by this study of variations in chamber pressure at the hands of mixture ratio. The effect of mixture ratio is seen to be a reduction of c* efficiency at the lower chamber pressures. The values obtained indicate that, with the experimentally verified nozzle efficiency, the overall specific impulse of the aerospike thrust chamber with this injector design will meet the performance goals at both rated and throttled conditions.

(C) Film Cooled Results. It was possible to operate the water-cooled thrust chamber up to 900 psia without encountering peak throat heat flux that would exceed the burnout heat flux for this geometry. Gaseous hydrogen film coolant was utilized so that tests could be conducted up to 1500-psia chamber pressure.

(U) The film coolant was introduced normal to the combustion flow field and at a velocity, which resulted in a velocity vector parallel to the nozzle converging walls. Such an arrangement of injection with the annular throat gap was expected to lead to uniformly mixed product flow through the nozzle. The characteristic velocity efficiencies could then be calculated easily by taking into account the influence of film coolant on the thrust chamber flow field. An energy balance was made between the combustion products generated upstream from the start of nozzle convergence and the point where gaseous hydrogen was injected. This yielded a temperature that represents conditions upstream of the nozzle entrance. Characteristic velocity efficiency was taken to be proportional to the ratio of the temperature obtained from the energy balance and the adiabatic flame temperature corresponding to injector end mixture ratio and chamber pressure. The latter portion of the analysis may be shown to hold for sufficiently small variations in flow field molecular weight and specific heat ratio.

(U) Three equations were required to accomplish the data reduction. These expressions were:

$$\eta^2_{c^*_t} = \frac{T_t}{T_t \text{ (theoretical)}} \tag{12}$$

$$T_{inj} = \frac{\dot{w}_{f_c} C_{p_{f_c}} (T_t - T_f) + \dot{w}_{inj} C_{pinj} T_t}{\dot{w}_{inj} C_{pinj}} \tag{13}$$

$$\eta^2_{c^*_{inj}} = \frac{T_{inj}}{T_{inj} \text{ (theoretical)}} \tag{14}$$

(U) Application of Eq. 12 through 14 to the test data yielded the characteristic velocity efficiencies shown in Table 64. A complete description of the analytical method is presented in Appendix I. Confidence in the performance efficiencies calculated by the aforementioned method was given by comparison of characteristic velocity efficiencies with and without film coolant present during a given test. Such a comparison showed that performance efficiency calculated, as described above, differs from the nonfilm-cooled case by less than 1 percent. This excellent agreement is shown in Table 64 where the film-cooled data reduction is summarized.

(U) The high characteristic velocity efficiencies discussed above apply to an injector operating in a perfect combustion chamber. Addition of fuel film coolant at the nozzle entrance can only lower thrust chamber performance because the coolant will only have the opportunity of contributing energy that will be reflected in the characteristic velocity during transit through the converging portion of the nozzle. Because the converging portion of the nozzle has a constantly decreasing pressure and characteristic velocity is directly proportional to the pressure, the contribution to characteristic velocity by the film coolant will be less than that contributed by the same mass of fuel at the injector end. This loss in thrust chamber performance is illustrated in Fig. 189. A list of all film-cooled tests is presented in Table 64.

(C) Hot-Gas Tapoff. The feasibility of hot-gas tapoff was investigated in the 2.5K chamber segment. The objectives of the tapoff tests were to determine the dependence of chamber pressure, mixture ratio, and tapoff geometry on the tapoff temperature with several tapoff variations. The first design was a single-hole configuration and the second, a two-hole unit, both units designed for a tapoff exit velocity of a Mach number equal to 0.2 for a nominally 1500 F fuel-rich gas. The tapoff temperature as a function of chamber pressure is shown in Fig. 190 for both of these configurations. The first test results indicate an increase

TABLE 64

(C) THRUST CHAMBER PERFORMANCE SUMMARY FOR FILM-COOLED TESTS*

Test No.	Injector	Chamber Pressure, psia	Injector Mixture Ratio	η_{c^*}	η_{c^*} (After Film-Coolant Off)
105	1-3B	1494	6.85	0.985	
106	3-2A	1505	7.11	0.981	
107	4-1B	1507	8.05	0.965	
108	4-1B	724	6.97	0.913	0.907
111	3-2A	294	4.54	0.979	0.969
112	3-2A	304	5.72		0.977
113	3-2A	969	6.03	0.977	
114	3-2A	946	6.16	0.988	
117	3-2A	639	5.14		0.977
118	3-2A	650	6.93	0.986	0.981
119	3-2A	324	4.27		0.984
120	3-2A	316	5.92	0.979	0.974
121	3-2B	649	5.57	0.953	
122	3-2B	1042	5.81	0.973	
123	4-2A	615	5.63	0.990	
124	4-2A	596	5.35	0.990	

*Corrected to throat stagnation pressure condition

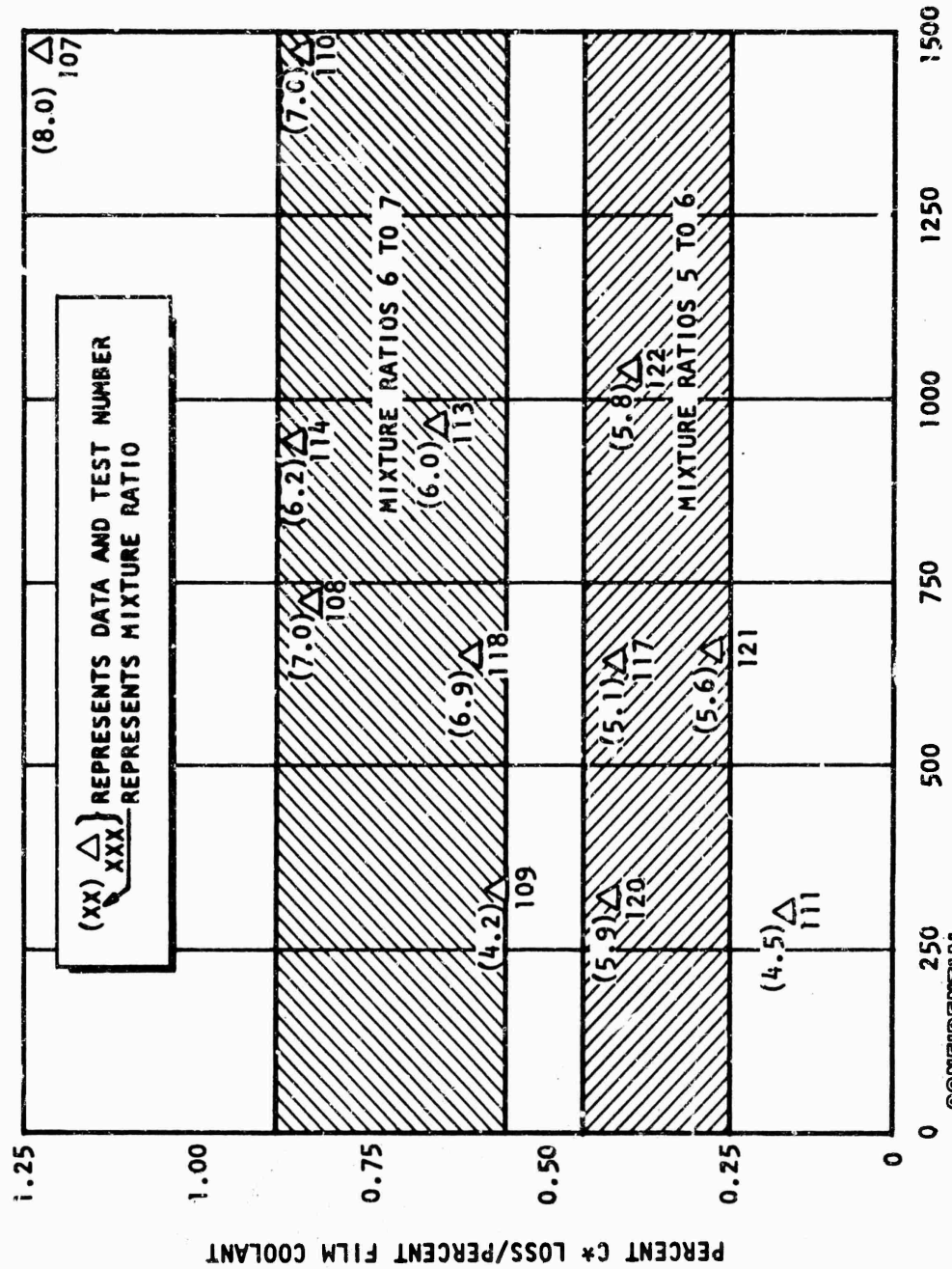

Figure 189. Effect of Chamber Pressure

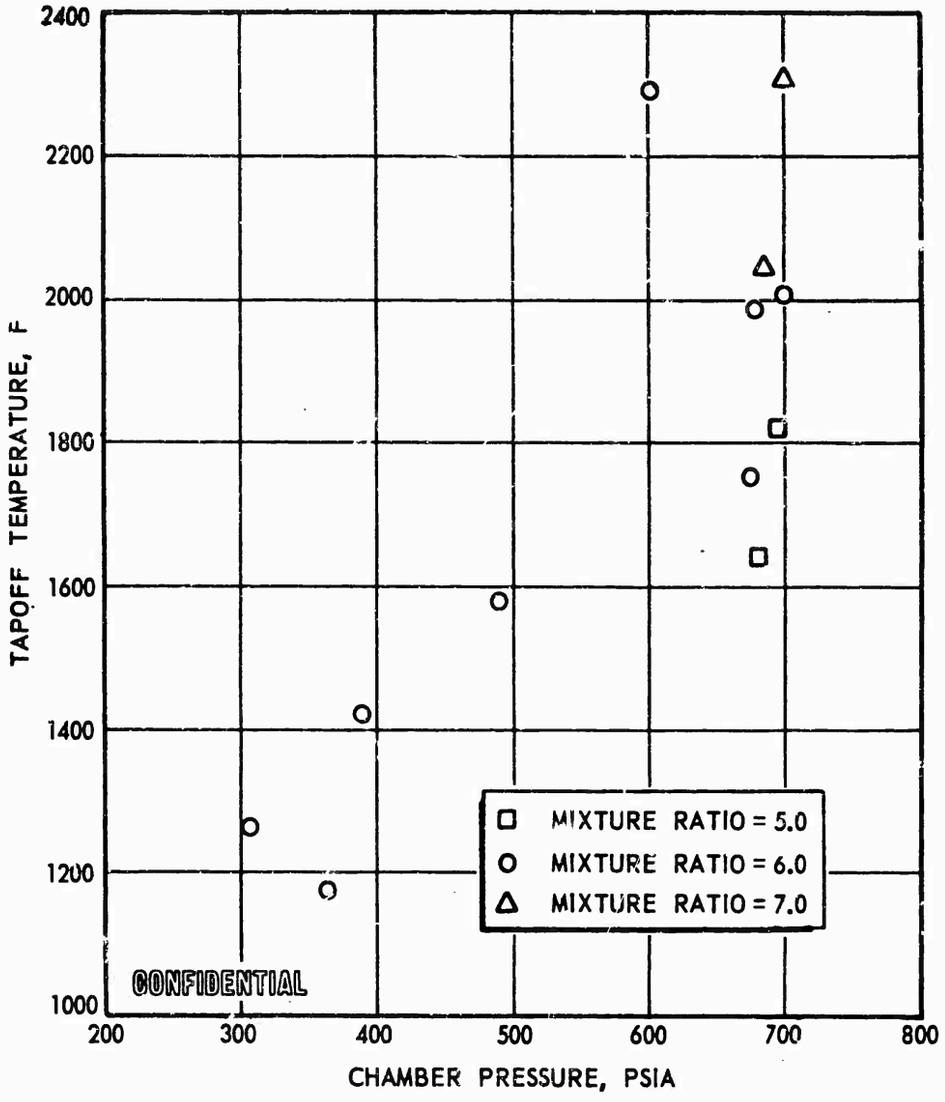

Figure 190. Measured Hot-Gas Tapoff Characteristics (2.5K Chamber)

in temperature with increasing chamber pressure and increasing mixture ratio (5 to 7). The third configuration is shown in Fig. 191. This configuration straddles the injector pattern as shown and is designed to provide for a more positive flow of fuel-rich gas than were the first two configurations. Five initial gas tapoff tests were conducted with the triplet injector pattern. These tests were 089, 091, 092, 093, and 095. Gas tapoff configuration and instrument locations for these tests are shown schematically in Fig. 192 and 193.

(U) The gas tapoff thrust chamber data reduction was accomplished in three steps. First, the oxidizer and fuel flowrate through the injector was determined. Second, the gas tapoff flowrate was calculated, and finally the net thrust chamber flowrate was calculated by taking the difference between the injector flowrate and the gas tapoff flowrate. Tapoff was evaluated as described in Appendix II.

(U) Gas tapoff flowrates were deducted from thrust chamber injector flowrates and adjusted thrust chamber performance was then determined. These data are presented in Table 60, and it may be seen that the results for tests 089, 091, and 092 are in excellent agreement with prior data for this injector. The adjusted results for tests 093 and 095 are subject to some question due to an indeterminate GN_2 purge.

(C) Later in the test program hot-gas tapoff tests were conducted with three basic modifications of an injector incorporating strips made on tooling used for 250K strips. The tapoff gas was found to be oxidizer-rich with the first modification to a standard injector (four oxidizer orifices plugged in vicinity of tapoff ports). The second modification consisted of addition of two tapoff bias orifices (0.070 inch diameter) drilled into the fuel strip to direct fuel into the tapoff ports. The tapoff temperature was 1840 F and was fuel-rich. The third modification consisted of enlarging the tapoff bias orifices to 0.0935 diameter. Finally, the number of plugged oxidizer holes was reduced to three. Tests

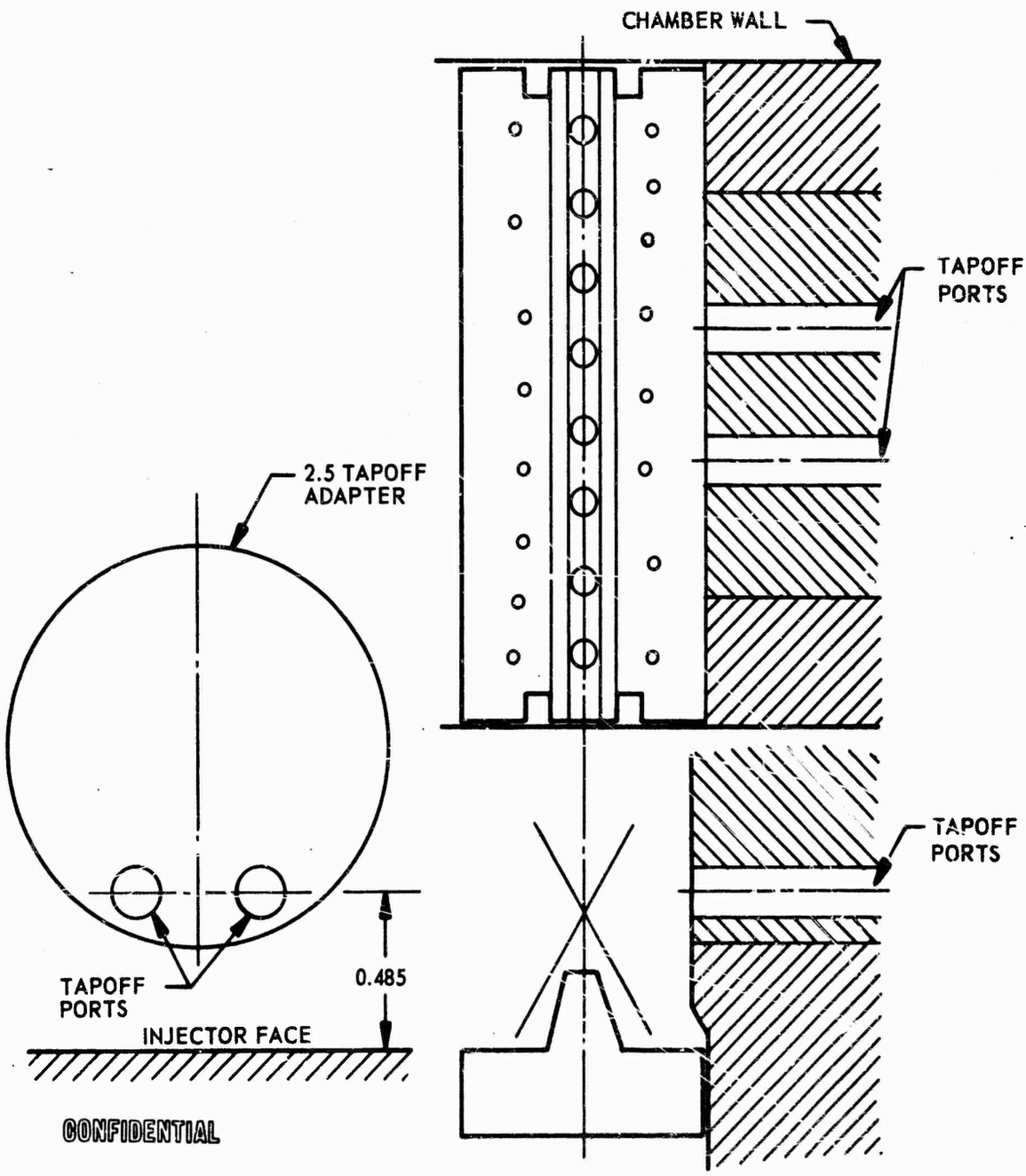

Figure 191. Simulated 250K Hot-Gas Tapoff Ports in 250K Thrust Chamber

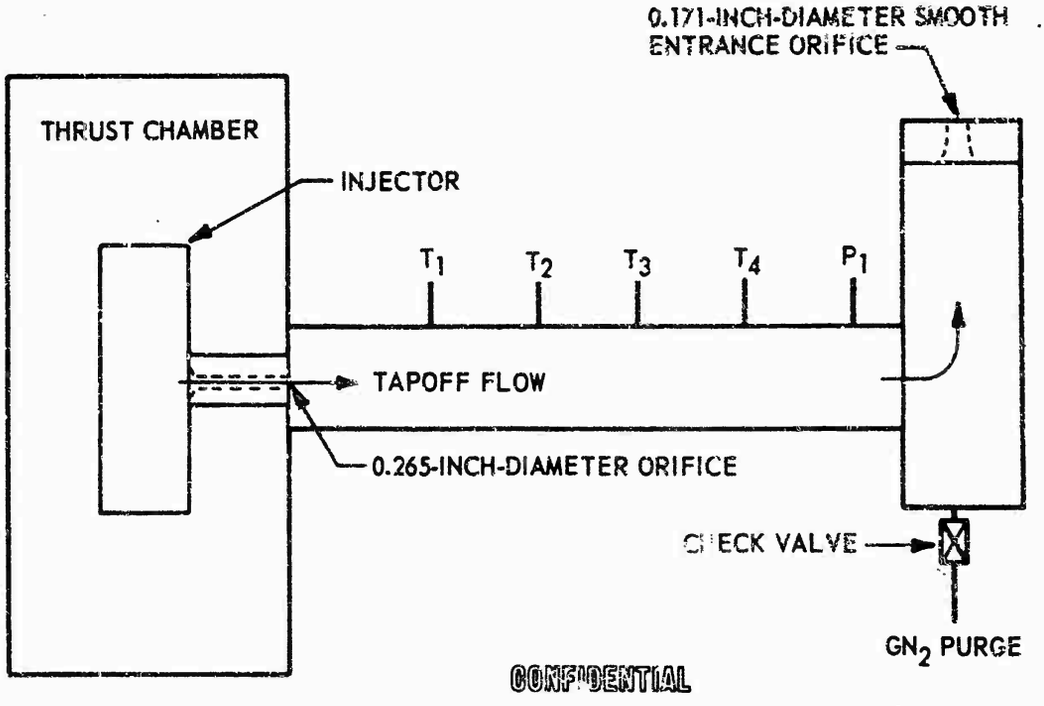

Figure 192A. Gas Tapoff Configuration for Tests 088 Through 092

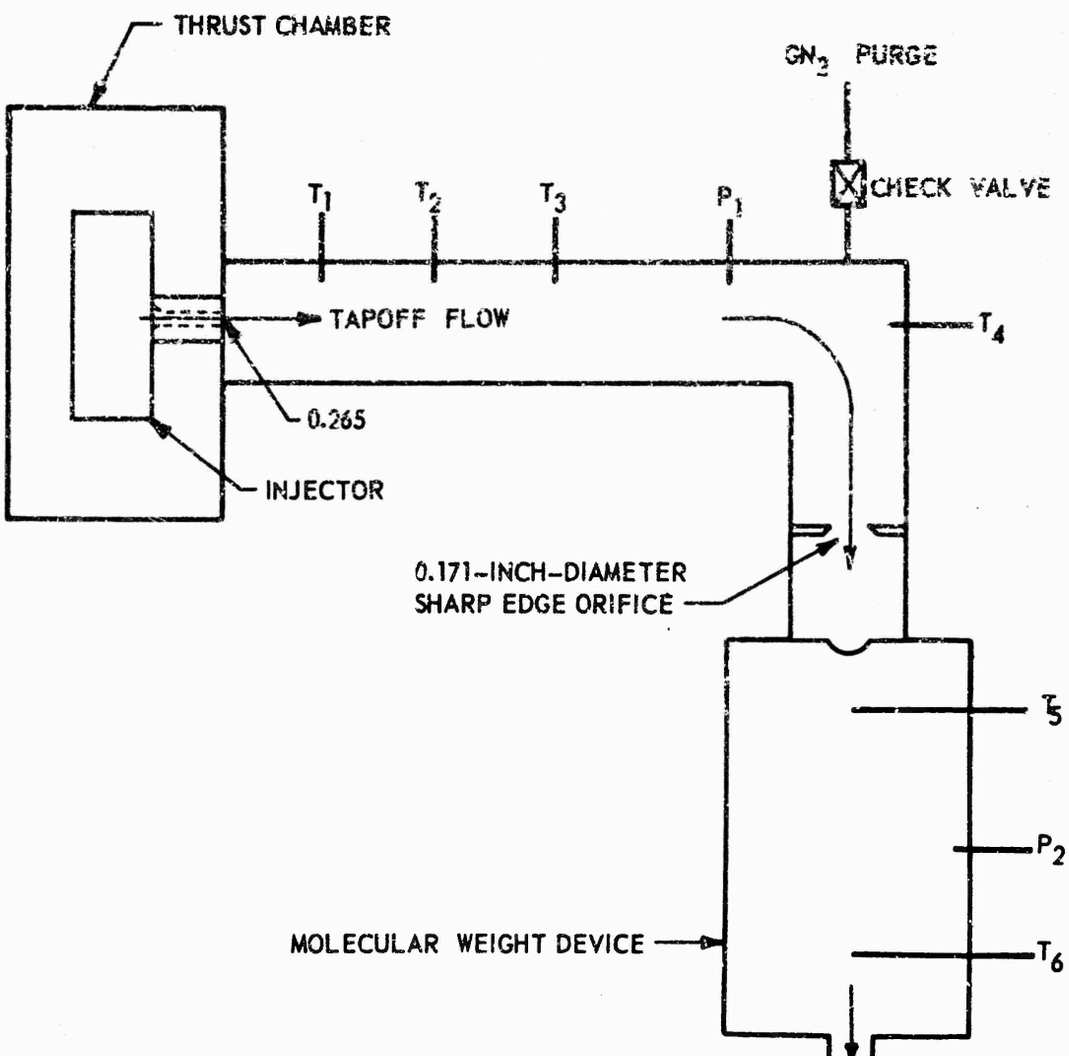

Figure 192B. Gas Tapoff Configuration for Tests 093 Through 099

were conducted over a chamber pressure range of 282 to 1290 psia. Tapoff temperature over the operating range can be expected to be between 1300 and 1600 F (Fig. 193).

(U) Two injectors were used to obtain the data shown in Fig. 193. The first injector was fabricated with strips from early experimental tooling and with four oxidizer holes plugged. The second injector was fabricated from the final 250K injector strip tooling with only three oxidizer holes plugged. (The plugged holes were reduced to three based upon geometrical examination of the tapoff port area.) The results from both injectors show that the results are corroborated and consistent, and show that the tooling effects are reproducible.

(C) The tapoff temperature appears to be fairly insensitive to chamber pressure and mixture ratio. The tapoff gas has been conclusively proven to be fuel-rich with the present injector hot-gas tapoff configuration. The technique used to determine whether tapoff gas was oxidizer-rich or fuel-rich consisted of introducing gaseous hydrogen into the tapoff duct during mainstage and measuring the resultant downstream temperature. A rise in temperature downstream of the point of gaseous hydrogen introduction indicated that the tapoff gas was oxidizer-rich, and the resultant tapoff gas mixture ratio (o/f) was moved toward stoichiometric. Conversely, a decrease in resultant tapoff gas temperature indicated that the tapoff gas was fuel-rich, and the resultant mixture ratio (o/f) was lowered.

(U) Heat Transfer Results. To obtain heat transfer data in the 2.5K solid-wall segment effort, a water-cooled chamber was utilized as described at the beginning of this section. This chamber is provided with coolant passages as shown in Fig. 194 with letter designations indicating passage location. The water flowrates into the passages are measured, and the bulk temperature rises indicated by three element chromel-alumel thermopiles. Primary emphasis is placed on the nozzle contour passages. The method of data reduction is outlined in Appendix III.

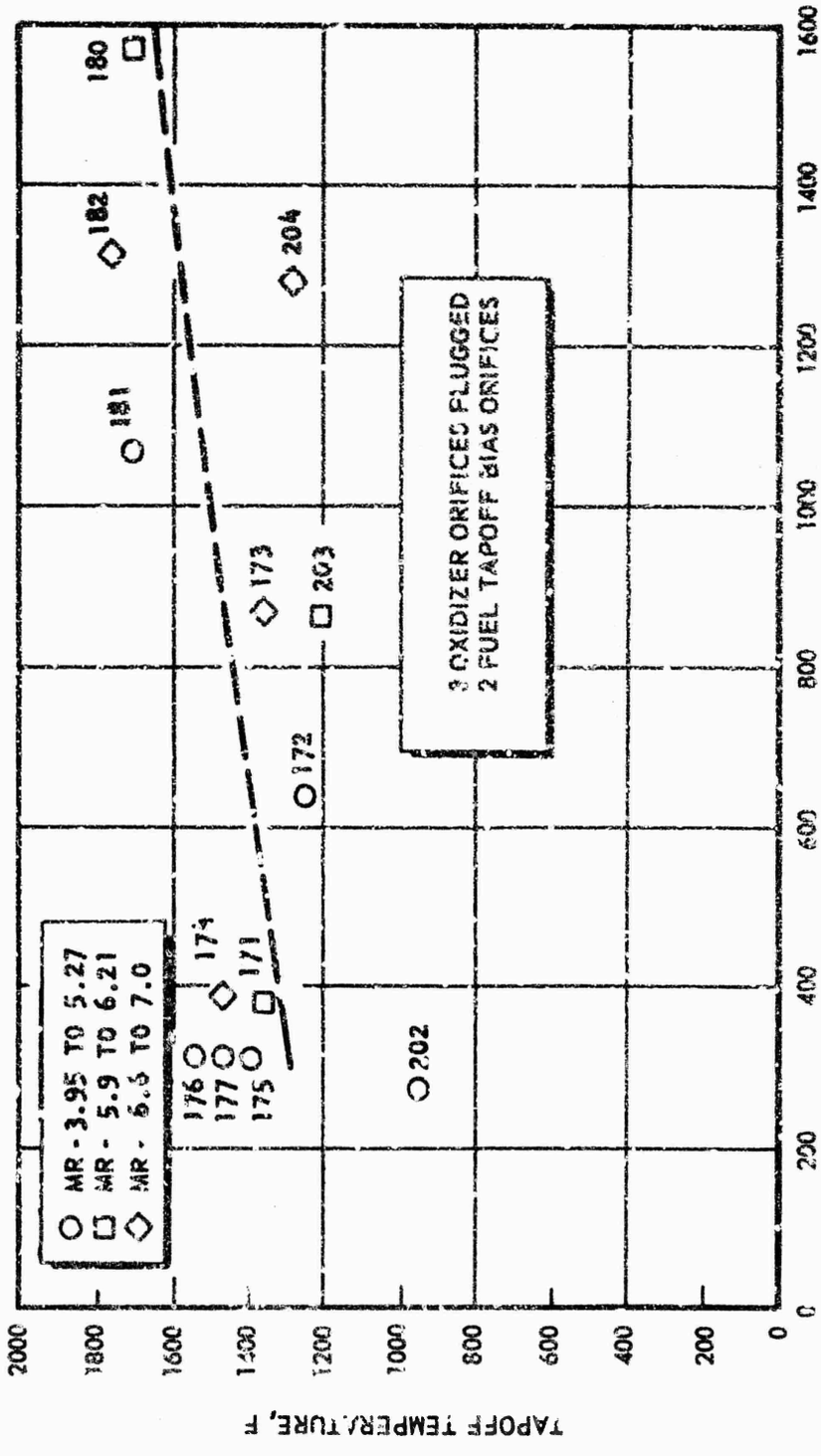

Figure 193. 2.5K Segment Tapoff Temperature vs Chamber Pressure

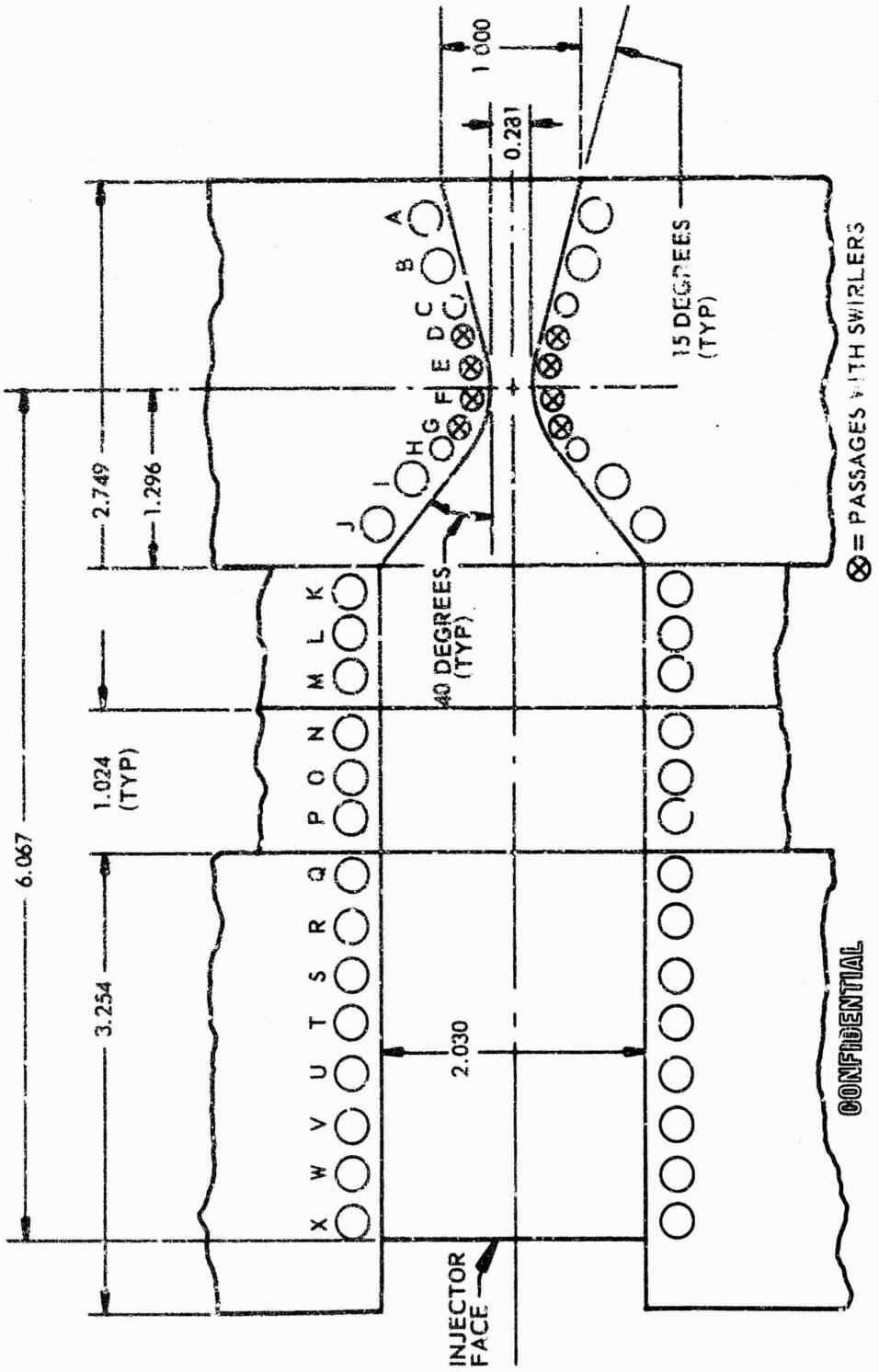

Figure 194. 2.5K Film-Cooled, Solid-Wall Segment Coolant Passage Location

(U) The reduced throat heat flux values are indicated in Table 60, 61, and 62. Values are subject to additional interpretation to obtain expected peak throat heat flux values for the operation. Early in the performance program it was observed that certain throat heat transfer abnormalities were occurring. Repeated firings under identical operating conditions of mixture ratio and chamber pressure indicated nonrepeatable heat fluxes. The general characteristics observed were that the heat flux increased from one run to the next run. A number of hypotheses were postulated for exploration of this phenomenon. These included corrosive attack of the copper chamber by the CTF ignition technique, thermal mechanical roughening of the contour surface, gross injector effects, and a segment contour mismatching disrupting the boundary layer.

(U) For ease of interpreting the results, the heat transfer data were reduced to a dimensionless Stanton and Prandtl number parameter,

$$N_{ST} N_{PR}^{2/3}$$

and this parameter was plotted as a function of run number for a series of runs during which various specific surface effects were investigated. Particularly, it was observed that the throat surfaces appeared to be roughened after a series of firings. Following the hypothesis of surface roughening through CTF ignition product attack, the throat was electroplated with nickel on one side and smoothed by rubbing with fine grit cloth on the other side, a number of times. The results are indicated in Fig. 195. It is observed that the Stanton number parameter increased more rapidly on the uncoated side than on the coated side. The limiting values coincide. Also of interest is the fact that the act of simply smoothing the throat resulted in a decrease in heat flux. The nickel surfacing did not appear to solve the problem.

(U) Further analysis of the data indicated that the increase in heat flux from run to run appeared to take place in discrete jumps rather than

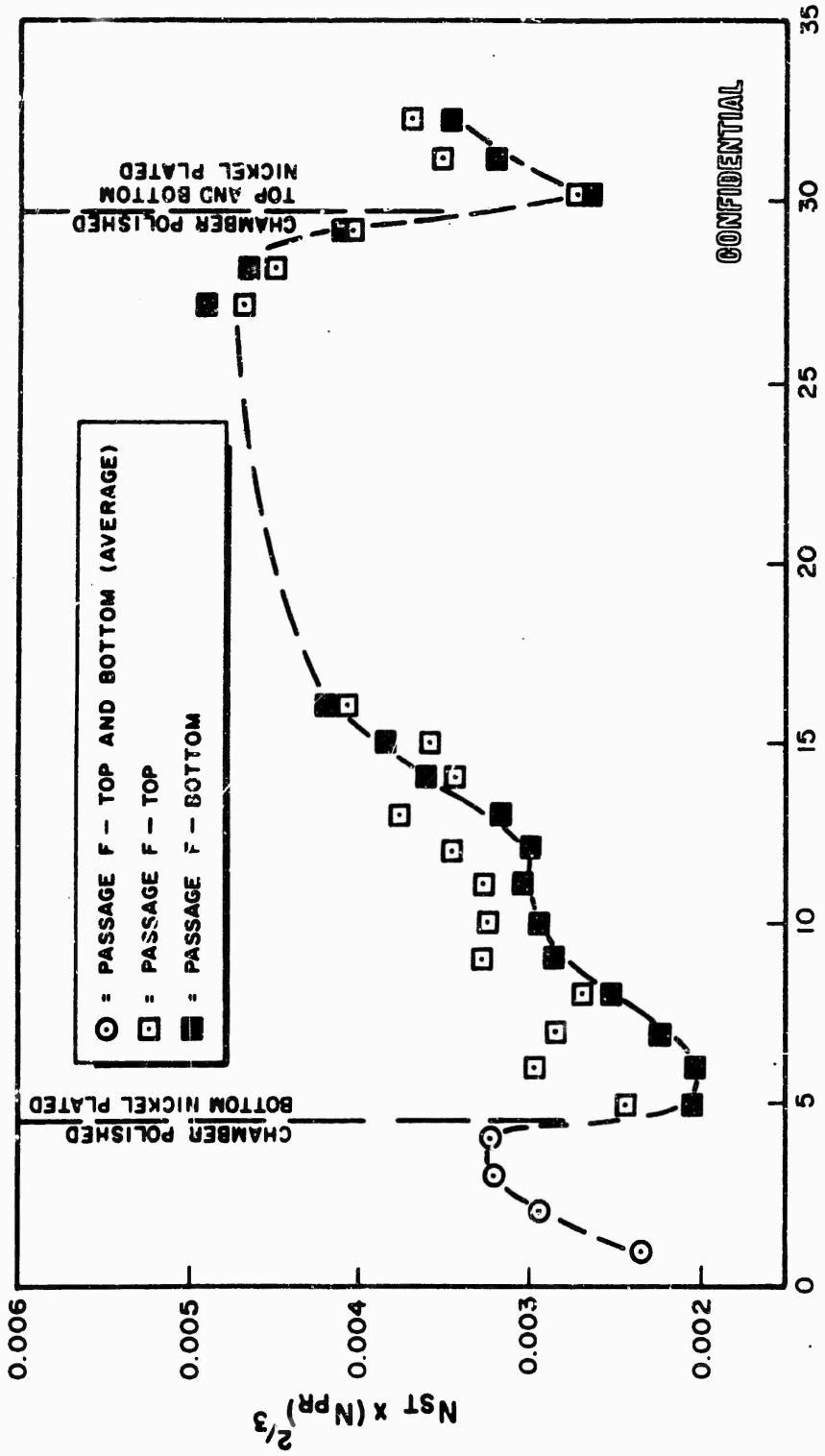

Figure 195. Variation in Heat Transfer Rates Into Passage Immediately Upstream of Throat

in a smooth manner. This led to a hypothesis of the effect being caused primarily during ignition. Two long-duration tests were conducted to determine if this was so, and the results are given in Fig. 196. It is observed that a large increase in heat flux was incurred, and it apparently was associated with ignition.

(U) At this time, a chemical analysis was conducted of the roughened throat surface, and it was found that the deposits were primarily nickel. Further close examination of the nozzle contour and throat surfaces showed that the roughening effects could not be described by distributed roughness, but instead would best be described by discrete surface protuberances. The CTF tube used as an igniter tube in the injector face was found to be pure nickel and the end eroded 1/16-inch to 1/8-inch behind the injector face. This small amount of erosion was found to be sufficient to account for most of the deposit coverage of the throat. To eliminate further difficulty, the CTF ignition tube was retracted to a position 0.125 to 0.200-inch behind the injector face.

(C) With these results in mind, a series of tests with a chrome-plated (0.0005 inch) throat was conducted to determine if reproducibility of heat transfer data could be obtained. The results are tabulated below for both the triplet injector and the LO_2 fan injector both as raw data and as normalized data to one common operating point.

	LO_2 Fan Injector		Triplet Injector	
Run No.	117	121	123	124
P_c, psia	639	649	635	596
MR	5.14	5.57	5.63	5.35
Q/A_{Exp}	31.6	30.8	28.3	27.0
Normalized Q/A (at 6.0 MR and 650 P_c)	29.7	30.2	27.8	26.3

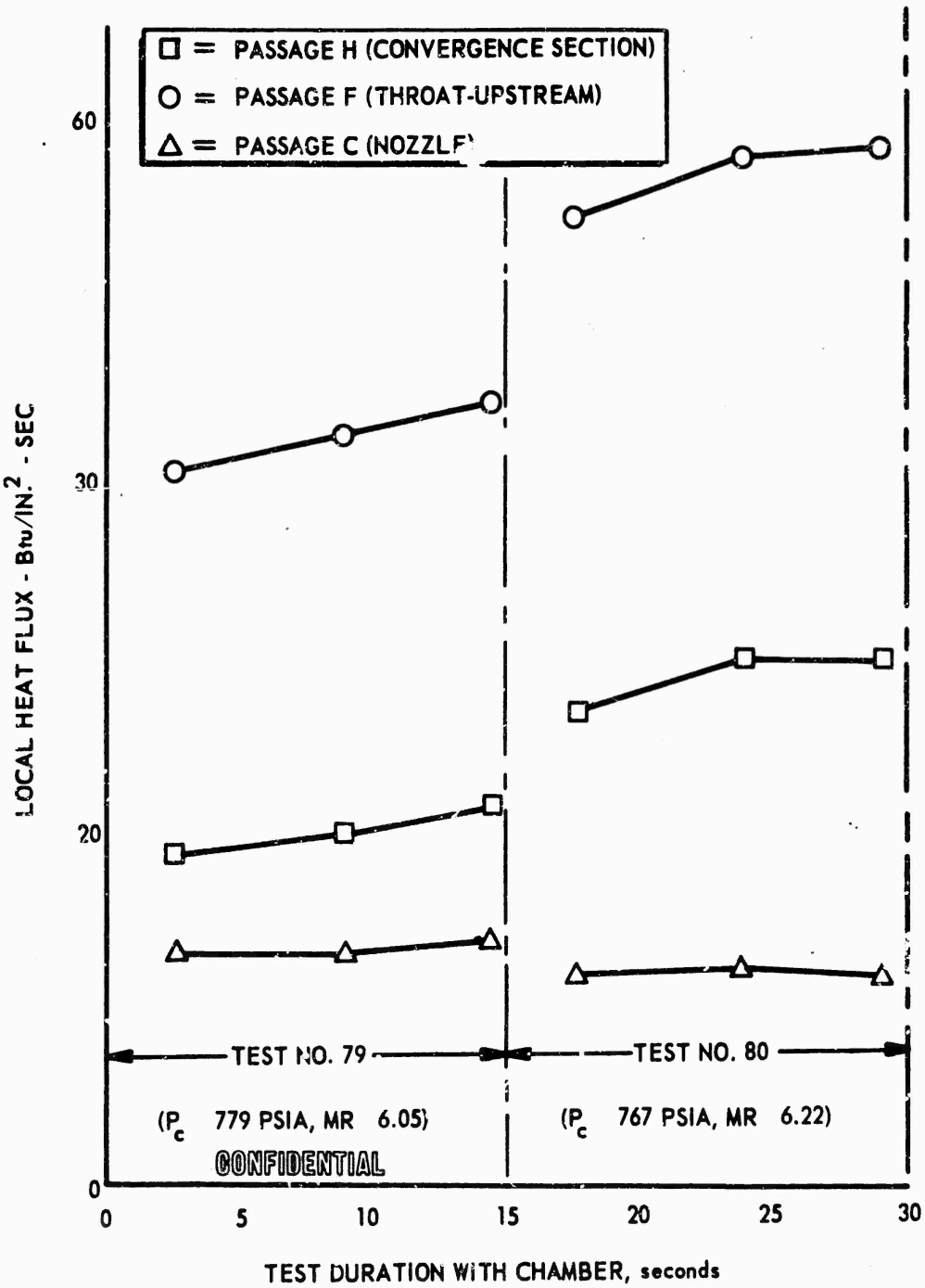

Figure 196. Variation in Local Heat Fluxes During 2.5K Water Cooled Segment Firings (Tests No. 79 and 80)

(C) Run 118 was a run at nominally 600 psi, but instrumentation read out in the throat was lost. Runs 119 and 120 were conducted at 300 psi with repeatable heat flux. Run 122 was a nominally 1000-psi run. This series of runs were considered to be as severe a test of the ignition hypothesis as could be devised in the hardware. The nominally 600-psi runs with the normalized values to a MR of 6.0 and a P_c of 650 psi indicate that the previously observed run-to-run increases in heat flux had been eliminated.

(U) It is noted here that these heat fluxes are higher than the results for a smooth contour. It was found that this particular throat contained flats in the throat region. The results, however, serve to prove that burning of the CTF tube tip was responsible for the increased heat fluxes. Of interest also is the fact that the chromium plate was virtually lost on the first two runs of the series and cannot be considered as a part of the improved heat flux behavior.

(C) To obtain a true comparison and prediction of the heat fluxes for the candidate injectors only data for known smooth contours were used. These include data for plated throats and those cases where the throat was purposely smoothed. The chromium-plated throat was smoothed after the above-discussed series of runs to eliminate the flats and utilized to obtain additional heat transfer data. The results are shown in Fig. 199 for the copper segment as a function of total flowrate. The data correlate quite well and show an average prediction of 54 Btu/in.^{2}-sec at the aerospike operating conditions. Reduction of the data to effective Stanton numbers shows that the heat flux in the stainless steel chamber will be 52 to 56 Btu/in.^{2}-sec with an average value of 54 Btu/in.^{2}-sec.

Problem Areas and Solutions

(C) In the entire 2.5K segment testing program, only two problems were encountered. One problem was the higher than anticipated throat heat flux

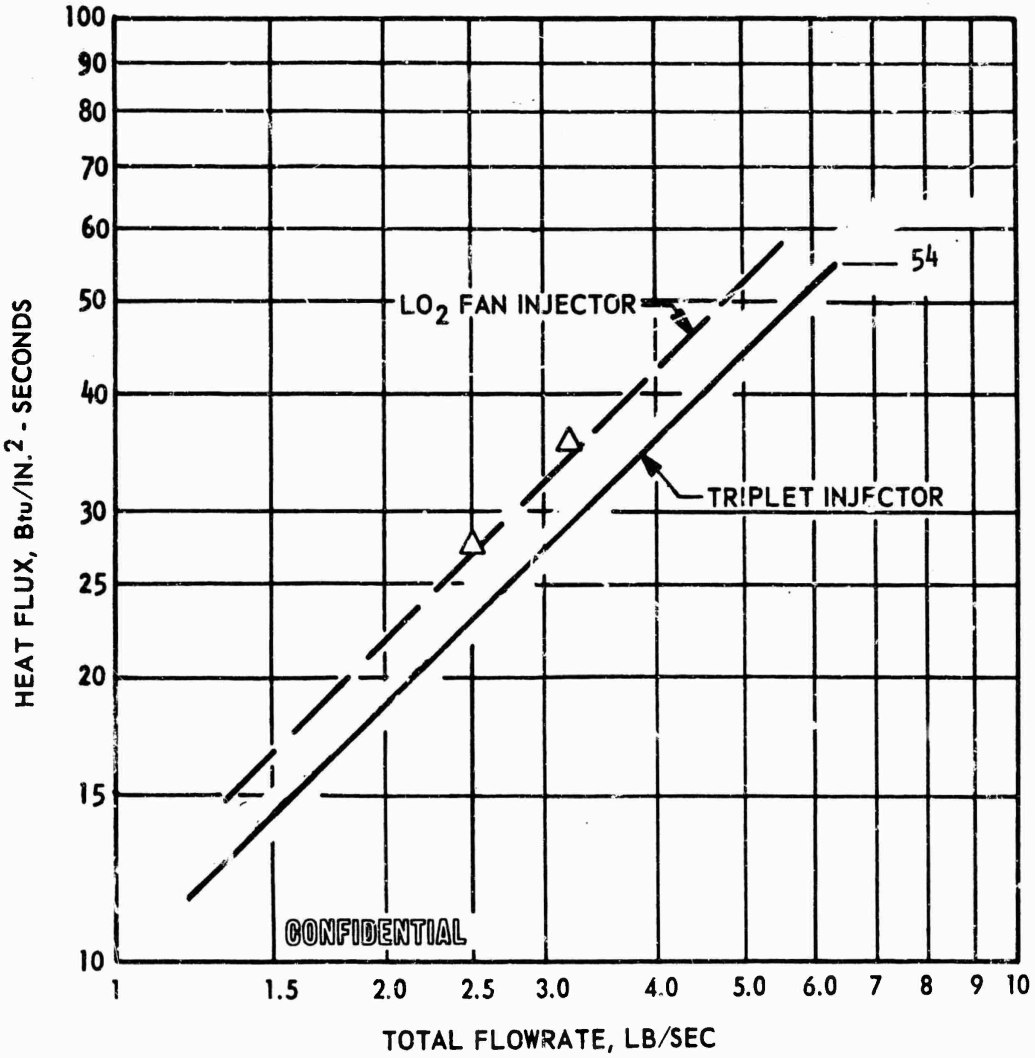

Figure 197. Comparison of Q/A for Triplet and Fan Injectors

that precluded testing above a chamber pressure of 900 psia. This difficulty was overcome by introducing gaseous hydrogen into the thrust chamber at the start of nozzle convergence to provide a cool film coolant, thereby permitting the attainment of 1500-psia chamber pressure.

(U) A series of tests with injectors 2-1G and 4-1B experienced buzz-type instability. The cause of this was found to be a fuel leak between the injection strip and the injector body. This problem was eliminated by using other injectors that did not have such leakage. In general, the 2.5K segment testing was not marred by any serious problem and all minor problems were corrected.

THRUST CHAMBER COOLING INVESTIGATION (2.5K TUBE-WALL SEGMENTS)

Objectives and Requirements

(C) The requirements of this subtask were as follows. Cooled 2.5K segments of the demonstrator combustion chamber were to be fabricated to determine the regenerative cooling limits for candidate tube materials including nickel, copper, and stainless steel. Supplementary cooling was to be investigated on a limited basis to evaluate the advantages and penalties associated with this technique for an annular throat chamber. The cooling tests were to be conducted with overall mixture ratios over the range from 5:1 through 7:1. The effects of throttling on cooling capability, as well as performance at the 20-percent thrust level and two intermediate points, was to be determined. The same injector configuration used in 250K workhorse chamber was to be used in the regenerative chamber segment. The coolant tubes used in the chamber segments were to the same configuration in critical areas as the tubes planned for the Demonstrator Module to ensure meaningful results.

(C) Accordingly, the thrust chamber cooling investigation consisted of a combined analytical and experimental effort to accomplish the following objectives:

1. Evaluate the regenerative cooling limits of the aerospike thrust chamber
2. Select tube materials to cool and meet life requirements
3. Predict the cyclic life of the selected tube material
4. Determine tube operating conditions to yield 100 reuses and 10 hours time between overhauls
5. Demonstrate the reuse life of a thrust chamber designed to these operating conditions

Summary of Work Accomplished

(U) These objectives were all successfully accomplished. The overall plan to meet the objectives made use of a combination of heat transfer analysis, stress, and materials analysis, materials laboratory evaluations, a tube tester simulating hot-fire conditions, and actual hot fire of 2.5K tube-wall segments.

(U) The limits of regenerative cooling were analytically determined for two basic tube materials. Cooling feasibility at the Demonstrator Module rated conditions was then demonstrated on 2.5K hot-fire segments. The durabilities of several candidate tube materials were evaluated through the combination of analytical effort and experimental results. The fatigue life of a selected tube material was demonstrated by the cyclic hot firing of a 2.5K tube-wall segment. The experimental life thus determined was in agreement with the analtically predicted life.

(U) Additional life limit tests were conducted on a unique thrust chamber tube tester such that preliminary maps of life vs chamber operating conditions could be made. These maps were then used in conjunction with other primary considerations to select the Demonstrator Module rated operating conditions.

(U) A systematic approach was used which called for the proper phasing of the overall effort. The initial task was the selection of candidate tube materials which provided adequate cooling and had promising durability. A preliminary heat transfer, plastic strain, and fatigue analysis was used in this effort. Two materials were ultimately selected as representative of these candidates, and 2.5K tube-wall segments were fabricated of each. These segments were hot fired to demonstrate cooling feasibility.

(C) Parallel with this effort, a material selection program was conducted which would enable the selection of highly durable tube materials for the 20K and Demonstrator Module thrust chambers. This program employed detailed analysis, laboratory evaluations, literature surveys, and related studies. The Nickel 200 tube material was selected for immediate thrust chamber application as a result.

(C) A nickel tube thrust chamber was hot-fire tested over 300 times for thermal fatigue life demonstration tests. Complementing the segment cycling tests were life limited evaluations on the Nickel 200 material conducted on the tube tester. The effects on tube life of off-nominal operating conditions and fatigue creep phenomena were explored.

(C) The results of these hot-fire and thrust chamber tube simulation tests were then compared with life predictions based on analysis and laboratory tests. A good overall correlation was established, lending confidence to the analysis. From this, parametric life and cooling studies on the Nickel 200 material were completed, enabling a rational balance between life and performance to be accomplished in the design of the Demonstrator Module.

Description of Hardware and Fabrication

(C) Design and Operational Limits, 2.5K Segments. The initially proposed aerospike thrust chamber design called for the use of tube materials which would cool and provide durability at high chamber pressures. Tube materials which were successful in previous high-heat-flux applications and which had promising fatigue properties were analyzed in a preliminary way for cooling feasibility. Three materials which were representative of these candidate tube materials in cooling effectiveness were intially selected for detailed heat transfer analysis and cooling feasibility tests.

Three 2.5K segment thrust chambers were designed which employed these representative tube materials, i.e., type 347 stainless steel, Nickel 200, and OFHC copper

(C) Tube Design. Tube wall thicknesses were established from known allowable hydraulic stresses for each material and from fabrication considerations. The chamber geometry from the injector to the throat simulated the 250K aerospike thrust chamber outer body contour. Hydrogen coolant was introduced from the injector end at a pressure of about 2300 psia and a bulk temperature of 250 to 300 R, again to simulate the cooling conditions on the 250K outer body. The tube sizes were typical of flightweight tubes as then conceived.

(C) Unformed diameters in the combustion zone and throat are tabulated below:

Parameter	Copper	Stainless	Nickel
Thickness, inches	0.020	0.008	0.014
Diameter, Chamber, inches	0.193	0.100	0.125
Diameter, Throat, inches	0.093	0.058	0.075
Tubes/Segment Wall, inches	36	59	44

(C) Figure 117 indicates the design wall temperature, heat fluxes, hydrogen velocities, and curvature enhancement values based on heat transfer data available at the start of the program. Low wall temperatures near the injector face were also based on heat transfer data, and indicated incomplete combustion in this region.

(U) It is noted that the throat tube diameter size yielded hydrogen velocities of approximately Mach 0.5.

(U) Combustion zone sideplates were water cooled and the nozzle convergent and divergent side plates were hydrogen cooled.

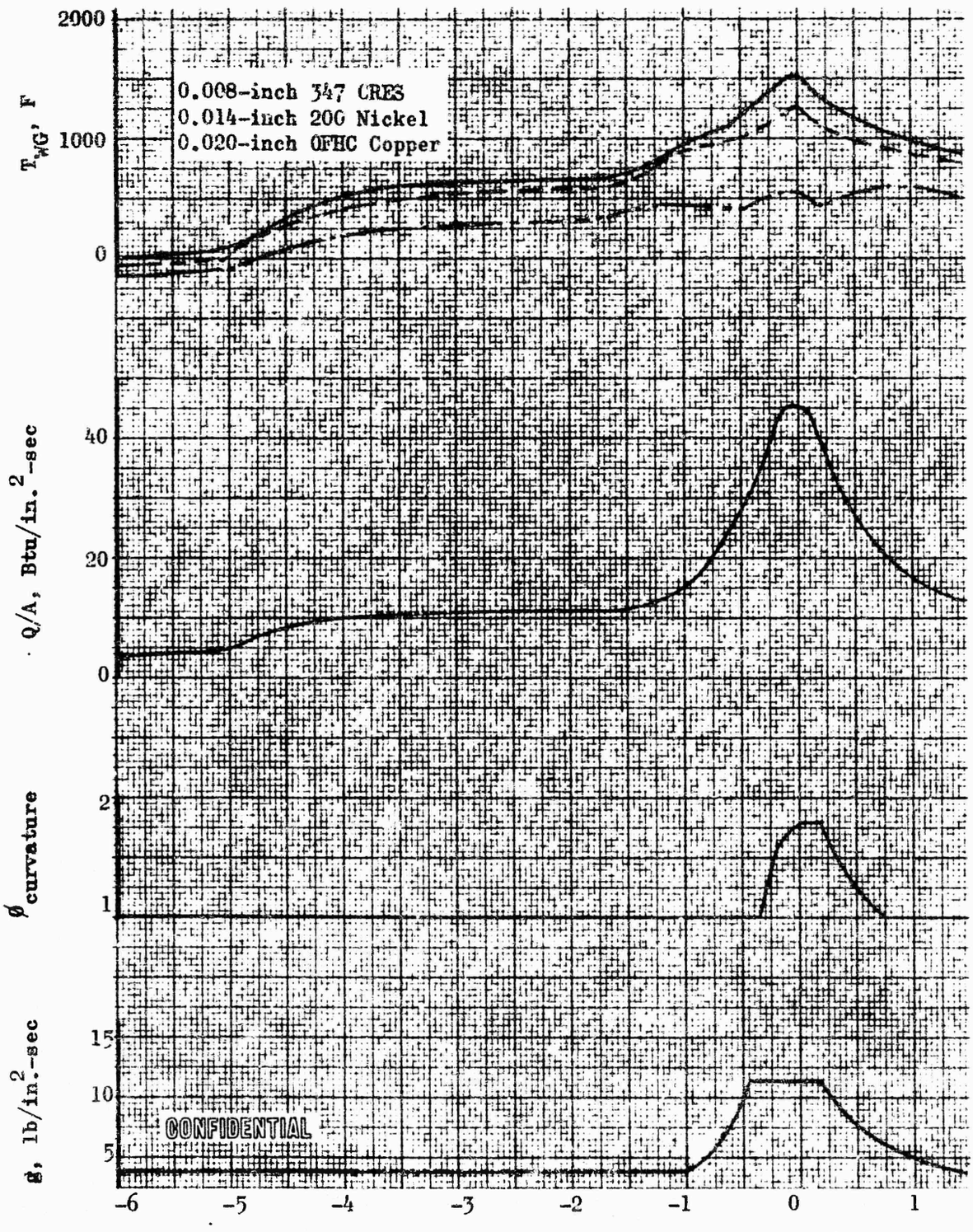

Figure 198. Initially Predicted Gas-Side Wall Temperature, Heat Flux, Curveture Enhancement, and Mass Velocity Profiles for 2.5K Experimental Segment (O_2/H_2, P_c = 1500 psia, MR = 6.0, W_{ct} = 0.956 lb/sec)

(U) Heat transfer studies indicated the most critical area of high heat flux in the Demonstrator Module to occur in the throat region of the outer body where the hydrogen coolant is flowing as a "downpass." To simulate this critical region it was only necessary that the 2.5K segments duplicate the Demonstrator Module Chamber geometry from the injector face to the throat and need not incorporate the outer body shroud or inner body spike. Thus the design was simplified by permitting the chamber to be symmetrical about an axial center line.

(C) Segment Design. A 2.0 by 3.5 inch rectangular chamber cross section with a 0.281-inch throat located 6 inches downstream of the injector face having a 40-degree convergent half angle and a 15-degree divergent half angle to an expansion ratio of 3.5 was selected.

(U) Separate cooling circuits were provided to each contoured tube wall with the flow direction being from the injector end to the nozzle end. The ability to measure both inlet and outlet pressure and temperature in each tube wall was provided. The coolant required for the side plates would also be provided by independent circuits. The chamber was designed to accommodate the same injectors as those being evaluated in the 2.5K solid wall investigation. To fulfill the requirements of the 2.5K tube-wall investigation, three segments were designed differing only in the tube material and dimensions related to the tubes. The fabrication was further simplified by the use of identical rather than mirror image parts for each side. Figure 199 shows the essential feature of the design.

(U) The design and fabrication philosophy employed for these segments was that (1) all detail components were to be fabricated complete per drawing and (2) specific operations were prescribed at established assembly levels and requirements were to be accomplished at these levels only. In addition, specifications were written to define the detail brazing

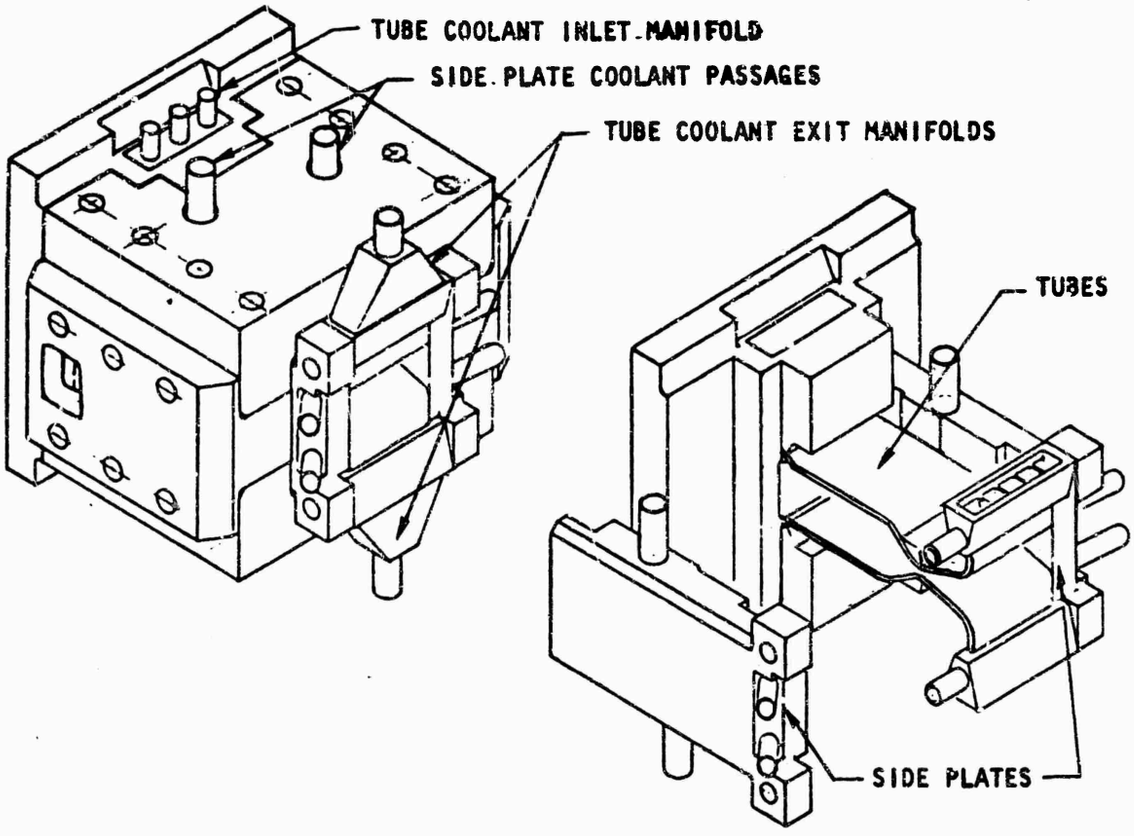

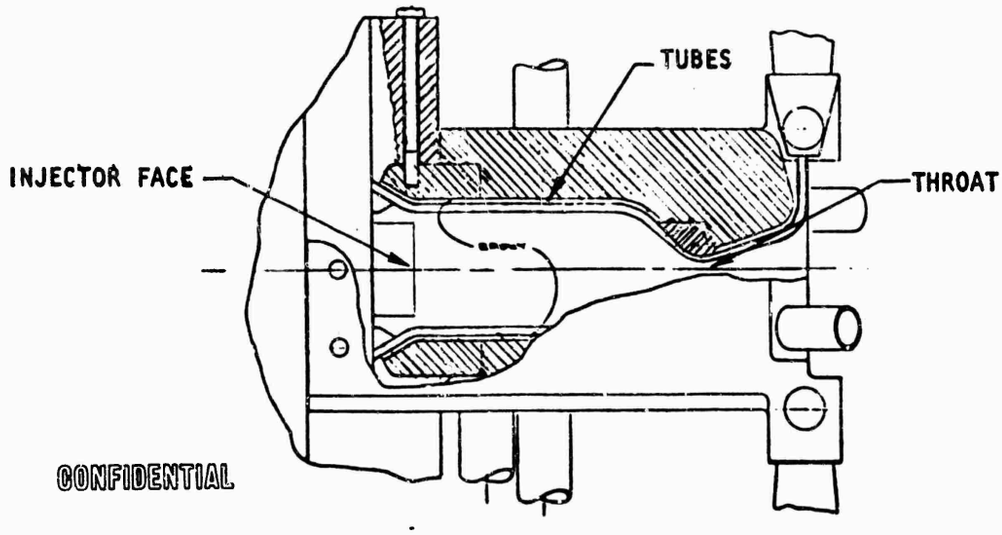

Figure 199. 2.5K Tube-Wall Segment Design

and assembly requirements. Thus, better program control and system quality were afforded during the program fabrication cycle.

(U) A two-phase furnace-brazing procedure was employed. The brazing of the copper end plate bodies was accomplished prior to the brazing of the thrust chamber body assembly. This permitted pressure testing of the complex end plate assemblies and subsequent repair, where required, to be accomplished without limited access. An additional advantage gained was that the completed end plates could act as a braze fixture for the tubes and manifolds of the thrust chamber braze assembly. This procedure represents somewhat of a compromise by using the highest-melting-temperature brazing alloy, but was deemed to be the superior method of obtaining a reliable chamber assembly.

(U) The 2.5K tube wall segment design consists of a brazed assembly of tubes, copper end plates, a type 347 stainless-steel injector end block, and type 347 stainless-steel exit end manifolds. Both inlet and outlet manifold closures were welded in place to eliminate one braze cycle. Access for good placement of braze alloy as well as inspection was incorporated. In addition, the ability to pressure test at various stages of fabrication was provided. The brazed assembly is reinforced by a bolted-in-place backup structure of SAE-4130 steel. Transfer of loads from the tube stack to the backup structure is through a bearing block bolted to the backup structure and making intimate contact with the tubes through an epoxy and glass fiber filler.

(U) Fabrication.

(U) Tubes. Conventional methods were employed during the fabrication of the tubes. A round tube of uniform wall thickness having a circumference equal to the perimeter of the final formed tube was reduced in diameter to the throat dimension. Tapered regions on either side form

the converging and diverging sections of the tapered tube configuration. This tube was then preformed by bending to the combustion chamber geometry and finally the preformed tube was placed in a die and sized to the required width.

(C) Heat transfer, pressure drop, and stress studies were conducted to determine the final tube configuration. Drawings containing these requirements were completed in April 1966 and materials were ordered for tube fabrication. Tubes were fabricated from nickel and copper only.

(C) Tapering of the nickel tubes began early in June 1966 and metallographic examinations indicated the tapered tubes to be of excellent quality. An examination of the first preformed and final-formed tubes indicated the preformed tube to be dimensionally satisfactory; however, slight buckling in the bend areas as a result of work hardening and tube pinching in the form die was observed. Annealing of the tubes was specified after preform. In addition, the handling techniques were improved to prevent damage of the tubes after the annealing process. To eliminate the pinching of the tubes, the die plates were combined on the base plate eliminating the center die parting line. Upon completion of forming, the tubes were trimmed to length by electrical discharge machining.

(U) Tapering and preforming of the copper tubes were accomplished per process specification. Metallographic examinations revealed the tube quality and wall thicknesses to be in agreement with drawing requirements.

(U) High-pressure final forming was selected as the method for forming of the copper tubes. All of the formed tubes were examined under white light using 20K magnification, and were categorized acceptable, marginal, and unacceptable. A thorough metallurgical examination was conducted on two tubes from the unacceptable group, one tube from the acceptable group and one tube from the marginal group. Seventy tubes from the acceptable category and 27 tubes from the marginal category were accepted for use. All tubes evaluated were OFHC copper, and the general quality of the acceptable tubes was excellent.

(U) Injector End Block. This component was designed to serve a threefold purpose:

1. Provide the support mount and sealing surfaces for the injector
2. Contain the H_2 inlet and distribution manifolds
3. Form the injector end support for the contoured tube walls

In addition, the test facility attach points were also provided on this block. Type 347 stainless-steel material was selected for strength, compatibility with the test fluids, good brazing qualities, and availability.

(U) The injector sealing was accomplished by means of a double-seal, 1/16-inch-diameter, metal O-ring inboard of a flexitallic seal. Two 0.75 by 3.60 inch openings were provided to form the H_2 manifold and access to the upstream ends of the tubes. The tubes were designed to protrude 1/4 inch into these cavities for good braze alloy placement and as a safeguard against alloy flowing into and restricting the tubes. Approximately 0.75 inch of braze engagement with the tubes was provided. A rectangular shoulder area, 0.5 inch deep, was cut by electrical discharge machining at the entrance to each of the manifold closeout block, which was welded in place.

(C) End Plates. The cooled copper end plates utilized experience gained during the fabrication of the 2.5K cooled-wall segments. The design used drilled coolant passages of small diameters (0.159 inch) precision deep drilled (approximately 6 inches).

(C) Two distinct coolant circuits, one each for the combustion zone and the throat region, were provided. The circuit for the combustion zone employed water in the thirteen 0.250-inch-diameter coolant passages. These coolant passages were fed by two 5/8-inch-diameter cross-drilled

passages which supplied the coolant. The direction of flow was from either side. The coolant circuit for the throat region was composed of thirteen 0.159-inch-diameter holes. Swirlers were provided in each of these holes to take advantage of the curvature effect of the hydrogen coolant. These coolant passages were joined together by 5/8-inch-diameter cross-drilled holes which provided the inlet and outlet for the coolant through 3/4-inch-diameter feed tubes. Open ends of all drilled passages were closed by brazed plugs.

(U) Figures 200A through 200E show the segment thrust chamber in various stages of fabrication.

(U) Braze Assembly. Inspection of the prebraze assembly disclosed that the tubes did not extend far enough into the nozzle end manifolds. A dimensional check of the components revealed that the tubes were trimmed too short.

(U) As a solution, the manifold positioning holes in the side plate were plugged by electron beam welding copper slugs in place. The holes were then repositioned inward, thus moving the manifolds inward to allow the tubes to extend farther into the manifolds. On the outermost tubes of the four corners, the tube end was plugged with refrasil cord and Nicro Braze stopoff to prevent alloy from flowing into the tube end.

(U) A brazing alloy was applied and the assembly was brazed in a furnace equipped with a vacuum retort at a temperature of 1800 F. Following this braze cycle, a 10-psig helium leak check revealed tube-to-tube and tube-to-manifold leaks. The assembly was realloyed and a second braze cycle was accomplished at 1790 degrees.

(U) Following the second braze cycle, a helium leak check verified that all tube-to-manifolds joints were sealed; however, random tube-to-tube leaks existed in the throat area. These leaks were repaired using a stylus silver-plating process.

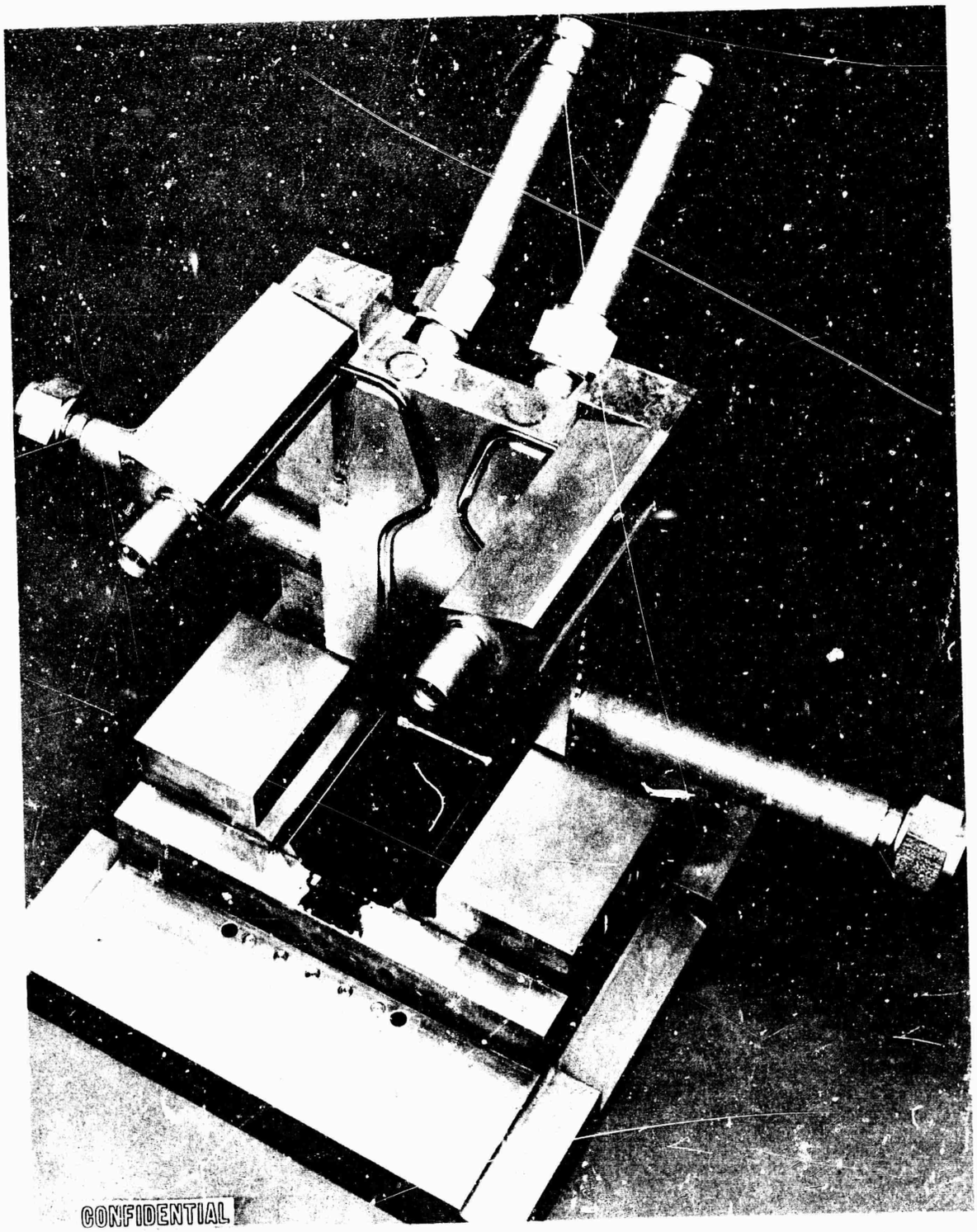

LXE32-9/1/66-C2

Figure 200A. 2.5K Nickel Tube-Wall Segment in Process Fabrication

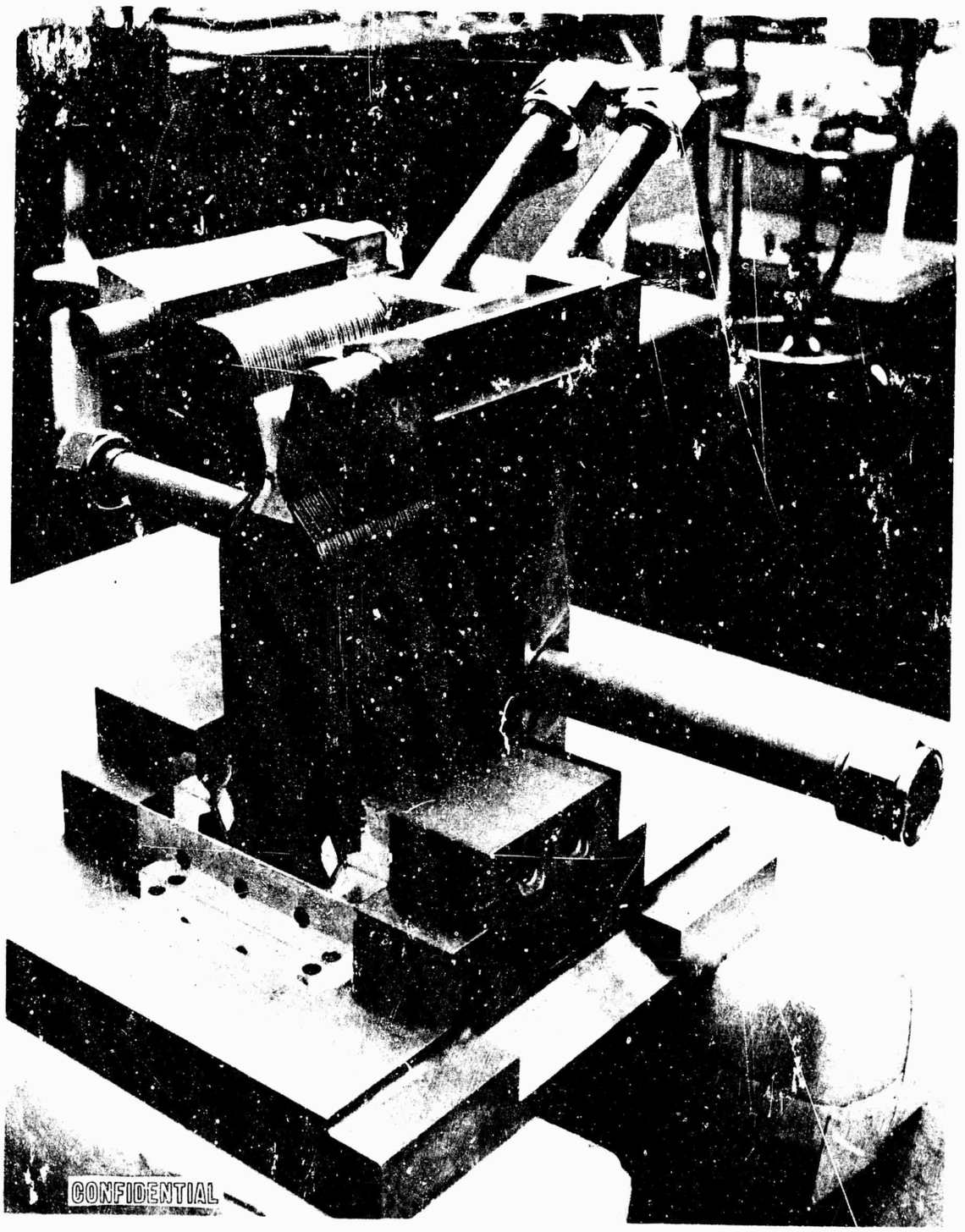

1XE32-9/12/66-C1

Figure 200B. 2.5K Nickel Tube-Wall Segment in Process Fabrication

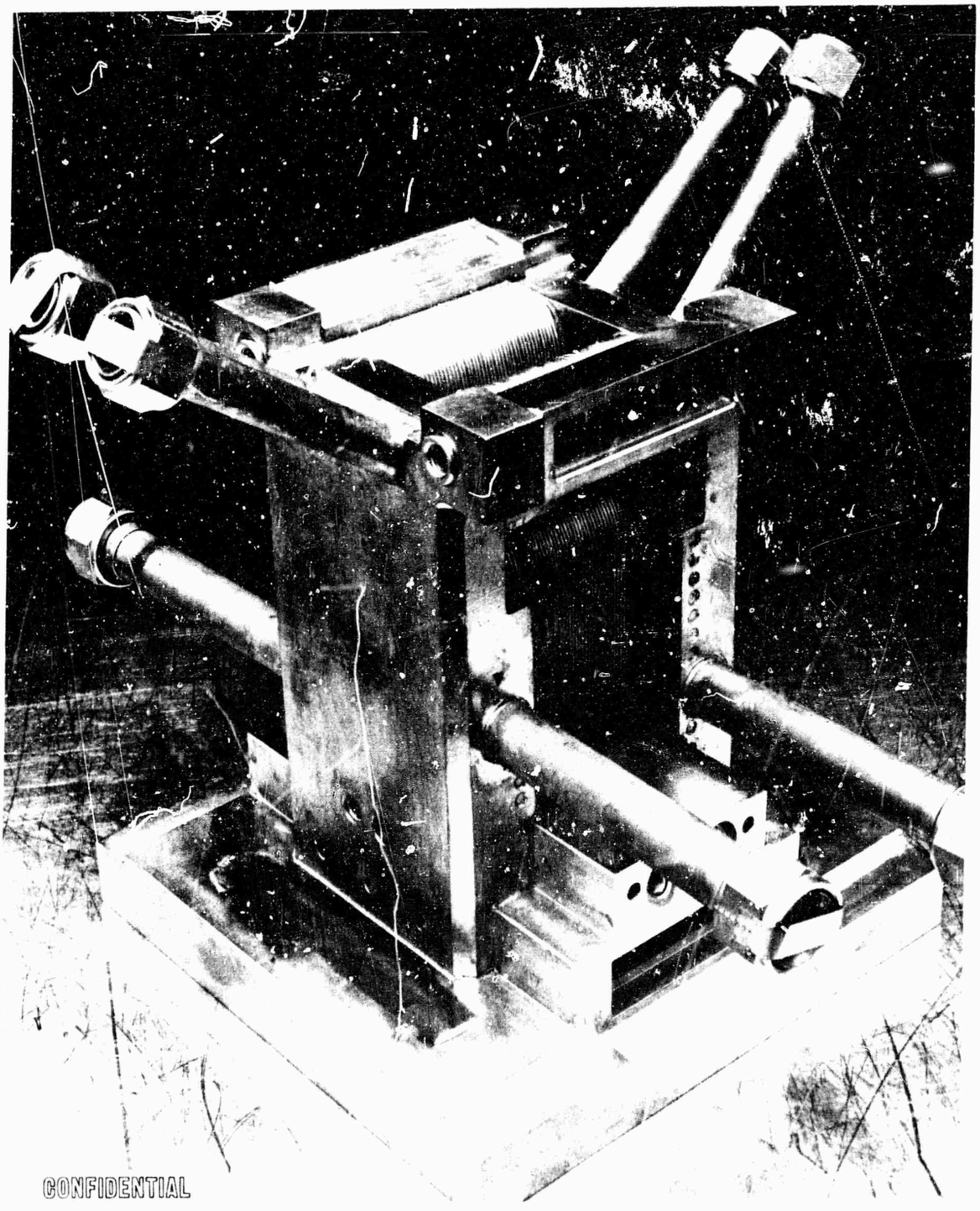

1HZ92-9/20/66-C1

Figure 200C. 2.5K Nickel Tube-Wall Segment in Process Fabrication

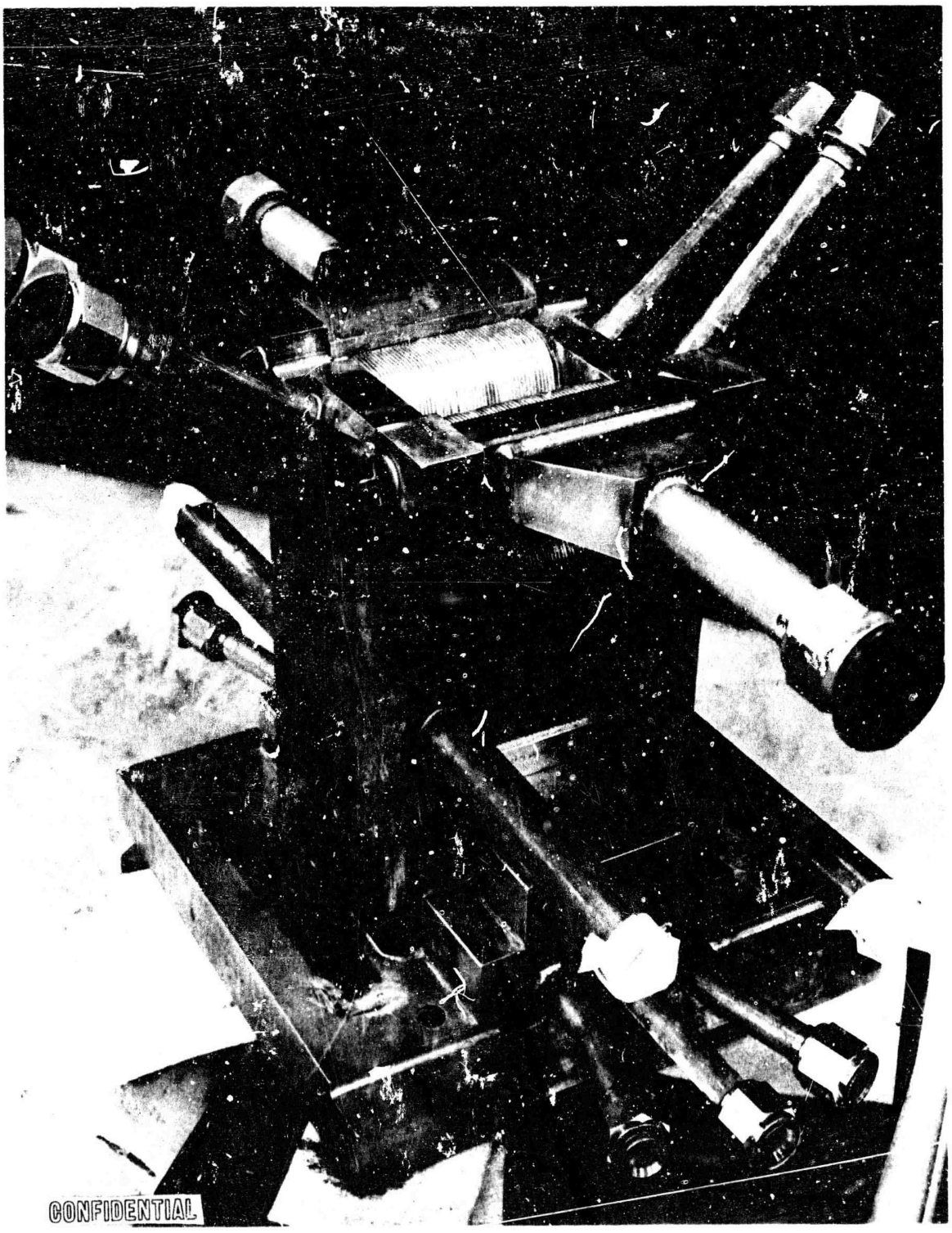

1XE38-10/14/66-C2A

Figure 200D. 2.5K Nickel Tube-Wall Segment in Process Fabrication

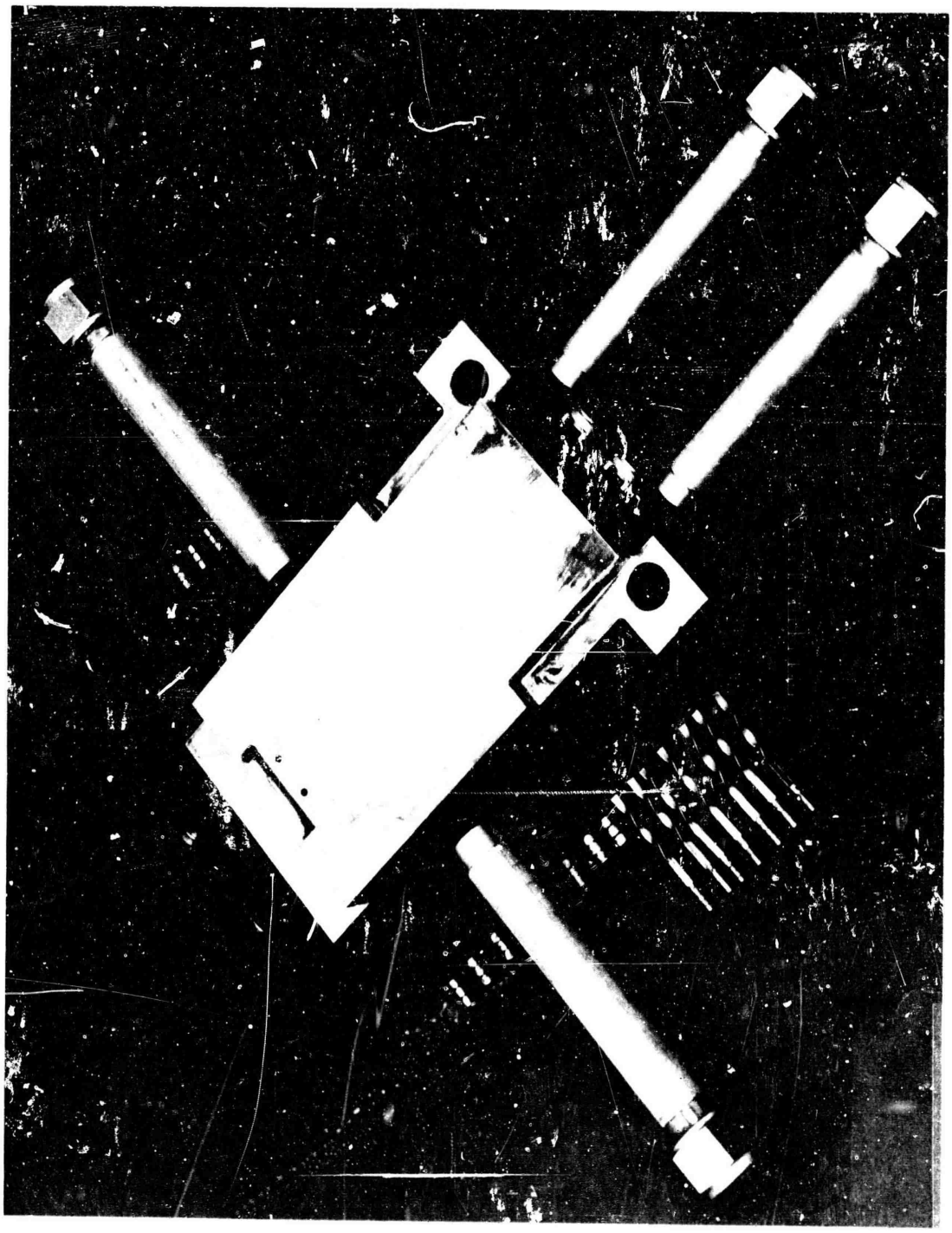

(U) The assembly and brazing of the copper tube segment utilized the same general techniques as the nickel-tube segment. Fabrication was completed with the two planned brazing cycles.

Testing

(U) Instrumentation. Two methods to measure hot-gas-side tube-wall temperatures were evaluated. These methods were: (1) placement of small, thin, braze alloy deposits on gas-side tube crowns as temperature indicators, and (2) installation of microminiature thermocouples on gas-side tube crowns.

(U) Thirty microminiature thermocouples were evaluated for installation techniques and possible employment on tubular segments.

(U) Thermocouple installation methods evaluated included: (1) furnace brazing, (2) electron beam welding, (3) lazer brazing, (4) induction brazing, (5) selective plating, (6) quartz lamp brazing, and (7) several types of hand brazing. The most successful methods were induction brazing and hand brazing. Both of these techniques were evaluated further to reduce the installation mortality rate and refine the installations.

(U) The feasibility of applying small, thin. braze alloy deposits on tube walls as T_{wg} indicators has been demonstrated on a high-chamber-pressure chamber at Rocketdyne. If properly and selectively applied, a determination of T_{wg} within 100 degrees is possible.

(U) To refine the assessment of T_{wg}, the remelt temperature of these alloys was experimentally determined. This was accomplished by resistance heating two instrumented stainless-steel tubes employing various braze material deposits (spots). The solidus remelt temperature was determined by probing the braze spots with a glass rod while the tube was heated gradually to elevated temperatures. This should closely approximate the remelt or braze washing temperature in a combustion chamber.

The remelt temperatures of the 12 braze materials evaluated varied between 1105 and 1810 F. When applied selectively, these 12 braze materials should be capable of defining gas-side, tube-wall surface temperatures. The 12 brazes and their remelt temperatures are given in Table 65.

(C) The evaluation of braze alloy remelt temperatures and their application were completed. These temperature indicators were applied post furnace brazing of the assembly. This was necessary because the furnace braze alloy melting temperature is higher than that of applicable temperature indicators. Braze alloy deposits were used in accessible (divergent region) areas only.

(C) Microminiature thermocouple installations using high-temperature (1900 F) braze were unsuccessful. This high-temperature application was necessary because the thermocouples must be installed prior to furnace brazing the tubular chamber assembly. The installations resulted in gas-side tube surface discontinuities which were not acceptable for the operating conditions of the thrust chamber.

(C) Microminiature thermocouples were mounted, however, to the tube back wall for determining gas-side heat fluxes. The design permitted easy assembly of the backup structure.

(C) Copper Tube-Wall Segment Cooling Feasibility Tests. A test plan was written for the 2.5K tube-wall chambers. The primary objective of this test program was to evaluate regenerative-cooling capability of each tube material to chamber pressures of 1500 psia.

(C) All tests were run at a chamber mixture ratio of 5.0 because this approximates the maximum heat fluxes. Test duration was 5 seconds to ensure steady-state instrument readings. Hardware instrumentation included heat transfer and performance measurements. Direct gas-wall temperature measurements were attempted using braze alloy spots on the tube surface.

TABLE 65

BRAZE ALLOY REMELT TEMPERATURE

Alloy	Composition	Published Solidus-Liquidus Melting Temperature, F	Experimental Remelt Temperature, F
Specimen No. 1			
Premabraze 403	Au - 20 Cu	1634 to 1634	1695
Braze 603	60 Ag-30Cu-10 Sn	1115 to 1325	1245
N. E.	25 Ag-52.5Cu-22.5 Zn	1500 to 1575	1410
Premabraze 615	61.5Ag-24Cu-14.5 In	1155 to 1305	1220
Braze 752	Ag-25 Zn	1300 to 1330	1275
Ag-15 Zn	Ag-152n- 3/4 Ni-1 Cu	1350 to 1420	1430
Easy Flo	Ag-15.5Cu-16.5Zn-18 Cd.	1160 to 1175	1105
Specimen No. 2			
Nicoro	Cu-35Au-3Ni	1814 to 1877	1810
Braze 051-TE	5Ag-58Cu-37Zn	1575 to 1600	1605
Palcusil No. 10	50Ag-32Cu-18 Pd	1515 to 1566	1550
Premabraze 615	61.5 Ag-24Cu-14.5 In	1155 to 1305	1235
Palcusil No. 20	52 Ag-28Cu-20 Pd	1615 to 1650	1610
Nioro	Au- 18 Ni	1742 to 1742	1775
Easy Flow 45	Ag-15Cu-16 Zn	1125 to 1145	1110

Coolant measurements included a flowrate and inlet and outlet temperatures and pressures. For performance, thrust, chamber pressure, injection flowrates, and hydrogen injection, temperature was measured. A CTL ignition system was employed.

(C) Seven hot tests were conducted on the 2.5K copper tube-wall segment on the ADP test effort. The test series consisted of six mainstage tests between 540- and 1500-psig chamber pressure, plus an ignition checkout test. Inspection of the hardware after the test series revealed the copper tubes were in good condition. The performance was typical of that obtained on the solid-wall segment performance evaluation and is shown in Table 66.

(C) Copper Tube-Wall 2.5K Segment Cycling Tests. Nineteen cyclic tests were made at over 1500-psia chamber pressure, mixture ratio 5 on a related program. These cycling tests, combined with the previous seven cooling feasibility tests, brought the total number of hot-fire pressure cycles on this thrust chamber to 26. Testing was terminated because of excessive tube coolant leaks.

(C) Nickel Tube-Wall Segment Cooling Feasibility Tests. A test plan identical to that followed on the copper tube-wall segment was followed on the initial tests. A CTF ignition system was again employed.

(C) The first test conducted on the nickel chamber was at a chamber pressure of 170 psia and was successful in that the facility hydrogen and water-cooling circuits were proved to function satisfactorily. These circuits also functioned properly during the second test, which was targeted for a pressure of 450 psia. During this test, injector burnout was experienced at the 2.5-second point. The heat transfer in the tubes appeared to be normal and reasonably consistent with the data from the 2.5K solid-wall segment effort up to the 2.5-second point. The cooling circuit data and high-speed movies indicate a general injector failure at the 2.5-second point.

CONFIDENTIAL

TABLE 66

(C) 2.5X COPPER TUBE-WALL SEGMENT PERFORMAN

Test No.	Test Date, 1966	Injector S/N	Test Duration, Seconds	Thrust Stagnation Pressure	Thrust	Oxidizer Injector Inlet Temperature, F	Fuel Injector Inlet Temperature, F	Tube Bundle Inlet Temperature (Top), F	Oxidizer Injector Inlet Pressure, psig	Fuel Injector Inlet Pressure, psig	Tube Bundle Inlet Pressure, (Top), psig	Tube Bundle Exit Pressure, (Top), psig	Chamber Pressure Injector End, psig	Oxidizer Flowrate, lb/sec	Fuel Flowrate Injector, lb/sec	Fuel Flowrate Tube Bundle (Top), lb/sec
030	12-6	4-1A	Ign only		N/A											
031	12-7	4-1A	1.5	538.0		-268	64	-216	630	750	1980	1750	540	1.87	0.398	0.64
032	12-8	4-1A	1.5	876.7		-267	64	-216	1080	1225	2220	1770	880	3.02	0.596	0.93
033	12-8	4-1A	1.5	597.3		-265	65	-215	665	810	2170	1750	600	1.95	0.408	0.98
034	12-15	4-1B	1.5	981.4		-266	63	-255	1200	1380	2220	1680	985	3.50	0.673	1.14
035	12-15	4-1B	1.5	1295.2		-261	63	-255	1620	1770	2250	1710	1300	4.47	0.895	1.11
036	12-16	4-1B	1.5	1494.5		-263	67	-260	1920	1950	2180	1650	1500	5.20	1.02	1.03

NOTE: N/A = Not Available

MENT PERFORMANCE DATA

izer rate, sec	Fuel Flowrate Injector, lb/sec	Fuel Flowrate Tube Bundle (Top), lb/sec	Total Flowrate Injector, lb/sec	Injector Mixture Ratio, o/f	η_{c^*} P_c	Momentum Ratio, o/f	Oxidizer Injection Velocity ft/sec	Fuel Injection Velocity, ft/sec	Tube Bundle Inlet Temperature (Bottom)	Tube Bundle Inlet Pressure (Bottom)	Tube Bundle Exit Pressure (Bottom)	Fuel Tube Bundle Flowrate (Bottom)	Tube Bundle Outlet Top Temperature, F	Tube Bundle Outlet Bottom Temperature, F
97	0.398	0.64	2.268	3.00	0.953	.1295	74.21	2693.2	-216	1980	1750	0.64	-369	-369
92	0.596	0.93	3.616	3.25	0.987	.2344	118.17	2554.3	-216	2220	1770	0.93	-372	-372
95	0.408	0.98	2.358	2.00	1.025	.1001	77.96	2498.0	-215	2175	1750	0.98	-332	-332
60	0.673	1.14	4.173	3.07	0.960	.3061	138.45	2351.9	-255	2220	1680	1.14	-400	-400
97	0.895	1.11	5.365	4.03	0.974	.3735	178.08	2381.3	-255	2250	1710	1.11	-435	-435
00	1.02	1.03	6.22	5.04	0.970	.4462	204.93	2341.4	-260	2180	1630	1.03	-470	-470

2

(U) Failure analysis indicates that the injector failed because of extended duration firing with insufficient liquid oxygen cooling of the LO_2 injector strips. Previously, 2.5K solid-wall evaluations have shown that the selected design will operate satisfactorily with gaseous oxygen cooling for short durations; however, for long-duration runs, liquid oxygen is required. The cooling capability of the liquid oxygen is approximately nine times that of the delivered oxygen on the failure test. The presence of gaseous oxygen into the mainstage period of the test is attributed to a combination of the stand configuration and sequencing producing inadequate chilldown at the low flowrates used for the initial tests. Subsequent to this failure, the sequencing of oxygen to the test stand was changed substantially to ensure a delivery of proper quality LO_2 to the injector. A series of simulated starting sequences proved that the new approach delivered oxygen in an identical manner to that obtained on the 2.5K solid-wall evaluations.

(U) Repair possibilities were reviewed for the nickel chamber. The thrust chamber damage consisted of tube splits near the injector and an eroded side plate cooling passage at the injector (Fig.201).

(C) The regenerative cooling capability of a nickel-tube-wall chamber was then explored on the cyclic life series, described in the following section. A nickel segment was operated repeatedly at over 1300-psi chamber pressure at stabilized conditions and at a maximum of 1350-psi chamber pressure and wall temperatures as described in that section. This testing thus demonstrates the regenerative cooling capability to 1350 psi but does not define the limits of cooling. On a related program, the damaged nickel tube segment, previously described, was repaired to explore repair techniques and tested to explore general cooling margins. In this series, 12 tests were conducted over a range of 310- to 2050-psi chamber pressure and mixture ratios up to 7.2, under stabilized conditions. Operating conditions produced computed tube-wall temperatures closely duplicating those predicted for the Demonstrator Module chamber (Fig. 202). Posttest condition of the tube walls and injector was excellent, clearly showing that the limits of regenerative cooling have not been reached at 2050 psi and adequate margin exists even at this pressure.

Figure 201. Injector End 2.5K Repaired Nickel Segment After Cleaning and Machining Upper Coolant Wall

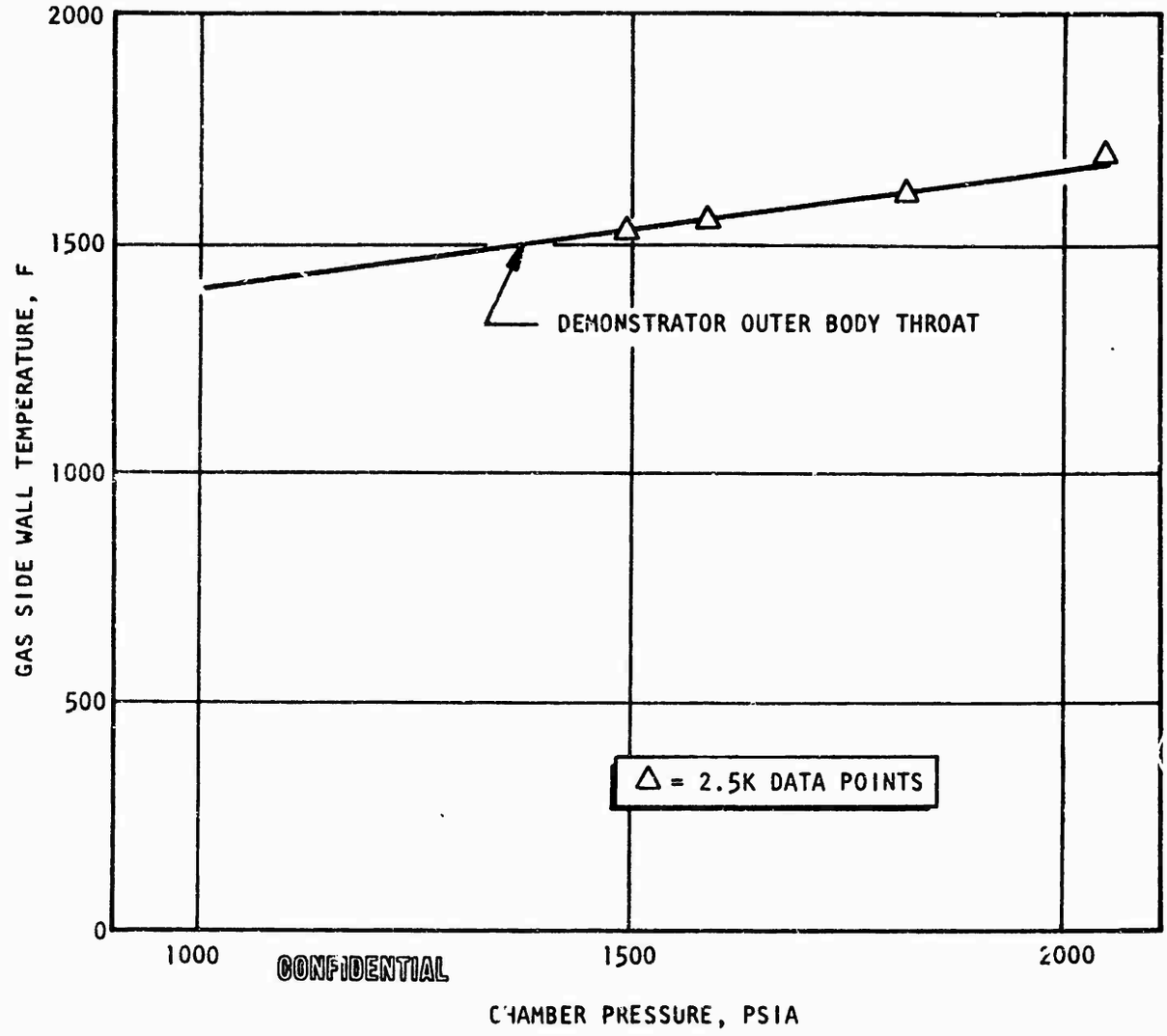

Figure 202. Repaired 2.5K Nickel Tube-Wall Temperature Simulation of 250K Demonstrator

Nickel Tube-Wall Thrust Chamber Cycling Tests.

(C) Test Conditions. An experimental determination of the thermal fatigue life of a 2.5K segment thrust chamber was completed. The goal of this 2.5K tube-wall segment cycling program was to demonstrate by actual hot-firing tests the life expectancy of the Nickel 200 tube material selected for the Demonstrator tubes. A further benefit derived from this tests series was an experimental verification of the analytical tube life predictions.

(U) To achieve these goals, it was necessary to reproduce operating conditions which simulated the critical fatigue life parameters of the Demonstrator at rated operation in a segment thrust chamber having an identical tube material. The analysis establishing the operating conditions is contained in the Analysis of Results section below.

(C) The second nickel tube-wall 2.5K thrust chamber was made available from a related program and used for these cycling tests. This segment was fabricated of Nickel 200 tubes which were drawn, tapered, and pressure formed following a process planning which closely resembled that described for the Demonstrator Module. The segment thrust chamber experienced two-step furnace braze cycles, using the braze alloy systems selected during the tube material selection program. The total furnace time at high temperature was adequate to ensure that tube material grain growth effects were simulated.

(C) Ignition was obtained by the use of TEA-TEB hypergol. The current plan for the Demonstrator Module ignition makes use of O_2/H_2 1800 F hot gas. No appreciable differences in environmental effects were predicted as a result of the substitution of the hypergolic ignition fluid. During the test series, no deposits resulting from the combustion of TEA-TEB were found in the thrust chamber except in very minute quantities.

(C) It was concluded that the effects of chemical and temperature environment on the metallurgy of the Demonstrator Nickel 200 tube material were simulated in the 2.5K segment.

(U) Instrumentation. The 2.5K segment used for the cyclic test series was instrumented to ensure the aquisition of the necessary data. Some redundancy in the instrumentation was employed to increase confidence and reliability. A schematic of the tube bank coolant flow circuit, injector flow circuit, and related instrumentation is shown in Fig.203. An indication of the type of equipment used to record the data is also given. Where needed, fast response recorders were employed in parallel with the more usual direct-inking recorders so that dynamic effects were not lost. A photograph of the segment thrust chamber mounted on CTL-3 cell 18-A is shown in Fig.204.

(C) Testing Procedure. The 2.5K segment was tested by cycling chamber pressure, and thus tube wall temperature, in a series of cyclic test groups. During each test group, the fuel flow through the injector and tube banks remained unchecked, while the LO_2 flow was intermittently stopped. Ignition was obtained at the start of each test group with TEA-TEB hypergol, and was maintained during the idle phases of each test group by a small, continuous, gaseous oxygen flow. During these cyclic idle phases, the heat flux to the walls was very low, and by analysis, a tube-wall and adjacent-structure average temperature which approached -230 F was realized. The upper cyclic tube-wall temperatures were near those predicted for the Demonstrator throat. Figure 205 shows a typical plot of the key operational parameters during a mainstage cycle test as a function of time. Table 67 presents a summary of 2.5K segment cycle tests. A tabulation of the operational, tube cooling, and life parameters for each test is given in Table 68.

(C) Figure 206 shows a nozzle end photograph of the segment chamber after 243 hot-fire cycles.

(C) The chamber segment was still in operating condition at the conclusion of the 315 hot-firing cycles. However, since the program goal of demonstrating the feasibility of obtaining 300 hot-fire cycles with the Nickel 200 tube material selected for the Demonstrator Module chamber had been exceeded, the hardware was removed from the test facility in favor of a detailed metallurgical analysis of the chamber and injector.

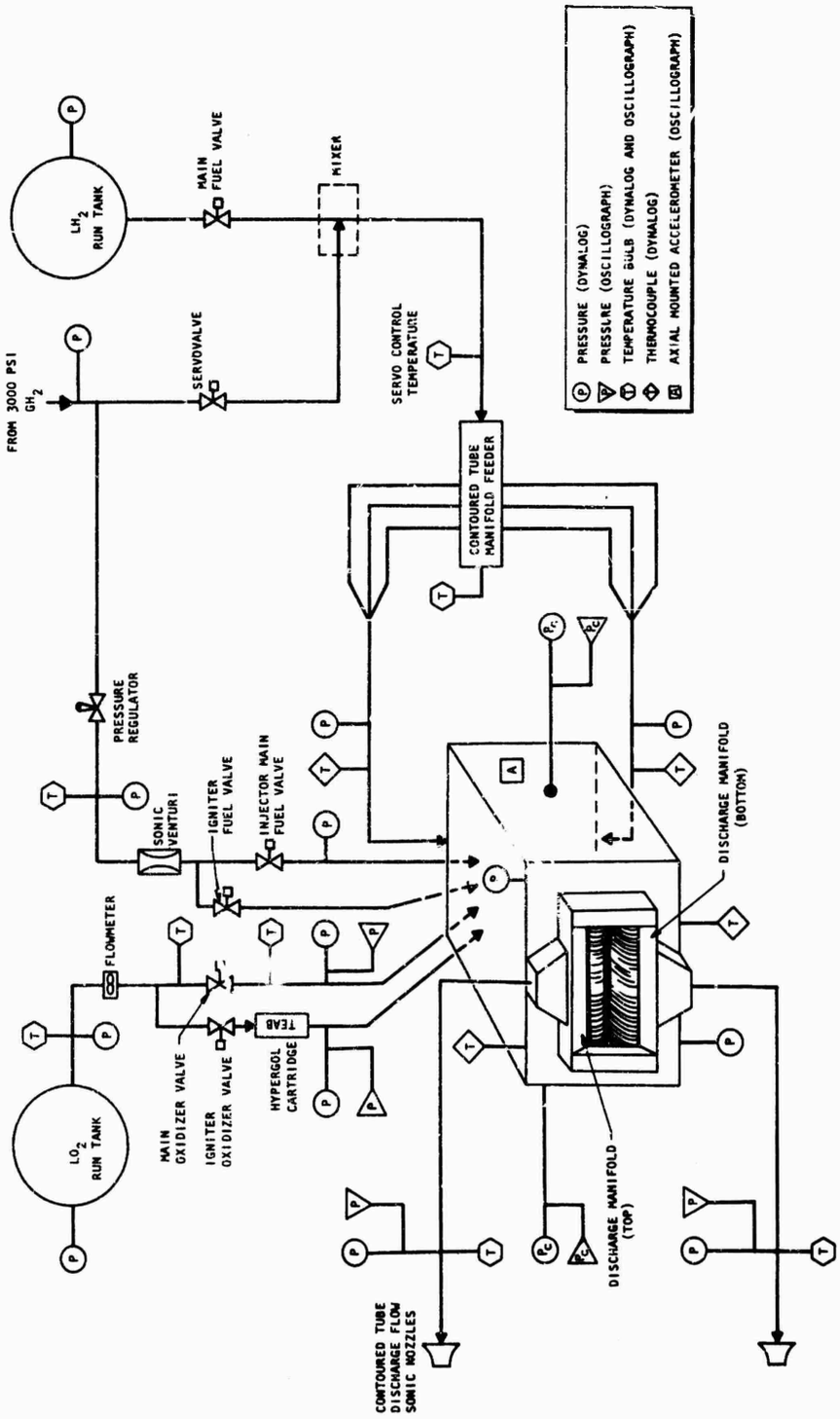

Figure 203. Cycling Test Instrumentation and Flow Circuit Schematic Nickel Tube-Wall Segment

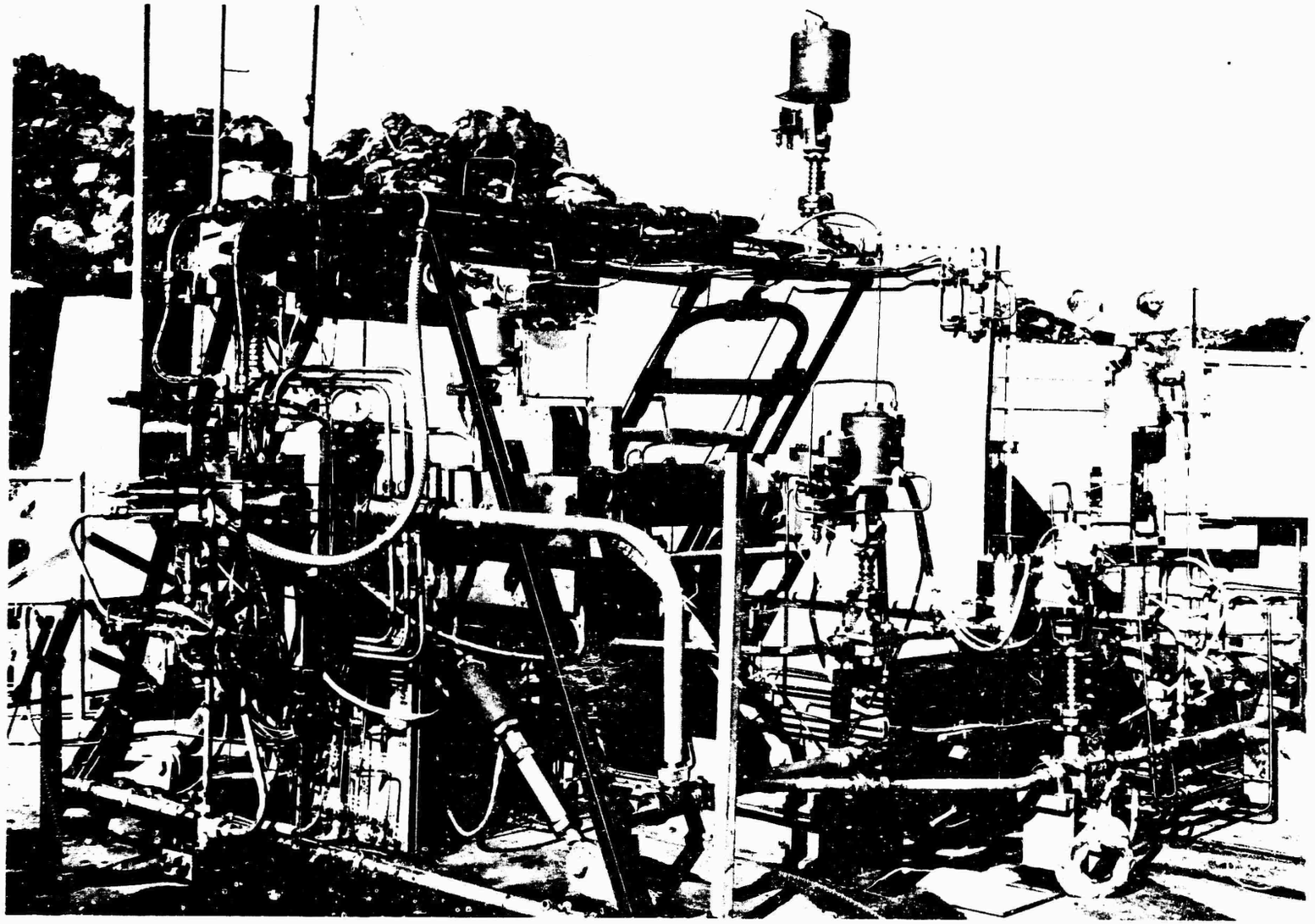

1CT23-11/14-66-SID

Figure 204. Segment Thrust Chamber Mounted on CTL-3

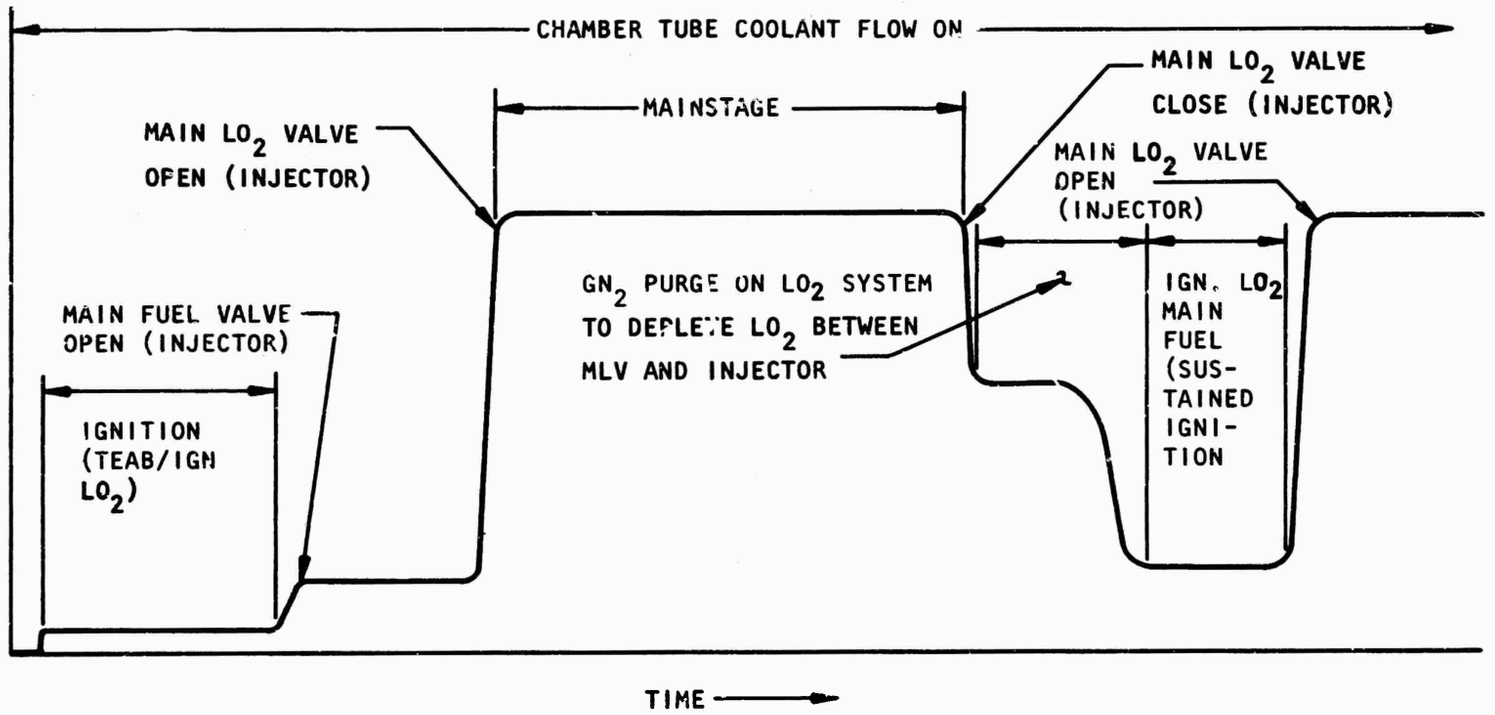

Figure 205. Typical Chamber Pressure Trace During 2.5K Tube-Wall Segment Mainstage Cycling Program

TABLE 67

(C) SUMMARY OF 2.5K SEGMENT CYCLE TESTS

Test No.	Cycle No.	Chamber Pressure, psia	Injector Mixture Ratio*	Coolant Mass Velocity	Tube Gas Wall Temperature*, F	Tube Hydraulic Temperature*, psi	Tube Hydraulic Stress*, psi	Approximate Life Simulation* Ratio
1				Ignition Only				
2	1	610	6.05	12.55	810	524	3836	3.091
3	2	930	5.30	11.28	1195	828	3375	1.522
4	3-17	956	5.06	12.45	1140	758	3335	1.595
5	18	1320	5.04	11.50	1550	1108	2814	0.944
6	19-35	1322	5.31	12.13	1525	1058	2810	0.971
7	36-51	1303	5.22	12.13	1505	1062	2940	0.983
8	52-67	1230	5.07	11.28	1490	1064	2945	1.020
9	68-84	1071	5.42	10.68	1360	964	3175	1.213
10	85	1210	4.47	10.63	1510	1090	2971	1.011
11	86-116	1309	4.96	12.03	1520	1075	2900	0.968
12	117-147	1330	5.00	12.03	1535	1087	2795	0.948
13	148-178	1230	5.14	10.40	1545	1123	2950	0.975
14	179-209	1260	4.94	10.85	1545	1117	2640	0.967
15	210-242	1310	5.31	10.96	1585	1144	2830	0.942
16	243-277	1330	5.00	10.53	1620	1178	2800	0.890
17	278-314	1270	4.45	10.64	1560	1129	2890	0.954

*Average values

CONFIDENTIAL

TABLE 68A

(c) COMPARISON OF 2.5K SEGMENT CYCLE TESTS TO DEMONSTRATOR MODULE

Operational Parameters				Tube Cooling and Life Parameters at Throat				
Test No.	Cycle No.	Chamber Pressure, psia	Injector Mixture Ratio	Coolant Mass Velocity	Tube Gas Wall Temperature, F	Tube Mean Wall Temperature, F	Tube Hydraulic Stress, psi	Approximate Life Simulation Ratio
Demonstrator Module								
		1500	6.0	10.6* 11.2**	1520	1116* 1030**	2340* 3560**	
2.5K Segment								
1		Ignition Only →						
2	1	610	6.05	12.55	810	524	3836	3.091
3	2	930	5.30	11.28	1195	828	3375	1.522
4	3	1070	4.60	12.45	1275	880	3173	1.365
↓	4	960	5.22	↓	1130	752	3333	1.625
	5	940	5.22		1110	724	3361	1.654
	6	950	5.04		1120	740	3346	1.644
	7	945	5.20		1115	736	3354	1.657
	8	940	5.21		1110	724	3361	1.654
	9	950	4.95		1120	740	3346	1.644
	10	940	5.21		1110	724	3361	1.654
	11	950	5.22		1120	740	3346	1.644
	12	955	5.06		1125	744	3341	1.631
	13	960	5.06		1130	752	3333	1.625
	14	940	4.90		1110	724	3361	1.654
	15	940	5.00		1110	724	3361	1.654
	16	960	5.07		1130	752	3333	1.625
↓	17	940	4.92	↓	1110	724	3361	1.654
5	18	1320	5.04	11.50	1550	1108	2814	0.944
6	19	1360	5.52	12.13	1550	1096	2756	0.930
6	20	1300	5.51	12.13	1505	1057	2843	0.976

*Outer Body
**Inner Body

TABLE 68B

(C) COMPARISON OF 2.5K SEGMENT CYCLE TESTS TO DEMONSTRATOR MODULE

Operational Parameters				Tube Cooling and Life Parameters at Throat				
Test No.	Cycle No.	Chamber Pressure, psia	Injector Mixture Ratio	Coolant Mass Velocity	Tube Gas Wall Temperature, F	Tube Mean Wall Temperature, F	Tube Hydraulic Stress, psi	Approximate Life Simulation Ratio
6	21	1340	5.25	12.13	1530	1078	2785	0.949
	22	1320	5.28		1517	1069	2814	0.965
	23	1310	5.34		1511	1066	2830	0.975
	24	1300	5.40		1505	1061	2843	0.982
	25	1320	5.28		1517	1069	2814	0.965
	26	1325	5.27		1521	1073	2806	0.961
	27	1320	5.27		1517	1068	2814	0.964
	28	1315	5.25		1514	1066	2282	0.969
	29	1330	5.27		1523	1075	2298	0.961
	30	1330	5.29		1523	1075	2798	0.961
	31	1310	5.29		1511	1063	2830	0.972
	32	1320	5.30		1517	1068	2814	0.964
	33	1330	5.36		1523	1075	2798	0.961
	34	1325	5.41		1521	1073	2806	0.961
	35	1320	5.41		1517	1069	2814	0.965
7	36	1285	5.49	12.13	1500	1058	2864	0.988
	37	1290	5.15		1503	1061	2856	0.985
	38	1290	5.19		1503	1062	2856	0.986
	39	1295	5.21		1505	1063	2851	0.984
	40	1290	5.16		1503	1061	2856	0.985
	41	1320	5.10		1517	1071	2814	0.968
	42	1300	5.04		1505	1060	2843	0.980
	43	1330	5.24		1523	1075	2798	0.959
	44	1295	5.17		1505	1063	2851	0.984
	45	1320	5.30		1517	1068	2814	0.964
	46	1325	5.24		1521	1073	2806	0.963
	47	1300	5.20		1505	1058	2343	0.979
	48	1305	5.24		1507	1061	2835	0.978

CONFIDENTIAL

TABLE 68C

(C) COMPARISON OF 2.5K SEGMENT CYCLE TESTS TO DEMONSTRATOR MODULE

Operational Parameters				Tube Cooling and Life Parameters at Throat				
Test No.	Cycle No.	Chamber Pressure, psia	Injector Mixture Ratio	Coolant Mass Velocity	Tube Gas Wall Temperature, F	Tube Mean Wall Temperature, F	Tube Hydraulic Stress, psi	Approximate Life Simulation Ratio
7	49	1305	5.24	12.13	1507	1061	2835	0.978
↓	50	1310	5.24	12.13	1511	1064	2827	0.973
↓	51	1290	5.25	12.13	1503	1061	2856	0.985
8	52	1240	5.00	11.28	1500	1073	2929	1.008
↓	53	1220	5.00	↓	1485	1063	2958	1.030
↓	54	1220	5.00	↓	1485	1063	2958	1.030
↓	55	1215	5.00	↓	1480	1060	2966	1.040
↓	56	1215	5.01	↓	1480	1060	2961	1.040
↓	57	1218	5.01	↓	1483	1063	2961	1.037
↓	58	1215	5.01	↓	1480	1060	2966	1.090
↓	59	1230	5.02	↓	1490	1064	2942	1.021
↓	60	1235	5.12	↓	1495	1069	2937	1.016
↓	61	1215	5.03	↓	1480	1060	2961	1.040
↓	62	1215	5.06	↓	1480	1060	2961	1.040
↓	63	1220	5.15	↓	1485	1059	2958	1.026
↓	64	1260	5.08	↓	1510	1077	2900	0.992
↓	65	1235	5.08	↓	1495	1069	2937	1.016
↓	66	1255	5.27	↓	1505	1072	2908	0.997
↓	67	1275	5.32	↓	1525	1086	2879	0.970
9	68	1035	5.25	10.86	1315	927	3225	1.286
↓	69	1040	5.25	↓	1325	936	3217	1.422
↓	70	1045	5.25	↓	1335	946	3210	1.257
↓	71	1055	5.36	↓	1345	954	3196	1.241
↓	72	1070	5.56	↓	1370	973	3173	1.198
↓	73	1075	5.34	↓	1375	977	3168	1.188
↓	74	1080	5.56	↓	1380	982	3160	1.182
↓	75	1080	5.56	↓	1380	982	3160	1.182
↓	76	1075	5.56	↓	1375	977	3168	1.351

CONFIDENTIAL

TABLE 68D

(C) COMPARISON OF 2.5K SEGMENT CYCLE TESTS TO DEMONSTRATOR MODULE

Operational Parameters				Tube Cooling and Life Parameters at Throat				
Test No.	Cycle No.	Chamber Pressure, psia	Injector Mixture Ratio	Coolant Mass Velocity	Tube Gas Wall Temperature, F	Tube Mean Wall Temperature, F	Tube Hydraulic Stress, psi	Approximate Life Simulation Ratio
9	77	1070	5.56	10.86	1370	972	3173	1.194
	78	1075	5.56		1375	976	3168	1.186
	79	1085	5.56		1385	986	3152	1.174
	80	1080	5.45		1380	982	3160	1.182
	81	1085	5.35		1385	986	3152	1.174
	82	1080	5.35		1380	982	3160	1.182
	83	1085	5.16		1385	987	3152	1.178
	84	1085	5.56		1385	986	3152	1.174
10	85	1210	4.47	10.63	1510	1090	2971	1.011
11	86	1315	5.12	12.03	1525	1086	2822	0.970
	87	1300	5.01		1510	1069	2843	0.982
	88	1300	4.94		1510	1069	2843	0.982
	89	1300	4.94		1510	1069	2843	0.982
	90	1302	5.01		1512	1071	2840	0.980
	91	1302	4.94		1512	1071	2840	0.980
	92	1304	5.01		1514	1073	2837	0.978
	93	1305	4.94		1515	1074	2837	0.977
	94	1307	4.94		1517	1076	2832	0.976
	95	1307	4.86		1517	1076	2832	0.976
	96	1308	4.92		1518	1077	2832	0.975
	97	1310	4.94		1520	1079	2827	0.973
	98	1310	5.01		1520	1079	2827	0.973
	99	1310	4.92		1520	1079	2827	0.973
	100	1312	4.92		1525	1085	2824	0.969
	101	1312	5.00		1525		2824	
	102	1312	4.90		1525			
	103	1312	4.94		1525			
	104	1312	5.00		1525			

CONFIDENTIAL

TABLE 68E

(C) COMPARISON OF 2.5K SEGMENT CYCLE TESTS TO DEMONSTRATOR MODULE

Operational Parameters				Tube Cooling and Life Parameters at Throat				
Test No.	Cycle No.	Chamber Pressure, psia	Injector Mixture Ratio	Coolant Mass Velocity	Tube Gas Wall Temperature, F	Tube Mean Wall Temperature, F	Tube Hydraulic Stress, psi	Approximate Life Simulation Ratio
11	105	1312	4.92	12.03	1525	1085	2824	0.969
	106		4.92					
	107		4.94					
	108		5.00					
	109		5.02					
	110		4.92					
	111		4.97					
	112		4.97					
	113		4.90					
	114		4.97					
	115		4.97		1522			
	116	1315	5.06		1528	1088		0.967
12	117	1320	5.00	12.03	1530	1087	2814	0.960
	118	1325	5.05		1535	1093	2806	0.956
	119	1330	5.00		1540	1098	2798	0.952
	120		4.97			1097		0.951
	121		4.97					
	122		4.94					
	123		4.94					
	124		4.97					
	125		5.00					
	126		5.12					
	127		4.94					
	128		4.97					
	129		4.97					
	130		4.93					
	131		4.94					
	132		5.00					

CONFIDENTIAL

TABLE 68F

(C) COMPARISON OF 2.5K SEGMENT CYCLE TESTS TO DEMONSTRATOR MODULE

Operational Parameters				Tube Cooling and Life Parameters at Throat				
Test No.	Cycle No.	Chamber Pressure, psia	Injector Mixture Ratio	Coolant Mass Velocity	Tube Gas Wall Temperature, F	Tube Mean Wall Temperature, F	Tube Hydraulic Stress, psi	Approximate Life Simulation Ratio
12	133	1330	5.00	12.03	1540	1097	2798	0.951
	134		5.00					
	135		5.09					
	136		4.97					
	137		5.05					
	138		5.06					
	139		5.03					
	140		5.00					
	141		4.97					
	142		5.03					
	143		5.04					
	144		5.00					
	145		5.00					
	146		5.00					
	147		5.03					

TABLE 68G

(C) COMPARISON OF 2.5K SEGMENT CYCLE TESTS TO DEMONSTRATOR MODULE

Operational Parameters				Tube Cooling and Life Parameters at Throat				
Test No.	Cycle No.	Chamber Pressure, psia	Injector Mixture Ratio	Coolant Mass Velocity	Tube Gas Wall Temperature, F	Tube Mean Wall Temperature, F	Tube Hydraulic Stress, psi	Approximate Life Simulation Ratio
13	148	1215	5.48	10.4	1530	1112	2966	0.994
	149	1220	4.80		1535	1120	2958	0.995
	150	1235	5.00		1550	1126	2937	0.969
	151	1235	5.00		1550	1126	2937	0.969
	152	1235	4.98		1550	1131	2937	0.976
	153	1235	5.02		1550	1126	2937	0.969
	154	1235	5.36		1550	1127	2937	0.970
	155	1235	5.05		1550	1126	2937	0.969
	156	1235	5.06		1550	1126	2937	0.969
	157	1230	5.07		1540	1118	2945	0.981
	158	1240	4.94		1555	1134	2929	0.969
	159	1235	5.36		1550	1126	2937	0.969
	160	1240	4.83		1555	1137	2929	0.974
	161	1235	5.44		1550	1126	2937	0.969
	162	1235	5.18		1550	1127	2937	0.970
	163	1245	5.00		1560	1126	2919	0.968
	164	1235	5.23		1550	1126	2937	0.969
	165	1240	5.12		1555	1130	2929	0.962
	166	1240	5.26		1555	1131	2929	0.963
	167	1240	5.25		1555	1129	2929	0.961
	168	1240	5.30		1555	1129	2929	0.961
	169	1240	5.02		1555	1130	2929	0.962
	170	1240	5.06		1555	1130	2929	0.962
	171	1235	5.32		1550	1130	2937	0.963
	172	1230	5.36		1540	1114	2945	0.975
	173	1245	5.00		1560	1136	2921	0.959
	174	1235	5.14		1550	1125	2937	0.967

TABLE 68H

(C) COMPARISON OF 2.5K SEGMENT CYCLE TESTS TO DEMONSTRATOR MODULE

Operational Parameters				Tube Cooling and Life Parameters at Throat				
Test No.	Cycle No.	Chamber Pressure, psia	Injector Mixture Ratio	Coolant Mass Velocity	Tube Gas Wall Temperature, F	Tube Mean Wall Temperature, F	Tube Hydraulic Stress, psi	Approximate Life Simulation Ratio
13	176	1245	5.43	10.4	1560	1134	2921	0.957
↓	177	1235	4.85	↓	1550	1135	2937	0.981
	178	1235	5.40		1550	1126	2937	0.969
	179	1230	5.12		1540	1116	2945	0.977
14	180	1235	5.22	10.85	1515	1088	↓	0.994
↓	181	1245	5.28	↓	1525	1098		0.985
	182	1255	4.87		1535	1111		0.982
	183	↓	4.95		↓	1110		0.981
	184		4.94			↓		↓
	185		4.95					
	186		4.95					
	187	1255	5.02			1106	2908	0.974
	188	↓	4.90			1111	↓	0.982
	189		4.90			1111		0.982
	190		4.95			1110		0.981
	191		4.90			1111		0.982
	192		4.90			1111		0.982
	193		5.02			1106		0.974
	194		4.95			1110		0.981
	195		4.90			1111		0.982
	196		4.90			1111		0.982
	197		4.90			1111		0.982
	198	1265	4.95		1545	1118	2892	0.968
	199	↓	4.90		↓	1118	↓	0.970
	200		4.92			1118		0.970
	201		4.88			1119		0.971
	202		4.90			1118		0.970
	203		4.95			1118		0.968
	204		4.90			1118		0.970
↓	205	1275	4.90	↓	1555	1128	2879	0.959

CONFIDENTIAL

TABLE 68I

(C) COMPARISON OF 2.5K SEGMENT CYCLE TESTS TO DEMONSTRATOR MODULE

Operational Parameters				Tube Cooling and Life Parameters at Throat				
Test No.	Cycle No.	Chamber Pressure, psia	Injector Mixture Ratio	Coolant Mass Velocity	Tube Gas Wall Temperature, F	Tube Mean Wall Temperature, F	Tube Hydraulic Stress, psi	Approximate Life Simulation Ratio
14	205	1270	4.90	10.85	1550	1123	2887	0.963
	206	1270	4.92		1550	1123	2887	0.963
	207	1270	4.88		1550	1123	2887	0.965
	208	1270	4.88		1550	1123	2887	0.965
	209	1275	4.88		1555	1128	2879	0.961
	210	1275	5.54	10.96	1545	1110	2879	0.957
15	211	1285	5.53		1555	1118	2864	0.946
	212	1305	5.06		1570	1130	2835	0.931
	213	1305	5.24		1570	1128	2835	0.929
	214	1305	5.32		1570	1128	2835	0.929
	215	1305	5.37		1570	1128	2835	0.929
	216	1310	5.24		1575	1133	2830	0.929
	217	1310	5.36		1580	1133	2830	0.929
	218	1315	5.36		1580	1138	2827	0.919
	219		5.37					0.919
	220		5.30					0.919
	221		5.28					0.919
	222		5.21					0.920
	223		5.28					0.920
	224		5.42					0.919
	225		5.33					
	226		5.33					
	227		5.33					
	228		5.25					
	229		5.28					
	230		5.25					
	231	1320	5.42		1585	1141	2814	0.913
	232		5.25					
	233		5.33					
	234		5.30					
	235		5.28					

TABLE 68J

(C) COMPARISON OF 2.5K SEGMENT CYCLE TESTS TO DEMONSTRATOR MODULE

Operational Parameters				Tube Cooling and Life Parameters at Throat				
Test No.	Cycle No.	Chamber Pressure, psia	Injector Mixture Ratio	Coolant Mass Velocity	Tube Gas Wall Temperature, F	Tube Mean Wall Temperature, F	Tube Hydraulic Stress, psi	Approximate Life Simulation Ratio
15	236	1315	5.25	10.96	1580	1138	2827	0.920
	237	1315	5.25		1580	1138	2827	0.920
	238	1320	5.30		1585	1141	2814	0.913
	239							
	240							
	241							
	242							
	243	1315	5.00	10.53	1605	1167	2822	0.905
16	244	1335	5.00		1620	1178	2793	0.889
	245	1340	4.95		1630	1189	2785	0.883
	246	1345	4.95		1640	1200	2777	0.876
	247	1350	4.98		1645	1204	2772	0.872
	248		4.95			1203		0.869
	249							
	250							
	251							
	252							
	253							
	254							
	255		4.98			1202		0.868
	256		4.95			1203		0.869
	257		4.98			1202		0.868
	258		4.92			1203		0.869
	259		4.92					
	260		4.90					
	261		4.97					
	262		4.90					
	263		4.89					
	264		5.00			1202		0.868

TABLE 68K

(C) COMPARISON OF 2.5K SEGMENT CYCLE TESTS TO DEMONSTRATOR MODULE

Operational Parameters				Tube Cooling and Life Parameters at Throat				
Test No.	Cycle No.	Pressure, psia	Injector Mixture Ratio	Coolant Mass Velocity	Tube Gas Wall Temperature, F	Tube Mean Wall Temperature, F	Tube Hydraulic Stress, psi	Approximate Life Simulation Ratio
16	265	1345	5.05	10.53	1640	1197	2777	0.872
	266		5.24			1196		0.875
	267		4.90.			1199		0.875
	268		5.11			1197		0.872
	269		5.11					
	270		5.11					
	271		5.11					
	272		5.10					
	273		5.07					
	274		4.80			1202		0.877
	275		5.24			1197		0.872
	276		5.04			1200		0.876
	277		5.07			1200		0.876
	278	1240	4.51	10.64	1540	1116	2929	0.977
17	279	1255	4.54		1555	1128	2908	0.959
	280	1265	4.40		1565	1141	2892	0.956
	281		4.50					
	282		4.51					
	283		4.49					
	284		4.51					
	285		4.43					
	286		4.43					
	287		4.50					
	288	1275	4.43		1575	1149	2879	0.946
	289		4.47					
	290		4.43					
	291		4.43					
	292		4.45					
	293		4.40					
	294		4.45					

TABLE 68L

(C) COMPARISON OF 2.5K SEGMENT CYCLE TESTS TO DEMONSTRATOR MODULE

Operational Parameters				Tube Cooling and Life Parameters at Throat				
Test No.	Cycle No.	Chamber Pressure, psia	Injector Mixture Ratio	Coolant Mass Velocity	Tube Gas Wall Temperature, F	Tube Mean Wall Temperature, F	Tube Hydraulic Stress, psi	Approximate Life Simulation Ratio
17	295	1275	4.43	10.64	1575	1149	2879	0.946
	296	↓	4.47	↓	↓	↓	↓	↓
	297		4.47					
	298	1280	4.45		1580	1154	2871	0.941
	299	1275	4.43		1575	1149	2879	0.946
	300	1275	4.43		1575	1149	2879	0.946
	301	1275	4.43		1575	1149	2879	0.946
	302	1280	4.43		1580	1154	2871	0.941
	303		4.47					
	304		4.43					
	305		4.50					
	306		4.43					
	307		4.47					
	308		4.43					
	309		4.43					
	310		4.43					
	311		4.50					
	312		4.47					
	313		4.47					
↓	314	↓	4.47	↓	↓	↓	↓	↓

(C) The life simulation ratio of the segment thrust chamber test series was computed as the arithmetic average of the approximate life simulation ratio for each test. The value of this overall ratio was determined to be 1.006. Thus, the fatigue generated during the 314 cycles of the test series is equivalent to the fatigue damage of the Demonstrator Module being tested 312 times.

CONFIDENTIAL

LXR36-6/5/67-S1

Figure 206. 2.5K Nickel Tube-Wall Segment, Posttest 243

(C) Two injectors were used for the test series. The first unit developed minor oxidizer strip leakage after 86 tests and was replaced by the second unit for the final 229 tests. Posttest inspection of the second unit did not reveal any leakage (Fig. 207). However, erosion of the body was noted adjacent to the chamber end-plates and was attributed to an excessive gap between the injector body and the chamber wall.

(C) The injector used for the segment cycling tests was the raised fuel strip design which was selected for the Demonstrator. No provision for the application of film coolant was made in the combustor end walls or tube walls. The injector design included a bias flow from the ends of the fuel strips which prevented LO_2-rich combustion products from burning in the small recesses around the injector body. During the copper 2.5K solid wall tests it was shown that the strip end bias flow had no effect on performance or heat transfer at the throat but did provide tube protection near the injector face. It was concluded that the throat gas-side heat transfer coefficients were representative of those predicted for the Demonstrator Module.

(U) Tube Tester Program. The tube simulation fatigue tests were conducted on a unique tube tester. A typical formed tube and completed tube specimen is shown in Fig. 208. An instrumented tube specimen is installed in the tube tester prior to installation of the pressure chamber is shown in Fig. 209. A spring-loaded chromel/alumel thermocouple located on the tube crown (center of specimen) is used for the programmed cycling control. Other instrumentation shown includes voltage pickups and electrically insulated thermocouples at the ends of the heated specimen. Similar instrumentation is employed on the diametrically opposed tube crown.

1XE45-6/7/67-C1A

Figure 207. 2.5K Injector Unit 4-4, After 229 Cycles

Figure 208. Typical Tube Tester Thermal Fatigue Crack (347 CRES Specimen After 300 Cycles at 70 to 1100 F)

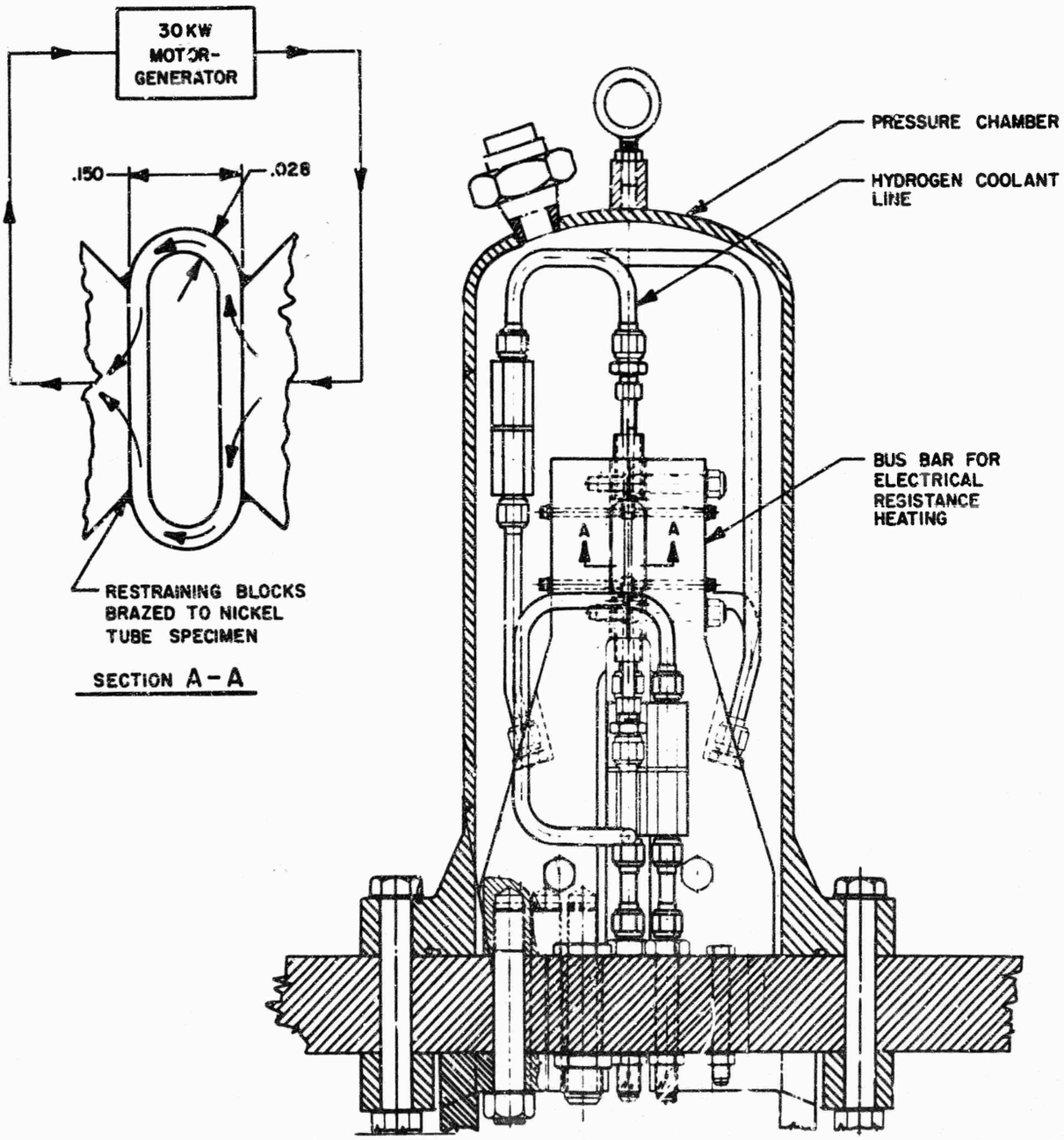

Figure 209. Thrust Chamber Tube Tester (High Pressure)

(C) Several tube tester specimens were thermally cycled to failure to check out the facility and establish an experimental-analytical correlation. These include three 347 CRES tubes and one Hastelloy-X tube, all of 0.010-inch wall thickness. These materials were tested prior to nickel and copper because of material availability. Most of the available experimental data were on stainless steel. Cyclic fatigue data which were obtained agreed with the analytical technique and data used for predicting the fatigue life of tubular chambers.

(C) Start-Stop Simulation Fatigue Tests. The objective of the tube tester experiments was to evaluate the thermal fatigue life and hydraulic stress adequacy of the nickel material under simulated chamber operating conditions. Some of the tests were representative of operating conditions more severe than those anticipated on the Demonstrator Module and thus were conducted as material limit tests. Other tests were as close to the predicted operating values of the Demonstrator Module as the test equipment would permit.

(C) The electrically heated, hydrogen-cooled, thermal fatigue tube tester was the experimental tool used for these tests (Fig. 209). Five thermal fatigue temperature cycle ranges were employed either individually or in combination to evaluate six tubular specimens. The temperature cycle ranges were selected to demonstrate the life capability of Nickel 200 under various cyclic chamber pressure operating conditions.

(C) The first four tests were designed to verify the thermal fatigue life of the throat tubes when subjected to a continuous series of engine start-stop sequences. Two of these tests utilized cyclic gas-wall temperatures of 100 to 1400 F, and thus approached the predicted gas-wall temperature range of the Demonstrator Module throat tubes. One specimen was in the "as received," small-grained condition, while the other was furnace processed with the resulting enlarged grain size. Penetrating crack failures occurred at 315 cycles in the "as-received" specimen, while the

furnace-processed specimen was run a total of 320 cycles without failure. Fatigue cracks were initiated, however, and further testing was deemed unnecessary. These tests were run at temperature conditions somewhat less severe than the Demonstrator Module throat tubes (T_{wg} = 1400 vs 1520 F, T_B = 100 vs -230 F); consequently, the induced cyclic plastic strains were less. The experimentally determined life, however, was in excess of the Demonstrator Module predicted life, and thus the selection of Nickel 200 as a tube material was supported.

(C) The other two engine start-stop sequence tests employed 0.012-inch wall tubes in the furnace-processed condition with cyclic gas-wall temperatures of about 100 to 1800 F. Such a temperature range on the Demonstrator Module tubes would be representative of an ambient to over 2000 psi chamber pressure start cycle. The fatigue failures occurred at 142 and 143 cycles. These tests demonstrate the safety margin of the chamber tubes for overtemperature conditions which may occur as a result of malfunction or abnormal conditions.

(C) Intermediate Throttling Fatigue Tests. Two other tests on a related program were intended to explore the limits of the Nickel 200 tube material under more complex operating conditions. Two cyclic temperature ranges were employed on the first specimen. A cyclic temperature range of 620 to 1140 F was initially applied to the specimen a total of 800 times with no evidence of failure. The same specimen was then additionally cycled 193 times between 100 to 900 F. Although the heated tube crown still showed no visible evidence of fatigue cracks, testing was stopped because of a breakdown of the specimen in another area.

(C) Steady-State Creep and Fatigue Tests. The last test employed an 0.028-inch wall sepcimen which was designed for high heat flux continuous testing. The objective was to verify the limits of Nickel 200 in

combined thermal fatigue and hydraulic stress induced creep. A severe steady-state gas wall temperature cycling condition of 1365 to 1435 F at a frequency of about 1 cps, in combination with a heat flux of 50 Btu/in.^{2}/sec and a hydraulic stress of 4500 psi, was applied to the specimen. Testing continued for 7 hours, accumulating 22,500 thermal cycles without fracture or leaks. Routine inspection revealed that microcracks were initiated, however, and further testing was stopped. Table 69 summarizes the results of these thermal fatigue tests.

(U) A tube tester data reduction computer program was developed under separate funding. This program gave an accurate measure of the specimen wall temperature drop. Included in the wall drop numerical solution were the variables of thermal and electrical conductivity with temperature, and variable current distribution in the bimetallic bus bars.

(U) A computation of the plastic strains was also included in the program, based on the plastic strain analysis, the measured test gas wall cyclic temperatures, and the program computed wall drop. These values are given in Table 69 which also includes a computed equivalent fatigue life for the demonstrator throat tubes. This computed life is based on an extrapolation of the tube tester data, using the relationship $N_F^k \Delta \epsilon_p = C$, where k was assumed to have a value of one-half.

(U) It is seen that the technique gave a lower life (about one-third) for the Demonstrator tubes than was realized in the 2.5K segment start-stop cycling tests. This difference was attributed to nonuniform specimen tube crown cyclical heating in the tangential direction, resulting in tangential strain concentrations at the tube crown, and perhaps other effects unresolved at this time. The "steady-state" creep and fatigue test results, however, were thought to reasonably represent the Demonstrator tube life, if such steady-state temperature fluctuations were actually realized in service.

TABLE 69

(C) THERMAL FATIGUE TUBE TESTER RESULTS ON NICKEL 200

Type of Test	Tubular Specimen Metallurgical Condition	Cyclic Gas Wall Temperature, F	Wall Temperature Drop, F	Hydraulic Stress in Heated Tube Crown, psi	No. of Thermal Cycles	Final Appearance of Heated Tube Crown	Equivalent Cycles at Demonstrator Conditions
Demo Module Start Simulation	As received	100 to 1400	74	1000	315	Intergranular and transgranular cracks, rupture	86
Demo Module Start Simulation	Furnace Processed	100 to 1400	65	1000	320	Intergranular and transgranular cracks, no rupture	94
Overtemperature Limit Test	Furnace Processed	100 to 1800	87	1000	142	Intergranular cracks, rupture	80
Overtemperature Limit Test	Furnace Processed	100 to 1800	92	1000	143	Intergranular cracks, rupture	86
Exploratory Limit Test	Furnace Processed	620 to 1140 100 to 900	200	3300 3300	800 193	No visible cracks, no leaks or rupture	Not applicable
Steady-State Limit Test	Furnace Processed	1365 to 1435	520	4500	22,500 over 7 hours	Cracks initiated, no leaks or rupture	22,500

CONFIDENTIAL

Analysis of Results

(C) Heat Transfer Data Input From 2.5K Solid-Wall Tests. The solid-wall chamber heat transfer data acquired later in the program showed that the heat transfer rates were generally higher than the initial analysis predicted. The existing 2.5K segment tube design was then evaluated using these improved data, and the increased cooling requirements were determined. The revised heat flux made type 347 stainless-steel a less attractive tube material since the conduction limits were approached at high chamber pressures with the 0.008-inch wall thickness. This circumstance, coupled with the reduced thermal fatigue life determined from the material selection program, led to the elimination of this material from further consideration for any tube-wall chambers constructed in the program. Analytical efforts were concentrated on the more conductive tube materials of nickel and copper.

(C) Cooling Limits and Heat Transfer Maximum Potential. The 2.5K chamber capability was analyzed extensively in terms of coolant flowrates required in the contour tubes as a function of chamber pressure, wall temperature, coolant bulk temperature, and throat curvature enhancement factor. Typical requirements for the nickel and copper tubes are shown in Fig. 210 and 211, respectively. The indicated mixture ratios are coolant mixture ratios (combustion oxidizer flow/hydrogen coolant flow). The maximum coolant flow which can be obtained was limited by test stand pressure capability.

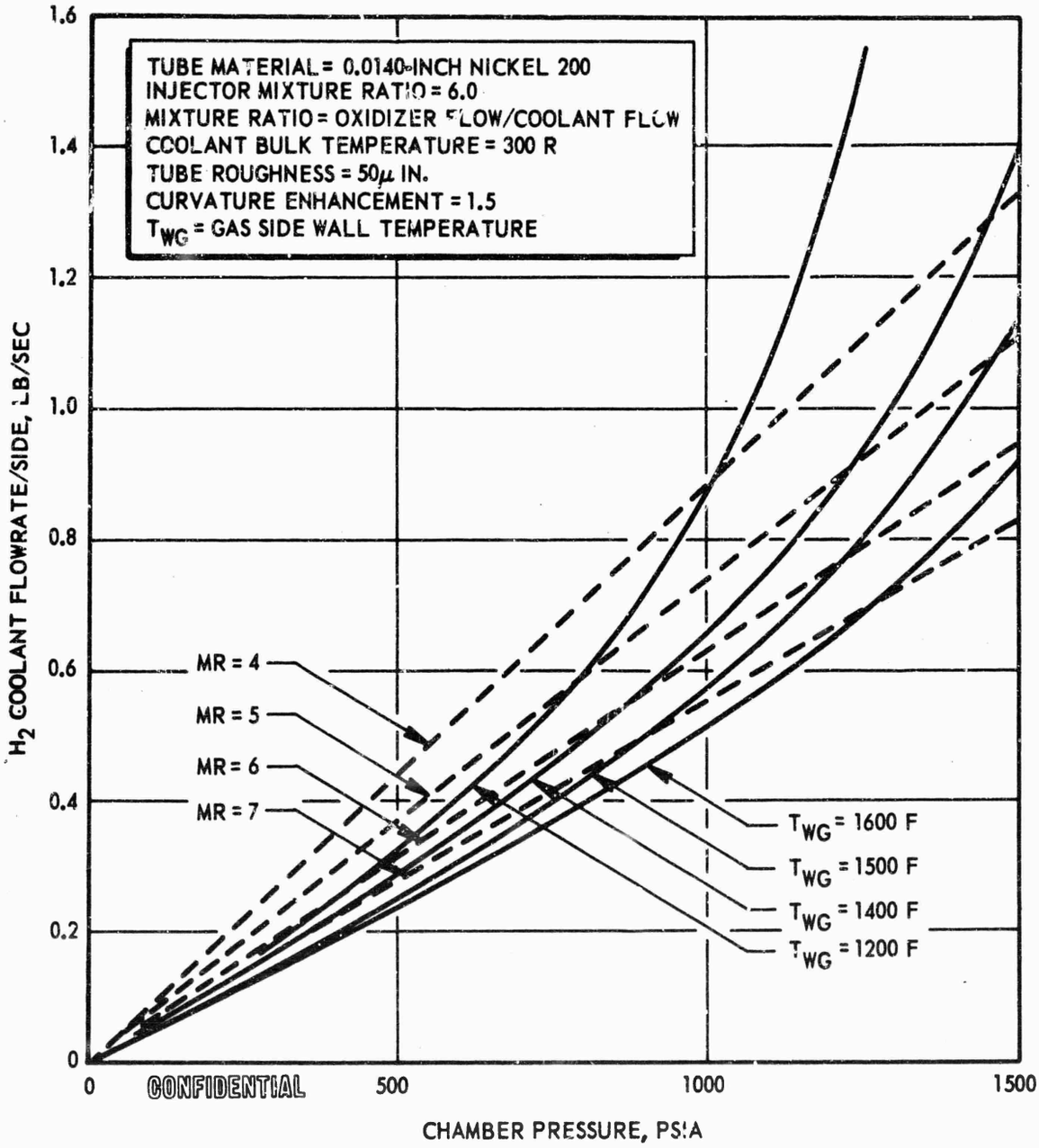

Figure 210. Typical Throat Cooling Requirements for 2.5K Contour Wall LO_2/H_2 Thrust Chamber

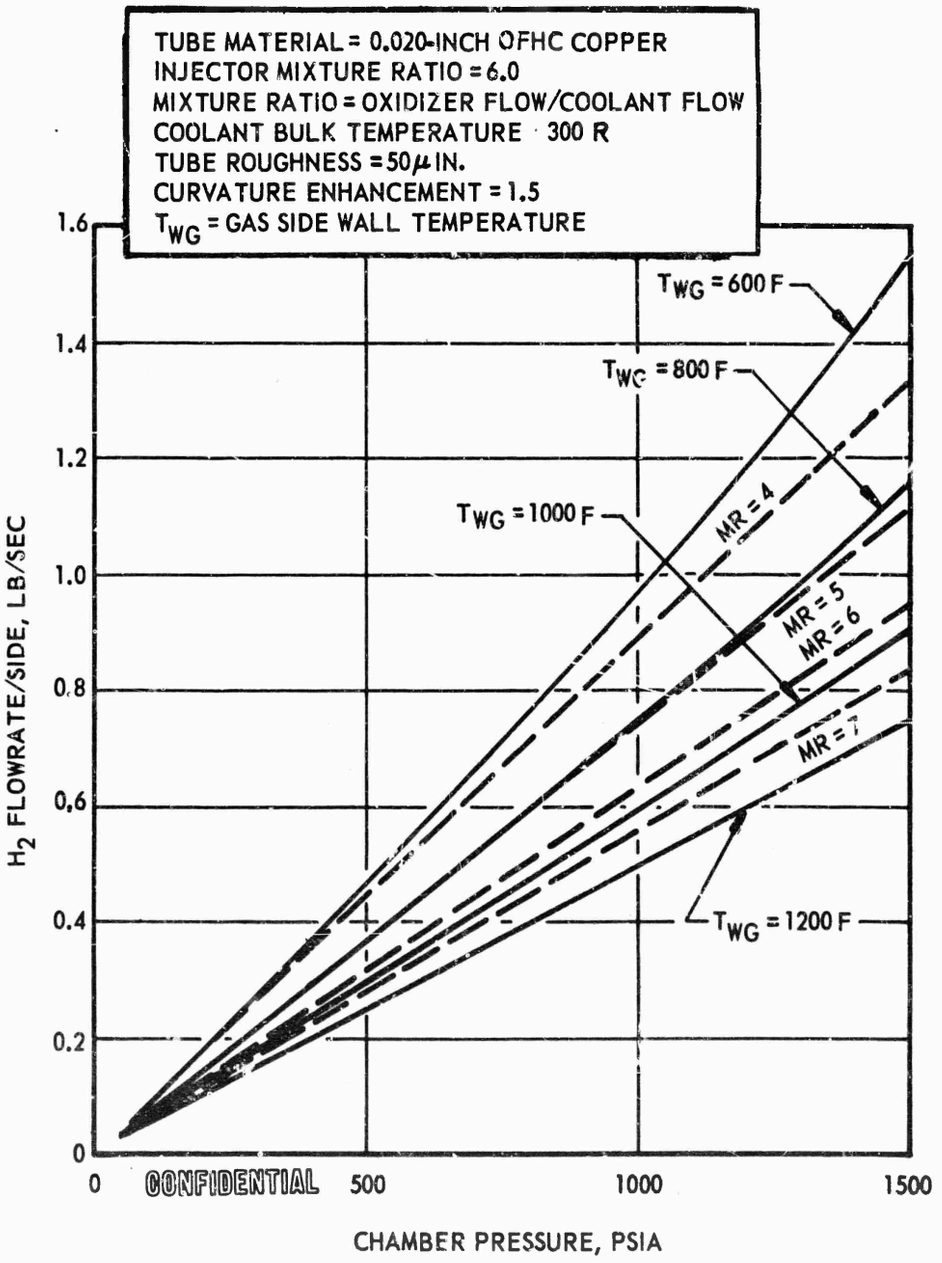

Figure 211 Typical Throat Cooling Requirements for 2.5K Contour Tube-Wall LO_2/H_2 Thrust Chamber

(C) Combustion zone operation was sensitive to coolant inlet temperature (Fig.212). Consequently, these values were monitored during later tests. Side walls were cooled with water satisfactorily up to 1100-psia chamber pressure. Above 1100 psia, hydrogen was used in the throat region to take advantage of curvature enhancement induced by swirl vanes.

(C) The maximum heat transfer potential for H_2/O_2 propellants is determined through the maximization of the product of the gas-side film coefficient and the temperature difference between the adiabatic wall temperature and the wall temperature. The film coefficient has a maximum value at low mixture ratios, whereas the temperature difference is a maximum at stoichiometric. The combined maximum occurs at a mixture ratio of approximately 6:1 as shown in Fig.213. As seen in Fig.214, it is this condition to which the tube design must be tailored. Operation at other mixture ratios, such as 7:1, results in wall temperatures cooler than these at a mixture ratio of 6:1. It is also apparent that a tapoff engine design is not penalized at any mixture ratio because all the coolant passes through the coolant circuit.

(C) A study of the heat flux capability of materials, OFHC copper (0.020 inch) and Nickel 200 (0.013 inch), showed that the heat flux capability of these materials was in this order indicated, copper being the best. The results are shown in Fig.215 and 216. For the purposes of this study, a coolant bulk temperature of 450 R was used (this approximates the anticipated value in the outer body throat of the 250K thrust chamber), and a tube roughness of 50 microinches was assumed. Coolant mass velocity of 11 $lb/in.^2$-sec is based on a coolant Mach number of about 0.5 for 450 R and 2200-psia (total pressure) hydrogen.

(C) The results for nickel 200 incidate it can conduct with a 1600 F wall temperature, a heat flux of 44, and 60 $Btu/in.^2$-sec for curvature enhancements of 1.0 and 1.75, respectively. Thus, Nickel 200 can operate at conditions of the Demonstrator Module which has a curvature factor of

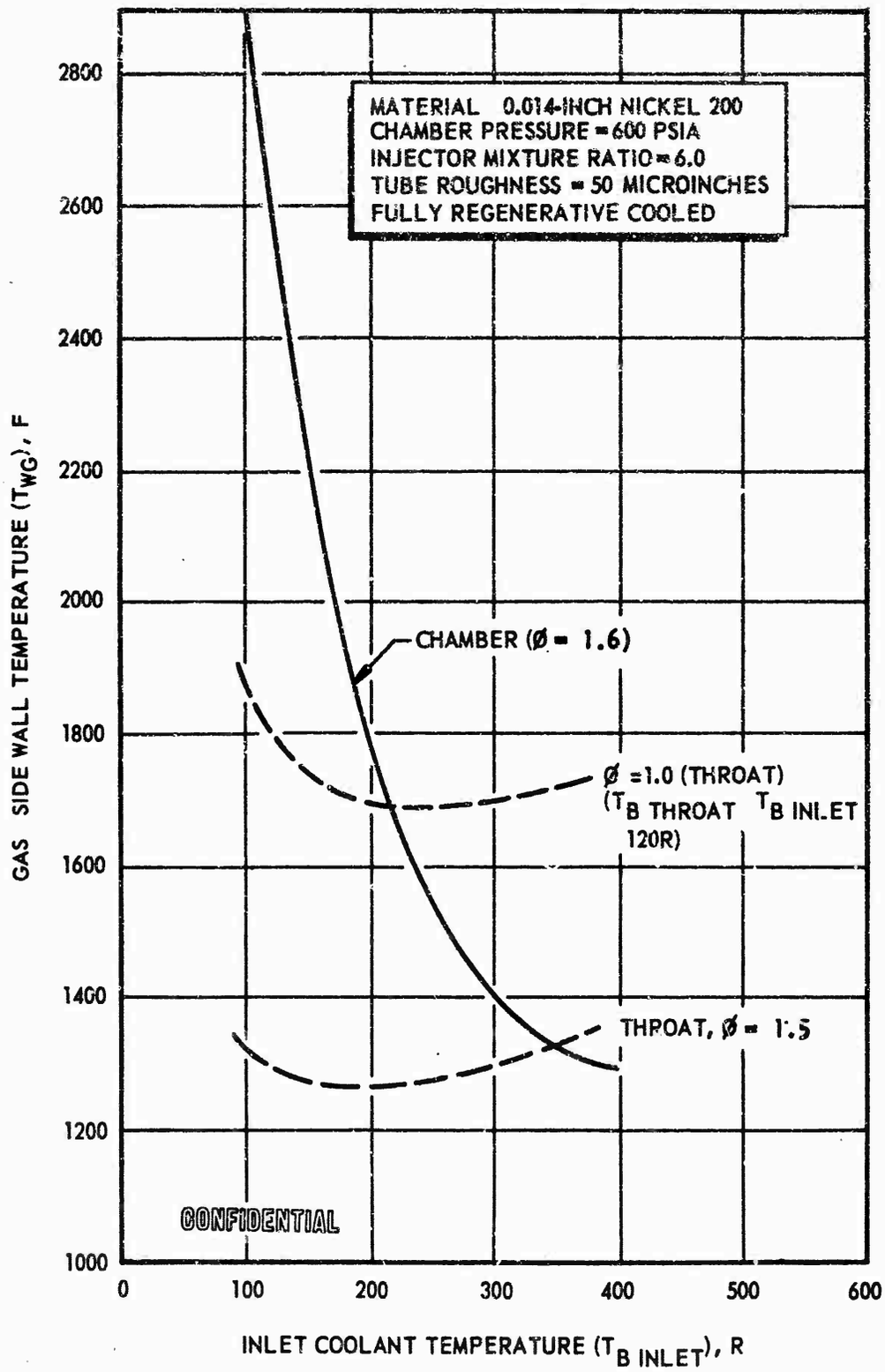

Figure 212. Gas Side Wall Temperature for 2.5K Contour Tube Thrust Chamber

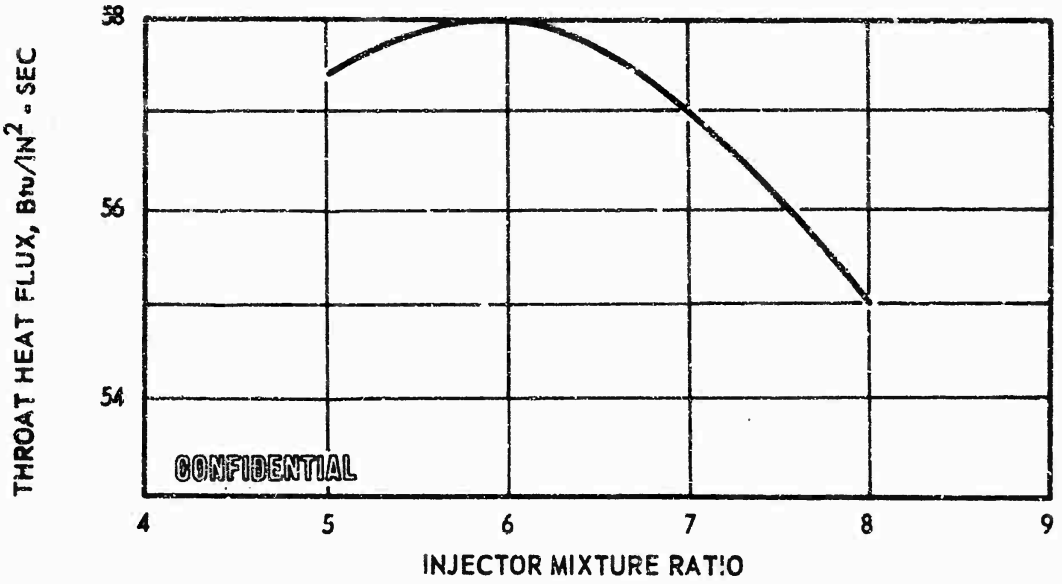

Figure 213. Throat Heat Flux for LO_2/H_2 With Gas Side Wall Temperature of 1450 F at Chamber Pressure of 1500 psia

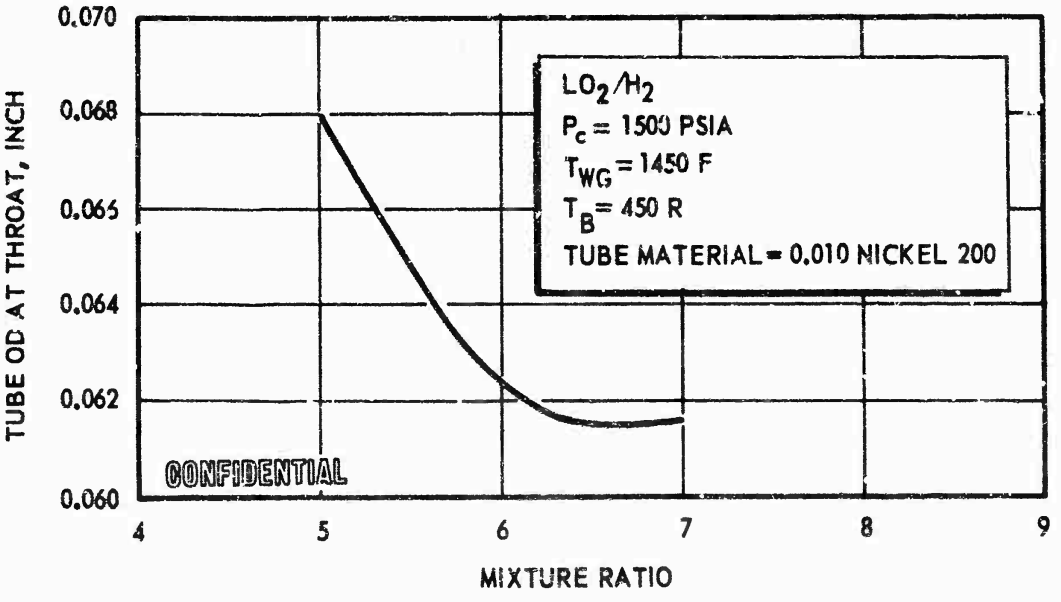

Figure 214. Maximum Outside Tube Diameter at Throat

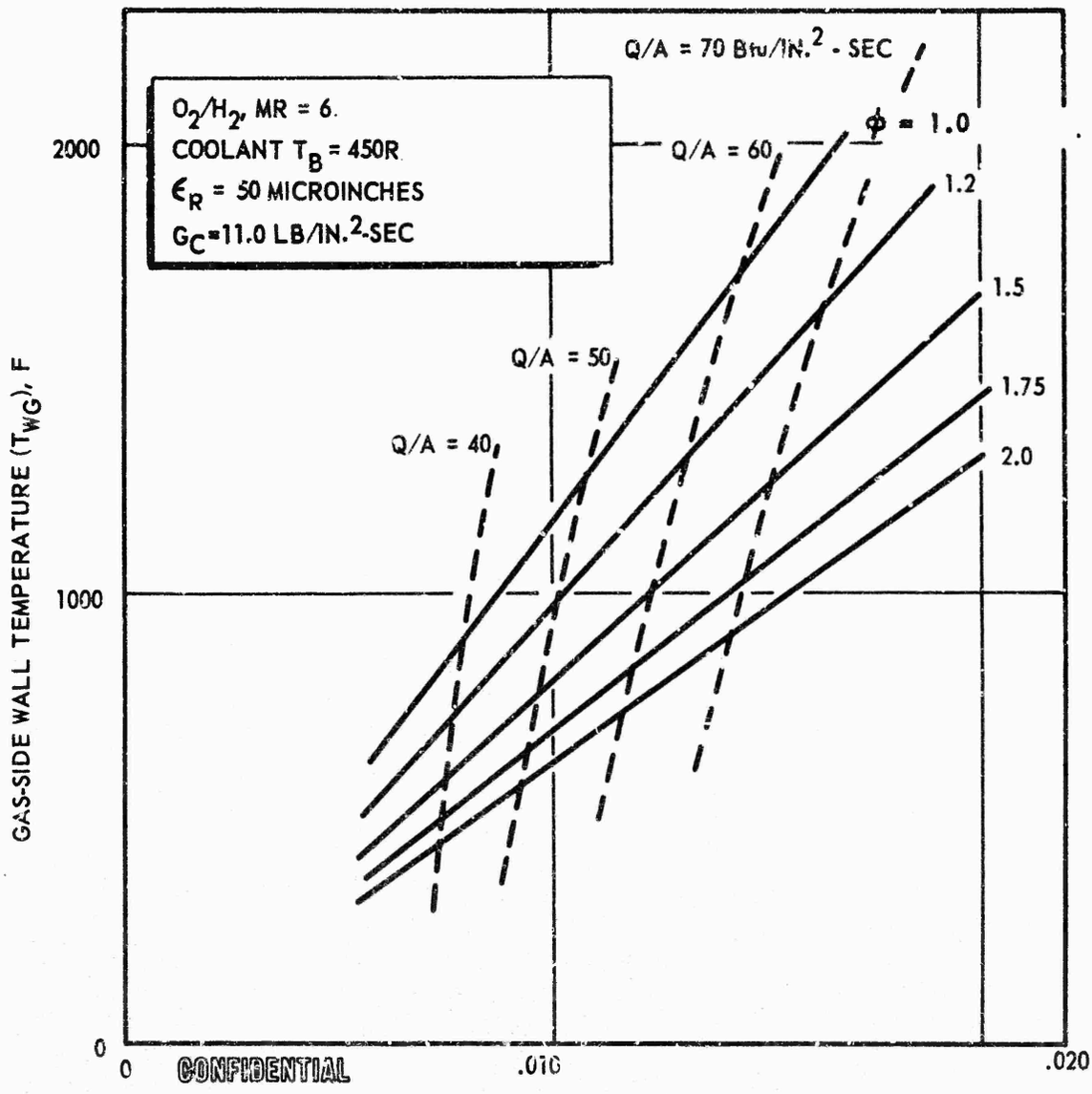

Figure 215. Cooling Limit Results for OFHC Copper

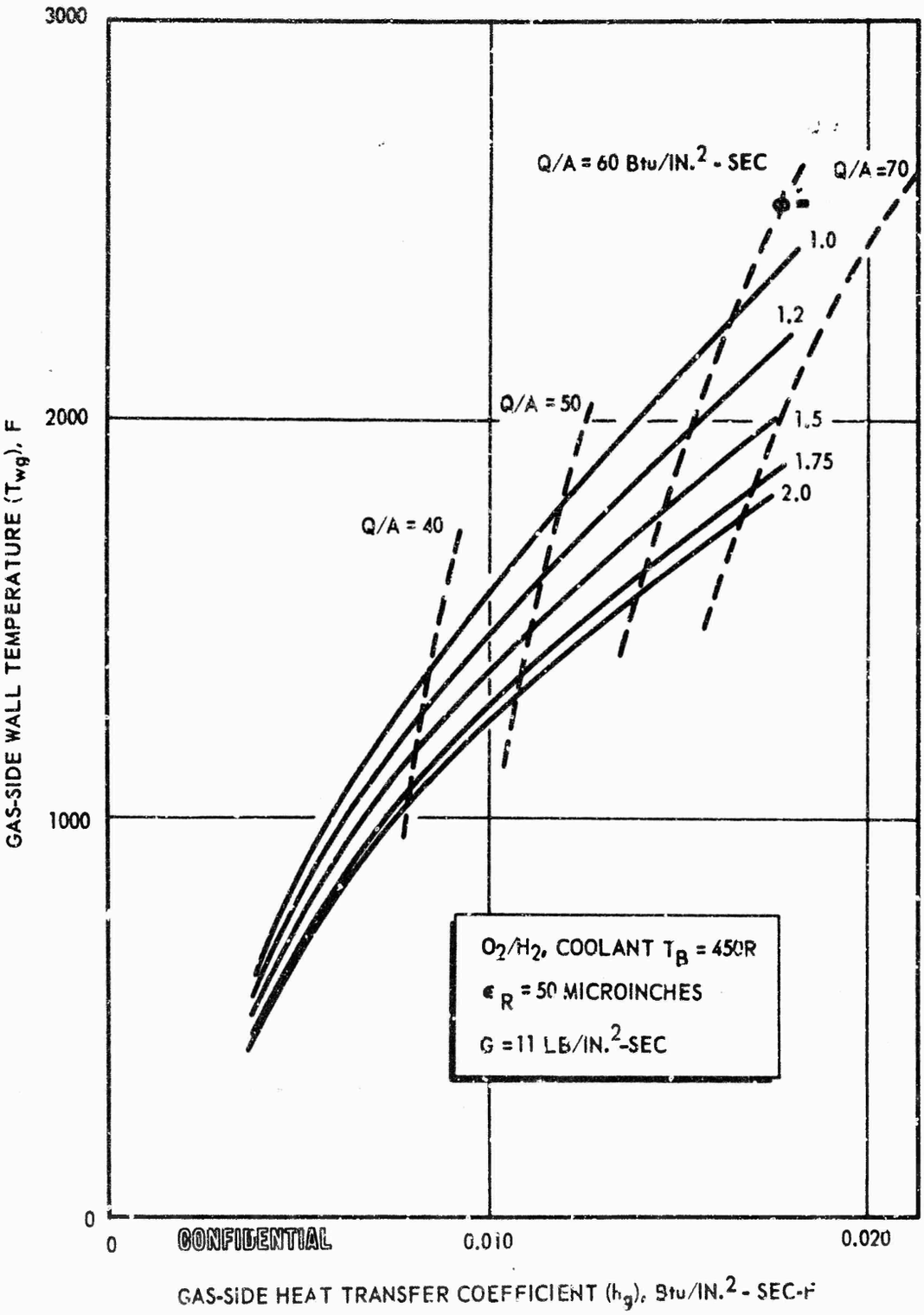

Figure 216. Cooling Limits for Nickel 200

at least 1.45, and a wall thickness at the throat of 0.010 inch. It is noted that Nickel 270, due to its somewhat higher conductivity, would operate at lower wall temperature.

(C) Copper conduction capability using the annealing temperature of about 900 F is 40 and 67 Btu/in.^{2}-sec for the range in curvature examined. Thus, copper can also handle the anticipated throat heat fluxes.

(C) The temperatures indicated are typical of what would be expected in the outer body throat region. The inner body will operate at lower wall temperatures because of the more desirable hydrogen coolant temperature existing in the inner body throat region (200 to 250 R).

(C) The nickel contoured tube overall heat transfer rate was significantly lower than obtained on the copper tube-wall segment. The experimental heat transfer characteristics of both tube wall thrust chamber segments and the solid wall hardware are shown in Fig. 217. The reduction noted on the nickel segment was attributable to a higher gas-side tube-wall temperature, resulting in reduced heat transfer rates. The overall heating rate for the No. 1 repaired nickel chamber was essentially the same as was obtained for the No. 2 nickel chamber and also the water-cooled, solid-wall hardware. Consequently, heat flux profiles generated from the solid-wall data were applicable to the tube wall.

(U) It has been found, in extensive calorimetric heat flux profile measurements, that the total overall flux is directly proportional to the throat values. Therefore, these heat transfer correlations obtained on the tube-wall program reinforce the demonstrator module cooling tube analysis.

(C) Conclusions to be drawn from the 2.5K segment cooling analysis and tests are that the 250K Demonstrator Module tubes can be run at chamber pressures of 2100 psia. However, it should be realized that there is a tradeoff between maximum operating conditions (high chamber pressure) and cyclic fatigue life such that a tube life somewhat less than 300 cycles

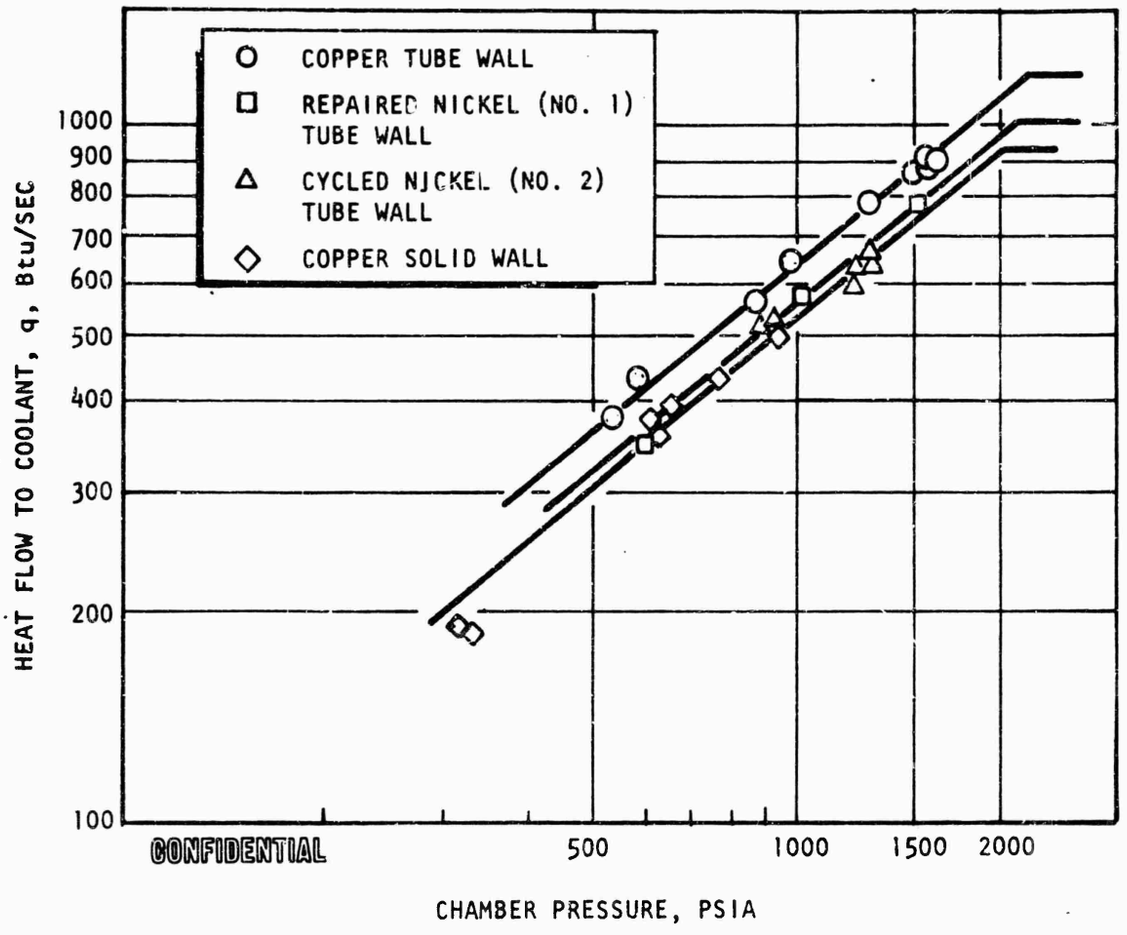

Figure 217. Contoured Tube Overall Heat Transfer Characteristics (2.5K Copper and Repaired Nickel Segments)

and a 10-hour between overhaul requirement would be realized at 2100 psia. To obtain the same life at 2100 psia as compared to 1500 psia requires thinner tubes of smaller diameter so that the plastic strain and temperature levels remain unchanged.

(C) It was also concluded that effectual tube repairs are feasible in the combustion zone of a 250K thrust chamber employing the Nickel 200 material.

Material Selection Program.

(U) Background Survey. To utilize all available Rocketdyne experience, a survey was made of all regeneratively cooled production thrust chambers to study their life-limiting processes. Particular note was made of the J-2 liquid oxygen-hydrogen thrust chamber life history. This survey led to a summary of thrust chamber life-limiting processes as given below:

1. Axial Tube Splits Cause Rapid Failure
   a. Hydraulic pressure spikes can burst tubes.
   b. Hydraulic pressure can burst tubes if steady stress at high temperature causes creep or creep fatigue.
   c. Either of the above failure modes is aggravated by oxidation-erosion which thins the tube wall.
2. Transverse Tube Microcracks Cause Gradual Degradation
   a. Cyclic thermal strains can cuase plastic flow which eventually results in transverse tube microcracks.
   b. These microcracks are not self-propagating and are closed during steady-state operation.

(U) Program Plan. A materials evaluation and selection effort was then planned to provide the critical data needed to select a long-life, high-performance, fabricable tube material. The logic flow diagram for the material selection program is shown in Fig. 218.

(U) To complete the analtyical selection of candidate materials described in the flow diagram, it was necessary to develop a tube-wall plastic strain analysis.

(U) Plastic Strain Analysis. The plastic strain analysis was directed toward the prediction of the plastic strain-time history of a thrust chamber tube during a typical engine run of a specified duration. It is known that the primary plastic straining occurs at engine start and shutdown; however, some cumulative plastic straining may occur during steady-state run conditions. The goals of the program were therefore directed toward the complete accounting of plastic strain accumulation. Following the hypothesis of linear strain damage accumulation, a prediction of life was possible from laboratory test fatigue data on the selected tube material.

(U) To furnish a workable analytical tool for preliminary analysis and material comparison purposes, a simplified analytical approach was developed which allowed the rapid prediction of plastic strains which occur during the start and shutdown sequence. This approach employed the assumptions of elastic strain invariance and infinite rigidity of the tube backup structure.

(U) The assumption of "elastic-strain invariance" was based on the observation that the elastically computed strain distribution does not depend on the elastic modulus if the modulus is constant throughout the body. Elastic theory may then be used to compute the total strains even if they are partly plastic.

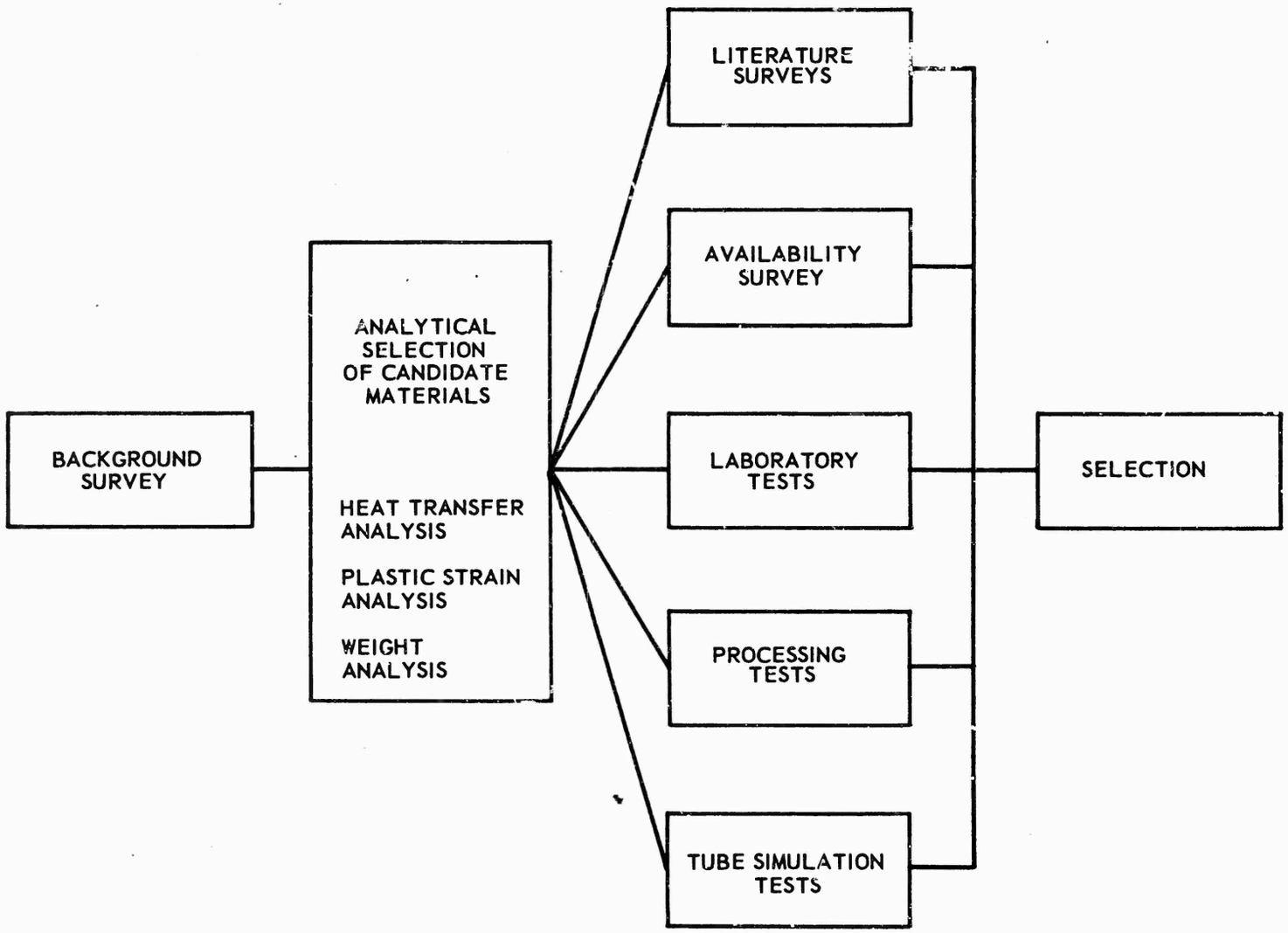

Figure 218. Material Selection Program

(U) If the form of the body and temperature conditions are such that there would be no stresses except for the constraint of external forces, the elastic strains may be found by determining the shape and dimensions the body would assume if unconstrained, and then calculating the strains produced by forcing it back to its original shape and dimensions.

(U) Following this type of model, an elemental part which has been removed from the crown of the tube was considered as a flat-plate free body. The application of a temperature gradient through the thickness

$$\Delta T_1 = T_{wg} - T_{wc} \tag{15}$$

would cause the element to assume a spherical curvature. The length and width dimensions, as measured along the curvature at the midplane, would also increase by an amount proportional to the average temperature rise. If the element was originally at the coolant bulk temperature, the average temperature rise was given by

$$\Delta T_2 = \frac{T_{wg} + T_{wc}}{2} - T_B \tag{16}$$

(U) The constraints against this thermal deformation and growth were applied by the geometry of the thrust chamber tube and jacket. Complete restraint against curvature change was afforded by the curved tube wall. Restraint against growth is realized, for the most part, in the axial direction only. Applying the necessary restraints against curvature to force the element back to its original shape yielded the familiar relation

$$\sigma_{th} = \pm \frac{E \alpha (\Delta T_1)}{2 (1 - \nu)} \tag{17}$$

(U) Applying the restraints against growth so that the element was forced back to its original dimensions gave $\sigma_{th} = E \alpha (\Delta T_2)$. Superimposing the results of both restraints in the axial direction gives (for the tube gas wall)

$$\epsilon_{TOT} = \frac{\alpha\,(\Delta T_1)}{2\,(1-\nu)} + \alpha\,(\Delta T_2) \quad \text{(total elastic strain)} \tag{18}$$

(U) Similarly, the restraint against curvature change only in the tangential direction gave

$$\epsilon_{TOT} = \frac{\alpha\,(\Delta T_1)}{2\,(1-\nu)} \tag{19}$$

The plastic strain components of the total strain were approximated by

$$\epsilon_p = \epsilon'_{TOT} - \epsilon_e = \epsilon_{TOT} - \frac{\sigma_y}{E} \tag{20}$$

Substituting the previous relationships for ϵ_{TOT}, ΔT, and ΔT_2 gives for the axial plastic strain at the gas wall, $\epsilon_{p_{axial}}$:

$$\epsilon_{p_{axial}} = \alpha \frac{(T_{wg} - T_{wc})}{2\,(1-\nu)} + \alpha \left(\frac{T_{wg} + T_{wc}}{2} - T_B \right) - \frac{\sigma_y}{E} \tag{21}$$

while for the tangential plastic strain, $\epsilon_{p_{tang}}$:

$$\epsilon_{p_{tang}} = \alpha \frac{(T_{wg} - T_{wc})}{2\,(1-\nu)} - \frac{\sigma_y}{E} \tag{22}$$

From the theory of plasticity, it was known that the maximum or "effective" plastic strain at the tube gas wall is greater than either the axial or tangential plastic strain individually. To apply uniaxial cyclic fatigue test data to the prediction of the tube fatigue life, a relationship between the uniaxial test data and the real case was used. This relationship

was taken from the "deformation" theory of plasticity. Accordingly, the effective plastic strain is given by

$$\epsilon_{p_{effective}} = \frac{2}{\sqrt{3}} \sqrt{\left(\epsilon_{p_{axial}} - \epsilon_{p_{tang}}\right)^2 + \left(\epsilon_{p_{tang}} - \epsilon_{p_{rad}}\right)^2 + \left(\epsilon_{p_{rad}} - \epsilon_{p_{axial}}\right)^2} \quad (23)$$

(U) This expression was simplified by the introduction of the "no volume change" basic assumption of all plasticity theory. Then,

$$\epsilon_{p_{rad}} = - \epsilon_{p_{axial}} - \epsilon_{p_{tang}}$$

Substituting the previous equation gives:

$$\epsilon_{p_{effective}} = \frac{2}{\sqrt{3}} \sqrt{\epsilon_{p_{tang}}^2 + \epsilon_{p_{tang}} \epsilon_{p_{axial}} + \epsilon_{p_{axial}}^2} \quad (24)$$

This value is commonly known as the plastic strain range. If the total plastic strain occurring during one engine run is that incurred from the start and shutdown temperature cycle, the cyclic plastic strain per engine run is given by

$$\epsilon_p = 2 \epsilon_{p_{effective}}$$

Table 70 shows the results of the plastic strain analysis as applied to the revised candidate tube materials.

(U) Selection of Candidate Materials. In the selection of the candidate tube materials for thrust chamber usage, an effort was made to utilize basic analysis as a means of screening a broad range of materials. The previously described plastic strain analysis, in conjunction with an

TABLE 70

(C) SUMMARY OF RESULTS, PLASTIC STRAIN ANALYSIS

Parameter	Type-347 Stainless Steel	Nickel 200 & 270	OFHC and Boron Deoxidized Copper	Beryllium Copper, Alloy 10
Wall Thickness, inches	0.008	0.015	0.029	0.016
Heat Flux, Btu/sec-in.^{2}-F	44.5	46.5	54.0	54.0
Gas Wall Temperature, F	1650	1450	750	750
Coolant Wall Temperature, F	400	400	530	530
Coolant Bulk Temperature, F	-260	-260	-260	-260
Tangential Plastic Strain, in./in.	0.01170	0.00825	0.00183	0.00
Axial Plastic Strain, in./in.	0.02370	0.01700	0.01053	0.00103
Plastic Strain per Cycle	0.07200	0.05150	0.02680	0.00205

analysis of high-temperature ductility and fatigue data, was used to select the candidates. In general, a candidate material was evaluated by comparing the predicted cyclic plastic strain against its fatigue properties over a range of temperatures. Other considerations, such as ease of fabrication, mechanical properties, and estimated cost and availability, influenced the selection.

(U) The candidate materials thus selected were then the subject of preliminary studies in processing, availability, and cost. As a result of these preliminary studies, a further screening of the original candidates was made. The original candidate materials which survived the preliminary screening are also shown in Table 71.

(U) Literature Survey. A survey was made of all available data on the physical and mechanical properties of the candidate materials. All existing valid data were compiled using, wherever possible, the properties of the material in the as-furnace-brazed condition. The results of the literature survey are shown in Table 72. In some instances, the required data were not available. Testing was therefore scheduled to obtain these data on the remaining candidate materials, as indicated by the shaded boxes. As stated earlier in this section, four of the candidate materials were eliminated. Chrome copper and zirconium copper were eliminated because of difficulties in furnace brazing. TD-nickel and Hastelloy-X were eliminated because of the shortage of supply in tube stock and long lead time to procure samples and stock. Also, TD-nickel cost was excessive when procured in bar stock as necessary for this effort.

(U) Oxidation-Erosion and Surface Protection Studies. The oxidation-erosion studies revealed that from strictly thermocynamic considerations, copper and nickel should not oxidize in a water vapor environment. With excess hydrogen in the water vapor, copper and possibly nickel should not oxidize, even under the flow conditions characteristics of thrust chambers. It seems probable, then, that the oxidation-erosion problem, if it appears, centers around such practical considerations as nonuniform

TABLE 71

(C) CANDIDATE MATERIALS FOR THRUST CHAMBER USAGE

Original Candidates, Selected by Analysis		
	Nickel	200 270 TD
	Copper	OFHC Boron Deoxidized Beryllium Alloy 10 Zirconium Alloy Chromium Alloy
	Stainless Steel	347
Screened Candidates, Evaluated by Tests		
	Nickel	200 270
	Copper	OFHC
Additional Candidates for Long-Range Application, Evaluated by Tests		
	Copper	Boron Deoxidized Beryllium Alloy 10

CONFIDENTIAL

TABLE 72

(C) SUMMARY OF RESULTS,
MATERIAL PROPERTY LITERATURE SURVEY

Alloy	Thermal Conductivity	Total Thermal Expansion and Contraction	Modulus of Elasticity	Poisson's Ratio	Tensile Data Before Braze (Annealed)	Tensile Data After Braze	Stress-Strain Curves to 3 Percent	Percent R.A. Data Brazed Condition	Creep Tubing or Sheet
Ni 200	Have data	[redacted]	Have data	R.T. Elastic only, need data	Have data	Have data	Have data	[redacted]	Need data
Ni 270	Have data	[redacted]	R.T. only, need data	Need data	[redacted]	[redacted]	[redacted]	[redacted]	Need data
TD Ni	Have data	Need data	Have data	R.T. only, need data	Have data	Have data	Have data to 0.3 percent	Need data	Need data
Hastelloy-X	Have data	Need data, have mean linear only	Have data	-108 F and R.T. only, need data	Have data	Have data	Have data	Need data	Need data
347 SS	Have data	Have data	Have data	Have data, elastic only	Have data	Need new data	Have data	Need data	Need data
OFHC Cu and Boron Deoxidized Cu	Have data	Have data	Have data	Have data, elastic only	Have data	Have data	Have data to 2 percent	[redacted]	Need data
Be-Cu	Have some data, need data	[redacted]	[redacted]	Need data	[redacted]	[redacted]	[redacted]	[redacted]	Need data
Zr-Cu	Have data	Need data, have mean linear only	Need data	Need data	Need data	Need data	Need data	Need data	Need data

mixture ratio distribution and adverse perturbations in tube temperature. These efforts can only be determined by tests, and are characteristic of injector design, start sequence, throttling range, and other system-controlled effects.

(U) The diffusion layers and coating studies were intended to reveal those state-of-the-art processes which might be applied to nickel or copper tubes to enhance their oxidation-erosion resistance. Two different approaches were explored. Studies indicated that braze alloy wetting may increase the oxidation resistance of nickel and copper since these alloys are essentially composed of noble metals. A concurrent literature review revealed the existence of several state-of-the-art intermetallic diffusion processes which would be applicable to nickel and possibly copper. Diffusions of aluminum appear particularly attractive because such diffusions reputedly have ductilities close to that of the base metal. Other diffusion systems in current use employ chromium and aluminum-chromium combinations. All diffusion coatings would adversely affect thermal conductivity to some degree. The significance of this degradation could only be determined by heat transfer tests and analyses.

(U) As a result of the oxidation-erosion and diffusion layers and coatings studies, a decision was made to eliminate the surface protection screening tests until a firm requirement was established by hot-firing tests.

(C) Mechanical Property Tests. The mechanical property and ductility tests were simple tensile tests on rod and tube specimens, both in the annealed condition, and were also processed in a way similar to a furnace-brazed tube. Tests were conducted at room temperature in air and also at elevated temperature in an argon environment. The results of these tests are shown in Table 73. Some significant findings from these tests were the excessively low yield stress of Nickel 270 and the effects of grain size on the tube materials apparent tensile properties. The grain structure of Nickel 200 and 270, OFHC copper, and beryllium copper No. 10 prior to brazing and postbrazing is shown in Fig. 219 through 222. All except the Cu-Be No. 10 are tubular specimens.

TABLE 73

(c) SUMMARY OF RESULTS,

MATERIAL PROPERTY LITERATURE SURVEY

Bar Stock Tensile Properties							
Material	Condition	Test Temperature, F	0.2 Percent Yield Strength, psi	0.5 Percent Yield Strength, psi	Ultimate Strength, psi	Elongation (1-Inch Gage Length), percent	Reduction of Area, percent
Ni 200	Annealed	*	21,700	29,500	67,600	47.5	85.4
Ni 200	Brazed	*	20,300	23,700	67,900	41.0	64.0
Ni 200	Annealed	1400	6,500	7,200	13,400	92.0	99.1
Ni 200	Brazed	1400	6,100	7,200	14,200	78.0	96.0
Ni 270	Annealed	*	21,700	24,400	50,800	66.5	88.5
Ni 270	Brazed	*	14,600	16,500	46,100	31.5	55.9
Ni 270	Annealed	1400	3,000	3,600	6,200	75.5	99.9
Ni 270	Brazed	1400	-	-	7,950	53.0	80.5
OFHC	Annealed	*	10,300	11,900	32,000	50.0	84.1
OFHC	Brazed	*	8,300	9,400	34,900	41.0	76.3

Tubing Tensile Properties								
Material	Condition	Test Temperature, F	0.2 Percent Yield Strength, psi	0.5 Percent Yield Strength, psi	Ultimate Strength, psi	Elongation (1-Inch Gage Length), percent	Uniform Reduction of Area, percent	Local Reduction of Area, percent
Ni 200	Annelaed	*	20,500	22,700	73,700	39.0	46.2	95.0
Ni 200	Brazed	*	9,500	11,100	50,900	28.2	27.8	95.0
Ni 200	Annealed	1400	-	-	18,200	89.0	79.9	95.0
Ni 200	Brazed	1400	7,100	7,900	12,100	14.4	18.9	18.9
Ni 270	Brazed	*	4,500	6,200	37,900	25.0	29.6	95.0
Ni 270	Brazed	1400	4,500	4,600	8,600	25.4	19.4	50 to 99
Ni 270	Binder Brazed Without Vacuum	1400	5,700	5,900	9,500	24.0	33.4	90 to 99
Ni 270	Binder Brazed With Vacuum	1400	4,400	5,000	9,100	29.6	37.9	99.0
OFHC	Annealed	*	6,100	7,400	32,700	-	-	-
OFHC	Brazed	*	4,600	5,600	26,200	18.6	24.0	99.0

*Room Temperature

(a) OFHC Copper Annealed

(b) OFHC Copper After Simulated Braze Cycle

Figure 219. Comparison of OFHC Copper Tube Grain Size in the

CONFIDENTIAL

(a) Prior to Brazing (b) After Brazing

Figure 220. Comparison of Beryllium-Copper Grain Size Prior to Brazing and After Brazing

(a) Nickel 270 Annealed

(b) Nickel 270 After Simulated Braze Cycle

CONFIDENTIAL

Figure 221. Comparison of Nickel 270 Tube Grain Size in the Annealed Condition and After Simulated Furnace Braze Cycle

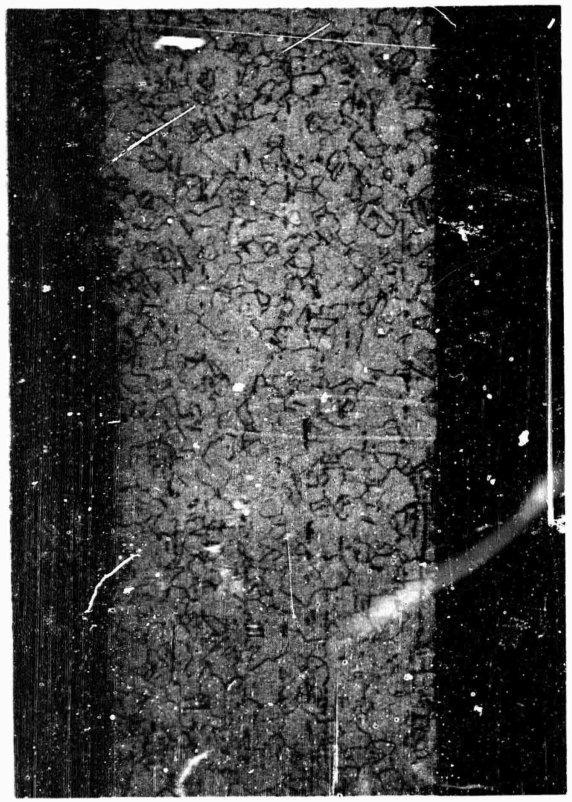

(a) Nickel 200 Annealed

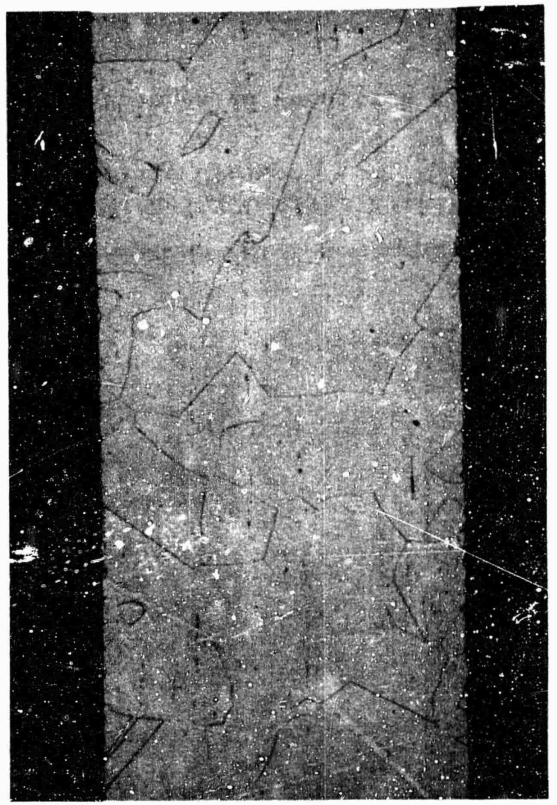

(b) Nickel 200 After Simulated Braze Cycle

Figure 222. Comparison of Nickel 200 Tube Grain Size in the Annealed Condition and After Simulated Furnace Braze Cycle

(U) It is not apparent from published data nor from the fatigue results reported here that large grains have a deleterious effect upon life. However, where the grain boundaries extend completely across the tube wall as shown (Fig. 219 through 222) for Nickel 270 and OFHC copper, mechanical behavior becomes erratic and intergranular penetration of contaminants becomes more hazardous.

(C) As a result of these tests and posttest metallographic analyses, further investigations of the effects of grain size on the mechanical properties and fatigue life of Nickel 200 in the furnace-brazed condition were conducted. These investigations were conducted on the thrust chamber tube tester, and are described in a later section.

(C) Brazing Feasibility Studies. The braze process and contamination studies and tests were intended to define initially proposed furnace step braze cycles for each candidate tube material. These initially proposed braze cycles were then applied to test specimens to determine the alloy wetting and flow characteristics, and to determine any tendencies for the braze alloys to induce tube alloying or intergranular penetration. The results of these tests are shown in Table 74. The results of these tests indicate that while Nickel 200 and 270 apparently may be successfully furnace brazed with current technology, brazing of the OFHC and beryllium copper is limited by tendencies of the common braze alloys to dissolve part of the base metal.

(U) Mechanical Strain, Elevated Temperature Fatigue Studies. The mechanical strain at elevated-temperature fatigue tests were designed to simulate the strain cycle experienced by a thrust chamber during the start and shutdown sequence. These tests were run at constant elevated temperatures, and utilized rod specimens which were axially strained. Materials in the annealed and furnace-brazed condition were tested. The plastic strain analysis described previously was used to predict the equivalent axial strains which each material would experience as a thrust chamber throat tube. The tests were run at temperatures which represented the

TABLE 74

(C) BRAZING FEASIBILITY TESTS, NICKEL 200, 270, AND BERYLLIUM COPPER

Tubing Material	Braze Filler Metal	Braze Temperature, F	Braze Atmosphere	Visual Examination		Microstructure Examination	
				Wetting	Flow	Alloying, inch	Intergranular Penetration, inch
Nickel 200 and Nickel 270	90%Ag-10%Pd (RB0170-062)	1975	Hydrogen	Good	Good	< 0.001	< 0.001
	82%Au-18%Ni (RB0170-064)	1800	Hydrogen	Good	Good	< 0.0015	< 0.001
	90%Ag-5%Pd-4% Cu-1%Ni (RB0170-105)	1800	Hydrogen	Good	Good	< 0.001	< 0.001
	72%Ag-28%Cu (AWS, BAg-8)	1500	Argon*	Good	Fair	< 0.001	< 0.001
	60%Ag-30%Cu-10%Sn (Handy and Harman Braze 603)	1350	Argon*	Good	Fair	< 0.001	< 0.001
	61.5%Ag-24%Cu-14.5%In (Handy and Harman Braze 615)	1350	Argon*	Good	Fair	< 0.001	< 0.001
Beryllium Copper	62%Cu-35%Au-3%Ni (RB0170-065)	1900	Hydrogen*	Good	Good	Grain Boundary Melting	
	50%Au-50%Cu (Handy and Harman Premabraze 402)	1800	Hydrogen*	Good	Good	0.006	< 0.001
	72%Ag-28%Cu AWS, BAg-8)	1500	Argon*	Good	Fair	0.003	< 0.001
	60%Ag-30%Cu-10%Sn (Handy and Harman Braze 603)	1350	Argon*	Good	Fair	0.004	< 0.001
	61.5%Ag-24%Cu -14.5%In (Handy and Harman Braze 615)	1350	Argon*	Good	Fair	0.005	< 0.001
OFHC Copper	62%Cu-35%Au-3%Ni (RB0170-065)	1900	Hydrogen	Good	Good	0.0056	< 0.001
	50%Au-50%Cu (Handy and Harman Premabraze 402)	1800	Hydrogen	Good	Good	< 0.001	< 0.001
	72%Ag-28%Cu (AWS, BAg-8)	1500	Argon*	Good	Fair	0.002	< 0.001
	60%Ag-30%Cu-10%Sn (Handy and Harman Braze 603)	1350	Argon*	Good	Fair	0.0015	< 0.001
	61.5%Ag-24%Cu -14.5%In (Handy and Harman Braze 615)	1350	Argon*	Good	Fair	0.002	< 0.001

*Flux applied to specimens

maximum predicted tube gas wall temperature for each material. Tests were also run at a reduced temperature known to represent a condition of minimum ductility for each material. All tests were run in an argon environment. Table 75 shows a summary of the test conditions.

(U) A record of each load-strain cycle was continuously printed out by automatic equipment. Typical load strain cycles recorded in these tests are shown in Fig. 223. The unsymmetrical curve developed after a large number of cycles represents the load-deflection behavior of the progressing fatigue crack alternately stressed in tension and compression. As the crack grows, the tensile load-carrying ability decreases as strain remains constant, thus providing a convenient technique for recording crack progression.

(U) While it is customary in tests of this nature to report the number of cycles to complete fracture, a more meaningful technique was used which gave a measure of the development of internal fatigue damage, as well as the conventional cyclic life. This was obtained by plotting the ratio of maximum cyclic tension (compression loads in the specimen vs the number of tests cycles). These load values were obtained from the load-strain hysteresis loops (Fig. 223). Groups of curves for each common material and process condition were then drawn for each specimen run at various test temperatures.

(C) Figure 224 shows two such curves for furnace-brazed Nickel 200. Since the thermally induced strain in a thrust chamber tube actually occurs over a range of temperatures, an average temperature fatigue curve has been estimated. The arithmetic average used was felt to be conservative for this case.

(U) The average curves for each material, both in the annealed and processed condition plotted together for comparison purposes, are shown in Fig. 225. These curves are useful in comparing materials, as well as for estimating the number of start sequences required to cause transverse through-cracks in a thrust chamber tube.

TABLE 77

(C) MECHANICAL STRAIN AT ELEVATED TEMPERATURE FATIGUE TESTS, SUMMARY OF TEST CONDITIONS

Material	Condition	Total Strain Range, in./in.	Test Temperature, F	No. of Specimens
Type 347 Stainless Steel	Annealed, 1975 F	0.0360	1650	2
Nickel 200	Annealed, 1350 F	0.0257	1400	2
Nickel 200	Annealed, 1350 F	0.0257	1100	2
Nickel 200	ADP Step Braze Cycle, 1975 F	0.0257	1400	1
Nickel 200	ADP Step Braze Cycle, 1975 F	0.0257	1100	1
Nickel 270	ADP Step Braze Cycle, 1975 F	0.0257	1400	2
Nickel 270	ADP Step Braze Cycle, 1975 F	0.0257	1100	2
OFHC Copper	Annealed, 900 F	0.0134	750	2
OFHC Copper	Annealed, 900 F	0.0134	500	2
OFHC Copper	ADP Step Braze Cycle, 1900 F	0.0134	750	1
OFHC Copper	ADP Step Braze Cycle, 1900 F	0.0134	500	1
Beryllium Copper Alloy 10	ADP Step Braze Cycle, 1800 F	0.0098	750	1
Beryllium Copper Alloy 10	ADP Step Braze Cycle, 1800 F	0.0098	500	1
Beryllium Copper Alloy 10	Heat Treat to Optimum Properties	0.0098	750	2
Beryllium Copper Alloy 10	Heat Treat to Optimum Properties	0.0098	500	2

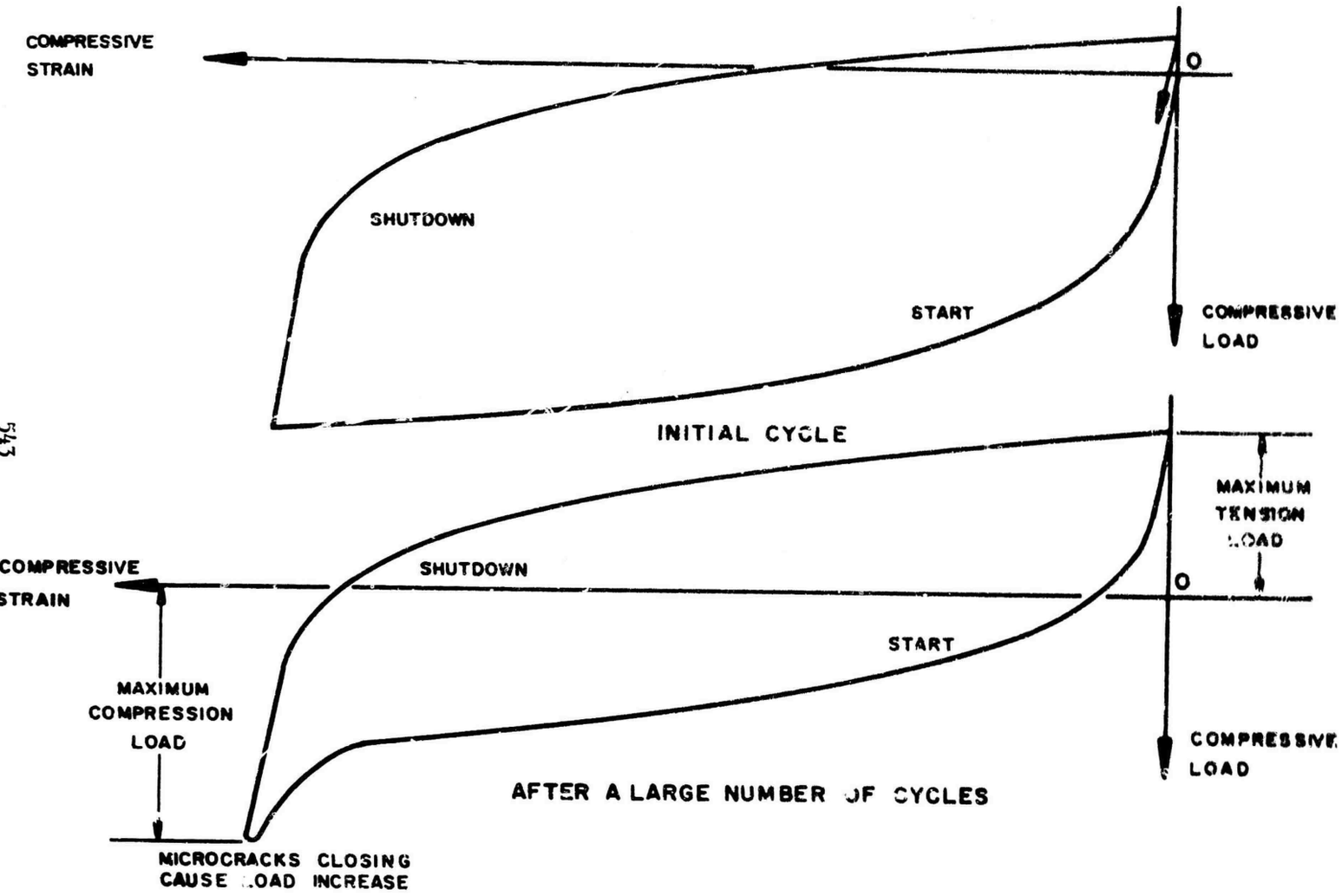

Figure 223. Axial Load, Strain Cycle for a Thrust Chamber Tube

Figure 224. Mechanical Strain at Elevated Temperatures, Test Results on Brazed Nickel 200

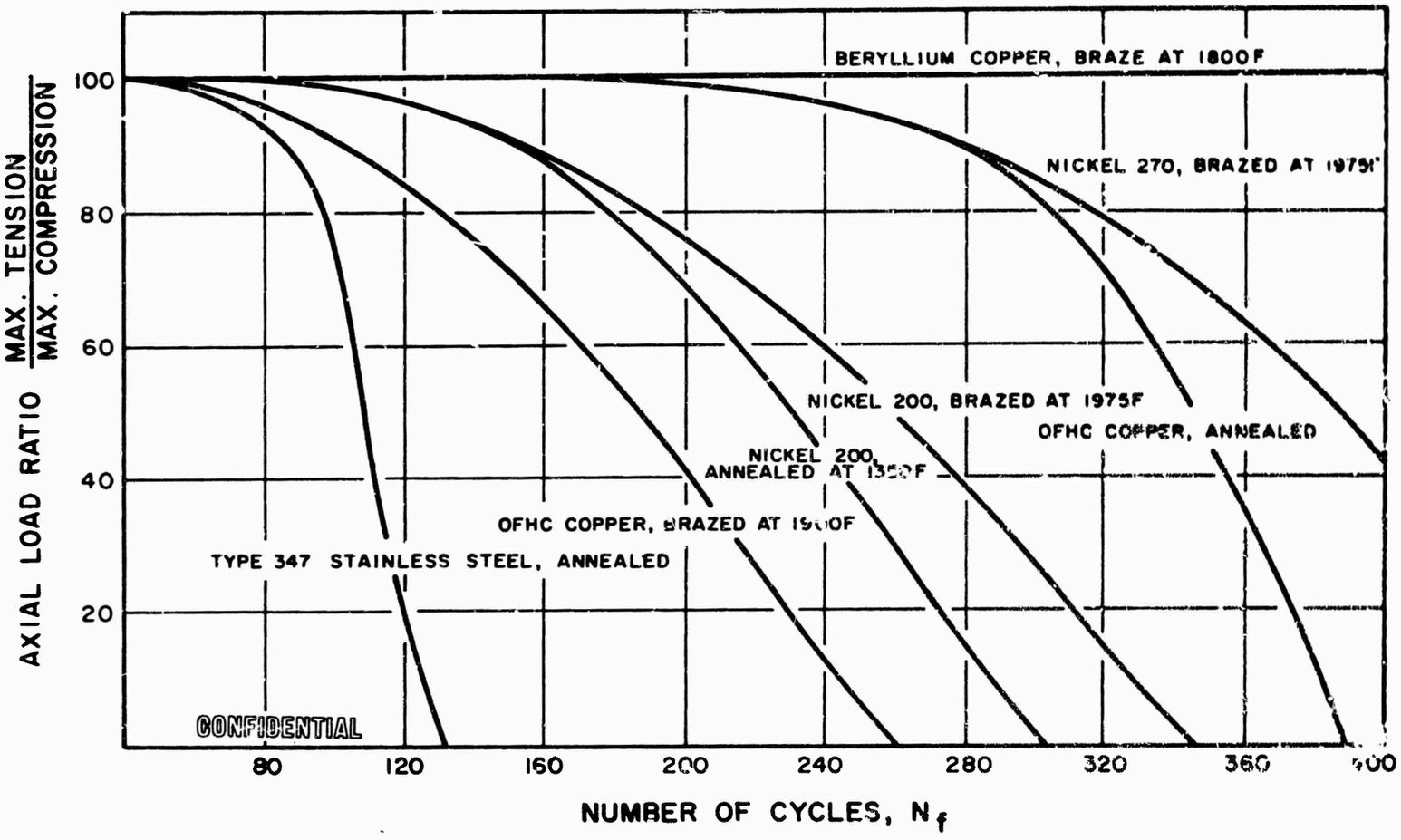

Figure 225. Mechanical Strain at Elevated Temperatures, Test Results of Candidate Materials

(C) Tube Tapering and Forming Feasibility Study. A separately funded tube-tapering feasibility program was also completed, and the results were made available for the material selection program. The materials evaluated in this program were type 347 stainless steel, Nickel 200, Nickel 270, and OFHC copper. These materials were experimentally tapered to required tube dimensions and tolerances. Inspection of the finished tubes yielded an initial estimate of tube-tapering confidence with regard to process time, tolerance control, lubricant contamination, and the effect of inclusions in the material.

(U) Material Selection. To select a tube material for the demonstrator segment thrust chamber, a criteria list was developed as an aid. The criteria were taken from life, performance, and fabrication considerations. Each tube material was then evaluated by these criteria, as determined from the results of the Materials Selection Program, from previous experience, from published literature, and from the results of the hot-firing tests.

(C) A comparison of the demonstrator segment thrust chamber tube materials, as determined by these criteria, is given in Table 76. It was concluded that Nickel 200 offered the best combination of necessary features for this application. This material was therefore selected, in combination with a process cycle which produced the best obtainable properties.

(U) A similar comparison was made of the long-range candidate materials (Table 77). It was seen that the beryllium copper alloy No. 10 material offered a large increase in thermal fatigue resistance in either the partial or fully heat-treated condition. This is due to the fact that a low plastic strain is induced in this condition. Its practical thrust chamber use, however, awaits the development of suitable manufacturing processes.

Copper Tube-Wall Results.

(U) Heat Transfer. A summary of the test results is presented in Table 66. These data were reviewed to define the heat transfer distribution of the tube-wall segment. The overall heat transfer characteristics

TABLE 76

(c) FACTORS AFFECTING SELECTION OF 20K-SEGMENT TUBE MATERIAL

(Based on State-of-the-Art Fabrication Technology and Aerospike Operating Conditions)

Criterion \ Material	Type 347 Stainless Steel	Nickel 200	Nickel 270	OFHC Copper
Strength to Withstand Hydraulic Stress	Good	Good	Poor	Good
Thermal Stress Fatigue Resistance	Poor	Good	Poor	Fair
Metallurgical Stability	Excellent	Good	Poor	Poor
Oxidation-Erosion Resistance	Good	Good	Good	Good
System Compatibility	Excellent	Good	Good	Fair
Comparative Coolant Pressure Drop	1.0	0.85	0.75	0.95
Comparative Weight	1.0	1.05	1.05	1.20
Uprating Capability	Poor	Fair	Fair	Good
Drawing, Tapering, and Forming Confidence	Good	Excellent	Excellent	Good
Brazing Confidence	Excellent	Good	Good	Poor
Availability	Good	Good	Good	Good
Total Cost	Low	Low	Low	Low

TABLE 77

(C) FACTORS AFFECTING SELECTION OF LONG-RANGE TUBE MATERIALS

(Based on Current Knowledge and Operating Conditions)

Material / Criterion	Boron Deoxidized Copper	Beryllium Copper Partial Heat Treat	Beryllium Copper Full Heat Treat
Strength to Withstand Hydrualic Stress	Good	Excellent	Excellent
Thermal Stress Fatigue Resistance	Good	Excellent	Unlimited
Metallurgical Stability	Good	Excellent	Excellent
Oxidation-Erosion Resistance	Fair	Good	Excellent
System Compatibility	Fair	Good	Good
Comparative Coolant Pressure Drop	0.95	0.95	0.95
Comparative Weight	1.20	1.05	1.05
Uprating Capability	Good	Excellent	Excellent
Drawing, Tapering, and Forming Confidence	Good	Unknown	Unknown
Brazing Confidence	Poor	Poor	Poor
Availability	Fair	Good	Good
Total Cost	Low	Moderate	Moderate

(end point data) were well-behaved and showed that the heat transfer was of an expected turbulent nature (Fig. 226) throughout the chamber pressure range. Unfortunately, the local coolant bulk temperature measurements were not within the required accuracy to asses the heat transfer distribution. Therefore, the solid-wall water-cooled data (Q_{local}) employing the same injector were reviewed. The ΣQ_{local} of solid-wall segment tests are compared with tube-wall Q_{total} in Fig. 227. As noted in Fig. 226, a difference of approximately 11 percent between solid-wall and tube-wall data exists which is attributable to the difference in local gas-side wall operating temperatures. Using the established heat transfer distribution of the solid-wall segment, the local heat transfer distribution of the copper tube-wall chamber was determined and is shown in Fig. 227. The associated gas-side tube-wall temperature profile, utilizing a maximum coolant curvature enhancement of 1.5, is also presented in Fig. 227. The data show that regenerative cooling capability was definitely determined.

(C) Cooling Limits. During the cycling tests at 1500-psi chamber pressure of the related program, the 2.5" copper tube-wall chamber operated at higher temperature than initially designed for as a result of (1) increased heat flux, (2) reduced curvature enhancement, and (3) roughening of the hot-gas crown. The increased wall temperature resulted in the operating hydraulic stress exceeding the material yield stress and the noted tube crown failure in the throat region. A summary of the tube operating conditions for the 2.5" copper segment and the Demonstrator Module is presented in Table 78. The operating of the tube at a hydraulic stress greater than the yield stress was confirmed by a metallurgical examination of the tubes. Tubes in various stages of expansion to burst were sectioned and analyzed. Ruptures were ductile and exhibited bulging and wall thinning in early stages and in later stages extreme wall thinning, rupture, and bending of the wall outward relieving the hydraulic pressure.

1. Nickel Tube-Wall Thrust Chamber Results Analysis.

(C) Analysis of Test Conditions. The most severe limitation to the extended usage of well-designed, regeneratively cooled thrust chamber is imposed by the fatigue of the coolant tubes. The fatigue phenomenon

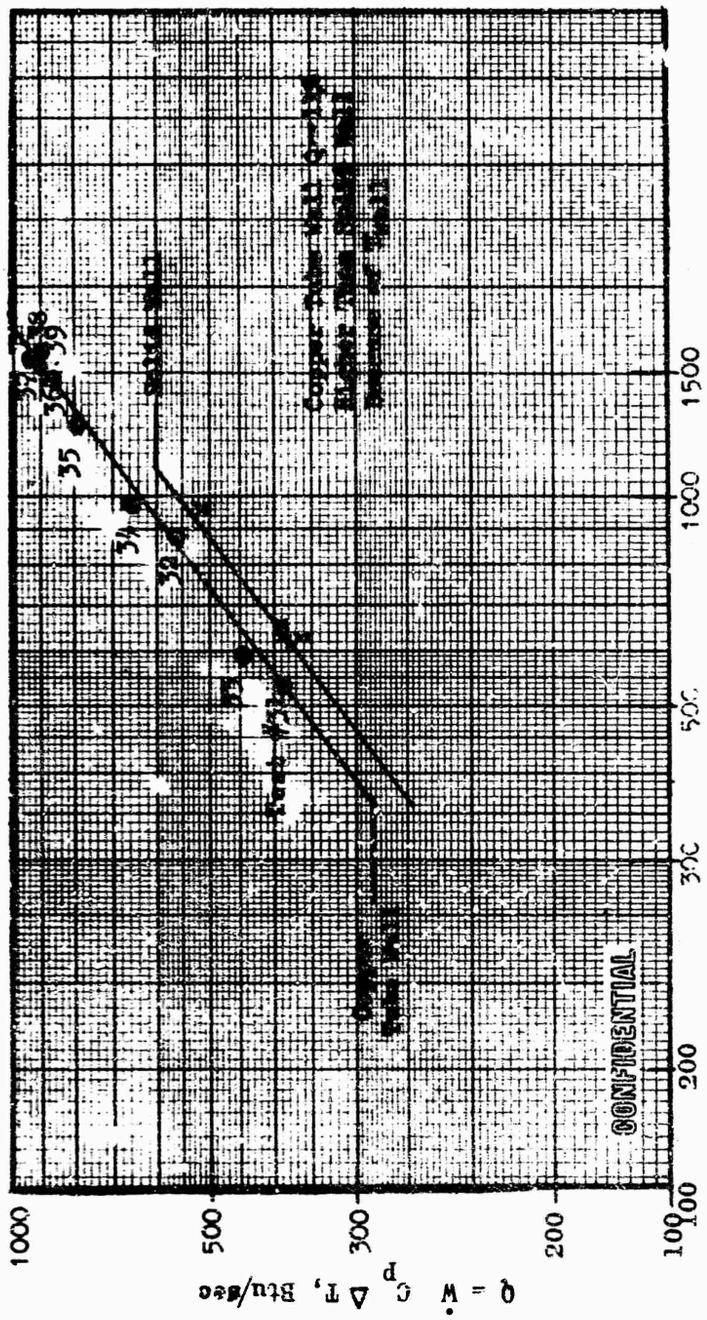

Figure 226. 2.5K Copper Tube-Wall Overall Heat Transfer Characteristics

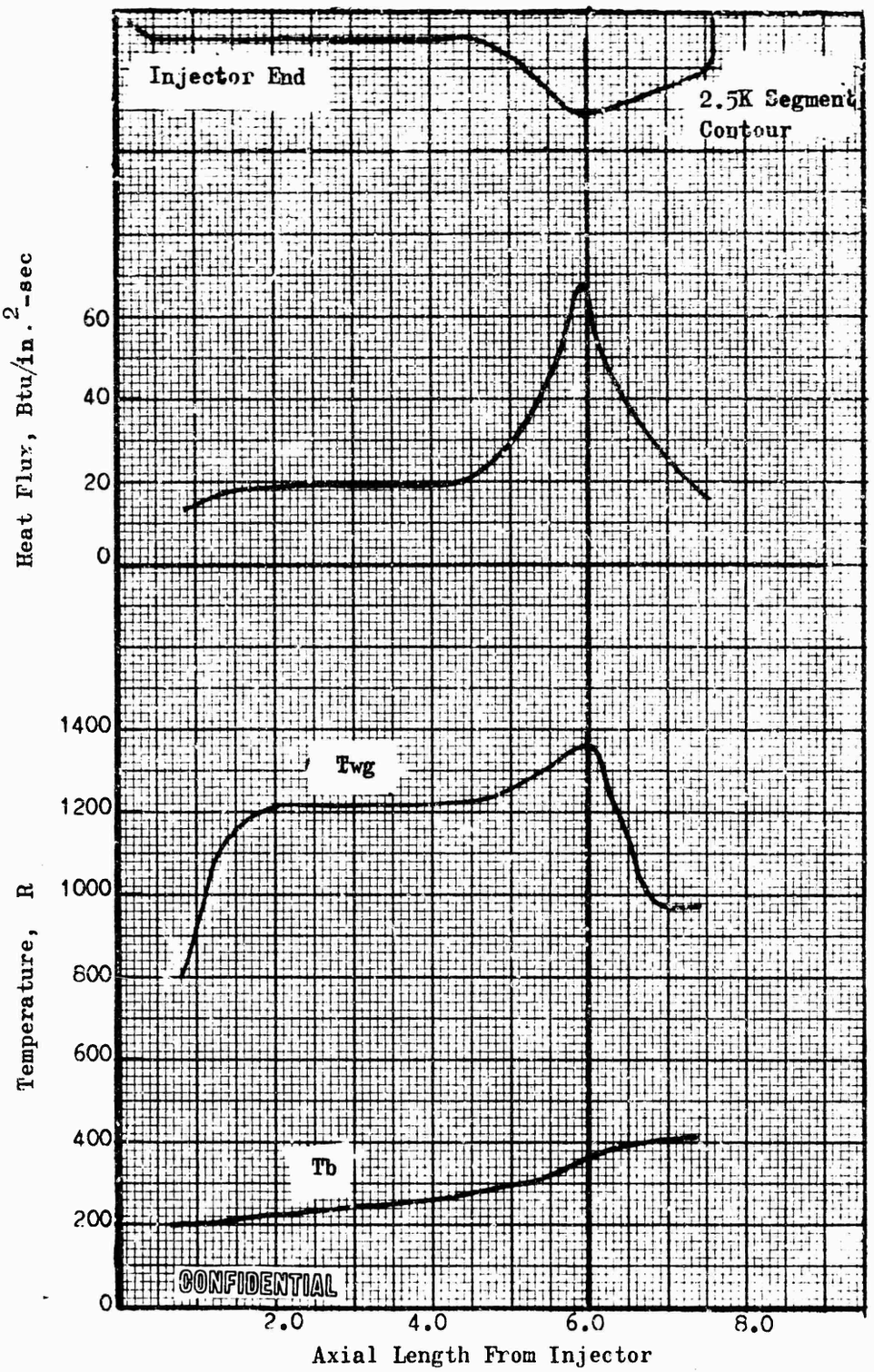

Figure 227. 2.5K Copper Tube-Wall Thrust Chamber Heat Transfer Distribution

TABLE 78

(C) COMPARISON OF OPERATING CONDITIONS

2.5K COPPER TUBE-WALL AND 250K DEMONSTRATOR

	2.5K Segment OFHC Copper		250K Demonstrator Design Nickel 200	
	Design	Operation	Inner Body	Outer Body
Wall Thickness, inch	0.020	0.020	0.012	0.030
Gas Wall Temperature, F	750	1200 to 1300	1520	1320
Average Wall Temperature, F	650	1100 to 1200	1030	1116
Yield Strength (σy 0.2 percent), psi	4500	1400 to 900	9000	8000
$\frac{\sigma Hyd}{\sigma Y}$ at 1500 P_c	0.4	1.1 to 1.6	0.40	0.29

CONFIDENTIAL

ordinarily manifests itself in the form of tiny transverse cracks which nucleate and grow through the hot wall of the tube. The primary cause may be described as the gradual destruction of the material's internal bonding due to plastic strain or slip.

(U) Thermally induced plastic strains in the Demonstrator tubes occur during the engine start and shutdown sequence, especially near the throat plane. Here a transient gas-wall temperature ranging from near the coolant bulk temperature to the nominal operating value occurs with the rapid heat flux buildup which follows ignition.

(U) An approximate technique for calculating the "equivalent uniaxial" strain resulting from these tube-wall, multiaxial strains was outlined in a previous section of this report. The uniaxial strain referred to here is the plastic strain in a low-cycle fatigue test measured along the axis of applied cyclic mechanical strain. An analytical relationship between the tube wall plastic strains and the plastic strain of a laboratory fatigue test is thus established. A tube life prediction based on laboratory test data is then possible.

(U) Since the test objective was the accurate modeling of the Demonstrator thrust chamber thermal fatigue, the most important criterion of test design was that the maximum value of the gas-wall cyclic plastic strain be reproduced in the test segment. Other important test design criteria were the simulation of the cyclic temperature range which the Demonstrator tube gas wall experiences, and the simulation of the tube-wall environmental conditions. These environmental conditions included those experienced during fabrication as well as those during operation. A high tube-wall pressure stress in combination with cyclic thermal strain can also be critical, causing the axial crack fatigue failure mode to predominate over the transverse crack failure mode. This complex fatigue creep failure mode was effectively simulated on the tube tester, as previously described. In the selection of the 2.5K segment cycling test conditions, consideration was given to all of the above criteria so that these life parameters for the Demonstrator Module were simultaneously matched as closely as possible in the 2.5K segment.

(U) The throat tubes of the Demonstrator Module outer body were selected as the reference base for test design because the operating conditions of the outer body tubes afford a more basic limitation to the thermal fatigue life of the Demonstrator.

(C) The predicted peak tube gas-wall temperature at the Demonstrator outer body throat is 1520 F, which occurs in combination with a peak heat flux of 56.8 Btu/in.^{2}/sec. and a tube wall pressure stress of about 2400 psi. A reasonable value for the lower temperature limit of the Demonstator tubes and structure immediately prior to ignition would be -200 to -250 F.

(U) The 2.5K segment test conditions were then selected to simulate this gas-wall thermal cycle in combination with the pressure stress. The down-pass (injector to nozzle) flow direction was chosen to match the flow direction of the Demonstrator outer body.

(C) The criterion which was primary in the selection between series or parallel coolant flow was tube-wall pressure stress. The total coolant pressure drop was also considered because of test stand limitations. Figure 228 shows the pressure stress resulting in the upstream tube bank of a series flow scheme with a separate cooling circuit. The pressure stress in the tube crowns was unrealistically high compared to the Demonstrator value of 2400 psi. The tube crown pressure stress in a parallel flow scheme, however, yielded a more realistic value of about 2800 psi.

(C) The 2.5K segment nickel tube actually represents an earlier version of the Demonstrator tube configuration. Since the original design of the 2.5K tube, segment and tube curvature tests have provided valuable additional gas- and coolant-side heat transfer data. Water-cooled segments have provided accurate combustion chamber and throat heat flux data; tubular segments have verified coolant bulk temperature rise predictions; and tube curvature tests have indicated methods of increasing the coolant side enhancement.

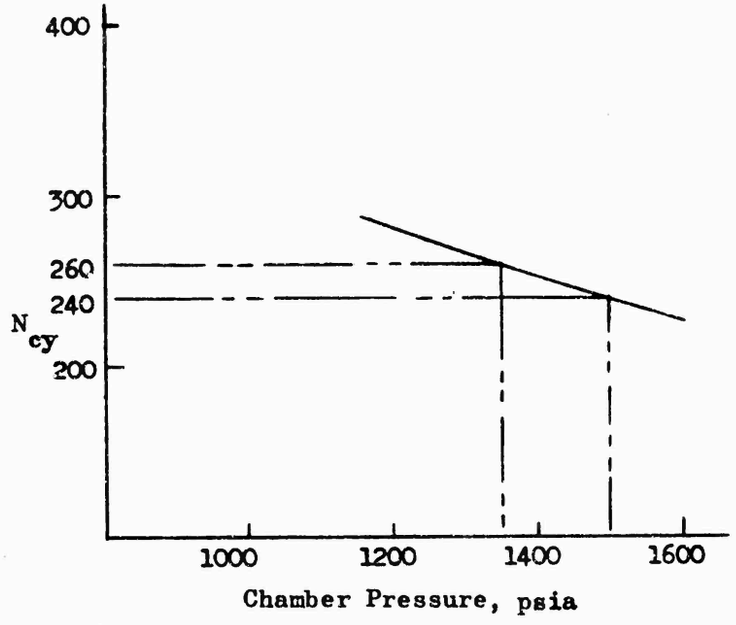

(Maximum Chamber Pressure vs Number of Cycles to Fatigue Cracking N_{cy})

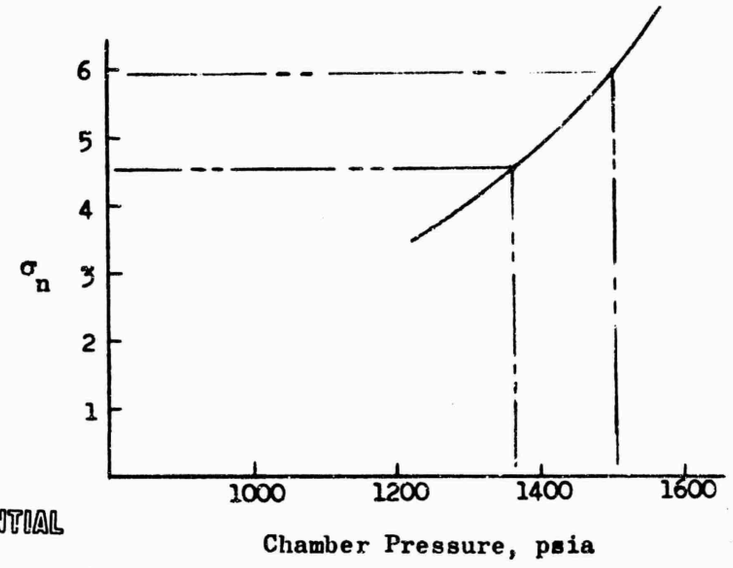

(Maximum Chamber Pressure vs Hydraulic Stress at Throat σ_n)

Figure 228. Effect of Chamber Pressure on Tube Life, 2.5K Segment (Constant Gas-Wall Temperature Case, T_{wg} = 1520 F)

(C) As a result of these findings, the Demonstrator tube design has evolved. The inner body currently has a 0.012-inch Nickel 200 wall, a coolant mass velocity of 11.2 lb/in.^{2}/sec, and curvature enhancement of 1.5. The outer body design has a 0.010-inch Nickel 200 tube, 1520 F wall temperature, a coolant mass velocity of 10.6 lb/in.^{2}/sec, and a curvature enhancement of 1.45.

(C) By comparison, the 2.5K tube wall chamber had a wall thickness of 0.012 inch, mass velocity of 10.5 lb/in.^{2}/sec at a flowrate of 1.0 lb/sec, and a curvature enhancement of about 1.25 (about 15 percent lower than the Demonstrator outer body). Even if the coolant mass velocities were the same in the 2.5K tube wall and the Demonstrator outer body, the 2.5K tube-wall gas-side temperature would be higher than on the Demonstrator outer body because of the increased curvature enhancement (achieved by shifting the outer throat) and reduced wall thickness in the latter. With a maximum coolant flowrate of 1.0 lb/sec, the 2.5K tube would have a predicted wall temperature of 1750 F at a chamber pressure of 1500 psia and a mixture ratio of 6.0. The required wall temperature to simulate the required life cycles is 1520 F. To achieve this temperature, it was necessary to reduce chamber pressure to 1250 to 1350 psia with a coolant flowrate of about 1.0 to 1.2 lb/sec within a mixture ratio range of 4.5 to 6.0 (Fig. 229). This chamber pressure and heat flux also correctly simulated the temperature drop across the wall.

(C) The consideration of matching the cyclic wall temperature and pressure stress thus led to further evaluation of the downpass, parallel flow, cooling scheme in regard to matching the cyclic plastic strain. It was again found that a good correlation between the analytical model and experimental results was realized when chamber pressure was 1250 to 1350 psia at a mixture ratio of 4.5 to 6.0 with a coolant flowrate of about 1.0 to 1.2 lb/sec (Table 79). The fact that these strains were matched at a reduced chamber pressure was due primarily to the difference in tube-wall thickness and curvature cooling enhancement of the Demonstrator and 2.5K segment. The mean tube-wall temperature, and thus the tube-wall yield strength, was also found to be comparable at these operating conditions.

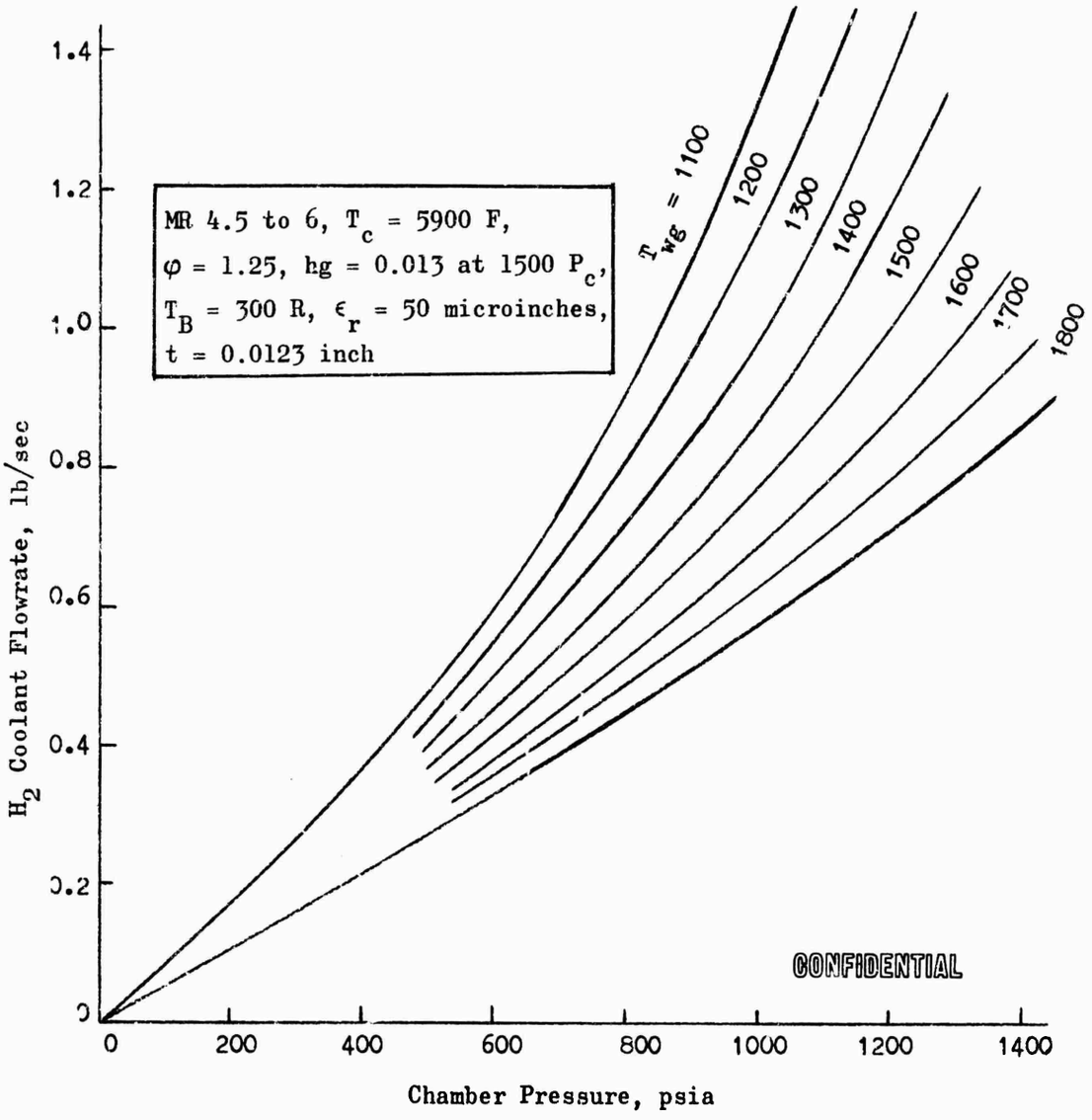

Figure 229. Throat Tube Gas-Wall Temperatures Nickel Tube-Wall Segment Cycling Tests

TABLE 79

(C) COMPARISON OF 250K DEMONSTRATOR AND 2.5K SEGMENT COOLING AND LIFE PARAMETERS

Thrust Chamber	Geometry and Heat Transfer Conditions					Temperature Parameters		Plastic Strain and Life Parameters			
	Tube Outside Diameter, inch	Tube-Wall Thickness, inch	ϕ_c, Curvature Cooling Enhancement	Coolant Mass Velocity, $lb/sec/in^2$	Chamber Pressure, psia	Gas Wall Temperature, F	Mean Temperature, F	Axial Plastic Strain, in./in.	Tangential Plastic Strain, in./in.	Cyclic Plastic Strain, in./in.	Life Simulation Ratio
Demonstrator Outer Body	0.066	0.010	1.45	10.6	1500	1520	1116	0.01652	0.00642	0.0473	1.000
Demonstrator Inner Body	0.068	0.012	1.50	11.2	1500	1520	1030	0.01706	0.00776	0.0503	0.916
2.5K Segment Case 1	0.075	0.012	1.25	12.7	1350	1520	1060	0.01675	0.00725	0.0492	0.962
2	↓	↓	↓	10.6	1250	1550	1125	0.01695	0.00675	0.0489	0.973
3				12.0	1310	1520	1075	0.01678	0.00708	0.0490	0.970
4				10.6	1350	1630	1210	0.01767	0.00667	0.0503	0.916
5	0.075	0.012	1.25	12.5	950	1120	740	0.01225	0.00575	0.0368	1.710

(C) Life Prediction. By use of the thermal fatigue diagram (Fig. 230) with the computed cyclic plastic strain, a tube-wall life in thermal cycles was predicted. The ductility of nickel, as illustrated on the lower half of Fig. 230 in the desired operating range of temperature is an important factor in its ability to absorb the high orders of plastic at these temperatures. Each engine start corresponded to a tube gas-wall thermal cycle of -230 to 1520 to -230 F. This predicted life was consistent with the Demonstrator Module restart requirements.

(U) Table 68 includes a calculated life simulation ratio for each test. This number is defined as the ratio of the predicted life of the segment thrust chamber cycling from -240 F to the peak heat transfer conditions of that case to the predicted life of the Demonstrator outer body. Life simulation ratios less than one indicate test conditions were more severe than those expected on the Demonstrator Module design. The predicted lives used to compute this ratio were in all cases obtained by identical use of the plastic strain equations and fatigue diagram. Because the computed values of these ratios are less than unity for most cases, it was seen that the segment operated under conditions which were, for the most part, more severe from a thermal fatigue standpoint than the Demonstrator outer body.

(U) While these comparative observations could be readily made, it was desirable to obtain a quantitative measure of the relative life of the complete segment test series to the life of the Demonstrator. This involved a computation of the life simulation ratio for each test so that an average ratio for the test series could be obtained. For purposes of data analysis, a technique for the rapid computation of an approximate life simulation ratio for each test was used. An expression for the approximate life simulation ratio was found to be

$$\frac{(\text{Fatigue Life})_1}{(\text{Fatigue Life})_2} = \frac{(\text{Heat Flux})_2\ (\text{Mean Wall Temperature})_2\ (\text{Wall Thickness})_2}{(\text{Heat Flux})_1\ (\text{Mean Wall Temperature})_1\ (\text{Wall Thickness})_1}$$

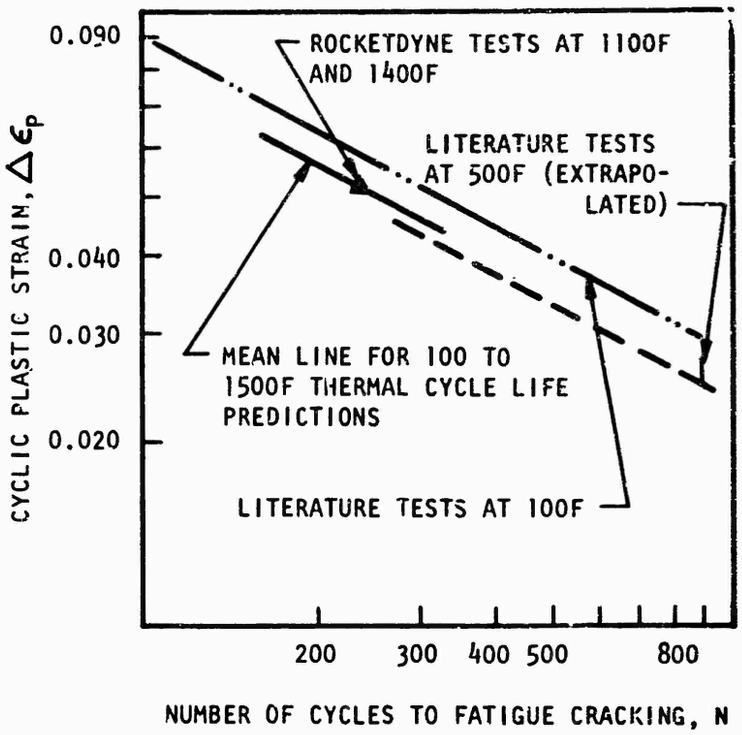

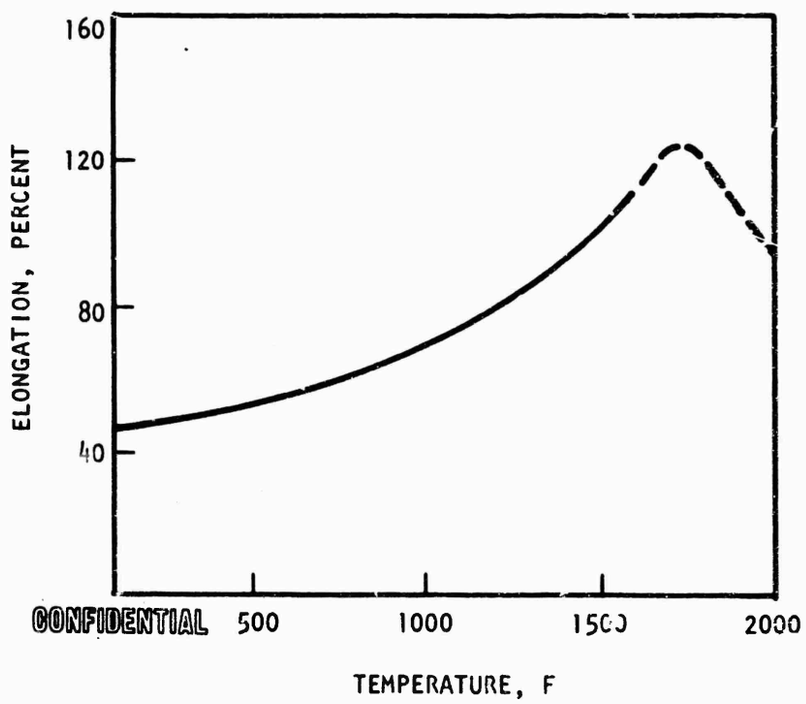

Figure 230. Low Cycle Fatigue Characteristics, Nickel 200

above the subscripts , and I refer to the segment and Demonstrator thrust chambers, respectively.

(U) The life simulation ratio of the segment thrust chamber test series was computed as the arithmetic average of the approximate life simulation ratio for each test. The value of this overall ratio was determined to be [illegible]. Thus the fatigue generated during the 516 cycles of the test series is equivalent to the fatigue damage of the Demonstrator Module being tested 511 times.

(U) Degradation Life. By observing the chamber throughout the test series, a record of the fatigue progression was obtained. The general appearance of the overall tube was generally excellent and well-progressed fatigue cracking were only noted at a narrow band near the throat. In some tubes, initial evidences of fatigue were also visible on sections near the injector. At the conclusion of the testing there little or [illegible] fatigue cracking [illegible] were evident on the injector [illegible]. Operation of thrust chamber tubes containing microcracks generally has no noticeable effect on chamber flows, cooling, or performance. This result was again verified during this test series. Comparison of the appearance of microcracks in the [illegible] powder-bonded channel proof verification. Figure 23 plots the percentage of tubes with microcracks as a function of test number. Statistical data has predicted that 50 percent of the tubes would have microcracks after 100 cycles.

(U) There was a [illegible] progression in the appearance of the two sides of the chamber. The fatigue [illegible] on [illegible] were an [illegible] progression with microcracks appearing at about 40 cycles [illegible] the usual [illegible] experienced in thermal fatigue data. In [illegible], it appeared that there was an [illegible] in throat [illegible] temperature such that a portion of the tubes were undergoing [illegible] than normal temperature cycling. [illegible] of the remainder of tubes were undergoing [illegible] temperatures were nearer that for nominal. Midway through the tests, [illegible] microcracks appeared on a small percentage of the tubes as [illegible]. These [illegible] [illegible]

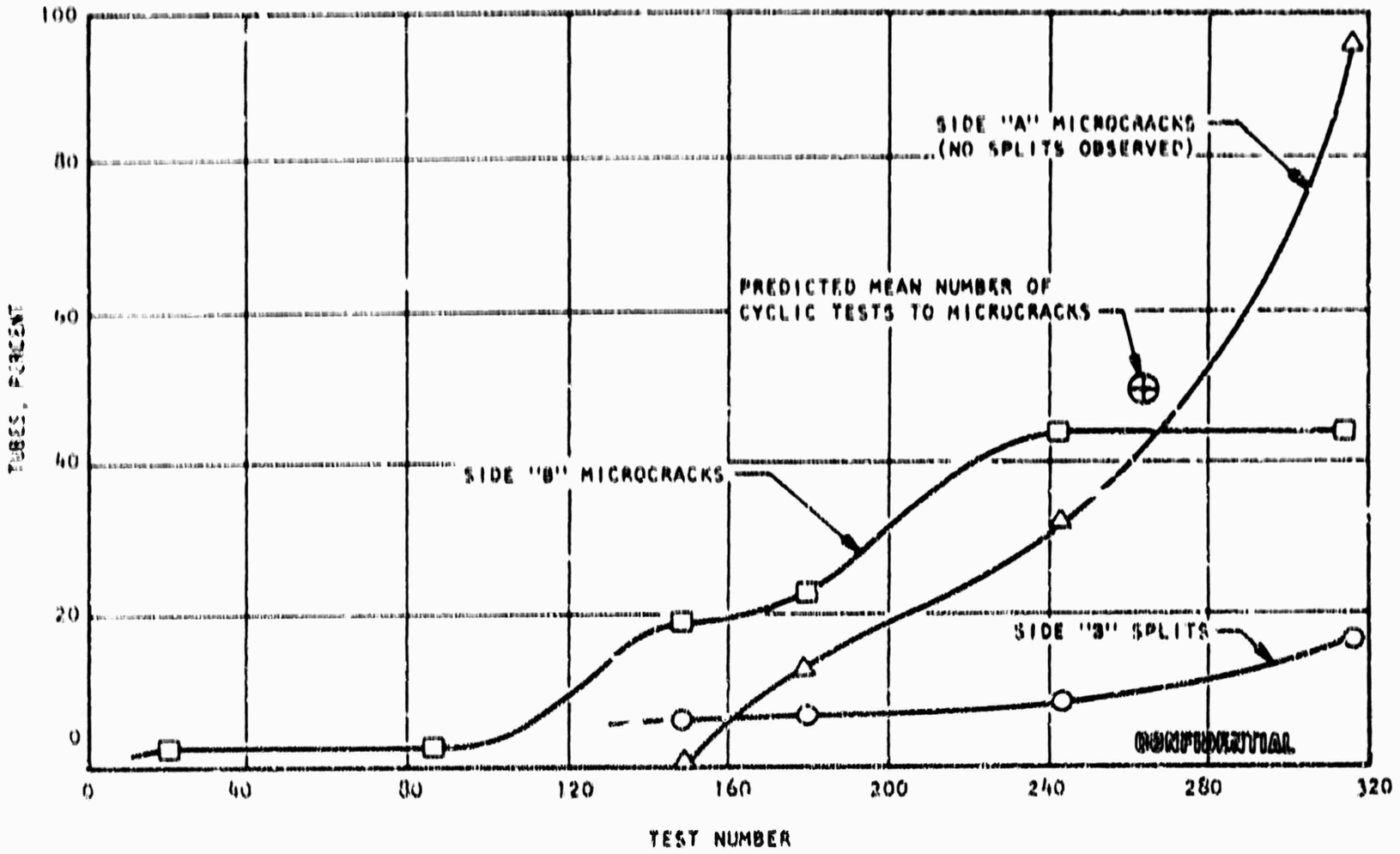

Figure 231. Order of Appearance of Tube Microcracks and Splits
Nickel Tube-Wall Segment Cycling Tests

into sources of leakage as testing continued. All of these tubes appeared to the left of the centerline of Side B, while the tubes to the right of the centerline on Side B generally indicated less fatigue than any other portion of the chamber. The reason for this temperature unbalance was not accurately determined. However, it appears to relate to manifold fabrication repairs which could have influenced coolant distirbutions.

(U) Injector Performance. Combustion performance efficiencies (η_{c^*}) were reviewed for the mainstage cycling tests but were not included in Table 68 because these values were affected by the tube leaks as discussed herein. However, the data support previously observed performance trends of the selected triplet injection pattern.

(U) The combustion efficiency is a computation of c* based on injector fuel and oxidizer flows. During the latter tests in the series, additional fuel was added to the combustion products near the throat plane through nine tubes on Side B which developed leaks. A leakage flowrate through these primary leaks was computed, based on sonic velocity conditions at the minimum flow area and properties of the coolant which were known from the heat transfer analysis. The c* efficiency of the segment thrust chamber without these major leaks was then computed by removing from the efficiency computation the effects of this added fuel coolant. The efficiency computation was based on the conservative assumption that no heat was added to the leaking coolant (theoretical c* remains unchanged while the actual is reduced).

(C) The c* efficiency during the test series was found to remain between 97 and 100 percent. Figure 232 shows the variation of the c* efficiency with test number. The rise of combustion efficiency during the initial phase of the test series is attributable to the buildup of chamber pressure to the nominal value, with a corresponding in combustion efficiency. This was followed by a decay attributable to an oxidizer leak which developed at the injector braze joint. Injector repairs were attempted

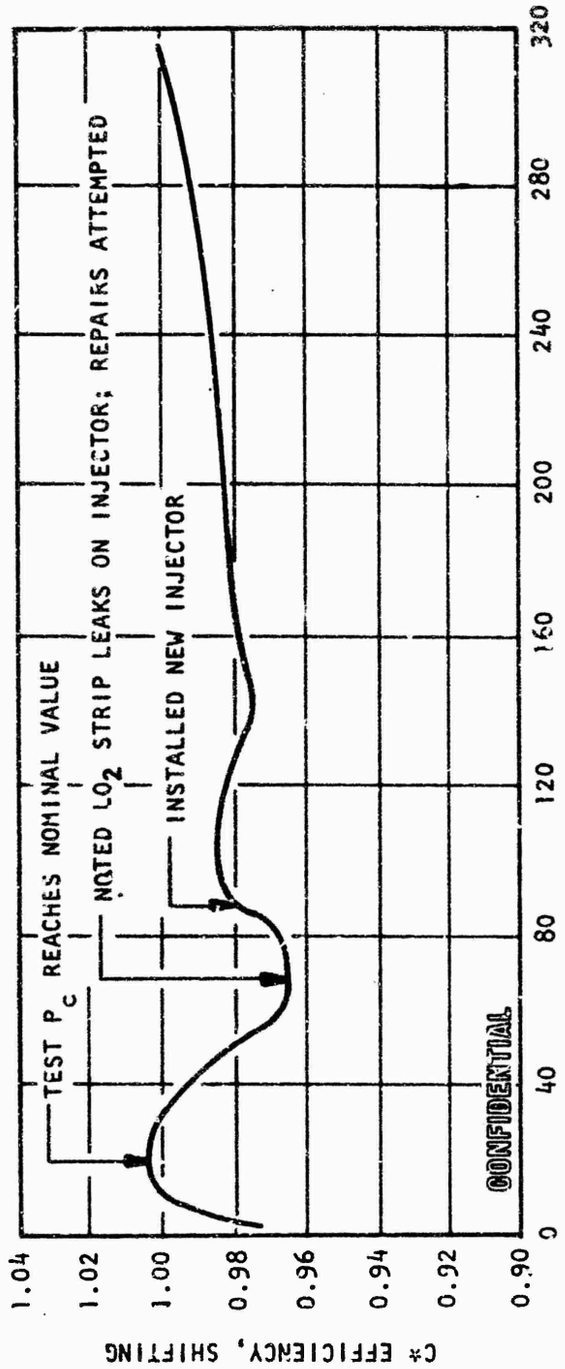

Figure 232. Combustion Efficiency vs Cyclic Test Number
Nickel Tube-Wall Segment Cycling Tests

after test 68. While these repairs halted the further development of LO_2 leaks, the injector performance was not restored to the original value. A new injector of identical design was then installed after test 87, resulting in an improved efficiency value, which was maintained throughout the test series.

(U) Metallurgical Examination. A detailed metallurgical examination of the segment thrust chamber was conducted after test 315. The chamber was cut in half by sawing through the center of the copper side plates. Following photography of the two chamber halves, additional saw cuts were made to expose the throat area tube hot and cold side to sterobinocular examination. This examination showed that no gross melting or erosion of the tube crowns in the throat had occurred. All but five tubes in the A side appeared to have microcracks in the throat area. The appearance of the tubes was remarkably uniform on the A side (Fig.233). Unlike the A side, there was considerably more tube crown damage in the left side of the throat of the B side than in the right side (Fig.234). Extensive, highly localized metal movement had occurred in the hot-gas surface of the tubes in the A and B side throat area, which is characteristics of low-cycle thermal fatigue. The four tubes brazed to the copper side plates suffered axial cracks near the throat apparently caused by additional restraint imposed by the side plates. On side B, these axial cracks developed into major leaks during the latter tests.

(C) A metallographic examination was made of sections across the throat. Figure 235 shows two such sections, which are typical of most of the tubes on the A side. Two tubes were also split to examine a longitudinal section in the throat area, as shown in Fig.236. The hot-gas crowns showed an alternate increase and decrease of thickness which is typical of metal movement caused by thermal cycling. Typical variations were between 0.010 and 0.015 inch compared to the original 0.012 inch. Examination at high magnification confirmed the lack of sulfur contamination or braze alloy penetration. There was some erosion damage to a few tubes

IXE35-6/8/67-C1B

Figure 233. Nickel Tube-Wall Segment Throat Condition
After Cycle 315

LXE35-6/8/67-C1C

Figure 234. Nickel Tube-Wall Segment Throat Condition
After Cycle 315 (Side B)

Mount 7-3578 Etch: Anaconda Mag: 50X

(a) Tube B43

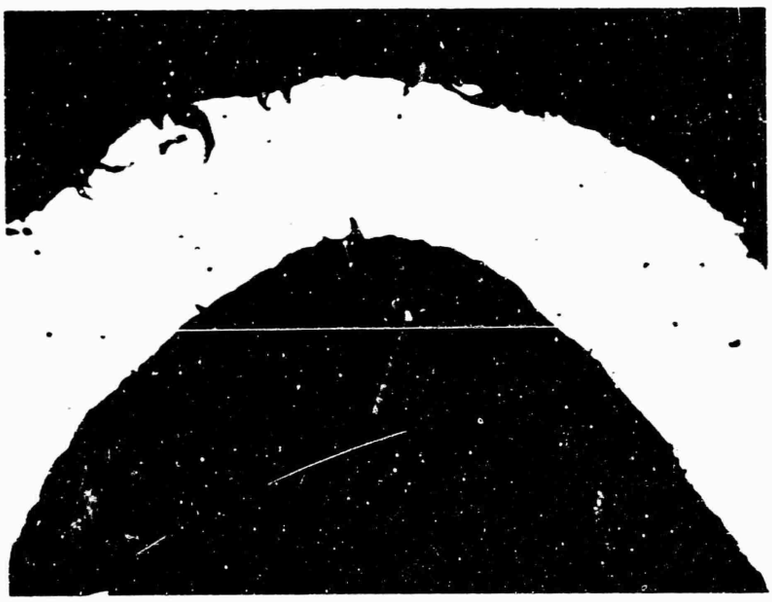

Mount 7-3576 Unetched Mag: 100X

CONFIDENTIAL

(b) Tube A6

Figure 235. Hot-Gas Crowns of Two Tubes at the Throat

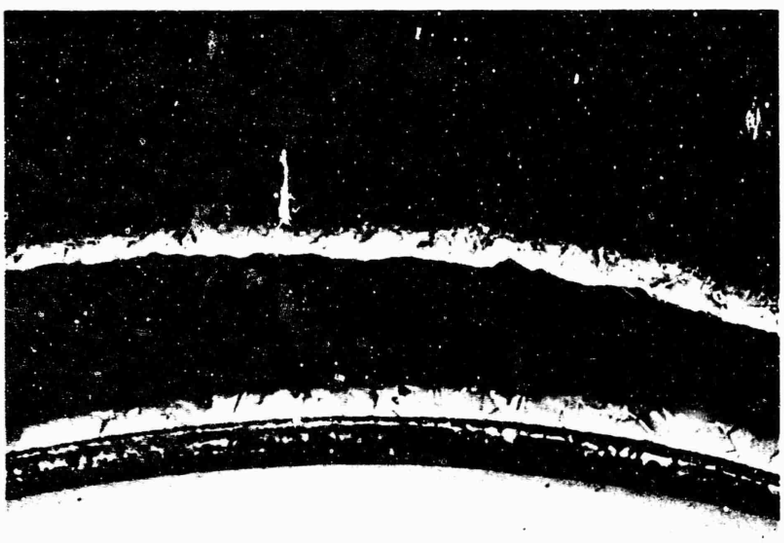

CONFIDENTIAL

Mount 7-3577 Etch: Anaconda Mag: 16X

Figure 236. Longitudinal Section of Tube A28. The Section is not Exactly on the Axis, so That it Falsely Indicates a Tapering Tube Crown Height

which protruded about 0.020 inch into the combustion zone (Fig. 237). This erosion is normal where direct flame impingement occurs.

(U) A microhardness survey was made at regular intervals along the section of a tube at the throat. A portion of the survey is shown in Fig. 238, with the observed hardness values. These microhardness values are typical in magnitude and distribution for all tubes, both in the throat and combustion zone. The observed variations in hardness are attributable to strain cycling under variable conditions of temperature and restraint around the tube crown.

(C) A thin black film had formed on the tube surfaces in the convergent and throat areas, as seen in Fig. 239. A spectrographic analysis of this film indicated that this deposit contained no major component (over 10 percent); it contained minor quantities of chromium, nickel, iron, copper, aluminum, gold, boron, and other trace elements. No nickel corrosion products formed from the TEA/TEB hypergol were found. The spectorgraphic analysis also confirmed that the tubes were originally unalloyed nickel, with no alloy additions.

(U) There was general evidence of thermal fatigue, with a few tubes split by hoop stresses. There were no failures from erosion and/or melting of tube crowns in the throat.

(C) The choice of braze alloy and the brazing operation appear correct. Tube wetting was good, and yet the penetration of braze alloy into the nickel was almost nil. No differences in tube materials, fabrication, or service-produced metallurgical changes could be detected in the throat area. The nickel tube segment was judged to have been well made and assembled, and to have good life performance in the test program.

(C) Conclusions to Nickel Tube Fatigue Results. The cyclic firing of a 2.5K nickel tube-wall segment thrust chamber to demonstrate the thermal fatigue life of the Demonstrator Module was successfully completed. A total of 314 tests were conducted in which the cyclic temperature

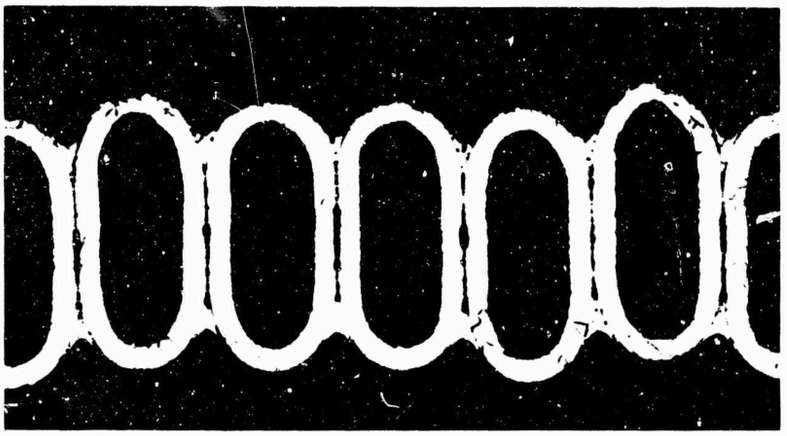

Hot-gas crowns

Cold side

Tube No. A4 A5 A6 A7 A8

Mount 7-3417 Etch: Anaconda Mag: 10X

(a) The Tubes With the Most Damage Projected Farthest into Hot-Gas Stream

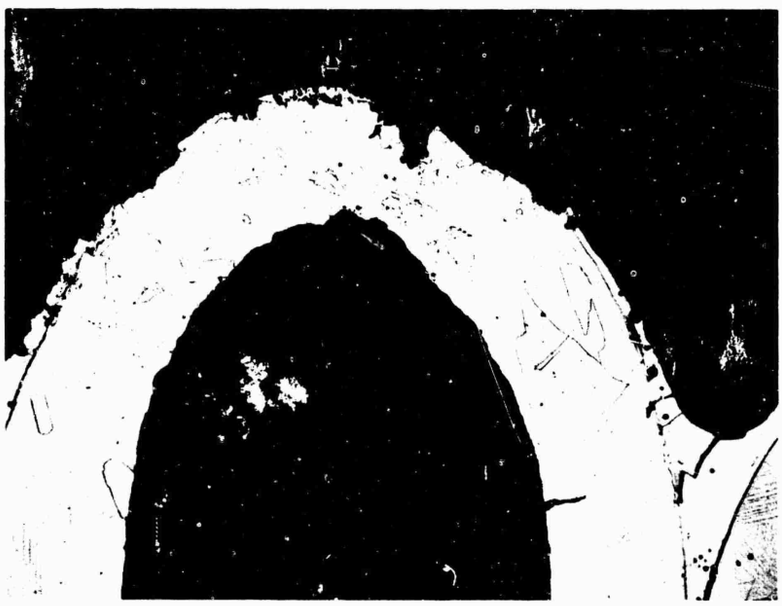

Mount 7-3417 Etch: Anaconda Mag: 10X

(b) The Thin Light Layer on the Crown is Braze Alloy, While the Outer Surface to the Right of the Crack is Oxidized

Figure 237. Cross Section of "A" High in the Combustion Zone, Where There was Moderate Damage from Impingement

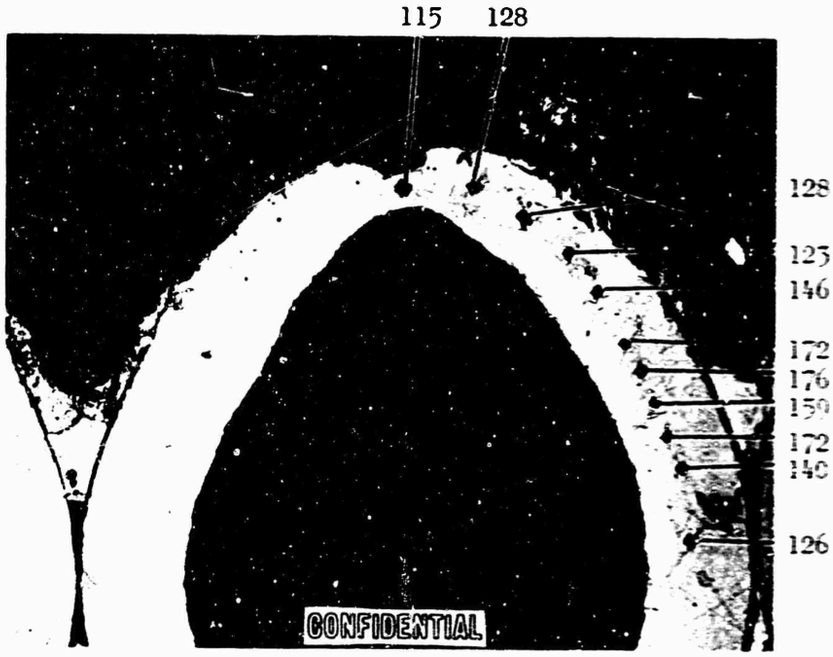

Mount 7-3578 Etch: Anaconda Mag 50X

Figure 238. Tube B43, With Microhardness Readings in Diamond Pyramid Hardness Numbers

and pressure ratio conditions predicted for the demonstrator were examined. The take-off, subsonic climb, supersonic cruise, metallurgical conditions, and environmental effects were also examined.

(U) A method of predicting the thermal fatigue life of the demonstrator was established and by the use of this analytical model, the test conditions for the segment thermal chamber were determined so that an accurate simulation was provided. An analytical analysis of the cyclic test data, a life prediction for the segment tests was also made and found to be close to that of the demonstrator.

(U) The experimentally determined thermal fatigue life of the segment thermal chamber was compared to the predicted value. A good correlation was found, especially as the test data would experience considerable scatter. It was concluded that the thermal fatigue tube life experimentally determined on the segment is then representative of the demonstrator tubing as was required. Confidence in the analytical technique was also established, and that parameter life studies could be made of the demonstrator thermal chamber tubes.

(U) Burner Tube Temperature Life Studies. The parametric fatigue life of advanced metropolis thermal chambers employing Nickel 200 as the thermal tube material was explored, using a heat transfer and pressure stress analysis combined with fatigue test results. Heat transfer and fatigue data from the segment cycling tests were used for gas data, and the fatigue diagram constructed from re-duced and extrapolated tests in the laboratory were utilized.

(U) The analysis parametrically explored the tube temperature versus fatigue life. The tube life of the chamber is greater than the temperature versus fatigue life. This is because local relaxation and fatigue of the hot gas side of the thermal chamber, and non-uniform distribution of the segment cycling tests. If local thermal fatigue cracks develop, the tube life of the chamber is diminished. In a multi-fatigue thermal chamber however, the local

crack does not appear the tube wall crack is the first positive indication of fatigue.

(f) The effect of the thrust chamber gas-wall temperature on the tube transverse crack fatigue life of the Demonstrator Module at the nominal operating condition is shown in Fig. 246. In the analysis, chamber pressure was fixed at the nominal 1500 psia value, and the thrust tube temperature varied by changing the design coolant pressure drop and velocity. This study indicated that a relatively small gain in tube life is obtained by increasing the cooling effectiveness to lower the gas-wall temperature below 1200 F.

(g) A study of the relative fatigue life of the Demonstrator tubes when operated at off-nominal chamber pressure was then completed. A diagram of the relative transverse crack fatigue life vs chamber pressure for the Demonstrator thrust tube is shown in Fig. 247. The analysis assumed a fixed tube design, while chamber pressure and the parameters of heat flux and coolant mass flow were varied for the throttling environment.

(h) It was noted that for a mission spectrum which included a number of runs at reduced pressure, the transverse crack fatigue life was extended well beyond the nominal 500 runs.

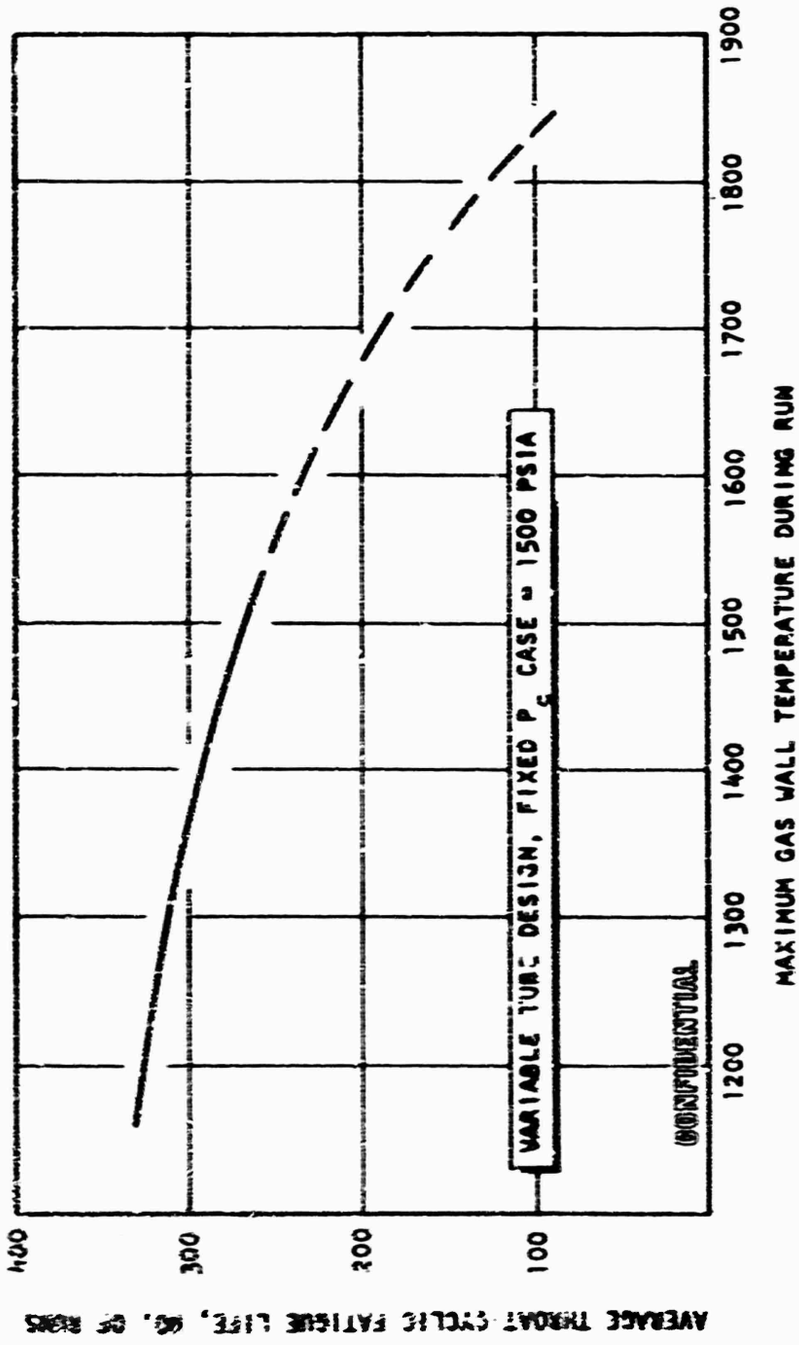

Figure 240. Effect of Wall Temperature on Tube Fatigue Life
Demonstrator Module

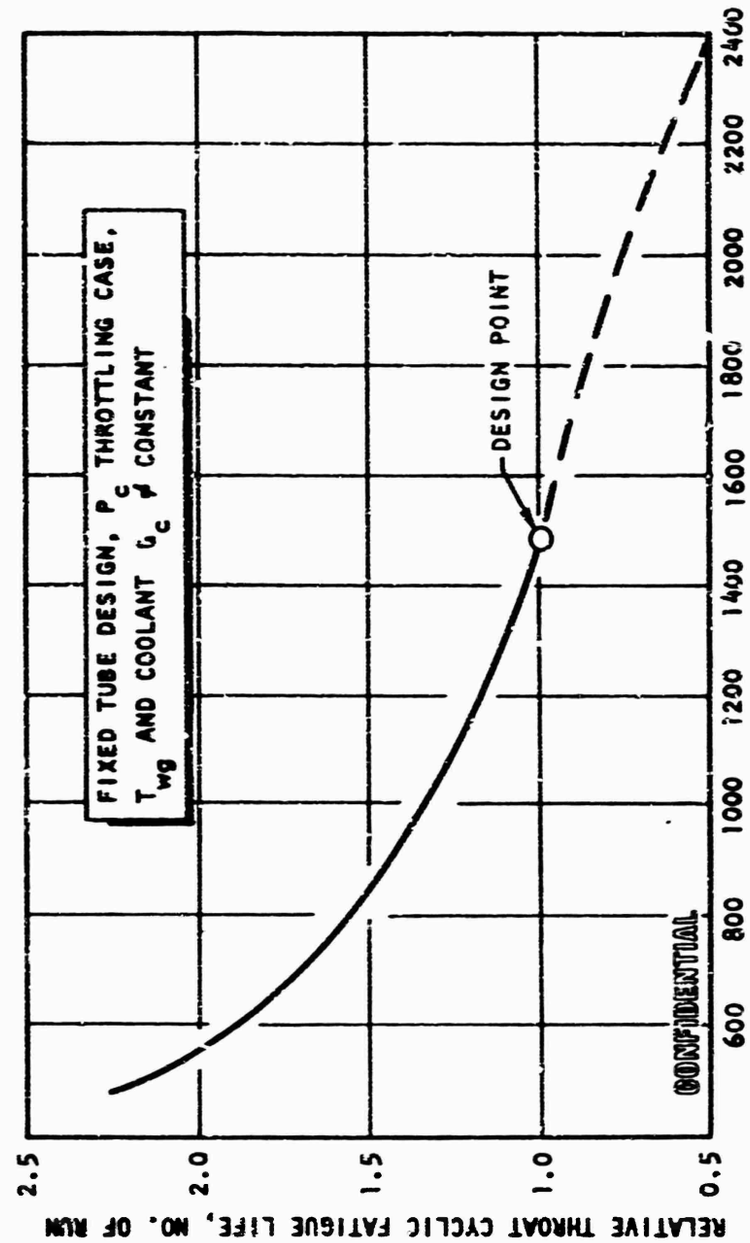

Figure 241. Effect of Chamber Pressure on Tube Fatigue Life
Demonstrator Module

Problem Areas and Solutions

(C) An injector burnout on the second test of the nickel chamber resulted in damage to the nickel chamber. The damage summary was: (1) approximately 30 percent of the tubes were split near the injector, (2) a water-cooling passage was burned through near the injector, and (3) the injector close-out surfaces were eroded. Analysis showed that oxygen delivered to the injector failed to reach the required temperature for cooling during the test. The injector burned out 2.5 seconds into a 4-second run. Previous experience with these injectors had shown capability of running at least 1 second with gaseous oxygen before liquid oxygen is required. The test stand and sequencing were modified to ensure liquid oxygen delivery to the injector within 500 to 1000 milliseconds. The problem was successfully eliminated.

(C) Fuel leaks between tubes and injector end manifold required removal from the nickel tube-wall segment from the test stand during the test. Hand-braze repair on one side (side B) was made, and vent grooves adjacent to the manifold were added to relieve any slight leakage. A machining error had resulted in a substandard braze joint at this particular manifold, which was the cause of the leak.

(C) Hydraulic ruptures occurred in the copper tubes at the throat during cooling limits cyclic tests at over 1500 psia chamber pressure on the copper tube segment. Ruptures resulted from overheating caused by reduced curvature cooling enhancement and surface deposits, in combination with the low yield strength margin of copper. No solution is proposed because copper was not selected as the material for the Demonstrator Module chamber.

THRUST CHAMBER-NOZZLE DEMONSTRATION

Objectives and Requirements

(C) The requirements of this subtask were as follows: Solid-wall and tube-wall 250K workhorse thrust chambers were to be fabricated and tested at or near the chamber pressure associated with the regenerative-cooling limit. The workhorse chambers and nozzles were to have internal dimensions identical to those planned for a Demonstrator Module. Duration capability of the tube-wall chambers was to be sufficient to obtain steady-state performance data. The workhorse chamber was to utilize approximately a 25-percent nozzle length and have an overall engine diameter of approximately 100 inches. Combustion efficiency, nozzle efficiency, specific impulse, base bleed effects, hot-gas ignition, and combustion stability for the annular chamber-aerospike nozzle were to be evaluated. The goal of the combustion stability evaluation was to be recovery of chamber pressure within 40 milliseconds following detonation of a high explosive tangential pulse. Testing was to cover a range of overall mixture ratios extending from 5:1 through 7:1 and with base bleed flowrates from zero base bleed to approximately 5 percent of the total flowrate. Preliminary heat transfer and structural effects data were to be acquired during these tests. The workhorse chamber and nozzle were to be tested at a simulated-altitude condition to gain information on the degree of altitude compensation.

(U) The approach adopted was to use the solid-wall chamber for facility checkout, injector checkout, initial and hot-gas ignition tests, priming and start transient tests, stability checks, and obtaining tapoff data. The tube-wall testing with a self-pumped diffuser would be utilized for obtaining the performance data.

(U) The plan provided that injector details would come from the Injector Performance Investigation subtask. Therefore, scheduling of these two subtasks was to be coordinated. Because the tube-wall chambers were

"workhorse" types, no attempt was made to coordinate cooling tube details with the Cooling Investigation subtask which served the Demonstrator Module design. Gaining experience with fabrication of large, tube-wall aerospike thrust chambers was a definite objective of the work.

Summary of Work Accomplished

(C) One water-film-cooled, solid-wall chamber and two hydrogen-cooled tubular chambers were constructed to accomplish the contractual objectives. The length of these chambers was 12 percent of an equivalent conical nozzle. The length of these chambers was extended to the desired 25 percent of an equivalent conical nozzle by an uncooled nozzle extension. The external dimensions of the chamber were equivalent to a 100-inch-diameter flight engine. The internal geometry of the combustor closely duplicated the proposed configuration for the Demonstrator Module, and the thrust chamber cooling tubes were optimized for serving the workhorse function and cost.

(C) Two injectors, one with provisions with hot-gas tapoff and hot-gas ignition, were constructed. The injector strip configuration and pattern design were based on the results of the 2.5K solid-wall portion of the program. As in the Demonstrator Module design, the annular combustor was divided into 40 compartments. These compartments were separated by cooled baffles; however, the design of these baffles differed in some respects from the Demonstrator configuration. For the Demonstrator Module, the baffle length is 4.5 inches and the baffle is sealed to both the inner and outer body. In the experimental thrust chambers, the baffles were attached to the injector. With this cantilevered arrangement, baffle lengths were 3.0 inches and clearance was provided between the baffles and the inner and outer combustor bodies. (The exact combustor and baffle configuration of the Demonstrator were simulated in the 20K structural model.)

(U) The fabrication of all thrust chamber components was successfully completed during the program. Dimensional control was accurately maintained for these full-scale components. The construction of these injectors and tube-wall thrust chambers demonstrated the feasibility of many of the construction techniques for building Demonstrator Module and flight hardware.

(C) A total of 14 mainstage tests were conducted with the 250K experimental chambers. The duration (above 90 percent of peak chamber pressure) of these tests was limited; only one test exceeded 1 second mainstage duration. This test series covered a range of mixture ratios from 5 to 7 and a range of operating pressures from 353 to 1289 psia.

(C) Analytically predicted values of nozzle efficiencies (C_t) were repeatedly verified during the test series. A high level of altitude compensation was demonstrated during a throttled (609 psia chamber pressure) site test. The specific impulse during this test was 343.6 seconds. The higher degree of the altitude compensation was also verified by the achievement of ambient base pressures while under various amounts of secondary flow.

(C) Significant performance data were achieved during three tests of the tube-wall thrust chamber test series. During test 023, a combustion efficiency of 97.4 percent was achieved at a chamber pressure of 609 psia. The duration of this test was 400 milliseconds, and experience indicates that short durations at this thrust chamber test stand adversely affect measured performance, i.e., an increase of at least 1 percent combustion efficiency would be anticipated for a longer operating duration. Despite the adverse effects of reduced duration, the nozzle performance and combustion efficiency achieved during this test were sufficient to fulfill the specific impulse objectives of the Demonstrator Module configuration.

(C) Two other tube-wall tests (027 and 028, durations 275 and 800 milliseconds, respectively), provided information relative to the injector combustion efficiency. During each of these tests, combustion efficiency was adversely affected by: (1) the short duration and, (2) the leakage of fuel into the chamber from tube splits and baffle erosion. Fuel leakage adversely affects the uniformity of the mixture ratio in the chamber and supplies a large amount of hydrogen into regions of the chamber where it is unlikely to combust with the remaining propellants. In each test, large amounts (13 and 25 percent of the total hydrogen) were injected into the combustor through these leak paths. Despite these adverse factors, combustion efficiency during these two tests was 96.2 and 94.9 percent, respectively and the delivered specific impulse was 336 lbf-sec/lb and 330 lbf-sec/lb, respectively. An attempt was made to normalize the effect of the fuel leakage to interpret the actual combustion efficiency of the injector. This was done by utilizing empirical factors developed during the 2.5K solid-wall effort. Based upon these data, the combustion efficiency for propellants which passed through the injector was greater than 98 percent during both tests. The results of this test series, although qualified by duration and hardware damage, were positive indications of the aerospike performance capability. The data indicated that no change in the performance prediction techniques or the predicted specific impulse values was warranted.

(U) The 250K test series also provided data in structural and heat transfer areas pertinent to future aerospike absence designs. One of the most important results of the test was the virtual absence of side loads during sea level operation with the high expansion ratio nozzle. Unlike the bell thrust chambers, the aerospike configuration showed that it could be operated over a wide range of conditions without this undesirable symptom. The total heat transferred into the chamber was closely predicted by analytical studies. Total temperature rises corresponded closely with predicted values.

(U) Hot-Gas tapoff feasibility was successfully demonstrated on three tests. Transient temperature data indicated that tapoff temperatures would be comparable to values achieved on 2.5K segment tests.

(U) Satisfactory CTF ignition and start transient were achieved on all tests. Film and pressure data indicate that successful ignition was repeatedly achieved on the full annular chamber. Hot-gas ignition demonstration was not attempted during the test series.

(C) Two pulse gun tests at chamber pressures of 353 and 1289 psi were conducted and resulted in no instability being induced. Analysis of the test data revealed a tendency for the system to oscillate in two frequency ranges: (1) 200 to 400 cps during transition and cutoff and in mainstage at lower chamber pressure levels, and (2) 1800 to 2000 cps during mainstage on some tests. The first mode of oscillation (200 to 400 cps) has been analyzed to be the common chug mode and correlates extremely well with an analytical model developed on the NASA Engineering Program (Ref. 5). Minor modifications to the feed system impedance will eliminate this mode of oscillation at the low chamber pressure operating condition. Analysis of the intermediate frequency mode (1800 to 2000 cps) revealed no correlation with the predicted fundamental modes of acoustic instability or structurally coupled modes of oscillation. This mode can be attributed to either a feed system-combustion process coupled oscillation (buzz), or a ninth harmonic of the annular acoustic mode. The mode should be eliminated by either minor modification to the feed system and/or the use of the longer baffles planned for the Demonstrator Module.

Description of Hardware and Fabrication

(U) The major components designed and fabricated for operation at the 250K thrust level were a solid-wall thrust chamber, two tube-wall thrust chambers, and two injectors. Other hardware designed and fabricated includes a thrust mount, an uncooled nozzle extension, a base closure, and various ducts and manifolds. These components will be reported separately in following sections. Specific location of components and instrumentation is described by referring to the degree orientation and some of the chamber as described in Appendix I.

(U) The major steps in the fabrication of the 250K hardware are described herein. However, the details of the processes utilized in fabrication are covered in the Materials and Processes Research and Development Report (Ref. 3).

(U) 250K Solid-Wall Thrust Chamber Design. The 250K solid-wall chamber is a workhorse chamber designed primarily to provide for injector checkout, determination of durability (structural and heat transfer), ignition characteristics, and stability evaluation. The chamber was utilized to provide advanced information regarding operational characteristics of a full 360-degree aerospike thrust chamber assembly. Specific items evaluated during hot-fire testing were:

1. Injector assembly performance, stability, and structural integrity at various operating conditions
2. Hypergolic ignition
3. Injector-combustion stability rating by pulse gun as well as operational test
4. Hot-gas tapoff

In addition, the inherent ruggedness of this type of hardware made it a valuable tool during test facility shakedown periods.

(U) The following basic design requirements were established for the solid-wall chamber:

1. Inner and outer body chamber contour identical to the Demonstrator Module Chamber
2. Ease of manufacture and repair
3. Maximum accessibility
4. Interchangeability with subsequent chamber hardware

(U) The solid-wall chamber is composed of two major units: one consists of the outer section of the combustion chamber and expansion skirt, and

the other consists of the inner section of the combustion chamber and expansion nozzle. Each unit was fabricated from 304L CRES steel forgings machined to the desired contour. Between machining operations, the combustor bodies were annealed to minimize residual stresses and ensure dimensional integrity. Radial and axial positioning of the inner and outer body are maintained by attachment to the injector. Thermal and pressure loads are transmitted through shear lips on the interface at the attach bolt circle. Thrust loads are transmitted through the inner chamber body, utilizing an eight-point thrust mounting structure.

(U) Duration at full thrust is made possible through the utilization of water film cooling and copper-lined throat. The inner and outer combustor body design (Fig. 242) incorporated film-coolant rings located 1.5 inches above the throat. The coolant flows through orifices in the ring which are directed toward the converging wall of the throat, providing a boundary layer of coolant along the surfaces of the throat and nozzle. To further improve the life capability of the chamber, the outer body throat is lined with 0.75-inch-thick, high thermal conductivity copper, and the inner body throat is lines with 0.75-inch nickel, which provides a margin of safety during operation and also the potential of brief operation without coolant.

(U) Provisions for stability testing were included in the combustor testing design. Stability testing was accomplished by pulse guns located 1 inch below the injector face. The pulse guns were chosen for their ability to provide a directional burst of energy in the region most likely to induce instability. Located on the outer wall of the thrust chamber (Fig. 243), the guns are easily serviced and insensitive to thermal detonation, allowing the chamber to be "pulsed" at any time during mainstage.

(U) The gun (Fig. 244) is designed to accept either a 300 H&R (rifle) or a 38 special (pistol) cartridge. The shell can utilize various powder loadings, and when utilized with burst diaphragms of 7500, 10,000, and 20,000 psi, provides varying values of overpressure.

(U) During the chamber run, an electrical squib is detonated, driving the firing pin into a standard rifle or pistol primer which ignites the

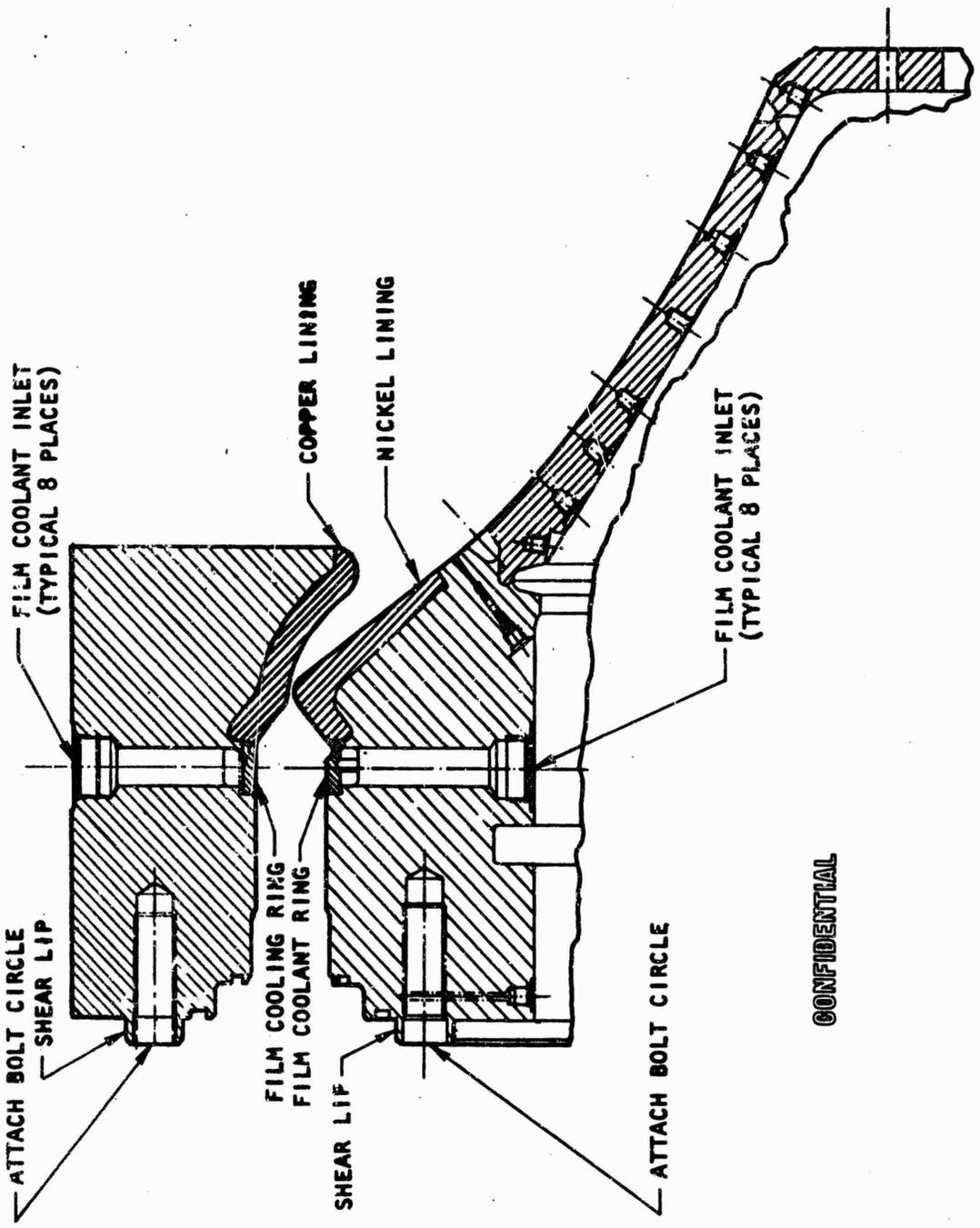

Figure 242. 250K Solid-Wall Thrust Chamber Body Assembly

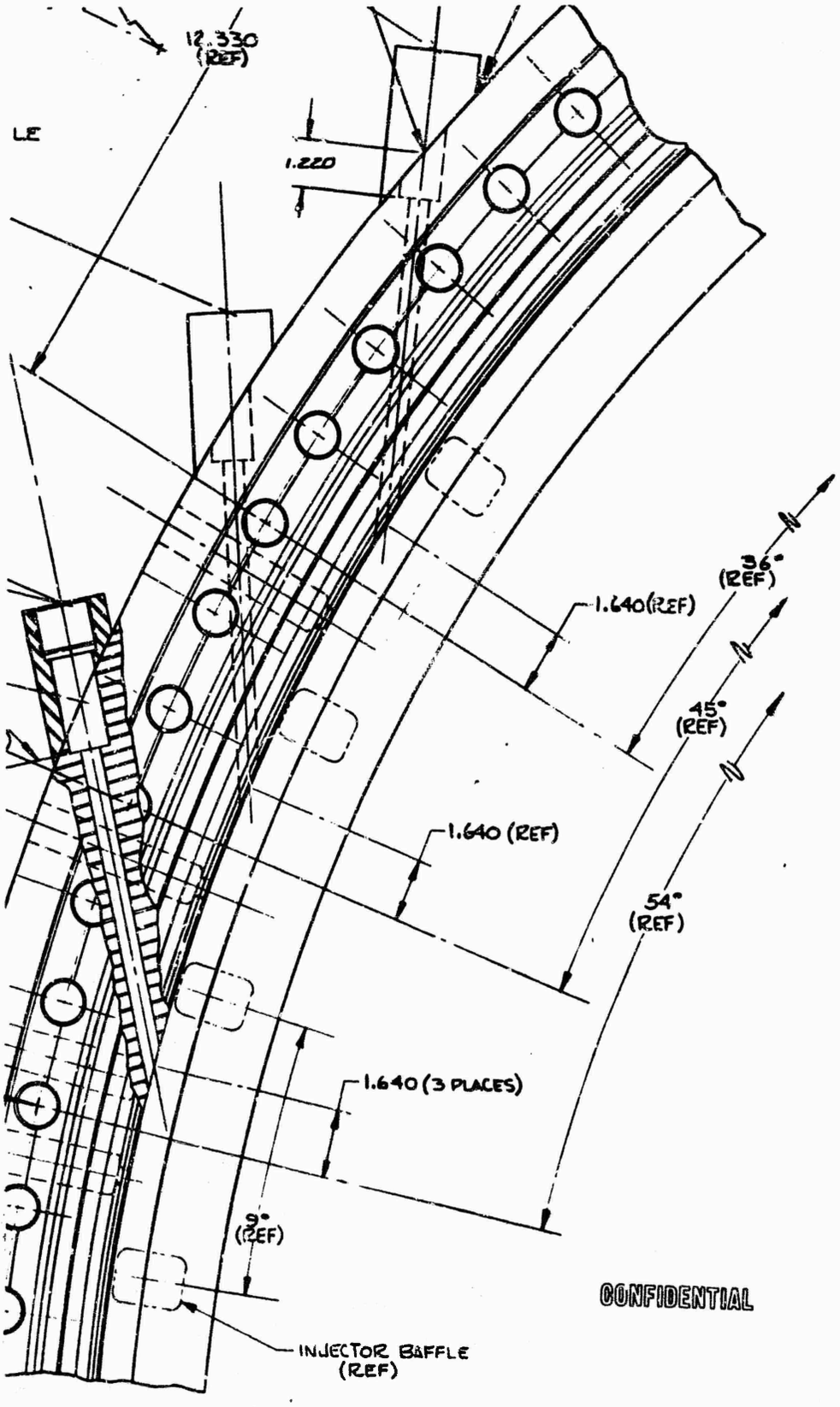

Figure 243. Chamber Locations of Pulse Gun Ports

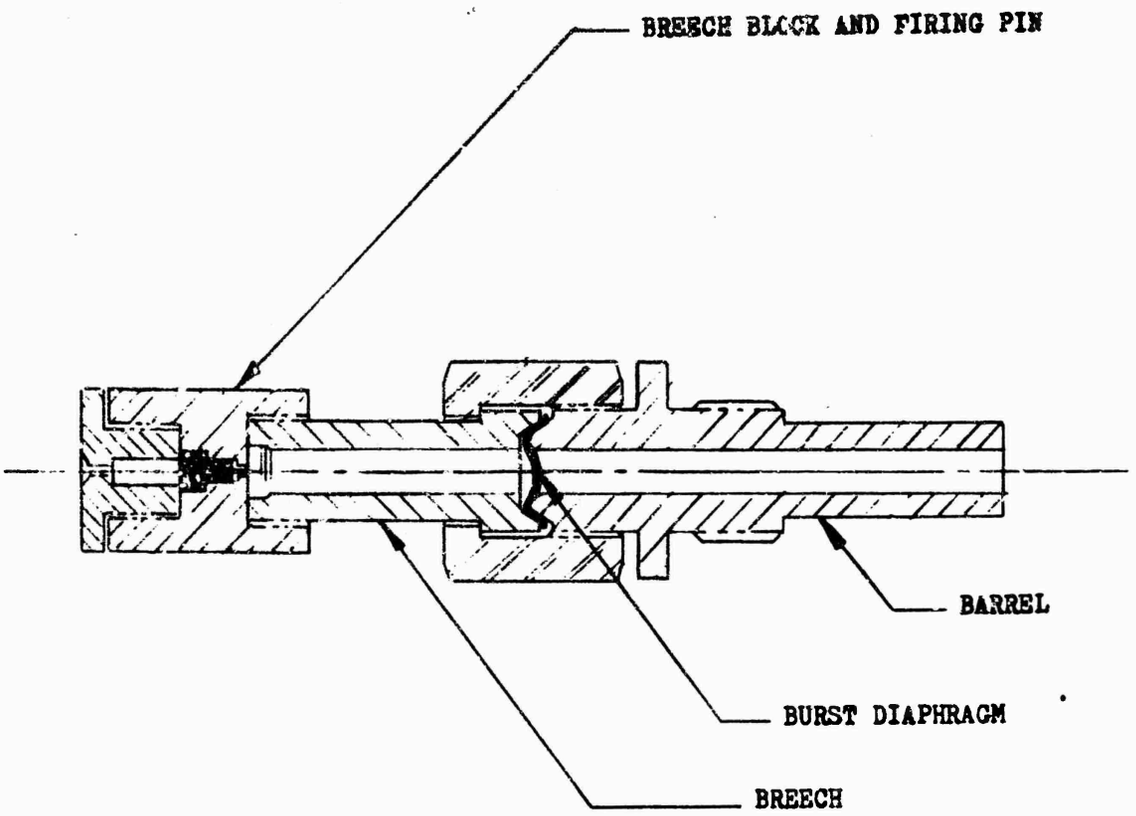

Figure 244. Pulse Gun

powder. The burst diaphragm prevents the gas charge from escaping into the chamber until the full charge is developed.

(U) The design includes provisions for high-frequency pressure transducers to provide data during stability runs for evaluation of overpressure and damping characteristics. The transducer ports (Photocon type) also may be adapted to streak photography windows.

(U) 250K Solid-Wall Thrust Chamber Analysis. The inner and outer combustor bodies, which comprise the 250K solid-wall chamber, have a contour identical to the tube-wall bodies, and use the same basic forgings machined to a thickness equivalent to the chamber mold line of the tube-wall bodies. The aerodynamic and structural work completed for the tube-wall combustors is directly applicable and is reported in a later section.

(C) The solid-wall combustor bodies were designed with copper throat inserts and film cooling in the throat so that the throat would not limit durations. A transient heat transfer analysis was conducted to analyze the 250K, solid-wall, water-film-cooled thrust chamber design in the throat. The film-coolant orifices have 0.043-inch diameters and are spaced 0.30 inch apart. For the transient analysis, it was assumed that the film-coolant streams do not spread, but cover 0.043-inch-wide strips along the chamber contour. The film-cooled strips in the throat region were maintained at 511 F, corresponding to the saturation temperature of water at a pressure of 750 psia. For the surfaces exposed to the hot gas, a film coefficient of 0.0105 Btu/in.^{2}-sec-F, with an adiabatic wall temperature of 5900 F for P_c = 1500 psia, and MR = 6.0 was used.

(C) The maximum gas-side wall temperature in the throat is shown as a function of time in Fig. 245. The value at t = 0.75 second of 1770 F is below the copper melting temperature of 1980 F. The temperature distribution through the wall after 0.72 second is shown in Fig. 246. The temperature decreases very rapidly into the wall, falling to 1500 F at a point 0.030 inch below the surface. Spreading of the coolant stream can greatly diminish these wall temperature values if sufficient flow velocity for nucleate boiling is maintained.

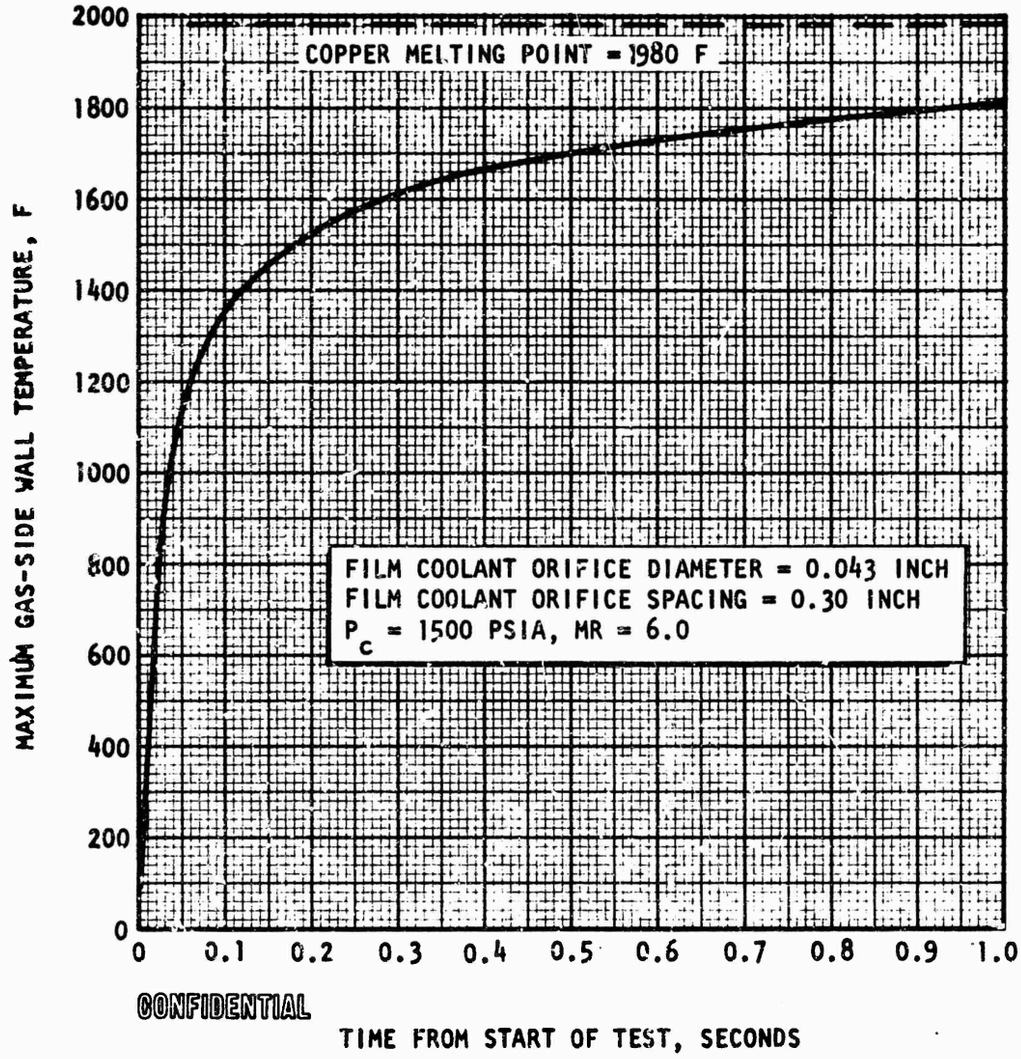

Figure 245. Maximum Gas-Side Wall Temperature vs Time for 250K, Solid-Wall, Film-Cooled Chamber

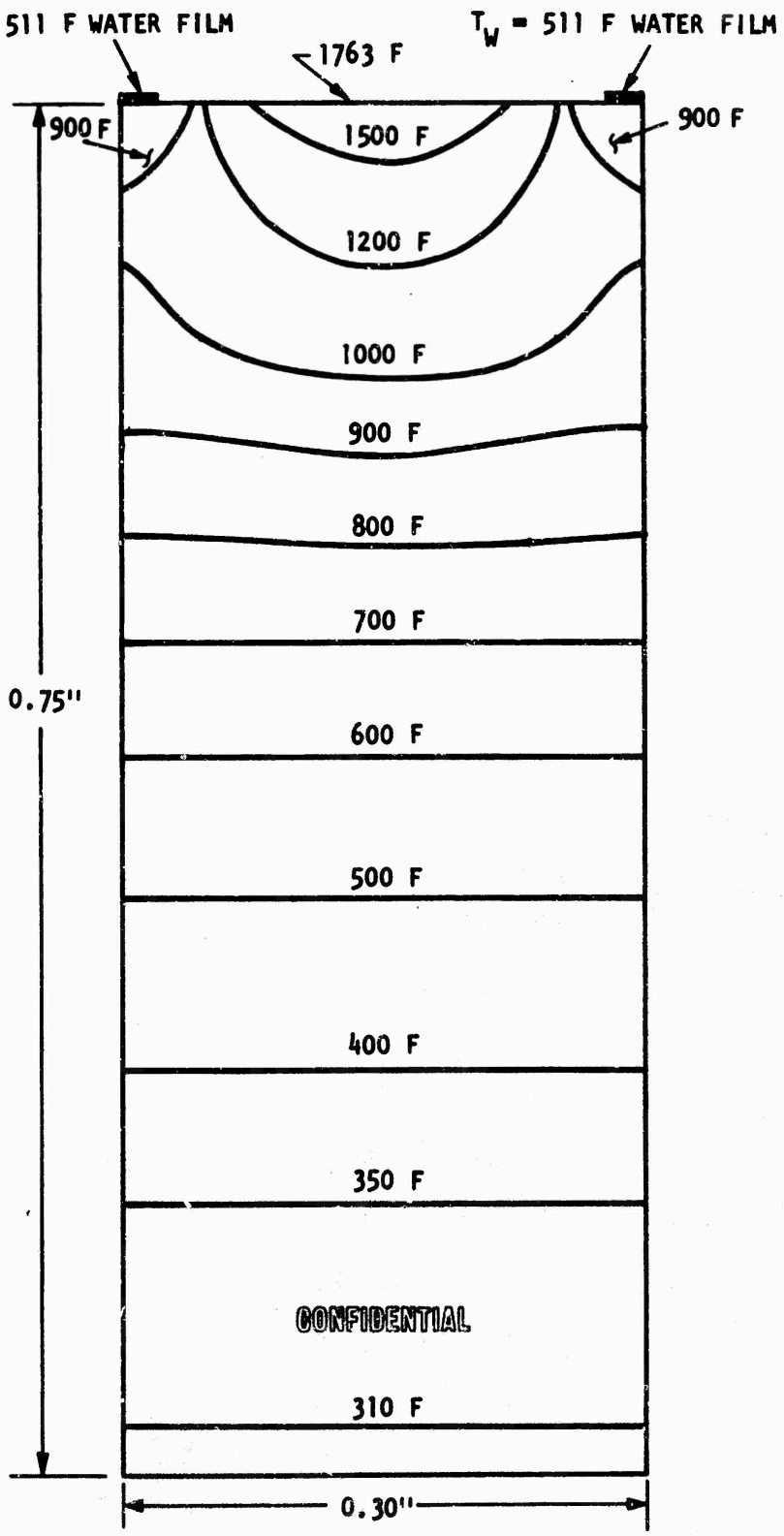

Figure 246. Wall Temperature Distribution in Throat of Water Film-Cooled Solid-Wall Chamber After 0.72 Second

(C) The design flowrate through each film-coolant orifice is 0.087 lbm/sec which gives an injection velocity of 138 ft/sec. If the film-coolant streams spread, completely covering the entire 0.30-inch width between orifices over the 5-inch length of surface to be cooled, the total coolant surface area of each stream exposed to the hot gas is 1.5 sq in. Using the film coefficent distribution of Ref. 10, the total heat input to each film-coolant stream at P_c = 1500 psi and MR = 6.0 is 78 Btu/sec. The maximum heat absorption capability of the film-coolant is 87 Btu/sec, thus indicating that most of the film coolant will be vaporized by the time it reaches the nozzle exit. However, water vapor should provide adequate cooling for the lower heat flux regions of the nozzle.

(U) A check was made to determine whether the heat flux to the coolant from the copper-wall side could exceed the burnout heat flux. If the film-coolant stream does not spread, this heat flux will be substantial, but the associated high coolant velocity will provide an acceptable margin on the burnout heat flux margin. Inspection of the copper deposition at the throat indicated high conductivity relative to that used in the analysis (Fig.247).

(U) Adequate test duration of approximately 0.7 second without erosion in the throat region is completely feasible with the present solid-wall design.

(U) 250K Solid-Wall Fabrication. Ring forgings of type 304L stainless steel were procured and the combustor bodies were rough machined to contour. The contour on the hot-gas side of each body was defined as the

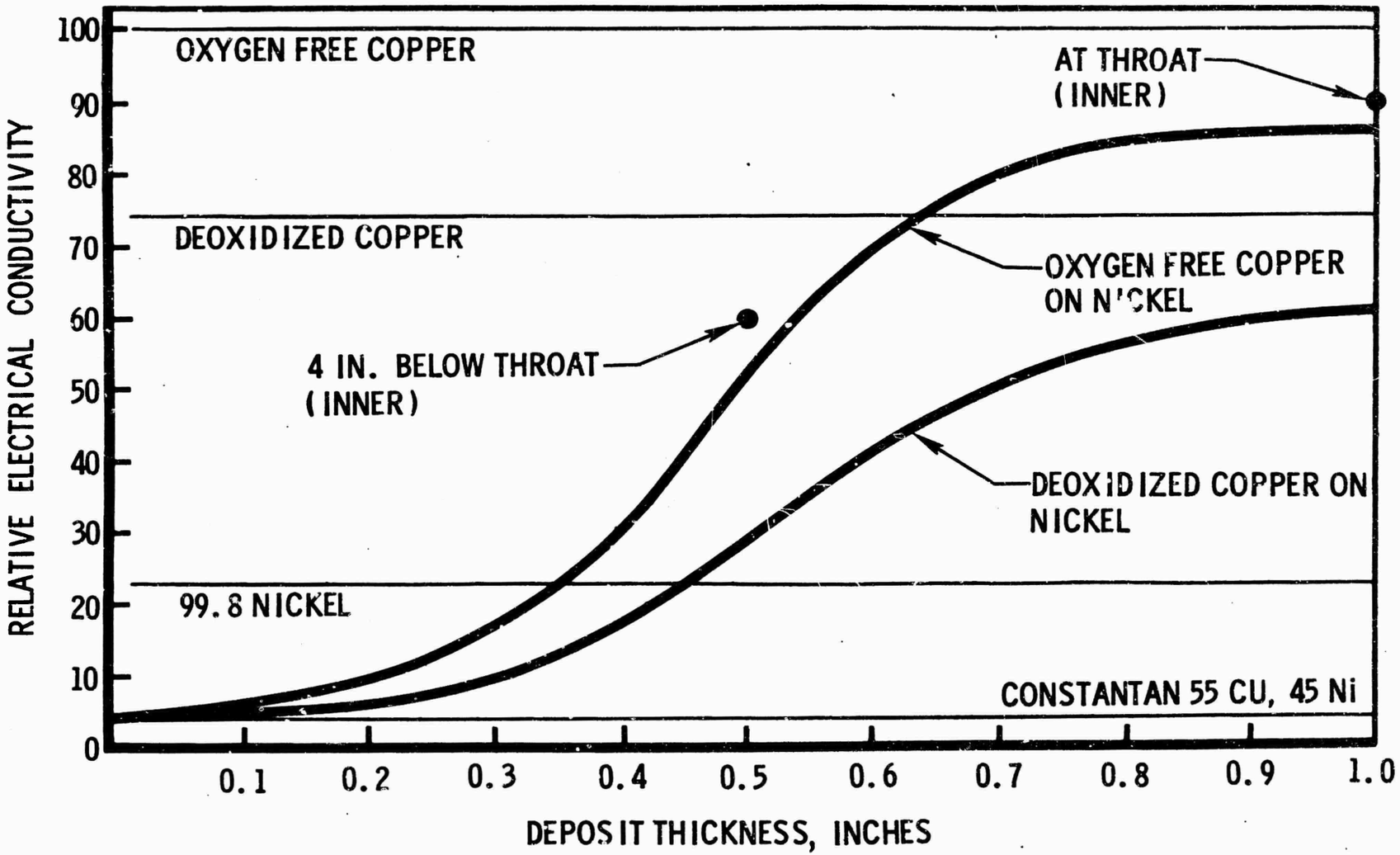

Figure 247. Predicted vs Measured Conductivity
Solid-Wall Outer Body

mold line of the hot-gas side of the tubes in the cooled chamber. During rough machining, drilled holes for introduction of film coolant and the manifold for distribution of coolant were installed. The film coolant rings were welded to each body and a pressure check was conducted to verify structural integrity. To accomplish this, holes in the film-coolant ring were sealed with a plastic resin compound, and the manifold behind the ring was pressurized to the equivalent of maximum operational pressure.

(U) The copper throat was applied by weld deposition to the 304L stainless-steel forgings, which had been previously surfaced with nickel to provide better copper adhesion. The copper deposited on the outer combustor body was inspected and found to be nonporous, high-conductivity copper which complied with the established requirements. The copper applied to the inner body was high conductivity; however, excessive porosity was evident in the welds. Machining of the porous areas and subsequent copper weld deposition was not successful. The body was then machined to accept an oxygen-free, high-conductivity (OFHC) copper ring which was to be welded to the forging. This method proved unsuccessful so nickel was weld deposited to the throat area of the inner body.

(U) Final machining of contour, seal surfaces and injector mating shear lips was accomplished by utilizing match machining techniques to ensure fit to the injector within defined limits. Also included in final machining was installation of a shear groove on the inner periphery of the inner body, straddled by eight equally spaced sets of six tapped holes. These provide shear restraint and attach points for clevises used to mount the eight-leg thrust mount in final assembly.

(U) Final cleaning operations included a water flow test of film-cooling orifices to verify distribution of film coolant. Excellent distribution and alignment of holes were evident in this test.

(U) The thrust chamber bodies (Fig. 248 and 249) and injector were then assembled with the thrust mount and other hardware to form the assembly. Figure 250 shows the inner and outer bodies on assembly fixture. The fit

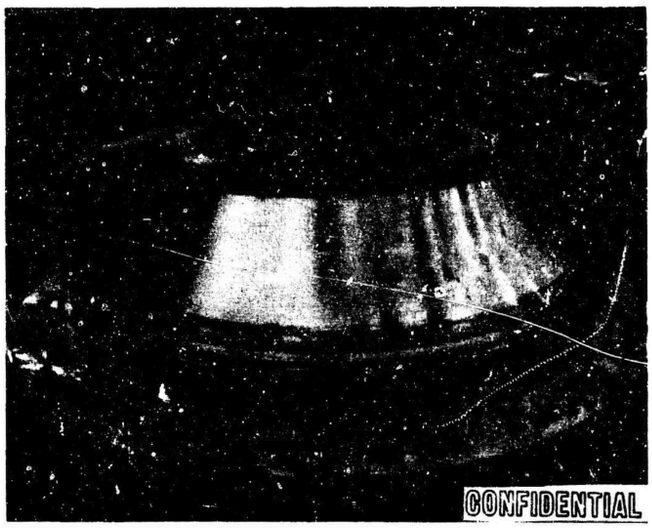

Figure 248. Inner-Body Solid-Wall Assembly

Figure 249. Outer Solid-Well No. 1

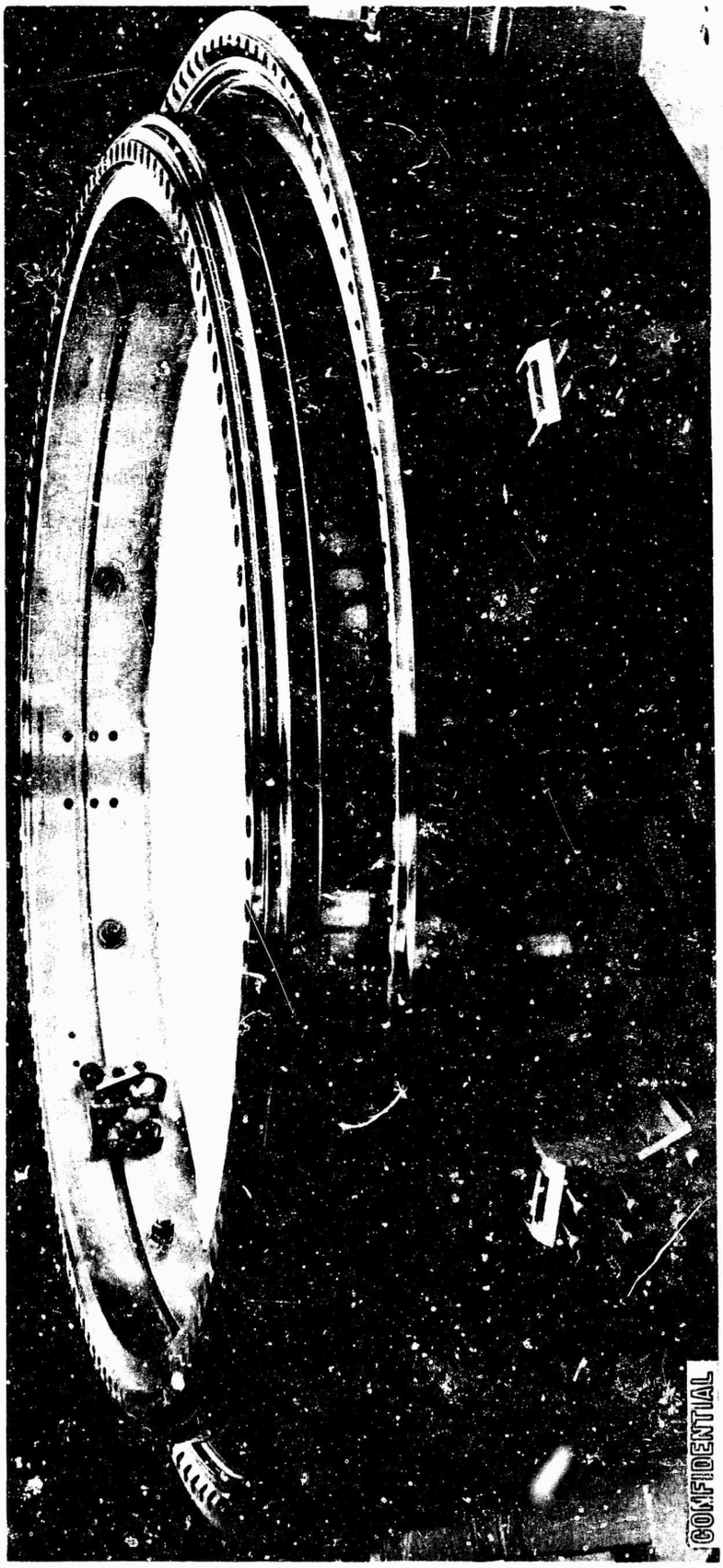

1XE32-2/21/67-C1B

Figure 250. 250K Solid-Wall Inner and Outer Bodies in Assembly Fixture

between all mating components during the assembly was excellent. Of particular interest was the matching of the shear lips on the inner and outer bodies to the injector unit. The matching of these components demonstrated the ability to maintain critical fabrication tolerances at large diameters.

(C) 250K-Tube-Wall Thrust Chamber Design. The tube-wall chamber is a regeneratively cooled assembly with heavyweight backup structure designed to provide nozzle and combustion operating data on extended duration runs over a 5:1 throttling and 5 to 7:1 mixture ratio ranges. The chamber provies the capability to obtain altitude compensation data with base bleed gases provided by an auxiliary gas generator.

(C) The thrust chamber is designed with a nozzle length the equivalent to 25 percent of the length of a 15-degree, half-angle cone of the same area ratio, and consists of concentric, regeneratively cooled inner and outer combustor assemblies. The combustor assemblies form an annular chamber leading to a converging throat, a shrouded outer tubular wall, and an inner tubular nozzle wall to the exit plane.

(C) Each of the combustor assemblies consists of contour machined, type 304 stainless-steel forgings to which the regeneratively cooled stainless-steel tubes are brazed. The inner body (Fig. 251) has a manifold at the exit end through which the hydrogen coolant enters the thrust chamber (Fig. 251, Sections R-R and C-C). The coolant then flows through the tubes toward the injector and emerges from the inner body at a manifold formed by the body and the injector (Fig. 252, Sections F-F). A double-seal arrangement ensures that hot gases cannot leak from the chamber since the hydrogen in the manifold is at a higher pressure than chamber pressure.

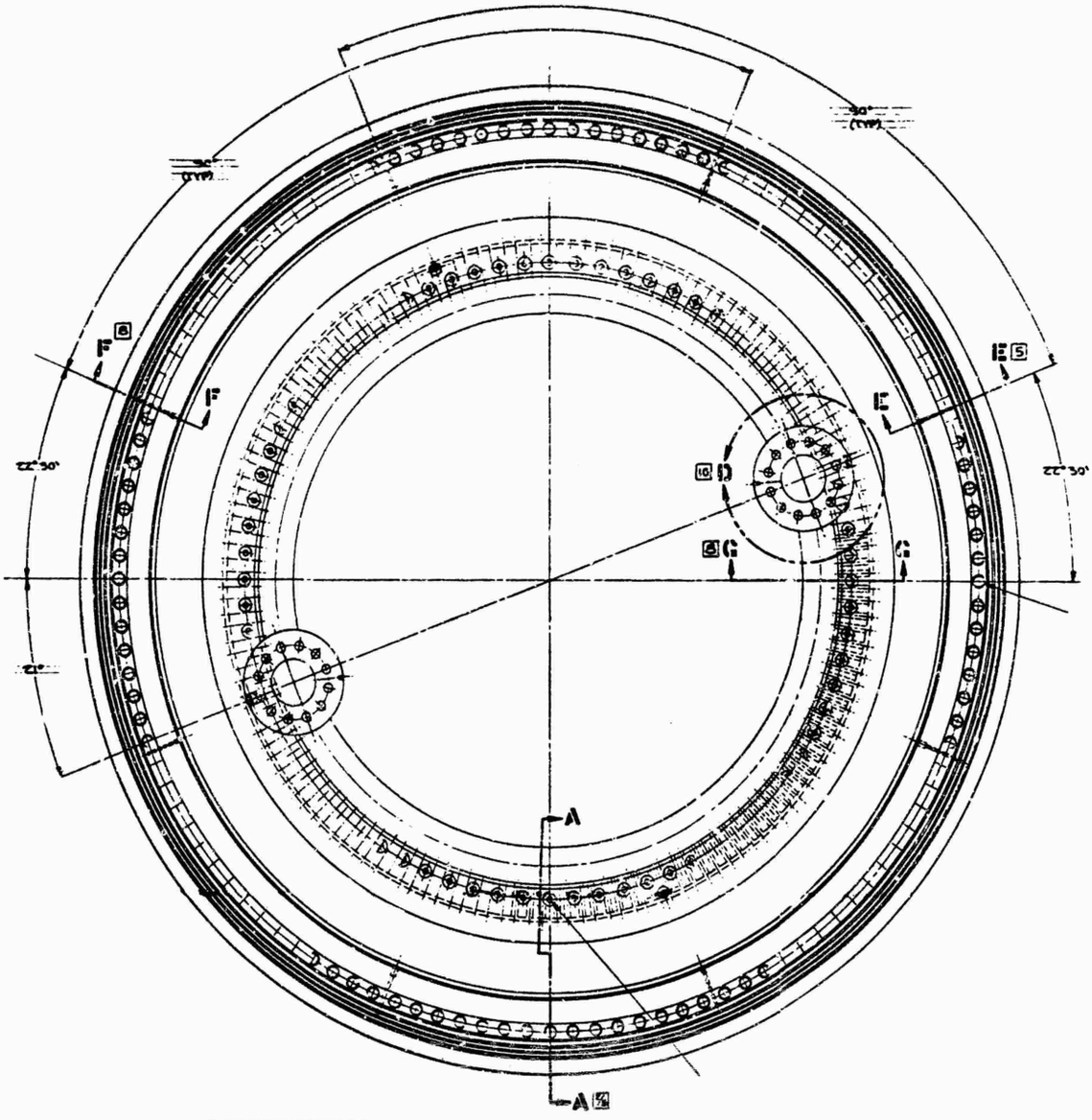

CONFIDENTIAL

Figure 251A. 250K Tubular Thrust Chamber Inner-Wall Assembly

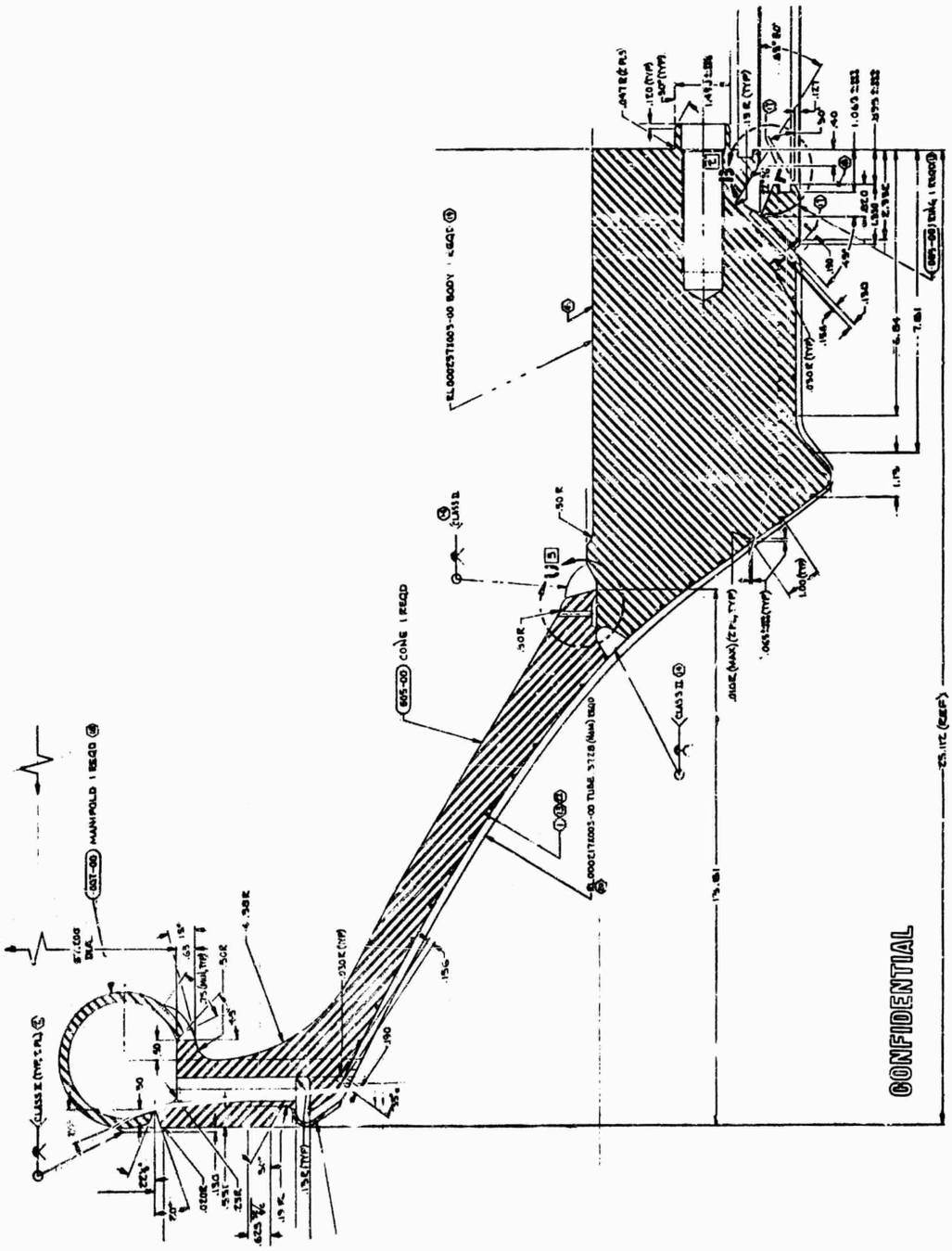

Figure 251B. 250K Tubular Thrust Chamber Inner-Wall Assembly

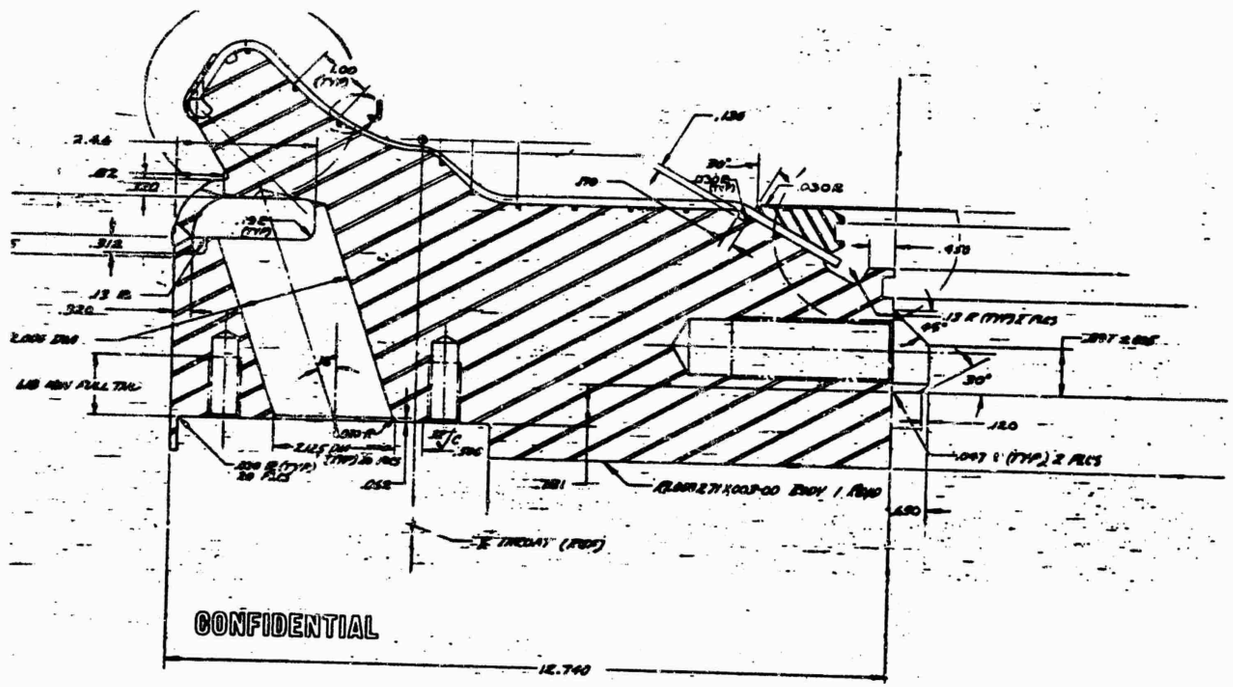

Figure 252. 250K Tubular Thrust Chamber, Outer-Wall Assembly

CONFIDENTIAL

(U) The outer body and injector form an analogous manifold (Fig. 252, Detail K). The coolant, after flowing through the injector, enters this manifold and then flows into the outer body tubes and to the exit end manifold (Fig. 252, Section B-B). This manifold is connected to the injector hydrogen inlet manifold by 20 riser ducts.

(U) Both combustor bodies were designed with provision for venting the cavities between the back of the tubes and the walls (Fig. 251, Sections F-F and S-S, and Fig. 252, Sections D-D and F-F). The bodies were circumferentially grooved at the upper and lower ends, and these manifolds were then ported to the atmosphere by drilled holes through the bodies.

(C) The inner and outer combustor tubes (Fig. 253 and 254) were fabricated from stainless steel because of the available tapering and forming experience with this material. The tube is tapered from 0.011-inch wall both sides of the throat to a 0.008-inch wall through the throat and for some distance either side of the throat centerline. After tapering, the tube is high-pressure formed to the final geometry.

(U) 250K Tube-Wall Thrust Chamber Analysis. The significant design analysis areas for the aerospike concept includes the expansion shroud, nozzle, combustion chamber contour, coolant tube, and thrust chamber structure. Empirical and analytical efforts were combined to achieve the optimum compromise between performance, heat transfer, and the total strain and deflection effects.

(U) Aerodynamic Analysis. The selected aerodynamic spike nozzle employs a double-expansion shroud design coupled with the ideal spike design procedure. The analysis method consists of starting with an ideal spike exit flow field and computing the nozzle required to give this flow

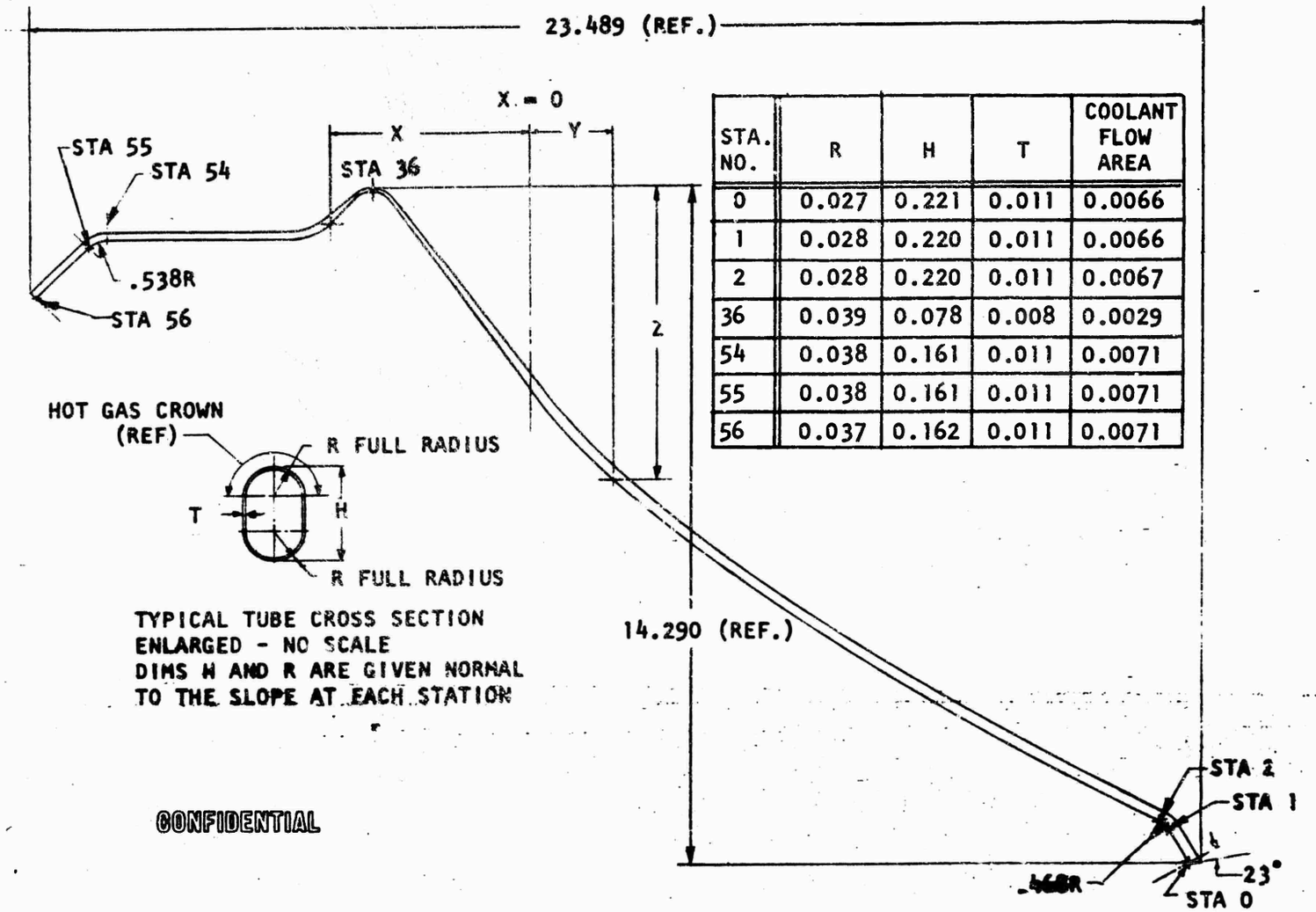

STA. NO.	R	H	T	COOLANT FLOW AREA
0	0.027	0.221	0.011	0.0066
1	0.028	0.220	0.011	0.0066
2	0.028	0.220	0.011	0.0067
36	0.039	0.078	0.008	0.0029
54	0.038	0.161	0.011	0.0071
55	0.038	0.161	0.011	0.0071
56	0.037	0.162	0.011	0.0071

Figure 253. Inner Tube, Aerospike Thrust Chamber

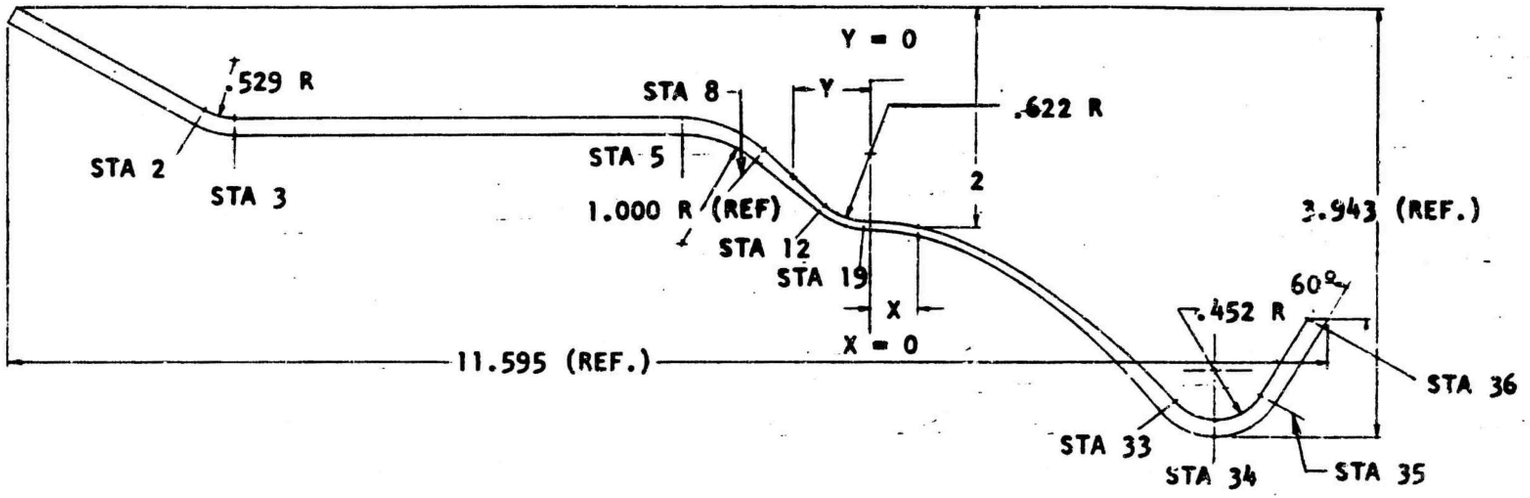

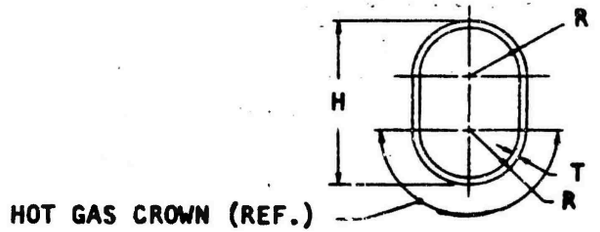

TYPICAL CROSS SECTION
(ENLARGED VIEW NO SCALE)
DIM'S H AND R ARE GIVEN
NORMAL TO THE SLOPE AT
EACH STATION

STA. NO.	R	H	T	COOLANT FLOW AREA
2	0.040	0.159	0.011	0.0073
3	0.040	0.159	0.011	0.0073
5	0.040	0.159	0.011	0.0073
8	0.040	0.129	0.011	0.0057
12	0.039	0.093	0.011	0.0048
19	0.039	0.078	0.008	0.0028
33	0.038	0.161	0.011	0.0069
34	0.037	0.161	0.011	0.0069
35	0.038	0.161	0.011	0.0069
36	0.038	0.161	0.011	0.0069

Figure 254. Outer Thrust Chamber Tube

field. A double-expansion shroud is then designed to match this flow field at some point downstream of the throat. Depending on the point in the flow field where this match is made, mean throat flow angles θ^* from approximately 5 to 90 degrees can be obtained. The advantage of this type of design is that a nozzle with nearly axial throat flow and a throat design suitable for maximum regenerative cooling can be obtained.

(C) Contours designed for mean throat flow angles of 4.5, 14.5, and 23 degrees are shown in Fig. 255. As the throat approaches an axial flow condition, the length at the shroud and overall length of the nozzle are increased. However, as the flow field downstream of the shroud approximates the flow field of an ideal spike, the nozzle performance is the same for all shroud lengths, provided that the spike length (positive X/RL, as shown in Fig. 255) is the same. The criterion to maintain a near-axial mean throat angle resulted in the selection of the $\theta^* = 4.5$-degree design.

(C) Shroud Length Reduction Study. As an alternate approach to obtaining reduced shroud lengths and maintaining the nearly axial mean throat flow angle, the shroud on the $\theta^* = 4.5$-degree nozzle was truncated to various lengths, as shown in Fig. 256. The method of characteristics nozzle analysis programs was used to generate the primary flow field and compute nozzle performance for each reduced shroud length case examined. Base pressure calculations were made to determine the change in base pressure for 1.7-percent secondary flow for a range of shroud lengths. The results of the reduced shroud length performance calculations for vacuum performance are shown in Fig. 257.

(C) The nozzle performance results, exclusive of base pressure contributions, clearly indicate that the full length shroud nozzle was not an optimum configuration for vacuum operation; otherwise, any change such

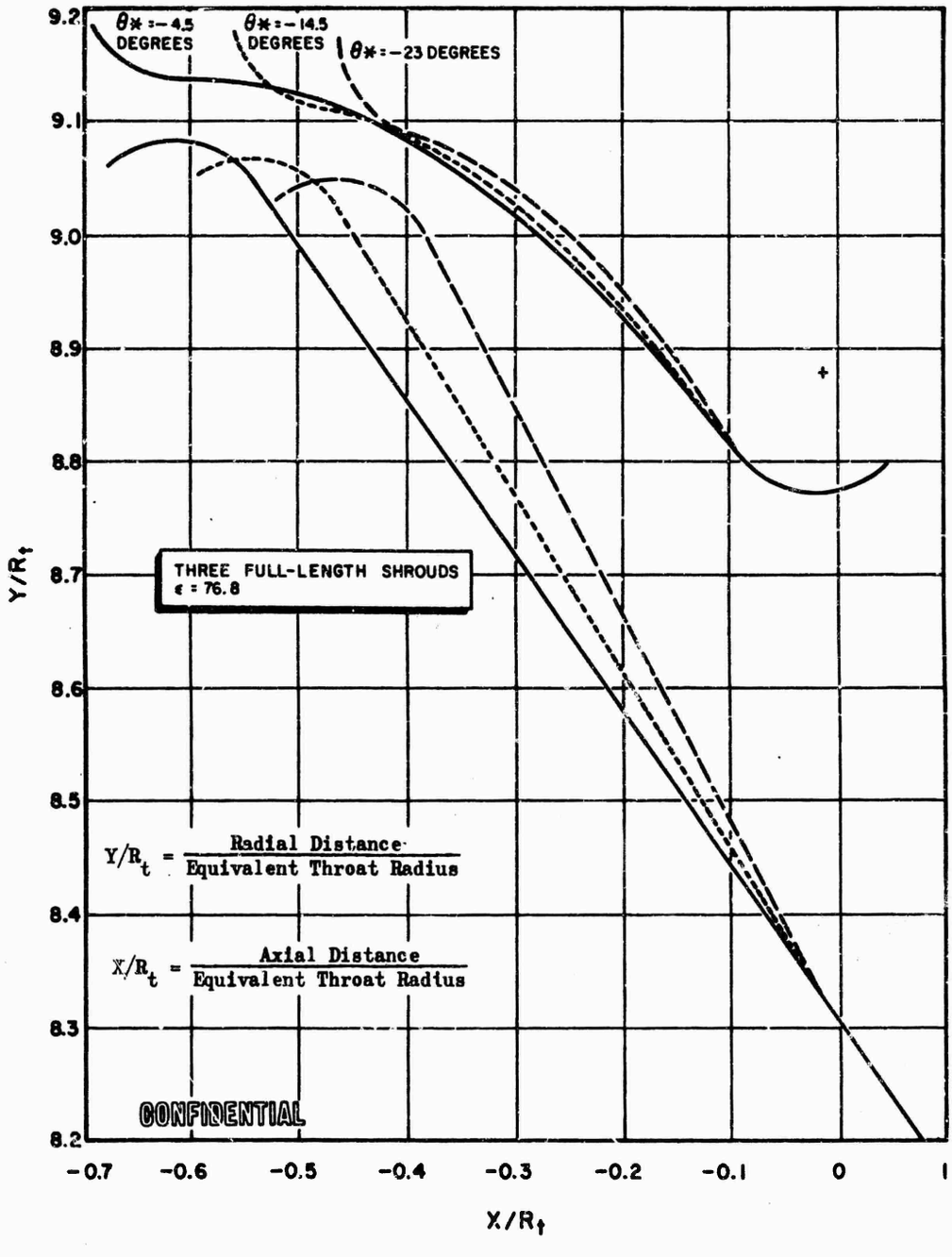

Figure 255. Nozzle Contour

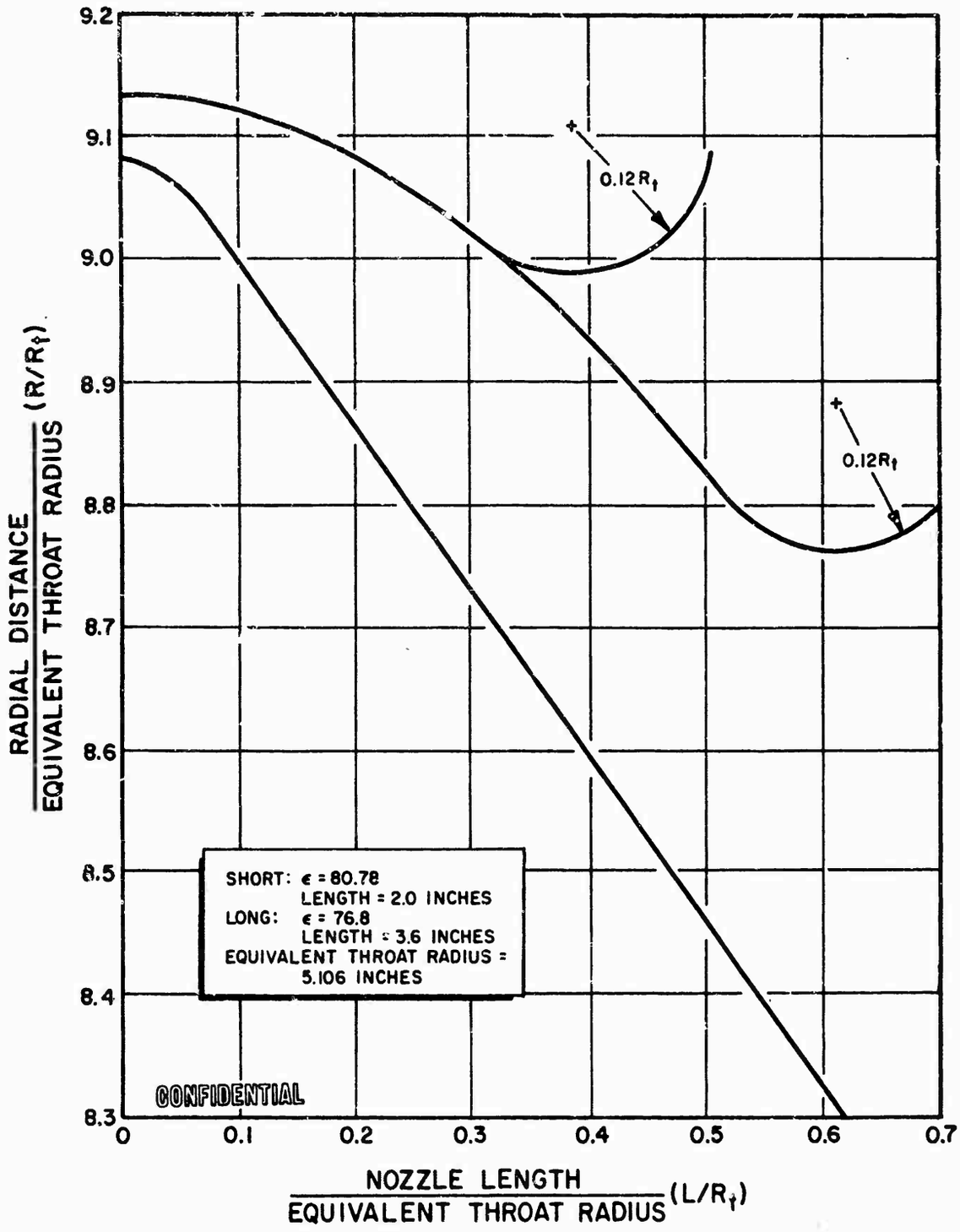

Figure 256. Shroud Length Comparison

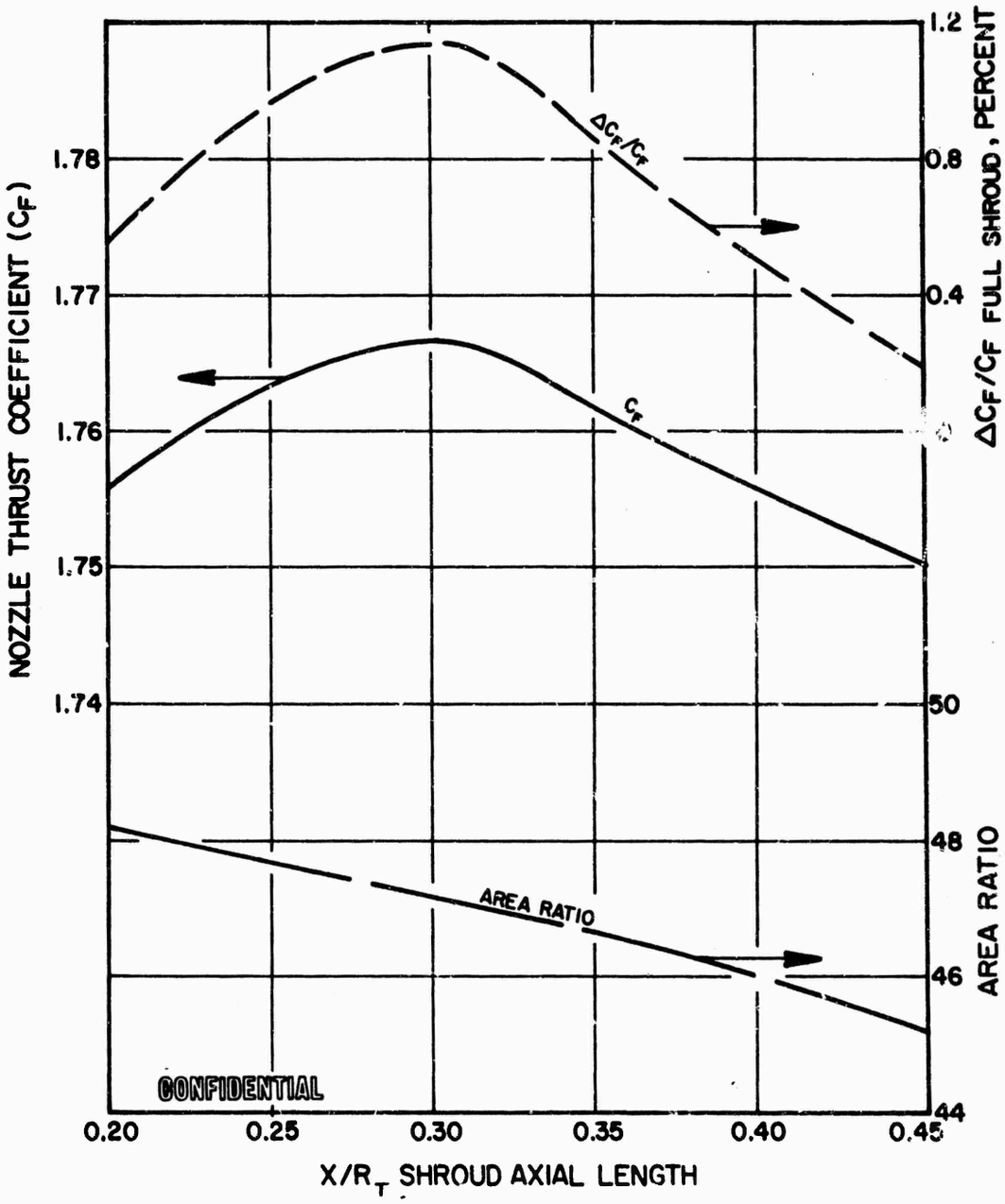

Figure 257. Performance vs Shroud Length

as reduced shroud length should produce a loss in thrust coefficient. The nozzle thrust coefficient (Fig. 257) shows a maximum for shroud axial length, $X/R_t = 0.3$. The base pressure was found to remain nearly constant from full length to $X/R_t = 0.3$, then drop for further reductions in shroud length. These performance results indicate that a reduced shroud length of $X/R = 0.3$ should be selected to obtain the optimum vacuum performance.

(C) Low-Pressure Ratio Performance Analysis. In addition to the vacuum analysis, a low-pressure ratio analysis (of the mean flow angle design of 4.5 degrees) of the effects of shroud length was also investigated. The shroud lengths (Fig. 256) corresponding to the vacuum optimum and full length were analyzed.

(C) Outer shroud and spike nozzle wall pressures are shown in Fig. 258 for the full-length shroud design, for chamber pressures of 300, 600 and 1500 psia, operating at test stand altitude and vacuum conditions. The increases in the low wall pressure are caused by a recompression effect. Typical flow patterns for an aerospike nozzle operating at low-pressure ratios are shown in Fig. 259. For the ideal case, as shown in Fig. 259 (View B), expansion waves from the shroud are reflected from the contour as expansion waves, and are then reflected from the free-jet boundary as compression waves. At high-pressure ratios, the compression waves from the free-jet boundary do not intersect the contour; however, at low chamber-to-ambient pressure ratios (Fig. 259), the compression waves from the free-jet may intersect the contour, resulting in recompression. The chamber-to-ambient pressure ratio below which there will be recompression on the contour is a function of the area ratio, the ratio of specific heats, percent length, the nozzle contour, and the geometry of the cowl. However, if the flow field downstream of the shroud does not approximate that of an

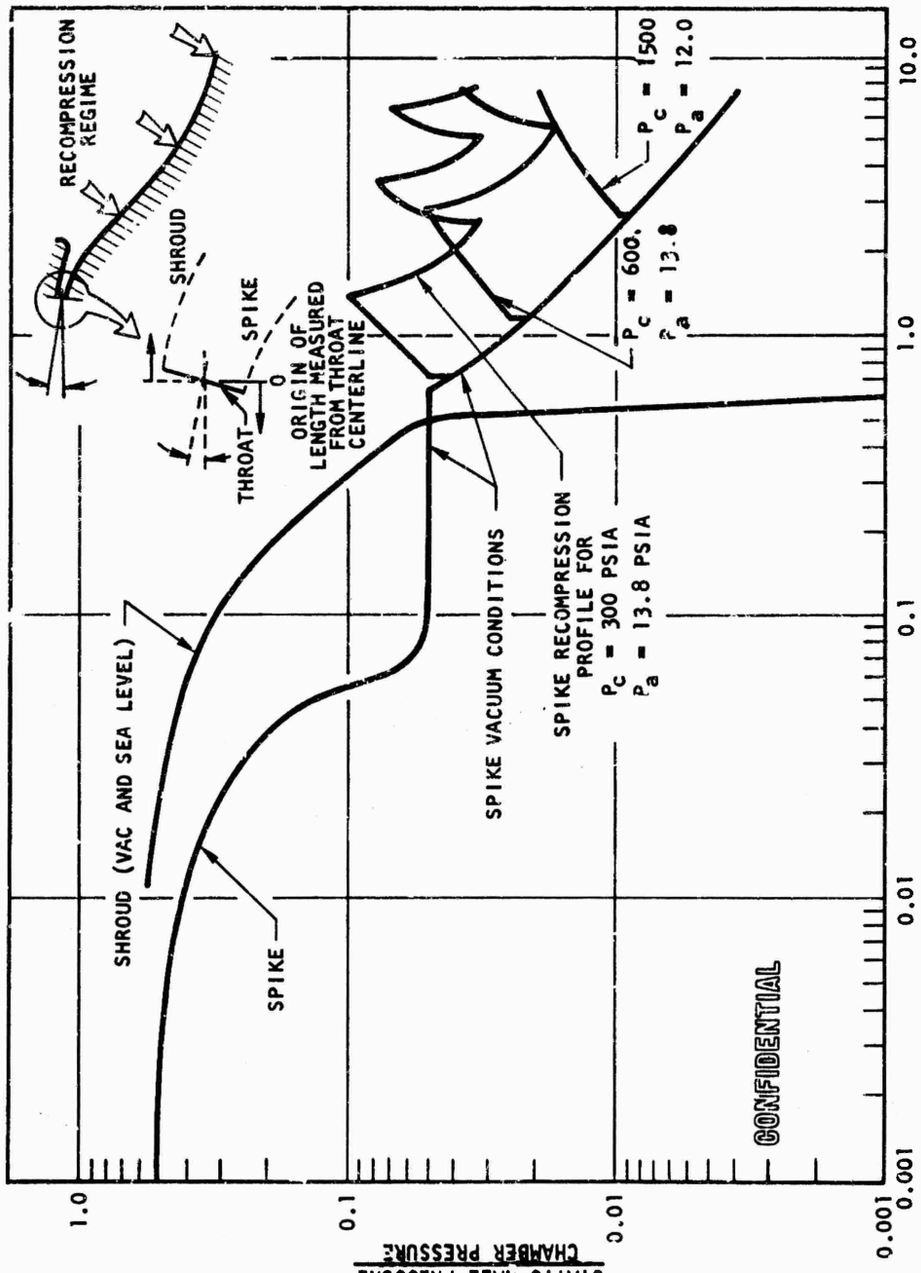

Figure 258. Shroud and Spike Pressure Profiles

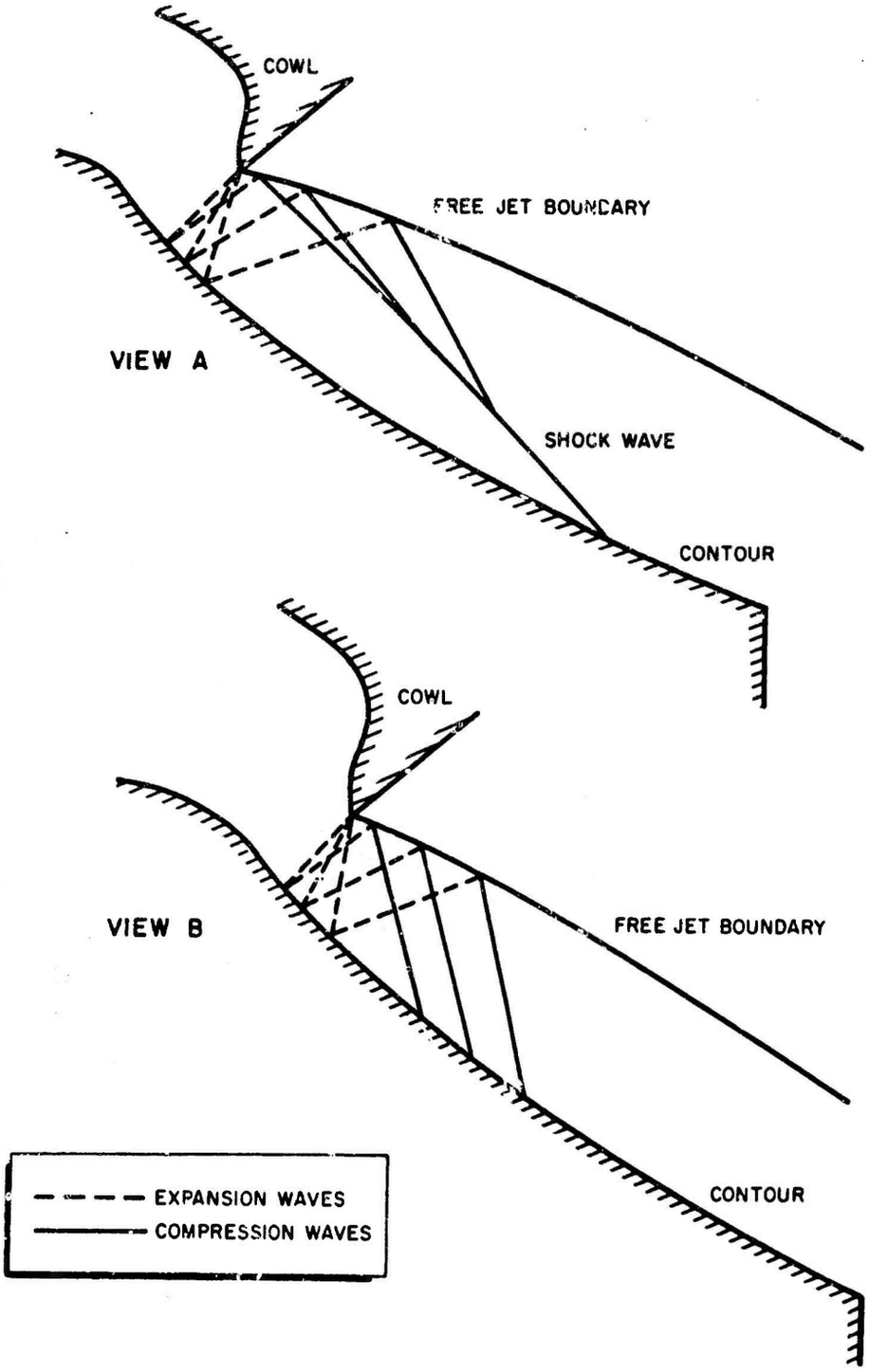

Figure 259. Expansion and Compression Waves in Aerodynamic Spike Nozzle Flow Field Analysis

ideal spike, the recompression waves coalesce into a shock wave (Fig. 259, View A). The strength of this shock wave depends on the nozzle flow field departure from that of the ideal spike.

(U) A comparison between the wall pressure profiles resulting from the short and full-length shrouds is shown in Fig. 260. The pressure rise associated with the long shroud is less severe than that of the short shroud. Although it is not apparent from the data given in Fig. 260, the wall pressure profiles associated with the long shroud are the result of isentropic recompression, while the short-shroud wall pressure profiles are the result of the impingement of strong oblique shocks on the nozzle wall.

(C) Tube Design Analysis. The 250K tubes were designed and released early in the program. Consequently, the heat flux profile used in the tube design was based principally on previous segment data (under contract NAS8-19) in the subsonic regime, and on theoretical aerodynamic and heat transfer analysis of the nozzle and shroud. The aerodynamic analysis used a method of characteristics, nozzle analysis, computer program. Once the aerodynamic flow field had been determined along the wall, a theoretical boundary layer analysis was performed to determine the gas-side heat transfer coefficients for the chamber. As shown in Fig. 261, the experimental data correlate with the theoretical heat transfer predictions very well in the subsonic region, although it deviates considerably in the throat. Consequently, the theoretical heat fluxes were used for the design of the 250K tube wall, with the exception of the throat where an experimental heat flux of 45 Btu/in.^{2}-sec was used.

(C) Two tube materials were considered for the 250K chamber, 347 stainless steel and Nickel 200. Of the two materials, Nickel 200 was most attractive from a heat transfer standpoint because of its higher thermal conductivity. Stainless steel was finally chosen, however, principally

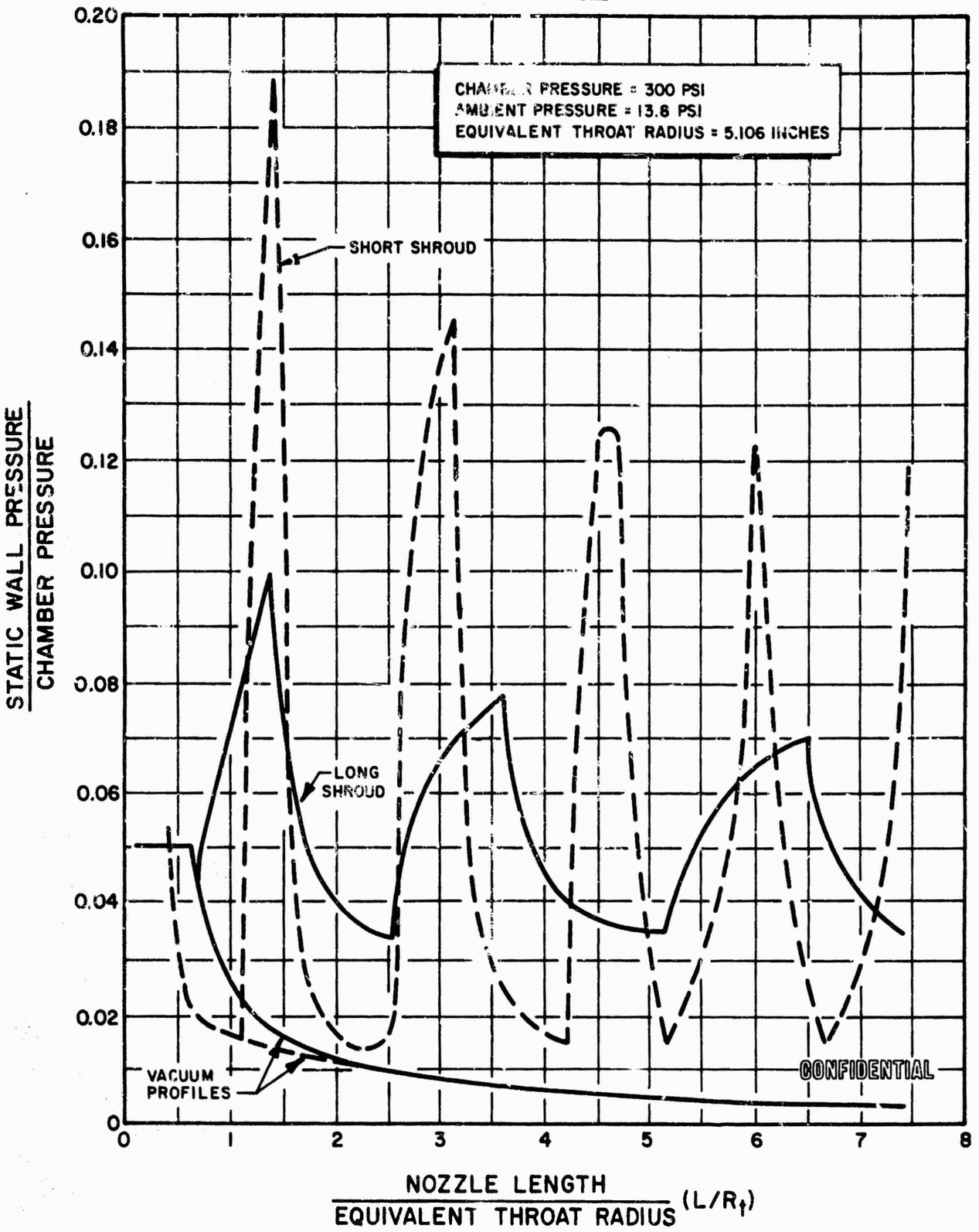

Figure 260. Sea Level Centerbody Spike Wall Pressure Profiles

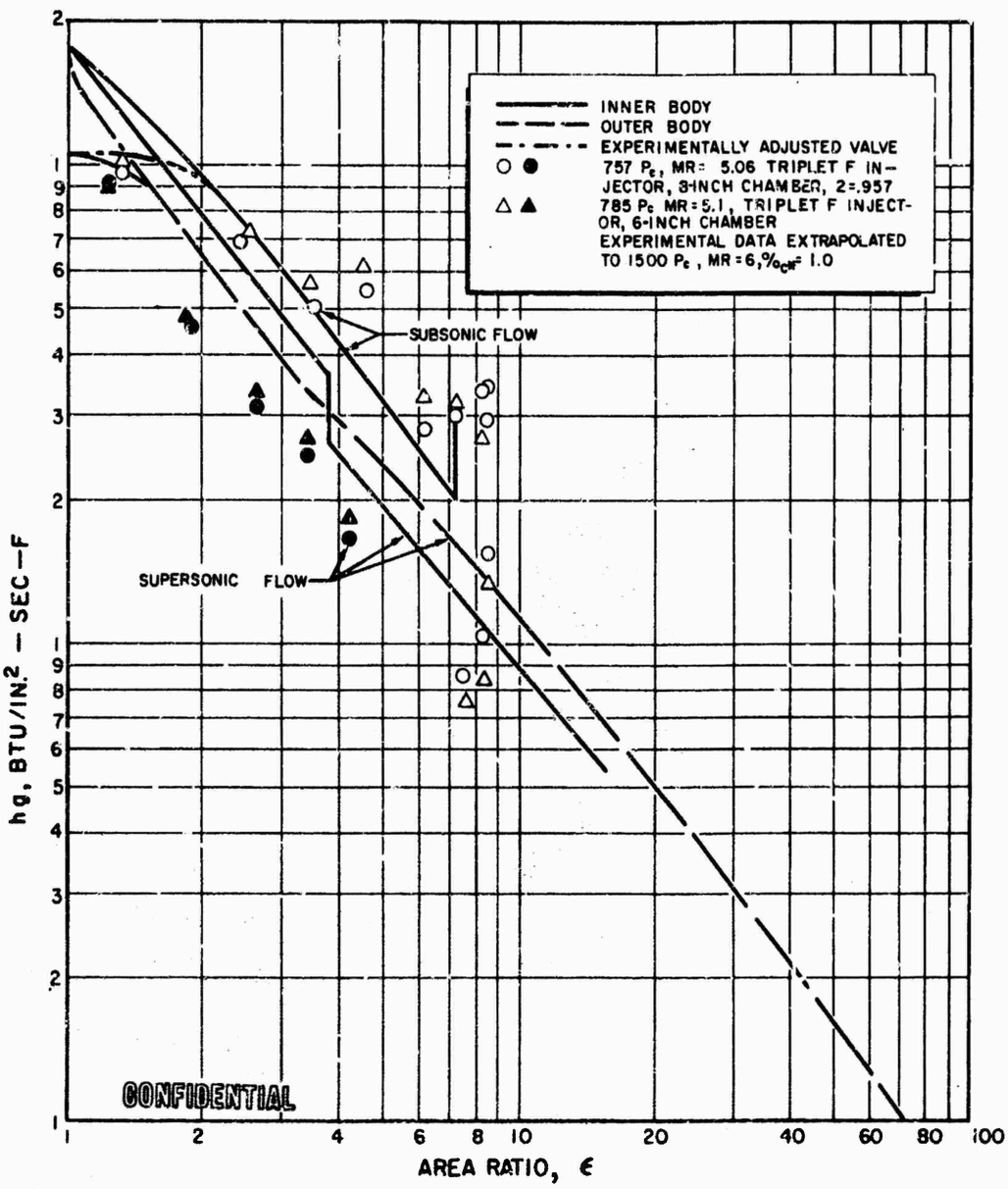

Figure 261. Theoretical and Experimental Heat Transfer Coefficients, 250K Experimental Thrust Chamber Breadboard Engine, O_2/H_2, MR = 6.0, P_c = 1500 psia, Vacuum Operation

because of manufacturing experience. Because of the lower thermal conductivity of stainless steel and the high heat fluxes occurring in the throat at the higher chamber pressures, the wall thickness was tapered from 0.011 inch to a nominal 0.008 inch in the throat region.

(C) To determine the coolant mass velocity requirements, a modified form of the Dipprey and Sabersky cooling correlation was used (Ref. 10) assuming an internal tube roughness of 50 microinches. The combustion zone and throat were designed for the maximum chamber pressure, with mixture ratio of 6 to 7 (o/f). The nozzle was designed for the lowest chamber pressure (300 psia), mixture ratio of 7.0, and sea level conditions. Whereas the highest heat flux occurs in the chamber and throat at the maximum chamber pressure ($Q/A \sim P_c^{0.8}$), the peak flux (at the first recompression) on an altitude compensating nozzle is nearly independent of chamber pressure. Consequently, the lowest chamber pressure is the hardest design point for the nozzle, since there is less coolant flow for the same heat flux.

(C) The tubes were sized based on a hydrogen flow of 125 lb/sec at the maximum chamber pressure. Since this is roughly 50 percent more than the injector fuel flow at a mixture ratio of 6.0, this design precludes the use of regenerative coolant flowrates through the tubes. However, the design based on 125 lb/sec does permit using about 25 percent fewer tubes, with a resultant savings in cost. Since demonstration of complete regenerative cooling was not an objective of the 250K tube-wall chamber, advantage was taken of the cost savings involved. The inner and outer body tubes have a linear taper upstream and downstream of the throat, with an 0.130-inch unformed diameter in the combustion zone, and an 0.078-inch unformed diameter at the throat. Because of the slower expansion of the combustion gases on the outer body, the maximum coolant mass velocity must be maintained for a longer length than on the inner body (1.90 inches vs 0.96 inch) with accompanying increase in coolant pressure drop. Since the density is also lower in the outer body, the outer body pressure drop is more than twice the inner body value, despite the greater length of the inner body.

(C) To verify the coolant-side heat transfer capability of the design, a tapered and formed tube was submitted to electrically heated tests with heat fluxes up to 31 Btu/in.^{2}-sec. This was done using inlet hydrogen temperatures from 152 to 451 R and pressures from 1000 to 1900 psia. Data were obtained with hydrogen flowing in both subsonic and supersonic flow regimes. A typical instrumented tube and experimental results are shown in Fig. 262 and 263, along with the values used in the 250K tube design. While the design values appear on the conservative side, part of the difference results from the different baseline values used. The experimental values are ratioed to the theoretical values predicted by the McCarthy-Wolf equation, whereas the design values are referenced to the Dipprey and Sabersky equation. This difference between the two reference heat transfer coefficients can amount to 20 to 30 percent.

(C) Later in the program, further electrically heated tube tests were conducted using one tapered and formed inner and outer body stainless-steel tube. Again local heat fluxes up to 31 Btu/in.^{2}-sec were achieved. Hydrogen was introduced into the tubes at about 150 R and 1500 to 2000 psia. Heat transfer enhancements were generally consistent with previous curved tube results. It is noted that the full length of the tube was not heated, but only the region near the throat to achieve the maximum possible heating rates.

(C) Typical results for these tests are shown in Fig. 264 and 265 for the inner and outer body tubes, respectively. One of the important points indicated is that the peak enhancement value occurs downstream of the throat on both tubes (relative to the coolant flow direction). This was responsible for the choice of the "shifted outer body throat" concept for the demonstrator chamber, which is intended to bring the peak curvature enhancement into the region where the peak heat flux occurs. This is done by moving the throat radius of curvature of the outer body relative to the

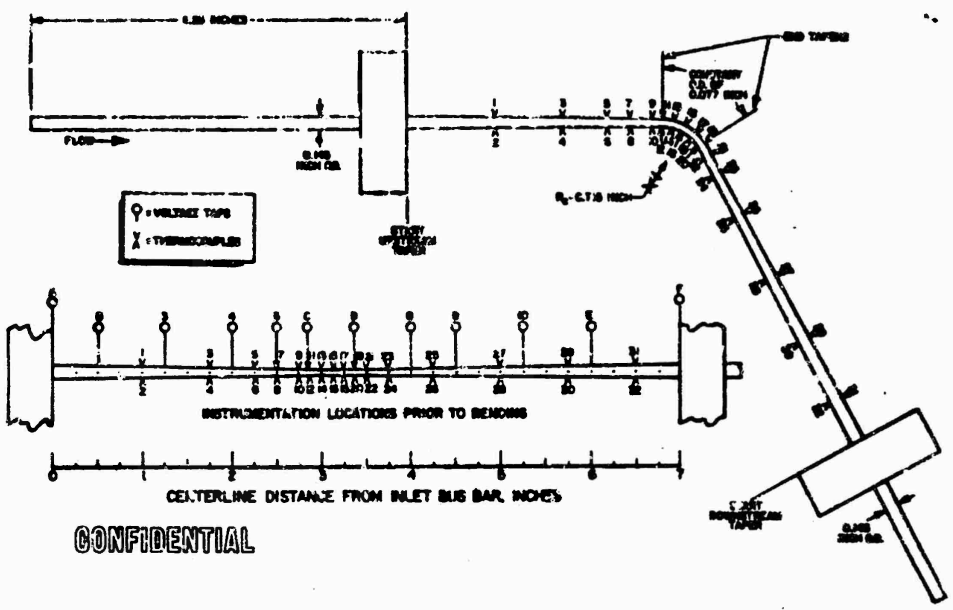

Figure 262. Simplified Curved Gaseous Hydrogen Heat Transfer Test Section (66-1)

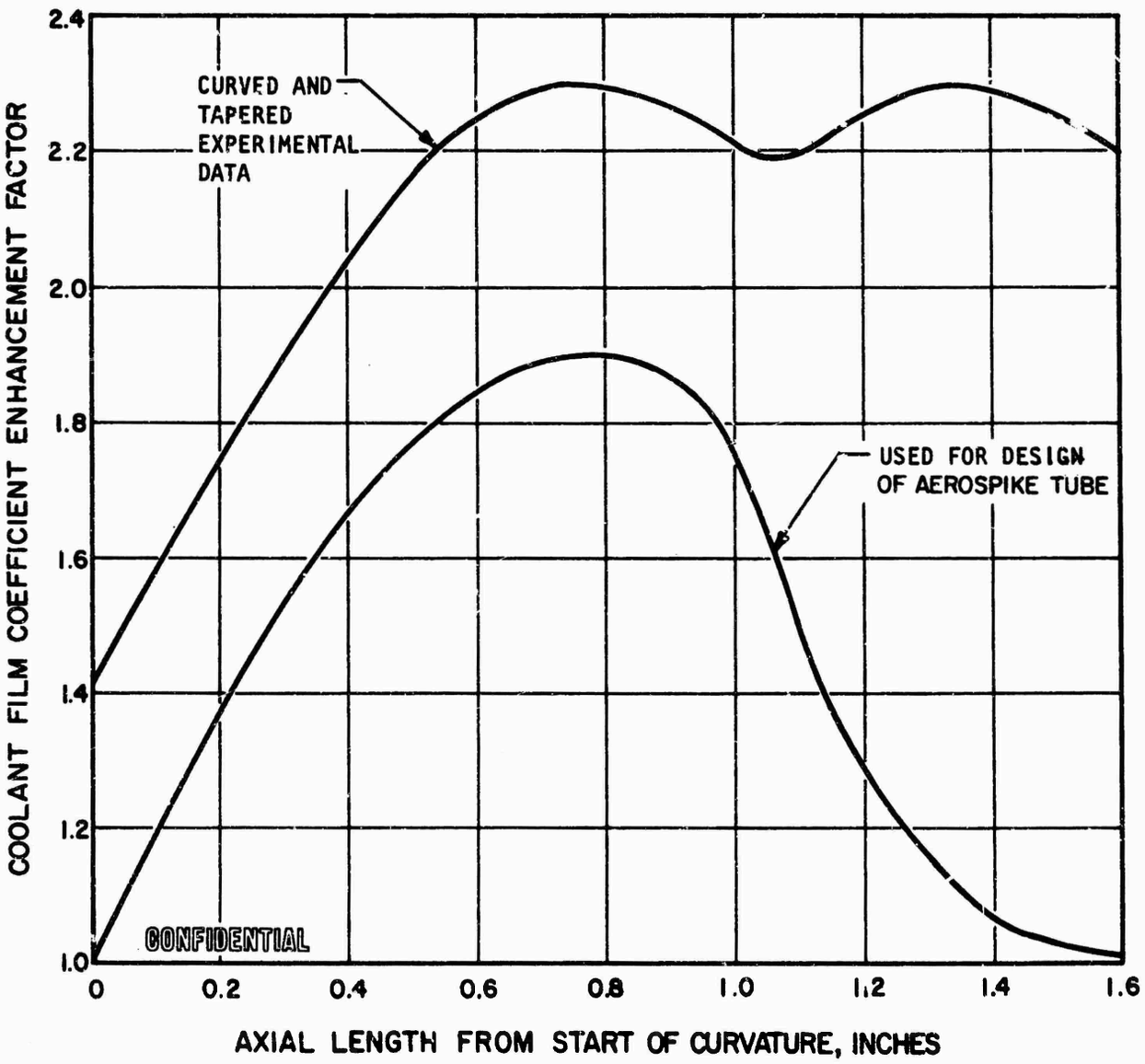

Figure 263. Comparison of Film Coefficient Enhancement Factor Used for Design With Experimental Results

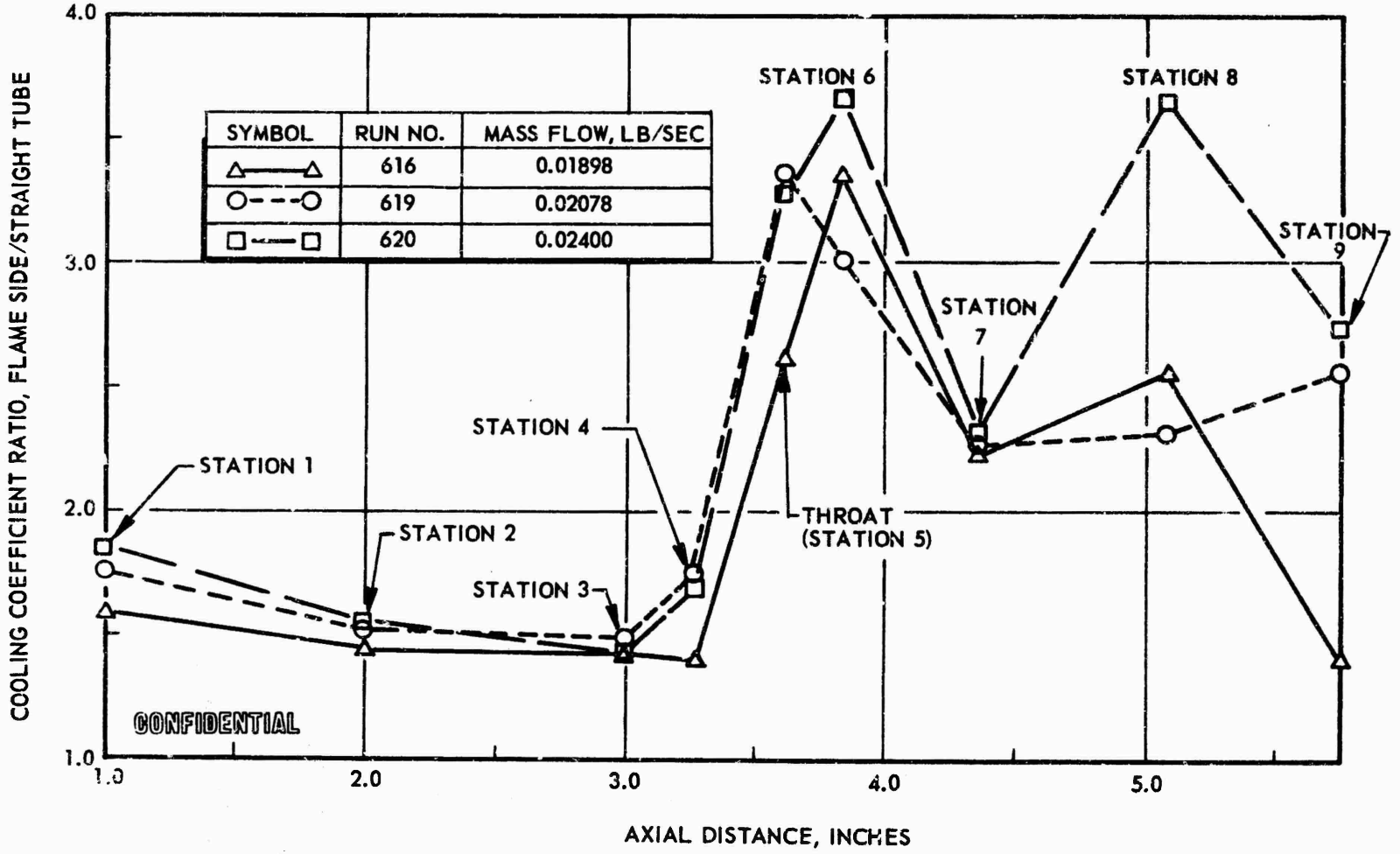

Figure 264. Heat Transfer Results for Inner-Body Coolant Tube; Ratio of Flame-Side Surface to Predicted Straight Tube Heat Transfer Coefficients

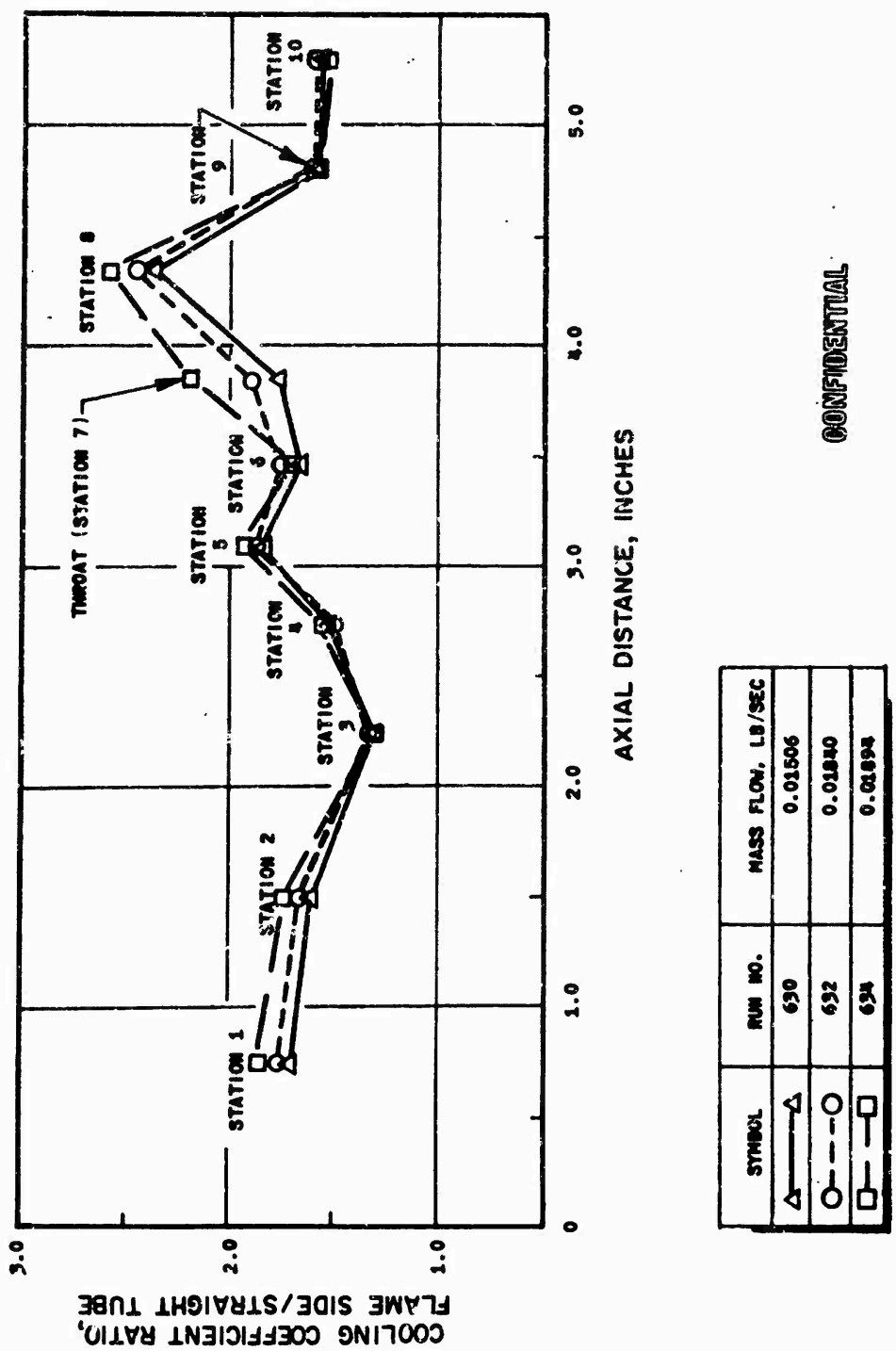

Figure 265. Heat Transfer Results for Outer-Body Coolant Tube; Ratio of Flame-Side Surface to Predicted Straight Tube Heat Transfer Coefficients

inner body. This concept was based on the data presented in Fig. 264 and 265. The curvature enhancements for both inner and outer body tubes and the values used in the tube design may be somewhat conservative. The design values at the geometric throat, compared to the experimental values (adjusted to the same reference straight-tube value), are 1.6 vs 2.0 for the inner body, and 1.45 vs approximately 1.5 for the outer body. This is good agreement, especially on the outer body. It is worth noting that, at least theoretically, the sonic line and the peak heat transfer point intersects the tube upstream of the geometric throat, where the curvature enhancement is lower on the outer body. Thus, on the outer body the maximum wall temperature should occur a short distance upstream of the geometric throat.

(C) Choice of Coolant Circuit and Inlet Temperature. The choice of coolant circuit for the tube-wall chamber is a result of a study including curvature enhancement, local hydrogen coolant temperatures, and manufacturing considerations. The main consideration was to obtain minimum tube-wall temperatures with a minimum pressure drop and a workable coolant circuit. It was convenient and desirable to cool the inner body first in an up-pass direction (toward the injector). This is convenient since in the Demonstrator Module the pumps will be located in the lower part of the chamber. It is also desirable from a heat transfer standpoint as a greater coolant curvature enhancement is obtained in the up-pass direction. Also, since hydrogen is not as good a coolant near its critical temperature, an up-pass design allows the hydrogen to heat up in the low heat flux area of the nozzle, so that it is near optimum condition in the higher heat flux zones of the throat and combustor.

(C) A down-pass configuration was selected for the outer body because of greater available curvature enhancement at the throat in this direction. Although a two-pass design on the outer body would be desirable from a

plumbing standpoint and because fewer tubes would be required, the disadvantages of higher pressure drop and an increase in up-pass wall temperature of about 150 F outweigh the advantages.

(C) It was desirable to choose the coolant inlet temperature to simulate approximately the demonstrator coolant temperature in the inner body throat. This would require a coolant inlet temperature of about 125 to 150 F. However, throat conditions were approximated and stand flow capability was maximized by a coolant inlet temperature of 100 R.

(C) Tube Tolerances. Before the 250K tube-wall design was released, an analysis was conducted to determine the effect of tube tolerances on operating wall temperature. Nominal tolerances in the throat included ±0.001 inch in wall thickness and tube height, and $^{+0.000}_{-0.002}$ inch in tube width. The tolerance on wall thickness is the most severe, since it affects the tube operating temperature directly (160 F increase/0.001 inch at maximum P_c), and it also changes the coolant cross-sectional area (about 6 percent/0.001 inch), the latter partially offsetting the former (net change of 80 F/0.001 inch). Figure 266 shows the effect of the various tolerances on the throat operating temperature.

(U) To ensure that none of the tubes in the stack would be starved, each tube used in the chamber was flow calibrated. A simple, but accurate, tube calibration device was utilized. This device consisted of a precision sonic venturi in series with the tube to be calibrated. Dry nitrogen was used to eliminate condensation effects. Inlet pressure to the sonic venturi was maintained at 80 psia to ensure that both the venturi and the tube were flowing sonic.

(U) Since both the venturi and the tube were flowing sonic, the venturi upstream pressure could be used directly to determine the minimum cross-sectional area of the tubes. This was used to select individual tubes

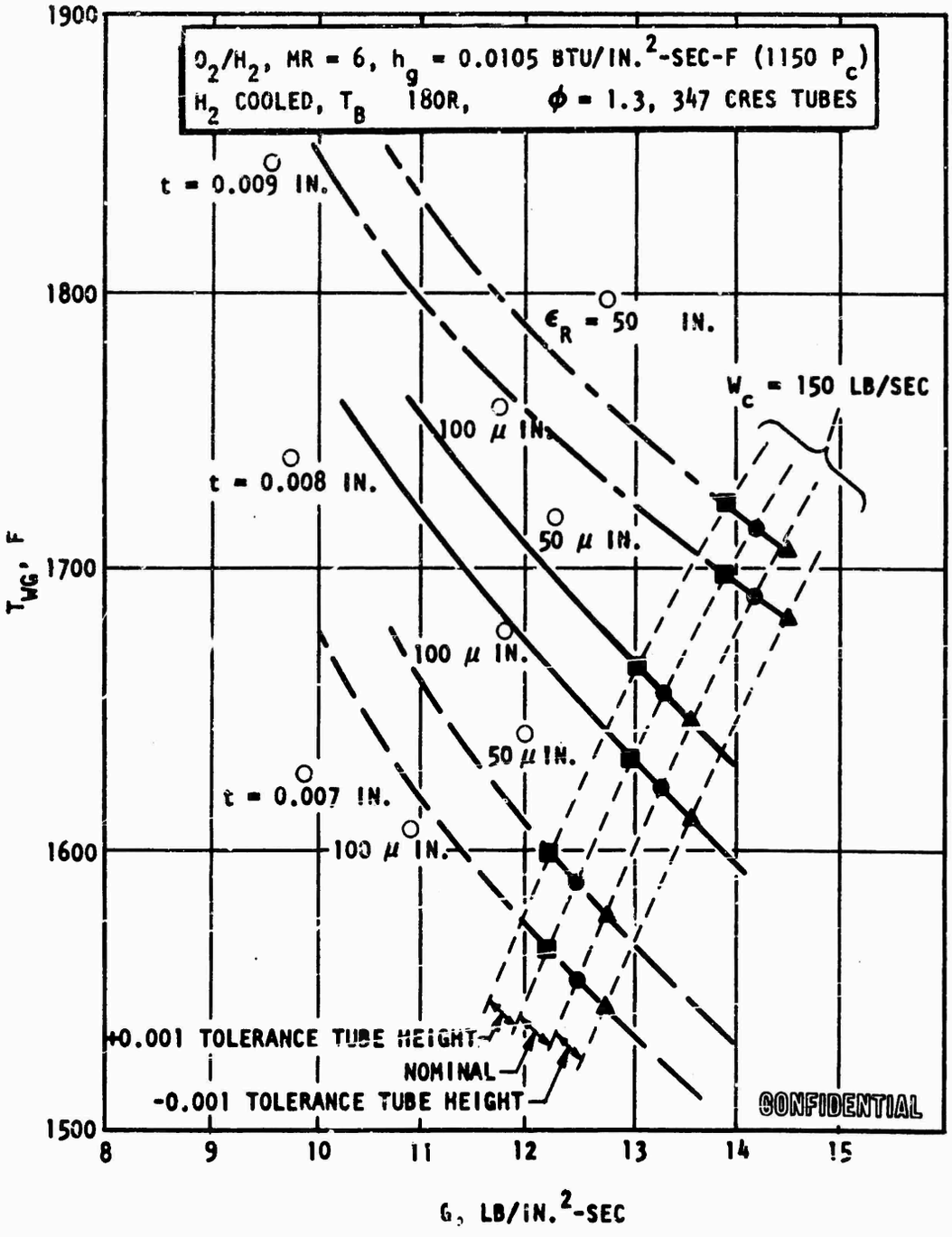

Figure 266. Effect of Tube Tolerances and Coolant Mass Velocity on Gas Wall Temperature

for a braze stack. This technique was also used after brazing and final machining to ensure that all tubes were flowing properly. This flow check device has been highly successful in achieving a uniform tube stack since none of the tested chambers have shown a non-uniform tube heating.

(U) Structure. A complete review of the structural arrangement for the 250,000-pound-thrust tube-wall thrustors was conducted. The area of stress analysis can be summarized through examination of Fig. 267, 268, and 269, which show the particular forces of concern on the structure. The forces result in moment, tension, and shear loads on the bolts connecting the inner and outer bodies and the injector. Primary pressure force restraint is in inner and outer body hoop-stress retention. Thermal loading accounts for only a small percentage of the available distortion forces.

(C) The temperature distribution of the tube backup structures is shown in Fig. 270 after a 5-second chilldown using 60 R hydrogen, and after a 5-second firing, the 350 R coolant bulk temperature corresponding to the outer body and the 200 R to the inner body throat region. An initial temperature of 100 F was assumed for the backup structure. A complete stress and thermal tolerance analysis of the throat gap shows that the throat gap will be 1.09 to 1.14 times the assembly dimension at 1500 psia.

250K Tube-Wall Thrust Chamber Fabrication.

(U) Machining and Annealing. The 304L stainless-steel forgings for the inner and outer thrust chamber body assemblies became a critical factor in the design considerations because of available size. Upon receipt of the inner and outer combustion chamber forgings and the nozzle cone forgings, these units were rough machined to dimensions which allowed for a

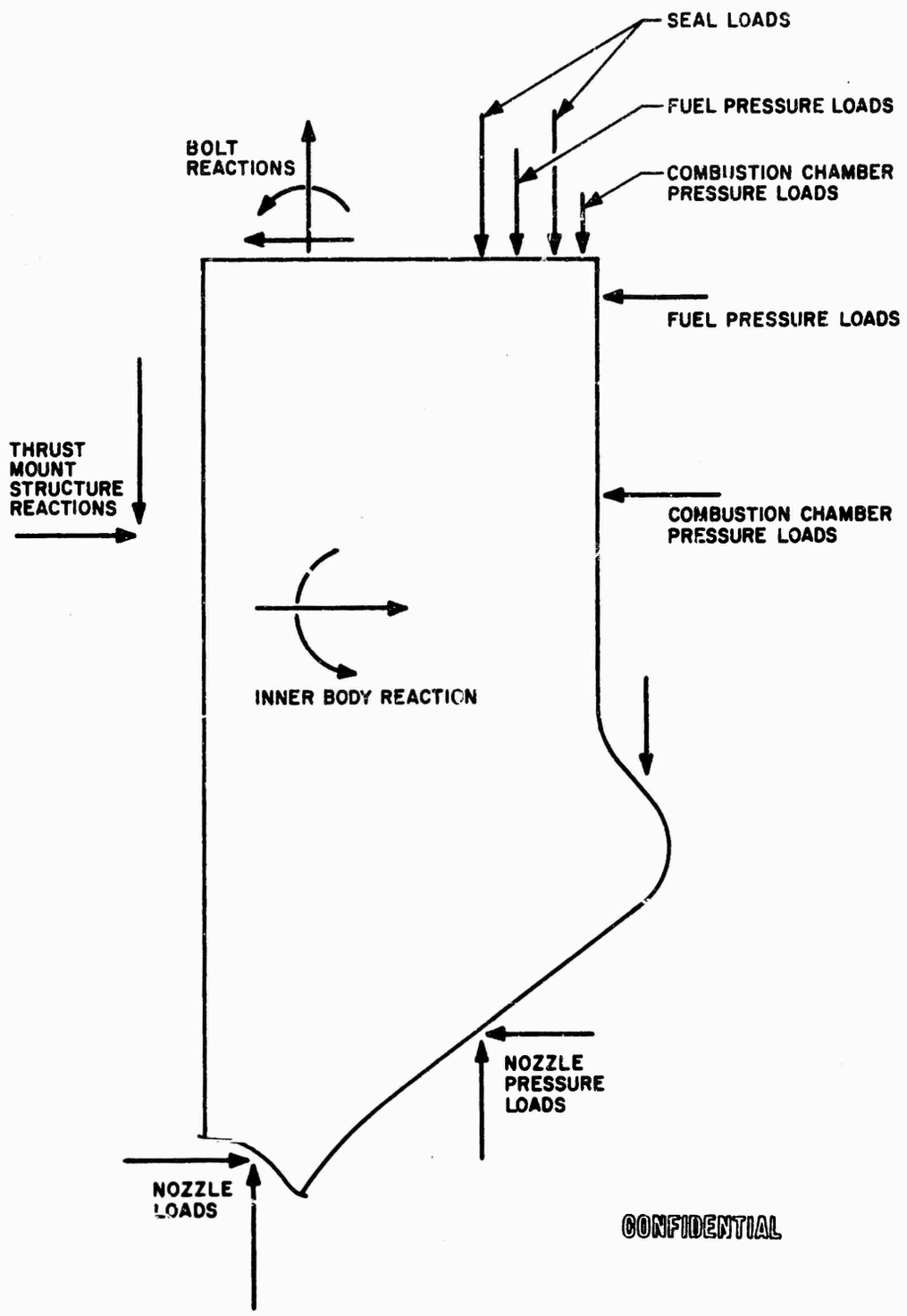

Figure 267. Forces Acting on Inner Body

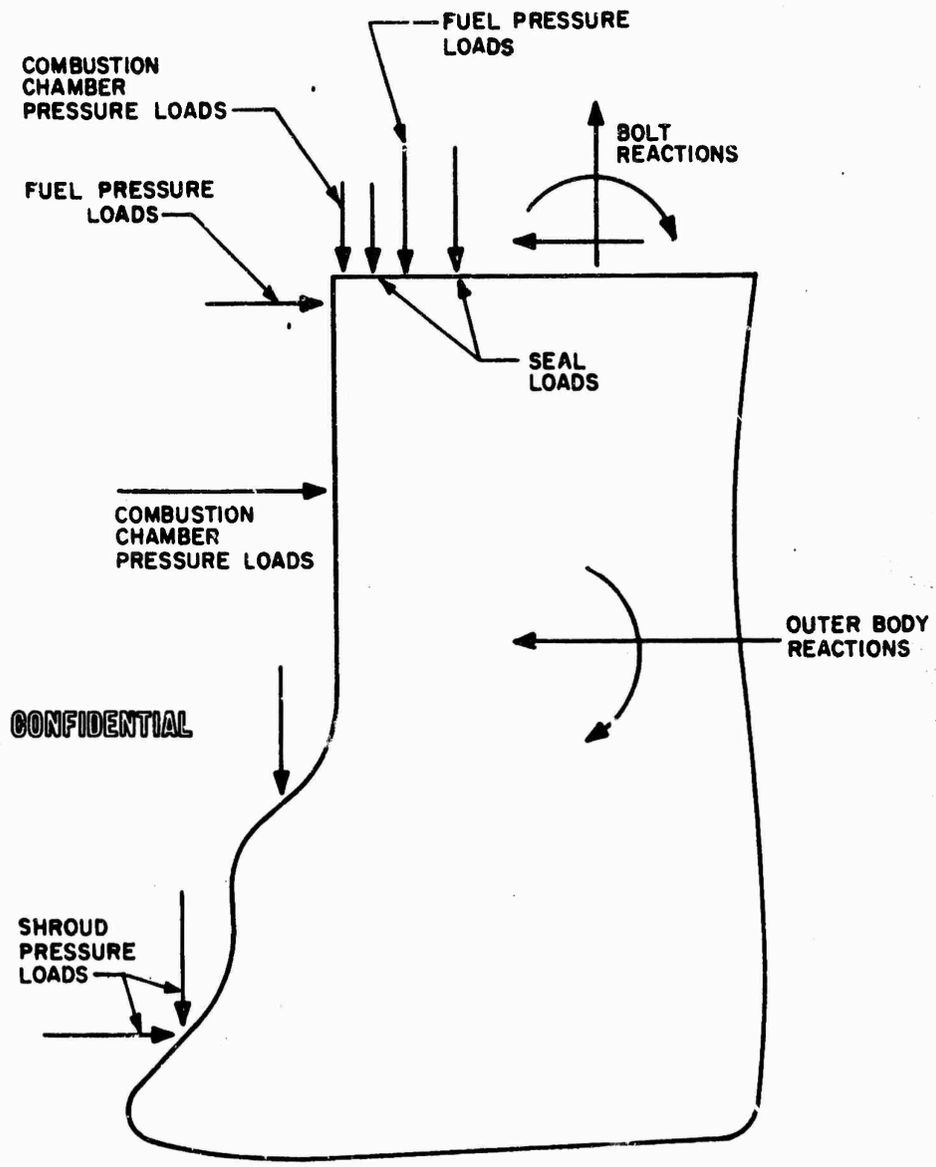

Figure 268. Forces Acting on Outer Body

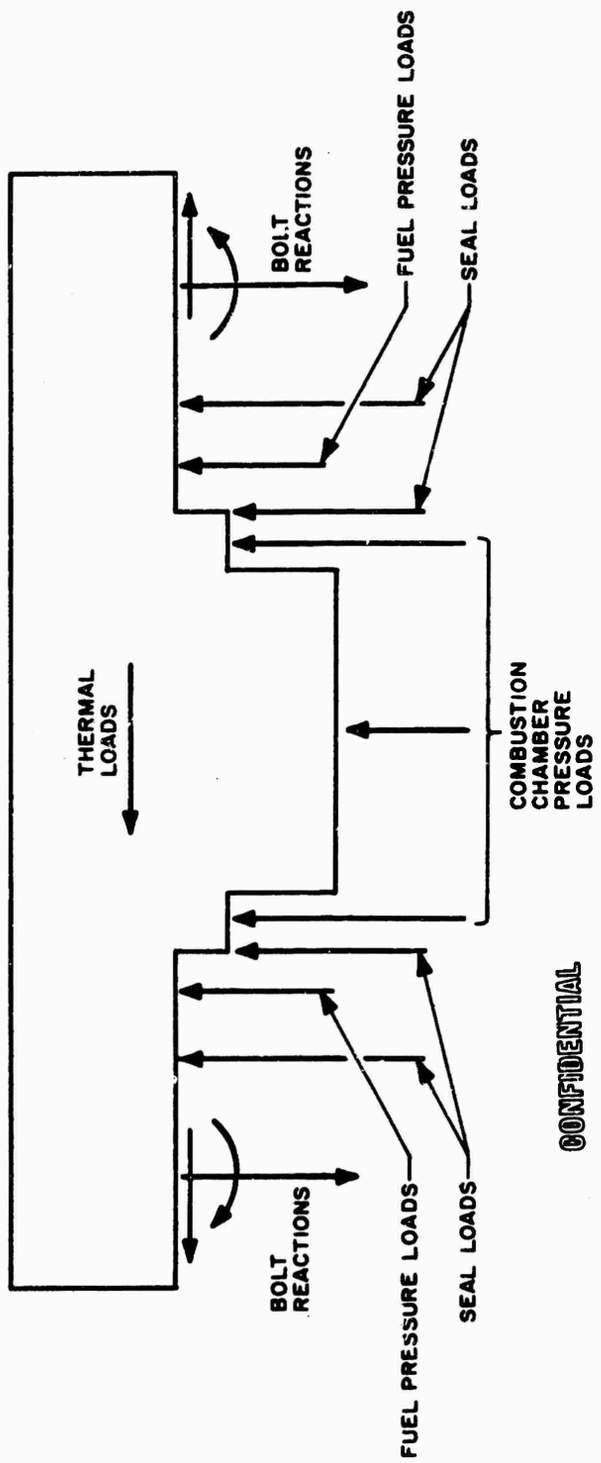

Figure 269. Forces Acting on Injector

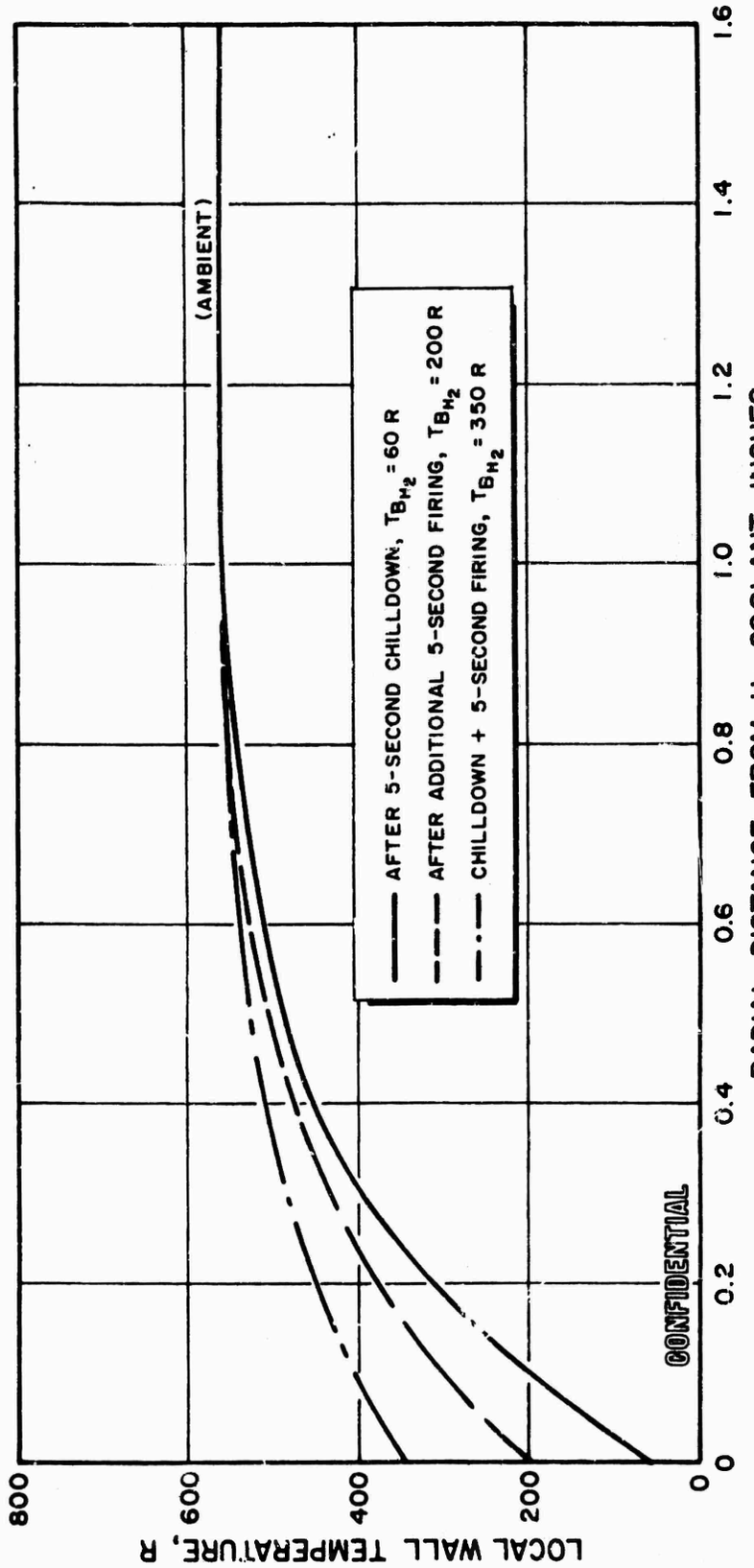

Figure 270. Transient Wall Temperature Profile (250K Solid Structural Backing for Tube Bundle, 304 L Stainless Steel)

final finish machining after weld and annealing. The nozzle cone was welded to the inner body forging after rough machining (Fig. 27). The units for the tube-wall assemblies were annealed at the anticipated brazing temperature of 2020 F following the rough machining and welding (in an inert atmosphere) to ensure that no residual stresses would be present during the brazing process.

(U) After the annealing cycle, the inner body forgings were finish machined at the aft fuel manifold region and 152 radial feed holes were drilled from the manifold area to the tube inlet manifold area. Following these operations, the fuel manifold and dual inlet feed flanges were welded in place. The inner-body forgings were again subjected to an annealing cycle at the planned braze temperature.

(U) Following the final stress-relieving operations, the inner and outer body forgings were machined to the final contour of the cold-wall side of the tube, and the manifold and feed passage holes were drilled using conventional machining techniques. A portion of the fuel-feed passages was drilled using special adapter plates and portable Quackenbush drill units. This provided the ability to drill more than one hole at a time, thus reducing the elapsed time of fabrication.

(U) Alloy grooves were machined circumferentially in predetermined locations along the axis which would provide a reserve of alloy for distribution during the brazing processes (Fig. 27). These locations had been verified by laboratory test prior to machining. In addition to the alloy grooves, venting grooves with passages to the atmospheric side of the system were machined to provide an escape rout for gases that could possibly leak into void areas behind the tube bundle. Upon completion of the machining operations, the body assemblies were cleaned in a vapor degreaser and the surfaces that join the tubes were nickel plated.

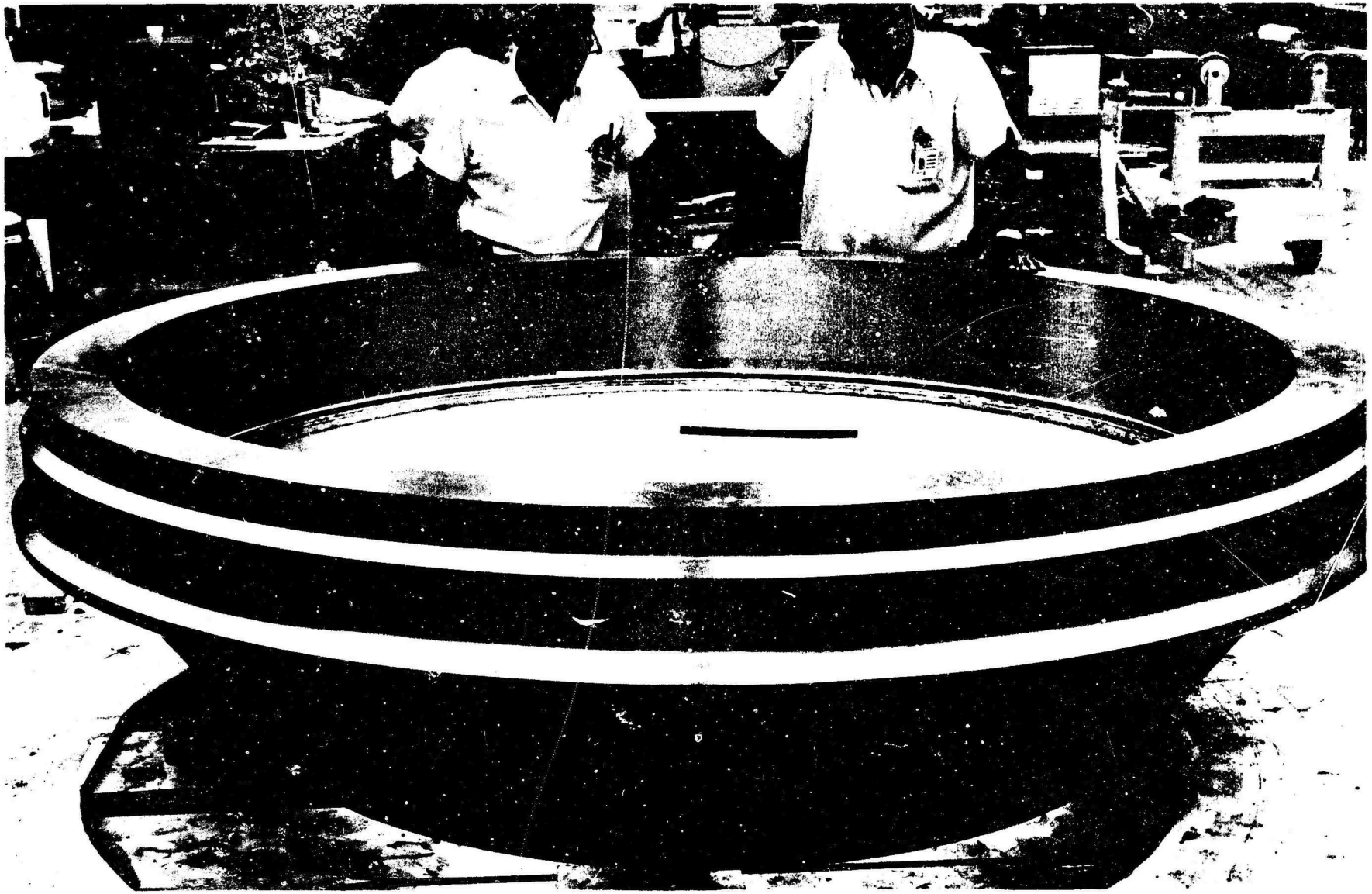

1XE39-10/27/66-C1C

Figure 271. 250K Tube-Wall Inner-Body After Rough Machining

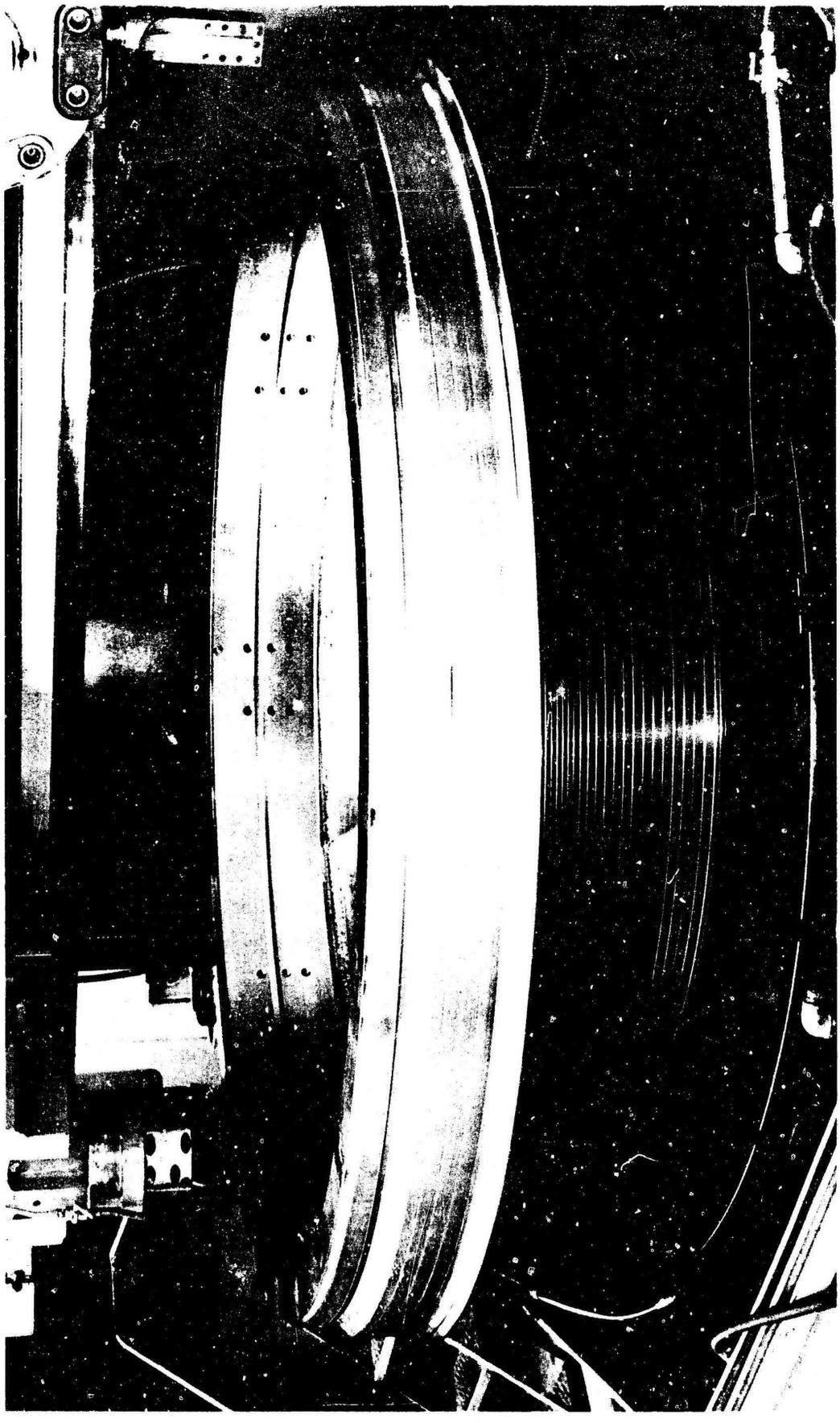

LXE32-2/2/67-C1B

Figure 272. 250K Tube Wall Inner Body Machined for Braze Assembly

(U) Tubes. The thrust chamber tubes for the inner and outer thrust chamber assemblies have a varying diametrical dimension, as well as a varying wall thickness dimension along the length of the tube assembly. Tubing to satisfy these requirements was procured in the tapered and preformed condition and also in an annealed condition so that the hydroform sizing can be accomplished without damage to the material. Surveillance of the metallurgical and dimensional quality control was accomplished on a sampling basis utilizing microsectional mounts for wall thickness determination and surface condition control. Samples were subjected to hydroforming operations equivalent to 6-percent stretching. Internal surface finishes were monitored on a surveillance basis also.

(U) A two-piece hydropressure forming die was fabricated for use in a 100-ton hydraulic press which has the capability of applying 50,000-psi hydraulic pressure for hydroforming (Fig. 273 and 274). Fixturing (Fig. 275) was fabricated which represented one-thirtieth (12 degrees) and one-tenth (36 degrees) segments upon which tubing groups were verified prior to acceptance for the final thrust chamber stacking.

(C) The small tube throat diameter (0.078 inch) and the necessity for adequate hydrogen velocities in the throat region dictated the necessity of a rapid nondestructive method of determining the tube inside dimensions. and surface character by utilizing a fluid flow technique. Dry nitrogen was used to flow calibrate the tubes at choked (Mach number = 1.0) conditions. The pressure drop through the tubes was calculated and the local total pressure at the downstream (flow) end of the minimum-area section (where the air would choke) was plotted as a function of the gaseous nitrogen flow per unit area. This was done for a maximum and a minimum cross-sectional area and variable tube surface roughness to find the outer flow limits, using the stackup of tolerances listed in Table 80.

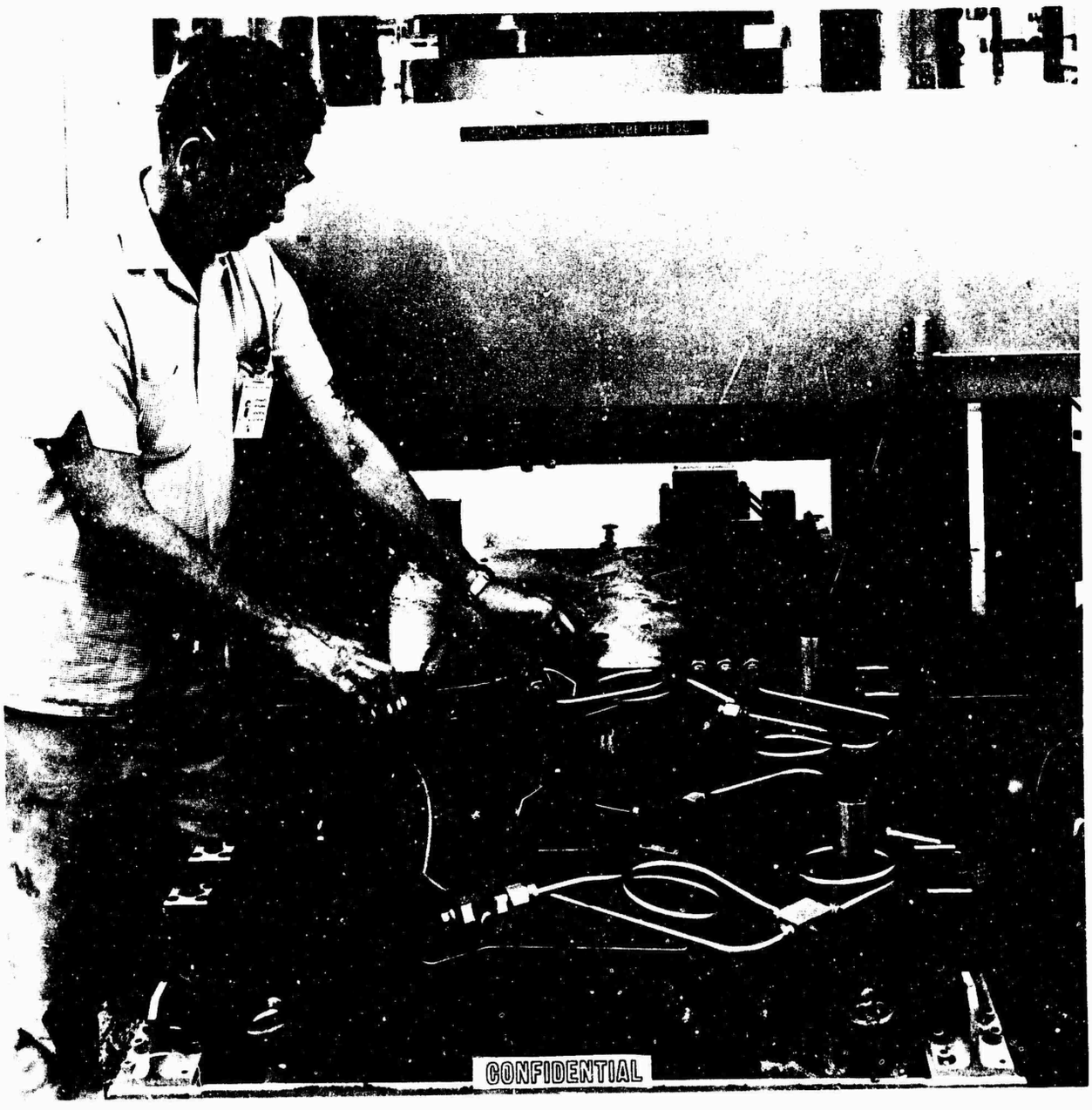

1XE42-8/26/66-C1J

Figure 273.250K Cooling Tube Pressure Forming

1XE31-8/8/66-C1

Figure 274. Inner and Outer Thrust Chamber Tubes

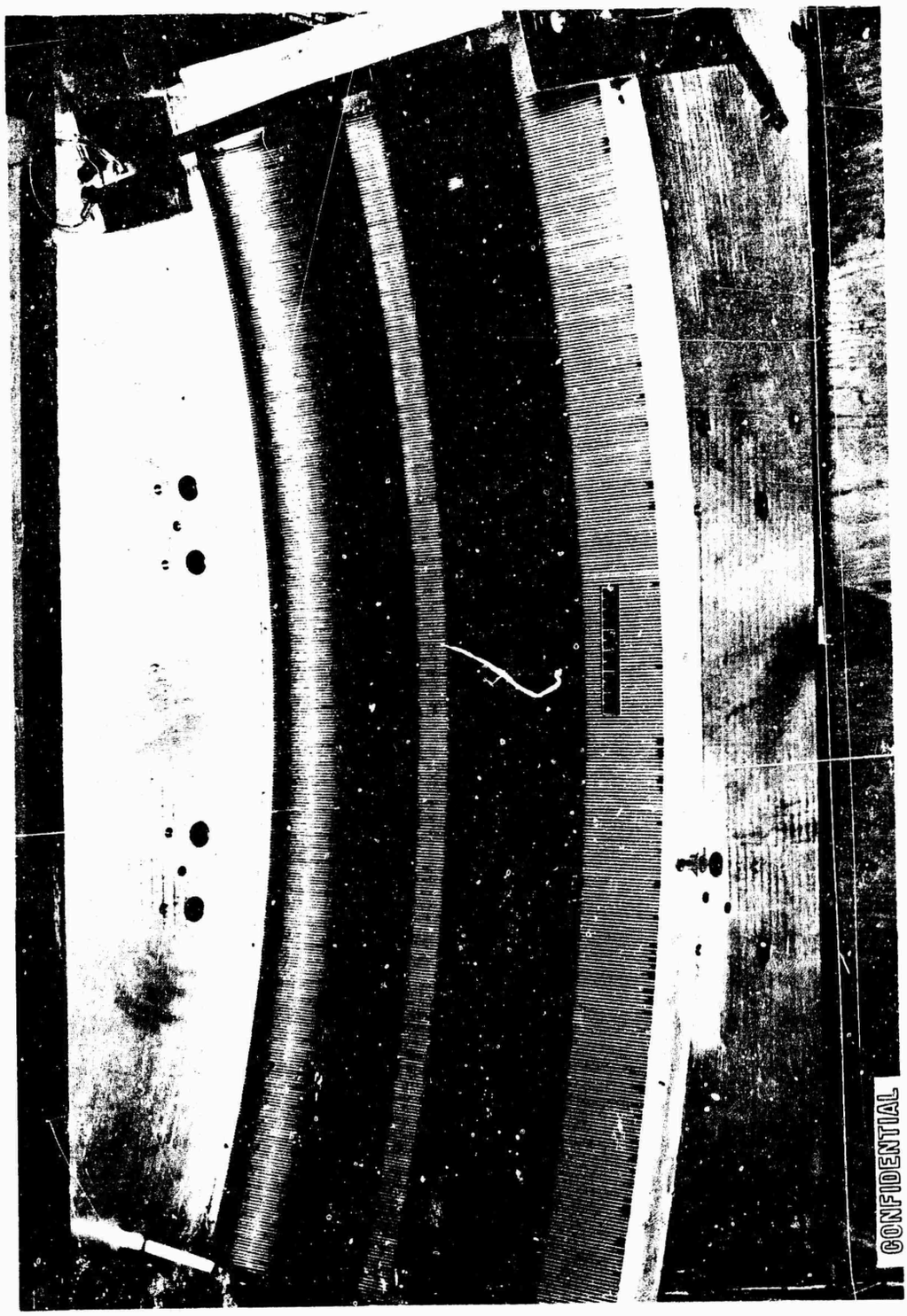

Figure 275. Stacking of Tubes for 250K Tube-Wall Thrust Chamber

TABLE 80

(C) TUBE TOLERANCE

	Outside Tube Height, inch	Outside Tube Width, inch	Tube Thickness, inch	Roughness, microinches
Minimum Area	-0.001	-0.002	+0.001	100
Nominal	0	0	0	75
Maximum Area	+0.001	0	-0.001	50

(C) The principal variation in the tolerance values results from the effect of tube roughness on the fraction factor. The effect of roughness is seen to be approximately ±2 percent on flowrates. By comparison, the stackup of the tube dimensions results in an area tolerance of +9 percent to -10.5 percent. The resulting GN_2 flow variations are presented in Table 81.

TABLE 81

(C) GN_2 FLOW VARIATION DUE TO TUBE TOLERANCE

	Roughness, microinches	Nozzle Up-pass, scfm	Nozzle Down-pass, scfm	Shroud Down-pass, scfm
Minimum Area	100	1.81 (+11%)	2.05 (+10%)	1.96 (+10%)
Nominal	75	1.63 (0)	1.87 (0)	1.78 (0)
Maximum Area	50	1.40 (-14%)	1.65 (-12%)	1.54 (-13%)

(U) The results of the study indicated that the sonic GN_2 flowrates were sufficiently sensitive to the dimensional variations to be worthwhile as an overall tube specification checking technique. The results also indicated the desirability of flowing the nozzle tube from the injector end, because the tolerance and roughness variations outside the minimum cross-sectional region have very little effect on the GN_2 flowrates for this orientation. However, flowing the nozzle tubes from the injector results in choked flow at the tube exit because of air pressure loss in the tubes, so that only the up-pass orientation will choke in the throat, and therefore the up flow was used.

(U) All of the tubes for both the inner and outer thrust chamber bodies were calibrated using the air-flow method (Fig. 276). The tubes were categorized into groups which represented 5-percent increments of the nominal flowrate required. Each tube was identified so that later reference could be made to the initial calibration. The flow group identification and the number of tubes from each group on each combustor is shown in Table 82.

(U) Upon completion of the individual tube calibration, the final fabrication operation of trimming the tubes to proper length was accomplished using the electrical discharge machining (EDM) equipment. This machining process was chosen because the method does not generate any metal chips or burrs. Final cleaning of the tubes for brazing was accomplished using the trichloroethylene vapor degreasing method.

(U) Brazing The brazing operations for each combustor consisted of two planned brazing cycles. The brazing sequence for all combustor bodies was identical. A detailed description of this procedure is contained in the final report, Materials and Processes Research and Development, Ref. 3.

(U) For the initial braze cycle, the stainless-steel bodies were nickel plated and alloyed, using 90 A_g-10Pd alloy. Alloy wire was placed in grooves prepared for this purpose, and alloy sheet was tack welded over the surface to which the tubes were to be brazed. The tubes were then stacked to the body and powdered alloy placed in all tube-to-tube and tube-to-body joints. Pressure bag tooling was then installed to ensure that all components were tightly held together at brazing temperatures, and the assembly was placed in a sealed retort within the furnace. A vacuum was pulled within the retort and an argon purge was initiated and maintained until a temperature of 700 F was reached. At this time, the purge was changed to hydrogen and maintained until the brazing temperature of 2000 F was reached. The furnace was then cooled in a controlled manner, maintaining hydrogen and then argon purges until 200 F. During the entire cycle, the temperature difference between various components was accurately controlled.

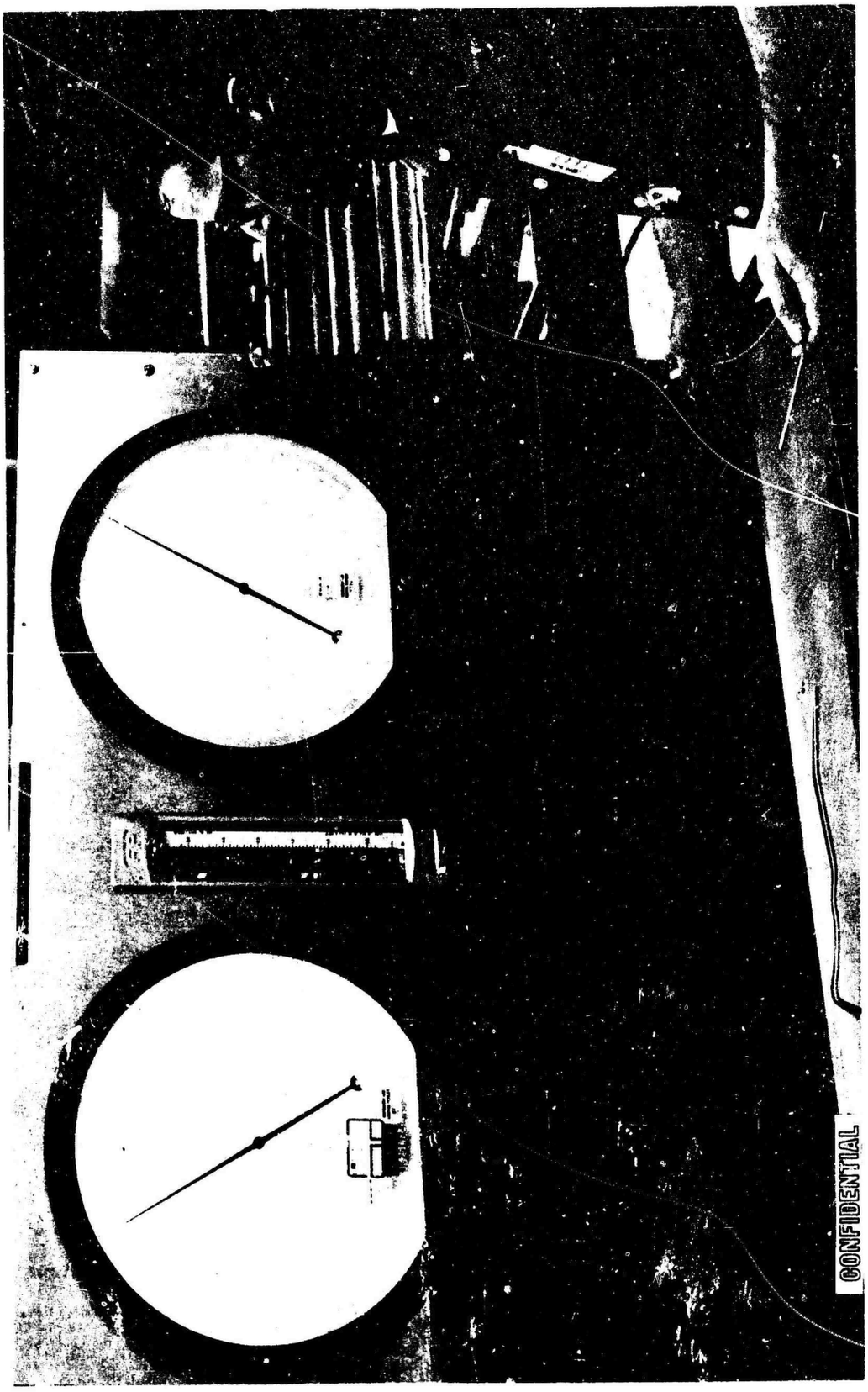

LXE42-8/26/66-C1K

Figure 276. Thrust Chamber Tube Calibration Console

TABLE 82

FLOW GROUP IDENTIFICATION

Flow category of each tube used in the following thrust chambers are:

Inner Body	Outer Body
D - 78.0 to 81.99 psia	U - 84.0 to 87.99 psia
E - 82.0 to 85.99 psia	U - 88.0 to 91.99 psia
F - 86.0 to 89.99 psia	W - 92.0 to 95.99 psia
	X - 96.0 to 99.99 psia
	Y - 100.0 to 103.99 psia

	Inner Bodies			Outer Bodies	
Group	Unit No. 1	Unit No. 2	Group	Unit No. 1	Unit No. 2
D	1821	1600	U	1850	378
E	1821	1800	V	1850	399
F		200	W		1307
			X		1437
			Y		119

(U) After the first furnace braze cycle, the bodies were inspected and all areas indicating insufficient alloy were realloyed with Nioro 82Au-18Ni. In addition, all tube-to-tube and accessible tube-to-wall joints were realloyed. The second braze furnace cycle was essentially the same as the first, except that brazing temperature was held to approximately 1800 F to ensure that the first cycle alloy would not remelt. Pressure bag tooling was not required during the second braze cycle.

(U) Final Machining and Processing. The inner and outer body tube-wall assemblies were final machined after completion of all brazing operations. In the case of the inner body, the first operation was to machine the thrust mount shear groove on the inside diameter. This groove was then used as a location reference for subsequent operations. A thermochromistic heat-sensitive coating was applied to the tubes to verify tube-to-backwall braze joint uniformity (Fig. 277).

(U) An individual tube flow check was performed to verify manufacturing process control capabilities. The results were checked to ensure that no tubes were plugged. Any tubes that looked restricted were opened up by pressure, hot water, and/or acid etch operations. The exit end tube manifold closures were then welded in place and penetrant inspected.

(C) The completed assemblies were installed into the hydrotest fixture, and subjected to a helium flow check in the tubes at three different pressure levels; 150 psig, 200 psig, and 300 psig. All of the combustor bodies passed this check with leakage at less than 10 scim. The bodies were proof pressure tested to pressures ranging from 4230 psig for the inner body, to 3755 psig for the outer body, and successfully fulfilled the hydrostatic test requirements.

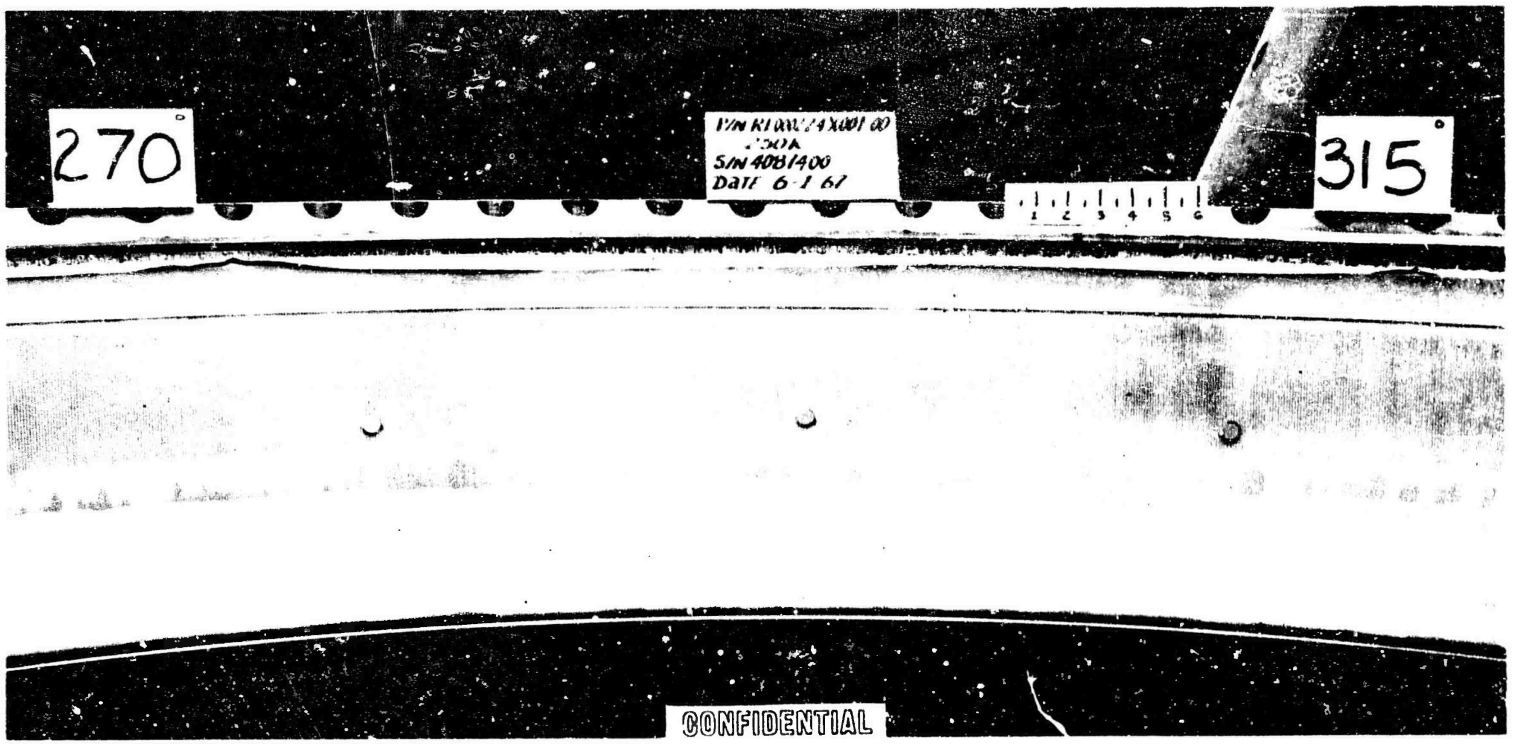

1XE32-6/1/67-C1G*

Figure 277. Thermochromistic Indication of Braze Bond; Outer Body, Tube Wall

CONFIDENTIAL

(U) The bodies were then flushed with trichloroethylene until a controlled sample taken from the effluent solution showed the contamination level to be within the required cleanliness levels. Upon completion of the trichloroethylene flush, the inner and outer body assemblies were water flushed. The combustor bodies (Fig. 278 and 279) were then complete and ready for assembly with the injector, thrust mount, and ducting.

(U) 250K Injector Design. Substantial basic aerospike injector design data were obtained from segment testing. Based on the heat transfer and performance results of the segment programs, the baffle and strip configuration, and design and fabrication techniques were selected identical to those segment configurations that showed the highest integrity and performance.

(U) The injector is a one-piece, stainless-steel, annular assembly, with a mean diameter of 93.00 inches and an injector face width of 2.00 inches. In addition to preparing and injecting propellants into the combustion chamber, the injector is a structural member that transmits the static, dynamic, and thermal loads of the outer combustor body assembly. Connection of the annular injector to the inner and outer combustion chamber section is accomplished with bolts on the inner and outer peripheries. A shear surface at each periphery is provided to restrain the thermal and pressure loads, thus reducing the bolt size requirement.

(C) To control deflection of the throat and prevent leakage through the injector body seals, the injector body is designed with a hinge groove. Normally, the bending would occur about the bolt centerline and produce excessive deflections (0.012 inch) that would completely unload the seals. The groove section modulus was designed to meet maximum load requirements, whereas the adjacent areas were purposely overdesigned, thus controlling the location of bending by design.

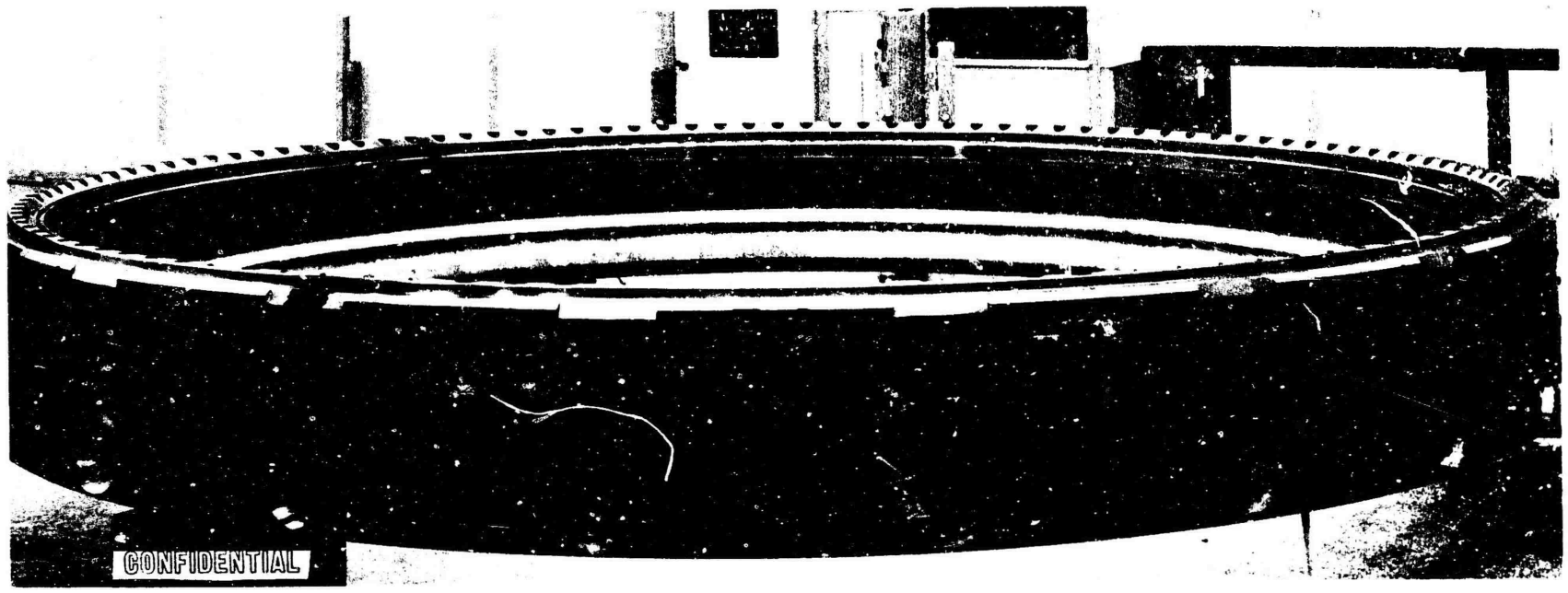

1XE32-4/12/67-C1B

Figure 278. Completed 250K Tube Wall Outer Body

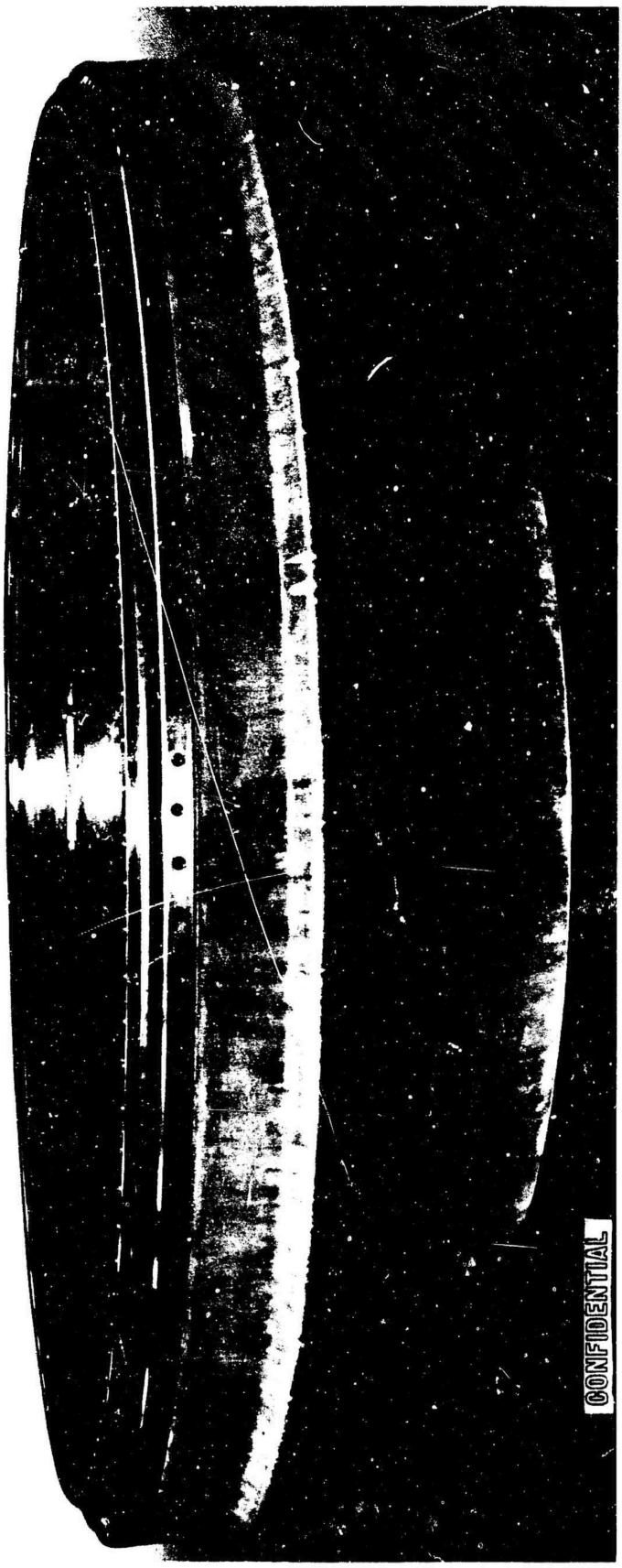

Figure 279. Completed 250K Tube Wall Inner Body

(U) The liquid oxygen inlet manifold design was established and the flow characteristics were verified on efforts performed under Contract NAS8-19 (Ref. 11). This manifold is welded to the top of the injector assembly. The liquid oxygen is distributed from this manifold via 120 equally spaced axial feed holes to a small circumferential groove that connects with the oxidizer strip cavities. The hydrogen is distributed to the fuel injector manifold through 80 feed holes from an externally mounted manifold. These holes contain an orifice plate that balances the flowrates between the baffle cooling circuit and the fuel injector manifold supply.

(U) The injector body also contains 160 radial feed holes which transfer the fuel from the inner to outer body as part of the regenerative-cooling circuit. The basic injector configuration is illustrated in Fig. 280.

(C) Baffles. The injector is uniformly divided into 40 compartments formed by copper baffles placed to simulate the internal support structure of the lightweight configuration. The results of the previous segment tests have indicated that overpressures of approximately 80 percent will not initiate an acoustical mode of unstable combustion when the compartments are of the approximate length of those formed by 40 baffles.

(C) The initial design of the baffles was based on a concept of electroforming or electroplating a type 347 stainless-steel core with OFHC copper to form a face with integral coolant passages. This design provided the capability of the baffle to withstand large overpressures that could occur during bombing tests of the thrust chamber. The baffles are regeneratively cooled by means of parallel flow circuits within the injector body, which bypasses approximately 24 percent of the injector fuel through the 40 baffle assemblies. This results in a coolant mass velocity of 4.8 lb/sec-in.^{2} within the baffles, and provides an adequate cooling margin at the

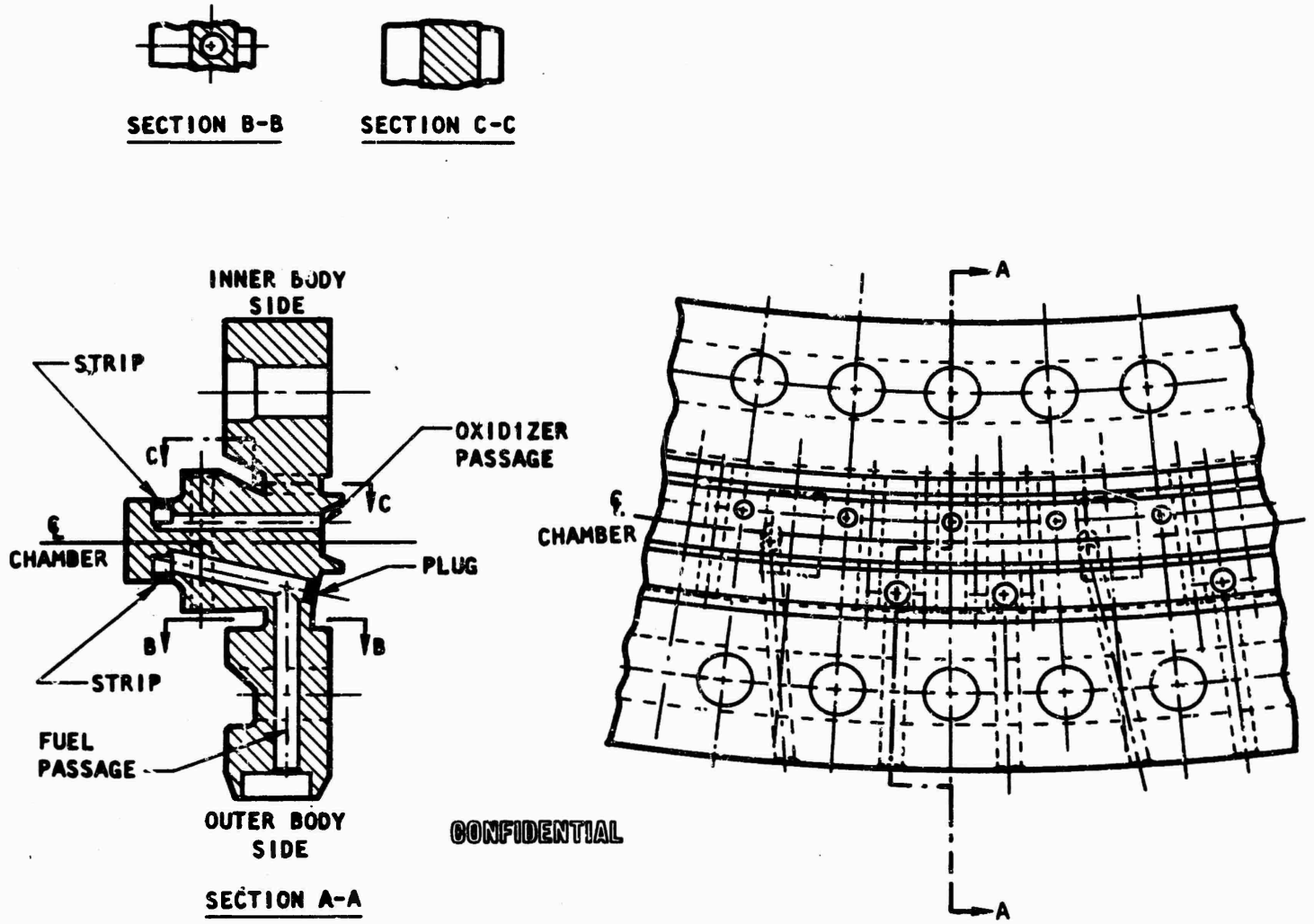

Figure 280A. 250K Injector Body

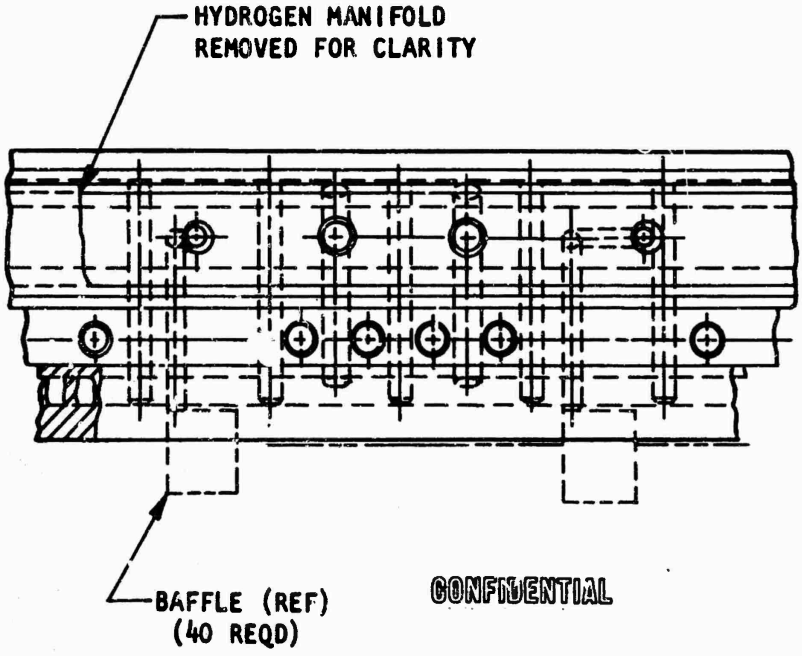

Figure 280B. 250K Injector Body

anticipated heat transfer conditions. The attempts to fabricate the baffles using the electroform techniques failed to produce assemblies with faces of copper that would meet the requirements of oxygen-free verification tests and the subsequent hydraulic pressure tests. Consequently, the design was revised to include baffles fabricated of solid OFHC copper which had the coolant passages integrally drilled within the body of the baffle (Fig. 281).

(U) Hypergol Ignition. The ignition ClF_3 hypergol is supplied to each baffle compartment via a passivated stainless-steel tube which is inserted through the injector body and extends to the face through the fuel strip at the center of the compartments (Fig. 282).

(C) Hot-Gas Ignition and Tapoff System. The hot-gas ignition and tapoff system was installed on the first of the two injectors. The system is a 360-degree peripheral manifold connected at 40 locations to the injector in line with the drilled copper baffles (Fig. 283). Insulating sleeves are installed within the injector to maintain the temperature of gases used for ignition and temperature of tapoff gases, and to minimize the thermal gradients in the injector body. The sleeves, fabricated of type 347 stainless steel, provide an air gap between the body and gas ports, maintaining ambient body and 1500 F hot-gas ignition temperatures.

(C) Injector Strips. Seven injector strips are incorporated within each baffle compartment. Each of these strips features a fuel stream impinging on doubled LO_2 streams, forming a triplet configuration (Fig. 284). The LO_2 streams impinge at a 60-degree included angle, 0.150 inch above a raised fuel strip. The raised fuel strip serves two purposes: (1) the point of fuel discharge is moved close to the point of LO_2 impingement to

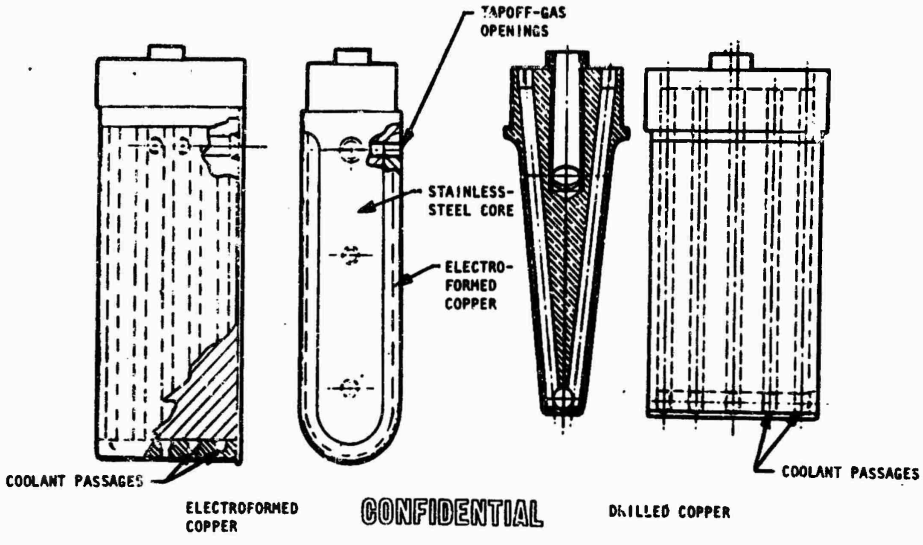

Figure Injector Baffle Configurations

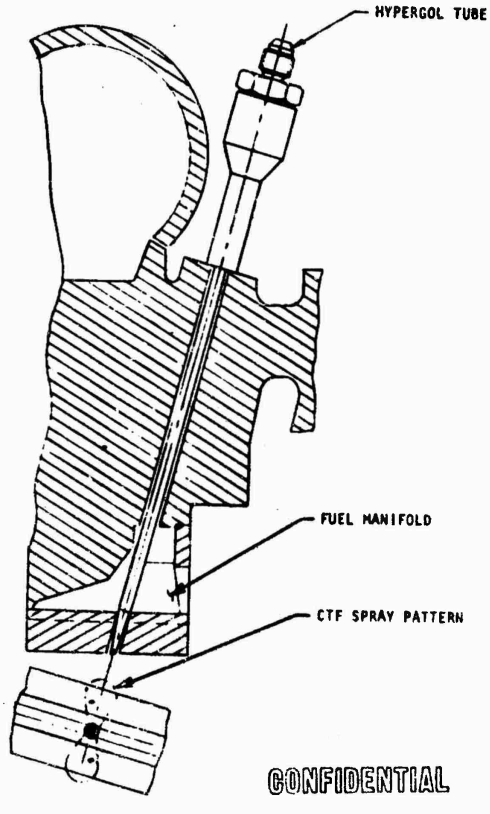

Figure 282. Hypergol Tube

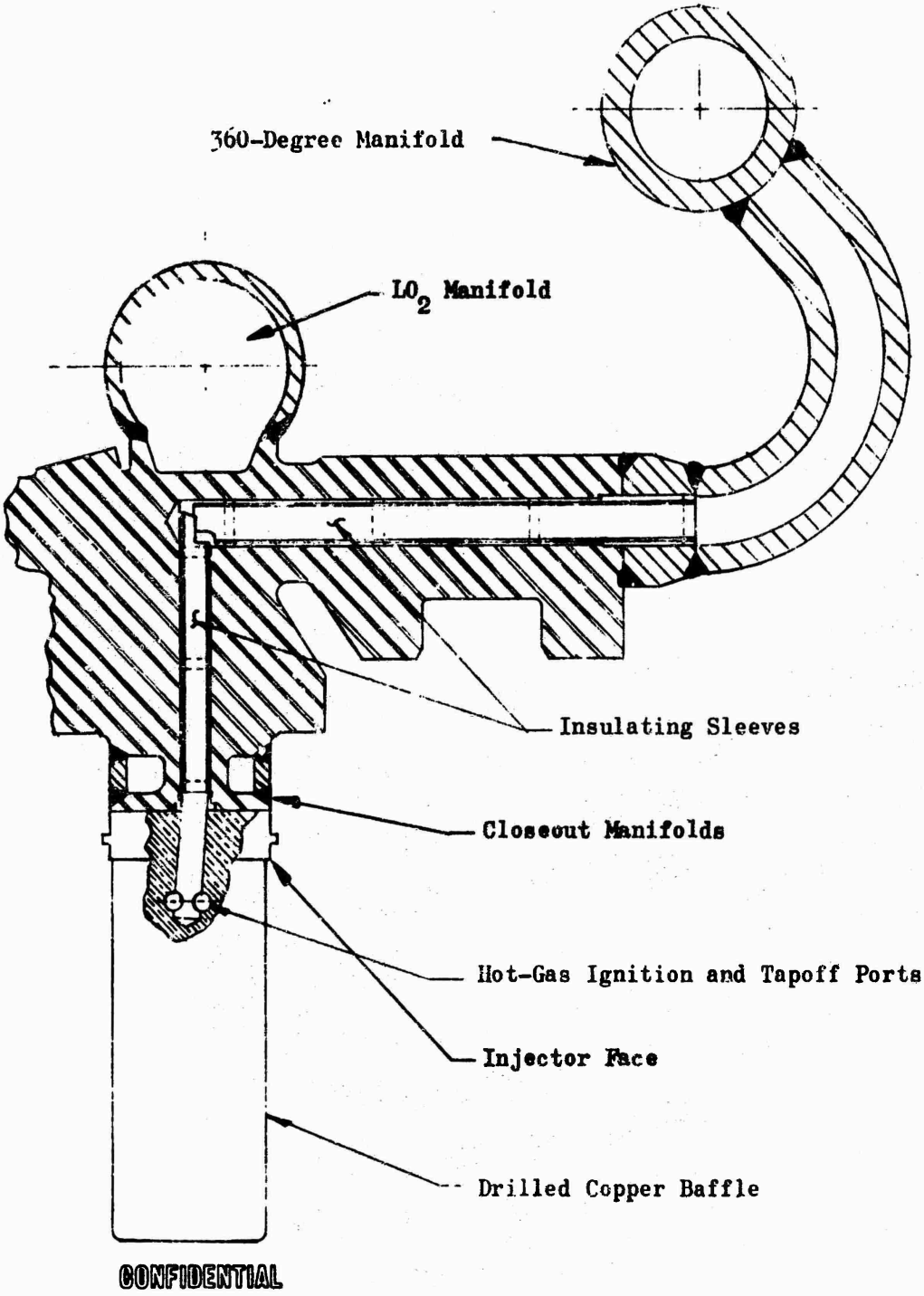

Figure 283. Hot-Gas System

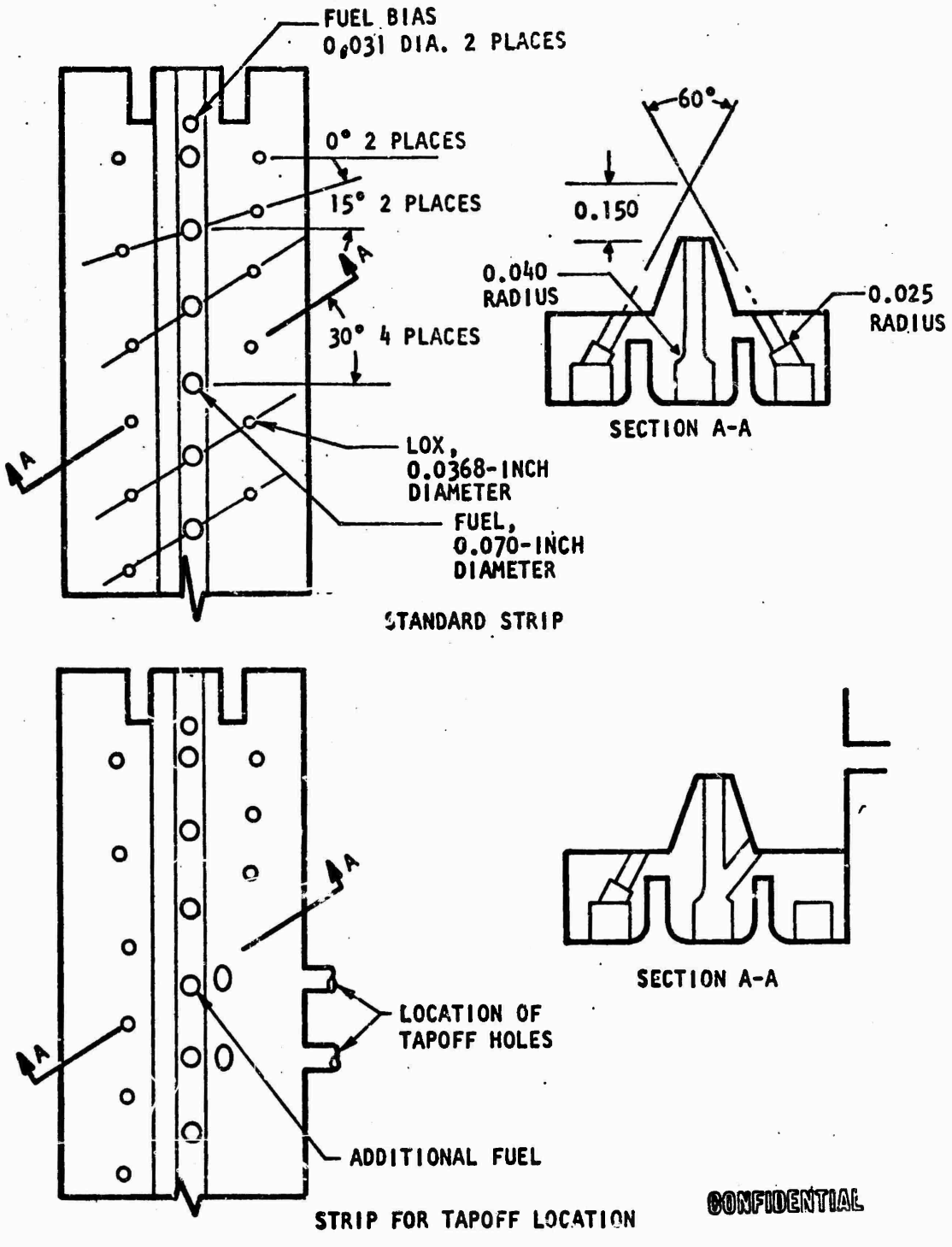

Figure 284. 250K Candidate Triplet With Fuel Post (No. 6-1A to 6-1D)

maintain fuel stream integrity for improved primary atomization, which produces high combustion efficiency; and (2) the raised fuel strip reduces recirculation across the face and maintains favorable temperatures near the oxidizer strips.

(C) Each strip contains eight triplet elements. The outermost elements are oriented 90 degrees to the strip, the second element from each strip end is canted 15 degrees, and the remaining elements are canted 30 degrees.

(C) The purpose of element canting is to separate each element to avoid propellant agglomeration. The outermost elements are oriented 90 degrees to the strip to provide adequate cooling at the strip ends.

(C) Numerous tests were conducted with the 2.5K segment to establish the performance and characteristics of this injector design concept. The advantages of the selected injector pattern and design are as follows:

1. High performance over the operating range
2. The combustion performance is relatively insensitive to mixture ratio excursion over the throttling range.
3. Demonstrated durability over the operating range
4. Excellent hydraulic characteristics over the throttling range (no hydraulic flip)
5. No occurrence of spontaneous instabilities during testing
6. Modifiable strip design for local mixture ratio control for hot-gas tapoff
7. Uniform mixture ratio obtainable by calibrating strips before installation in the injector
8. Demonstrated hot-gas ignition of a segment
9. All strips essentially identical for fabrication simplicity

(U) Injector Flow Calibration. The injector contains seven propellant orifice strips per baffled compartment. Each strip was inspected and flow calibrated with water for propellant stream appearance.

(U) This flow calibration procedure was conducted at the medium-flow facility. This flow facility is equipped to provide: (1) a constant flowrate to each strip through the use of cavitating venturis, and (2) quick strip removal and convenient visual access to the flow pattern.

(U) Cavitating venturis provided identical water flowrates to each strip. The fuel and oxidizer sides of each strip were supplied from a separate source. The differential pressure across the strips was measured and recorded and, because the flowrate to each strip was the same, the differential pressure across the strips was used as a measure of equivalent orifice area.

(U) Using the strip differential pressure as the criterion, the strips were statistically distributed around the injector to ensure uniform flowrate and mixture ratio. Misimpinging orifice elements or strips with excessive high or low differential pressure were easily detected during strip calibration. The consistency of results established this calibration technique as a satisfactory injector strip procedure to ensure uniform orifice patterns and flow characteristics.

Injector Fabrication.

(U) Body. The fabrication of the injector was performed in a method directed toward eliminating or at least minimizing the distortion which might occur after the injector strip placement or the brazing cycle of the injector strip. Consequently, the initial machining operations of the

304L forging did not reduce all areas to the final dimension. The manifold, closeout ring grooves, and the propellant transfer passages were machined. The other areas of the injector were machined, but a sufficient allowance was retained so that a final machining to finish dimension could be accomplished.

(U) The oxygen inlet manifolds, the peripheral fuel manifolds, and the oxygen and fuel injection manifold strips were then welded in place. In addition, the smaller closure welds of inserts in passages, instrumentation bosses, and orifices were accomplished. All of the welds were X-ray or dye penetrant inspected, and the system was hydrostatically tested to ensure structural integrity.

(U) On completion of all planned welding, the body assembly was subjected to a stress-relieving cycle. This stress-relieving cycle was accomplished using a retort in a furnace which had the capability of supplying an inert atmosphere during the cycle. The annealing of the injector body was accomplished at the planned temperature (1910 ±25 F) anticipated for brazing the strips into the body assembly. Thus, all the residual stresses should be relieved, and distortion would be minimal during the final brazing cycle.

(U) The preparation of the face slots and the integral feed passages for the baffles and strips was accomplished by using processes specifically designed for this injector. The 280 strip slots and 40 baffle slots were machined using a portable broach that was physically attached at tooling location holes within the injector body during the machining operation. This method ensured that each of the strip and baffle slots was identical and, also, that each of the 40 compartments within the injector was identical.

(U) The machining of the passages from the strip and baffle slots to the oxygen and fuel injection manifolds was accomplished by electrical discharge machining (EDM). The EDM machine was modified so that the injector could be positioned horizontally and rotated under the electrode head. A special electrode holding fixture was fabricated which contained 42 electrodes for strip passages and 4 electrodes for baffle-coolant passages. Each of the electrodes was configured to produce the desired passage shape. This fixture permitted the machining of two entire baffle compartments with one machine operation.

(U) The injector was subjected to a high-flow water flushing following the EDM process. Fixturing was attached to the injector which provided the capability of flushing in either direction with the intent of removing the foreign materials that could be present in the propellant passages. The flushing was repeated until samples of the effluent indicated a satisfactory contaminant level. Vapor degreasing and a 20-5-75 percent nitric acid-hydrofluoric-water descale to remove the carboniferous surface created by the EDM process were accomplished. Following these operations, the injector was nickel plated and prepared for the installation of the strips and baffles for the brazing procedure.

(U) Strips. The injector strips for the injector were fabricated from OFHC certified copper. The normal procedure for certifying the copper is to heat etch a representative sample of each lot of material. Because a sampling technique was considered unsatisfactory in this instance, all copper material was heat etched to 1900 ±25 F in a hydrogen atmosphere for 15 minutes. Each part was individually inspected for any discrepancies prior to being certified for use in the 250K injector.

(U) The machining to the correct configuration was accomplished using conventional machining equipment. However, the orifices were drilled by using a series of special drilling fixtures utilizing drill guide bushings

so that the holes could be made with hand-held equipment. These techniques produced satisfactory orifice conditions; however, the minute burrs or chips of copper created as a result of the copper material being very soft from the heat tinting process presented another problem. Manual removal of these chips proved to be unsatisfactory, both from a time and quality aspect. Consequently, an electrochemical deburring procedure and an EDM procedure were developed, which gave excellent results.

(U) Brazing. Assembly of the component parts prior to furnace brazing was conducted in the white room. Each strip was dimensionally checked prior to assembly using a precision gage. As the strips were placed in the mating area of the injector body, 0.001- and/or 0.002-inch braze alloy sheet was placed in the vertical joints, as needed, to equalize the gap widths. The strips were seated firmly and staked in position.

(U) The furnace braze operation was conducted in the same furnace as the thrust chambers and began by first evacuating the retort. The retort was then purged with argon gas during the heating cycle of 300 to 1400 F. Hydrogen gas was introduced into the retort from 1400 F through the braze temperature of 1900 to 1920 F.

(C) The integrity of braze joints was confirmed by pressure testing with helium at 60 psia. A method of plugging the injector strip holes using a styrene mineral wax blend material (Plastiwax 8969) was developed which permitted this type of pressure testing. The pressure tests of the first injector revealed that an excessive quantity of leakages existed at baffle and strip-to-land locations (Fig.285). The injector was realloyed and subjected to a second braze cycle. Realloying was accomplished by slotting the injector strips and parting the oxidizer and fuel sections into separate segments Fig.286). This permitted access to the body braze lands for insertion of alloy wire.

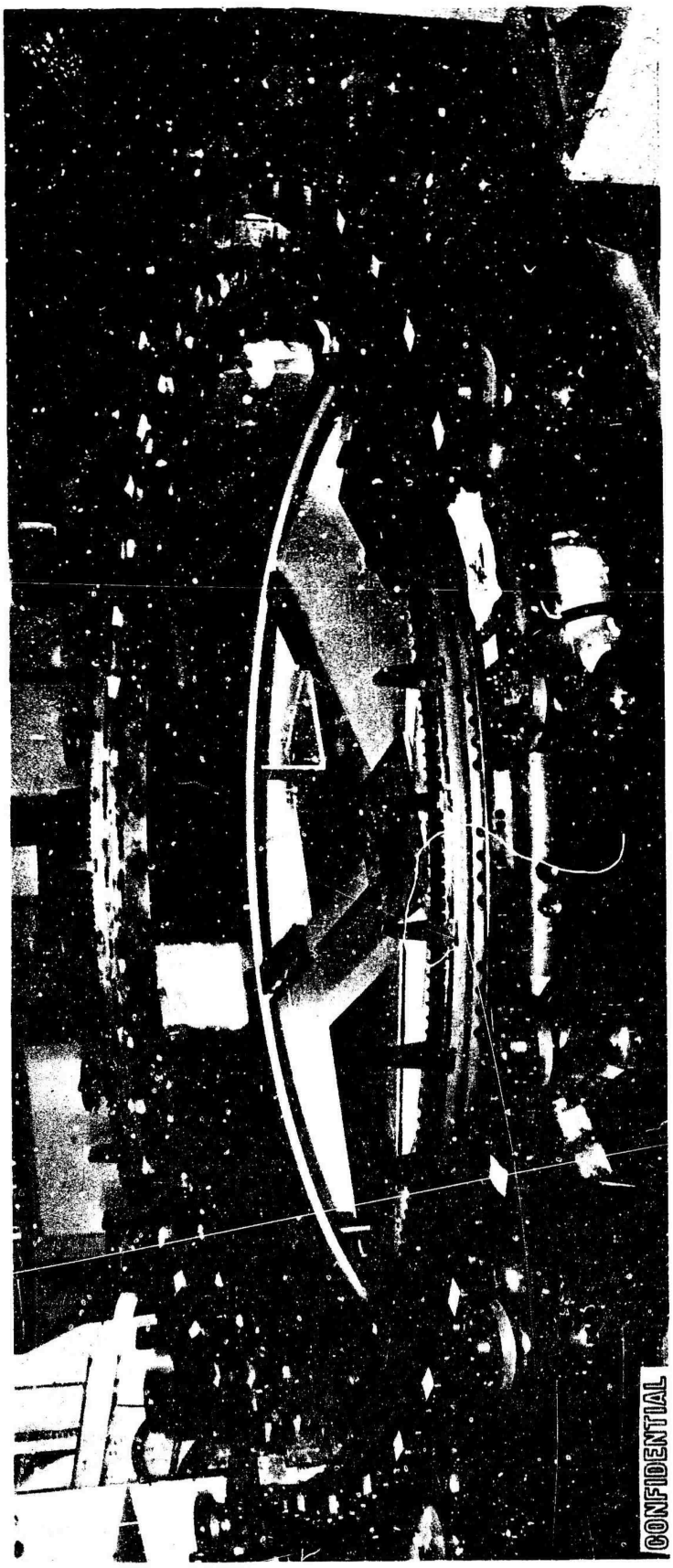

Figure 285. Injector After First Braze Cycle

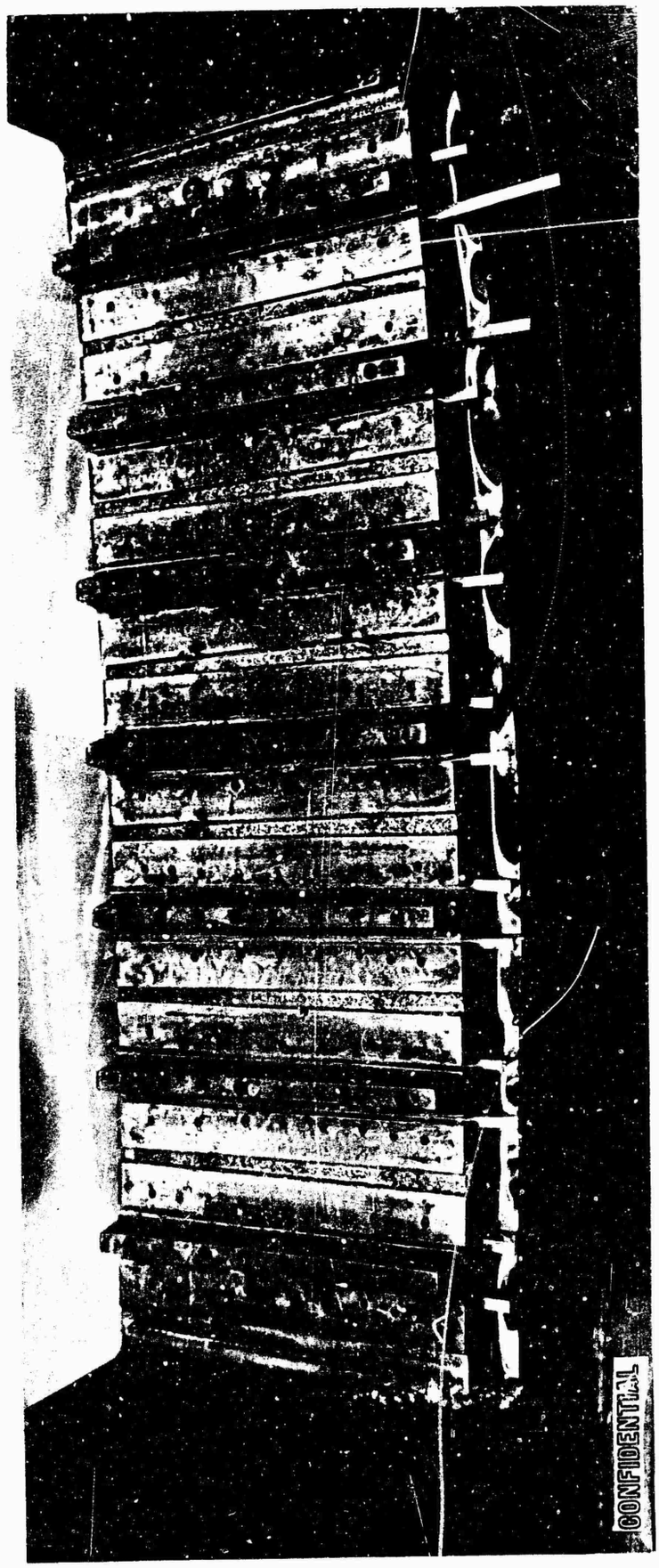

Figure 286. Realloying of Slotted Injector Strips

(U) Pressure test of the second injector after the first braze cycle revealed only a small quantity of strip end leaks and face leaks. Consequently, a second furnace cycle was not required. The strip end leaks were repaired by cutting a groove approximately 0.060-inch deep at the leak area. The area was then TIG brazed using 82Au-18Ni alloy filler. The face leaks were repaired by slotting the strip over the lands and machining out the copper strip material to gain access to the leak area. The repair was then accomplished using TIG brazing with 82Au-18Ni alloy filler.

(U) Final Machining. Final machining of the injectors was accomplished using conventional equipment. Match machining techniques were used to coordinate the injector shear lip dimensions of the solid- and tubular-wall chamber assemblies. Stacking and assembling have shown that excellent results were obtained.

(U) Hot-Gas Tapoff Manifold. The fabrication of the 360-degree hot-gas tapoff manifold for injector No. 1 was accomplished using inert gas welding techniques for the assembly of the preformed heavy-wall tubing components (Fig. 287). The completed manifold was welded to the injector assembly at the 40 fittings which were designed to minimize the heat input to the injector body.

(C) Calibration. The injector fuel and oxidizer flow circuits were both calibrated with the injector in a face-down position. The oxidizer system was water calibrated over a flowrate range of 1000 to 1900 gpm. The fuel system was calibrated over a flowrate range of 1100 to 2400 gpm. These flow calibrations showed excellent stream impingement and good correlation with analytically predicted pressure drop values. The final cleaning of the injectors was accomplished by vapor degreasing and deionized water flushing.

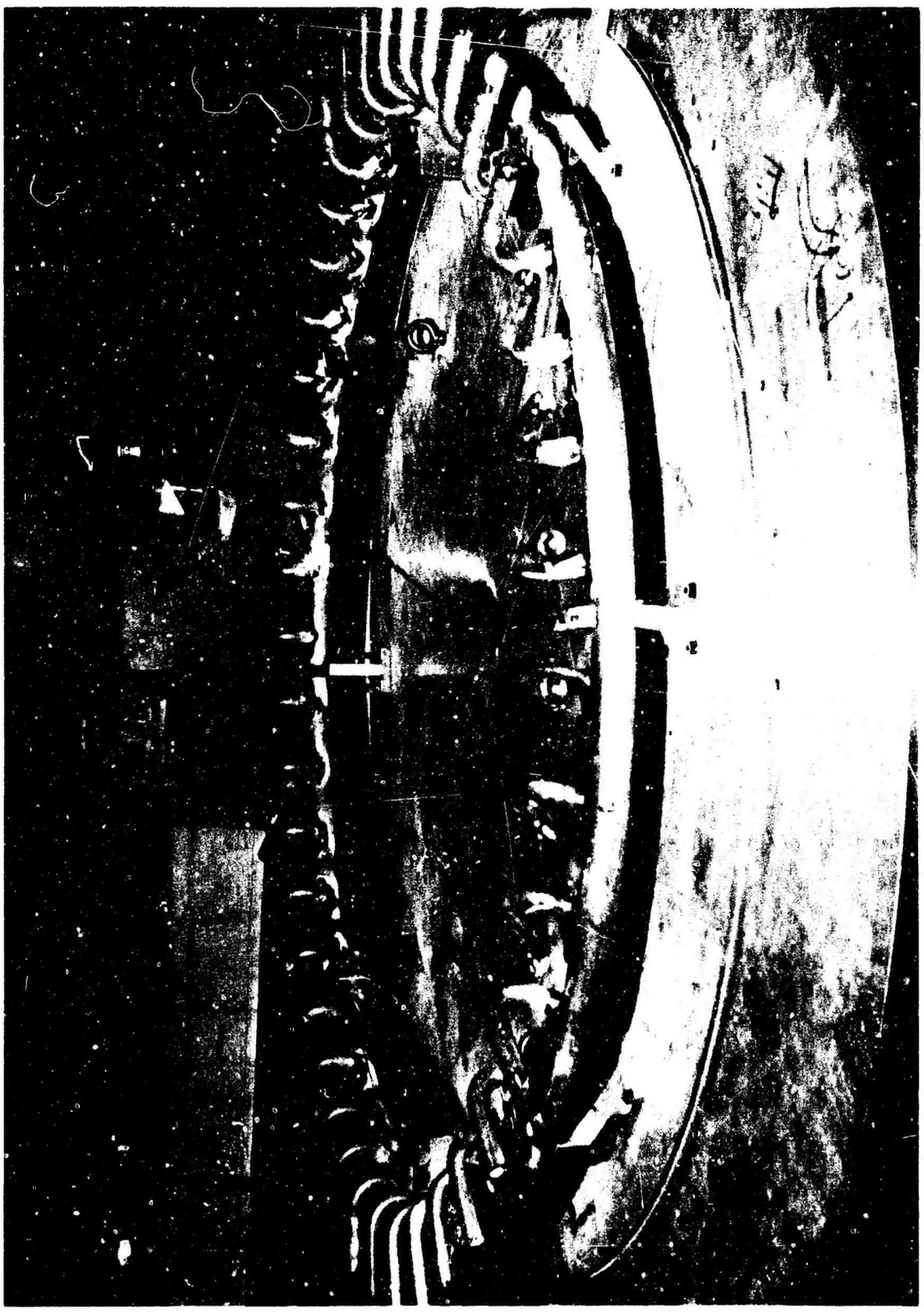

1XE32-10/20/66-C1G

Figure 287 . Hot-Gas Ignition and Tapoff Manifold

(U) Other 250K Components. In addition to the major items of hardware just discussed, several other pieces of hardware are of significance to the program. These include:

1. Uncooled nozzle extension
2. Base closure
3. Thrust mount
4. Ducting
5. Ignition system

(C) Nozzle Extension. The nozzle extension is designed to provide the length differential between the tube wall assembly (12 percent of a 15-degree half angle cone) and that required to provide desired thrust chamber performance (25 percent of a 15-degree half-angle cone). The nozzle extension provides for full-thrust operation for a 5.0-second duration.

(U) The nozzle extension (Fig.288) is fabricated as a contoured (defined by aerodynamic requirements) conical structure, having a flange at the larger diameter for connection to the solid- or tube-wall inner body, and a flange at the smaller diameter for connection to the perforated base closure. Provision for mounting pressure transducers is made at specified locations along contoured elements and about the circumference.

(U) The nozzle extension is fabricated as a welded 304L assembly, consisting of two 180-degree segments of a cone and a 360-degree upper flange ring.

(C) Base Closures. Two base closures were designed; a flat non-perforated closure for use with the 12-percent length solid- or tube-wall assembly, and a plenum-type base closure having a perforated flat face for use with the 25-percent length solid- or tube-wall assemblies.

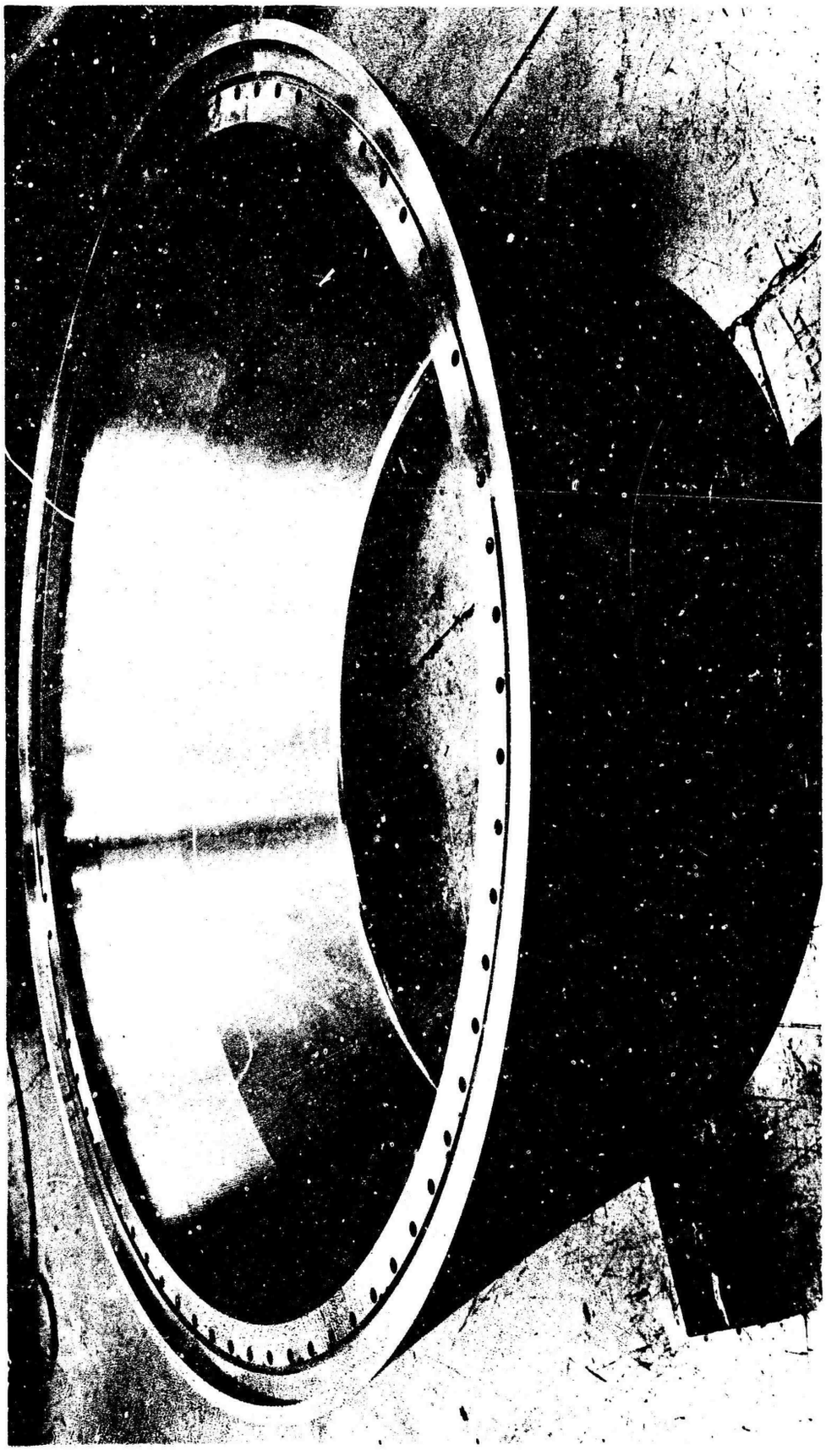

1XE32-12/21/66-C2F

Figure 288. 250K Uncooled Nozzle Extension

(This page is Unclassified)

(U) The flat closure, approximately 65.0 inches diameter, functions as a seal for the inner body cavity to protect instrumentation and the oxidizer system components against recirculating primary hot gases. The perforated base closure (10-percent porosity) was designed to accept secondary gases and distribute them uniformly across the base of the tube-wall assembly. These gases produce thrust, augmenting that normally produced by primary flow on the nozzle.

(U) The closure is designed as a plenum into which gases are introduced through a flanged inlet diffuser. The diffuser flow area may be varied to control sonically secondary flow at three different rates. Control is achieved by covering orifices in the diffuser pipe by three changeable sleeves, one of which is used for each flowrate. The base closure is attached to the uncooled nozzle extension by means of 48 bolts. Thermal expansion of the plenum is unrestrained due to the flexible joint between plenum and extension.

(C) The perforated base closure was analyzed for flowing up to 1.5 percent secondary flow products of combustion of a LH_2/LO_2 gas generator. Temperature and pressure predictions based on data extrapolated from previous aerospike chambers indicated a maximum temperature of 1200 F, a maximum differential across the perforated base of 38 psi, and a maximum internal pressure of approximately 45 psi.

(U) The flat base closure was fabricated from 1.00-inch CRES 347 plate to which a 1.50-inch CRES 347 flange ring is welded. Eight AND ports are tapped and drilled for the installation of five pressure transducers and three temperature probes.

(U) CRES 347 and 321 sheet and bar stock were used for fabrication of the perforated base closure. The entire assembly is of welded construction,

except the removal sleeves and cover plate. Figure 289 shows the base closure in the process of fabrication, and Fig. 290 shows the closure installed on the uncooled nozzle extension.

(U) Thrust Mount. The thrust mount is designed as an eight-legged welded structure interchangeable with solid- or tube-wall 250K assemblies (Fig. 291).

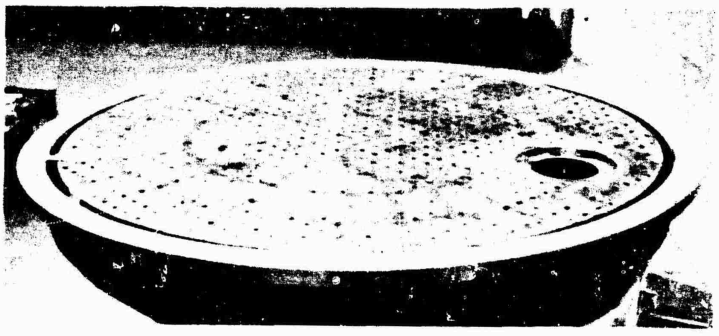

Figure 289. Base Closure Showing Perforated Plate

(U) Connection of the mount to the inner body of the solid- or tube-wall assemblies is made through eight clevises bolted (six bolts per clevis) to the body. Each clevis is designed with a tongue that mates with a circumferential groove cut into the inner diameter of the inner body and transmits the thrust through shear of tongue on groove. An assembly of pins, washers, and spacers tie the mount to the clevises and provide the dimensional restriction necessary to load transmission.

(U) Each of the eight legs and laterals connecting the legs are fabricated of 4135 steel tubing. Connection to the chamber and facility was originally designed using 4340 forgings and weldments, with fabrication of the mount initiated upon receipt of these forgings. Subsequent analysis indicated properties were slightly lower than desired but still satisfactory for use. Fabrication, including welding of all components, was accomplished without incident; however, after the final heat treat, cracks appeared in

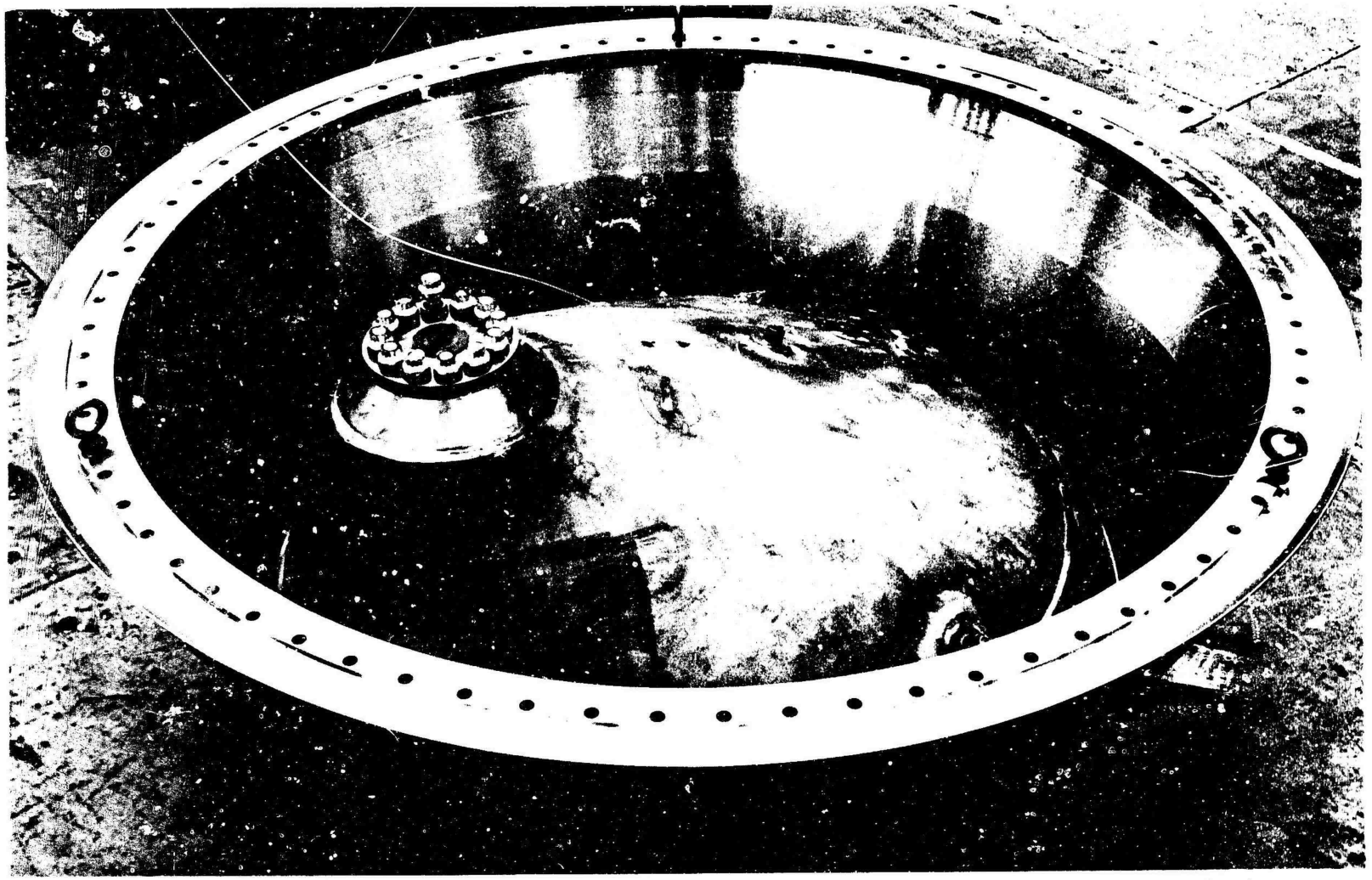

1XE32-4/25/67-C1

Figure 290. 250K Uncooled Nozzle Extension With Perforated Base Closure Installed

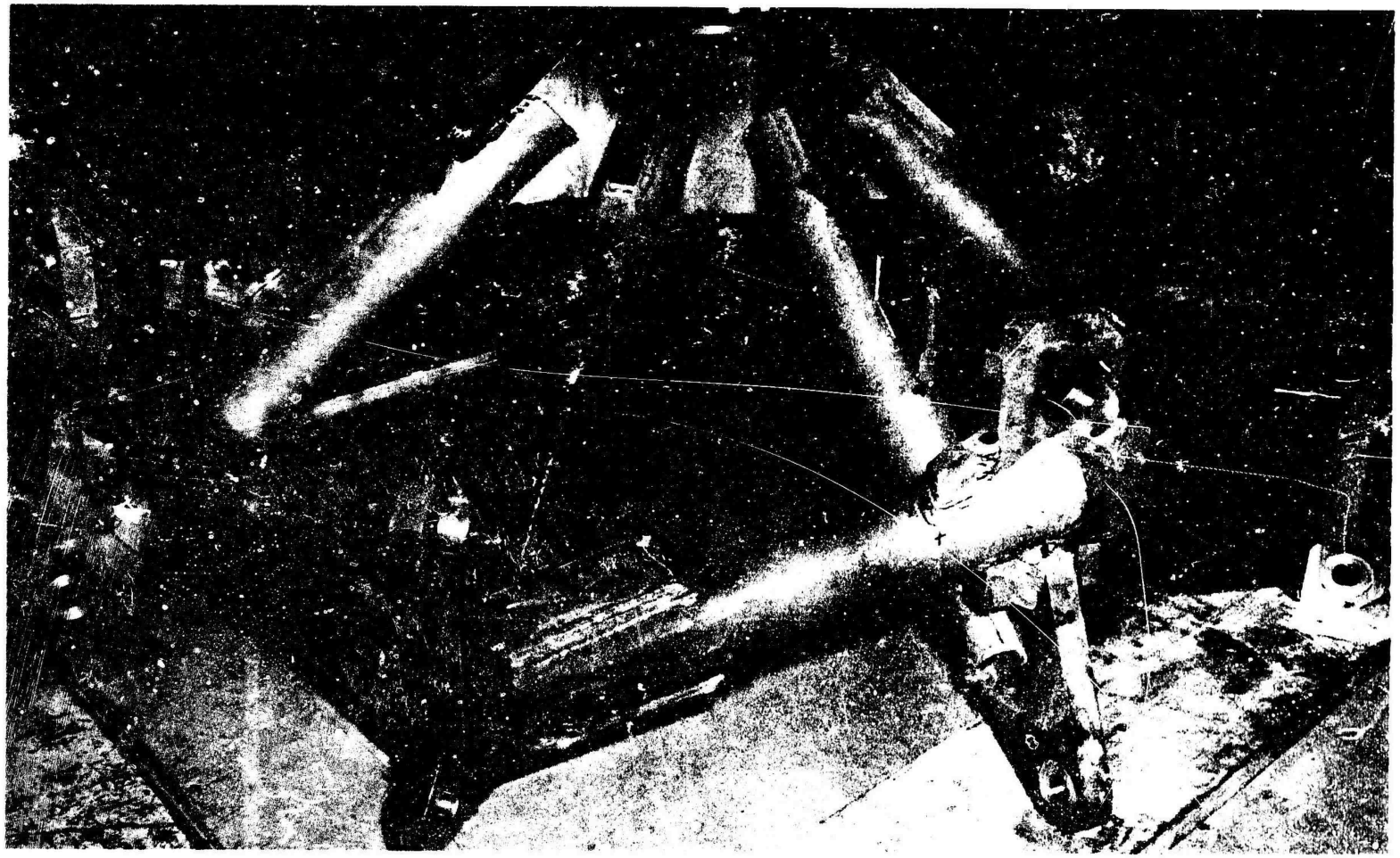

1XE32-1/24/67-C1D

Figure 291.250K Thrust Mount

several of the parent material 4340 forgings. The most severe of the cracks occurred at locations of connection to vertical and tangential test stand supports. These were removed and replaced by modified assemblies of 4135 wleded plate. A crack was also evident in one of the thrust calibration lugs. Both lugs were removed and dual removal U-frames were used for calibration on the stand.

(U) To verify the integrity of the mount in this condition, a structural load test was performed cycling the mount five times with a static proof load of 430,000 pounds. Locations and magnitude of the remaining cracks were noted and checked for propagation using magnaflux and dye-penetrant techniques. No propagation was noted.

(U) Ducting. The oxidizer propellant feed system, common to both solid- and tube-wall assemblies shown in Fig. 292 and 293, is composed of (1) an inlet duct connecting facility to the main LO_2 valve, (2) a J-2 oxidizer valve, (3) a diffuser plenum, and (4) four radial lines providing tangential inlet to the injector oxidizer manifold. Design of the oxidizer feed system was based upon the requirement for uniform feed into the four radial arms connecting the injector. Due to the location of the facility interface, an elbow inlet to the valve was mandatory creating an irregularly shaped velocity profile.

(U) To resolve this problem, a conical diffuser was designed as part of the oxidizer distribution plenum (Fig. 294). The device functions in the following manner. The throat area of the diffuser equals the effective flow area of the valve so that the diffuser throat will flow full without additional pressure loss. The perforated plate at the end of the conical section forces the flow out to the walls and prevents separation. The discharge from the perforated plate into the plenum chamber is axial and perpendicular to the outlets which are located on the circumference of

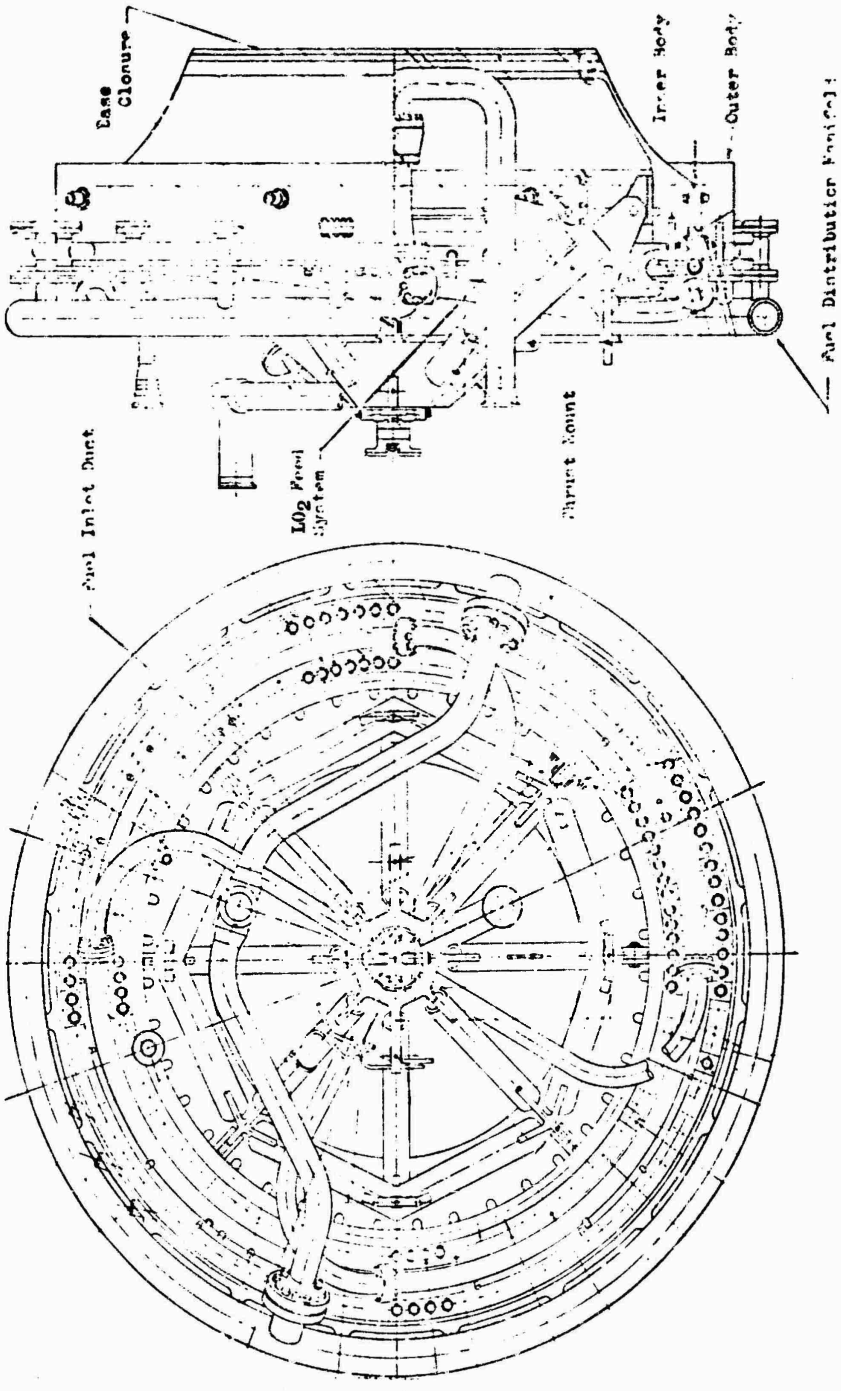

Figure 292. Solid-Wall Thrust Chamber Assembly

CONFIDENTIAL

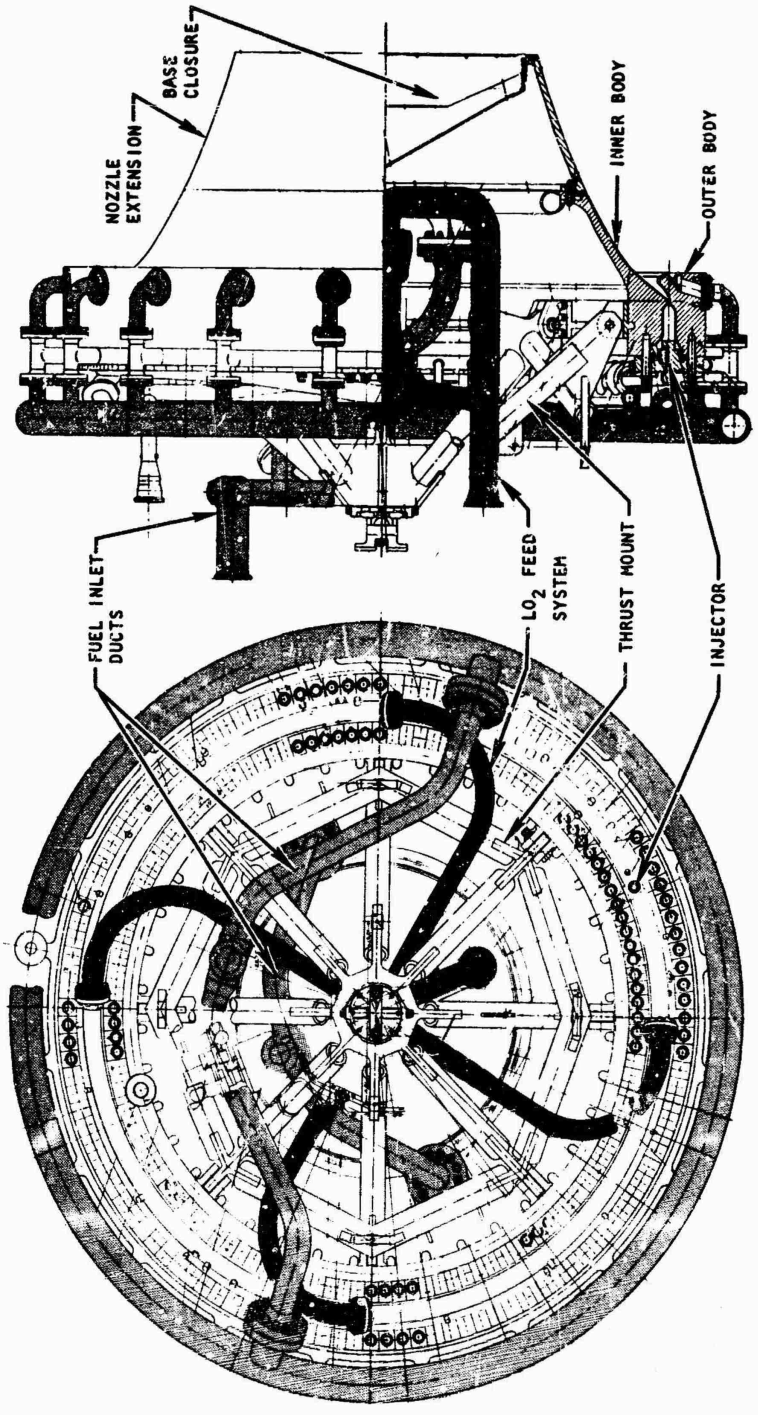

Figure 293. Solid-Wall Assembly

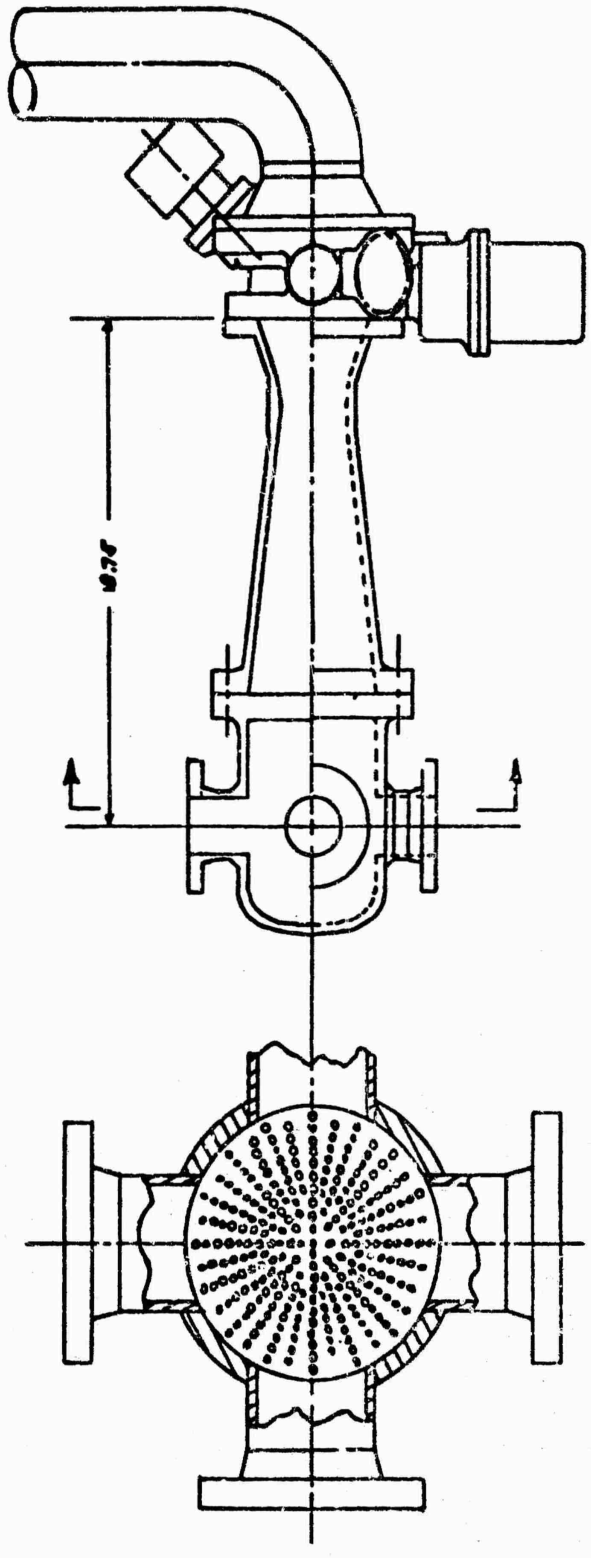

Figure 294. Oxidizer Manifold Center Plenum and Diffuser Section

(This page is Unclassified)

the circular plenum chamber. The holes in the perforated plate have a length/diameter ratio of at least 4:1, and will effectively cancel all eddies in the flow. Therefore, the flow in the plenum chamber will be axisymmetric, well distributed, and turbulent so that an even division of the flow between the individual outlets is achieved.

(U) Fabrication of all components of the oxidizer feed system was accomplished by conventional techniques using CRES 321 and 347 material. Upon completion of each component, hydraulic pressure check of integrity is made at 2550 psig.

(U) The fuel propellant feed system ducting for both solid-and tube-wall assemblies consist of (1) a tube-wall fuel inlet manifold, (2) 20 tube-wall fuel-return elbows, (3) an interchangeable solid-wall inlet distribution manifold (or tube-wall bypass distribution manifold), and (4) an interchangeable, solid-wall inlet manifold (or tube-wall discharge manifold). The fuel system for the solid-wall assembly (Fig. 292) consists of an inlet connecting a single facility feed to two diametrically opposed inlets, and a fuel distribution manifold, feeding the top (forward) of 20 inlet tees on the injector fuel manifold.

(U) These same components are used in a different capacity on the tube-wall assembly (Fig.293). On this assembly, fuel is introduced into two diametrically opposed inlets on the inner body by a fuel inlet manifold having a single facility connect. Twenty fuel-return elbows direct fuel from the outer body (after completion of its regenerative coolant circuit) to the underside (aft) of twenty inlet tees on the injector fuel manifold. Fuel not entering the injector for combustion is bypassed to 20 inlets of the distribution manifold described above, from which two outlets convey flow to a single facility interface. Large-diameter tubing was used whenever possible to keep velocities low and minimize flow unbalance. The large diameters also eliminated the necessity for any tapered ducting.

(U) Manifolds employ CRES 347 and 321 tubing and plate material, and use conventional techniques for fabrication and assembly. No noteworthy problems arose during the fabrication of the tube-wall or solid-wall inlet manifolds. Some rework was required to maintain proper alignment of the distribution manifold and the 20 feeder arms subsequent to the final welding operation. Each component of the fuel system was proof-pressure checked with water at 4230 psig upon completion.

(U) Ignition System. An ignition system was designed for the 250K aerospike to introduce chlorine trifluoride (CTF) into each of the 40 compartments of the thrust chamber assembly. Requirements of the overall system included the following: (1) the system must have the capability for removing individual elements from each of the 40 injection points to facilitate replacement or maintenance, (2) it must have uniform distribution and priming, (3) the igniter tube should be introduced through the injector in such a manner that the spray pattern does not impinge on the combustion chamber walls, and (4) the chlorine trifluoride is followed by GO_2 to recover corrosive hypergol from the ignition system and cool the igniter tube during mainstage conditions.

(U) Several systems were analyzed with respect to these requirements resulting in selection of a configuration feeding the injector in quadrants. Entrance to each of the quadrants is made through one of four legs of an internal manifold (denoted because of its position at the interior of the thrust chamber assembly). The manifold contains a single inlet plenum to which each of the four legs are welded. A B-nut and flared tube end enable connection of each leg to a quadrant outer manifold. Each quadrant in turn divides and distributes the flow to two adjacent plenums. One-eighth section of the combustor (five compartments) is then fed from each of the plenum.

(U) 250K Tube-Wall Assembly. The completion of the first tube-wall thrust chamber assembly was accomplished on 9 May 1967, and shipped to the Nevada Field Laboratory (NFL) test facility where initial checkout tests commenced 21 June 1967. Components, including fuel inlet lines and manifolds, oxidizer inlet lines, thrust mount, and ignition manifolds from the film-cooled, solid-wall chamber were utilized in the buildup of this unit. The assembly procedure, similar to that of the film-cooled, solid-wall thrust chamber, consisted of initially installing the outer body on the assembly jig fixture at the lowest position. In this position, the inner body may be installed with maximum clearance and located concentrically by means of lateral travel mechanisms on the assembly fixture.

(U) Figure 295 illustrates the inner and outer bodies on the assembly fixture subsequent to installation of the injector and prior to raising the outer body to the final position. Assembly of the injector to the inner and outer bodies was accomplished with no problems. Guide pins were used to achieve proper alignment of the bodies with the injector to ensure assembly clearances between the baffles and the chamber tubular walls.

(U) Subsequent to the installation of the fuel-distribution manifold and its outlet duct, and prior to installation of the fuel-return elbows, a fuel system leak check was conducted to determine the effectiveness of the injector-to-body seals. This was done by sealing the regenerative coolant circuit with pressure plates on the 20 outer body fuel outlets and pressurizing the cavity between the O-ring and Naflex seal on inner and outer bodies.

(C) Test results indicated essentially zero helium leakage to the vent cavities for both the inner and outer Naflex seals. The composite leakage of the metal O-ring seals and the bolts through the seal ring on the inner body was not obtained after assembly; therefore, leakage of the O-rings was indeterminable. The completed chamber assembly prior to the installation of the protective shipping covers is shown in Fig. 296.

1XE48-5/7/67-C1E

Figure 295. 250K Tube-Wall Inner and Outer Bodies During Assembly

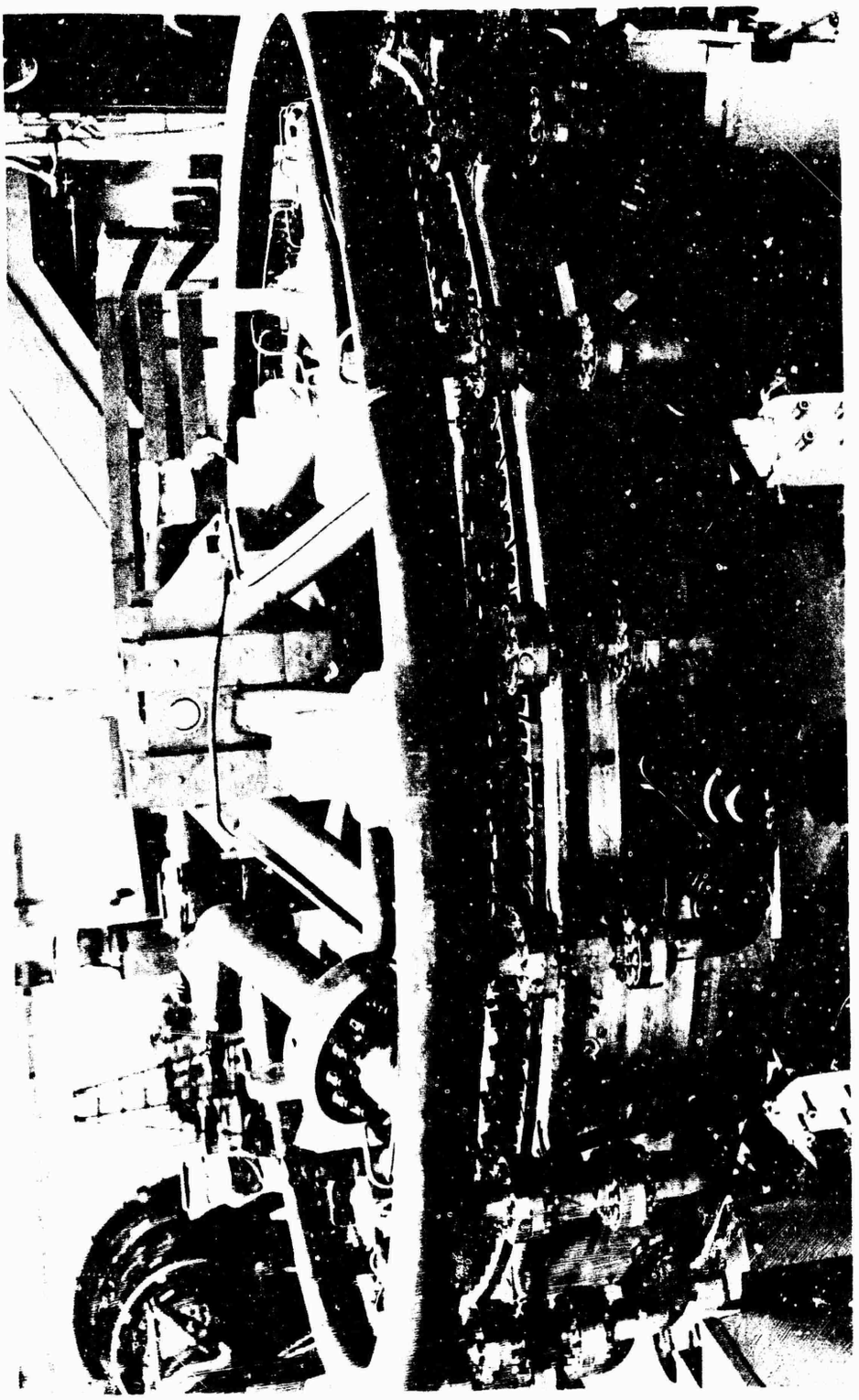

LXE32-5/8/67-C2C

Figure 296. Completed 250K Tube Wall Thrust Chamber Assembly

(This page is Unclassified)

(C) The solid-wall nozzle extension and porous base closure were packaged separately and shipped with the chamber. Installation was made at the facility to achieve the desired 25-percent nozzle length.

Testing

(U) Test Stand Description. The 250K solid-wall and tube-wall workhorse chambers were tested at the Nevada Field Laboratory, which is located northeast of Reno, Nevada. This high-pressure test facility offers the capabilities required for advanced concept high-energy programs. The high-pressure test stand, D-2, is a horizontal firing position stand (Fig. 297). Testing at simulated altitude is possible through use of a self-pumping diffuser. The altitude diffuser is mounted on tracks to permit easy access to the chamber.

(U) The propellant feed systems employ servocontrolled, balanced pressure regulators. Propellant flow was controlled further by a cavitating venturi at the chamber inlet in the oxidizer system and a sonic flow venturi at the chamber inlet in the fuel system. Flowrates were measured with turbine-type flowmeters in the liquid oxygen and liquid hydrogen systems. The methods of calculating propellant flowrates are described in Appendix VII. The capability of delivering hydrogen to the chamber at any desired temperature is provided by a servocontrolled, temperature-sensing, hydrogen, gas-mixing system, which introduces gas into the liquid hydrogen line. Gas flow to the mixer is measured with a subsonic flow venturi.

(U) The thrust-measuring system provides measurement of three forces and three moments in a six-component balance, thus permitting complete resolution of the thrust vector. The thrust-measuring system is shown schematically in Fig. 298. The system consists of a main load measuring cell (F_1) oriented coincident with the axis of the chamber, two vertical load cells (F_5 and F_6) (supporting the chamber weight), two horizontal load cells (F_2 and F_3) oriented parallel to the axis of the chamber, and a horizontal lateral load cell (F_4) oriented perpendicular to, but displaced from, the axis of the chamber. The main load cell connects to the chamber thrust mount through a gimbal bearing. The other five load cells connect to the legs of the chamber thrust mount through pinned joints.

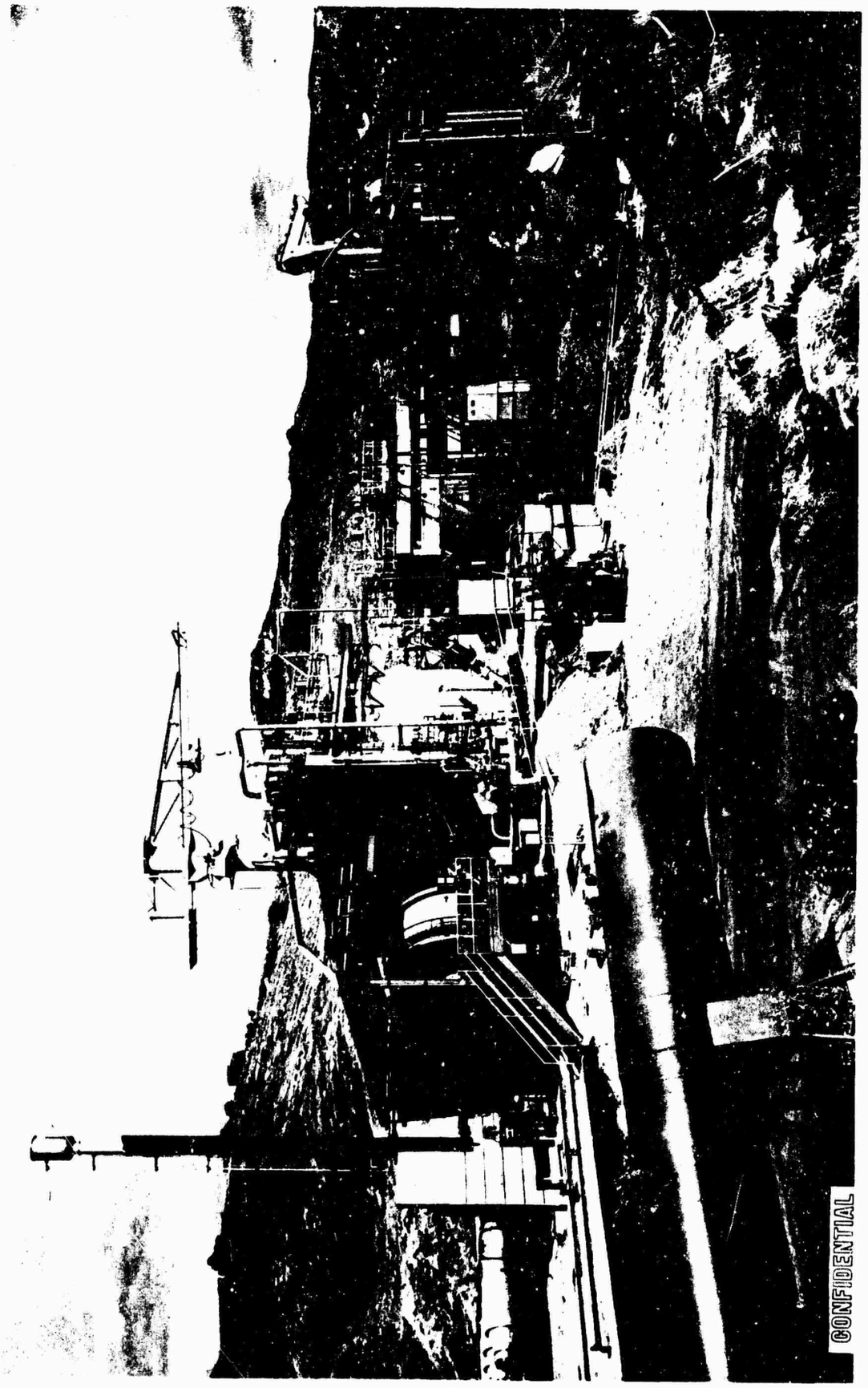

6RK36-3/11/66-R11

Figure 297. High-Pressure Facility, D-2

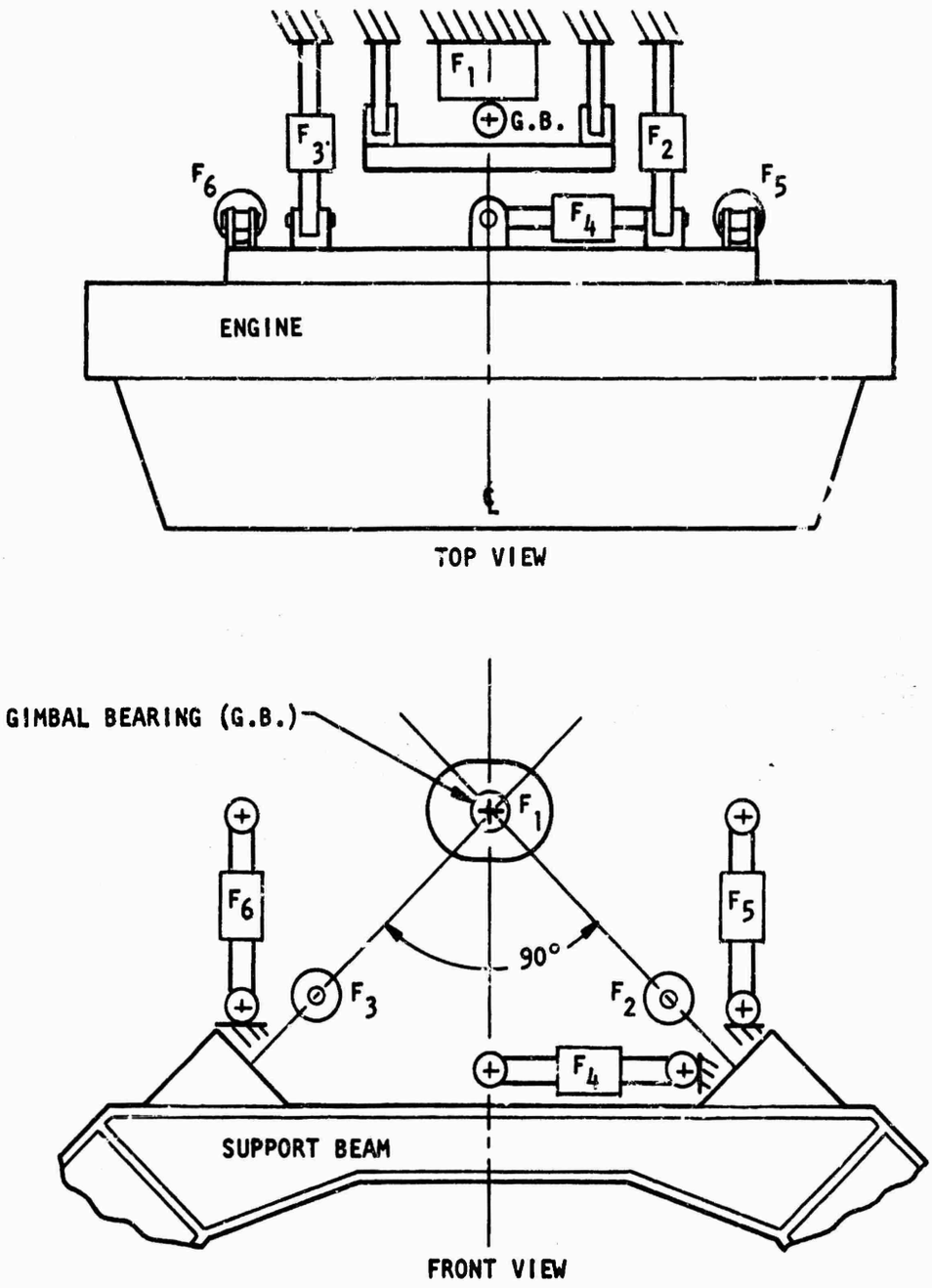

Figure 298. Thrust-Measuring System

(U) The capability of remote-controlled thrust calibration is provided by a servocontrolled hydraulic calibration system which uses a system of hydraulic rams and calibrated load cells. The calibration load cells are calibrated against secondary standards.

(U) Several systems were available for overboard flow of propellants. A fuel dump system and burnoff stack disposed of excess fuel coolant. A hot-gas line provided ducting capability for hot tapoff gases, and an oxidizer dump system downstream of the main oxidizer valve provided a means of achieving a rapid fuel-rich cutoff. The facility is also equipped with a servocontrolled hydrogen system to operate a gas generator which could be utilized for hot-gas ignition or for hot-gas secondary base bleed for the chamber.

(U) The test facility contains an oxidizer sampling system which permits taking two oxidizer samples at predetermined times during a test. The oxygen samples are analyzed in the facility chemistry laboratory for nitrogen dilution. The oxygen sample system is shown schematically in Fig. 299. Two such systems were installed to obtain oxygen samples at start and at cutoff to obtain a history of oxygen dilution during the tests. The oxygen samples were analyzed for nitrogen dilution by the Nitrometer method per MIL-P-25508D. The Nitrometer was calibrated against samples of oxygen of known purity.

(U) Chamber Handling. The handling equipment utilized for the 250K thrust chamber assemblies consists of a spreader bar, slings, and stabilizing cables to pick up the chamber by trunnions located on the outer body. The capability of rotating the chamber 360 degrees is thus provided. For installation on the test stand, the chamber is picked up from the shipping pallet and rotated 90 degrees from its horizontal position and moved by mobile crane to the thrust mount of the test stand for installation. The handling equipment in use is depicted in Fig. 300. The same handling equipment was used throughout the manufacturing process to handle the individual components also.

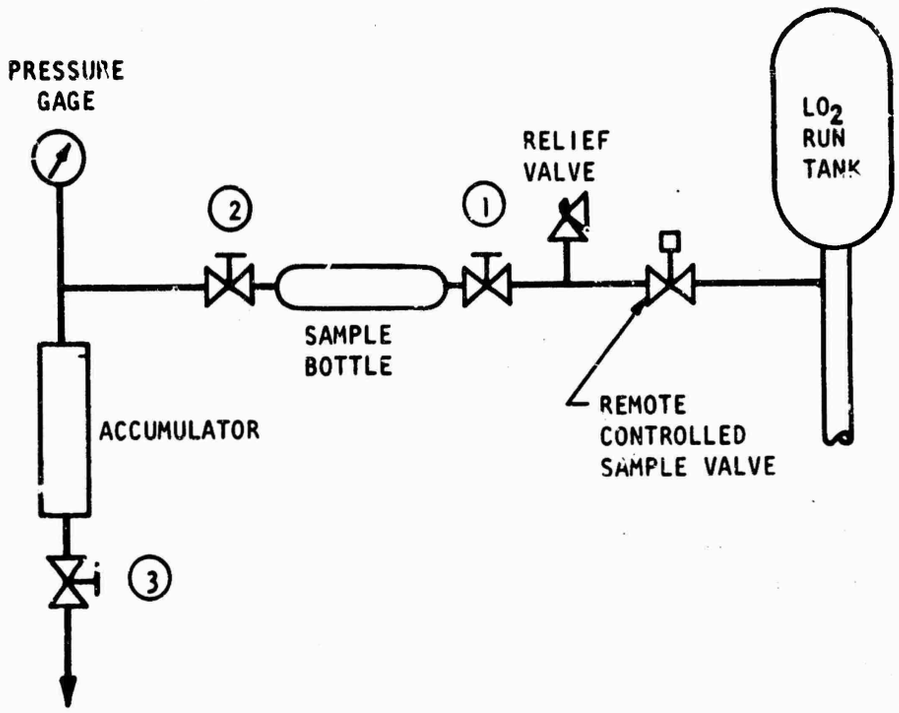

Figure 299. Liquid Oxygen Sample System Schematic

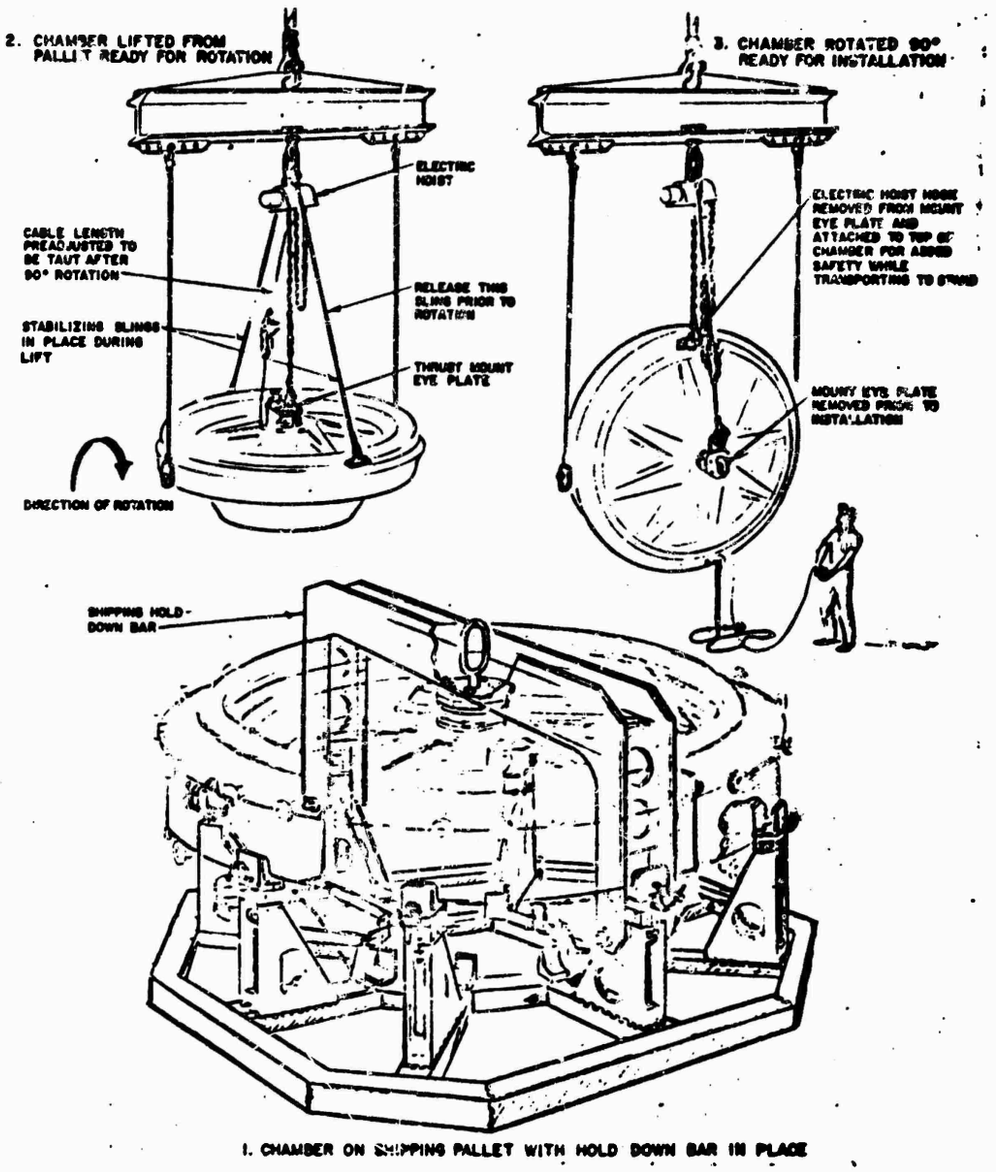

Figure 300. Aerospike Thrust Chamber Handling Equipment

(U) The shipping pallet also served the functions of assembly and disassembly. The chamber was assembled on the bed of the truck used to transport it to the test site. Disassembly on site was also possible with no extra handling equipment required.

(U) Solid-Wall Test Series. Nine mainstage tests were conducted during the solid-wall test program. The solid-wall chamber was operated with ambient gaseous hydrogen and liquid oxygen. These tests operated the injector over the design range of chamber pressure and mixture ratio. Three satisfactory hot-gas tapoff tests and two pulsing tests were conducted. There was no evidence from the oxidizer manifold pressure transducers that instability was initiated as a result of firing the pulse guns during mainstage. Figure 301 shows the solid-wall chamber operating during mainstage.

(U) Blowdowns. Before beginning the solid-wall tests, a series of propellant and water blowdowns was conducted to characterize each system and verify facility capabilities. Two hypergol (ClF_3) ignition tests were conducted in conjunction with fuel blowdowns. The blowdowns and ignition tests provided information concerning priming characteristics, pressure drops, ignition reliability, flow control system regulation, and cutoff purging characteristics. Consistent and predictable oxidizer and water priming was provided by cavitating venturi in each system. A sonic flow venturi was used in the gaseous hydrogen system for flow control and measurement.

(U) Ignition Tests. Hypergol ignition tests were conducted at the extremes of the intended operating conditions. Chlorine trifluoride (ClF_3) was used as the ignition source. The hypergol ignition system consisted of a 100 cu in. slug of ClF_3 pressurized by gaseous oxygen tapped off the main oxidizer system. The ignition combustion was sustained by gaseous oxygen and main fuel after the ClF_3 had been expelled. A schematic diagram

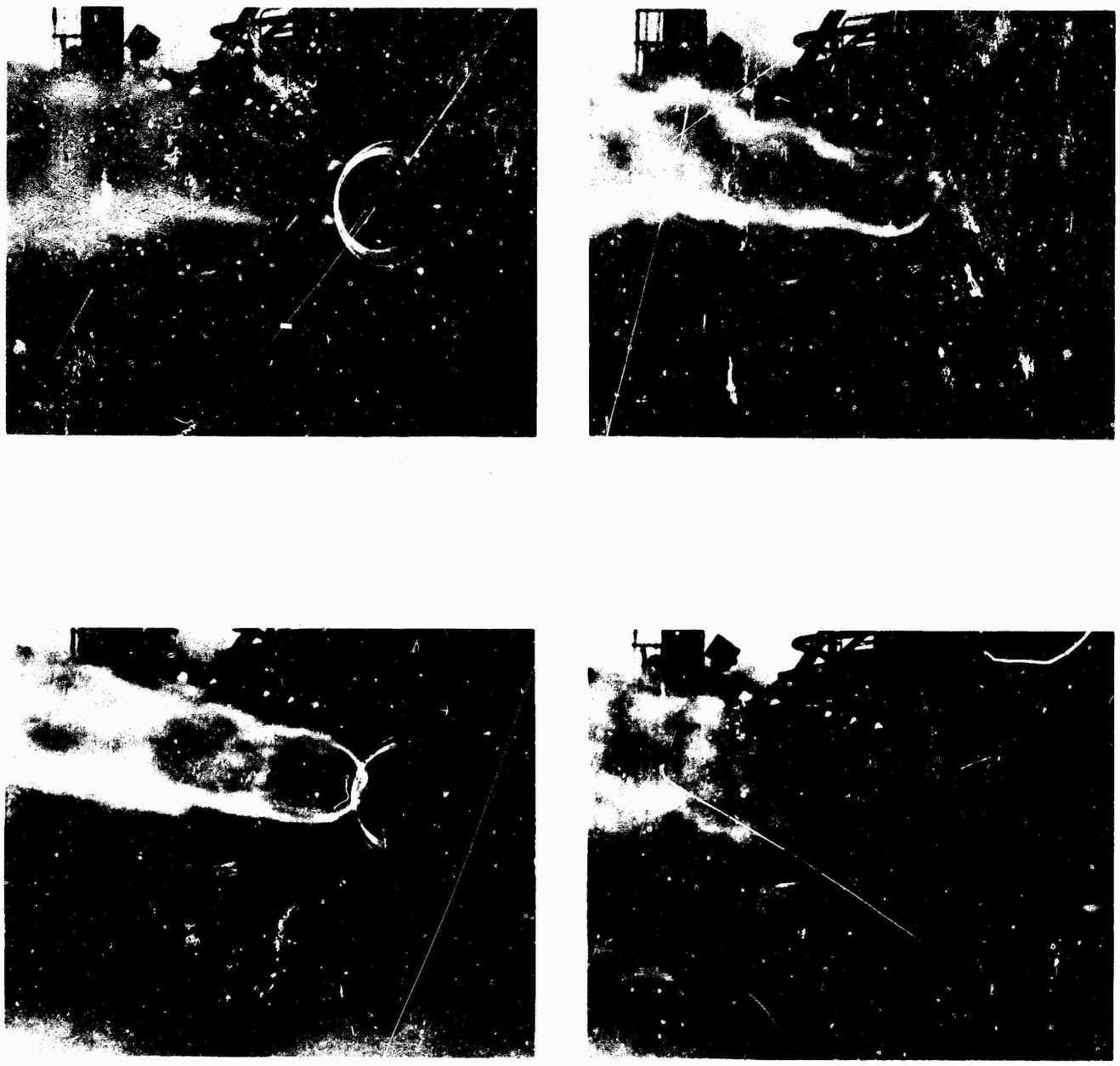

Figure 301. 250K Solid-Wall Operation on Nevada Field Laboratory Test Stand Under Different Test Conditions

of the hypergol system and a discussion of the solid-wall and tube-wall start sequences are presented in Appendix VIII.

(C) Hot-Firing Tests. A summary of the solid-wall mainstage test results is presented in Table 83. Chamber pressure and mixture ratio excursions over ranges from 353 to 1289 psia and 5.00 to 7.10 (o/f), respectively, were accomplished. Pulse guns were fired into the combustion chamber of one compartment at the extremes of chamber pressure with no instability initiated. Hot-gas tapoff was accomplished at the low and intermediate chamber pressures.

(C) The first test (No. 006) was scheduled to check out the facility and chamber and also to obtain performance data under throttled operating conditions (P_c = 908 psia) and low mixture ratio (5.0 o/f). Erosion of the diaphragms of two chamber pressure Photocons located 1/2 inch below the injector face resulted in burnout of the ports. Oxidizer-rich, hot-gas flow through one of the burned-out ports caused erosion damage to two adjacent injector oxidizer strips. The chamber was removed from the test stand, disassembled, and the damaged strips were repaired as described in detail in the Hardware Inspection section. The repaired area was carefully inspected by borescope after each subsequent test.

(C) The second mainstage test (No. 008) was conducted at throttled operation (P_c = 540 psia) and mixture ratio of 5.89 (o/f). No further obvious hardware damage occurred during this or any of the subsequent tests of the solid-wall test series.

(C) The third test (009) was scheduled to accomplish mixture ratio excursion (6.91 o/f) and stability rating. A mistimed signal fired the pulse gun prior to achievement of mainstage. Hot-gas tapoff was accomplished on test 010. The mainstage duration of 0.11 second proved to be inadequate to acquire tapoff temperature data. The schedule duration of

TABLE 83

(C) 205K SOLID-WALL TEST PROGRAM: SUMMARY OF MAINSTAGE TESTS

Test No.	Date, 1967	Chamber Pressure, psia	Mixture Ratio, o/f	$\dot{w}$ Fuel	$\dot{w}$ Oxidizer	$\dot{w}$ Water	Duration, seconds	Comments and Objectives
006	4-4	908	5.00	41.2	205.5	228.7	0.600	Chamber pressure Photocon burnthrough injector reparied posttest
008	4-13	504	5.89	21.3	125.1	214.6	0.120	Throttled operation
009	4-14	594	6.91	22.0	151.8	221.2	0.110	MR excursion, pulse gun misfired
010	4-17	423	5.20	18.8	97.6	229.3	0.110	Hot-gas tapoff, MR excursion
011	4-18	365	6.50	12.3	80.0	232.2	0.300	Hot-gas tapoff
012	4-19	353	6.10	12.1	74.3	237.8	0.240	Pulse gun
015	4-20	798	7.10	31.5	222.6	229.2	0.120	Hot-gas tapoff
016	4-21	1005	6.81	42.1	286.8	239.3	0.120	Throttled operation
017	4-22	1289	6.09	67.9	413.4*	239.8	0.060	Pulse gun

*Full flow as measured by the flowmeter was not achieved in the chamber.

CONFIDENTIAL

test 011 provided more stabilized chamber pressure and satisfactory hot-gas tapoff data. The measured tapoff temperature of 800 F was achieved at a chamber pressure of 365 psia. Stability rating with the pulse gun was accomplished on test 012 at a chamber pressure of 353 psia. There was no indication that instability had been induced. The oxidizer manifold high-frequency Photocons were relied upon to indicate pressure traces because the P_c Photocon ports were welded closed following burnout on test 006.

(C) Satisfactory hot-gas tapoff was again accomplished during test 015 at a chamber pressure of 798 psia and mixture ratio of 7.10 (o/f). The chamber pressure was increased to 1005 psia during test 016 at a mixture ratio of 6.81 (o/f).

(C) The final test of the solid-wall series was conducted at a chamber pressure of 1289 psia at near nominal mixture ratio (6.09 o/f). A pulse gun firing into one compartment during mainstage failed to initiate instability. An accelerometer installed on the pulse gun itself provided the indication of pulse gun firing. Posttest inspection of the hardware indicated that surface erosion of the oxidizer strip repair had been sustained.

(U) Posttest Hardware Inspection. The chamber was removed from the test stand following the first solid-wall test (test 006). The injector did not sustain damage other than in the area of the two burned-out Photocons. Figure 302 shows a typical area of the injector strips. The uncooled combustion zone walls (inner and outer) sustained erosion as shown in Fig. 303. Both the inner and outer throats were undamaged.

(C) Inspection revealed that two oxidizer strips adjacent to one of the damaged Photocon bosses sustained erosion which exposed the feed passages. Because it was obvious that heat flux and wall erosion in the vicinity of the Photocon location was more severe than anticipated, the Photocon bosses

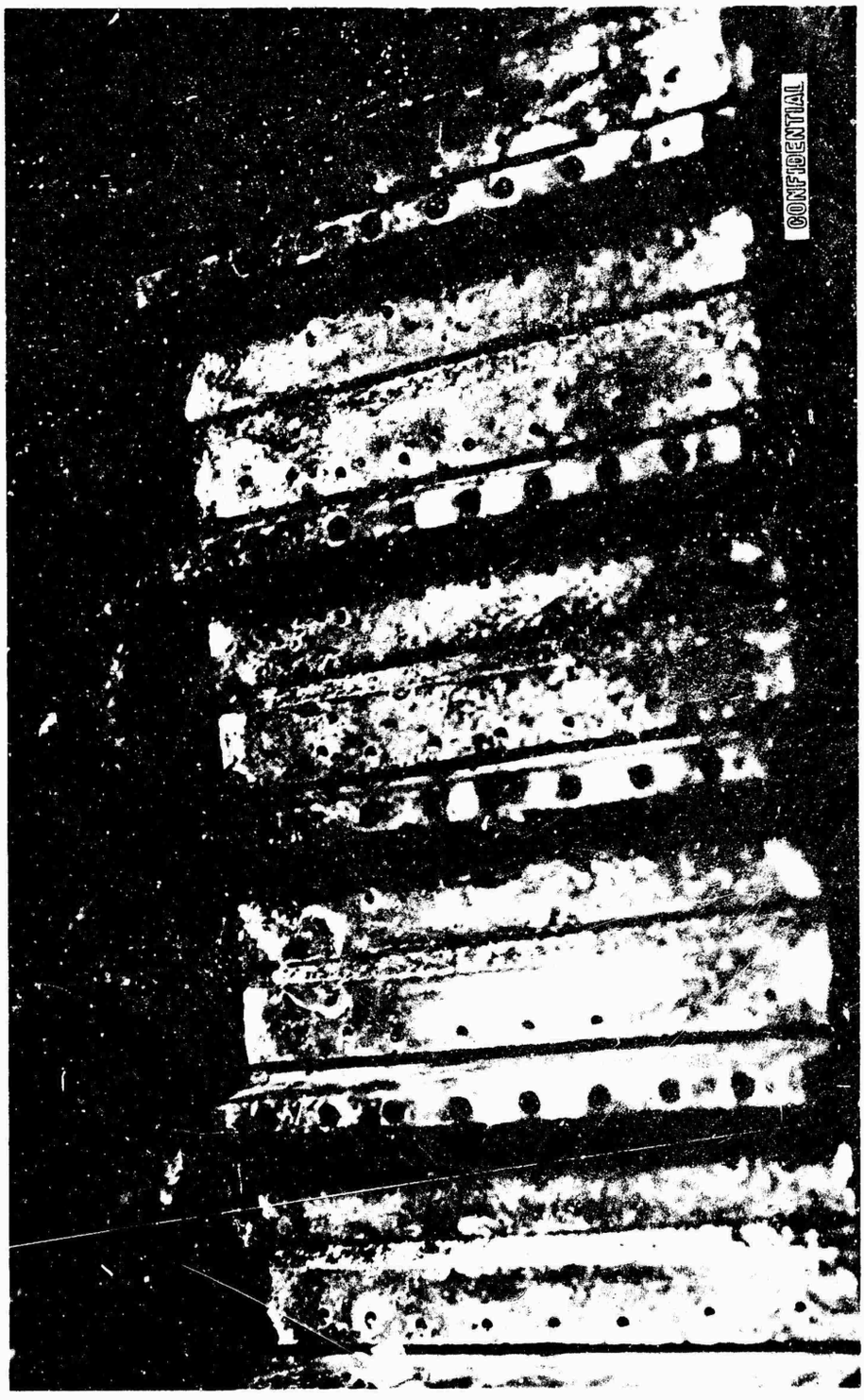

Figure 302. Injector Condition Posttest 006

Figure 303. Uncooled Chamber Posttest 006

were welded closed. The repair technique (Fig. 304) involved applying a gold-copper alloy braze over the strip surfaces to close off the erosion areas. Orifices were drilled into the adjacent fuel steeples to put an umbrella of fuel over the strip repairs. The oxidizer orifices were not redrilled in the repaired strips.

(C) The above-described repair technique was applied to the strips of a 2.5K segment and successfully tested over a range of chamber pressures up to 1500 psi to verify the durability of the repair technique prior to resumption of testing of the 250K chamber.

(U) Several systems were available for overboard flow of propellants. A fuel dump system and burnoff stack disposed of excess fuel coolant. A hot-gas line provided hot tapoff gas ducting capability and an oxidizer dump system downstream of the main oxidizer valve provided a means of achieving a rapid fuel-rich cutoff.

(U) Solid-Wall Series Posttest Inspection. Following satisfactory completion of the solid-wall test series, the injector and chamber were returned from the test stand and disassembled for inspection, repair, and modification.

(U) The two adjacent oxidizer strips which had been previously reworked at the test site following test 006 were completely removed from the injector body and replaced with new strips.

(U) Minor edge erosion and slag deposits were noted on all 40 baffles adjacent to the inner-body wall (Fig. 305). The edge erosion, which started approximately 1.5 inches downstream of the injector face, appeared to correspond with the start of a series of machining "steps" on the chamber wall contour. Postassembly measurement of the injector and inner chamber indicated the gap to be approximately 0.2 inch. Therefore, it was concluded

Figure 304. Injector Strip Repair Posttest 006

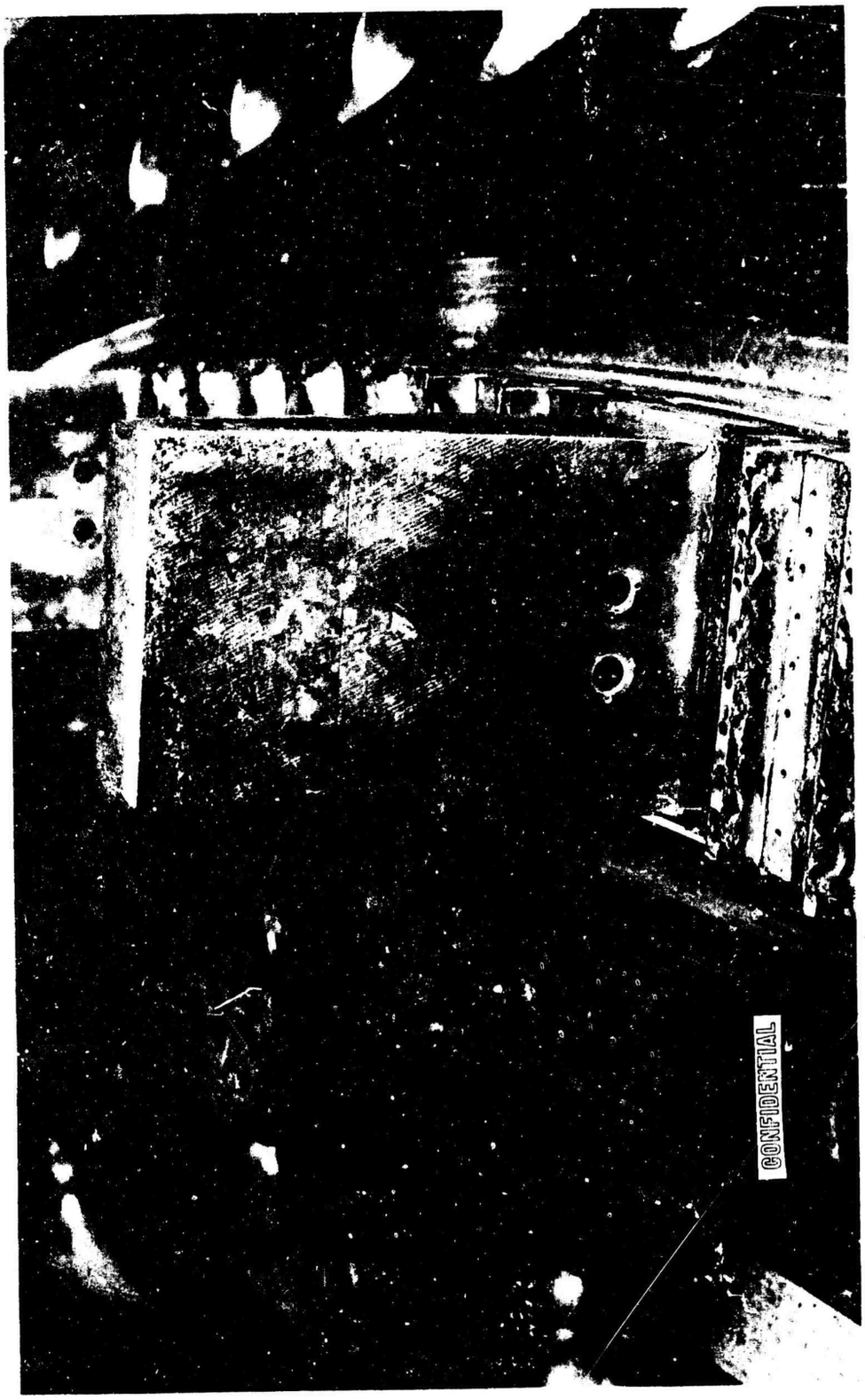

Figure 305. Erosion of Baffle Edges and One Tapoff Port

that an excessive baffle-to-chamber wall gap, together with the flow of slag from the chamber wall across the copper baffle surface, resulted in an increase in the local heat input and the noted baffle edge erosion. A layout of the eroded area with respect to the coolant passages indicated that an adequate wall thickness remained and no repair was necessary.

(U) Of the 160 tapoff ports, one sustained erosion of the liner at the entrance (Fig. 305). Cold-flow evaluation of the injector did not reveal misalignment of the tapoff fuel bias orifice to be the cause of erosion. Therefore, it was concluded that the erosion occurred because of a void in the sleeve-to-baffle braze joint, which impaired the heat transfer from the steel sleeve to the copper baffle body. Because the erosion appeared to be nonprogressive, and the intended structural function of the sleeve in the region of the baffle coolant passages was still effective, no repair was made.

(U) Shrapnel-type damage was observed on two of the baffle faces. The damage was in-line with the "pulse gun," which was mounted in the outer chamber wall and used to stability rate the injector during tests 009, 012, and 017. During preparation for repair, a fragment from the steel diaphragm used in the pulse gun assembly was found lodged within one of the copper baffle faces. It was concluded that both baffles were damaged by fragments from the pulse gun diaphragm, and the baffles were repaired.

(C) Light, random, oxidizer strip end and body land erosion was observed adjacent to the combustion baffles (Fig. 306). Further investigation revealed that the incidence of erosion was primarily in regions of maximum throat gap change; i.e., maximum intercompartmental gas flow. In cases where slag flow patterns were visible, it was apparent that secondary hot-gas flow fields existed in the cavity between the injector body and chamber wall. The noted erosion appears to be the result of oxidizer-rich gases being driven across the end of the oxidizer strip and body land by inherent discontinuities in propellant injection density and/or variations in throat

CONFIDENTIAL

Figure 306. Erosion of Strip Adjacent to Baffles

gap. A marginal cooling condition is likely to exist at these lands during tube-wall chamber testing because of the remoteness of the coolant passages. Therefore, to assist in cooling this area, the 0.043-inch-diameter fuel bias orifices at the side of the injector body were enlarged to 0.60 inch in diameter adjacent to each baffle.

(U) The condition of the combustor bodies was good, with expected general combustion zone erosion on both the inner and outer bodies. Figure 307 and 308 show typical erosion patterns. The extent of combustion zone erosion did not appear to have increased appreciably over that observed following posttest 006 disassembly. Heat transfer analysis of the uncooled combustion zone walls indicated that the chamber walls could have reached the melting point within 500 milliseconds of mainstage position. However, the erosion pattern revealed that local high heat flux areas existed at the propellant impingement point below fuel strips which probably started to melt early in the test. The slag-flow pattern on the chamber walls indicated that intercompartmental gas flow existed in several compartments around the chamber circumference. Analysis revealed that the direction of slag flow could be related to throat gap, i.e., slag flow from a small throat gap region to a larger gap region. Figure 309 is a plot of throat gap and indicated gas-flow direction from slag-flow pattern.

(U) The throat was in excellent condition with the exception of one small area of erosion caused by slag deposition on the convergent section which interrupted the water film. The throat gap variation was examined in connection with measured side loads. The directions of these loads were as expected from throat gap variation, i.e., toward the smallest throat area. Analysis is limited by the short duration and load oscillation.

(C) Tube-Wall Test Series. Five mainstage tests were conducted with two chamber assembles during the tube-wall test program. A summary of the tests is presented in Table 84. Tests were conducted at nominal 600- and

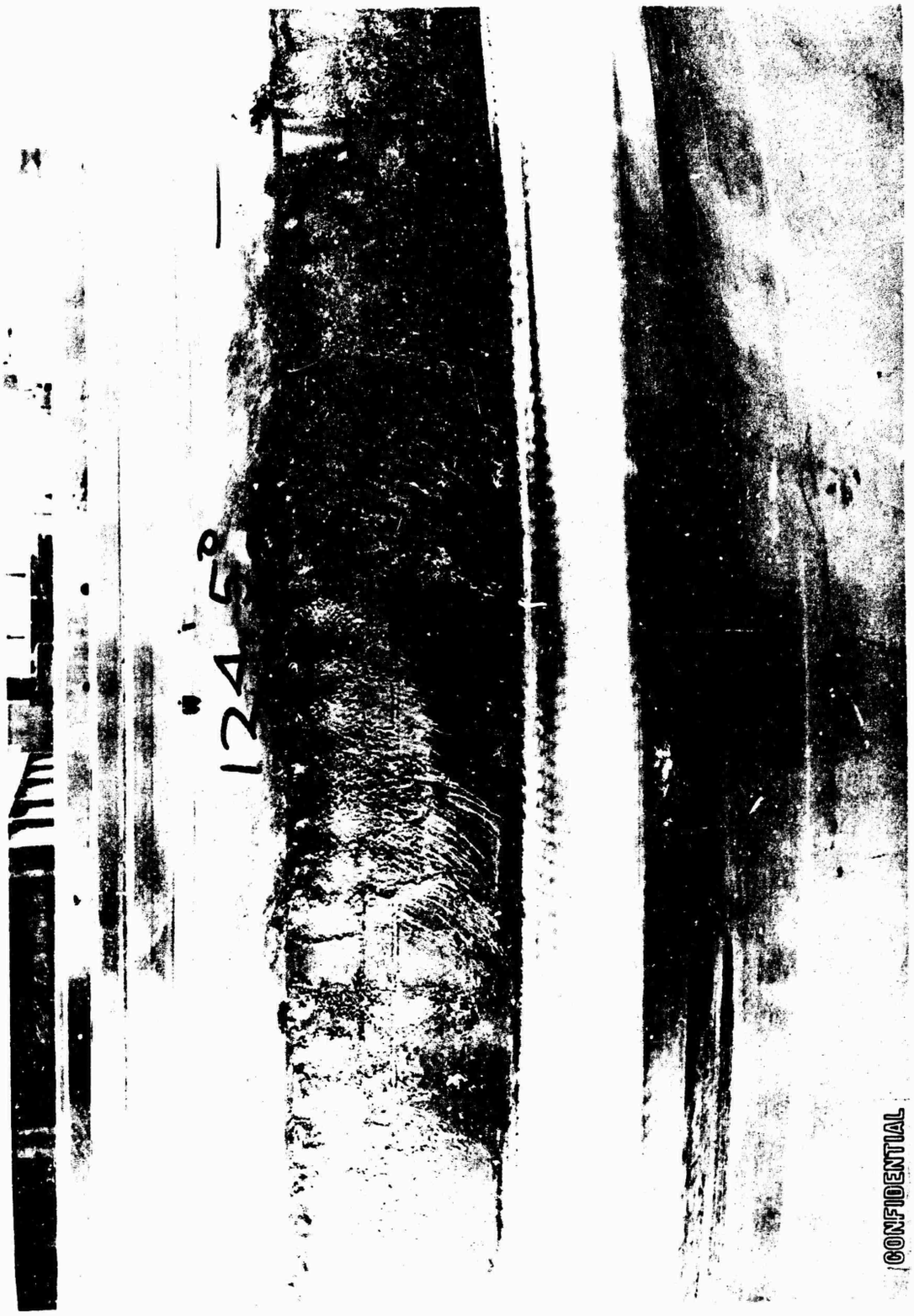

LXE35-4/25/67-C1

Figure 307. Erosion Pattern of Solid-Wall Innerbody, 124.5-degree Location

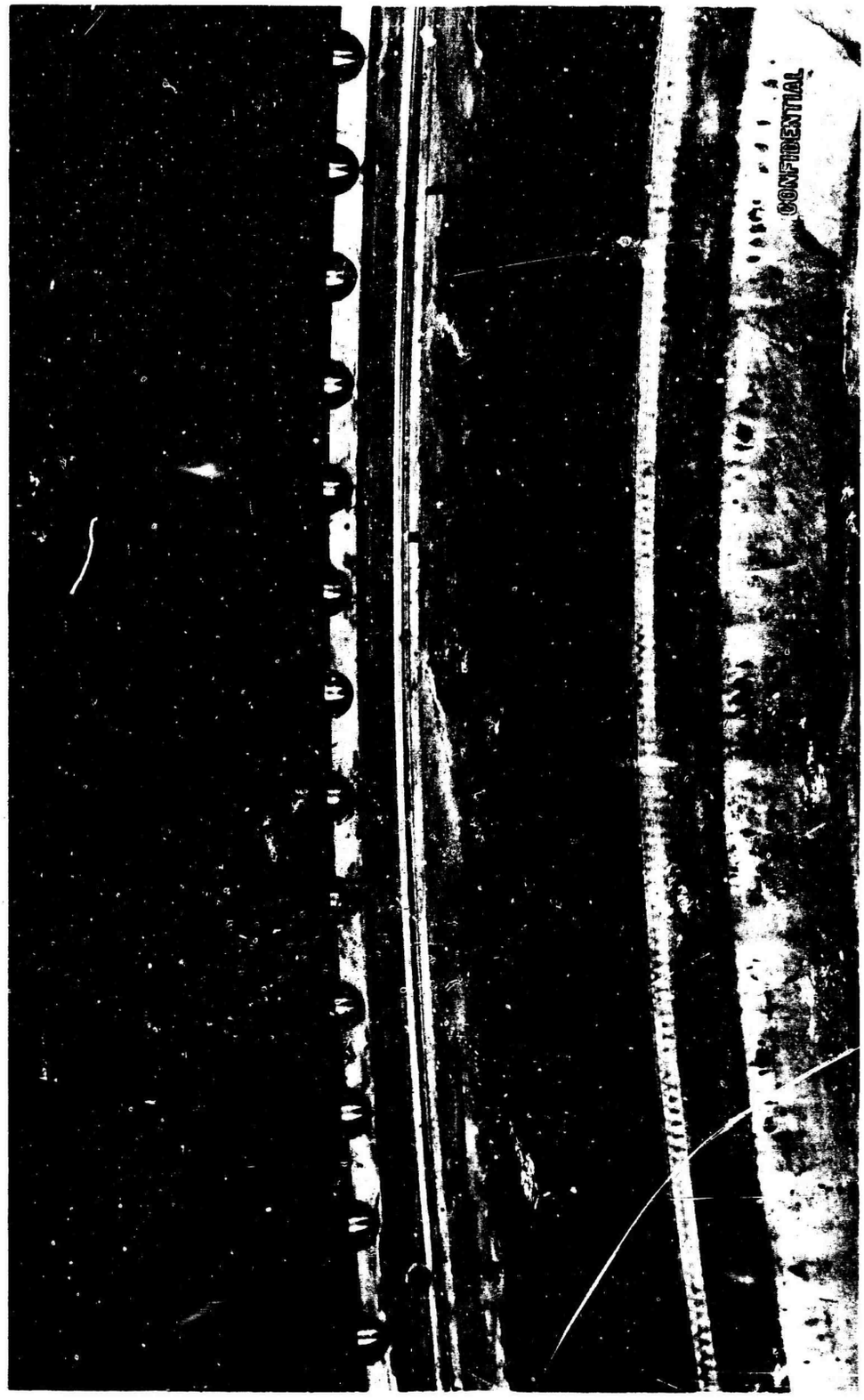

Figure 308. Erosion Pattern of Solid-Wall Outer Body

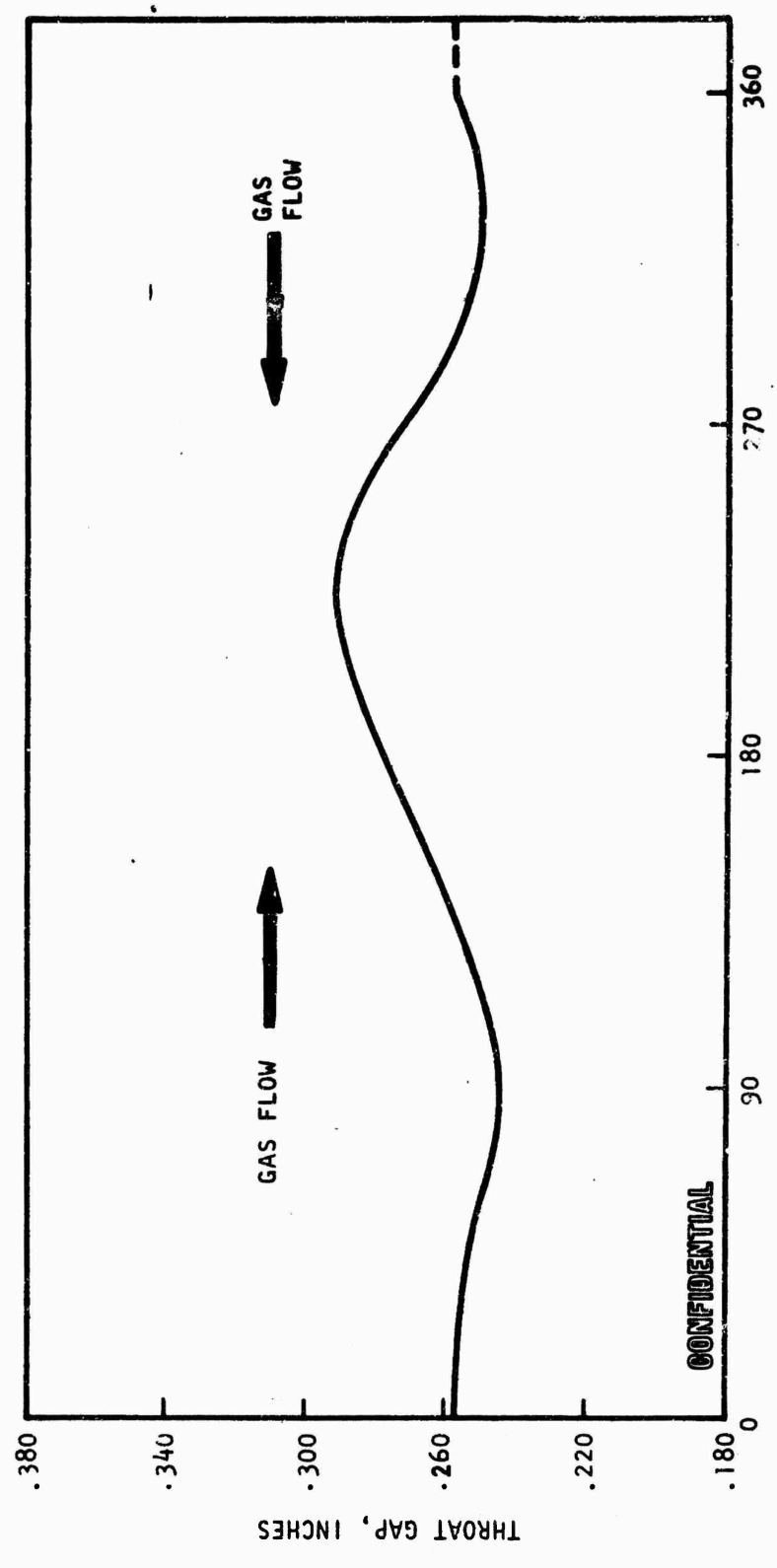

Figure 309. 250K Solid-Wall Thrust Chamber Throat Gap Variation, Posttest 004

TABLE 84

(C) 250K TUBE-WALL TEST PROGRAM SUMMARY OF MAINSTAGE TESTS

Test No.	Date, 1967	Chamber Pressure, psia	Mixture Ratio, o/f	Duration, seconds	Objectives and Comments
022	6/29	496.7	4.95	0.08	Transition checkout
023	6/30	608.8	4.95	0.40	Performance evaluation
024	7/1	—	—	—	Performance evaluation; terminated in transition by malfunction of redline cutoff device
025	7/2	816.7	7.07	1.60	Performance evaluation; hardware burnout
026	9/20	—	—	—	Ignition checkout
027	9/29	824.7	5.04	0.28	Transition checkout; chamber removed for inspection
028	10/7	897.9	5.90	0.80	Performance evaluation; cutoff due to high accelerometer readings

NOTE: Tests No. 022 through 025 were conducted with tube-wall chamber No. 1.

Tests No. 026 through 028 were conducted with tube-wall chamber No. 2.

900-psia chamber pressures at nominal mixture ratios from 5:1 to 7:1. Nozzle and combustion chamber performance and fuel bulk temperature rise data were obtained.

(U) The major difference between the two chambers used for tube-wall testing is that the No. 1 assembly was used for tests 022 through 025. The No. 2 assembly was used for tests 026 through 028. This unit only had tapoff provisions on two baffles. The injectors were otherwise identical. The tube-wall chamber installation on the test stand is shown in Fig. 310 .

(U) No. 1 Tube-Wall Test Series. A series of fuel and oxidizer blowdowns was conducted prior to mainstage testing. The purpose of these blowdowns was to verify system pressurization operation and fuel mixer system operation, and to establish system pressure drops. Because some of the systems were unchanged from the solid-wall test series, much of the data and experience gained during that program were directly applicable. Total fuel flowrate was controlled by means of a sonic venturi at the chamber inlet, and fuel temperature was controlled by a servo mixer system. Dump fuel flowrate was controlled by a sonic nozzle located at the chamber dump manifold outlet. The oxidizer flowrate was controlled by a cavitating venturi at the chamber inlet during the No. 1 tube-wall test series. Mainstage operation was achieved for a very short duration.

(U) The purpose of the first mainstage test (022) was to check out startup and shutdown sequences and general test stand operation. Figure 311 shows typical tube-wall thrust chamber operation (80 milliseconds). The data indicated that the targeted operating conditions were achieved and start and cutoff transients were as expected.

(U) Mainstage duration of 400 milliseconds was achieved on test 023. The objective of this test was the determination of mainstage performance with

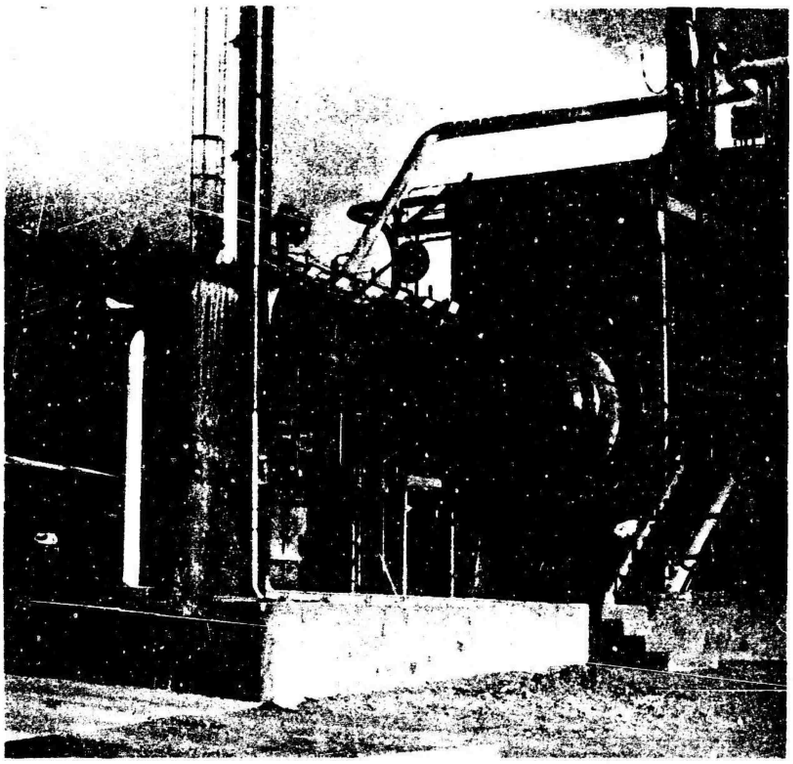

Figure 31C. Tube-Wall Thrust Chamber Mounted on Reno Test Stand

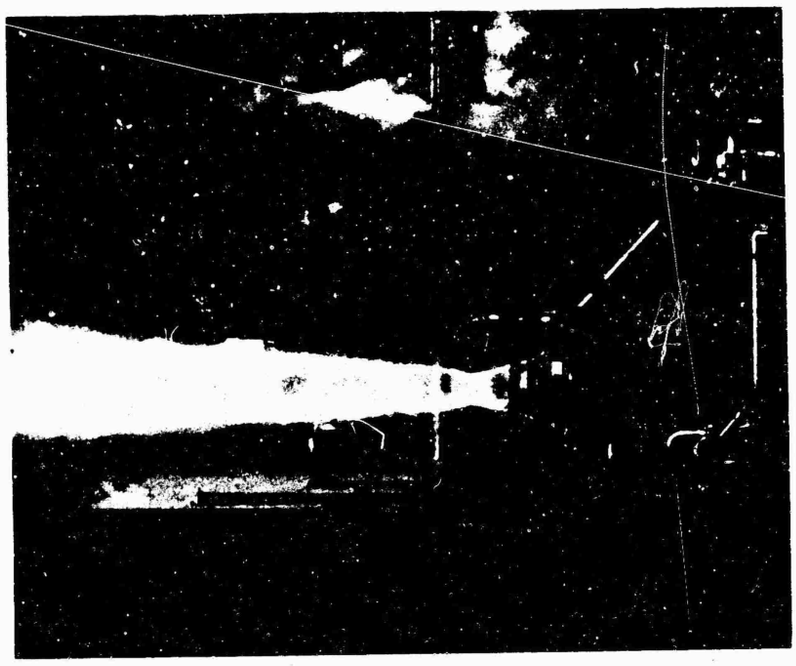

Figure 311. Tube-Wall Thrust Chamber Operation

secondary base bleed at site level. The data showed that the measured combustion efficiency was quite high despite the fact that the test was of short duration and chamber pressure had not reached stabilized value. The indications were that slightly longer duration would have increased performance and verified the high performance gained on 2.5K segment tests.

(U) Analysis of the data indicated that chamber operation was satisfactory except for a pressure rise in the inner-body, tube-to-backup structure cavity after cutoff. The significance of the rise in backup structure pressure is that it was an indication of fuel leakage on the backup structure side. Visual inspection revealed no damage other than minor tube crown braze wash at the throat. Subsequent (posttest 025) inspection revealed that these tubes had sustained splits on the hot-gas crown and on the backup structure side.

(C) Test 024 was targeted for a chamber pressure of 900 psia for a mainstage duration of 3 seconds. The targeted mixture ratio was 6.0 (o/f). The test was terminated during fuel lead because of failure of a facility fuel inlet temperature-sensing bulb. The corrective action taken was to replace the temperature-sensing bulb.

(C) Test 025 was an intended repeat of the previous test target conditions. Targeted and achieved conditions for test 025 are listed below:

	Targeted	Achieved
Chamber Pressure, psia	900	820 to 850
Oxidizer Flowrate, lb/sec	282.2	282.7
Fuel Flowrate, lb/sec	97	101.2
Injector Fuel Flowrate, lb/sec	47.5	40
Injector Overall Mixture Ratio, o/f	6.0:1	7.07:1
Dump Fuel Flowrate, lb/sec	45.6	37.5
Duration, seconds	3.0	1.5

The objective of test 025 was the determination of performance at site conditions with two secondary base bleed flowrates.

(U) Targeted mainstage duration was not achieved on test 025 because of early cutoff by a safety cutoff device. Considerable damage was sustained by the thrust chamber and injector as a result of internal burning of the hardware during mainstage. Burnout of the oxidizer and tapoff manifolds resulted in considerable facility damage within the altitude capsule.

(U) General Hardware Damage Incurred During Test 025. Following test 025, the No. 1 tube-wall chamber was removed from the test stand and returned to Canoga Park. The chamber was disassembled and thoroughly inspected to analyze the cause of chamber burning. Many of the component parts of the chamber were refurbished and used on the No. 2 tube-wall assembly.

(U) The area of greatest injector face damage occurred from approximately 025 to 130 degrees. (The chamber nomenclature and orientation system is described in Appendix VI.) Rather severe strip burning also occurred in compartments from 220 to 240 degrees and from 280 to 340 degrees. Strips were badly burned in these areas with the greater proportion of damage occurring on the outer end of the strips. An overall view of the injector is shown in Fig. 312. A view of the injector from 085 degrees to 105 degrees sustaining the greatest damage is shown in Fig.313 .

(U) Minor strip face erosion was sustained at several areas. The injector was essentially undamaged in areas from 005 to 015 degrees, from 140 to 200 degrees, and from 240 to 265 degrees. A typical undamaged section of the injector is shown in Fig. 314.

(U) The oxidizer closeout ring was burned out from approximately 063 to 099 degrees and from 225 degrees to 234 degrees. These two areas of

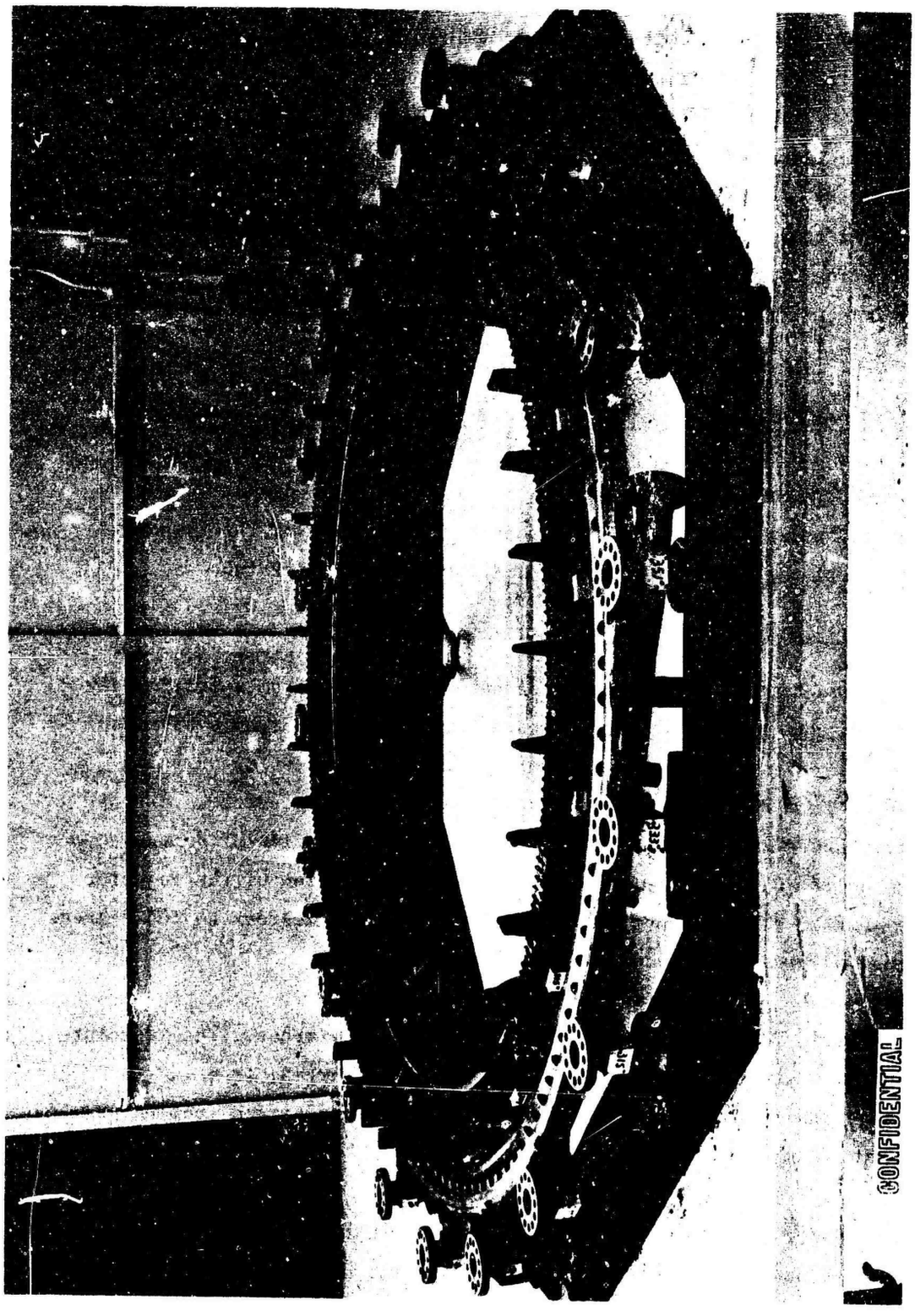

LXE25-7/6/67-C5A

Figure 312. Overall View of Injector

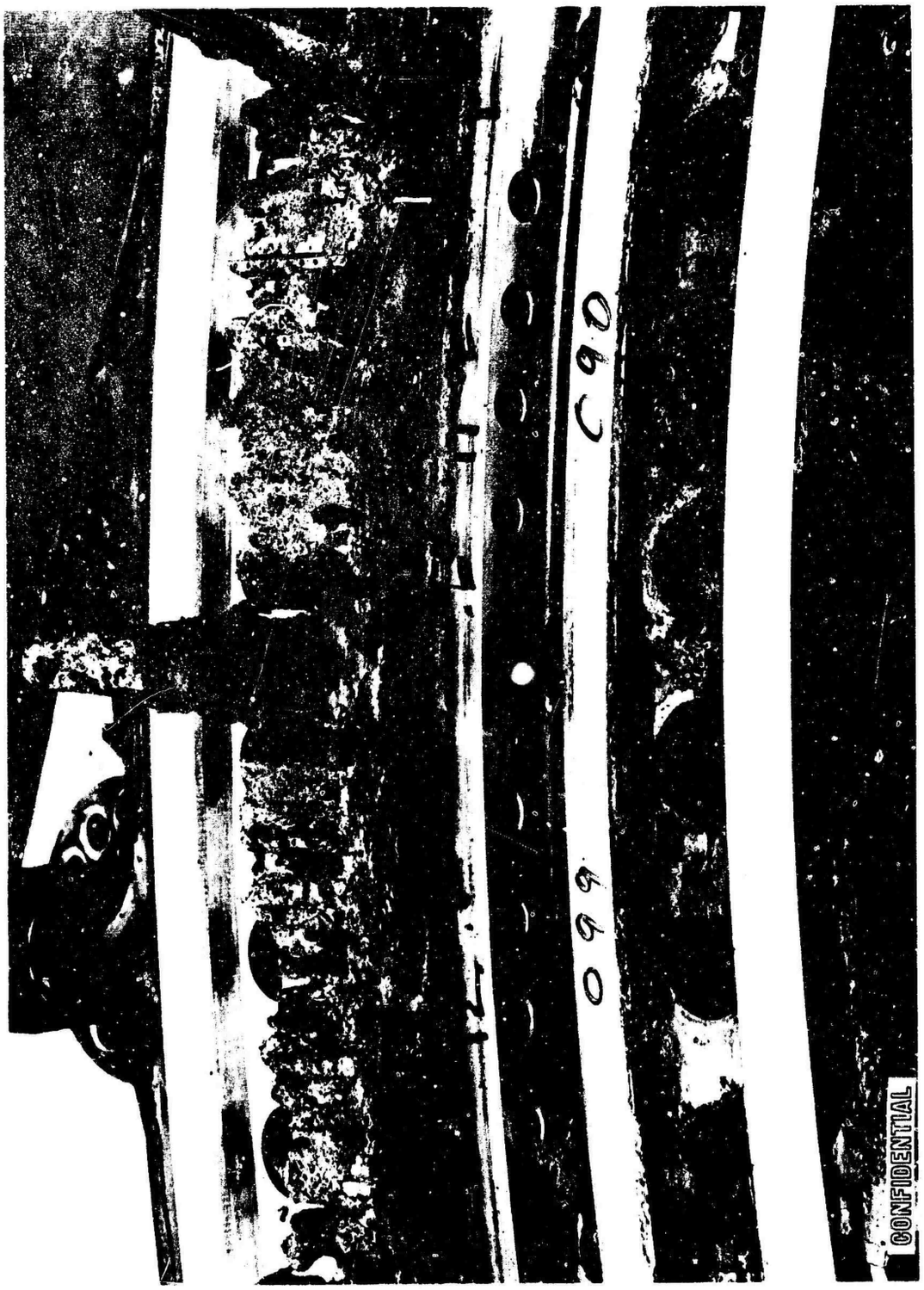

1XF25-7/6/67-C5U

Figure 313. Injector Damage (Inner), 085 to 105 Degrees

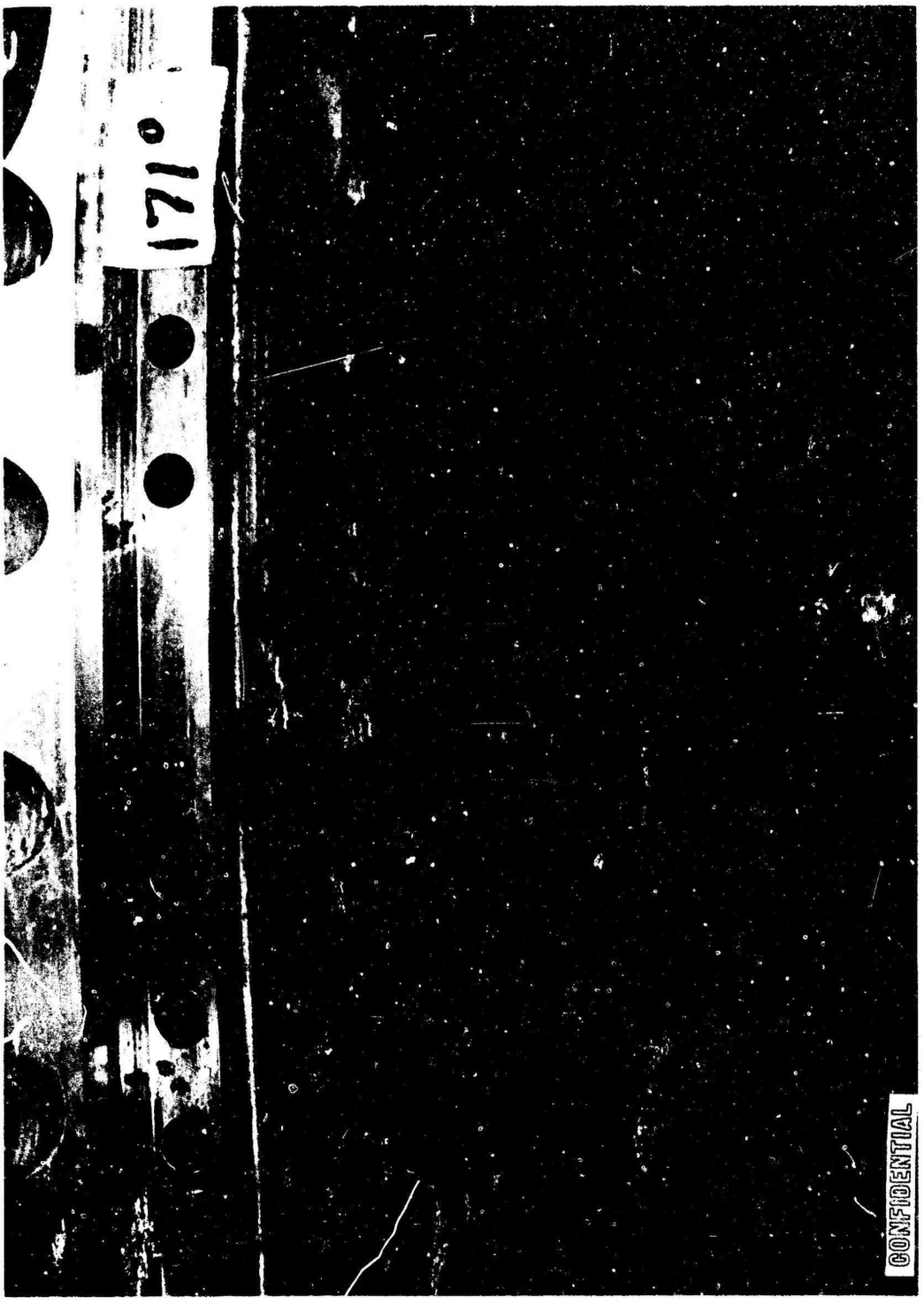

LXE25-7/6/67-C2Y*

Figure 314. Two Compartments of Chamber, Posttest 025

oxidizer closeout ring burning were the result of different burn paths. It is obvious that the closeout ring burnout from 063 to 099 degrees was burned from the inside out (Fig. 313). Injector face burnout progressed back into the body and oxidizer feed passage and through the closeout ring into the injector-to-chamber gap cavity. The oxidizer closeout ring was clearly eroded from the outside in, at the area from 225 to 234 degrees, because of combustion and erosion within the injector-to-chamber gap.

(U) The fuel closeout ring was burned out in areas from 036 to 043 degrees, at 048 degrees, from 082 to 085 degrees, and from 099 to 111 degrees. The fuel closeout ring weld was found to be cracked in several areas of severe closeout ring erosion.

(U) It is evident from hardware inspection that the fuel closeout ring was burned through from the outside in, as a result of burning and erosion in the gap cavity. The weld cracking was determined to be caused by high stresses induced by severe erosion of the weld and closeout ring combined with less than 100-percent penetration of the weld.

(U) The failure analysis revealed that burnout of the tapoff system was an effect and not a cause of the incident. The hot-gas tapoff legs to the tapoff torus manifold were burned through at eleven locations. A sketch showing the hot-gas tapoff system is shown in Fig. 283. Abnormal operating conditions within the combustion chamber resulted in pumping of oxidizer-rich hot gas into the tapoff system in certain compartments. Erosion within the tapoff ports progressed into the oxidizer manifold. Then, oxidizer manifold pressure being higher than tapoff manifold pressure, oxidizer was forced into the tapoff system, which resulted in burnout of the tapoff legs as well as extensive erosion of the baffle tapoff ports.

(U) The oxidizer manifold sustained external burnout in the areas from 038 to 062 degrees, from 80 to 110 degrees, and 320 degrees. The oxidizer manifold was burned through as a result of burnthrough of the tapoff manifold.

(U) The chamber outer body sustained tube burnout and erosion at the injector end in the throat area and in the shroud area. It appeared that the vast amount of tube damage was due to injector burnout. A great deal of injector slag was deposited on the tubes in the areas of gross injector burnout. The tubes appeared to be essentially intact under the slag. Several tube samples (several tubes wide) were cut from the outer body. These samples were selected to be representative of the areas of major failure, incipient failure, and visibly unaffected areas. Metallographical analysis indicated that tube failures on the outer body were apparently secondary in nature and were a result of liquid metal erosion from the injector and thrust chamber injector ring combined with reduced coolant flow late in test 025. There are several signs which indicate that the failures are predominantly due to the slag flow. These are:

1. Slag is present on all the failed tubes. Microphoto analysis detected generous quantities of copper in the slag (Fig. 315 and 316).
2. Tubes from the same zones, but not slag affected, are full wall thickness with no signs of incipient melting (Fig. 317).
3. The tube crown erosion is nonuniform across the crown, but related more to the slag impingement (Fig. 315).
4. The tube splits are not necessarily in the center of the tube crowns (Fig. 315).
5. The incipiently melted layer on the tube crown is extremely thin, indicating an intense but short-duration heat flux (Fig. 318).

(U) Slag-free failed tubes on the outer body turned out to be almost non-existent. Where there were large slag-free areas, the tubes in these areas were found to be perfectly intact. Failed tubes which were visibly free of slag, except in one instance, were found to have heavy slag deposition when viewed under the microscope.

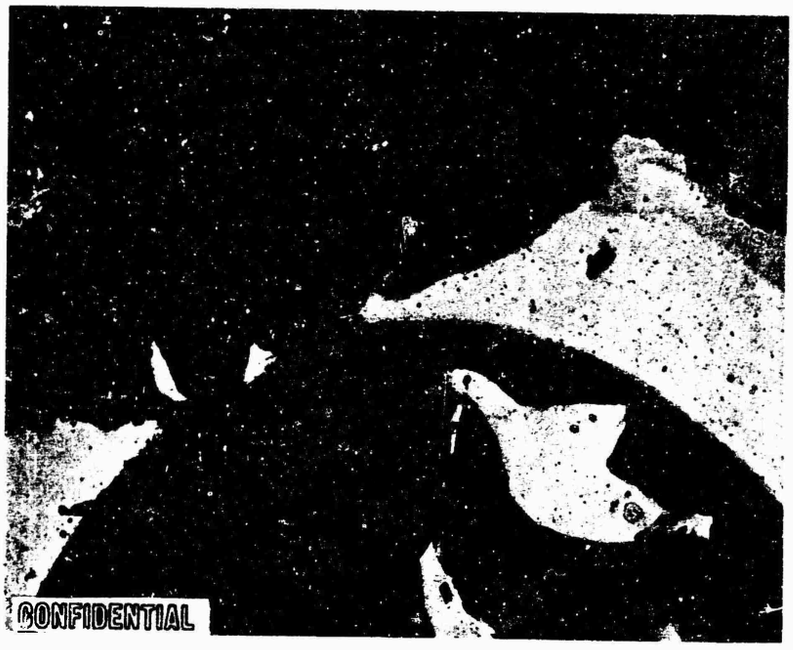

100X

Figure 315. Failed Tube With Slag Deposition at Injector Ring, Outer Body

100X

Figure 316. Failed Tube With Slag Deposition in Shroud, Outer Body

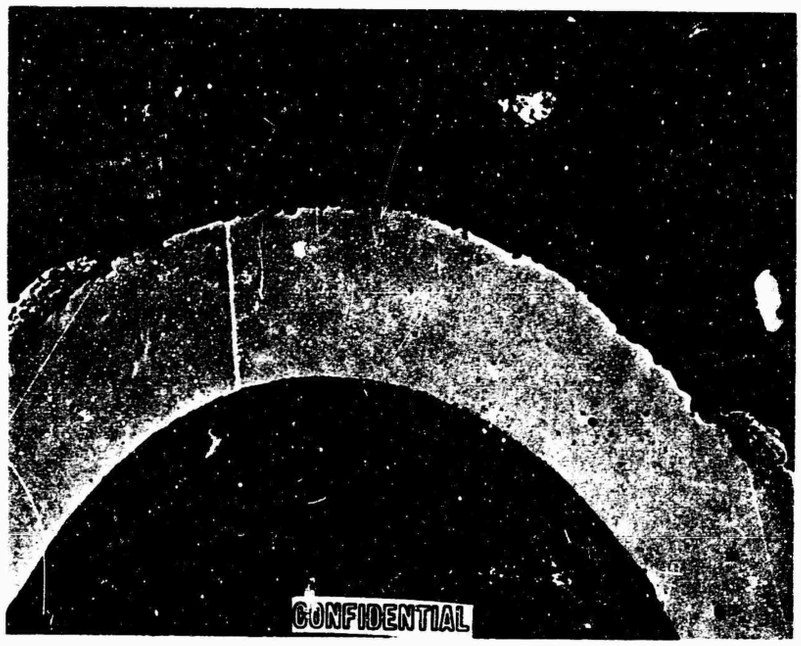

100X

Figure 317. Undamaged Tube at Injector End, Outer Body

100X

Figure 318. Tube at Throat, Outer Body With Incipient Melted Surface

(U) A general consistency of tube failure locations also added to the evidence that the outer-body tube failures were predominantly from slag. Wherever slag patterns were nonaxial, the tube failures followed the angular pattern with tubes above and below this line intact. A typical pattern would be failures at the injector ring, convergent contour, throat, and shroud along a 45-degree angle from axial. Failures would ignore zones of higher heat flux to maintain the above pattern.

(U) The chamber inner body sustained tube crown erosion on approximately 88 tubes. The majority of remaining tubes were essentially undamaged. Inner-body tube failures were not confined to areas of liquid metal flow. The majority of tube failures were in a zone 1/2 to 2 inches downstream of the injector ring and fairly consistently all the way around the combustor except for the following:

1. Areas between fuel strips
2. At and adjacent to baffle locations

Tube failures on the inner combustor body were predominantly due to hot-gas erosion in a localized band 1/2 to 2 inches below the injector face. Failures within this band are suspected to have occurred in runs 023 and 025, and probably a few in run 022. There were also tubes on the inner body which failed late in run 025 because of liquid metal erosion. These consisted of failures in the combustion, convergent, and throat sections in direct line with the injector failure.

(U) Tube samples were cut from the inner body 1 inch downstream of the injector ring at several locations. A typical photomicrograph of a failed tube is shown in Fig. 319 . There are definite indications here that these tubes failed because of hot-gas erosion. Significant observations in this regard are:

1. An absence of slag
2. Erosion in uniform

3. Tube splits in center of crown

4. Melted-in-place tube material on tube crowns

5. Evidence of incipient melting throughout remaining tube wall

6. High-temperature cracks in remaining tube material

(U) Upon chamber disassembly, the inner-body vent cavity was subjected to a leak check by pressurizing the cavity with 5.0-psig helium. Soap solution applications in the injector-end hydrogen manifold and exit-end manifold revealed that no leakage occurred in these areas. It was observed, however, that vent pressure gas was encaping through some of the larger tube crown splits in several locations on the assembly.

(U) Several tube crowns were removed to provide visual access to the back sides of the split tubes. Longitudinal cracks about 1/2 inch in length were observed in the tube walls at the tube-to-body interstices at several locations. Tube samples were removed from the body at these locations. Figure 320 shows a cross section through a typical area where cracks were found. Further microscopic investigation (Fig. 321) left no doubt that the cracks were caused by reverse bending fatigue of rather high amplitude (total life was probably on the order of 10^3 to 10^5 cycles).

(U) Calculations indicate that the natural frequency of the structure shown in Fig. 320 is in the range of 20,000 to 30,000 cps.

(U) The sequence of significant events of test 025 is presented in Fig. 322, views A through H. Analysis of data, high-frequency instrumentation, and film indicated that the fuel lead, ClF_3 ignition, oxidizer priming portions, and main propellant ignition appeared to be normal and satisfactory. Thrust chamber operation at the time of LO_2 prime is shown in view A. Transition appeared to be normal, based on data analysis; however, the exhaust flame showed more or less uniform bright yellow and white exhaust flame streaking completely around the chamber (view B). This streaking has been interpreted

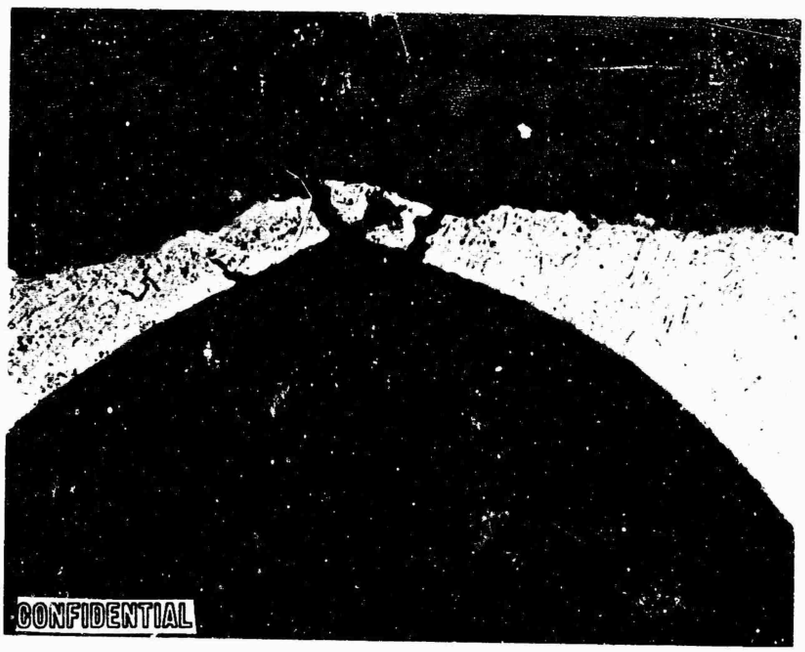

100X

Figure 319. Failed Tube in Combustion Zone, Inner Body Caused by Hot-Gas Erosion

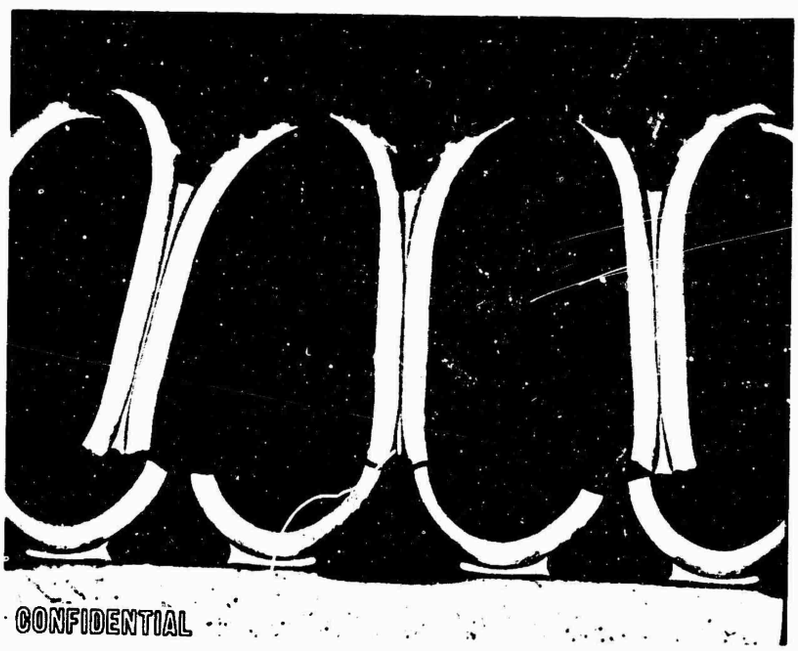

16X

Figure 320. Tube-to-Body Crack Location No. 1 Inner Body

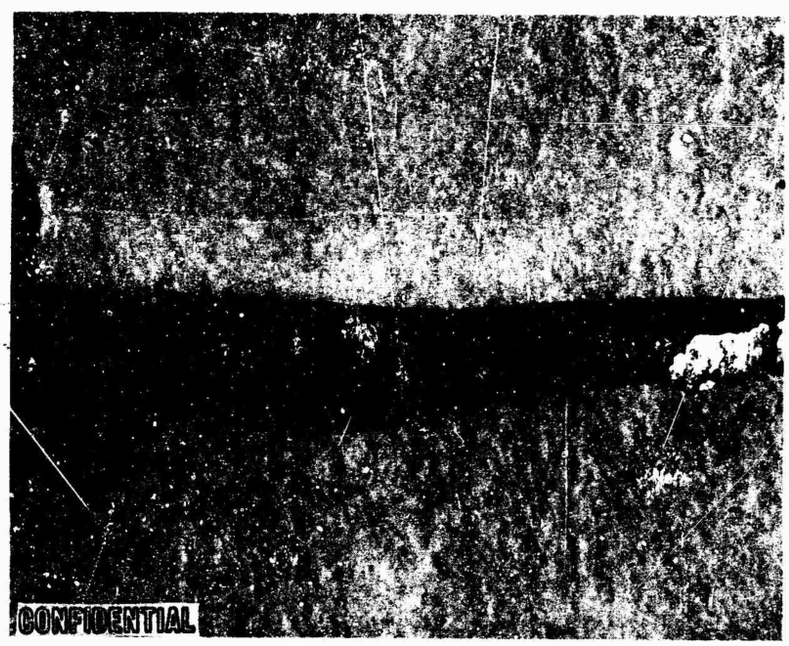

10X

Figure 321. Fractured Tube Walls Showing Multiplane Topography Typical of Reverse-Bending Fatigue

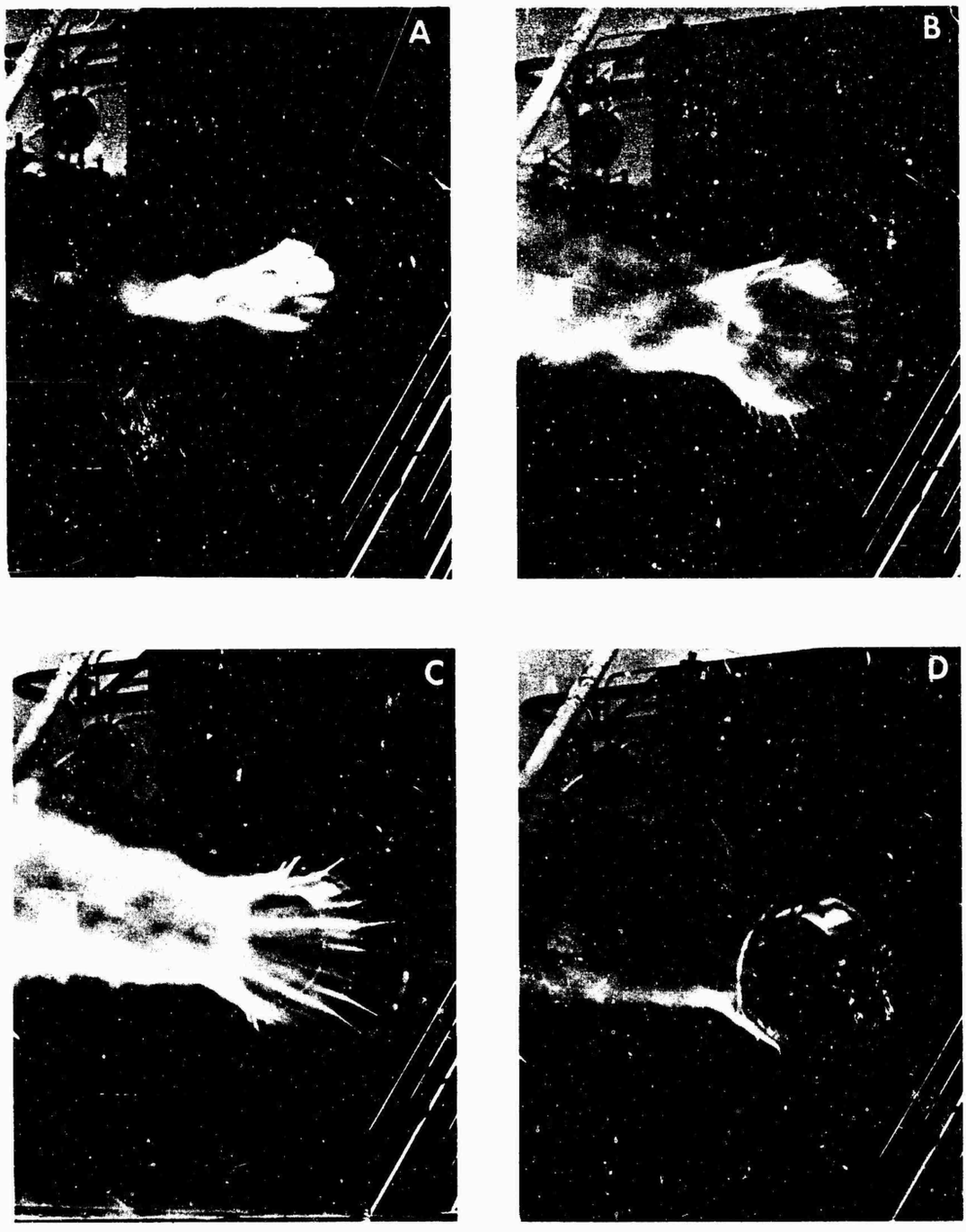

Figure 322A. Test 025 Mainstage Operation

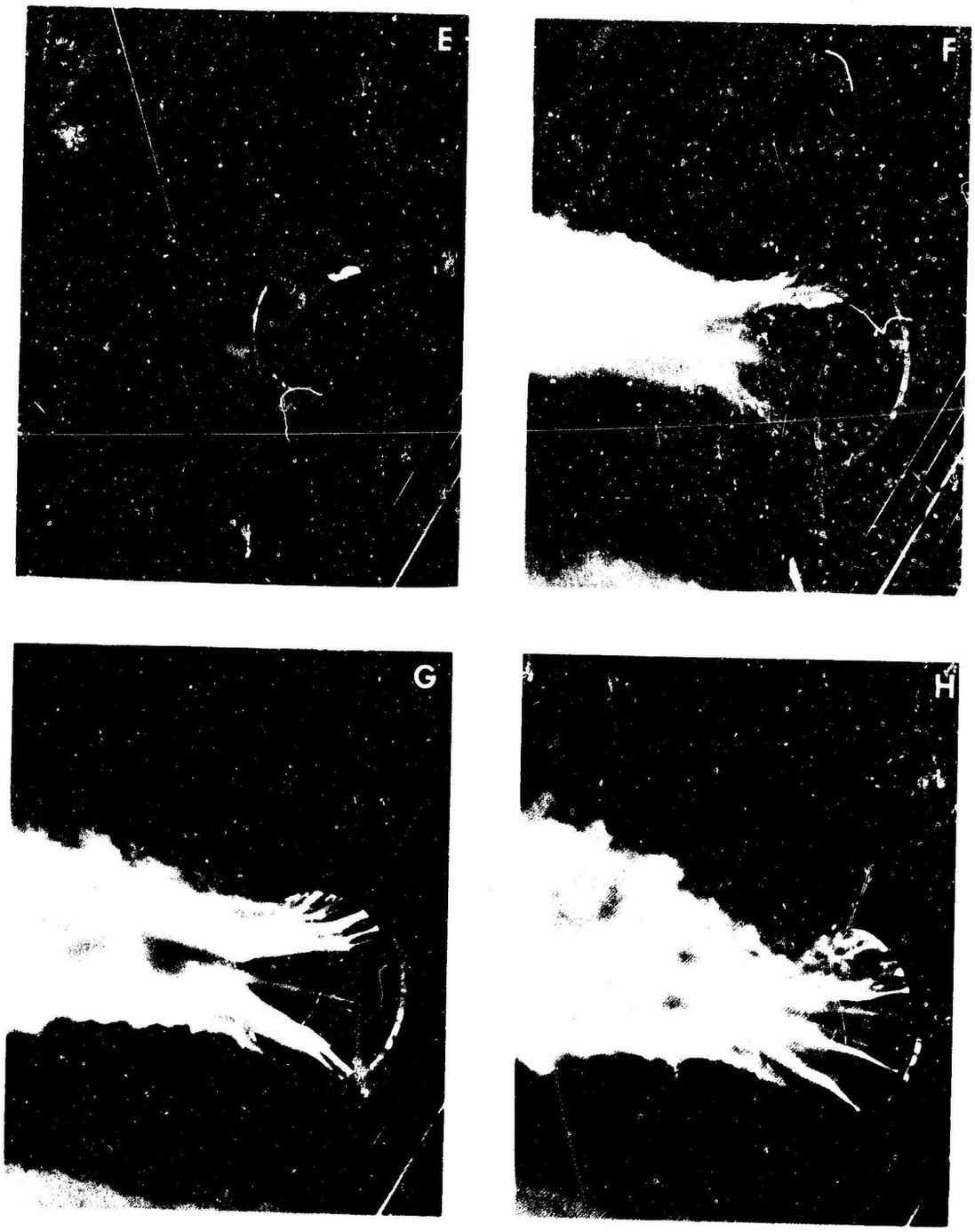

Figure 322B. Test 025 Mainstage Operation

to be evidence of tube and injector edge erosion. Predominant yellow and white streaks (indicating local chamber burning and/or mixture ratio variation, View C) more sparsely spaced appeared within a few milliseconds after transition and then tended to diminish in brightness (view D). Data show that fuel was lost from the flow circuit during or immediately after transition to mainstage.

(U) Green streaks (indicating burning of copper injector strips) appeared in the exhaust flame approximately 320 milliseconds into mainstage (view E). The high-frequency data do not reveal any unusual operational characteristics at this time. Internal chamber erosion continued as evidenced by bright yellow, white, and green streaking in the exhaust flame until a very bright flame appeared in the area from 030 to 090 degrees (view F) approximately 1.0 second into mainstage. It is quite evident, from examination of the time plot of events (Fig. 323) that major damage existed in the chamber at this time. All evidence indicates that erosion progressed through the hot-gas tapoff system and into the oxidizer manifold at this time. Heavy white streaking appeared in the exhaust flame at other locations around the chamber (view G) until external burnthrough of the tapoff manifolds occurred approximately 1.5 seconds into mainstage (view H).

(U) The posttest investigation revealed that failure was the result of several interrelated factors. The significant initiating and contributing factors to the incident and this interrelationship are shown in Fig. 324. The following is a brief discussion of the failure mode sequence. For clarity in understanding the causes and effects, this discussion will start with the terminal failure and trace the chain of events back to the initiating causes.

(U) Facility damage within the altitude was definitely caused by external burnout of the tapoff and oxidizer manifolds. Figure 325 shows a view of facility damage. The oxidizer and tapoff manifold damage occurred late

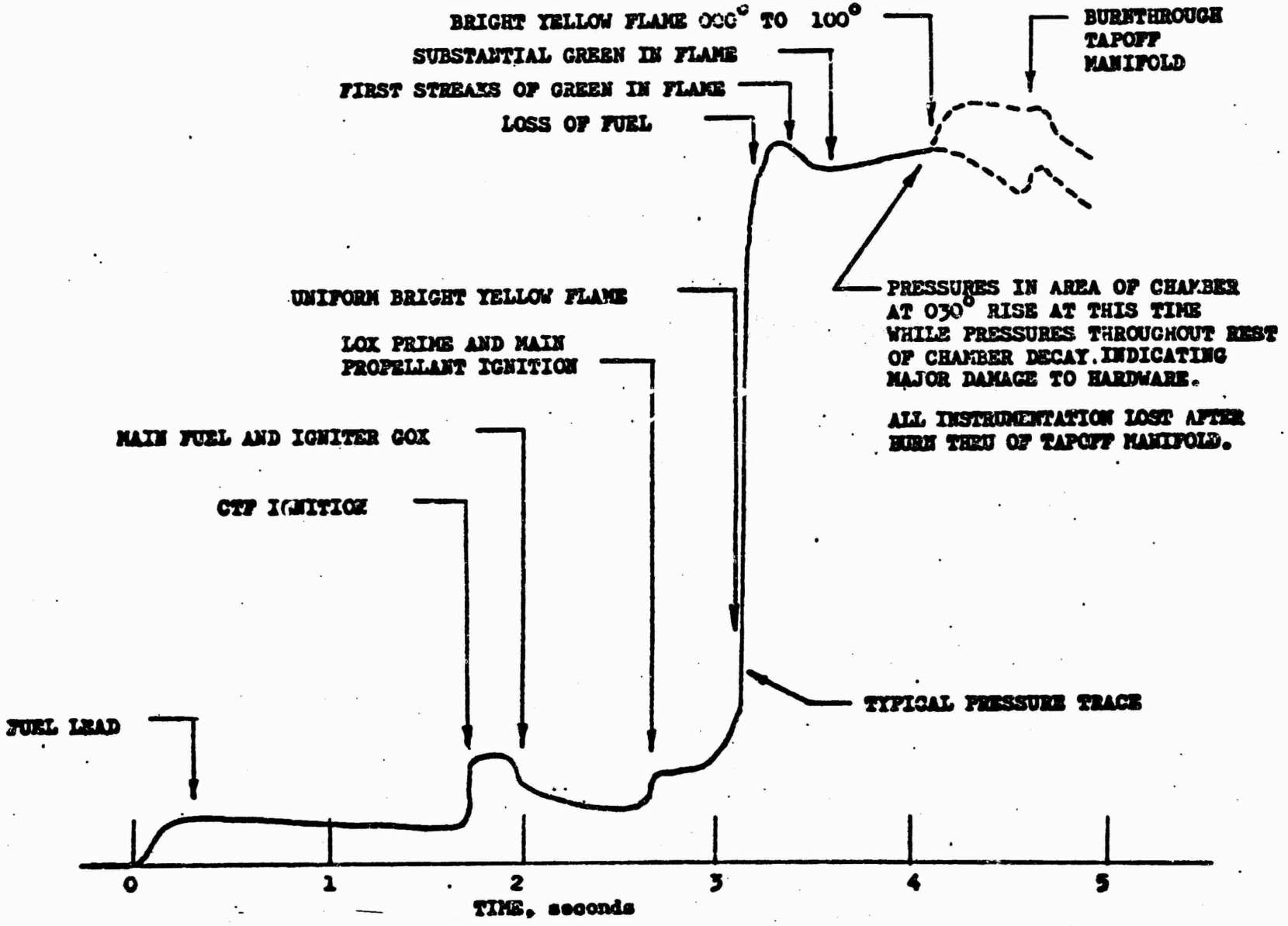

Figure 323. Test Events During Test 025

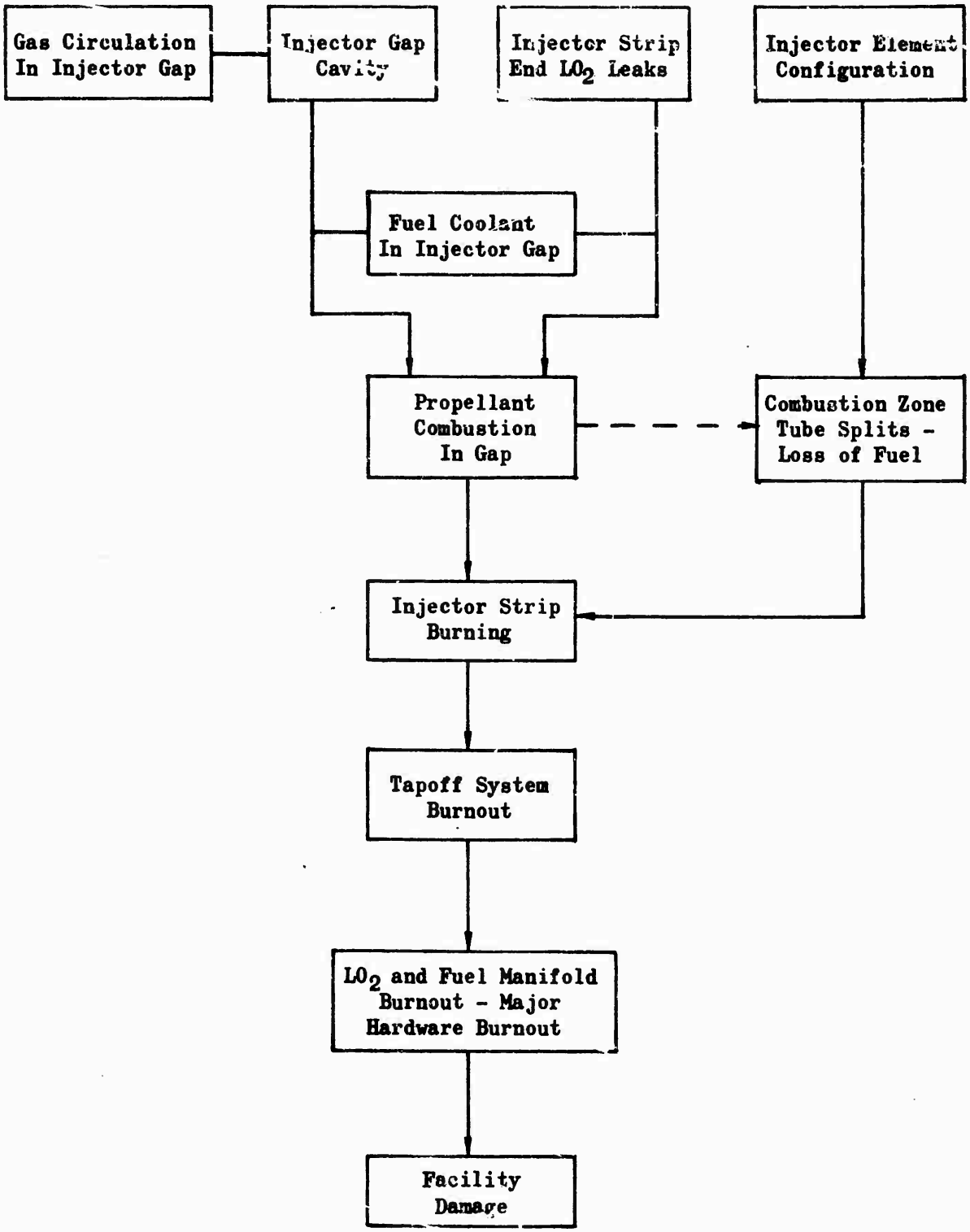

Figure 324. Test 025 Failure Mode Sequence

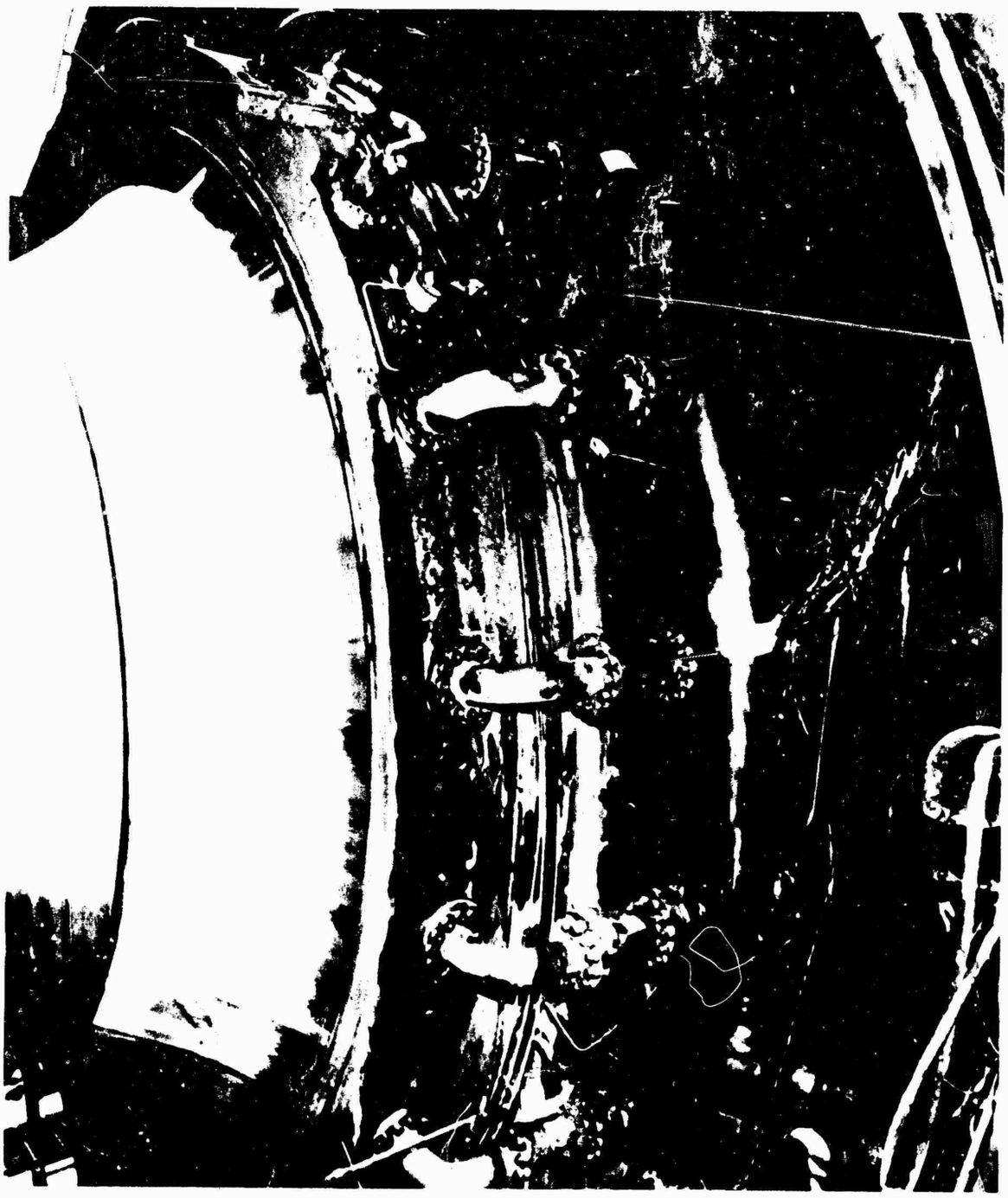

6RK38-7/2/67-R1B

Figure 325. Photo of Facility Damage Within Altitude Capsule

in the test. These manifolds burned through externally as a result of introduction of the oxidizer into the tapoff system through eroded tapoff ports in the injector. Figure 326 shows a sketch of the tapoff port erosion path within the injector body. Various stages of tapoff port erosion were found, extending from essentially undamaged ports to holes into the oxidizer manifold.

(U) Burning and erosion within the tapoff ports in the injector were caused by hot oxidizer-rich gases being pumped into the tapoff ports in certain compartments. The hot oxidizer-rich gas was a product of several causes:

1. Loss of fuel from the flow circuit at transition
2. Injector strip end and face burnout
3. Injector closeout ring burnout (secondary)

(U) Loss of fuel from the flow circuit is evidenced by: (1) higher-than-expected bulk fuel temperature rise, (2) lower-than-expected fuel system pressure drops (based on assumption of no fuel loss), and (3) low fuel pressures in fuel dump system. The fuel that was unaccounted for was lost from the flow circuit through tube splits and erosions. Tube splits and burnouts were caused by: (1) injector element configuration and wall gap causing combustion hot spots on the chamber walls, and (2) propellant combustion in the injector-to-chamber gap and resultant slag (from injector and chamber) erosion of tubes.

(U) The propellant combustion within the injector-to-chamber gap was a consequence of several factors. The injector-to-body gap is by nature oxidizer-rich. Oxidizer recirculating across the injector face was quite evident when hot gas was sampled from this zone during 2.5K segment testing and was found to be at a very high mixture ratio (approximately 100:1 o/f). Hot-gas circulation in the injector-to-chamber gap cavity is promoted by the existence of nonpressure producing regions within the injector-to-chamber gap and between the baffle ends and the chamber walls. Figure 327 illustrates the gas-flow path into the low-pressure regions and along the baffle end. Fuel introduced into this oxidizer-rich region to act as film coolant for the chamber body upper rings combined with an additional factor of oxidizer

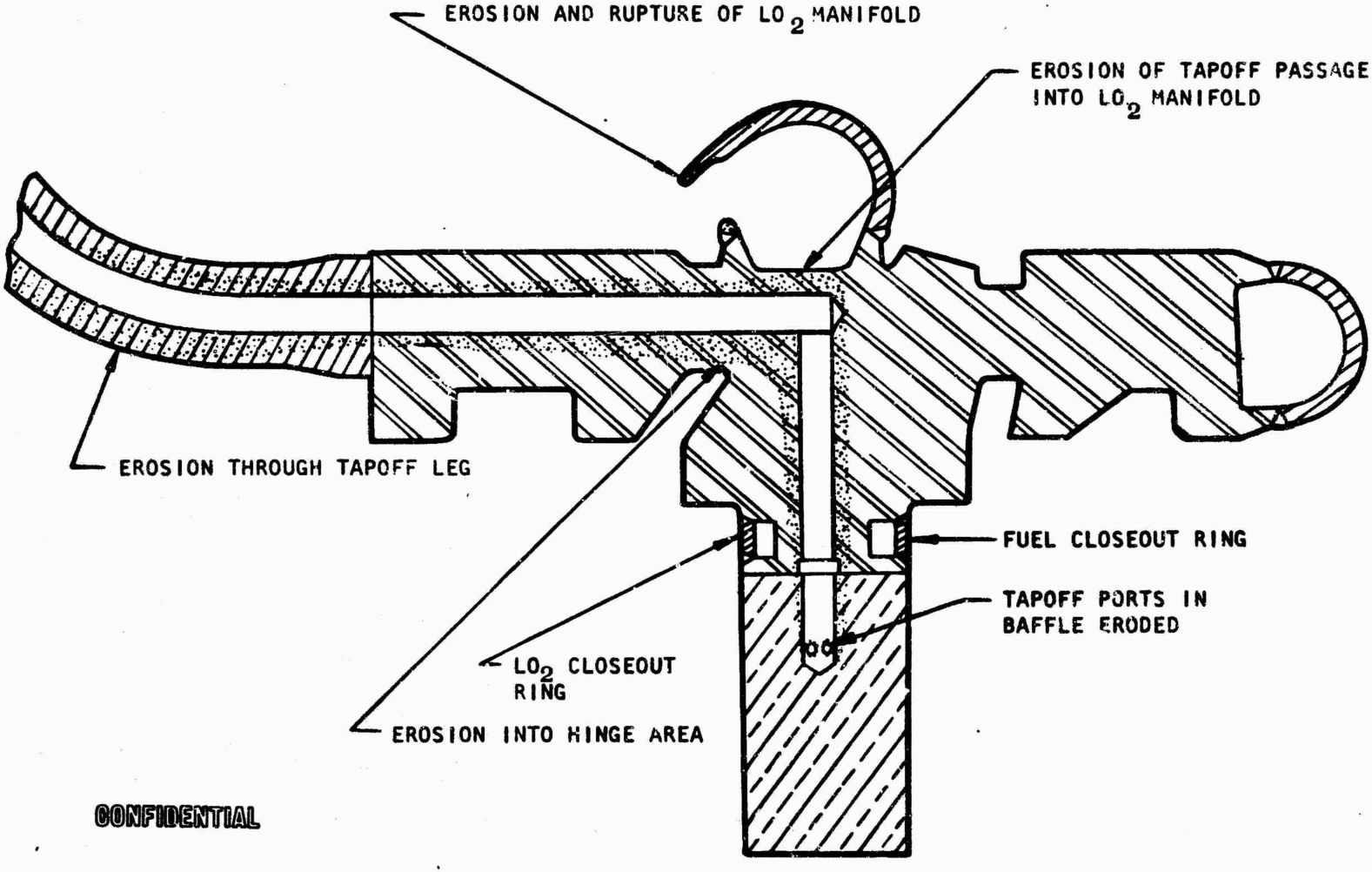

Figure 326. Major Tapoff Passage Erosion at Areas of Major Injector Damage

leakage from strip-end braze joints provided the necessary elements for combustion and erosion within the gap cavity.

(U) Injector face and strip-end burnout resulted from progression of combustion and erosion within the injector-to-chamber gap cavity. Loss of fuel from the flow circuit also tended to aggravate this condition by driving the injector mixture ratio (o/f) high and excessive local circulation to the gap at the tube splits. Likewise, burnout of the injector closeout rings was the result of combustion and erosion within the injector-to-chamber gap cavity.

(U) Oxidizer strip-end leaks and resultant injector and chamber erosion were found after testing in areas of the injector that did not sustain major damage. A typical area of erosion as a result of oxidizer strip-end leakage is shown in Fig. 328. A key cause of the damage appears to be the existence of a gap between the injector body and the chamber end ring and the resultant flow paths. Without this gap, oxidizer-rich hot gas and/or oxidizer from strip leaks could not combine with fuel in an area where it is not intended that combustion occur. All indications are that elimination of the injector-to-chamber gap and sealing of all strip-end leaks would have precluded the type of damage experienced in test 025. Extensive segment tests with a smaller gap showed no distress in this area, bearing out the analysis. It should be noted that intercompartmental gas flow near the injector and gas circulation behind baffles are not present in the Demonstrator Module or 20K segment because the baffles are sealed to the chamber walls. Accordingly, modifications were made to the No. 2 tube wall assembly to fill the gap between injector and chamber. A beryllium-copper lip seal was attached to inner and outer body injector end rings, as shown on Fig. 329, such that it prevented combustion gas from filling the gap and it directed the GH_2 from the injector strip-end orifices down over the strip ends, protecting them from erosion. A low temperature vulcanizing silicone ablative material was placed in gaps between baffles and bodies to reduce circulation as shown on Fig. 329. To reduce the tube overheating at the injector end, both inner and outer bodies were flame-sprayed with a tungsten-zirconia-silica coating to a depth of .010 inch and covering the area from injector to 2 inches downstream of injector face.

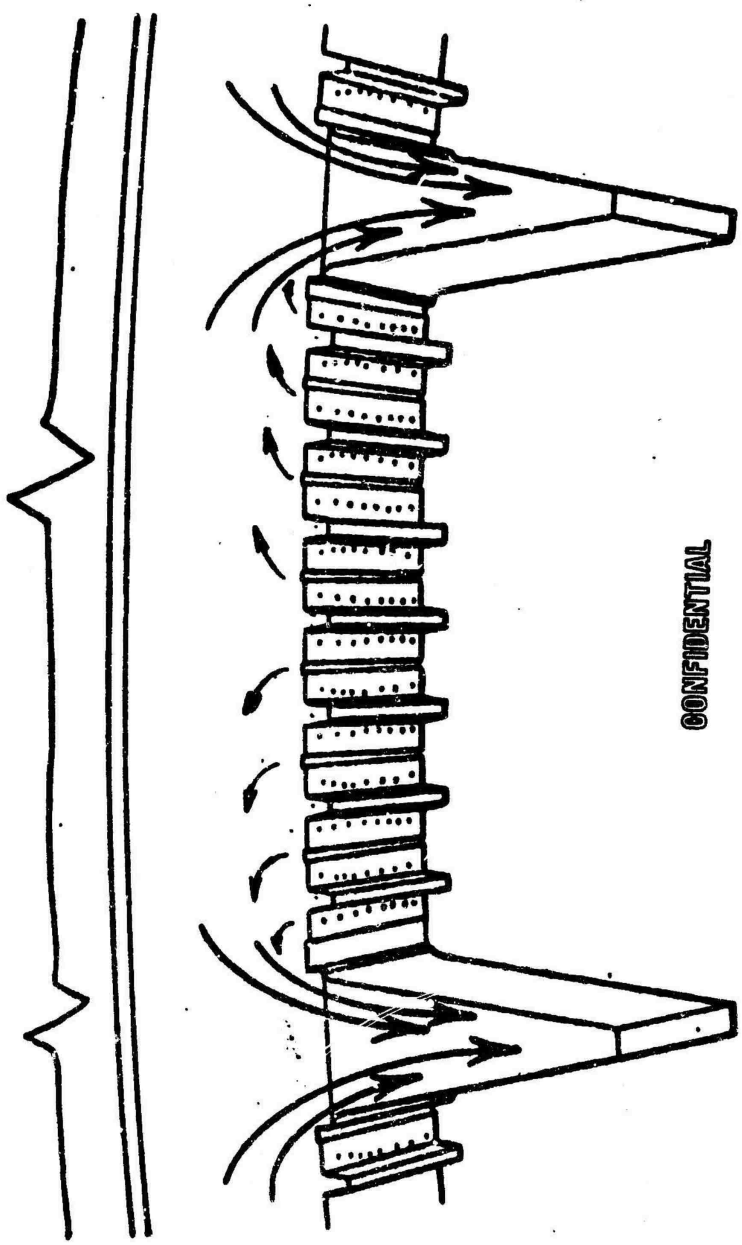

Figure 327. Hot-Gas Circulation Path in Injector Gap

1XE35-8/1/67-C1B

Figure 328. Chamber Erosion Caused by Strip End Oxidizer Leak

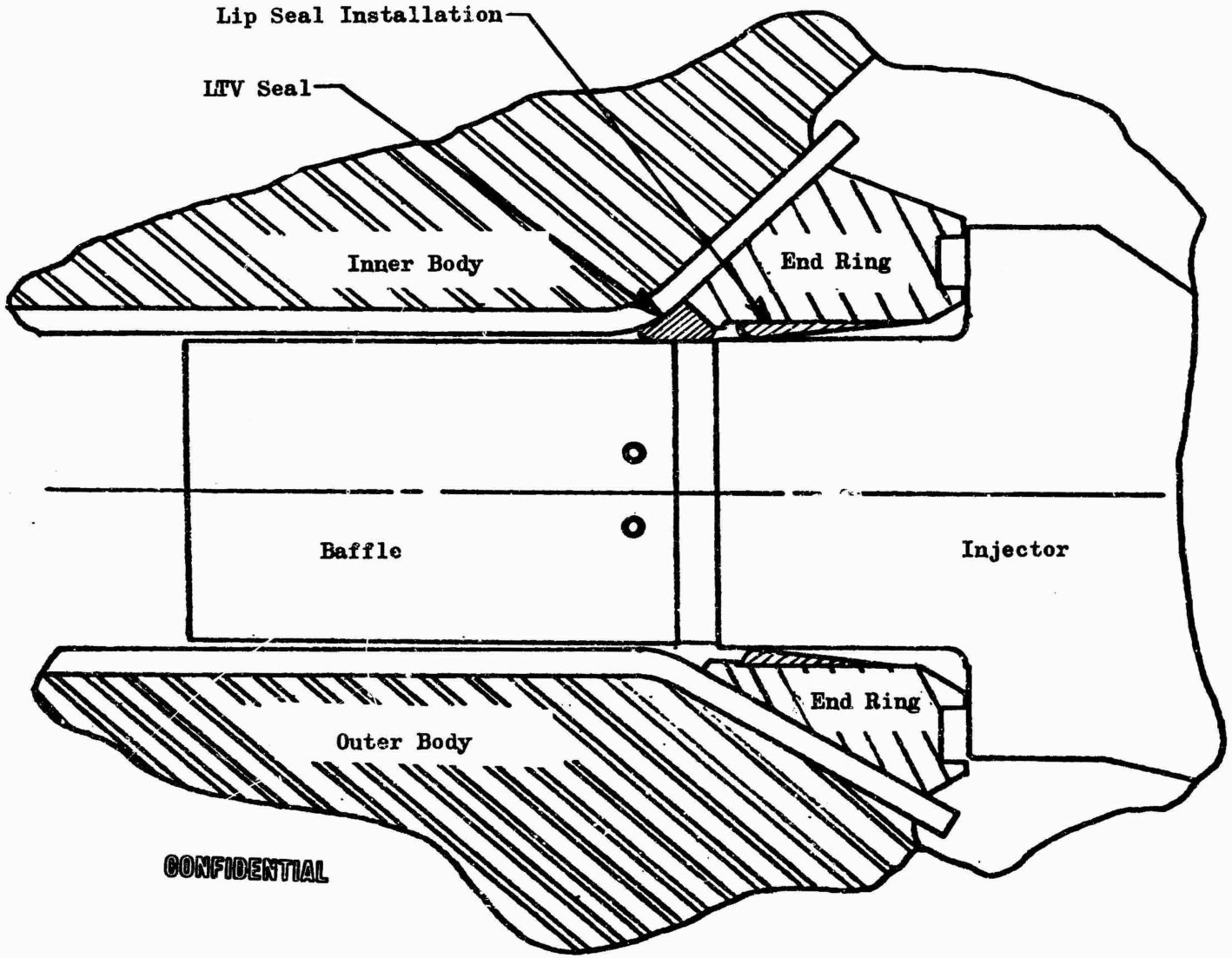

Figure 329. Cross-Sectional View of Injector Installation in Tube-Wall Thrust Chamber

CONFIDENTIAL

(U) No. 2 Tube-Wall test Series. During the solid-wall and No. 1 tube-wall mainstage tests, the greater portion of mainstage chamber pressure was developed within 50 milliseconds. Analysis indicated that a slower transition into mainstage was desirable. The sequence was therefore modified to achieve a two-stage chamber pressure start transient. Priming of the engine oxidizer manifold and transition to the intermediate chamber pressure level were achieved by using one-half of the mainstage oxidizer flowrate. At that time, the full oxidizer flowrate was sequenced in, and the final transition to mainstage was achieved. A series of oxidizer blowdowns was conducted prior to hot firing to verify system operation with two stages of flowrates, to obtain additional pressure drop data, and to determine priming characteristics at each stage of flowrate. The resultant start sequence is illustrated in Fig. 330 by comparing the start transients from tests 023 and 027. Test 027 utilized the step start sequence, whereas the start sequence for test 023 was similar to that utilized for the solid-wall chamber.

(U) Two mainstage tests (027 and 028) were conducted on the No. 2 tube-wall assembly. The purpose of the first mainstage test was to check out the modified step start sequence and to verify test stand operation. Mainstage operation of 280 milliseconds was achieved. Review of the data and films indicated that chugging occurred during start and cutoff. A 1900-cps tangential mode was observed during mainstage. The films also indicated that copper erosion occurred, as evidenced by green streaks in the exhaust flame.

(U) To fully ascertain the hardware condition, the chamber was removed from the test stand following test 027 and the outer body was lowered to permit access to the combustion zone. Visual inspection revealed that the injector was in good condition with the exception of the baffles. Overheating and erosion of the baffle edges was sustained, as shown in Fig. 331. An average of four tubes per baffle on the outer body were found to be split behind each of the baffles. The tubes were split up to 3/8 inch in

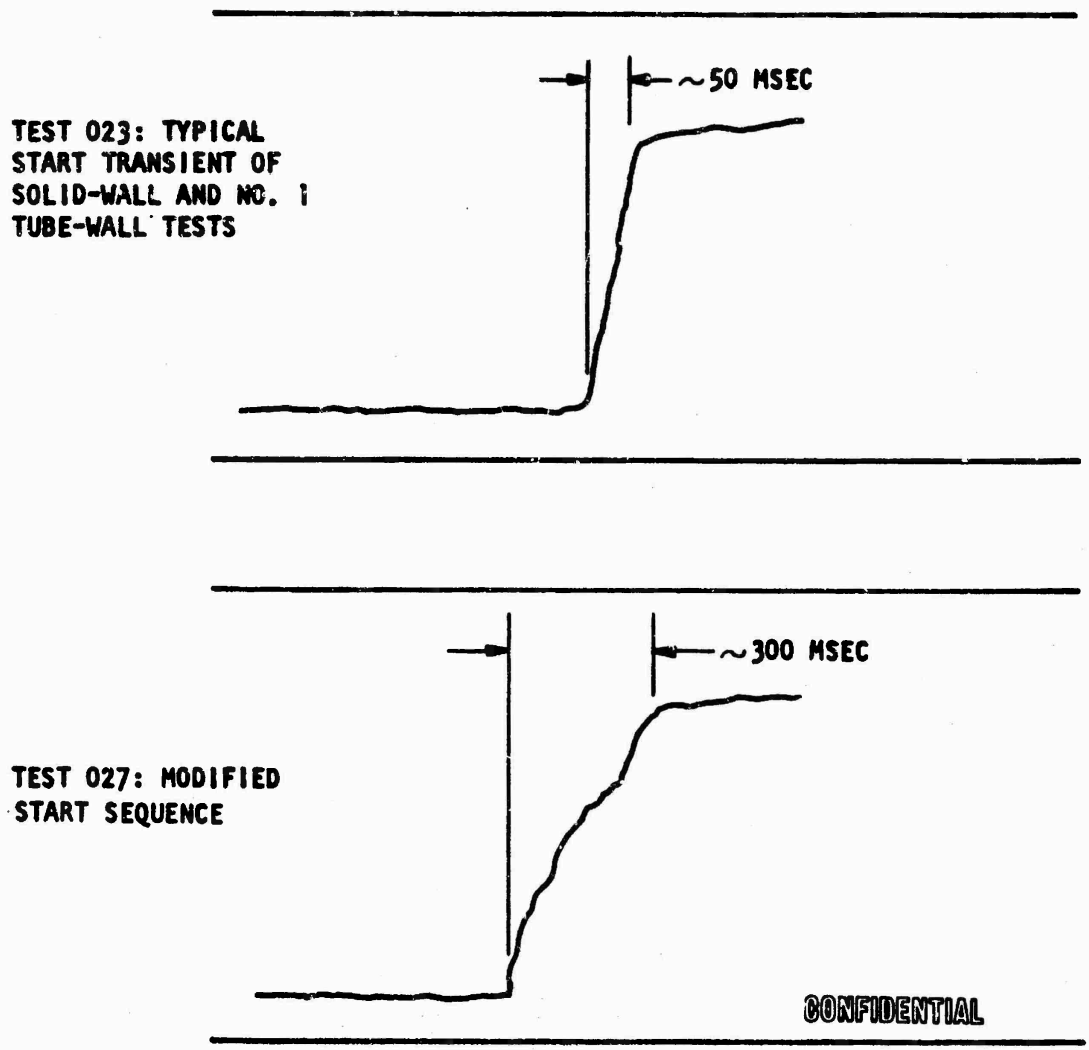

Figure 330. No. 2 Tube-Wall Modified Start Sequence

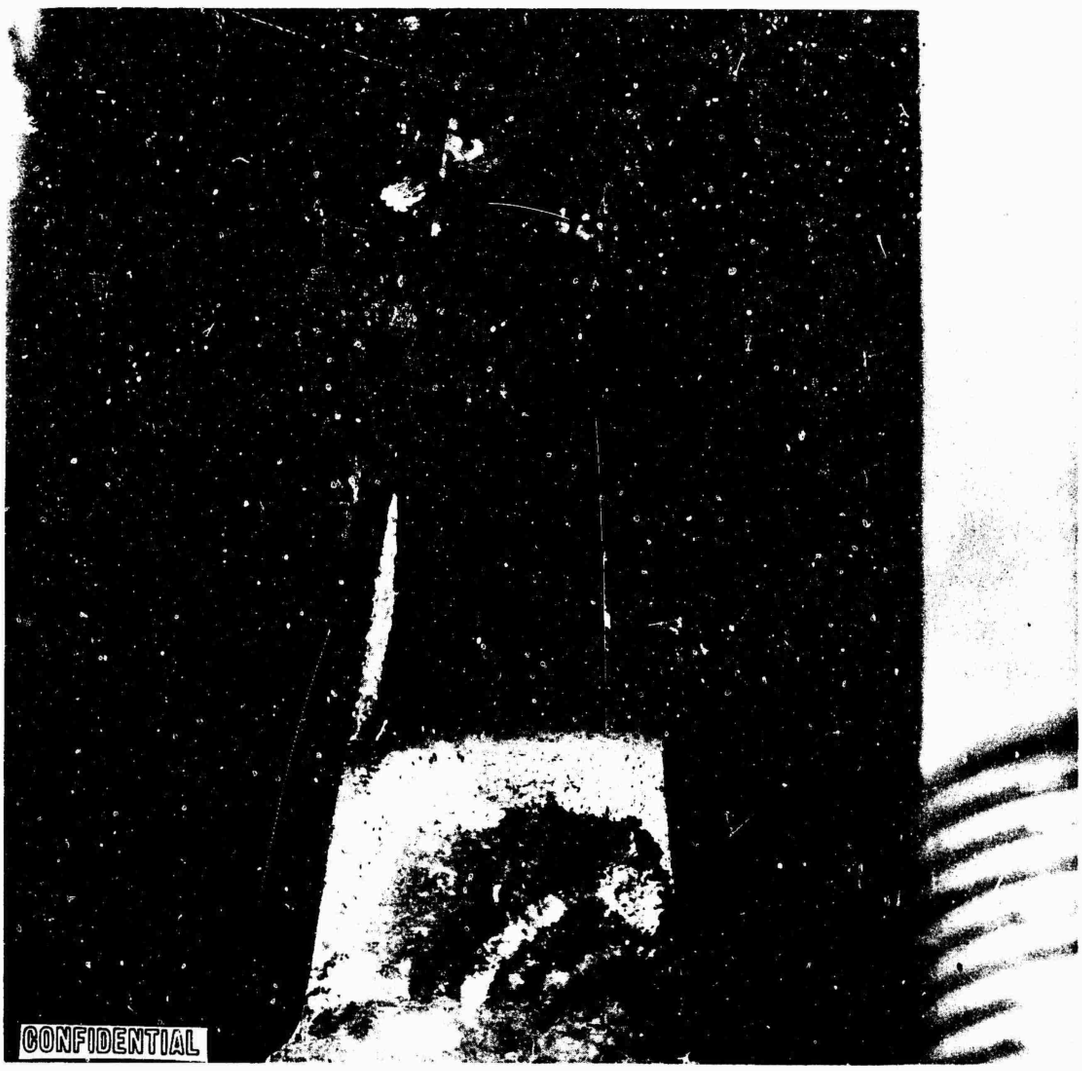

Figure 331. Posttest 027 Injector Baffle Condition

length. The plasma spray coating which was applied to the No. 2 chamber was found to be locally spalled, both behind baffles and within compartments on the outer-body tubes. The coating was in generally excellent condition on the inner-body tubes. Figure 332 shows a typical section of inner-body tubes and coating condition. Following completion of the inspection, the chamber was reassembled and reinstalled on the test stand for further testing.

(C) Testing was conducted at site level conditions with the No. 2 tube-wall chamber. The tube-wall test program was terminated following test 028. Test operating conditions for test 028 were: 898 psia chamber pressure, mixture ratio of 5.90 (o/f), and mainstage duration of 0.80 second. The targeted mainstage duration was 1.0 second; however, the test was terminated prematurely by the inner combustor body vibration safety cutoff (VSC) device. A 1900-cps combustion oscillation phased in approximately 0.50 second into mainstage, apparently tuning with the structural resonance of the inner body and causing a rise in vibration level and a VSC cutoff.

(U) Again, green flame could be seen in the test films. Inspection of the combustion zone with inspection periscopes revealed that the baffles had sustained erosion of the trailing edges and sides adjacent to the combustor bodies. The injector face and tubes within the combustion zone were in good condition.

(U) Posttest Hardware Inspection, Tube-Wall Chamber No. 2. The No. 2 tube-wall chamber was removed from the test stand and disassembled for complete inspection. The injector face was in generally excellent condition with no evidence of erosion. A view of the injector face showing two compartments is shown in Fig. 333. The baffles sustained overheating and erosion on the sides and along the trailing edges. The baffle coolant passages were exposed along the sides of two baffles (typically shown in Fig.334). The coolant passages were exposed on 27 baffles near the trailing edge on the inner-body side (typically shown in Fig. 335). The baffles were eroded to the coolant passage on the trailing edge (Fig. 333) on nine baffles.

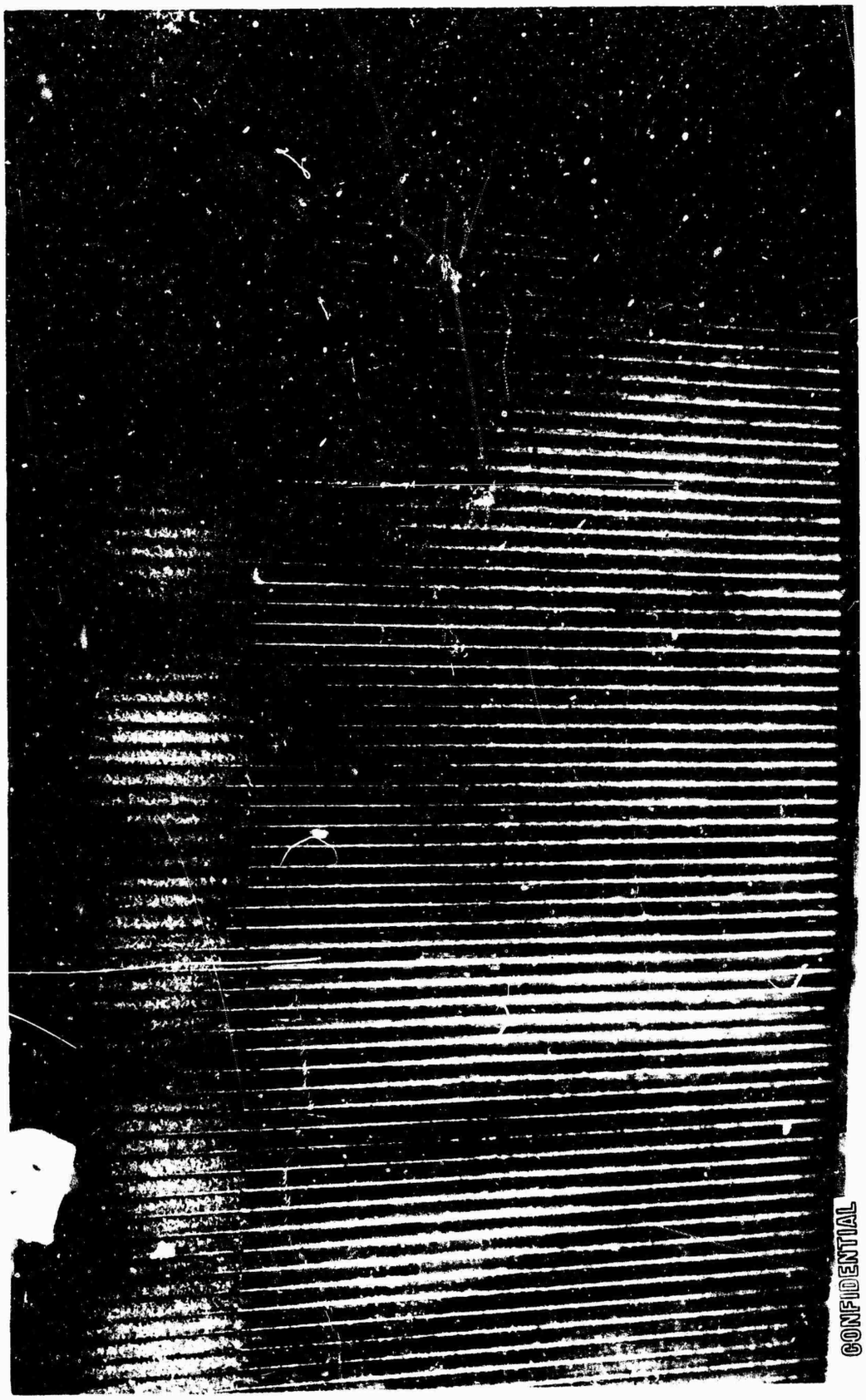

Figure 332. Chamber Inner-Body Posttest 027

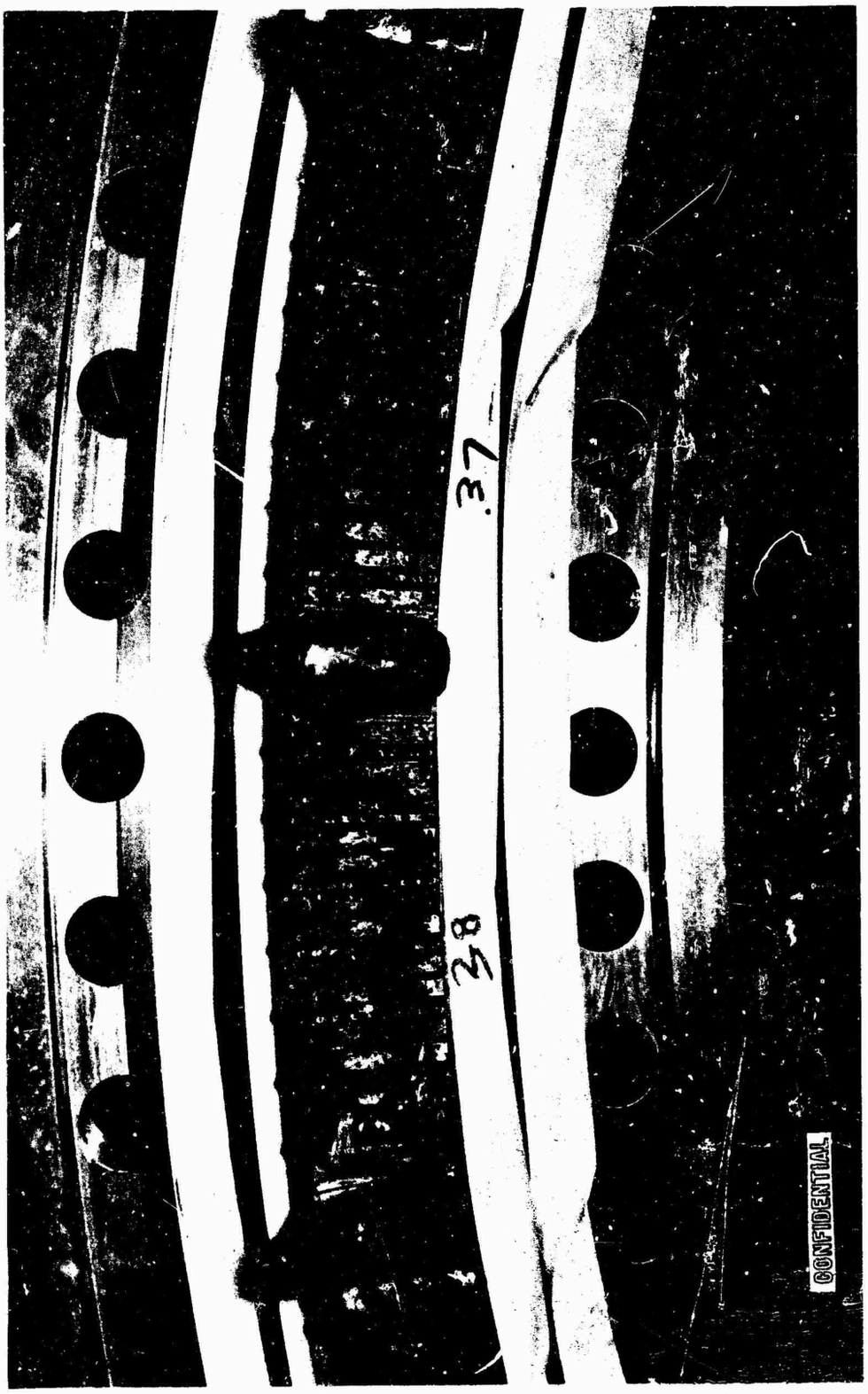

Figure 333. View of Injector Face Showing Two Compartments

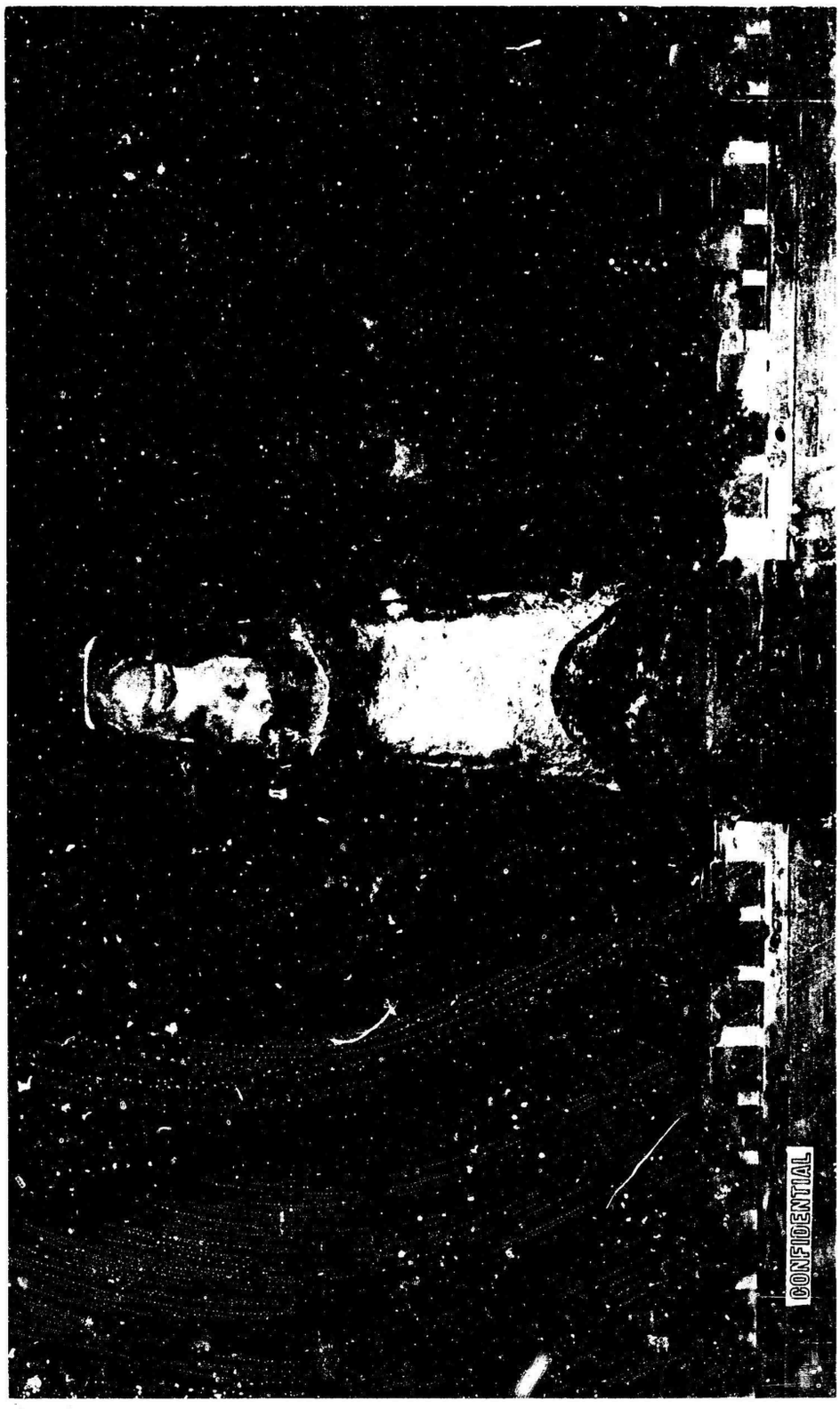

Figure 334. Exposed Baffle Coolant Passages

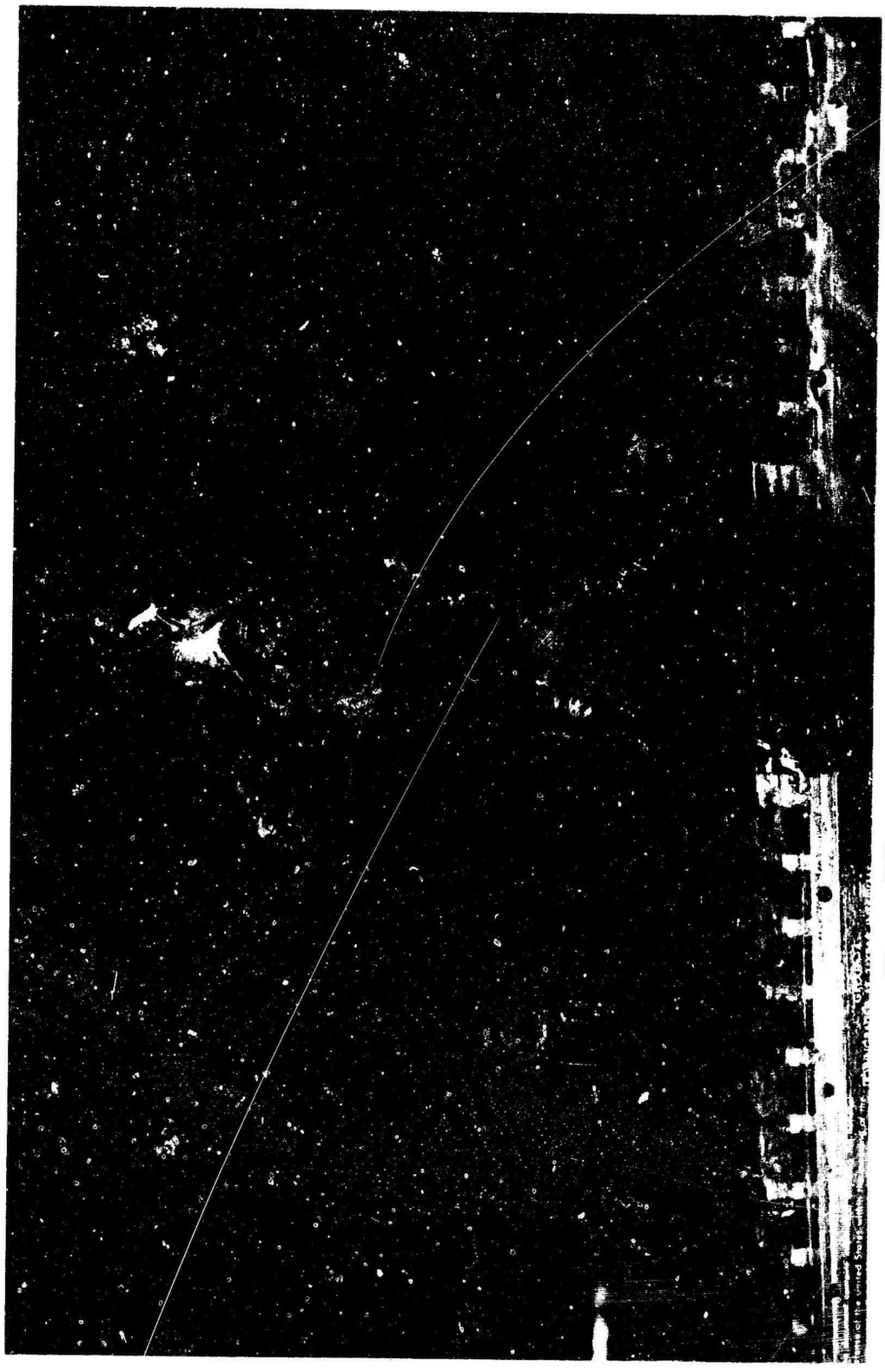

Figure 335. Exposed Coolant Passages

(U) Split tubes were sustained on both the inner and outer bodies behind baffles. An average of five split tubes per baffle was sustained on the outer body, and an average of four split tubes per baffle was sustained on the inner body. The tubes located within the compartments and at the throat and nozzle were in generally excellent condition.

(U) The combustion zone plasma spray coating was found to be spalled and thinned more severely on the outer body than on the inner body. The coating was still essentially intact on the inner body (Fig. 336). Copper removed from the baffles by erosion was found to be deposited on the inner- and outer-body tubes as well as on the injector face (Fig. 336). No other damage was sustained by any chamber component.

(U) The cause of the damage is analyzed in the Combustion Stability Analysis section (page 763) and the direction of solution discussed in Problem Areas and Solutions (page 777). Because this combustion oscillation and damage problem was present at the end of the contract period, this concluded the testing effort.

Analysis of Results

(U) The aerodynamic spike is an advanced nozzle concept which offers the advantage of high performance over the complete range of (sea level to vacuum) altitude operation. The goal of the 250K experimental thrust chamber effort was to demonstrate aerospike specific impulse, combustion efficiency, and nozzle performance of the concept. In addition, valuable data relative to base pressure, shock boundary layer interaction, thrust chamber base configurations, and scale effects on base pressure and thrust coefficient were attained.

(U) Nozzle Performance. Extensive cold-flow and hot-firing programs have been conducted to develop empirical and analytical formulations of aerospike nozzle performance. Through these efforts, the nozzle behavior has been well characterized.

Figure 336. Eroded Baffles

(C) The altitude-compensating process occurs regardless of the nature of the gas; however, the degree to which altitude compensation occurs does depend upon the nozzle geometry, and to a smaller extent, the nature of the working fluid and the amount of secondary flow used. Typical altitude-compensation results are shown in Fig. 337 (Ref.12). This figure shows the nozzle efficiency for a cold-flow model with an area ratio of 48.3 and a length of 30 percent of an equivalent conical nozzle tested with air. Data without secondary flow and with optimum secondary flow are presented. Maximum nozzle efficiency was approximately 98.5 percent at the design pressure ratio of 1400. The altitude-compensating ability of the aerospike nozzle is evident even at extremely low pressure ratios.

(U) The adequacy of nozzle performance techniques and the altitude compensation of the aerospike were demonstrated during tube-wall and solid-wall testing. The predictions of the 250K tube-wall chamber along with the measured values are given in Fig. 338. Altitude compensation is discussed in Appendix IX. It will be noted that altitude compensation is obtained, agreement (minor differences shown are largely due to mixture ratio and area ratio variations) between the experimental and measured thrust efficiency is achieved, and that experimental values are well above those attainable with comparable bell chambers.

(C) As noted previously, the degree of altitude compensation is affected only to a small extent by the nature of the working fluid. It is therefore possible to utilize and evaluate thrust coefficient data from the solid-wall thrust chamber. Figure 339 shows the values of the one-dimensional optimum C_F as a function of ambient pressure ratio $(P_c/1_a)$ for the solid-wall thrust chamber. The theoretical calculations also show the relative independence of the water film coolant on thrust coefficient (C_F). The

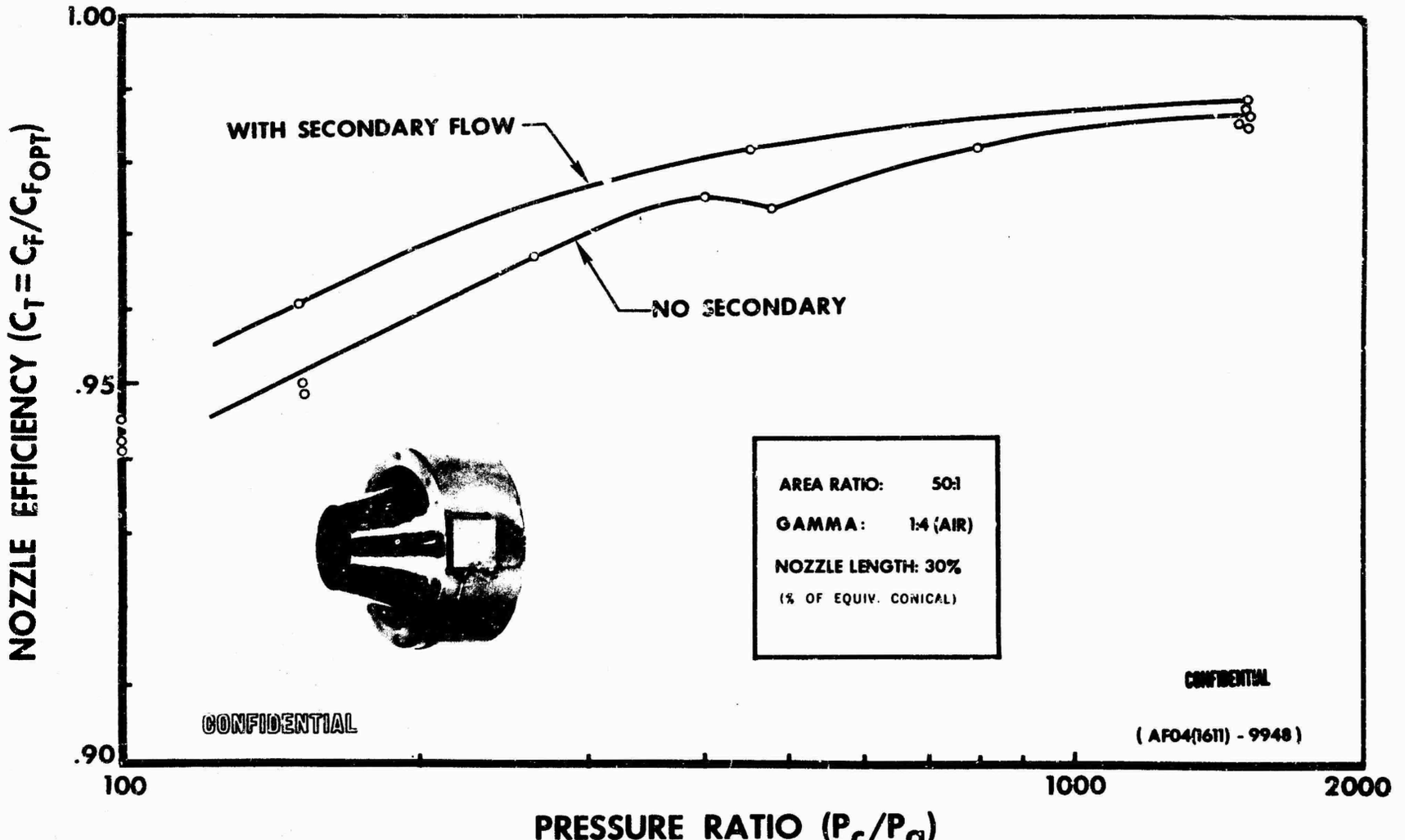

Figure 337. Aerodynamic Spike Performance, Altitude Compensation

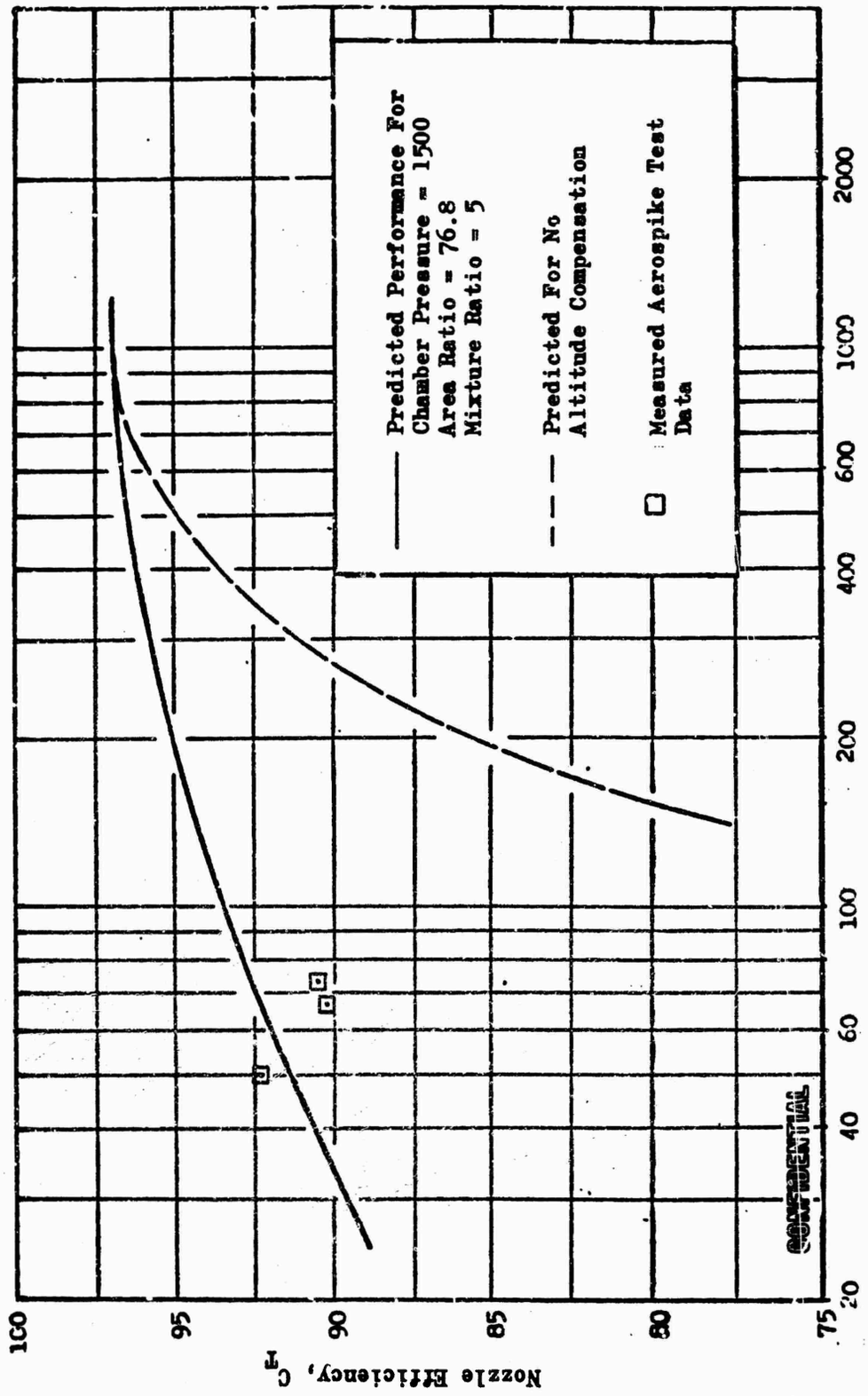

Figure 338. Tube-Wall Thrust Chamber C_T Performance vs Pressure Ratio

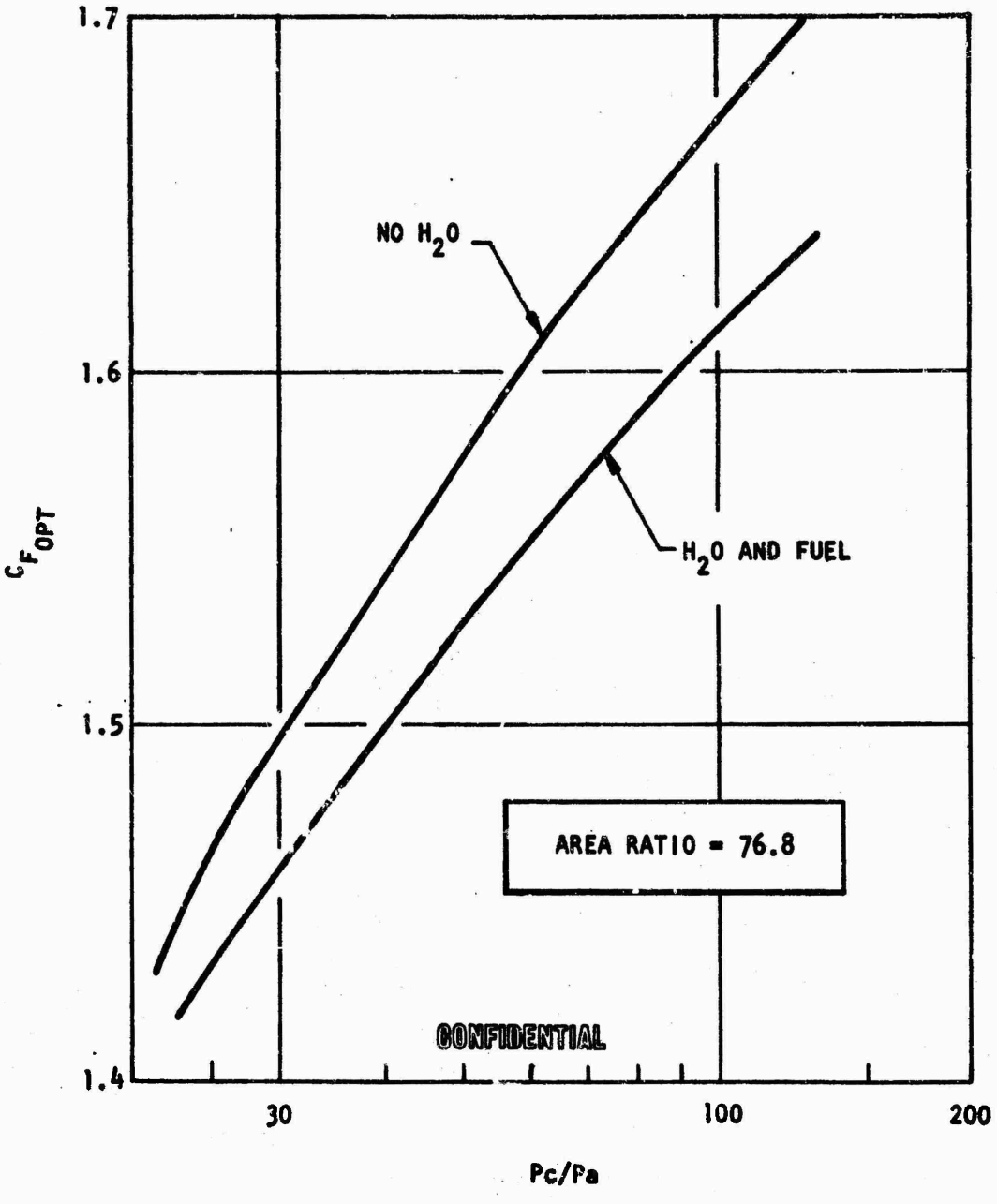

Figure 339. Theoretical Optimum Thrust Coefficient, Effects of Water

difference between the two extremes of thrust coefficient are approximately 1.0 percent at a pressure ratio of 20 and approximately 3.8 percent at a pressure ratio of 125.

(U) The experimentally determined primary nozzle thrust coefficients are shown in Fig. 340. This figure shows that the experimental data bracket the theoretical calculations.

(U) Base Pressure Analysis. The high performance levels of the aerodynamic spike nozzle are due in part to the base contribution. Considerable effort, both theoretical and experimental, has been expended in understanding the separated supersonic flow phenomenon, which is the mechanism of base pressure. These investigations have led to a comprehensive understanding of the base-flow phenomenon. These studies have shown the base pressure has two well-defined altitude or ambient pressure regions, generally referred to as the "open" and "closed" wake regions. The "open" wake is the altitude region where the base pressure is influenced by the ambient pressure, and the "closed" wake region is the altitude region where the base pressure is independent of the ambient pressure. When properly introduced, secondary flow improves the nozzle performance both at high and low pressure ratios. This increased performance is directly attributable to an increase in base pressure.

(C) Results of the ambient pressure dependence of base pressures are shown in Fig. 341. The data shown in this figure are for the 40K and 250K aerospikes for tests with durations greater than 0.25 sec. It will be noted that both the 40K and 250K data show that the open wake base pressure is near ambient. The short duration of the 250K test may have slightly lowered the base pressure on several tests.

(U) Since no high pressure ratio tests were conducted on the 250K chamber, no experimental verification of the closed wake base pressure was obtained.

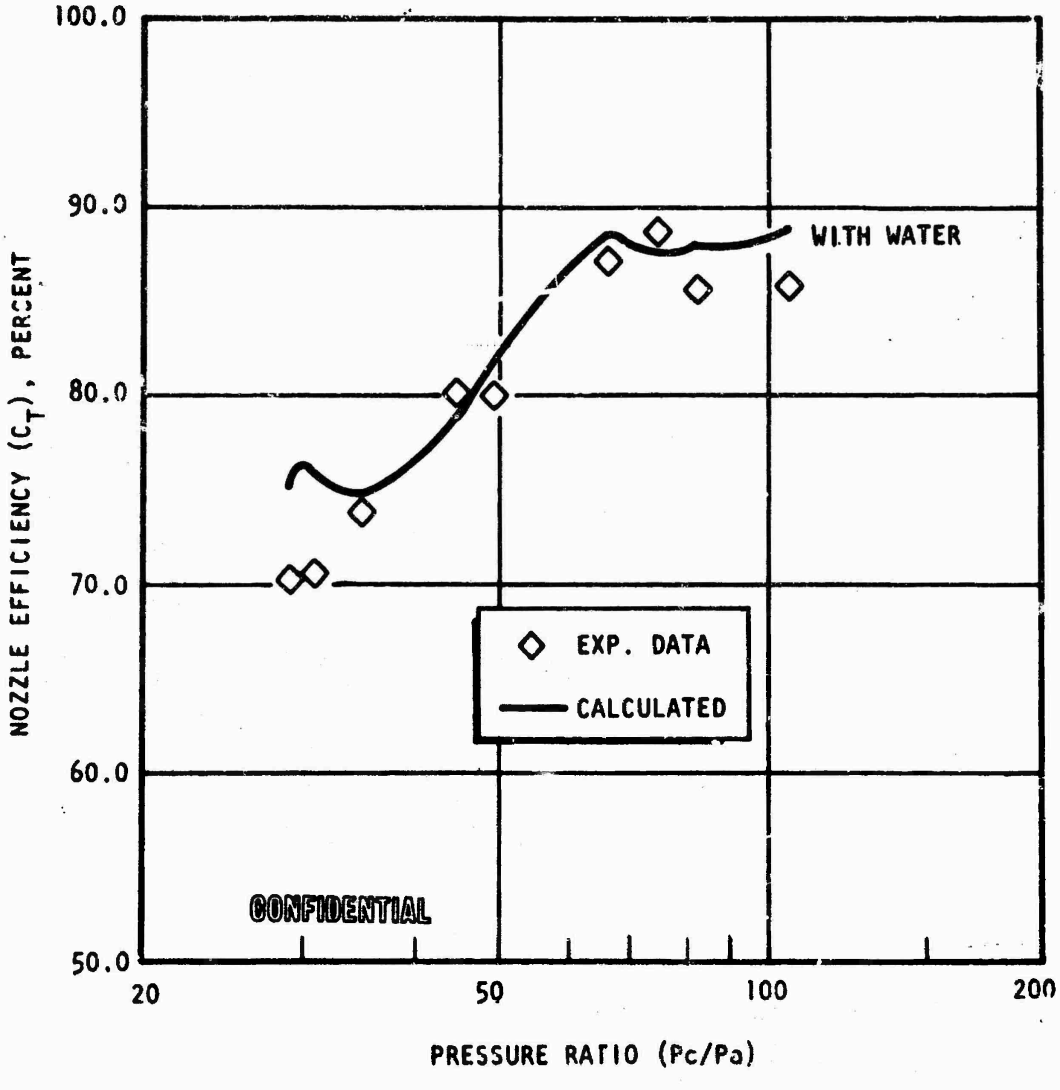

Figure 340. Minimum Model Nozzle Performance Test Results

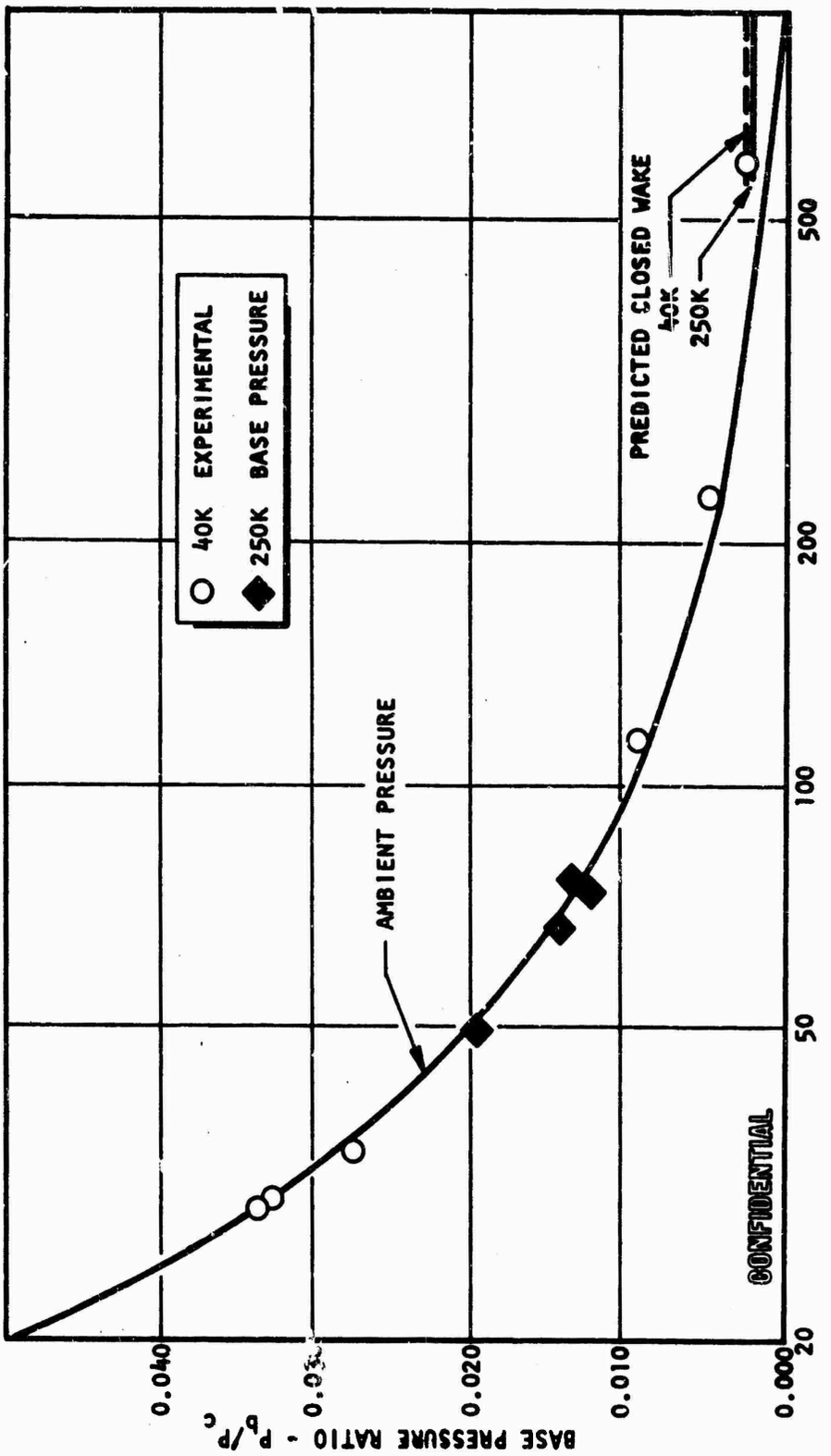

Figure 341. Experimental Base Pressure

(U) Nozzle Pressure Profiles. The altitude-compensating properties of the aerospike nozzle are, in part, due to reccmpression of the expanding gases. This recompression phenomenon results in nozzle wall pressures that are either above ambient (above the recompression zone) or near ambient (in the recompression zone). Verification of the ability to calculate the wall pressure is of prime importance because estimates of the thrust coefficients are obtained by integrating the calculated wall pressure profiles.

(C) One of the advantages of the solid-wall testing was the ability to experimentally determine the wall pressure profiles. Typical results are shown in Fig. 342 which gives the wall pressures with the chamber operating at 900 psia. This pressure rise downstream of the shroud is caused by the nozzle flow. The agreement between the experimental and calculated data provides additional support of the anticipated performance levels that can be realized with the aerospike engine.

(C) Experimental wall pressure profiles were measured on the uncooled nozzle extension of the 250K tube wall chamber. These results are given in Fig. 343 along with the theoretical results for a chamber pressure of 600 psia. The agreement between the theoretical and the calculated results shows that the calculation model can be used to obtain estimates of the inviscid thrust coefficient.

(U) One additional area associated with the nozzle pressure profile was the interaction of the recompression shock and the boundary layer. Recompression at low pressure ratios gives rise to oblique shock waves. The interaction of this shock wave with the nozzle boundary layer can lead to local separation of the boundary layer if the shock is of sufficient strength. Local separation of the boundary layer could lead to extremely high heat fluxes. Visual posttest investigations of tube-wall chambers and thermal measurements on the uncooled nozzle extension have shown that the recompression shock waves are not of sufficient strength to cause boundary layer separation.

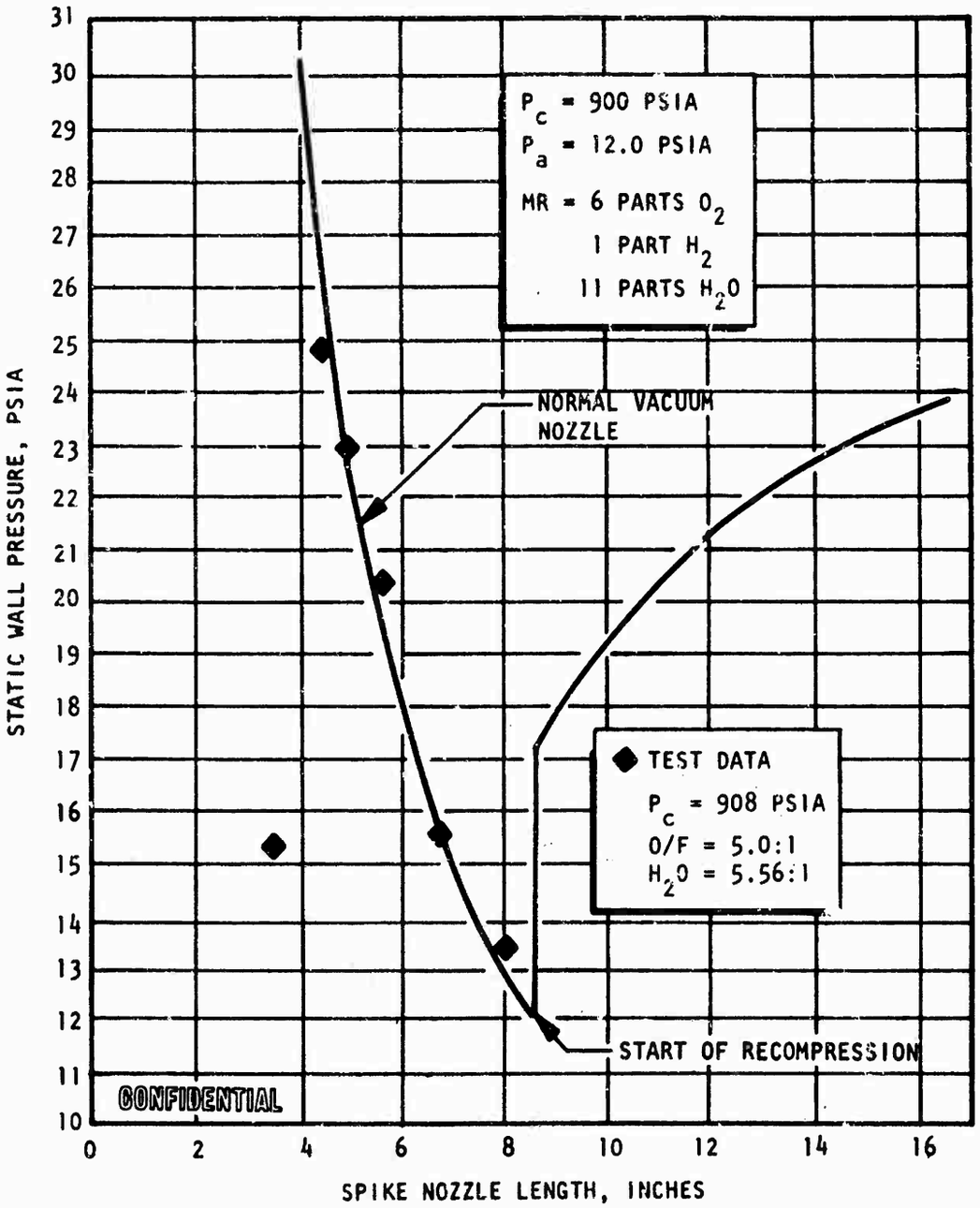

Figure 342. Wall Pressure Profile for Aerospike Utilizing LO_2/GH_2 with H_2O in Equilibrium

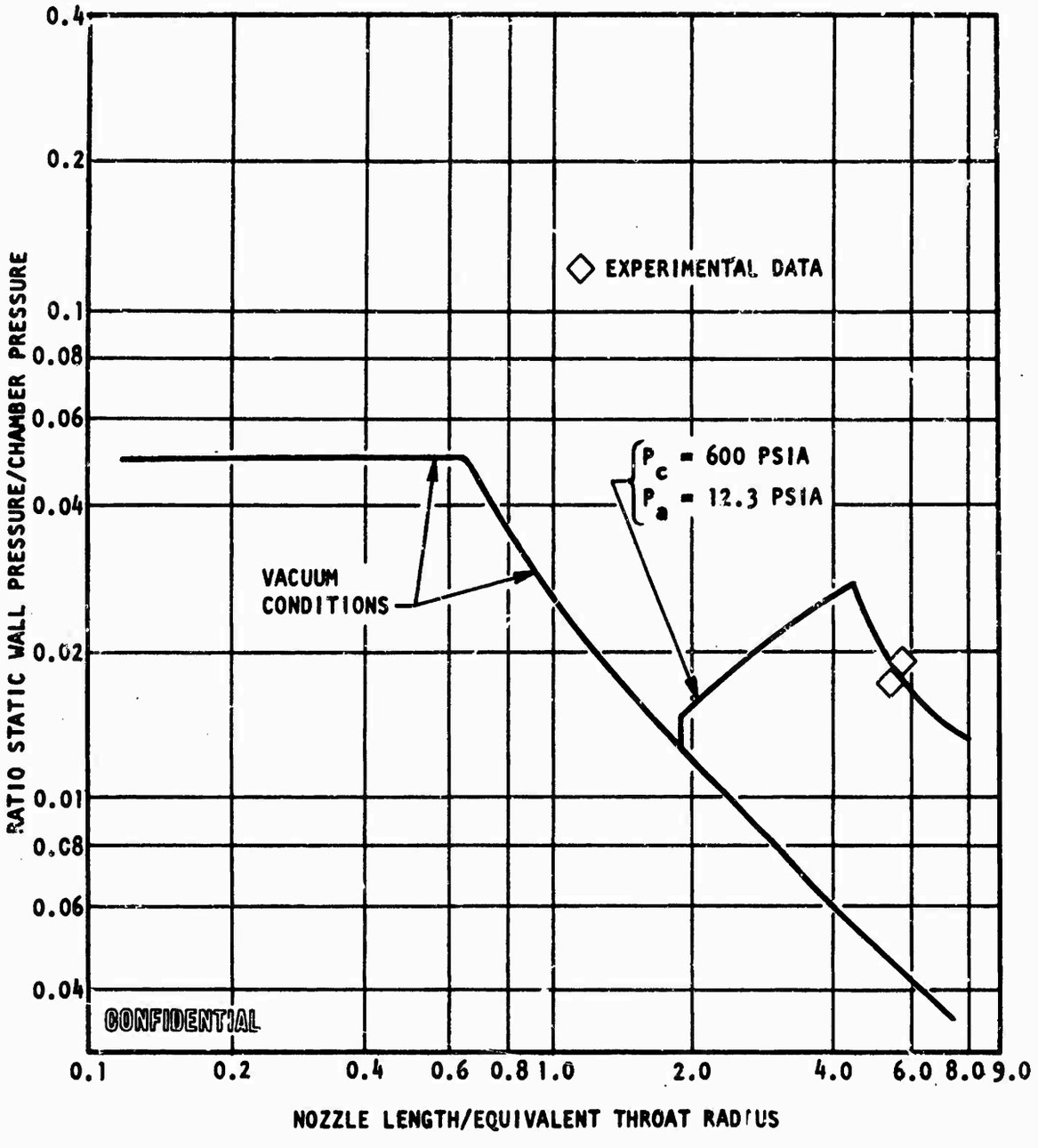

Figure 343. Wall Pressure Profiles

(C) Combustion Performance Analysis. The combustion efficiency obtained for LO_2 Hydrogen Aerospike combustion chamber configurations has been demonstrated in numerous tests. Many of these tests, i.e., the 2.5K segment, were performed specifically to determine combustion efficiency. The results have shown that optimized injector configurations produce combustion efficiencies above 99 percent at full thrust and in the 97- to 98-percent range at throttled conditions. The 2.5K segment designs were employed in the 20K segment and 250K designs. The same high c* performance obtained in the 2.5K segment was also obtained in the 20K segment and on the 250K tests which were not subject to excessive tube leakage, thereby demonstrating that the segment approach can be employed to develop injector performance

(U) For the final performance verification at the 250K level, a solid-wall (water film cooled) and a tube-wall thrust chamber were fabricated. The operational characteristics of the solid-wall thrust chamber (i.e., large amounts of water film coolant and short-duration test) precluded determination of the absolute c* efficiency of the 250K injector. Depending upon the assumptions concerning the behavior of the water film-coolant, efficiencies ranging from 80 to 132 percent were possible. Although it is not possible to obtain absolute values of c* efficiency from the 250K solid-wall testing, it is possible to obtain basic information on the calculation methods employed in evaluating the aerospike thrust chambers.

(U) For example, c* can be calculated from both the measured parameters of flowrate and chamber pressure and also from measured values of thrust. Because this method involves calculated nozzle losses, agreement between c* obtained from thrust and c* obtained from P_cA is verification that the nozzle calculations are reasonably accurate. Results of this calculation with the water effects included are shown in Fig. 344. The data scatter about the 45-degree line indicates that the data are consistent and that the calculation model employed on the solid-wall (and tube-wall) thrust chamber is valid.

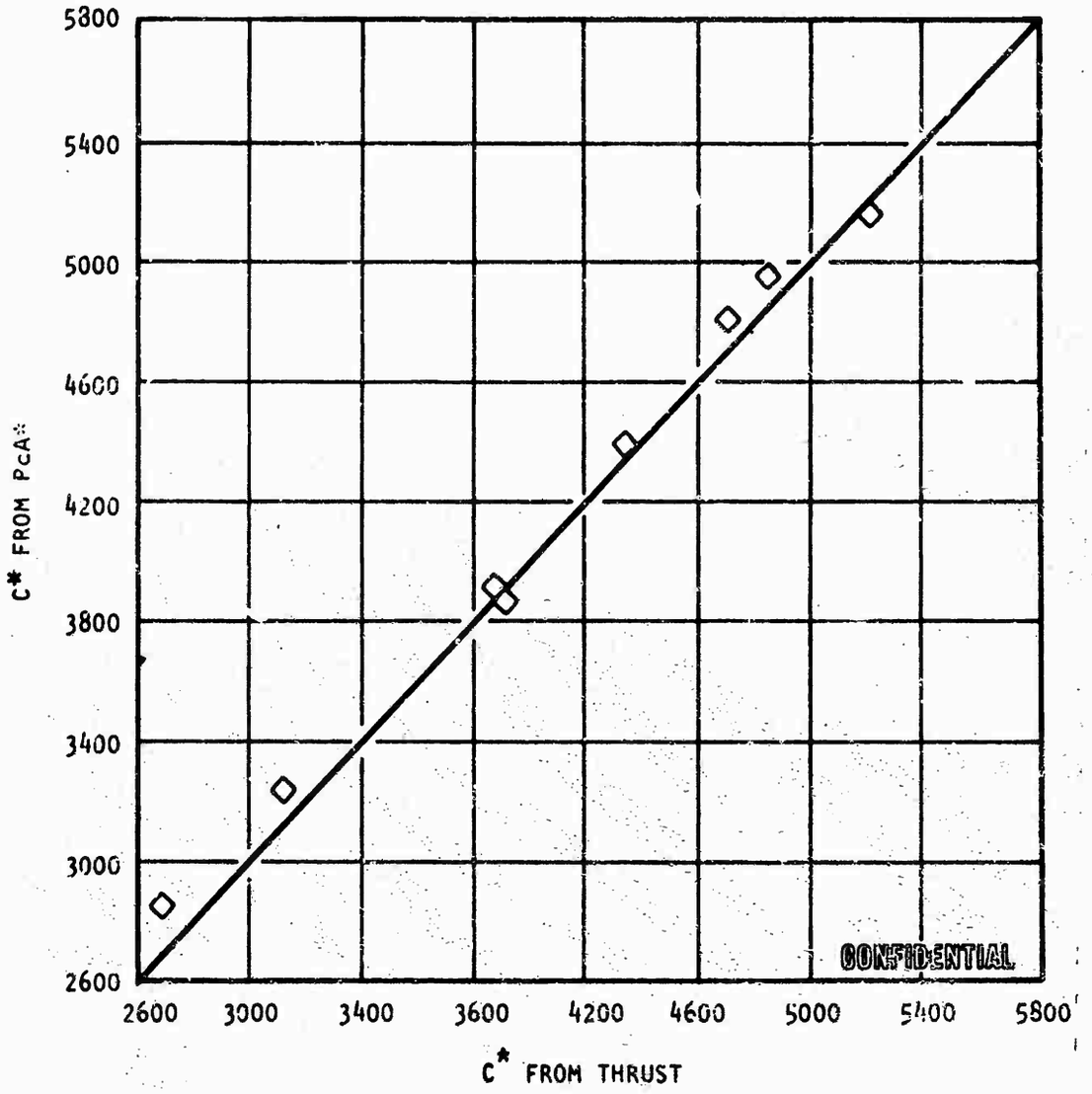

Figure 344. Combustion Performance, Comparison of Two Different Method Results

(C) In the tube-wall thrust chamber testing, three mainstage tests, capable of providing quantitative c* data, were obtained. These data (Table 85) show that c* efficiencies of 97.4, 96.2, and 94.9 percent were obtained for tests 023, 027, and 028. The c* efficiency of 97.4 percent obtained on test 023 was within 1 percent of the level that would have been expected based on the 2.5K segment testing. One adverse factor during this test was the limited duration (~0.4 second). In general, performance evaluation tests are of longer duration. Experience has shown that maximum efficiencies will be achieved after ~1 to 2 seconds of thrust chamber operation.

(U) Because of the nature of hardware damage incurred during tests 027 and 028, it is quite probable that quoted characteristic velocity efficiencies do not accurately portray the injector capability. Combustion efficiencies obtained during these tests are lower than values achieved during earlier short-duration 250K tests and are generally not in accordance with values projected from 2.5K and 20K segment testing.

(C) Besides the aforementioned effect of short duration, inspection after test 027 indicated numerous tube splits throughout the combustion chamber. Inspection after test 028 revealed tube splits plus substantial erosion and leakage at baffles. These two conditions are sources of fuel to the thrust chamber. By injecting fuel through split tubes or damaged baffles, chamber mixture ratio remains constant, but the injector operates at a high mixture ratio. Approximately 6 percent of the thrust chamber tubes were found to have splits. By estimating the total exposed area, it was found that these splits could account for up to 6.5 lb/sec of fuel. Similar analysis of the baffles indicated that the 0.77 sq in. of exposed baffle coolant area could account for up to 5.5 lb/sec of fuel.

(C) The manner in which fuel from the tubes and baffles enters into the combustion process is unknown. However, several calculations have been made to give an indication of the effect that may be expected. The

TABLE 85

(C) TUBE-WALL THRUST CHAMBER PERFORMANCE DATA SUMMARY

	Test Number		
	023	027	028
Test Duration (90-90% P_c), seconds	0.40	0.275	0.800
Specific Impulse, seconds			
Flight System at Test Pressure	343.7	342.2	334.7
Flight System at Vacuum	443.6	435.1	425.8
Specific Impulse Efficiency			
Flight System at Vacuum (Based on Shifting Equilibrium)	0.9548	0.9340	0.9156
Combustion Efficiency (Based on Shifting Equilibrium)	0.9743	0.9623	0.9493
Nozzle Efficiency			
Flight System at Vacuum (Based on Shifting Equilibrium)	0.9615	0.9502	0.9508
Ambient Pressure*, psia	12.30	12.20	12.30
Injector End Pressure*, psia	608.8	824.7	897.9
Nozzle Stagnation Pressure, psia	605.9	821.2	894.1
Overall Engine Mixture Ratio*, o/f	4.720	4.852	5.277
Injector or Primary Mixture Ratio*, o/f	4.930	5.017	5.884
Measured Thrust*, pounds	76140	96611	109251
Total Oxidizer Flowrate*, lb/sec	185.72	238.41	278.15
Total Fuel Flowrate*, lb/sec	62.26	100.91	106.67
Fuel Dump Flowrate*, lb/sec	22.91	51.78	51.76
Centerbody Flowrate*, lb/sec	1.68	1.61	5.43
Total Coolant Flowrate*, lb/sec	60.58	99.30	102.85
Oxidizer Injection Temperature*, R	232.8	215.0	212.2
Fuel Injection Temperature*, R	469.6	381.9	416.5
Coolant Inlet Temperature*, R	100.3	105.3	103.0
Oxidizer Injection Pressure*, psia	640.0	890.5	995.8
Fuel Injection Pressure*, psia	766.8	975.5	1042.3
Coolant Inlet Pressure*, psia	1611.6	2080.1	2171.2
Oxidizer Injector Pressure Drop*, psi	31.2	65.8	97.9
Fuel Injector Pressure Drop*, psi	158.0	150.8	144.4
Geometric Throat Area*, $in.^2$	87.570	81.515	81.895
Nozzle Area Ratio	72.06	77.40	77.04

*Measured Values

extreme case would be where only fuel injected through the injector contributes to performance. In this case, subtracting the flow through damaged areas would increase injection mixture ratio and decrease total flowrate. Based on this extreme assumption, the characteristic velocity efficiencies would be 100 to 105 percent for tests 027 and 028, respectively. A more realistic approach, based on previous segment experience, is to assume that the fuel from the tubes and baffles is 50 percent effective in the combustion process. In this case, the combustion efficiencies would be 97.6 and 98.6 percent for tests 027 and 028, respectively. These latter values not only appear consistent with the expected performance level of the injector but also indicate the slight improvements in performance that would be expected on the longer-duration test.

(U) Based on a review of the hardware and analysis of test data, it still appears that the current injector design will provide high values of characteristic velocity.

(U) General Performance Evaluation. Performance data for tests 023, 027, and 028 of the tube-wall thrust chamber are given in Table 85. Data are presented for: (1) the as-tested system, (2) the flight system at site conditions, and (3) the flight system at vacuum operation. Specific impulse efficiencies are referenced to engine mixture ratio at tank conditions. The equations and procedures used to evaluate the performance and definition of terms are given in Appendix V.

(C) Despite the adverse effects of short duration, the nozzle performance and combustion efficiency achieved during test 023 fulfilled the specific impulse objectives of the Demonstrator Module operation ($\eta_{I_s} > 95$ percent at throttled conditions). The specific impulse achieved at site conditions was over 343 seconds, and a comparable value for vacuum operation is 444 seconds.

(U) Performance values reflect total flow through the chamber. Tube splits were known to be present during runs 027 and 028. These tube splits inject substantial quantities of fuel into the combustor. Therefore, data on these tests are not an accurate presentation of ultimate injector or total (I_s) performance. By estimating the performance penalty associated with this tube and baffle damage, the ultimate performance predictions of the Demonstrator Module can again be verified.

(U) In the segment testing (from the 2.5K to the 20K level), it was repeatedly demonstrated that high combustion efficiencies were achievable with LO_2/H_2 propellants in an aerospike combustion chamber. This high combustion efficiency was verified by test 023 on the 250K thrust chamber.

(U) It was also shown that the anticipated nozzle efficiencies (C_T) were obtained for the 250K thrust chambers when operating at low pressure ratios. With these data, a high degree of confidence in the reliability of the calculational procedures used in estimating the altitude-dependent thrust coefficient is obtained.

(C) Figure 345 presents predicted specific impulse vs pressure ratio for the 250K tube-wall thrust chamber based on c* levels obtained on the 250K program supplemented by the 2.5K segment program. From this figure it will be noted that performance levels are consistent with the expected and previously quoted performance levels. A general conclusion of the 250K tube-wall chamber is that achievement of the specific impulse performance indicated in Fig. 345 is feasible on the 250K tube-wall chamber and that only the operational problems prevented the attainment of this level.

(U) Side Loads. A discussion of the thrust-measuring system is presented in the Facility Description section. The equations for the six components of force (three forces, three moments) were established from a diagram of the test stand (Fig. 298). It was thus possible to compute the six force

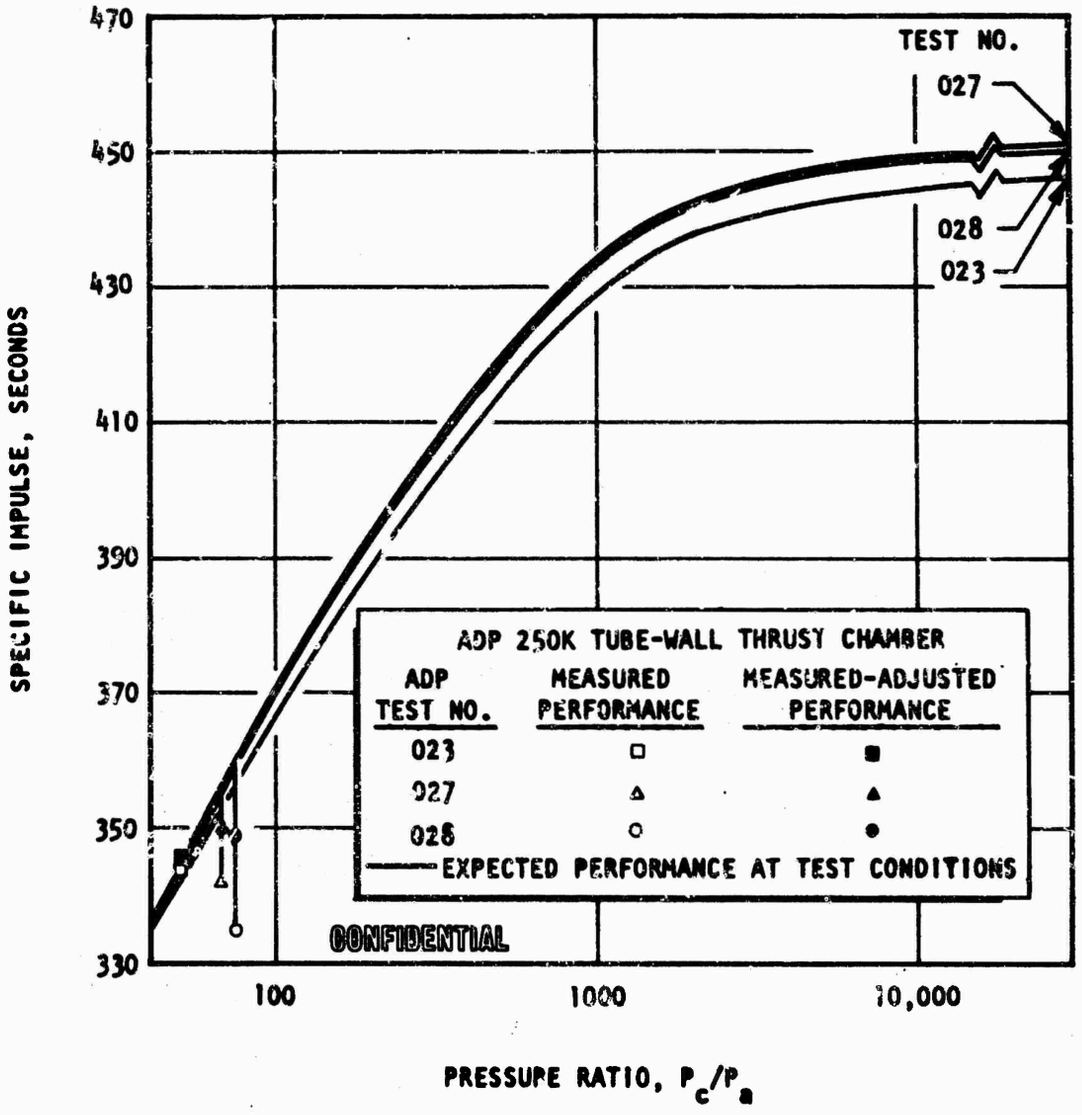

Figure 345. 250K Tube-Wall Thrust Chamber Specific Impulse vs Pressure Ratio

components as a function of run time. Load cell forces were recorded on the data-acquisition system, and the results were automatically printed out as plots of load cell force vs run time.

(U) One of the key items evaluated during this test series was the value of side loads. These loads were monitored during the start and cutoff transients, as well as during mainstage. For high nozzle area ratio bell chambers, the phenomenon of high side loads has influenced the chamber structure and development.

(C) It is significant to note that the side loads and moments obtained on the tube-wall chamber during the start transient, and also during steady-state operation, were very low. The three principal load components during the start transient of test 028 had the following values (in pounds):

Main Thrust	109,251
Peak Transient Vertical Side Load	557
Peak Transient Horizontal Side Load	92

(U) These load values are typical of the tube-wall tests.

(U) Side load forces were exceptionally small. Based upon the data obtained during the test series, it is expected that excessive side loads will not be a problem with this chamber.

(C) Throat Gap. A sensitive potentiometer was adapted to a bracket assembly to infer throat gap change during a test by measuring the relative radial displacement change between the inner and outer bodies at the throat plane. Figure 346 is a plot of throat gap change on test 028 which was conducted at a 900-psi chamber pressure. The measured throat gap change of 0.022 is in very good agreement with the predicted throat gap change

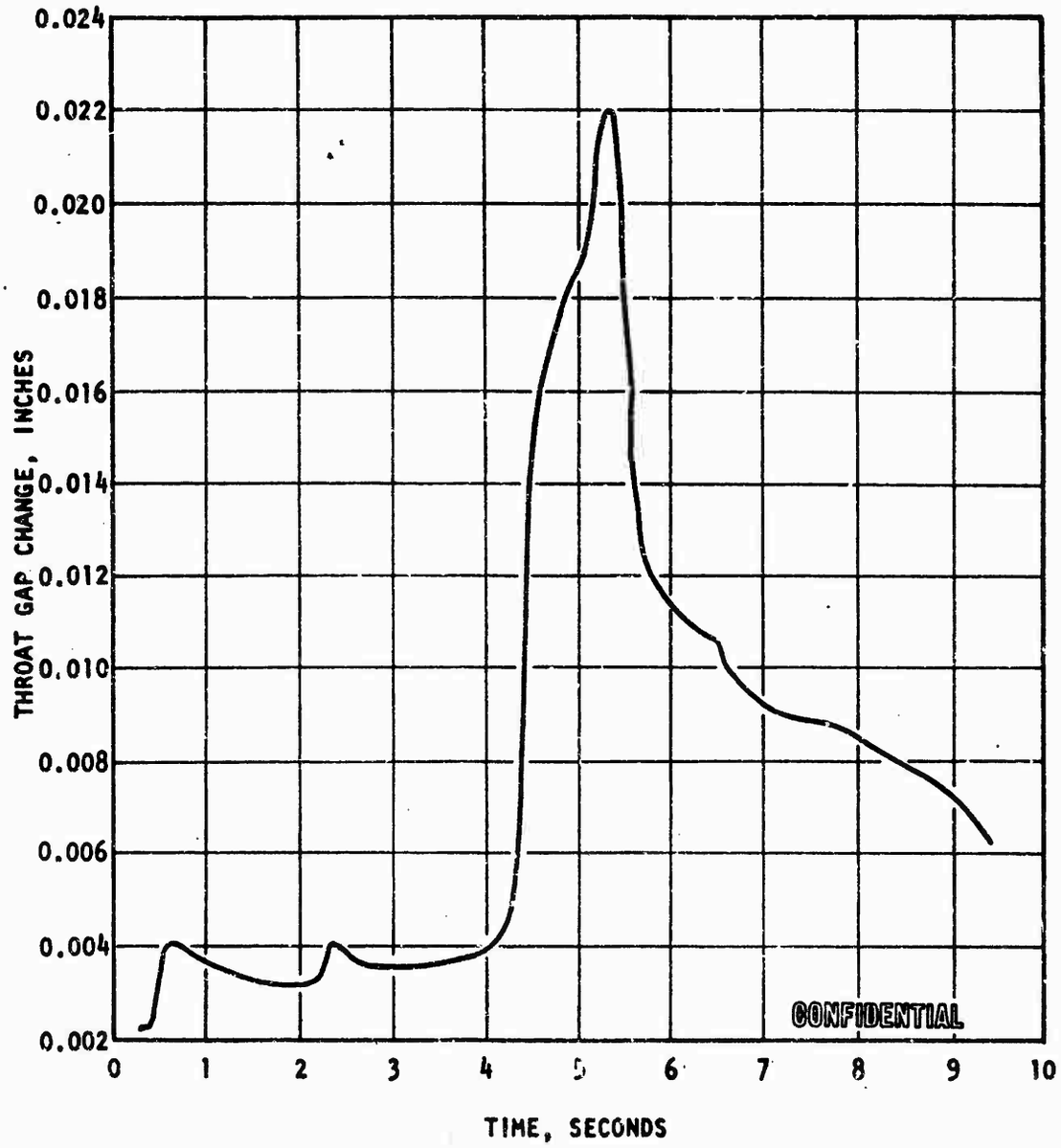

Figure 346. Throat Gap Variation During Mainstage of Test 028

of 0.020 to 0.025 at a 900-psi chamber pressure. These values of throat gap change are not directly applicable to the Demonstrator Module because of the difference in backup structures and the fact that the baffles attach to the chamber walls in the Demonstrator Module. The fact that the measured throat gap change agreed well with predicted values reaffirms the predicted throat gap control of the Demonstrator Module.

(C) Heat Transfer. The 250K chamber tubes, which were released early in the program, are designed for a peak heat flux of 50 Btu/in.^{2}-sec. The 2.5K solid-wall tests indicated that the heat flux in the throat was approximately 56 Btu/in.^{2}-sec at a 1500-psi chamber pressure with a wall temperature of 1600 F. As a result, an analysis was made to determine the actual operating characteristics of the throat and chamber. Selected parametric results are shown in Fig. 347 through 349 . Figure 347 shows the effect of coolant flowrate on the gas wall temperature of the outer-body throat at the 900-psia chamber pressure operating point. The outer-body throat was chosen as a critical test point, because theoretically, it is the hottest region in the chamber having higher theoretical wall temperatures than either the inner-body throat or the combustor. A curvature enhancement of 1.15 was chosen as being a somewhat conservative estimate of the value occurring near the aerodynamic area ratio, this being theoretically more severe than the geometric area ratio which has a higher curvature enhancement. Similar parametric analyses at other chamber pressure operating points were also conducted.
conducted.

(C) The effect of curvature enhancement on the theoretical operation of the tubes is evident by comparing Fig. 348 (ϕ curvature = 1.5) with Fig. 347 (ϕ curvature = 1.15). It can be seen that the coolant requirements can be reduced by up to 25 percent if the curvature enhancement is increased from 1.15 to 1.5.

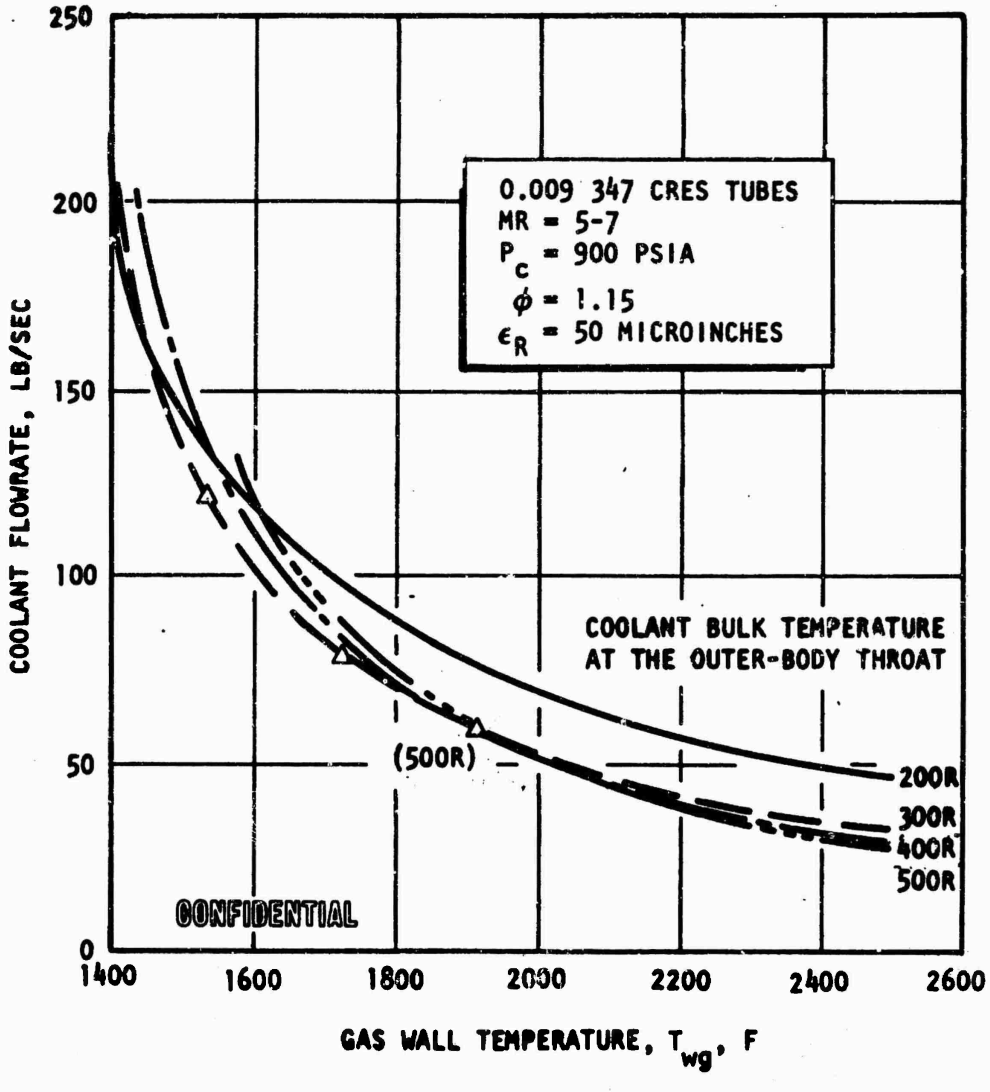

Figure 347. 250K Outer Body Throat Predicted Cooling Requirements

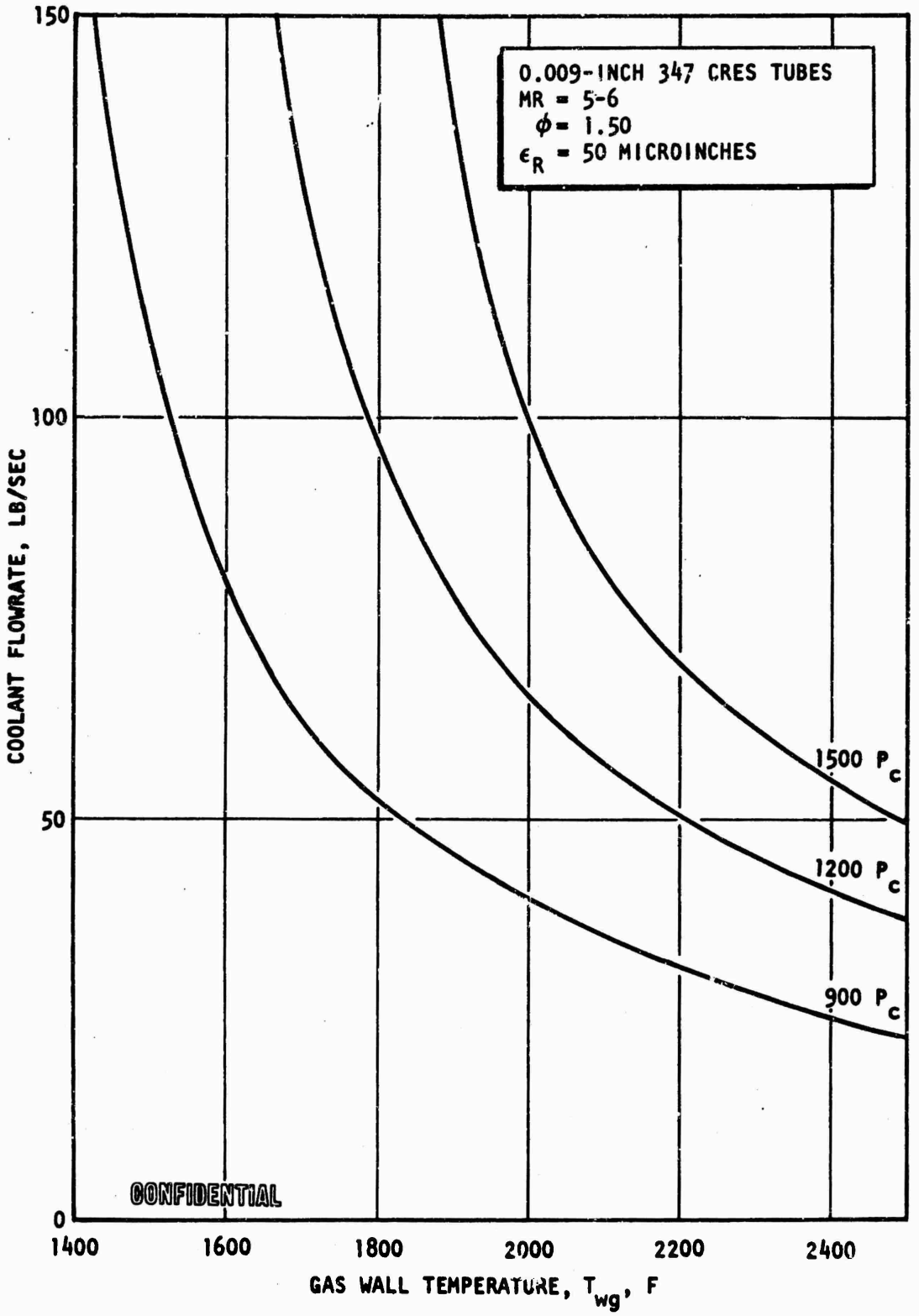

Figure 348. 250K Outer Body Predicted Throat Cooling Requirements

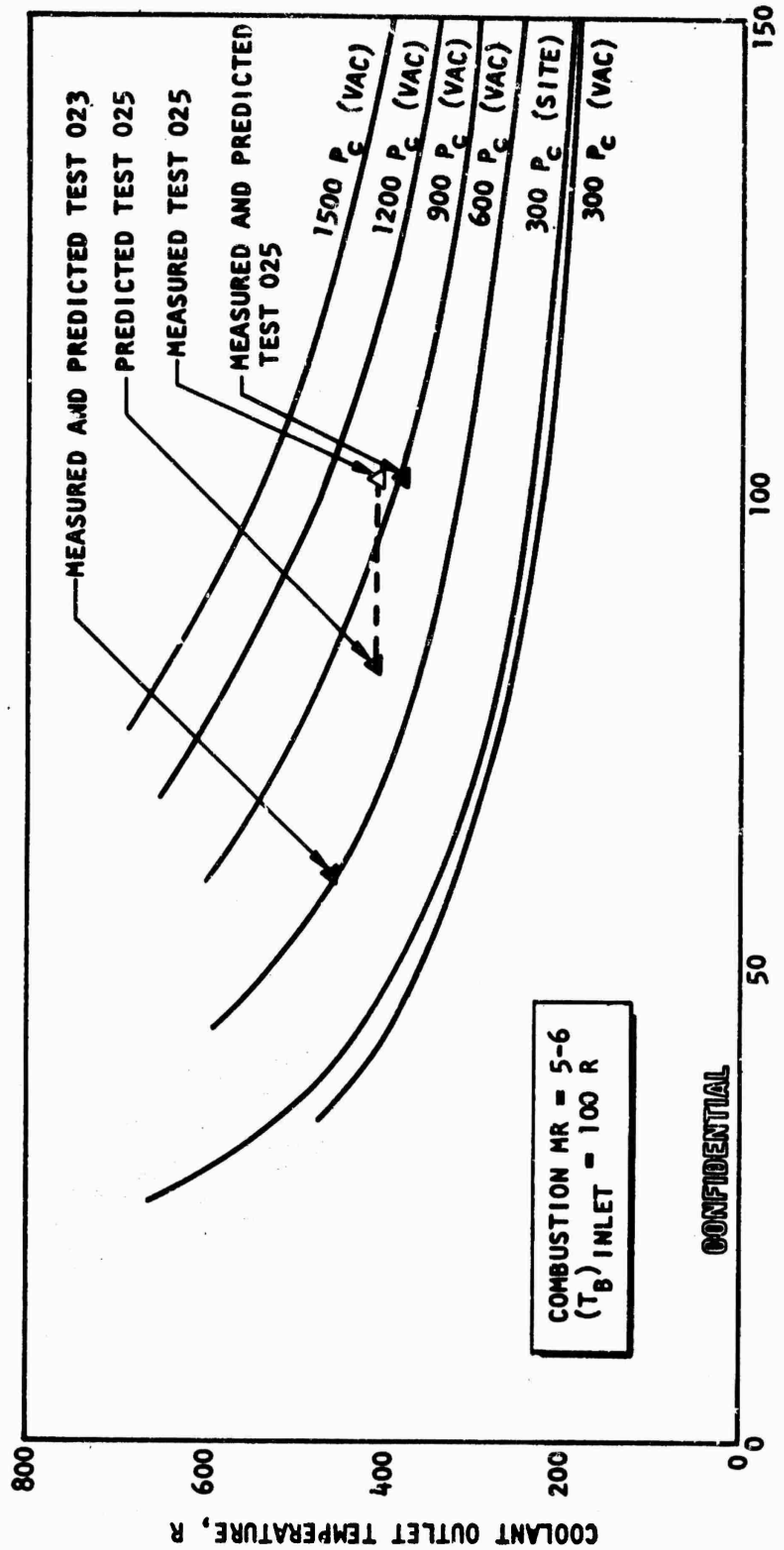

Figure 349. 250K Predicted Coolant Discharge Temperature, Outer Body C_2/H_2

(C) The predicted hydrogen discharge temperature from the outer body is shown in Fig. 349 for various coolant flowrates and chamber pressures. Also shown in Fig.349 are the experimental data points. The theoretical predictions agree extremely well with the experimental points. The apparent discrepancy of test 025 data can be fully accounted for if 20 lb/sec were lost from the coolant passages early in mainstage. It was determined from the test 025 failure analysis that 20 lb/sec hydrogen was indeed lost from the coolant circuit during transition.

(C) Hot-Gas Tapoff. The No. 1 injector unit was designed to evaluate hot-gas tapoff. This unit was equipped with tapoff ports on each baffle and a hot-gas manifold. The outlet of this manifold could be orificed to govern the amount of tapoff flow. During each test, sufficient gases were tapped from the chamber to fill the manifold. On three tests, tapoff gases were flowed through the manifold. Hot-gas flow was approximately 1.5 percent of the total flow through the chamber. Each tapoff test was of relatively short mainstage duration (100 to 300 milliseconds). The maximum tapoff temperature measured during these tests was 800 F. Extrapolation of this transient trace indicated that hot-gas temperatures were comparable with values achieved during 2.5K testing.

(C) Ignition and Start Characteristics. Fourteen hot-firing tests and five ignitions were conducted during the series of 250K tests. The thrust chambers were started over a range of mainstage chamber pressures from 353 to 1290 psia. Smooth transition and ignition were obtained in all cases, indicating adaptability of the thrust chamber to a variety of engine start conditions. Figures 350 and 351 represent starts to 340- and 1290-psia chamber pressures, respectively. Both of these traces are for tests conducted with the film-cooled, solid-wall thrust chamber.

(C) The chamber pressure trace for the No. 1 tube-wall chamber was again smooth on all tests. A step-start sequence was successfully utilized for

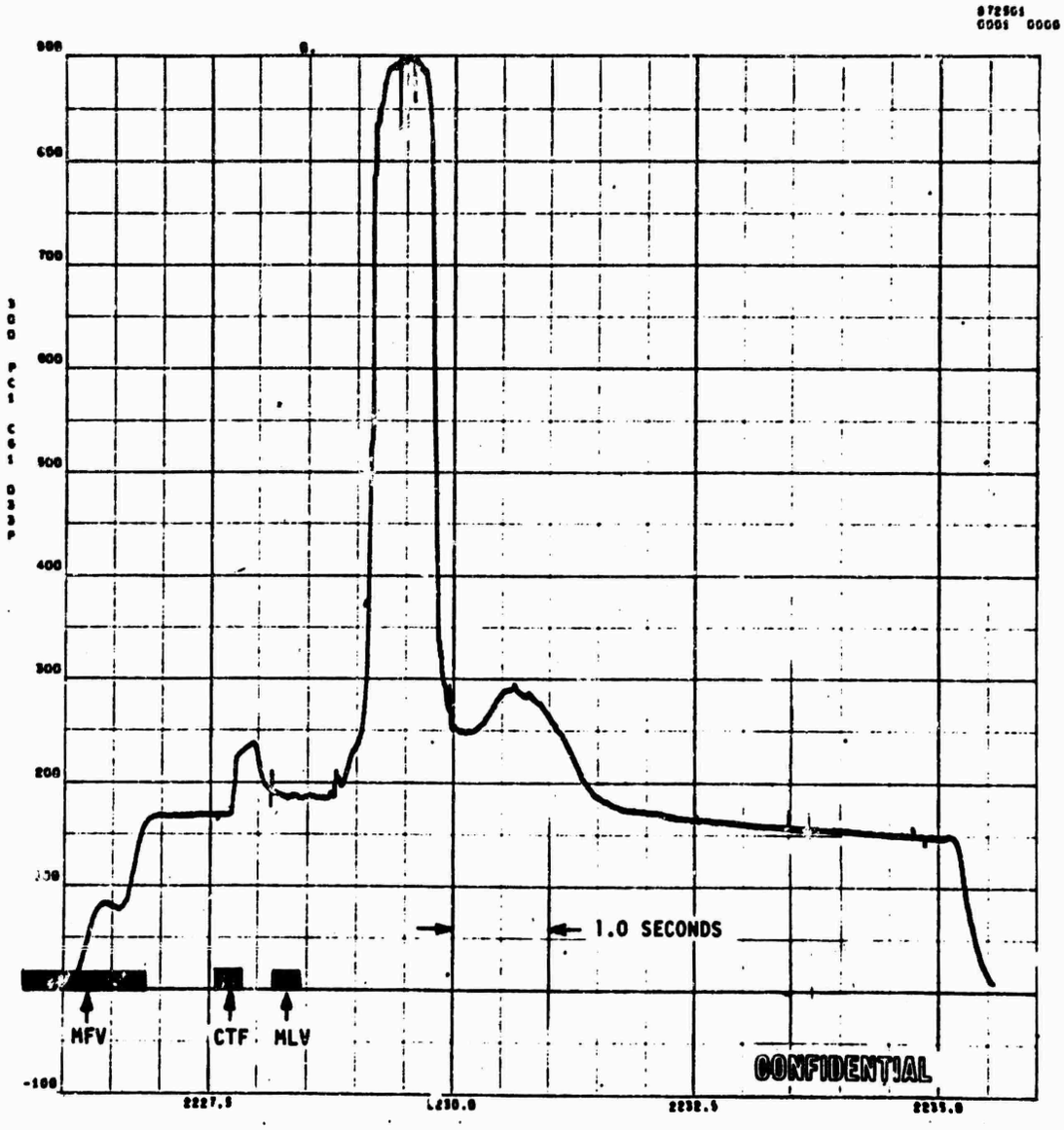

Figure 350. Chamber Pressure for Test 006

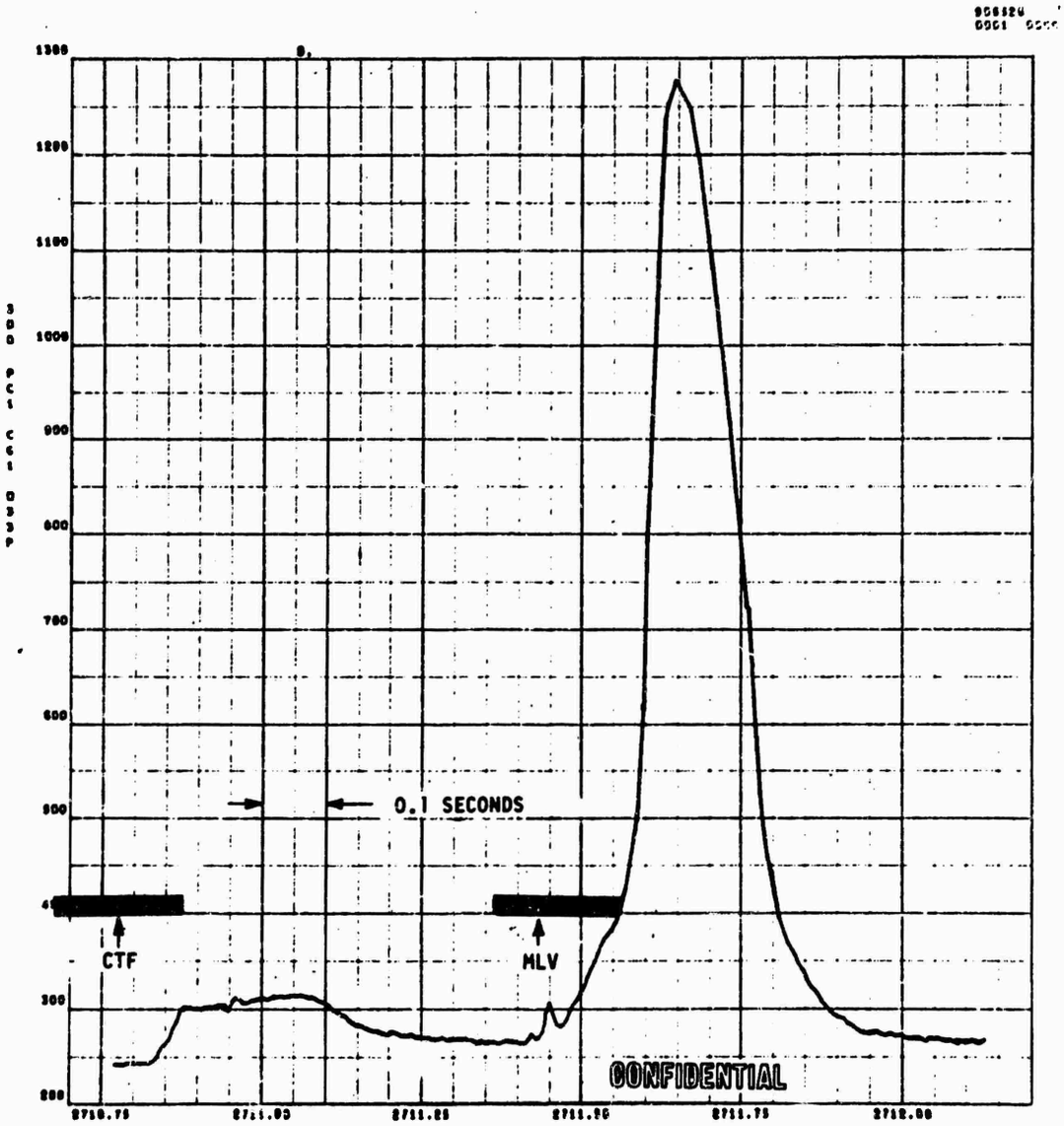

Figure 351. Chamber Pressure for Test 017

the No. 2 tube-wall test series to reduce the rate of chamber pressure rise and avoid possible excessive tube heat flux conditions during the start transient. The modified start sequence (Fig. 352) lengthened the transition to mainstage from approximately 50 to 500 milliseconds.

(U) Hypergol ignition of the annular chamber was satisfactory over the entire range of operating conditions as evidenced by test films and test pressure data. The films showed that all compartments were repeatedly ignited. The test records show that ClF_3 was expelled in approximately 200 milliseconds, and that the amount of hypergol was adequate to establish a good ignition flame.

(U) Based upon the test data accumulated, it is concluded that satisfactory prime and ignition of the 250K aerospike has been demonstrated.

(U) Hot-gas ignition was not accomplished. The No. 1 injector (which provided hot-gas ignition capabilities) was irreparably damaged on test 025. Hot-gas ignition feasibility was demonstrated during the 2.5K segment program.

(U) Combustion Stability Analysis. Thrust chamber dynamic performance was evaluated by analysis of high-frequency-response pressure transducers, accelerometers, high-speed fastax framing films, and streak photography. The first test on the solid-wall thrust chamber assembly employed flush-mounted, high-frequency-response chamber pressure transducers. Failure and burnout of these instruments necessitated their removal and no further flush-mounted chamber pressure measurements were made during the test series. Recess-mounted chamber pressure measurements were made for all tube-wall tests.

(C) Two pulse gun tests at chamber pressures of 353 and 1289 psia were conducted and resulted in no instability being induced. The first test

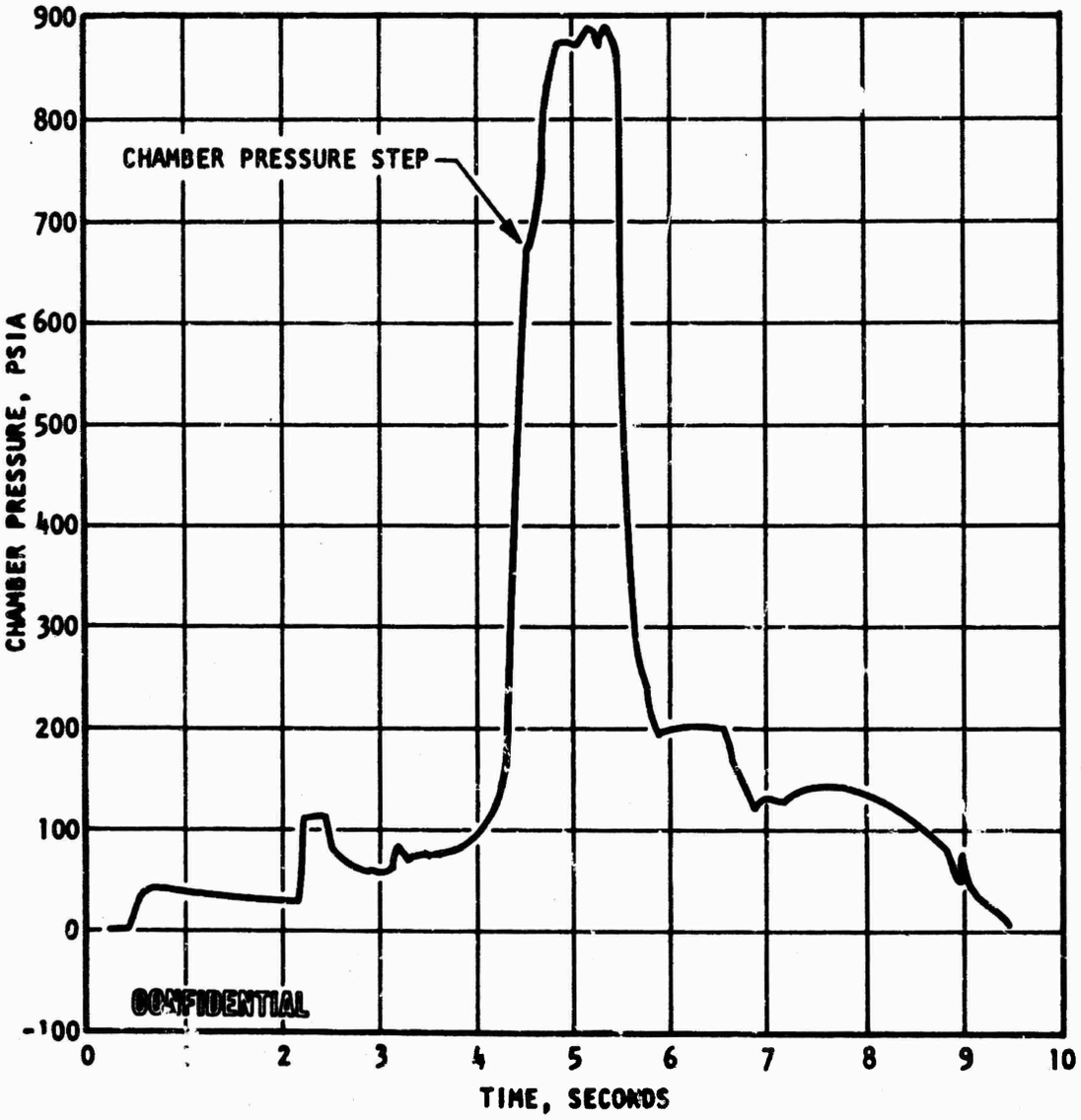

Figure 352. Test 028 Chamber Pressure Trace

used a 15-grain charge to burst a 7500-psi burst diaphragm, and although an instantaneous luminosity change was observed locally in the fastax film, no indication of disturbance was observed on accelerometers or feed system pressure transducers (Fig. 353). In the 1289-psi chamber pressure test, a 40-grain charge used to burst a 20,000-psi burst diaphragm produced similar results.

(C) Analysis of all test data revealed a tendency for the system to oscillate in two frequency ranges: (1) 200 to 400 cps during transition and cutoff and in mainstage at the lower chamber pressure levels, and (2) 1800 to 2000 cps during mainstage on some tests. Sonic traces from the last tube-wall chamber tests (027 and 028) illustrated both of these frequencies (Fig. 354).

(U) The first mode of oscillation (200 to 400 cps) has been analyzed to be the common chug mode and correlates extremely well with an analytical model developed on the NASA SDI program. Minor modifications to the feed system impedance will eliminate this mode of oscillation at the low chamber pressure operating condition.

(U) Analysis of the intermediate frequency mode (1800 to 2000 cps) revealed no correlation with the predicted fundamental modes of acoustic instability or structurally coupled modes of oscillation.

(U) Assuming a thrust chamber gas product acoustic velocity of 5500 ft/sec, the computed fundamental modes are:

First Tangential	~230 cps
Baffle Compartment Tangential	~4700 cps
Baffle Compartmental Radial	~16,000 cps
Longitudinal	~5500 cps

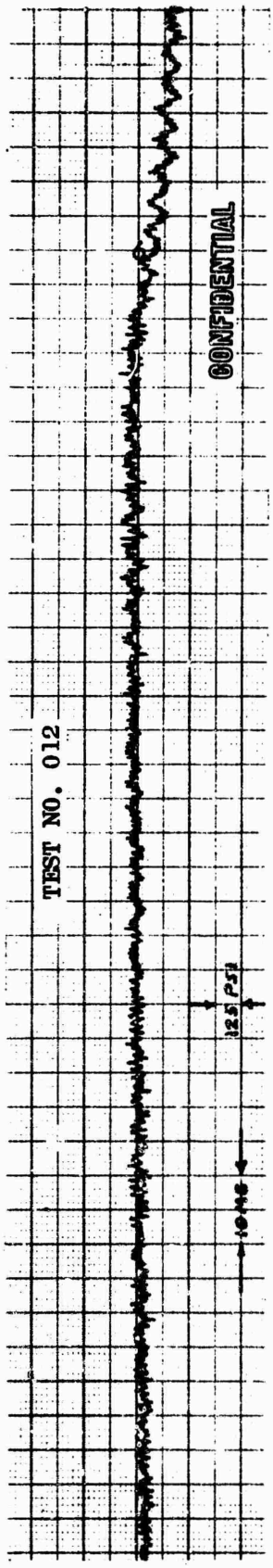

Figure 353. No. 2 LOX Manifold Photocon Traces, Mainstage

Instrument	Test 027 (Mainstage)	Test 028 (Ignition Stage)	Test 028 (Buildup to Mainstage)
Oxidizer Torus Manifold Pressure	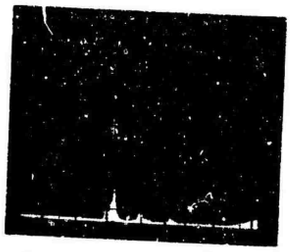 14.0 psi rms/div		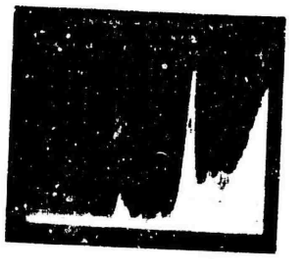 10.1 psi rms/div
Fuel Inlet Pressure	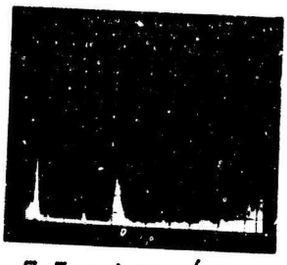 7.5 psi rms/div		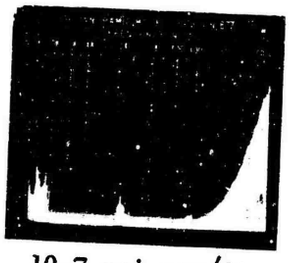 10.7 psi rms/div
Fuel Injection Pressure	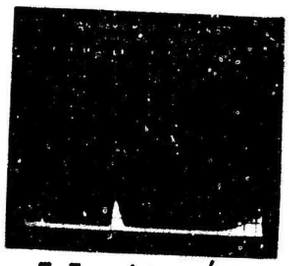 7.5 psi rms/div	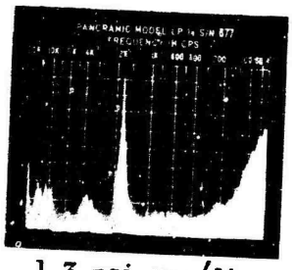 1.3 psi rms/div	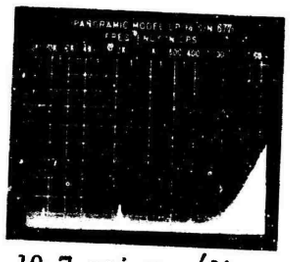 10.7 psi rms/div
Fuel Injection Pressure	 7.5 psi rms/div		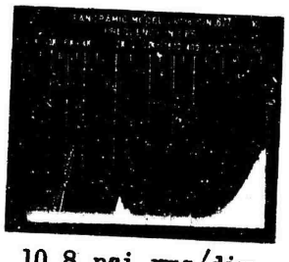 10.8 psi rms/div

Figure 354A. Sonics for Tube-Wall Aerospike Chamber

Instrument	Test 028 (Cutoff - 800 Milliseconds to Cutoff - 450 Milliseconds)	Test 028 (Cutoff - 450 Milliseconds to P_c Decay)
Oxidizer Torus Manifold Pressure	 5.1 psi rms/div	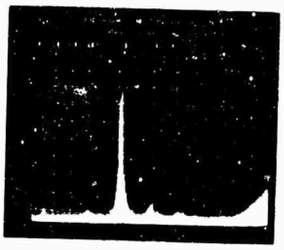 11.3 psi rms/div
Fuel Inlet Pressure	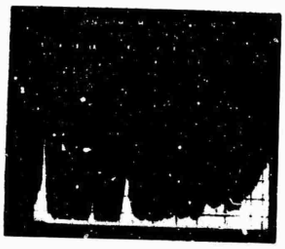 6.3 psi rms/div	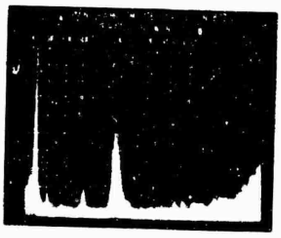 4.4 psi rms/div
Fuel Injection Pressure	 6.3 psi rms/div	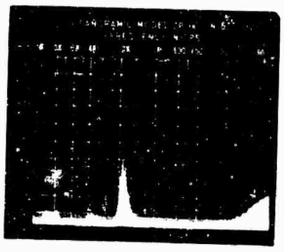 4.4 psi rms/div
Fuel Injection Pressure	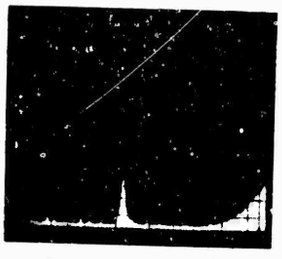 6.3 psi rms/div	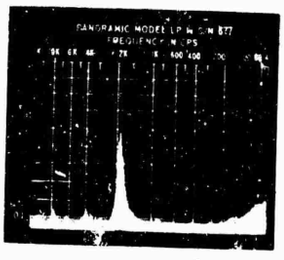 4.4 psi rms/div

CONFIDENTIAL

Figure 354B. Sonics for Tube-Wall Aerospike Chamber

Instrument	Test 027 (Mainstage)	Test 028 (Buildup to Mainstage)
VSC, Outer Body	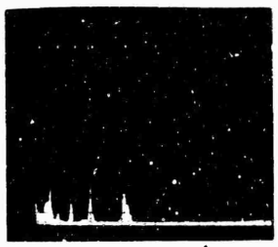 17.0 g rms/div	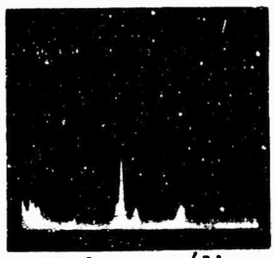 15.0 g rms/div
VSC, Inner Body	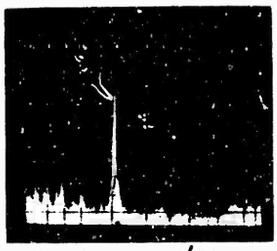 17.0 g rms/div	
Accelerometer, Axial	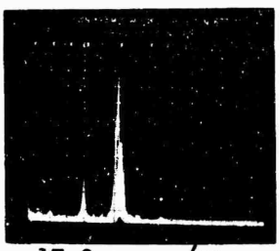 17.0 g rms/div	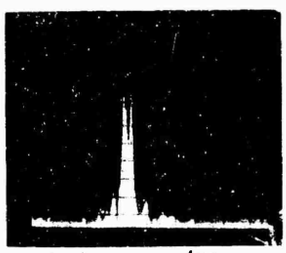 4.6 g rms/div
Accelerometer, Radial	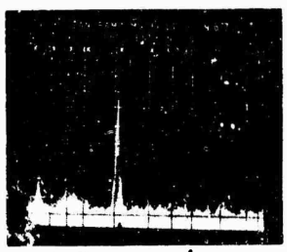 9.5 g rms/div	

CONFIDENTIAL

Figure 354C. Sonics for Tube-Wall Aerospike Chamber

Instrument	Test 028 (Cutoff - 800 Milliseconds to Cutoff - 450 Milliseconds)	Test 028 (Cutoff - 450 Milliseconds to P_c Decay)
VSC, Outer Body	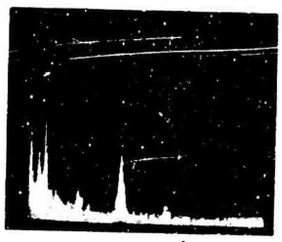 5.8 g rms/div	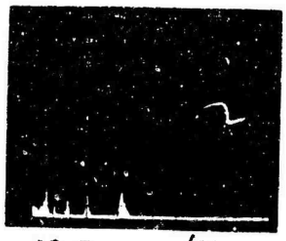 19.3 g rms/div
VSC, Inner Body	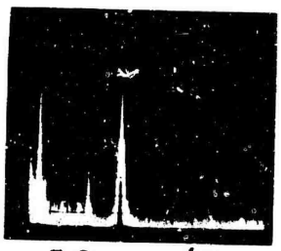 5.8 g rms/div	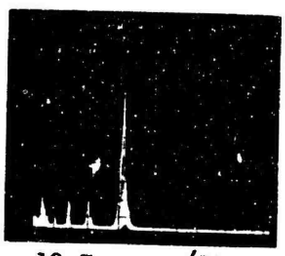 19.3 g rms/div
Accelerometer, Axial	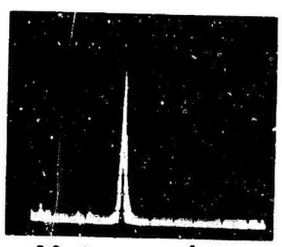 10.2 g rms/div	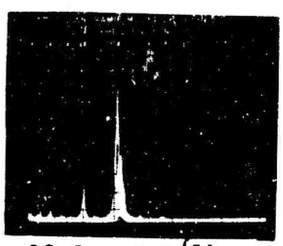 19.2 g rms/div
Accelerometer, Radial	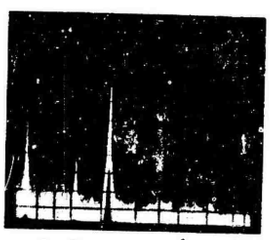 4.0 g rms/div	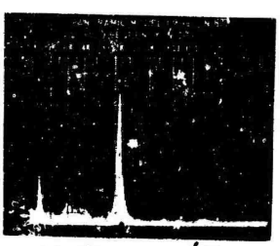 11.0 g rms/div

CONFIDENTIAL

Figure 354D. Sonics for Tube-Wall Aerospike Chamber

(C) No consistent phase relations among chamber pressure transducers or feed system transducers were observed. Accelerometer recordings indicated that in the 1800-cps range, outer-body accelerations were greater than inner-body accelerations, while the reverse was true when the oscillation frequency approached 2000 cps. Calculation of all theoretical fluid feed system resonances yielded no modes in the 1800- to 2000-cps range.

(U) High-speed fastax framing camera film review showed a rotating, flashing luminescence in the primary nozzle flow field in both solid-wall and tube-wall tests.

(U) To identify the oscillation mode further, a streak camera was employed in test 028. The film moved in the direction of gas flow and the plane of view was 115.5 inches. The image recorded was 3/4 inch by 9 feet in length, and the image position on the nozzle exit was 26 inches from the downstream end of the nozzle extension. Figure 355 illustrates the installation. A section of the streak photograph recorded during test 028 is shown in Fig. 356.

(C) Examination of the photograph reveals two dynamic patterns. The first is a series of bright lines parallel to the edge of the film, which appear and disappear at the rate of 2000 times per second. These streaks are radiation of copper molecules, which indicates a dislodging of copper from the baffles at a frequency of 2000 cps.

(C) A second pattern, apparent from the streak film strip, is the presence of dark lines with a period of 1/220 second. This correlates well with a combustion wave traveling at 5500 ft/sec. The distance between waves, however, is much less than the expected period and suggests a series of combustion waves traveling around the chamber. At a fixed point in space, nine waves traveling around the complete annular chamber would yield an apparent cyclic ratio of approximately 2000 cps.

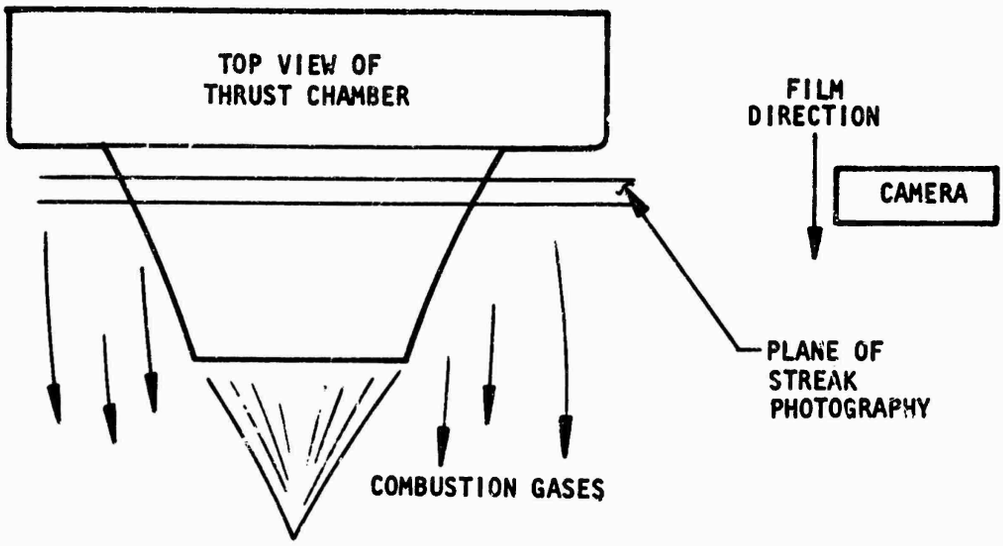

A. CAMERA LOCATION AND FILM DIRECTION

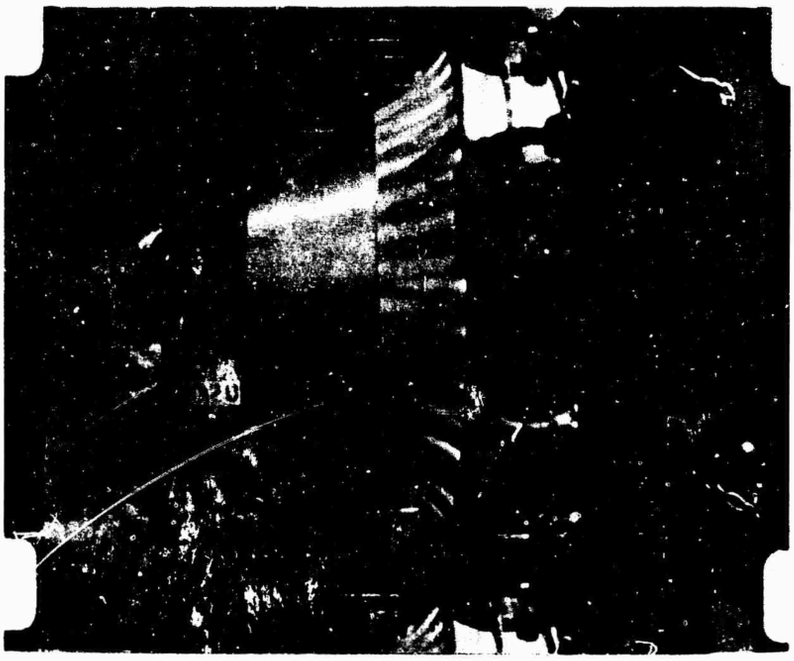

B. VIEW FROM STREAK CAMERA LOCATION

Figure 355. Orientation of Streak Camera

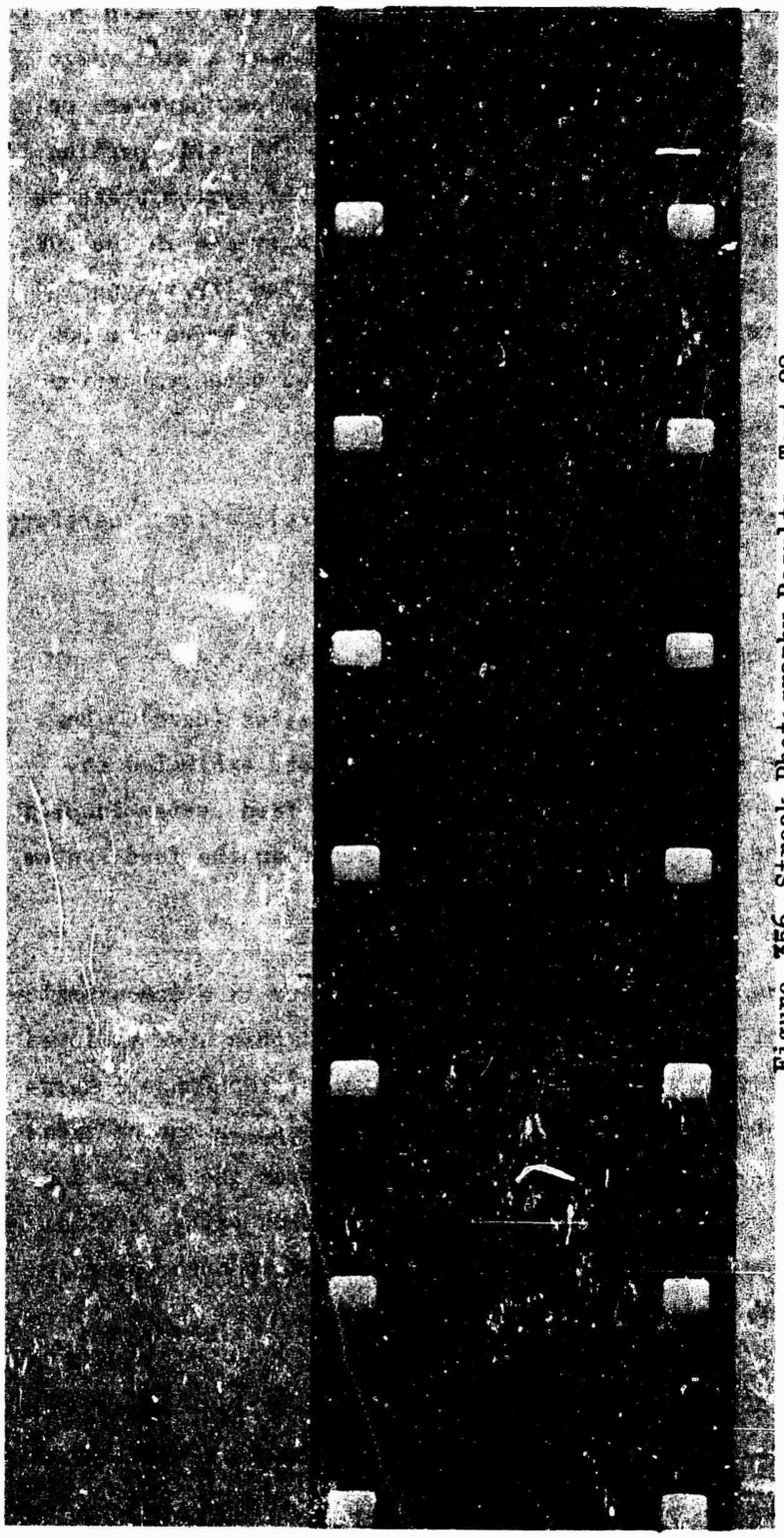

Figure 356. Streak Photography Results, Test 28

(C) Review of stability data obtained on the same injector pattern on the 20K and 2.5K segments showed that all 2.5K data were stable with no oscillation tendency in the 2000-cps range when tested over a wide range of chamber pressure and mixture ratio. The 20K data review, however, revealed an oscillation at 1800 to 2000 cps, apparent in the early portion of mainstage on almost all tests. Phase analysis of feed system pressure measurements showed that the mode was not the first transverse in the 20K. The wave character was indicative of a feed system-coupled "buzz-type" oscillation. Because injector and thrust chamber feed system on the 20K is quite similar to the 250K, it can be conjectured that both combustion systems exhibit a similar mode.

(C) The two proposed modes of the 1800- to 2000-cps oscillation, therefore, are:

1. Higher harmonics (~ninth) annular acoustic mode
2. Feed system-combustion process coupled oscillation (buzz). Because both the solid-wall and tube-wall chambers exhibited the same mode, it is hypothesized that if it is a feed system-coupled phenomenon, the oxidizer feed system, rather than the feed system, is more likely the coupling system.

(C) The higher-order annular mode is not likely to occur in a demonstrator engine system because of the presence of longer baffles than were employed in the Phase I hardware (4.5 vs 3 inches). In addition, the Phase I hardware permitted a communication between baffle compartments in the critical combustion zone area through the presence of a gap between the baffle and chamber wall. This gap, which permits an annular gas flow path, is eliminated in the demonstrator because the baffles are sealed to both inner and outer thrust chamber body walls.

(U) "Buzz-type" oscillation modes have been present in various experimental thrust chambers. The solution to these problems has generally been achieved

with slight alteration to feed system dynamical behavior and/or modification of the combustion zone sensitive time lag.

Problem Areas and Solutions

(U) The design and fabrication of a "first-of-a-kind" chamber usually entails problems peculiar to the specific chamber. Several such problems were encountered during fabrication of the 250K chambers.

(U) The original chamber concept utilized injector baffles that consisted of an inner core of high-temperature, high-strength material with cooled copper facing. Development difficulties precluded the use of this design for the 250K injectors and drilled copper baffles were substituted. Fabrication problems of the high-strength core baffle were overcome in time to be used successfully on the 20K segment, however.

(U) Other problems encountered during fabrication which required corrective action included the following items:

1. The inner-body forging (vendor supplied) consisted of welded pieces which contained welds with slag and porosity. It was necessary to machine away the weld which would be under tubes on the final chamber and apply new weld.
2. Thermochromistic check of the first tube-wall chamber after furnace braze indicated that complete braze adhesion of the tubes had not been attained. Addition of more chamber alloy grooves resulted in complete tube braze adhesion.
3. Tie bolts were added to the inner-body, end ring to reduce the load carried by the tube-to-end ring braze joint to ensure structural integrity.
4. A few tubes were plugged on the first chamber because of runoff of braze alloy during furnace braze. Stopoff applied to the ends of the tubes effectively eliminated tube plugging during the braze cycle.

(U) The solid-wall chamber utilized water-film-cooled throat sections fabricated by weld depositing copper on the chamber body. Fabrication of the outer-body throat was accomplished satisfactorily; however, copper welding of the inner body resulted in weld cracking. Attempts at weld repairing the throat and installing a copper ring were likewise unsuccessful. Consequently, the copper throat of the inner body was removed and the profile was achieved by nickel weld buildup. The problem with depositing copper on the inner body was that the weld deposition tended, thermally, to expand away from the body, resulting in cracking. This problem was not encountered on the outer throat because weld expansion tended to be constrained by the body since the weld was deposited on the ID of the chamber.

(U) Many potential problems concerned with testing (such as chamber pressure overshoot and water flowrate control) were anticipated and solved prior to delivery of the hardware to the test site. Other problems became evident during testing, and corrective action was taken as each problem was defined.

(U) It was noted during fuel blowdowns and during the first test that a vacuum was drawn on the inner-body, tube-to-backup vent cavity while fuel was flowing through the tubes. The pressure in the cavity spiked upon cessation of fuel flow. Analysis of this problem revealed that air in the backup structure cavity was liquefied by cold hydrogen flowing through the tubes. Liquefaction of air created a vacuum which drew more air into the cavity. Ambient purges through the tubes following cessation of cold hydrogen flow evaporated the liquefied air faster than the vents were capable of relieving the pressure. The problem was solved by inerting the inner-body vents with gaseous hydrogen and manifolding the vents (Appendix IV).

(C) Following the first tube-wall test, routine inspection revealed that liquid was standing in the chamber. A sample of the liquid was found to

consist of hydrofluoric and hydrochloric acids with a pH of 1.4. The chamber was flushed with water and thoroughly purged until a dew point check indicated that the chamber was dry. Analysis of the problem indicated that ClF_3 was flash frozen to the inner walls of the hypergol tubes. These tubes pass through the fuel manifold. The fuel temperature at ignition is approximately 100 R, whereas ClF_3 freezes at 355 R. Neither gaseous oxidizer propelling the ClF_3 nor fuel surrounding the hypergol tube reached a temperature high enough to melt or vaporize the frozen ClF_3 during mainstage. Acid was formed when ClF_3 vapors combined with water from melted frost after the chamber warmed to ambient following shutdown. Posttest securing procedures were modified to ensure that the ClF_3 system was warmed and purged prior to securing the chamber. It should be noted that no chamber damage resulted from acid contamination.

(C) Pressure spikes were observed to occur in the liquid oxygen manifold in the priming phase during solid-wall chamber testing. These spikes increased with an increase in chamber pressure. At high flowrates, the chamber was pressurized with hydrogen during fuel lead faster than the nitrogen purge could pressurize the oxygen manifold. Consequently, hydrogen, and possibly ClF_3, backflowed into the oxygen manifold where it reacted with the initial oxidizer flow. The oxidizer purge capacity was increased prior to tube-wall testing to provide adequate manifold purge. The start sequence was also changed prior to testing the No. 2 tube-wall chamber, as described in Appendix VIII.

(U) A major injector failure was experienced on the first tube-wall test series which resulted in facility and hardware damage and is described in detail in Tube-Wall Test Series (page 694). The cause was ascribed to gas circulation in the gap between injector and body and also to the pressure of combustion oscillations driving hot gas through this gap. These oscillations were identified later in the second tube-wall test series. Gas circulation in the gap was solved by installation of a lip

seal and ablative material in the gaps as described on page 723. Subsequent testing on this and the NASA Advanced Engine Aerospike Program showed this solution to be effective.

(U) The second tube-wall test series was terminated by damage to baffles and tubes resulting from combustion oscillations in start and mainstage. Although an analysis provided much information on the mode of oscillation (page 763), there was insufficient time on this contract to take corrective action. Subsequent to this contract, however, progress was made toward solution to this problem on the NASA Advanced Engine Aerospike Program. Modifications were made to the LO_2 feed passages immediately upstream of the injector face and to the baffles to improve compartmentation. These modifications attenuated the oscillations and reduced damage such that desired duration tests (7 seconds) were conducted.

SEGMENT STRUCTURAL EVALUATION

Objectives and Requirements

(U) The requirements of this subtask were as follows. The 20K segments were to be as light weight as practicable, simulating the structural characteristics of the Demonstrator Module thrust chamber (such as the ability to maintain throat dimensions) and combustion chamber weight. The tube material for the 20K segment was to be the optimum, selected from the 2.5K material evaluation test series. The objectives of the 20K test series were to evaluate chamber cooling and structures and to verify performance over the throttling and mixture ratio range.

(U) The objective was to select a segment approach which would allow simulation of the chamber structure and loads important to maintaining throat dimensions and the cooling, sealing, and performance factors associated with this structure.

(U) The three-compartment segment approach provides close simulation of the maximum tube-wall thermal stress which occurs in the throat region, maximum coolant bulk temperature rise in the high heat flux area of the throat and combustion chamber, and a close approximation of pressure loads that will occur in the 250K module.

(U) Structural integrity was to be demonstrated by two means. Strain gage measurements were to be compared with predicted values to determine the validity of the analytic model. Secondly, the throat gap was to be monitored to determine if plastic deformation was taking place in the cantilever section of the nozzle.

(U) Heat transfer was to be checked by comparing the total heat flux of the 20K segment with the scaled values observed in the life cycle tests of the 2.5K nickel tube-wall segment. Visual observations were to evaluate local heat transfer effects.

(U) Testing of the 20K segment over a range of chamber pressures and mixture ratios was to be conducted to check the throttling performance results obtained from 2.5K tests. Specifically, the test program would provide answers concerning the following baffle questions:

1. Can the baffles be cooled properly?
2. Will the baffles present a wake problem for the downstream tube bundle?
3. Will the baffles significantly effect performance?

Summary of Work Accomplished

(C) Two 20K tube-wall segments were fabricated and tested for a total of 18 successful tests. During these tests, key structural and heat transfer parameters of the 250K demonstrator module were matched. Chamber pressures ranged from 600 to 1550 psi and mixture ratios from 2.7 to 6.0. The lightweight structure evaluation test program demonstrated a combination of hardware compatibility, throat gap dimensional stability, heat transfer capability, and high-level of performance at all conditions.

(U) The first assembly, tested 13 times, used a paralled fuel circuit feeding the injector and tube bundle separately (nonregenerative). The paralled fuel circuit was used to gain greater control over the operating conditions.

Following the thirteenth test, the first assembly was found to have convex bulges in the tube bundle. The bulges were caused by hydrogen leakage from the back side of tubes where they were brazed to the throat support beam.

(U) With Air Force approval, the second 20K unit was tested during an in-house research program to investigate transients. Data from the five tests conducted during this effort are also presented.

(U) The 20K program demonstrated the feasibility of the demonstrator module cooling circuit, performance, structural integrity, and regenerative operation. Evaluation of the tubes to the backup structure bonding was inconclusive, because an interference problem in final assembly of the hardware precluded the necessary pressure required to attain a good bond.

(U) Strain gages on the backup structure and baffle bolts verified the calculated stresses in the lightweight structural design. These measurements confirmed the design analysis to a high degree. Excellent agreement exists between calculated and measured stresses in the baffle bolts, and the vertical and horizontal ribs of the backup structure. The stress levels in certain areas indicated potential weight reductions could be achieved.

(U) The throat gap measurements between tests indicated good dimensional stability and showed no signs of plastic yielding.

(U) The scaled bulk heat transfer data of the 2.5K nickel tube-wall compared closely with the 20K data. This demonstrated the scalability of the heat transfer data. The visual monitoring of the tube bundle baffles and injector throughout the tests showed no signs of erosion and/or overheating on the baffles, the tube bundle downstream of the baffles, and the injector.

(C) The 20K performance test demonstrated c* efficiency greater than 98 percent. The segment was operated from 600- to 1550-psia chamber pressure and 2.7 to 6.0 mixture ratio. These results are consistent with previous 2.5K testing and recent 250K full-scale thrust chamber data. This result verified the validity of segment testing and the ability to scale performance. Because the 20K segment utilized baffles, the 20K performance further substantiates the predicted performance for the 250K demonstrator module design.

(U) Tests demonstrated that the regenerative configuration does not exhibit problems, either heat transfer or otherwise, both during transition and extended mainstage. The 47-second extended mainstage test showed that this hardware does come very near to equilibrium in 2 seconds, thus confirming that steady-state conditions were reached in the earlier 2-second mainstage tests.

(U) All objectives of the 20K segment lightweight structural evaluation were achieved. The program demonstrated the advantage of gathering data for a final design with segments. The results validated earlier predictions and provided advanced information for the 250K demonstrator module design.

Description of Hardware and Fabrication

(C) Design Description. The 20K segment thrust chamber was designed to provide advanced structural, heat transfer, performance, and fabrication data for a lightweight demonstrator module chamber design. The segment is a three-compartment rectangular assembly which includes two subsonic struts or baffles but does not include the inner-body spike or the extended outer-body shroud. The regenerative coolant passages are formed

of Nickel 200 tubes which are brazed together and subsequently adhesive bonded to a titanium backup structure (Fig. 357).

(U) The three-compartment segment approach, without the spike or extended body shroud, allowed the use of a symmetrical combustion chamber; thus, one tube design and one tooling design were satisfactory for both the inner and outer bodies. This concept further provides close simulation of the maximum coolant bulk temperature rise in the high heat flux area of the throat and combustion chamber, and a close approximation of the pressure loads which occur in the 250K module.

(U) The segment design does not realize complete structural simulation of a 360-degree annular combustion chamber, but the rectangular as opposed to a curved segment resulted in design simplification at little loss of structural or heat transfer simulation. The three compartments with the two subsonic struts represent the shortest segment length required for continuous beam simulation.

(C) The design details of the Nickel 200 tubes selected for the 20K segment are identical to those of the 2.5K chamber. The injector design incorporates triplet orifice strips that have dimensions identical to the strips used during the 2.5K chamber tests.

(C) The segment design includes the following features:

1. A straight chamber length including three combustion zone compartments, the center compartment duplicating a compartment of the demonstrator module.
2. A symmetrical combustion chamber convergent nozzle, throat and expansion nozzle with a divergent half-angle of 15 degrees to an area ratio of 3.5.

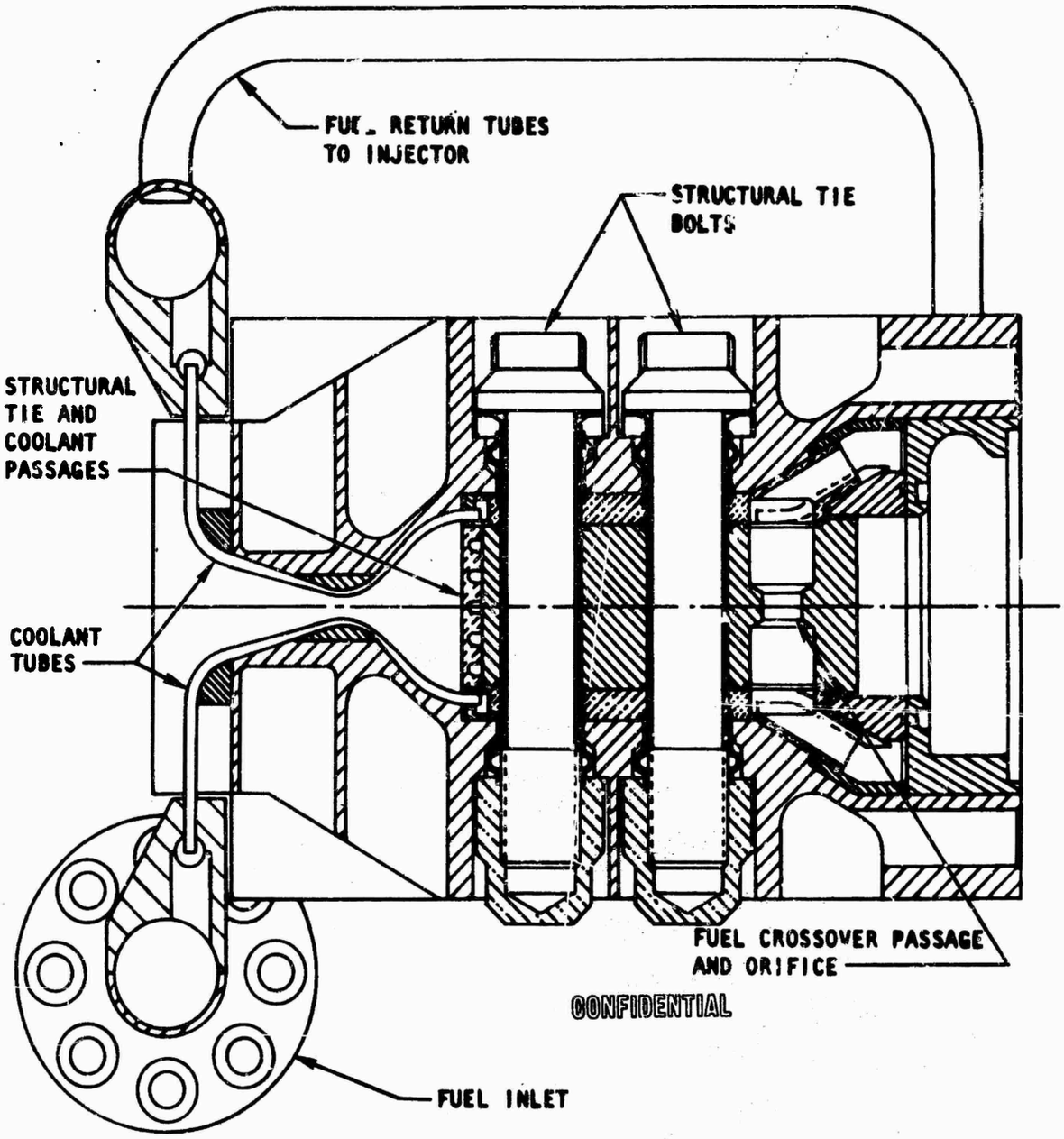

Figure 357A. Section Through Chamber at Structural Baffle, 20K Demonstration Segment

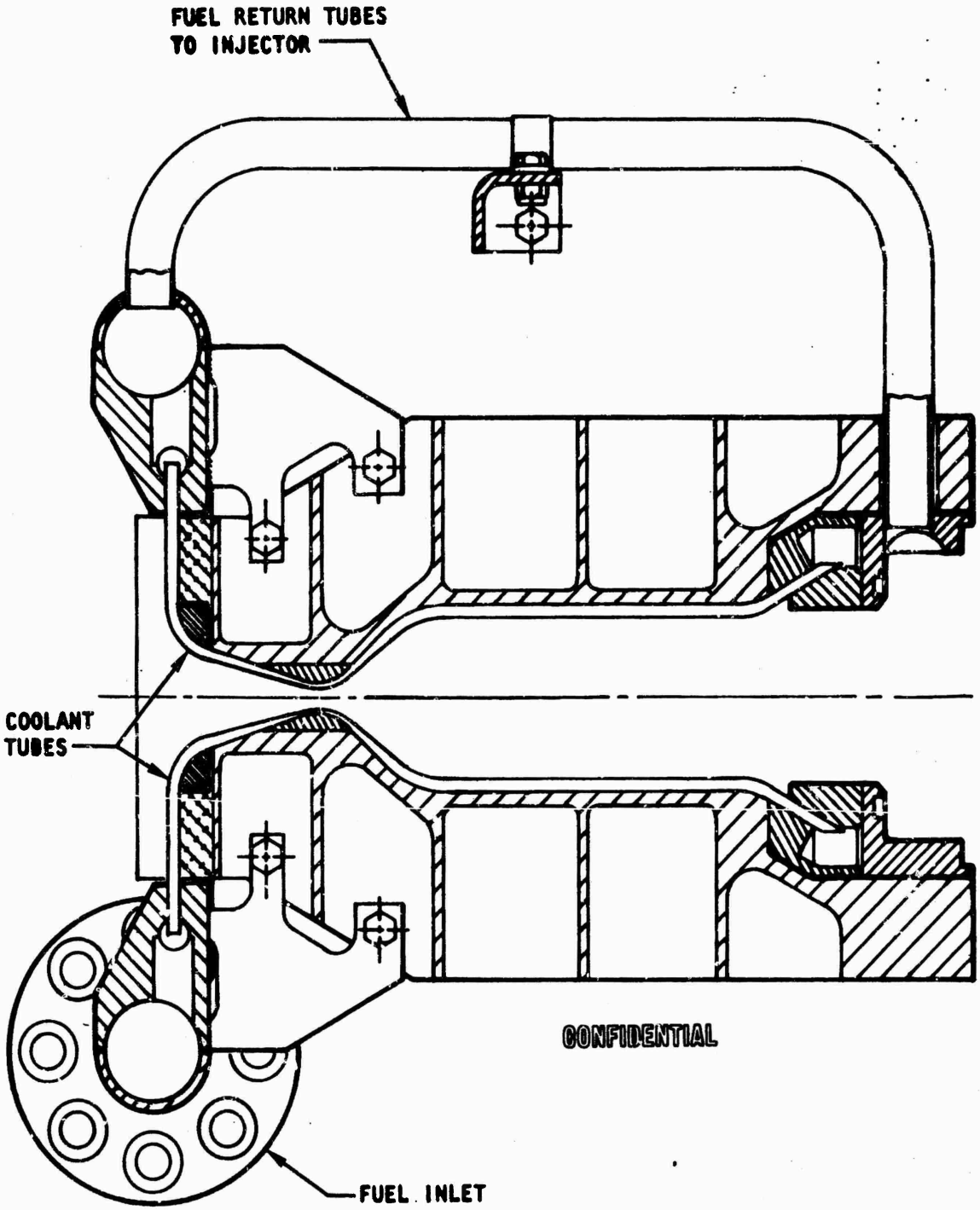

Figure 357B. Section Through Chamber Between Structural Baffles, 20K Demonstrator Segment

3. Two combustion baffles are utilized. In addition to providing a stabilizing influence to the combustion process, the baffles are designed to protect the structural tie-bolts from the combustion environment and to transfer the chamber coolant from the inner body to the outer body. The baffles are regeneratively cooled by diverting 25 percent of the coolant from the crossover circuit through passages within the copper shell which surrounds the baffle body. A parametric heat transfer study for the baffle geometry at the anticipated hot-firing conditions was conducted. The temperature distribution on the hot-gas side of the 20K baffle is shown in Fig. 358.

4. Copper end plates, although not a key component in the structural demonstration were necessary for successful segment operation. The end plate design is cooled with water in the area of the combustion zone upstream of the converging section and with 200 F hydrogen from the start of the converging section to the chamber exit. The hydrogen-cooled passages contain swirlers. A comparison of water as a coolant compared to 200R hydrogen with and without swirlers is shown in Fig.359 for a 0.070-inch-thick copper wall. If the side plates were water-cooled, swirlers would not be used because they do not appear to greatly enhance the heat transfer to a fluid undergoing nucleate boiling while having the disadvantage of greatly increasing the coolant pressure drop.

The disadvantage of water is that little warning is given when the cooling system becomes marginal, and a burnout can occur as soon as the burnout heat flux is exceeded either because of a chamber pressure spike at ignition or because of a lower water pressure for a particular run. The test stand where the engine is to be fired has a maximum water pressure capability of 2000 psia (tank). Although the wall temperature is higher at water

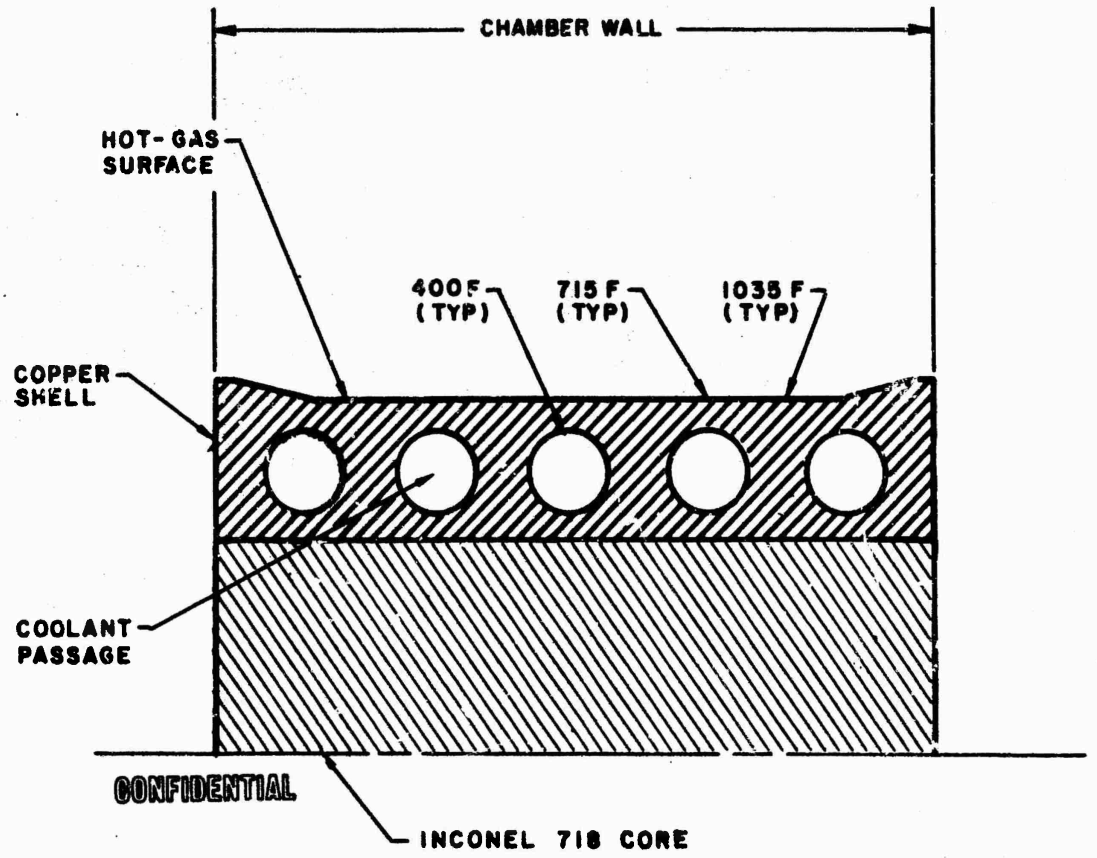

Figure 358. 20K Chamber Segment Maximum Baffle Temperature Distribution

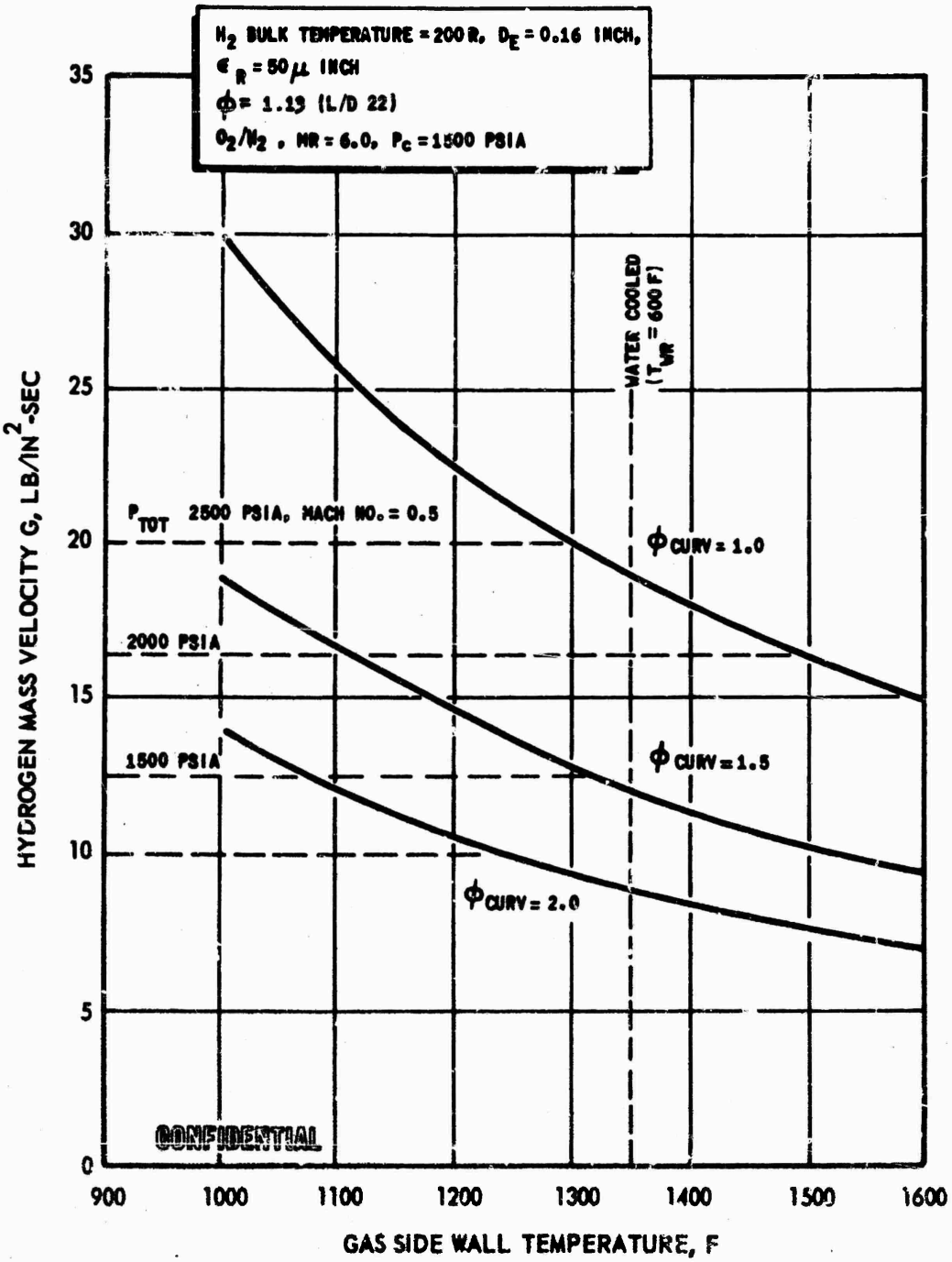

Figure 359. Hydrogen Mass Velocity Requirements vs Gas Wall Temperature (0.070-Inch Copper Wall)

pressures, higher heat fluxes can be handled because of the greater subcooling (higher saturation temperature). For a water velocity of 250 ft/sec, a heat flux of 50 Btu/in.^{2}-sec can be accommodated with a water static pressure of 700 psi. While this is sufficient to sustain normal engine operation, any local flux increase or coolant decrease will cause a heat transfer failure in the throat; thus, a margin of safety must be applied to the heat flux.

Hydrogen without swirlers has the same cooling capability as water. However, the hydrogen velocity is Mach No.= 0.50 for a pressure of 2300 psia, and choked flow would occur if the pressure dropped much lower. The use of swirlers will result in a curvature enhancement expected to exceed 1.5. This permits the hydrogen to cool as well or better than water with the available hydrogen pressures occurring in the side plate cooling passages.

5. To compensate for the different maximum bolt load between the 20K segment and the 250K demonstrator thrust chamber caused by the different shroud geometry (85,500 and 126,000 pounds respectively), a 1.0-inch-diameter bolt was selected for the 20K segment vs a 1.125-inch-diameter bolt for the 250K engine. The 1.0-inch-diameter bolt produced nearly the same stress and strain level in the 20K segment as the larger bolt developes on the 250K design.

Age-hardened INCO 718 material was selected as the bolt material because of its good ductility and fatigue properties at cryogenic temperatures. The bolt is designed with a reduced shank and a 5/32-inch-diameter torque gage hole down the bolt axis. Deflection measurements will be used to accurately apply the required bolt preload. Strain gages attached to the bolt shank were used to determine the maximum normal and shear stress levels occurring in the bolt during hot firing. The structural backup for the

combustion zone was designed to be fabricated from titanium forgings which were machined to an "egg crate" structure and then adhesively bonded to the tube-wall structures.

6. Baffle seats which are an integral part of the tube-wall assemblies provide the propellant manifolding, as well as the structural bearing and sealing surfaces.

7. The tube geometry selected was the same as that utilized on the 2.5K thrust chamber and the material selected was Nickel 200. The tube side wall subassembly sequence was divided into two steps. The baffle seat and the tubes that terminate at the baffle seat were initially brazed as a subassembly. This permitted flow and leak tests to be completed on these assemblies. Subsequent to completion of the baffle seat assemblies, the remaining tubes and the baffle seat assemblies, the remaining tubes and the baffle seat assemblies were brazed to form the tubular structure.

8. The regenerative coolant flow path which passes upward through the inner wall and diverts to the outer wall through the baffle passages, down the outer wall, then into the injector was selected to duplicate the demonstrator module (Fig. 360).

(U) Fabrication. Figure 361 is an exploded perspective drawing showing details of the 20K segment with the major components indicated. These are:

Baffle

Baffle Seat

Tube-Wall Braze Assembly

Titanium Structure

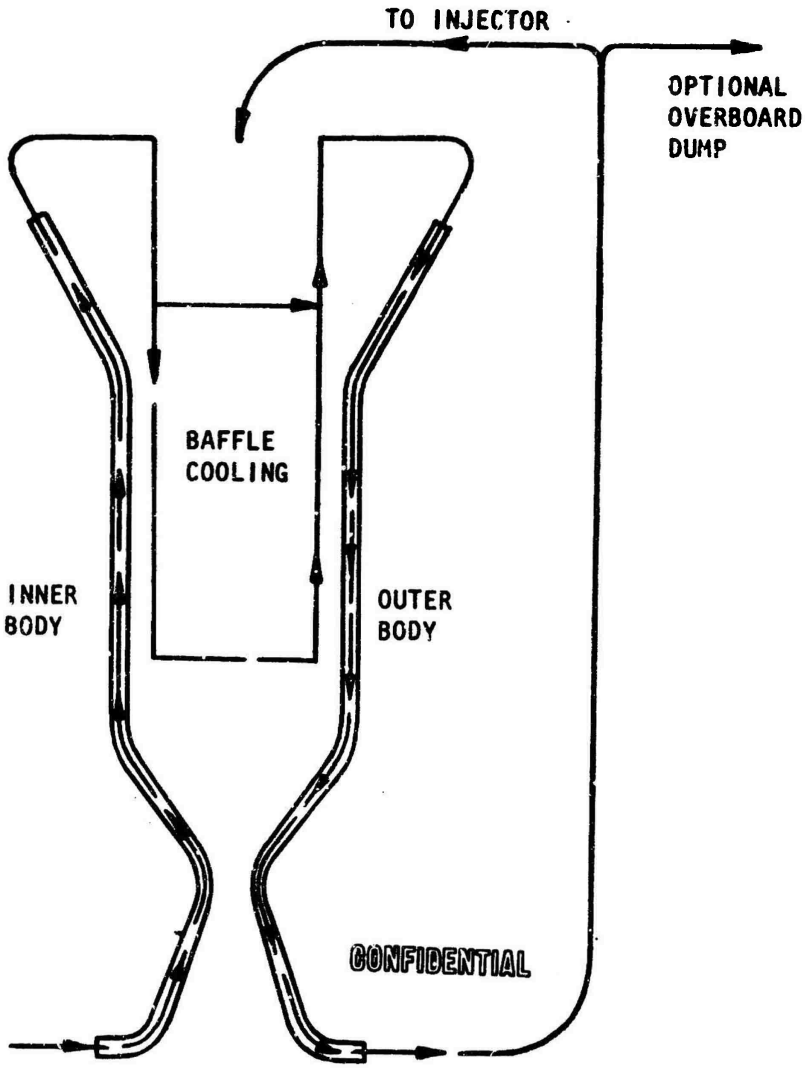

Figure 360. 20K Segment Flow Schematic

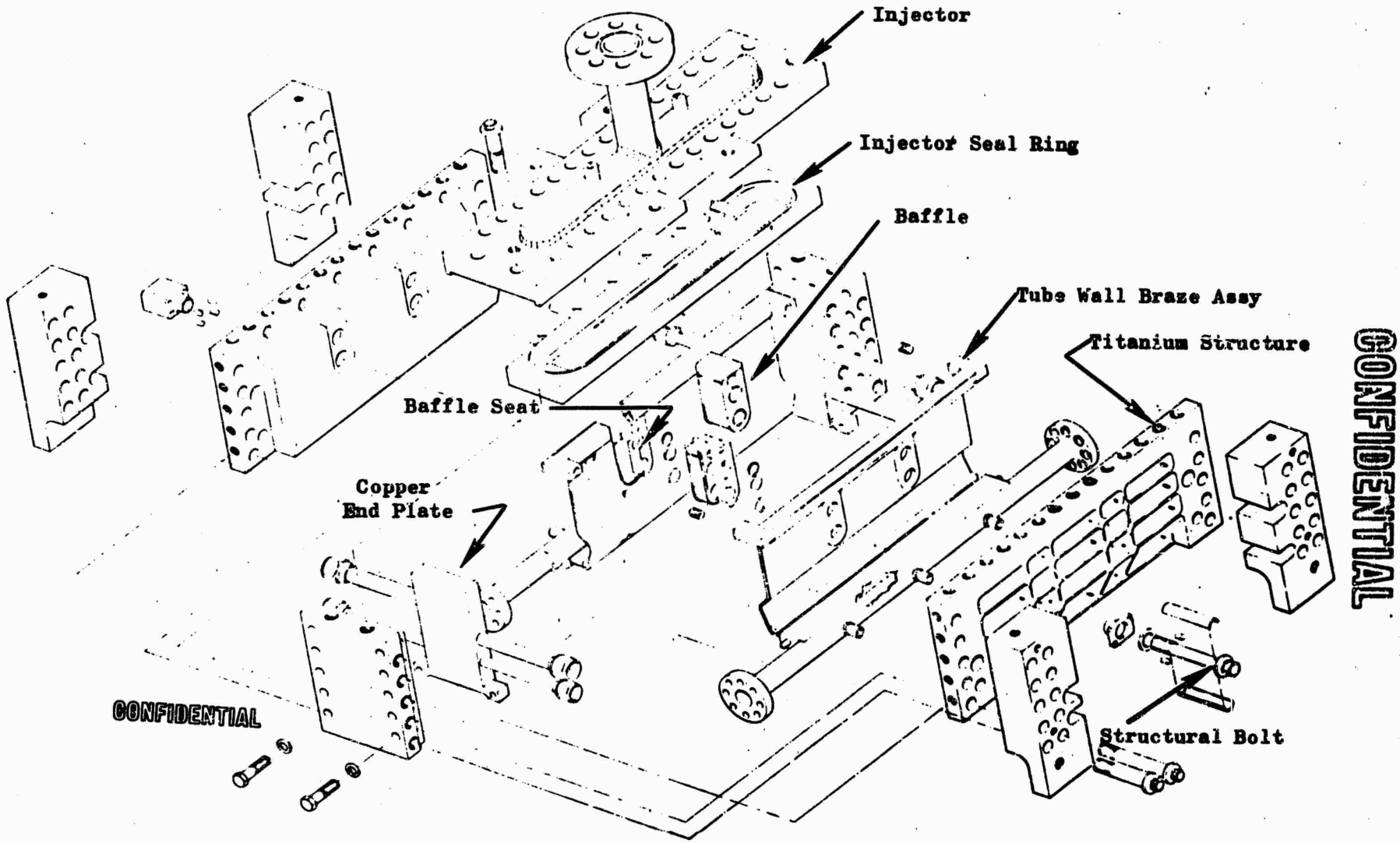

Figure 361. Perspective View of the 20K Segment Thrust Chamber

End Plate

Injector

Injector Seal Ring

Two segments were built. A description of the component parts with details of their fabrication follows.

(C) Tubes. Tubes were made of Nickel 200 material with a nominal wall thickness of 0.014 inch which was reduced to 0.012 inch in the throat region during the tapering process. Tube fabrication represented no departure from the conventional established method of forming rocket engine tubes. That is, starting with a round tube of uniform wall thickness, with a circumference equal to the perimeter of the final formed tube, a straight section of tube is reduced in diameter to the throat diameter of the final formed tube. The tapered region on each side of this section form the convergent and divergent section of the final formed tube. This is then preformed by bending to the combustion chamber geometry and finally the preform tube is placed in a die and sized to the required width. Drawing on the experience gained during the fabrication of the 2.5K tubes, these tubes were fabricated without difficulty and were of excellent quality. Each tube was subjected to a flow calibration process which was a measure of the quality of the formed tube as well as a means of determining its flow characteristics for final positioning in the tube-wall braze assembly. All processes and materials used for any aspects of the tube fabrication were rigorously controlled to ensure compatibility with the nickel material.

(U) End Plate Assemblies. Again drawing on the experience gained with the 2.5K tubular segment, a similar design was developed for use on the 20K. It consists of an OFHC copper body with deep drilled coolant

passages. Two distinct coolant circuits are provided; one for the combustion zone and one for the throat region. The one for the combustion zone employs fourteen 1/4-inch-diameter coolant passages spaced 0.355 inch apart. These are joined together by two 0.750-inch-diameter cross-drilled passages which on one side introduce the coolant from a 1-inch-diameter supply tube and on the other side collect and discharge the coolant through another 1-inch-diameter tube. Direction of flow may be from either side. The coolant circuit for the throat region is composed of fourteen 0.156-inch-diameter holes 0.220 inch apart and like the holes for the combustion zone, maintain a wall thickness of 0.070 inch with the hot-gas wall. Swirlers are provided in each of these holes to take advantage of the curvature effect on the cooling capability of the hydrogen coolant. As with the combustion zone circuit, these coolant passages are joined together by cross-drilled holes providing the inlet and outlet for the coolant through 3/4-inch-diameter tubes. The open ends of all drilled passages are closed by brazed in place plugs.

(U) Figure 362 shows the detail components. The four end plate assemblies required were furnace brazed with RB0170-065 (62Cu-35Av-3Ni) braze alloy. They were fabricated using conventional machining techniques as well as conventional brazing processes and posed no significant problems during fabrication. All four units were successfully proof-pressure tested without leakage after only one braze cycle.

(U) Baffle Seat Assemblies. The baffle seats were fabricated as separate braze assemblies consisting of 26 tubes and an Inconel 718 body and cover plate. Figure 363 shows the component details, and Fig. 364 shows the completed braze assembly. The body contains a milled passage for diverting the coolant flow around the structural bolts where it is

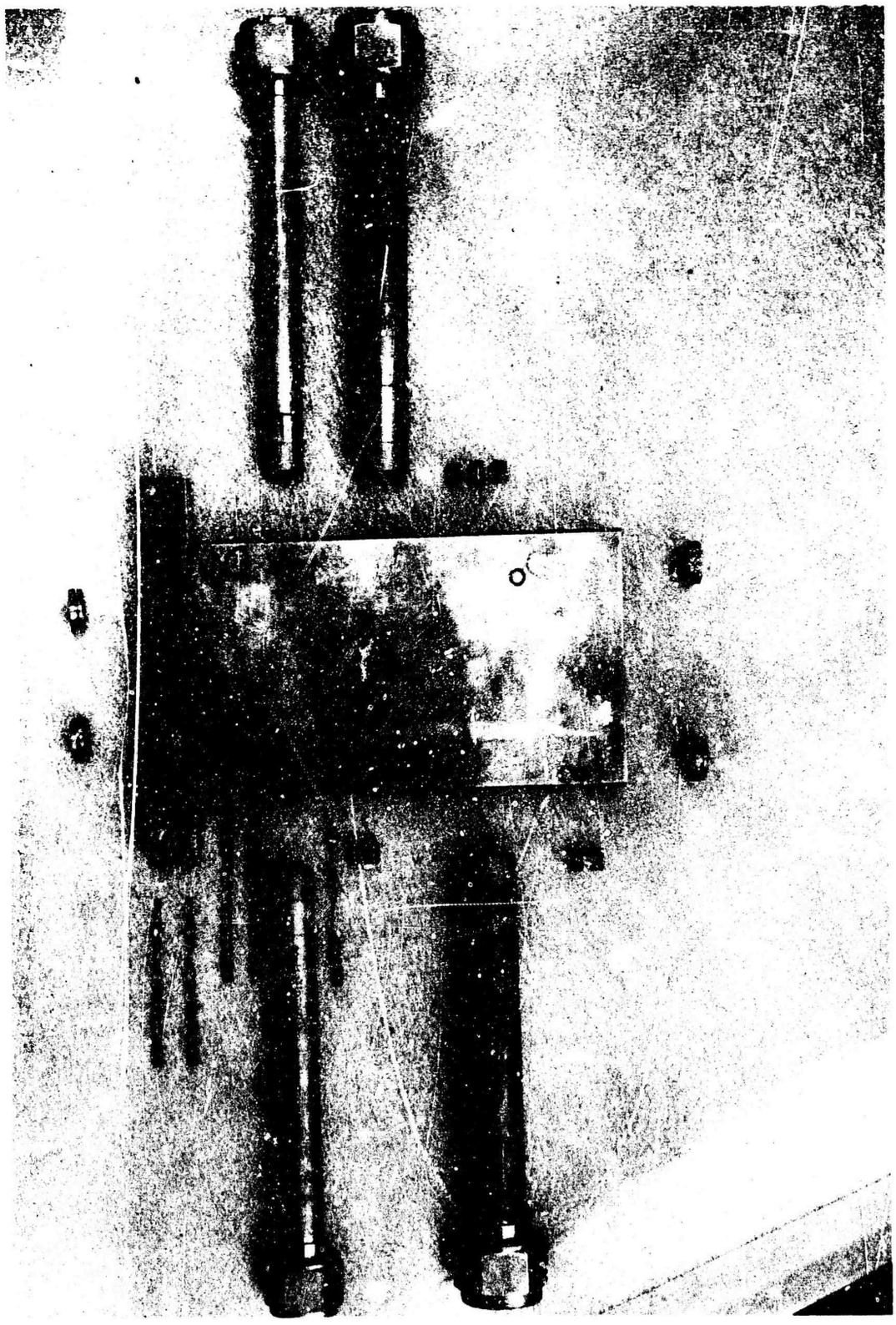

LXE32-2/27/67-C1B

Figure 362. 2UK End Plate Assembly

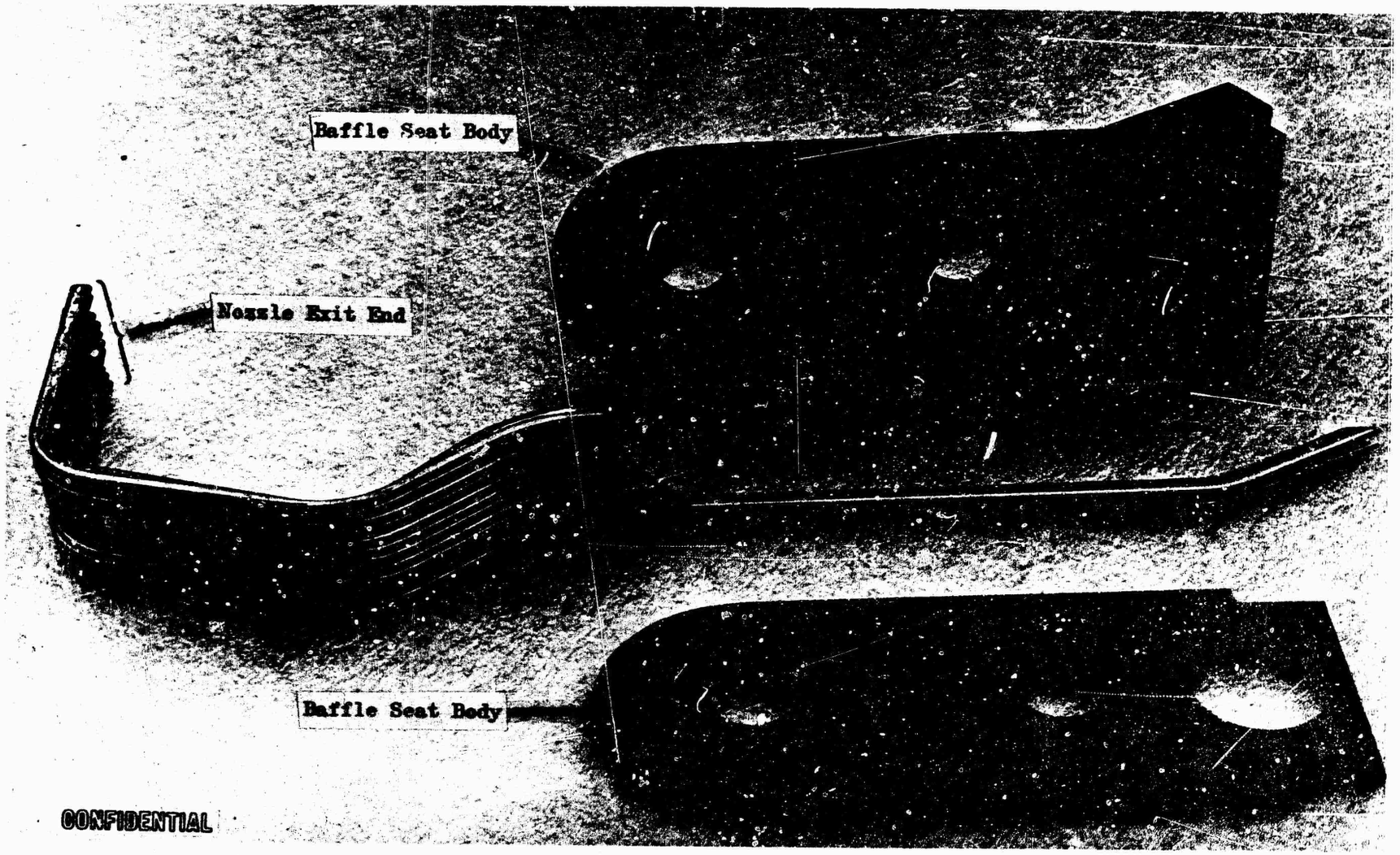

1XE32-1/9/67-CIE

Figure 363. 20K Baffle Seat Subassembly, Before Brazing

1XE32-2/20/67-03A

Figure 364. 20K Baffle Seat Subassembly Complete

joined with the balance of the coolant flow for introduction into the baffle on the up-pass side. It serves the reverse purpose on the down-pass side of the thrust chamber. Fabrication as a separate detail rather than as an integral part of the tube-wall assembly permitted verification of flow characteristics, finishing of sealing surfaces without risking damage to the chamber tubes, and assurance of the quality of the baffle seal prior to inclusion in the tube-wall braze assembly.

(U) Furnace brazing of the subject assembly was accomplished with a 50-percent gold/25-percent nickel braze alloy and at a brazing temperature of 2070 ±10 F. Selection of this brazing alloy was based on the need for a material that would not remelt during subsequent brazing of the baffle seats into the tube-wall assemblies.

(U) The furnace braze tooling concept selected was originally utilized in furnace brazing advanced design thrust chamber segment hardware. It was designed to apply a uniformly distributed dead weight load of approximately 3 psi on the components during the brazing cycle. Details of the brazing fabrication of the twelve assemblies required for the program are presented in Table 86.

(U) As shown in the table, the first two units were used subsequent to rejection, for evaluating methods of repair of post furnace braze leakage, exit end misalignment, and tube deformation. Tests were conducted to determine if localized repair could be accomplished utilizing the Plasma Arc and TIG processes with 50Au-25Pd-25Ni braze alloy. The large mass difference between the nickel tubes and INCO 718 body components was found to be a significant restriction upon the ability to achieve satisfactory repairs without subjecting the tubes to damage from overheating. As a result, re-furnace brazing was selected as the repair method for joint leakage.

TABLE 86

BAFFLE SEAT ASSEMBLY FABRICATION HISTORY

Unit No.	Number of Furnace Braze Cycles	Post-Furnace Braze Repairs	Remarks
1	1	Special furnace cycle for realignment of tubes at exit end. Not successful.	Unit rejected for braze joint leakage, tube misalignment at exit end, and tube end damage at injector end. Unit used to evaluate cold forming of tubes for realignment.
2	1	None	Unit rejected for excess braze alloy buildup on tube crowns and side walls of outer tubes and for exit end tube misalignment.
3	2	None	Three leaks repaired in second furnace cycle, unit assembled in RL000108X assembly, unit No. 1.
4	2	None	Two leaks repaired in second furnace cycle. Unit assembled in RL000108X assembly, unit No. 1.
5	1	Torch repaired two tubes damaged using 50Au-25Pd-25Ni braze alloy.	Unit statused as backup hardware.
6	2	Straightened tubes deformed during machining, using freeze-expansion technique.	One leak repaired in second furnace cycle. Unit statused as backup hardware.
7	1	Straightened tubes deformed during machining, using freeze-expansion technique.	Unit assembled in RL000108X assembly, unit No. 2.
8	2	Mechanically straightened tubes deformed during machining.	No leakage following first furnace cycle. Second furnace cycle used for braze buildup of tube crowns damaged in machining. Unit assembled in RL000108X assembly, unit No. 3.
9	1	None	Unit assembled in RL000108X assembly, unit No. 2
10	1	None	Unit assembled in RL000108X assembly, unit No. 3.
11	1	None	Unit assembled in RL000108X assembly, unit No. 4.
12	1	None	Unit assembled in RL000108X assembly, unit No. 4.

(U) Cold straightening was applied successfully to the correction of exit end tube misalignment. The use of a hydraulic press and suitable tooling resulted in satisfactory realignment of tubes with no effect on tube flow characteristics or tube-to-tube braze joints.

(U) A freeze-expansion forming technique was developed to repair deformed tubes on the finished baffle seat assemblies. Water was placed inside the deformed tube and frozen by immersing the assembly in liquid nitrogen. Expansion of the water upon freezing produced sufficient force to expand the tube and remove the concavity. A final forming operation was used to correct for overexpansion of the tube and restore the original configuration.

(U) Tube Wall Assemblies. The tube wall assembly consists of the injector end and exit end manifolds, two baffle seat assemblies, and the balance of the tubes required to form a contoured wall. Figure 365 shows these components during assembly prior to furnace brazing. Figure 366 shows a completed braze assembly with the tooling partially removed. Figures 367 and 368 show the assembled unit alloyed prior to its second braze cycle.

(U) The four required units were brazed utilizing the same fixturing concept that was applied to the baffle seat assemblies. Two furnace braze cycles were applied to each tube wall to obtain a leaktight structure prior to brazing the tube walls in the final chamber segment assembly. The first cycle was brazed with 90Ag-10Pd alloy at 1975 ±10 F, followed by a second cycle at 1805 ±10 F using 82Au-18Ni alloy.

(U) Results of the furnace braze cycles are shown in Table 87. Plugged tubes were evident on unit No. 3 and 4 following first cycle brazing. The plugging was located at the exit end of both units, and was a result of

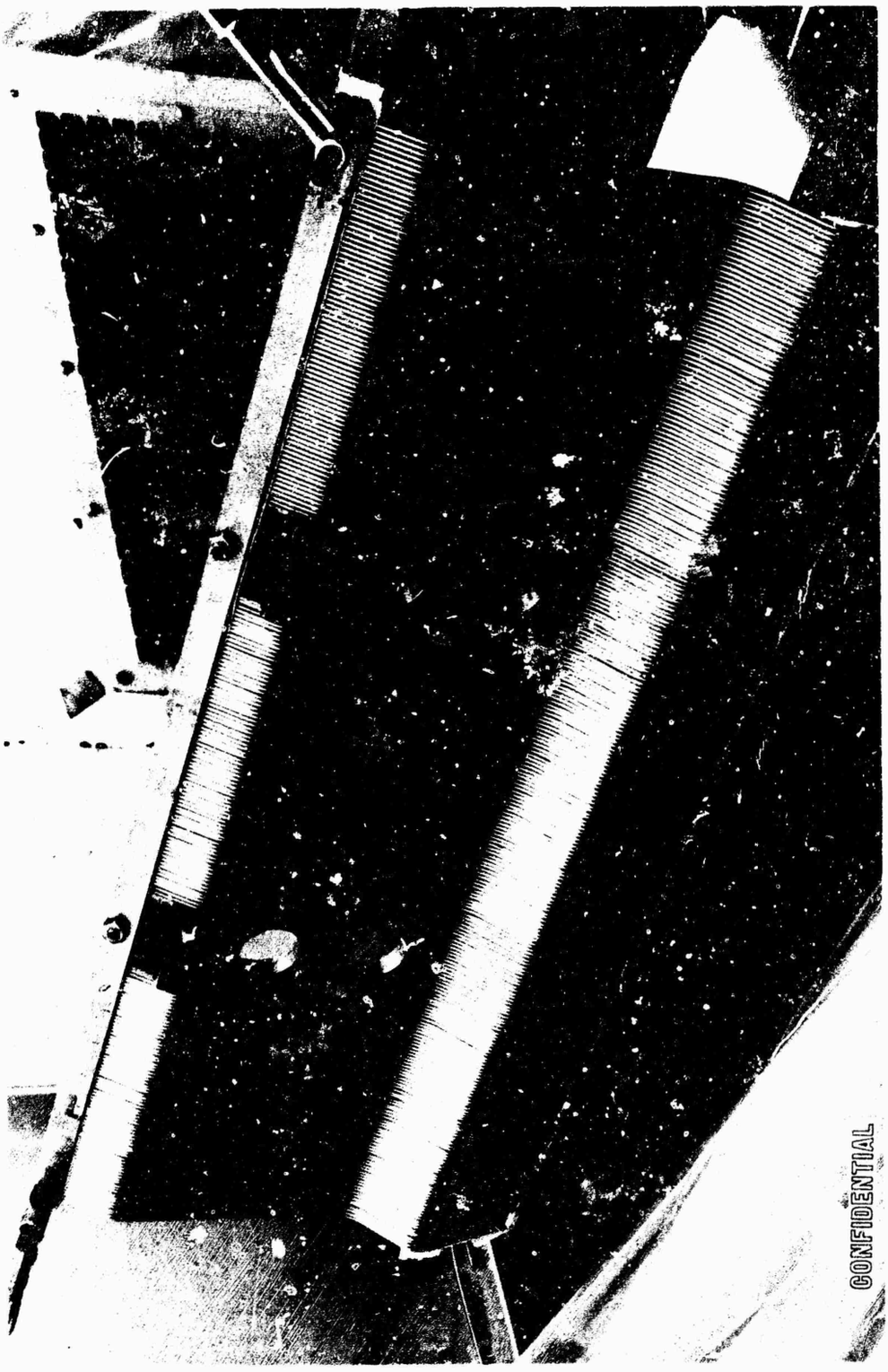

LXE32-2/27/67-C1C

Figure 365. 20K Tube Wall Subassembly Before Brazing

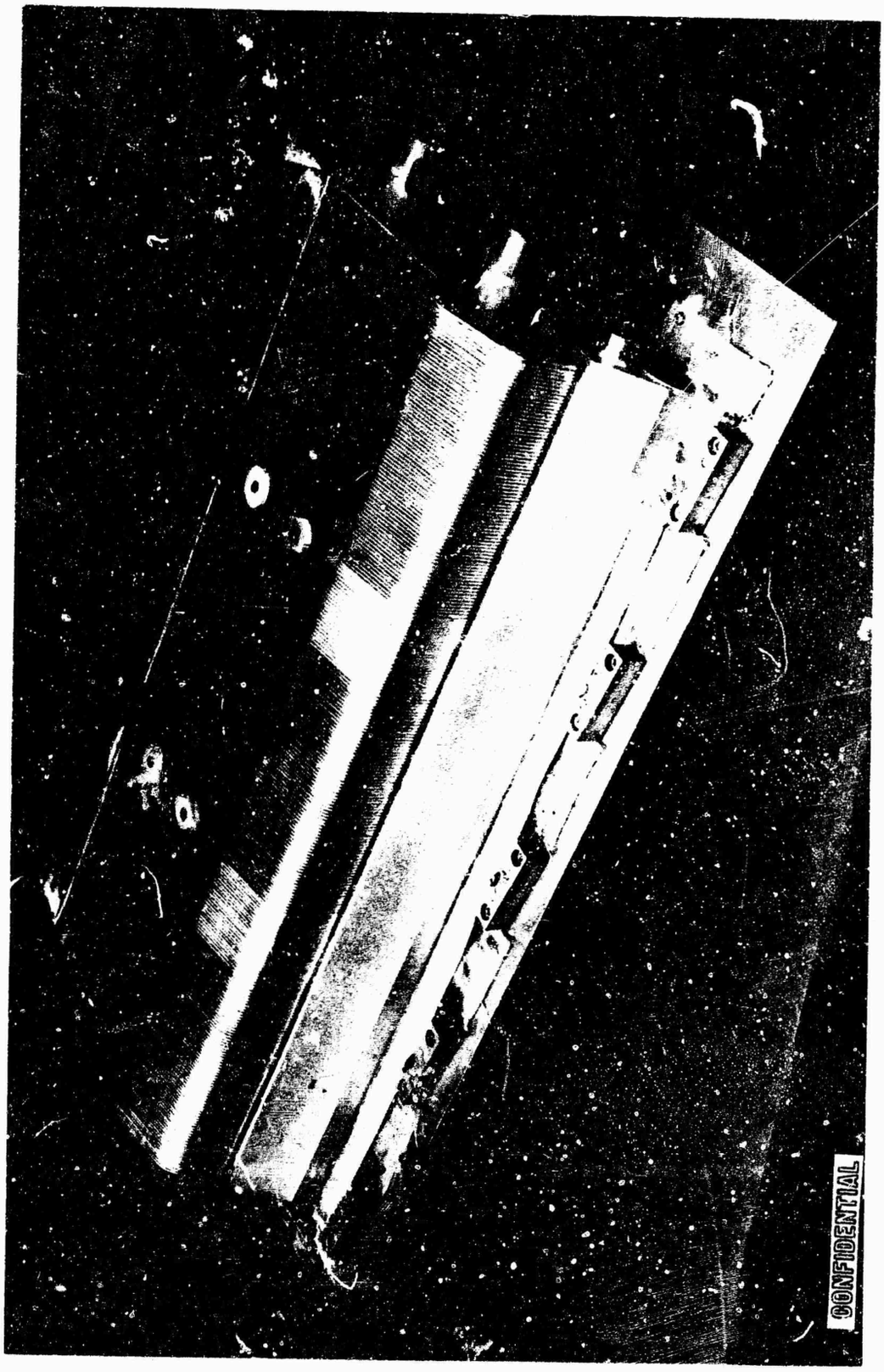

1XE52-3/6/67-C1C

Figure 366. 20K Tube Wall Subassembly in Brazing Fixture

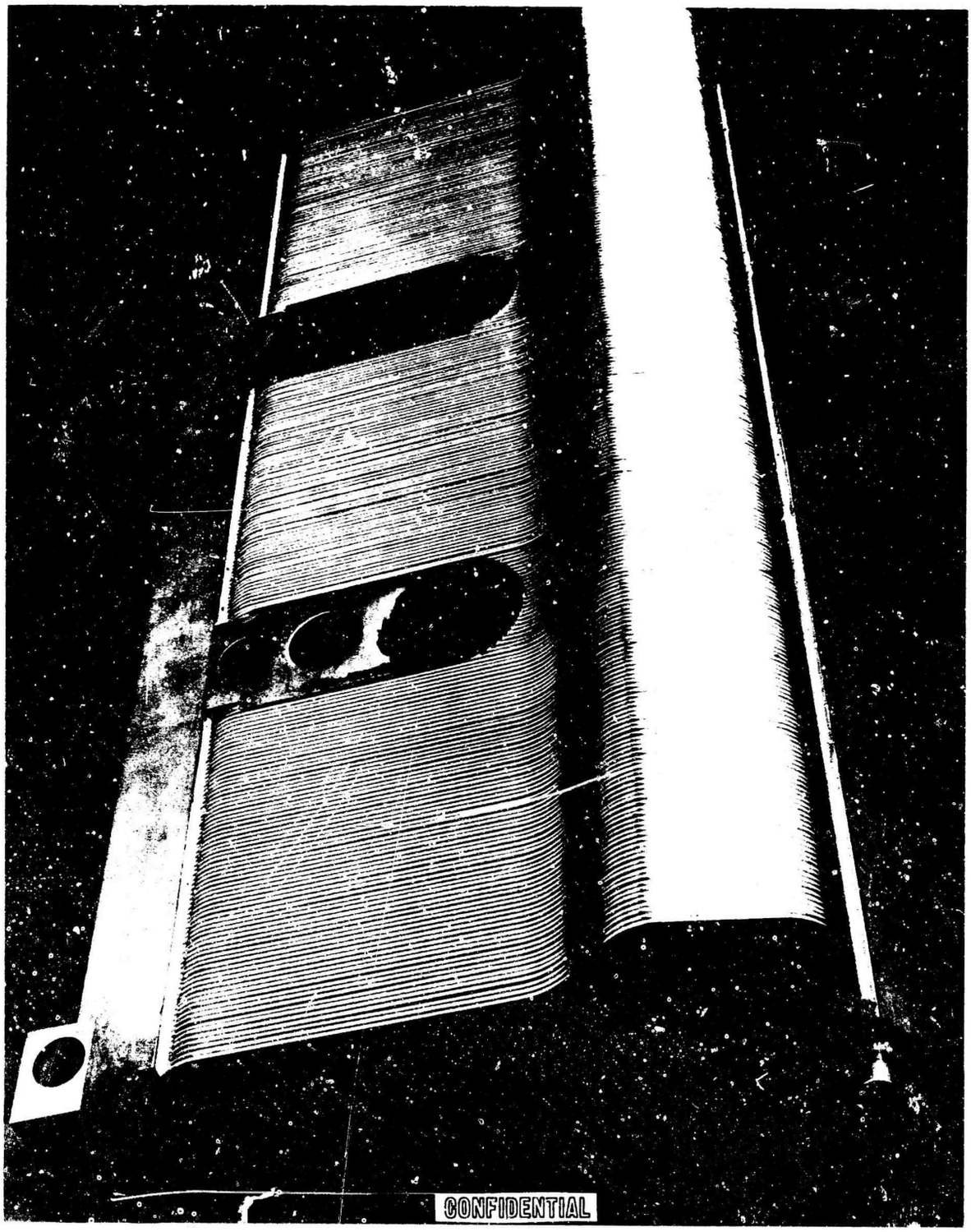

1XE32-3/30/67-C3B

Figure 367. 20K Tube Wall Subassembly Complete

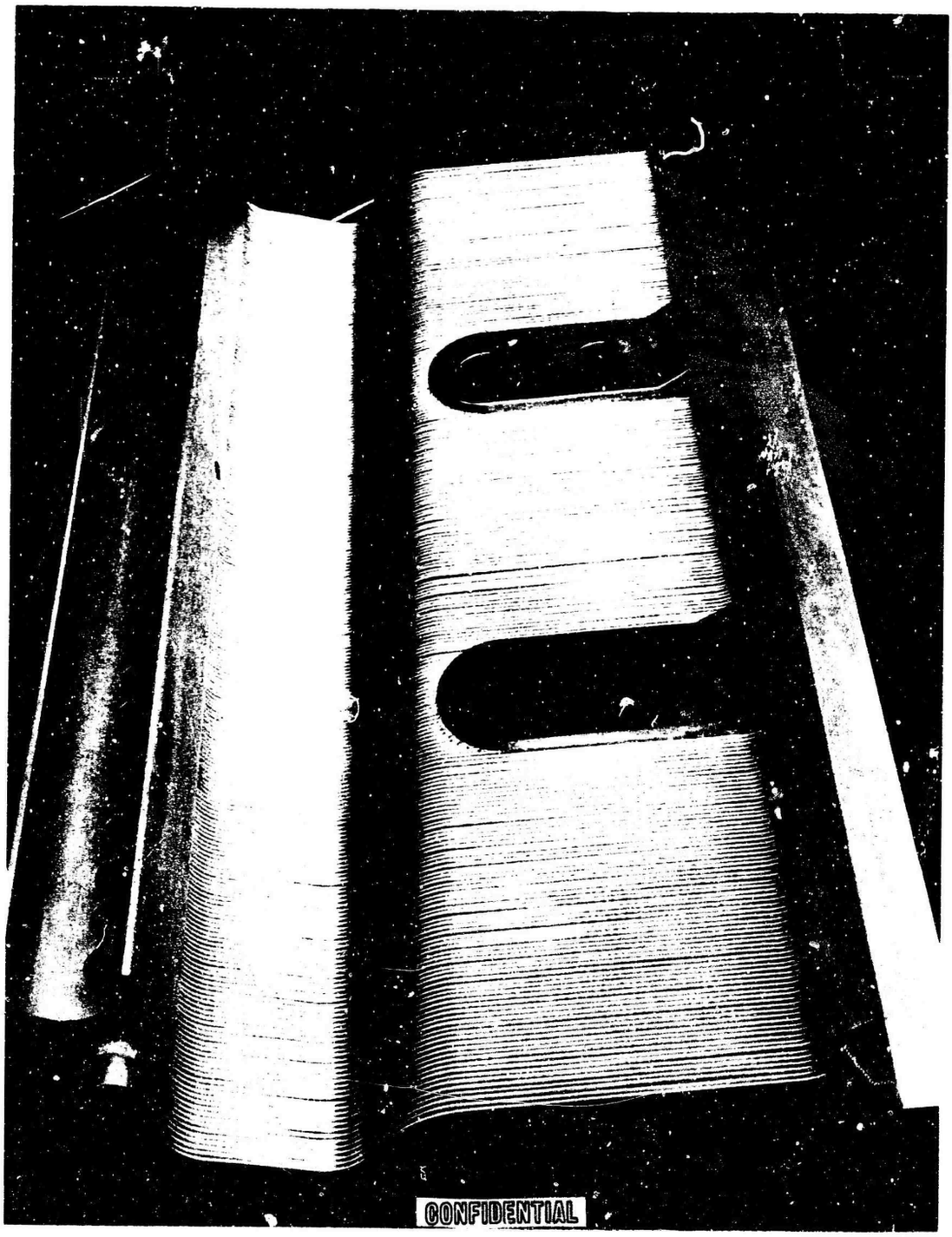

1XE32-3/30/67-C3C

Figure 368. 20K Tube Wall Subassembly, Structure Side

TABLE 87

(C) TUBE WALL ASSEMBLY BRAZE CYCLE RESULTS

Unit No.	Condition After First Furnace Cycle	Condition After Second Furnace Cycle	Remarks
1	Several leaks in tube-to-injector end manifold joints at hot-gas side of tubes; one tube-to-tube leak in throat area at one end of assembly	Seven leaks in tube-to-injector end manifold joints at cold-wall side of tubes	Seven leaks repaired by TIG brazing with RB0170-064 alloy.
2	Several leaks in tube-to-injector end manifold joints at cold-wall side of tubes; one hole in tube crown adjacent to injector end manifold at hot-gas side of tubes; gap between outer baffle seat tube and adjacent tube, at both baffle seats, inner compartment side	One tube-to-injector end manifold leak. One tube-to-tube leak at baffle seat	Tube-to-manifold leak repaired by TIG brazing with RB0170-064 alloy. Hole in tube (not repaired) in second furnace cycle intentionally repaired by Plasma Arc brazing with RB0170-062 alloy. Tube-to-tube leak repair made during furnace brazing of chamber assembly.
3	Baffle seat-to-manifold joint leak, both baffle seats	None	Tubes were plugged at exit manifold end with first cycle braze alloy; they were repaired by abrasive blasting.
4	Baffle seat-to-manifold joint	None	Tubes were plugged at exit manifold end with first cycle braze alloy; they were repaired by abrasive blasting.

CONFIDENTIAL

the braze alloy flowing into the tube ends or the inadvertent application of braze alloy paste in the tubes during preparation for brazing. The absence of tube plugging on the preceding units indicated possible omission of the required braze stopoff application. The tubes were unplugged by abrasive blasting (S. S. White abrasive unit). This operation was accomplished with no evidence of tube damage, and subsequent testing verified acceptable flow characteristics of these tubes.

(U) Thrust Chamber Braze Assembly. The thrust chamber braze assembly consisted of two contoured tube-wall assemblies, two copper end plates and the injector seal ring. Figure 369 shows this unit after furnace brazing.

(U) A 50Au-50Cu braze alloy was selected based on laboratory evaluation tests conducted in conjunction with the fabrication of the 2.5K chamber segment. Braze fixturing consisted of a flat base plate with means for locating and fixing one end of the chamber assembly and applying a constant load of approximately 5 psi normal to the copper end plate at the opposite end of the assembly.

(U) During the assembly and preparation for brazing of the first unit, several excessive joint gaps were observed. Shims were fabricated and installed to bring the gaps within normal brazing tolerances. However, during the brazing process, the shims moved out of position resulting in open joints in the shimmed area.

(U) The tube-to-end plate braze joint gaps observed during the assembly of the first unit were a result of the tube-wall width being undersize, predominantly in the throat area. This condition was also evident in units 2 and 3.

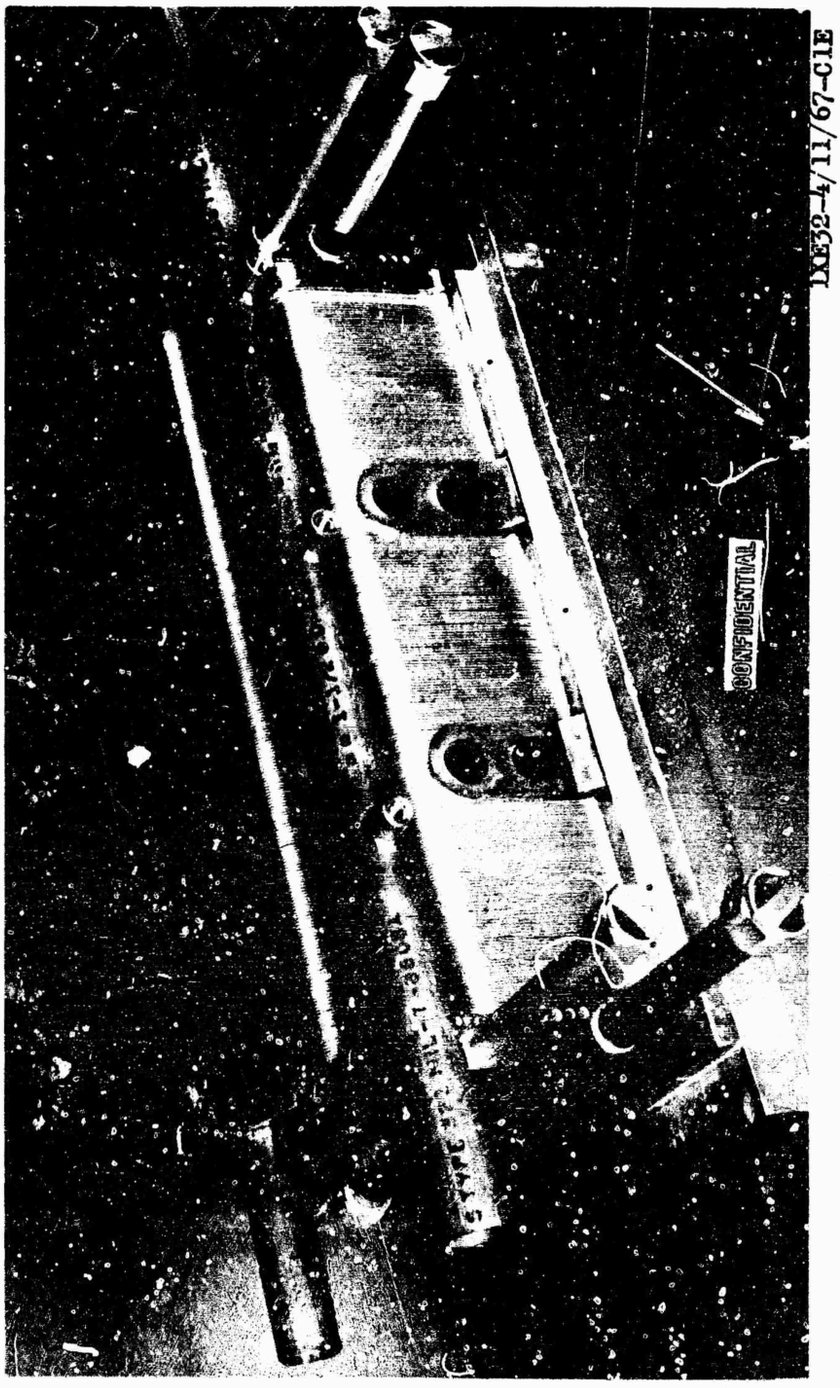

Figure 369. 20K Thrust Chamber Braze Assembly

(C) The tube-to-end plate braze joint gaps observed during the assembly of the first unit were a result of the tube-wall width being undersize, predominantly in the throat area. This condition was also evident in unit No. 2 and 3. Correction of this condition involved development of a torch brazing procedure for fitting OFHC copper shims and Nickel 200 coolant tubes in each corner to provide coolant to the throat area adjacent to the end plates.

(U) Baffle Assembly. The baffle assembly consists of 13 components; an Inconel 718 core, an OFHC copper coolant panel, a manifold closeout, and 10 braze sleeves connecting the manifolding to the copper panel (Fig. 370).

(C) Fabrication of the copper panel was initiated by deep-hole drilling 0.156-inch-diameter holes 14 inches long in flat OFHC copper plates milled to final width and thickness. These holes were packed with nickel powder, and the plate was formed around a radius block which also provided edge restraint to aid in preventing the holes from collapsing during forming. A final-finish machining was required to provide proper tolerances for brazing to the Inconel 718 core.

(U) The baffle core, fabricated from Inconel 718, provides the manifold and distribution system folding the copper panel and bolt cavities. The machining of this component was accomplished using conventional techniques with no noteworthy problems. Assembly of the core and panel are accomplished by braze CRES sleeves at the interface to ensure against leakage.

(U) A total of four of these assemblies were furnace brazed using RB0170-065 (62Cu-35Ag-3Ni) braze alloy. The braze fabrication history for these units is presented in Table 88.

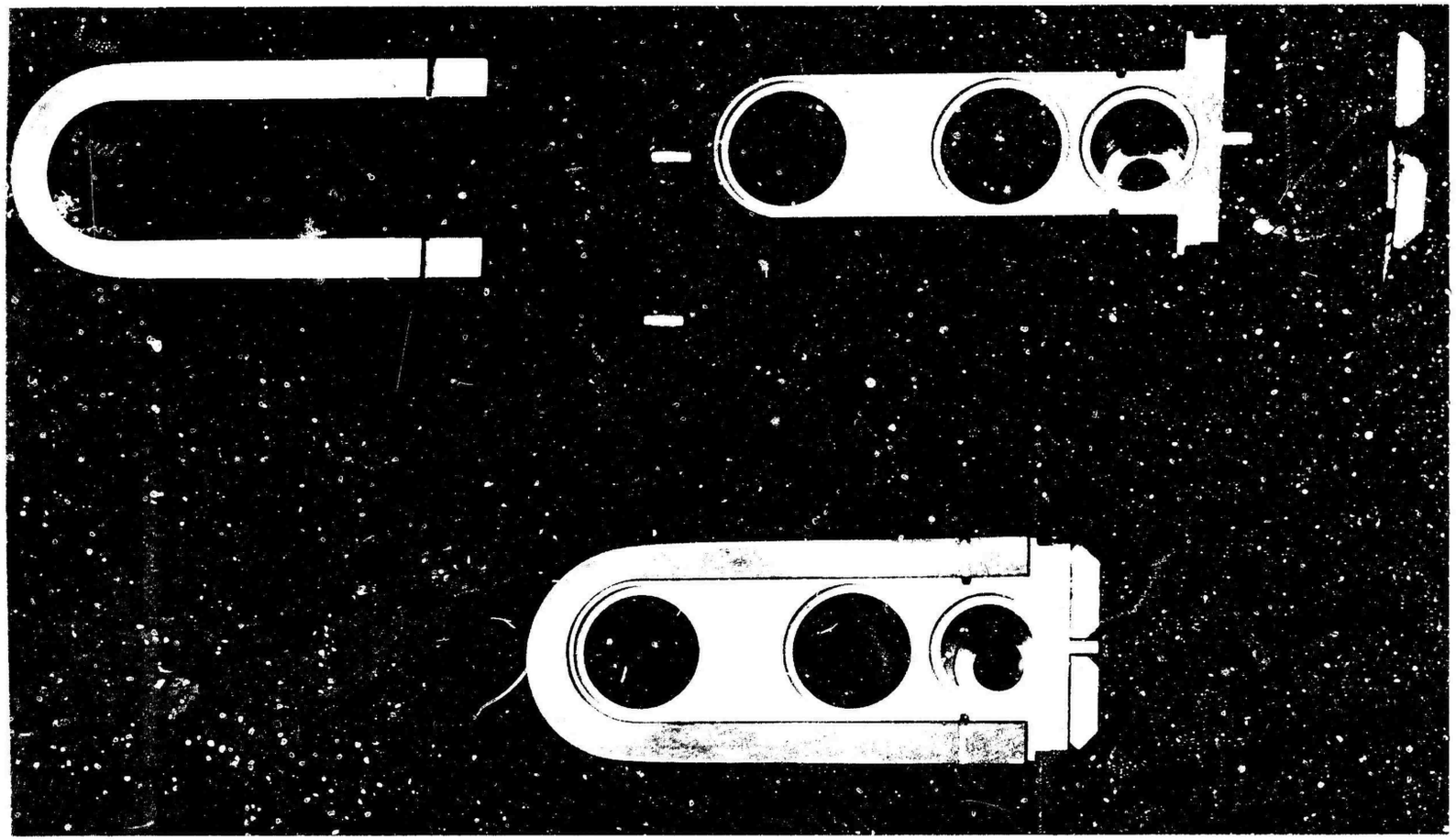

LXE32-3/30/67-C2

Figure 370. 20K Baffle Assembly

TABLE 88

RL000104X BAFFLE ASSEMBLY FABRICATION HISTORY

Unit No.	Number of Furnace Braze Cycles	Repair Procedure	Remarks
1	2	Realloyed all shell-to-body and sleeve-to-body joints with RE0170-065 alloy and rebrazed	No leakage after rebrazing.
2	2	Realloyed all shell-to-body and sleeve-to-body joints with RE0170-065 alloy and rebrazed	No leakage after rebrazing.
3	1	None required	Commencing with this unit, 0.002-inch braze sheet was placed in sleeve-to-shell joints. No leakage.
4	1	None required	No leakage.

(U) The first two assemblies exhibited leakage at the type 347 stainless-steel sleeve-to-OFHC copper sheel braze joints, which were sealed after subjecting these units to a second furnace cycle using RB0170-065 braze alloy. Leakage in these joints was attributed to excessive gap in the adjacent copper shell-to-Inconel 718 body joint (Fig.370), which resulted in braze alloy starvation of the sleeve-to-shell joints.

(C) Preparation of the third and fourth units was modified to include the preplacement of 0.002-inch-thick braze alloy sheet in the sleeve-to-shell joints, which eliminated the starvation and subsequent leakage in these joints. Subsequent to braze and leak check, the manifold closeout was installed using TIG fusion welding. A hydrostatic pressure test of 3750 psig was used to verify structural integrity of the final assembly.

(U) Tube-Wall Support Structure. The tube-wall support structures were machined from titanium 6AL4V forgings to provide a light-weight structure simulating the configuration anticipated on the 250K demonstrator module. Material removal producing the required contours and deep pockets with relatively thin webs (Fig.371 and 372) was accomplished on a numerically controlled milling machine. No problems were encountered during fabrication. However, it was determined that the time required using this technique would be excessive for a 250K demonstrator module shell, and that other techniques such as electrical discharge or electrical capacitance machining would probably be more applicable.

(U) Thrust Chamber Adhesive Bonding Process. The design of the 20K structural system provides for support of the tube bundle within the compartment areas between the baffles and end plates by using an adhesive bond joint made with an epoxy Nitrile adhesive. The properties of this material are controlled by the thickness of application and the load applied during the oven-curing cycle.

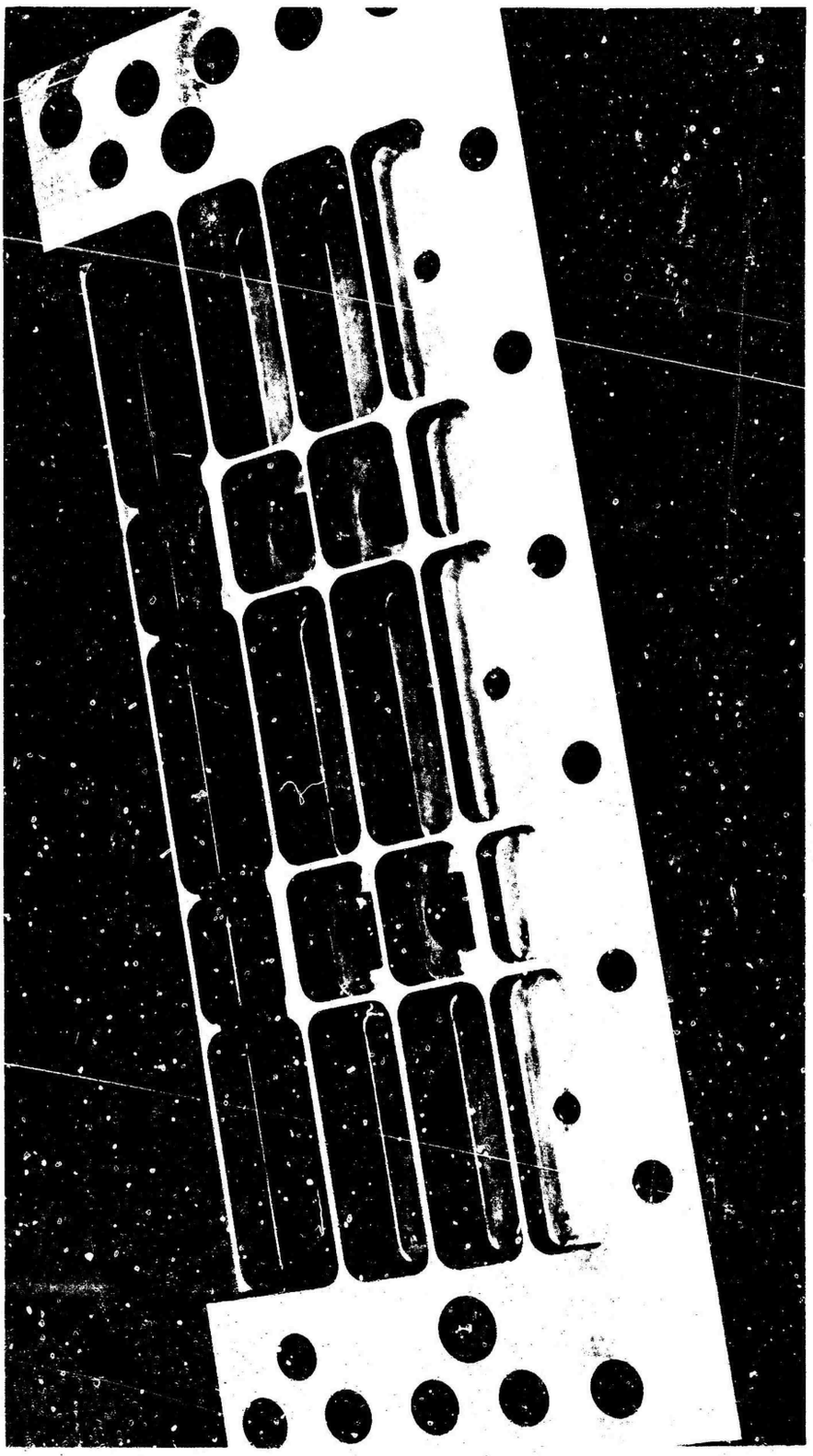

1XE32-3/30/67-C1A

Figure 371. 20K Titanium Structure, Outside

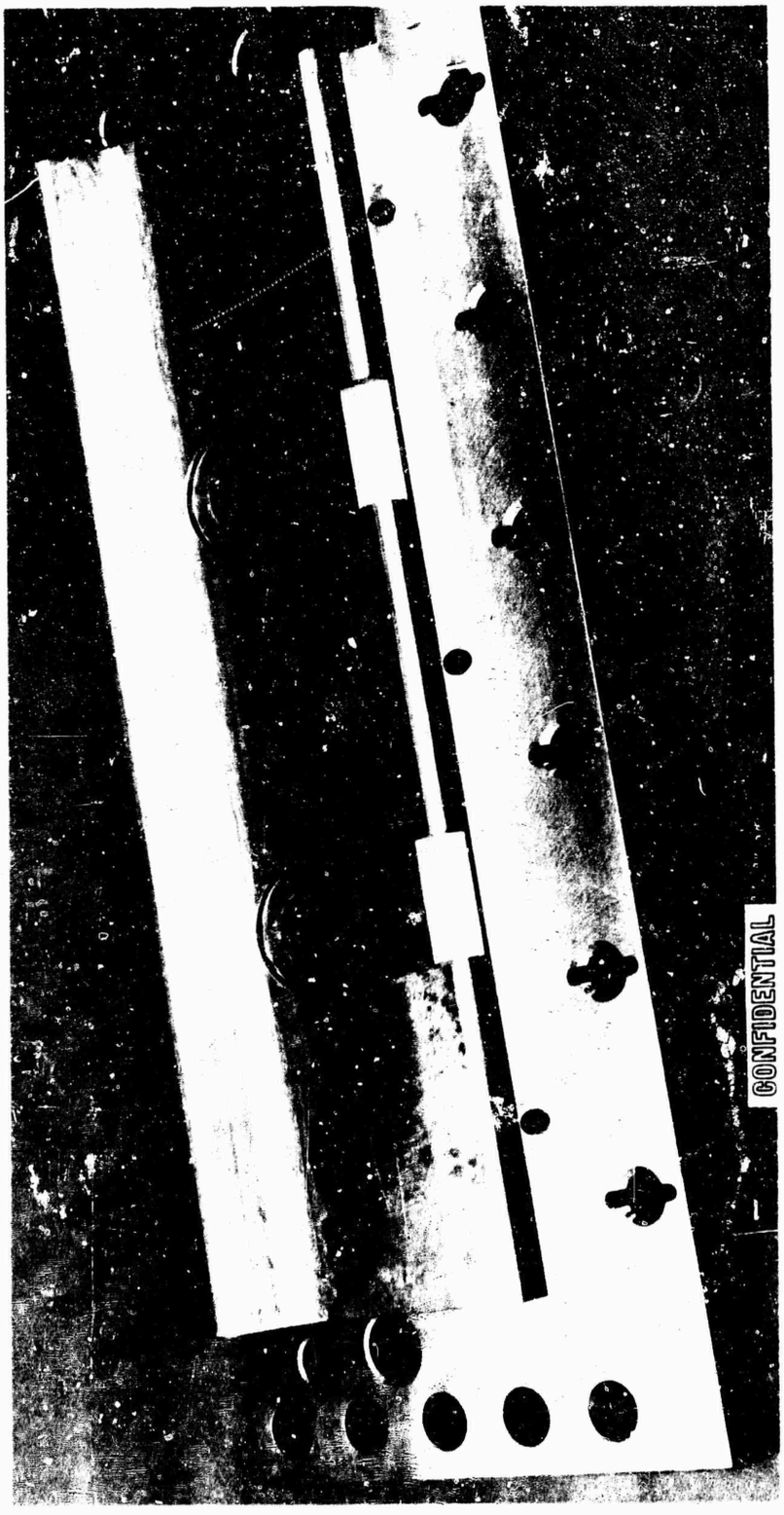

1XE32-3/30/67-C1B

Figure 372. 20K Titanium Structure, Tube-Side

(U) Thickness of application was determined after the titanium side wall structure and the tube-wall assembly had been cleaned by gaging the clearances between the side wall structure and the tube-wall surfaces. To accomplish this, a verifilm gaging material was applied to the surfaces (Fig.373 and 374). The chamber was installed in the bonding fixture then heated in an oven to 250 F. The components were then disassembled, the thickness of the verifilm measured, and the film thickness for the adhesive determined at all areas of the bond joint. The thicknesses measured were from tube crowns to structure; to compensate for additional adhesive required to fill tube interstices, epoxy nitrile adhesives were applied having a thickness 10 to 15 percent greater than the verifilm values. The thrust chamber was installed in the bonding tooling, and an equivalent of 25 lb/sq in. was applied through a pressure bag system. Adhesives curing was accomplished at a temperature of 250 F for 4 hours.

(U) Assembly, Final Machining and Pressure Test. The design of the 20K segment requires a series of assembly and match machining operations in order to obtain the dimensional tolerance limits. Upon completion of the bonding process, the end plate backup structures were assembled to the chamber. These structures support the copper end plates during the firing sequence and provide for the loads created by segmenting.

(U) The thrust chamber loads resulting from chamber pressure are carried by baffle bolts which attach to a bolt seat and cap assemblies. The baffle bolt seat and cap assemblies provide a means of transmitting the load from the one titanium backup structure through the adhesive bond joints and baffle without allowing leakage from the combustion zone. To accomplish this, a tube is welded to the baffle bolt seal or cap, passed through the titanium structure, adhesive bond joint and internally welded to the baffle seats of the tube-wall assembly (Fig.373 shows the assembly perspective). Thus, leakages to the adhesive joints are prevented. The torque

1XE32-6/2/67-C1C

Figure 373. 20K Titanium Side with Verafilm

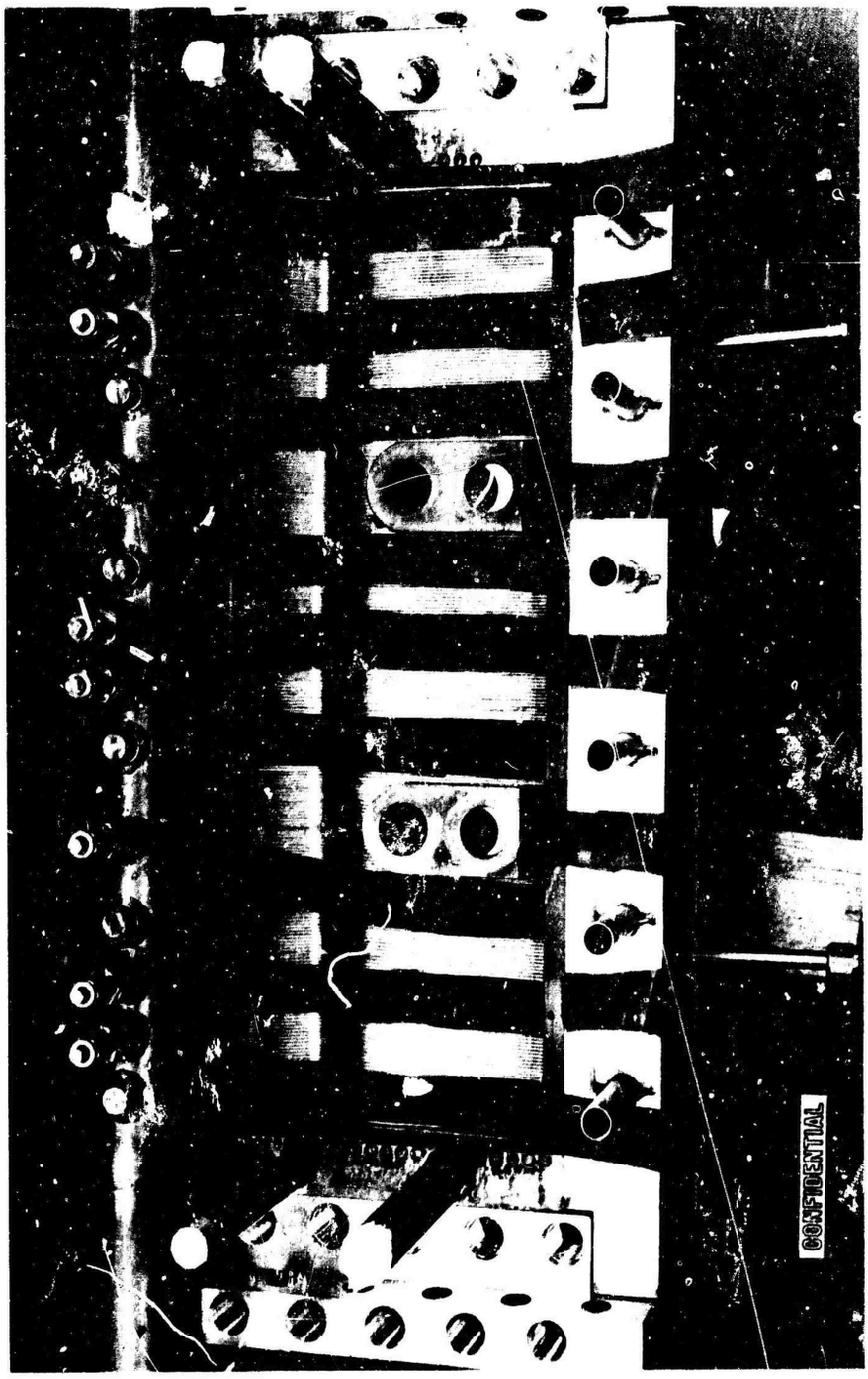

LXE32-6/2/67-C1D

Figure 374. 20K Chamber with Verafilm Applied

loads to the bolt seat or cap resulting from bolt installation is transferred to the titanium structure through pins which are installed into match drilled holes.

(C) The baffles were installed into the thrust chamber assembly, and the bolts were installed and torqued to a predetermined elongation value. Each bolt was calibrated to obtain a stress-strain curve, and the bolts were preloaded on assembly to 65K psi. These loads deflected the backup structure to the desired locations. The final machining for injector seal ring and mounting holes was accomplished (Fig.375). Upon completion of all machining and assembly, the thrust chamber assemblies were hydro-tested to 3180 psig and then cleaned for final assembly with the injector (Fig.376).

(C) Injector. The 20K injector assembly consists of a machined and welded CRES 347 body and 18 OFHC copper injection strips. The strips are arranged on the face of the injector to produce three compartments of six strips each when the injector is assembled to the 20K combustor assembly (Fig.377).

(U) The fabrication sequence was established such that critical feed passages and weldments could be proof-pressure tested without fabrication of costly tooling. Pressure test was conducted after welding of the oxidizer manifold and the oxidizer and fuel feed slots prior to EDM and broach for the injector strips.

(U) The latter operations as well as fabrication and installation of the injector strip were accomplished using techniques identical to those described for those items of the 250K injector.

IXE35-7/17/67-C1A

Figure 375. 20K Thrust Chamber With Baffles Installed

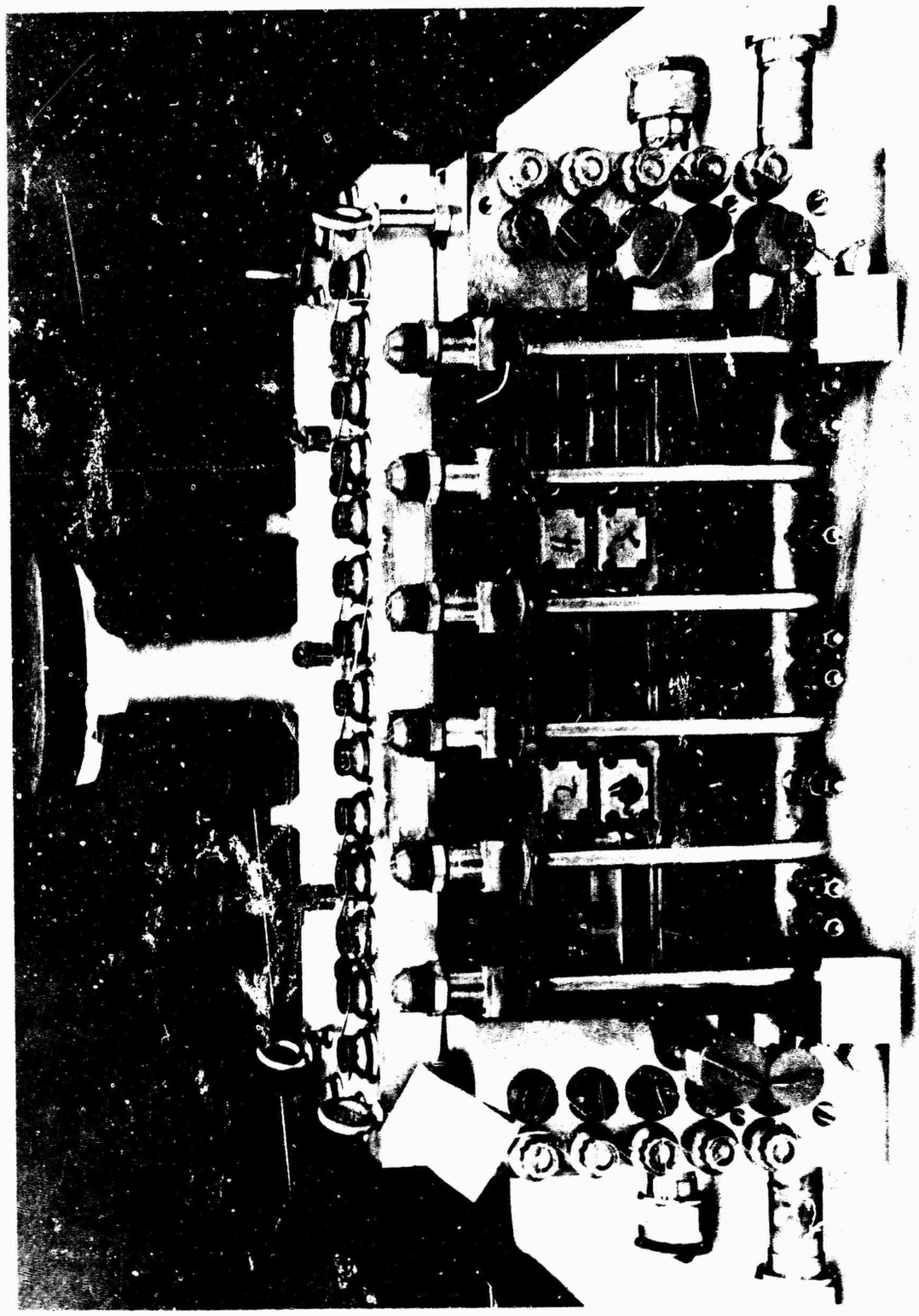

LXE32-6/7/67-C1B

Figure 376. 20K Structural Segment Assembly

(This page is Unclassified)

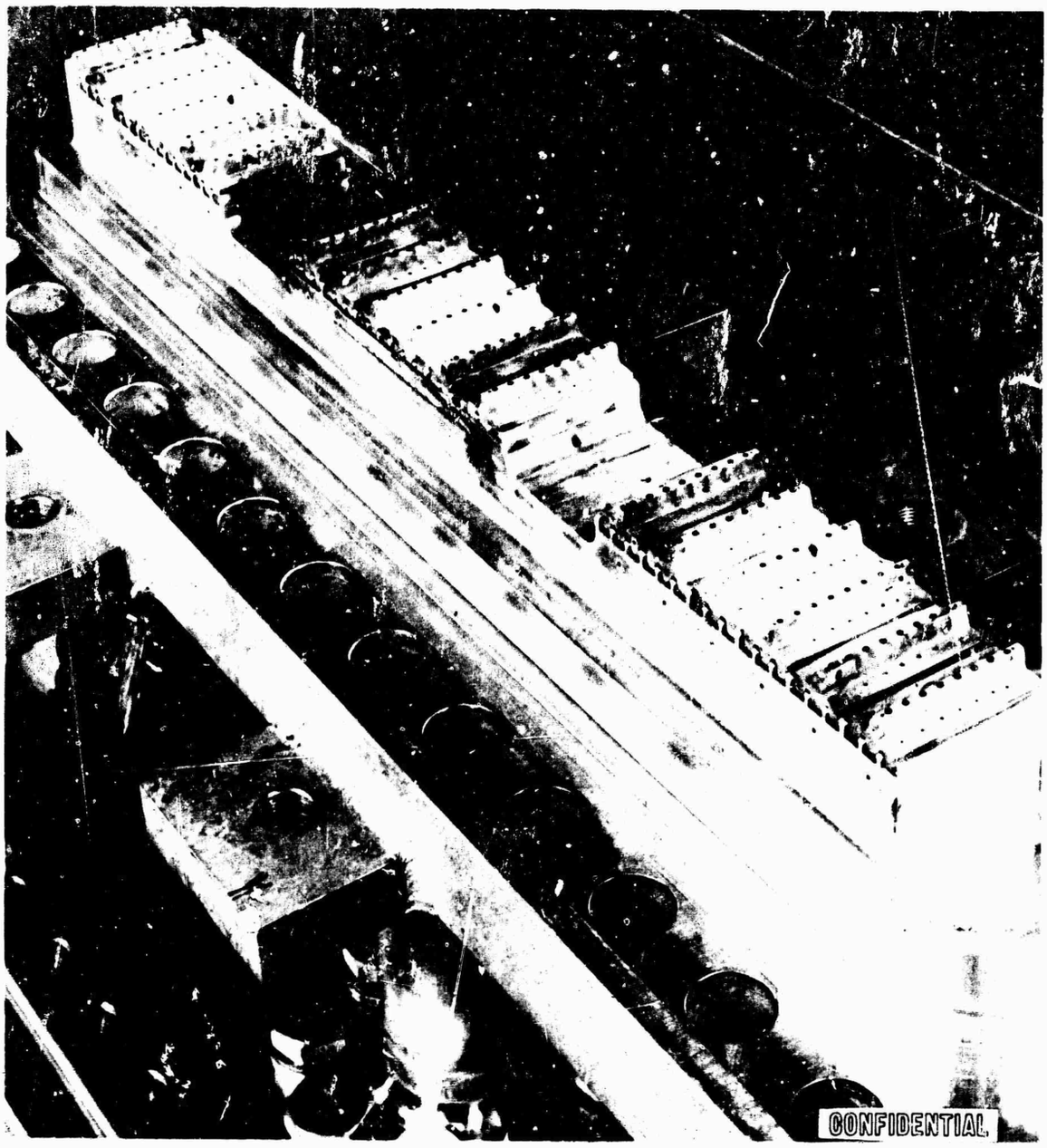

1XE35-7/17/67-C1G

Figure 377. 20K Injector Unit No. 2 Baffle Recess Erosion

Testing

(C) Test Plan. To provide meaningful cooling data, it was necessary for the 20K segment to simulate peak operating temperatures expected for the Demonstrator design and to demonstrate the adequacy of the coolant circuitry. By comparing results of the 20K segment tests with previous 2.5K segment results, the scalability of available heat transfer data was also evaluated. To demonstrate the structural integrity of the Demonstrator concept, it was necessary for the 20K segment to be operated over a range of chamber pressures up to the nominal design point, 1500 psi. In this manner, peak loading conditions of the structure will be evaluated and direct comparisons between analytical predictions and test data can be achieved. The third objective was to achieve performance data over a throttling range. The test program was designed to achieve these performance data concurrent with the heat transfer and structural objectives.

(C) A test plan was set up to achieve these objectives within the capabilities of the available test facility. The first portion of the test program provided performance data at throttled conditions, verified heat transfer and structural predictions, and demonstrated the adequacy of the coolant circuit design. This portion of the testing was conducted at chamber pressures between 600 and 1070 psia. During this series of tests, coolant flowrates were adjusted so that wall temperatures would correspond with values predicted for the Demonstrator Module. Fuel injection temperatures were maintained at ambient to correspond with values expected on the full-scale chamber configuration. Limitations in facility inlet pressure capabilities precluded operating in this same mode at higher chamber pressure values without exceeding hardware design conditions.

(C) To proceed to 1500-psia chamber pressures and maintain design wall temperatures within the tubular chamber, it was necessary to reduce chamber

mixture ratio and use lower temperature hydrogen to the injector. Tests 327 and 328 were conducted under these conditions. On test 328, a steady-state chamber pressure value of 1540 psi was achieved with a peak value of 1645 psi during the start transients. Achievement of these chamber pressures completed the evaluation of the chamber structural characteristics. Test of 20K unit No. 1 was then concluded.

(U) A subsequent research program effort resulted in a five-test series with 20K unit No. 2. The tests provided some data relative to the 20K segment operation with a fully regenerative-cooled chamber.

(U) Test Conduct. A series of 11 mainstage and 2 ignition tests were conducted on the 20K tube-wall segment (Table 89). During this test series, both the tube-wall temperature and tube hydraulic stress of the Demonstrator Module were matched (Table 90).

(U) Ignition (tests 316 and 326) was accomplished with 15/85 TEAB hypergol and igniter GO_2. A concentric tube igniter system was incorporated in each compartment. Igniter GOX was introduced through the center tube element with the hypergol propelled by GH_2, being introduced through the annulus of the concentric tube assembly.

(C) Tests 317 through 319 were successful mainstage tests at chamber pressures of 600 psi and varying duration. During test 320, stainless-steel erosion was noted for several milliseconds. The hardware was subsequently removed and inspected (Fig. 378). The erosion was caused by either a leaky capped-off instrumentation port or excessive volume in the port. As a result, fuel cooling from the injector was added in the baffle area. Special inserts were put in the ports, and tubular seals placed between the baffle and injector to prevent cross flow. Subsequently, two successful 600-psi chamber pressure tests (321 and 322) were made.

TABLE 89

(c) RESULTS OF 20K SEGMENT MAINSTAGE AND IGNITION TESTS

Test No.	Test Date, 1967	Duration, seconds	Thrust Chamber Pressure, psia	Injector Mixture Ratio, (o/f)	Thrust, pounds	$\dot{w}_o$ Injector, lb/sec	$\dot{w}_f$ Injector, lb/sec	$\dot{w}_f$ Coolant, lb/sec	LO_2 Injection Temperature, °F	Fuel Inlet Temperature, °F	Fuel Injection Temperature, °F	LO_2 Injection Pressure, psia	Fuel Inlet Pressure, psia	Fuel Dome Pressure, psia	Fuel Injection Pressure, psia	LO_2 Injection ΔP, psi	Fuel Injection ΔP, psi	LO_2 Dome Temperature, °F Det 1	Det 2	Det 3	R_{mr} (O/F)ss	γ_{ss}	$\dot{w}_{ox}$ (Mass O) lbm/sec	FAR Injection (Fuel
316	7-10	Ignition Only	996	5.0	93	96	96	96	96	96	96	96	96	96	96	96	96	96	96	96	96	96	96	96
317	7-11	0.15	996	5.0	93	96	96	96	96	96	96	96	96	96	96	96	96	96	96	96	96	96	96	96
318	7-12	0.98	996	5.06	93	96	15.99	13.16	8.89	6.74	-267	1000	2125	1090	2125	94	94	96	96	96	0.9984	1000	6360	63.15
319	7-13	1.18	985	5.56	93	96	16.27	13.39	8.98	6.74	-266	96	2125	1090	2125	94	94	96	96	96	0.9988	1000	6364	63.15
320	7-14	0.55	988	5.32	93	96	16.1	13.2	8.92	6.74	-266	96	2125	1090	2125	94	94	96	96	96	0.9988	1000	6364	63.15
321	7-18	0.55	988	6.0	93	96	16.1	13.2	8.92	6.74	-266	96	2125	1090	2125	94	94	96	96	96	0.9988	1000	6364	63.15
322	7-19	0.30	995	5.19	93	96	16.43	13.36	8.98	6.74	-266	96	2125	1090	2125	94	94	96	96	96	0.9988	1000	6364	63.15
323	7-20	1.05	988	5.83	93	96	15.95	13.0	8.78	6.74	-266	96	2125	1090	2125	94	94	96	96	96	0.9988	1000	6364	63.15
324	7-21	0.80	978	5.75	93	96	15.85	12.90	8.73	6.74	-266	96	2125	1090	2125	94	94	96	96	96	0.9988	1000	6364	63.15
325	7-1	2.17	1044	5.87	93	96	16.36	13.31	8.98	6.74	-266	96	2125	1090	2125	94	94	96	96	96	0.9988	1000	6364	63.15
326	7-5	2.36	1135	5.85	93	96	16.53	13.45	9.08	6.74	-266	96	2125	1090	2125	94	94	96	96	96	0.9988	1000	6364	63.15
327	7-6	2.36	1135	5.78	93	96	16.53	13.45	9.08	6.74	-266	96	2125	1090	2125	94	94	96	96	96	0.9988	1000	6364	63.15

Note: Mode data was not recorded
Mixer reduced due to manifold duration to achieve steady state

TABLE 90

(C) 20K/250K PRIMARY SIMULATION PARAMETERS

Parameters	250K Results	20K Results
Structural		
Chamber Pressure, psia	300 to 1500	600 to 1645
Heat Transfer (Throat)		
Tube Temperature (T_{wg}), F	1520	1560
Tube Wall ΔT, F	820	730
Coolant Temperature (T_B), R	550	560
Tube Hydraulic Stress (σ_{Hyd}), psi	3330	4100
Combustion Mixture Ratio	5 to 7	2.8 to 6.2

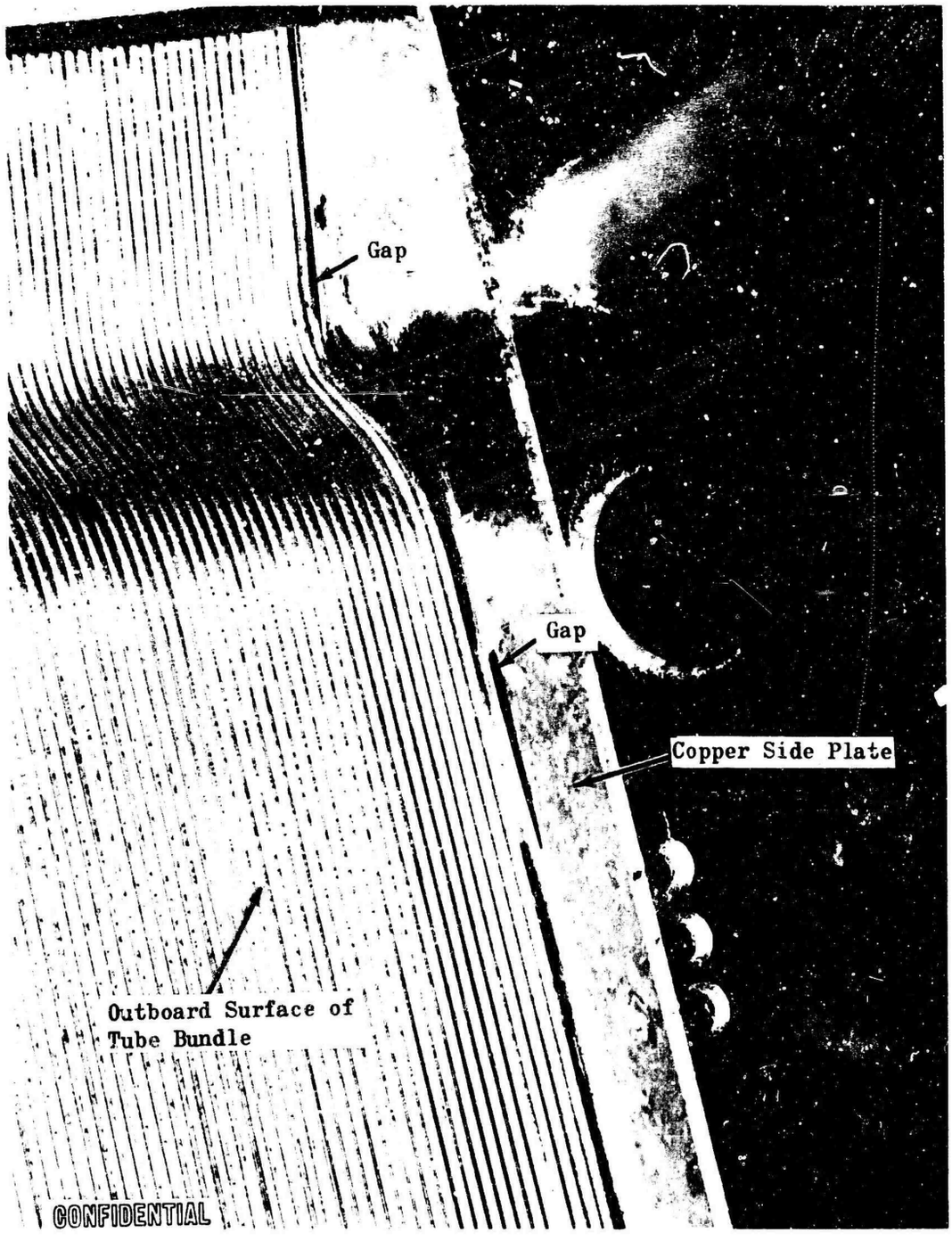

1EX32-4/11/67-C1A

Figure 378. 20K Thrust Chamber Braze Assembly, Gap at Tube-to-End Plate Joint

(C) Tests 323, 324, and 325 were successfully conducted at chamber pressures of 885, 935, and 1070 psia. It was noted that following test 323, the braze alloy between LO_2 injector strips showed indications of overheating. This condition existed in limited areas of diagonally opposite corners of each injector compartment. Braze alloy flow was also noticed on the outer body tubes adjacent to both baffles in the throat region. Prior to test 326, the injector fuel feed system was modified to condition the fuel. Test 326 was a satisfactory ignition test, which verified ignition for tests using cold gaseous hydrogen.

(C) Tests 327 and 328 were run at chamber pressures of 1175 and 1540 psia. These tests demonstrated that the lightweight structure could withstand maximum pressure stresses apparently without plastic deformation.

(C) Related Program. The second tube-wall chamber was used to conduct one transition and four mainstage tests on a related program. With a similar injector and fully regenerative cooling. Chamber pressures were 600, 900, and 1125 psi; mixture ratio varied from 5 to 6. The last test was an extended duration test with 47.25 seconds of mainstage at 1135-psi chamber pressure. No hardware damage was experienced.

(U) Posttest Hardware Inspection and Analysis. Just Prior to cutoff on test 328, leakage was noted from the titanium backup structure. This leak was at the location where shimming had previously been required (R-6537-5). Local heating had melted the braze holding this shim in place and created a hot-gas leak path. The leak from this crack eroded a hole in the titanium backup structure (Fig.379).

(U) In addition, the tube bundle was found to have a convex bulge in several places as a result of pressure buildup between the tube bundle and backup structure. The 20K thrust chamber was disassembled to determine the cause of the convex bulges (Fig.380). These bulges were found

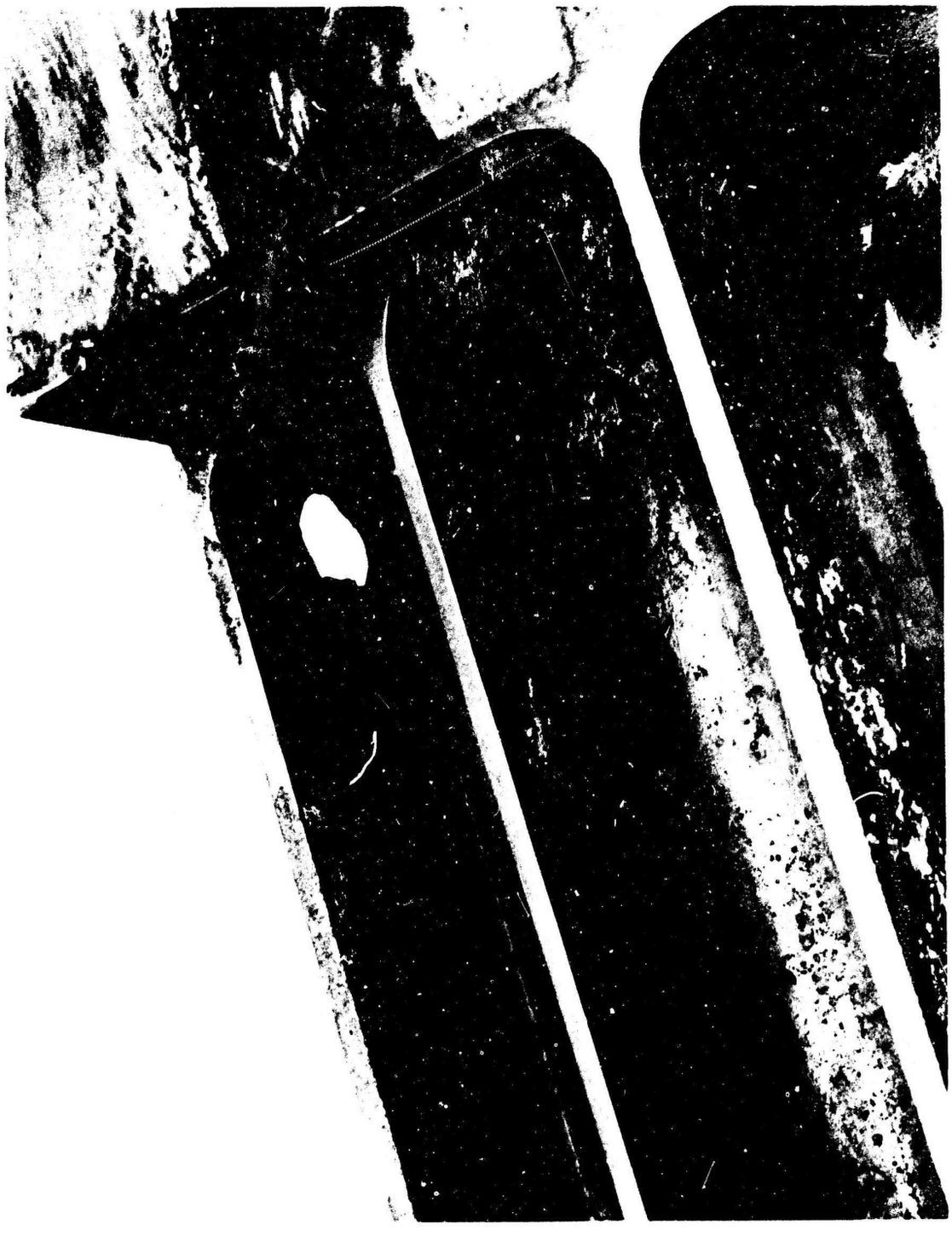

1XE35-9/22/67-C1D

Figure 379. Damage to Titanium Structure

(This page is Unclassified)

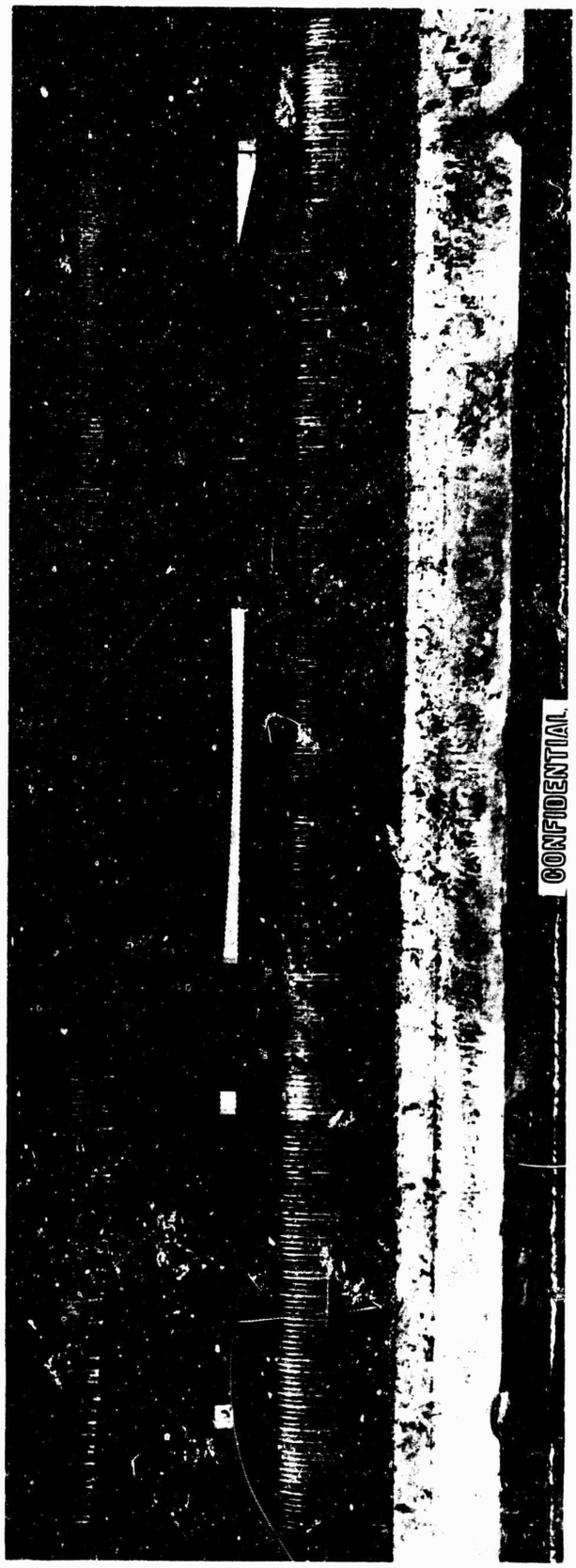

XB35-8/17/67-C1

Figure 380. 20K Thrust Chamber With Convex Bulges

to be caused by cold gas leaking between the tube wall and the titanium backup structure. The source of leakage was located. Approximately 70 tubes were leaking at their brazed joint to a fabrication support beam near the nozzle exit of the chamber. This support beam is unique to the 20K and not pertinent to the 250K Demonstrator design.

(U) Disassembly of the chamber also indicated that an effectively zero bond joint existed on both the uppas and downpass sides. Dimensional checks revealed that the bond joint had not failed, but rather that bonding had not been achieved during the initial assembly. Several factors indicate that this was caused by mechanical interference between the titanium structure and the brazed coolant circuit during final assembly:

1. The measured posttest thicknesses of the adhesive were all larger than the gap determined by preassembly verifilm measurements.
2. A casting resin, which was used subsequent to the bonding process, was found to be distributed on the adhesive film and on the baffle seats.

Neither of these events could have occurred if the parts were properly assembled because previous assemblies of the components had verified critical dimensions. Thus it is apparent that mechanical interference occurred during the final assembly.

(U) In spite of the mechanical interference, there were two small areas in the chamber where a successful adhesive bond was achieved. At these locations, the pressure bags used during the adhesive curing process created sufficient force to achieve contact between the nickel tubes, the adhesive, and the titanium backup structure. The fact that a good bond

was achieved under adverse conditions at these locations is a positive indication that if the unit had been assembled as intended, the surface would have had a good bond.

Analysis of Results

(U) Structural Weight Evaluation. One of the objectives of the 20K tube wall segment program is to demonstrate the feasibility and practicality of utilizing a light-weight structure adhesively bonded to the tube bundle.

(U) Portions of the 20K segment have been weighed, and an analysis made to determine what the weight of a full-scale 250K thrust chamber would be if the 20K actual weight were scaled up to a complete body. The injector was not included in the evaluation because of the wide differences in this workhorse-type injector and that of the Demonstrator Module Chamber. It has been necessary to delete portions of the 20K end plates and end fittings that would not exist in a full-scale model. In addition, comparison has been made (Table 91) to a 250K chamber (titanium shell) that has a short inner body nozzle section.

(C) TABLE 91

COMPARISON OF 20K AND 250K THRUST CHAMBERS

Item	Description	Thrust Chamber, pounds		Weight Differential, pounds
		20K (Scaled)	250K	
1	Fuel Manifold and Return Tube	163	60	103
2	Baffle Seat and Tubes	210	185	25
3	Injector Rings	289	130	159
4	Structural Backup	785	585	200
5	Structural Tie	390	403	-13
	Totals	1837	1333	504

(C) Table 91 indicates that if the applicable portions of the 20K segment were scaled up to a complete 250K thrust chamber (less the inner body nozzle), the assembly would weigh 504 pounds more than a comparable 250K demonstrator thrust chamber.

(C) Of the 504 pounds, 103 pounds difference is associated with the two exit end manifolds which, for the 20K, were designed as a facility item and have a safety factor twice as large as would be required; therefore, 51.5 pounds could be reasonable expected to be deleted from the difference.

(C) The 25 pounds difference associated with the baffle seat and tubes is associated with the difference in tube-wall thickness; 0.0146 inch in the 20K, and 0.008 inch in the demonstrator. It is expected that the weights would be exactly comparable with the same-size tubes. The 13-pound difference in the structural ties is accounted for by the smaller-size bolts used in the segment, the smaller size being used to produce the same deflection as on the Demonstrator Module with the shorter shroud.

(U) The injector rings were not pertinent to the structural simulation and were not designed for minimum weight. For a full-scale body, the injector rings would be designed exactly as the demonstrator and would weigh the same.

(U) One-hundred and one pounds of the structural backup weight difference can be accounted for by the extra material employed in the 20K for injector mounting. The rib/pocket design of the titanium structure was not minimized for reasons of economy and ease of fabrication. It is conservatively estimated that another 20 pounds could be deleted from the structure.

(C) Recapitulation of the weight difference would then proceed as shown in Table 92.

TABLE 92

(C) RECAPITULATION OF WEIGHT DIFFERENCE:
20K and 250K THRUST CHAMBERS

Item	Description	Thrust Chamber, pounds		Weight Differential, pounds
		20K (Scaled)	250K	
1	Fuel Manifold and Return Tube	111.5	60	51.5
2	Baffle Seat and Tubes	185	185	--
3	Injector Rings	130	130	--
4	Structural Backup	654	585	69
5	Structural Ties	403	403	--
	Total Difference			120.5

(C) This analysis therefore predicts that scaling the applicable portions of the 20K segment to a 250K thrust chamber would result in a weight within 120.5 pounds of the demonstrator thrust chamber. This is considered good correlation for a comparison between a segment design and a full-circumference design.

(U) Structural Analysis. To verify the calculated stresses acting on the light-weight backup structures on the 20K structural segment and the 250K demonstrator design, strain gages were installed on the 20K segment prior to the test series. Four strain gages were installed on each of two structural baffle bolts. These gages indicated both the total stress level and the amount of induced moments in the bolts. Additional strain gages were installed on the horizontal and vertical ribs of the titanium backup structure. The location of these gages was selected to provide data on load distribution paths, maximum stresses, and resultant moments.

(U) The conclusions reached from evaluation of strain gage data are:

1. The 20K Demonstrator segment light-weight backup structure and baffle bolts are structurally adequate and react as analytically predicted.
2. Excellent agreement existed between calculated and measured stresses at the baffle bolts.
3. Stresses measured at the vertical and horizontal ribs of the backwall structures indicated good agreement with calculated stresses.
4. Stress levels in some areas indicated potential weight reductions could be achieved.

(C) During the series of 20K hot-firing tests, a range of chamber pressures from 600 to >1500 psi were achieved. The baffle bolt stresses were measured on each of the tests. Results indicated excellent agreement between the measured and calculated bolt load (Fig.381). It should be noted that this figure represents the lower bolt. A large majority of the chamber loads are carried by this bolt. Stress values for the upper bolt are 16 percent less.

(U) As indicated in Fig.382, the bolt load is largely comprised of a preload imposed during assembly of the unit. This preload is set so that during peak operating conditions, the external load will not cause separation of the baffle from the baffle seat. As external loads are increased to the maximum operating conditions, the bolt load rises to a value above the initial preload condition. This value and the slope of the curve were calculated prior to the test series. Excellent agreement can be seen between the calculated bolt loads and measured values.

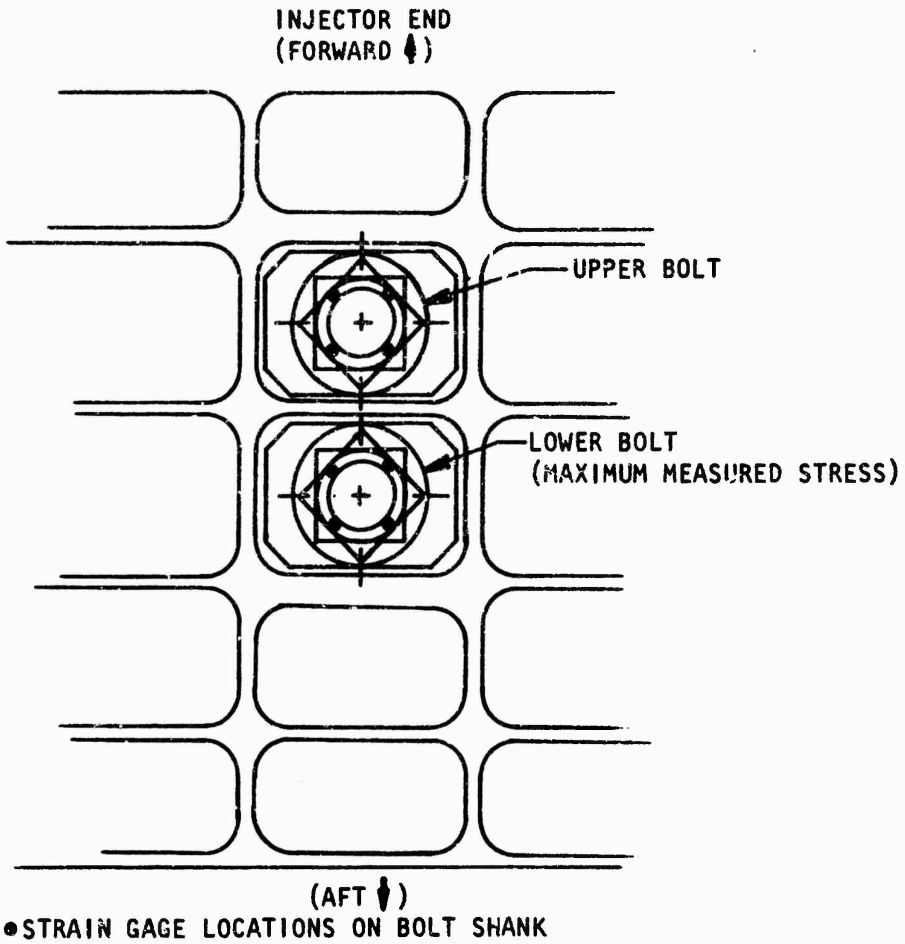

PRESSURE CHAMBER = 1540 PSI	
MAXIMUM MEASURED STRESS	CALCULATED STRESS USING MINUMUM DIMENSIONS
PSI	PSI
134,900	134,100

INCO 718 BOLTS

CONFIDENTIAL

ULTIMATE TENSILE STRENGTH = 200,000 PSI
TENSILE YIELD STRENGTH = 180,000 PSI

Figure 381. 20K Segment Strain Gage Results, Baffle Bolts

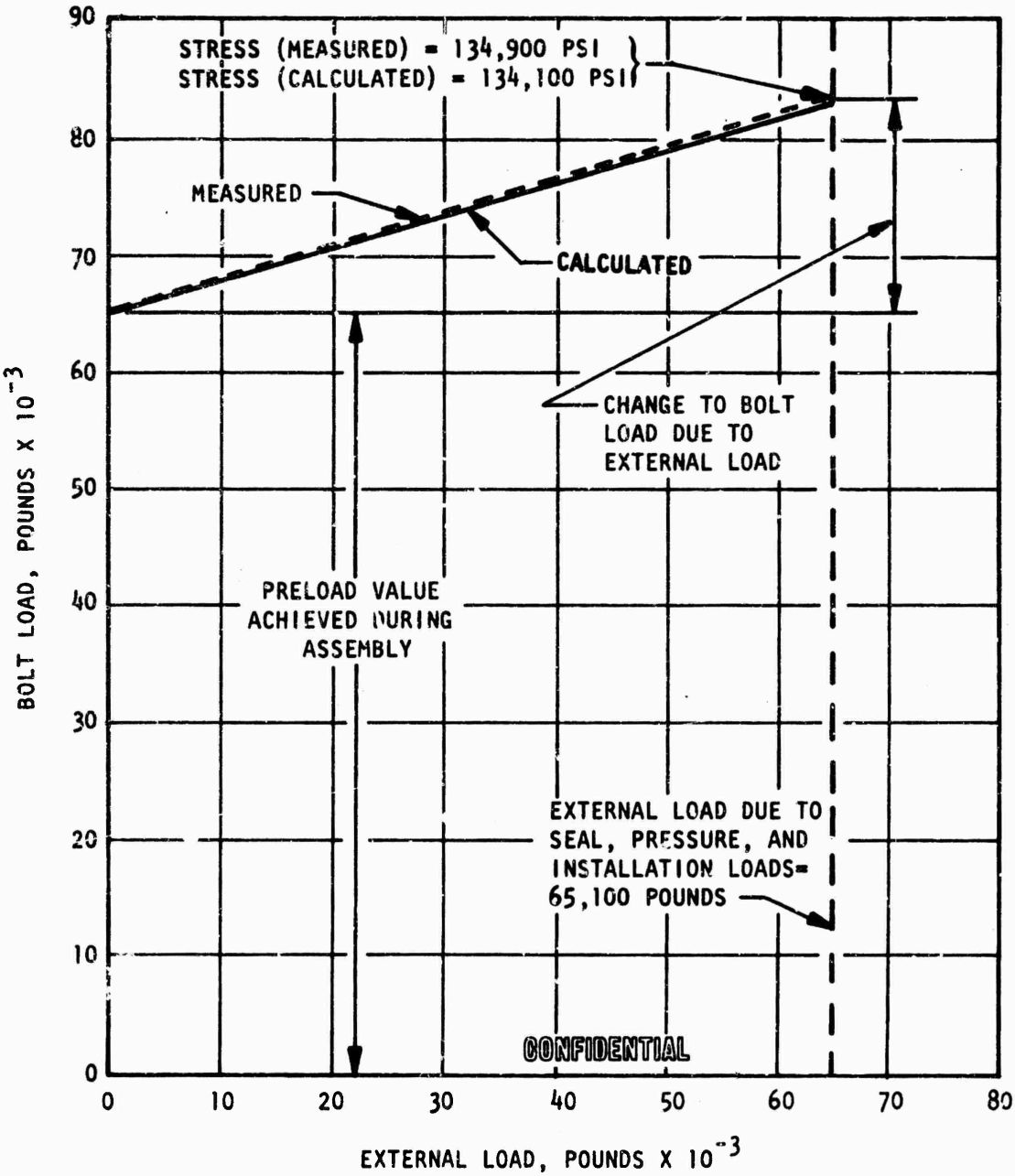

Figure 382. Lower Baffle Bolt Load Diagram

(U) Fourteen strain gages were placed on the titanium structure to evaluate load paths, moments, and maximum strains. Selected readings of these strain gages were taken on each test. Thus, throughout the test series, several readings of each strain gage location were accomplished.

(C) Strain gage data for the horizontal ribs of the backwall structure were recorded at a chamber pressure of 1065 psi. Extrapolating these data, a maximum horizontal web stress of 32,300 psi was obtained for P_c = 1540 psi at the bolt head side of the segment (Fig.383). This compares with the calculated value of 32,100 psi. Figure 384 shows the stress levels acting on the backup structure vertical ribs at the backside of the segment. A maximum vertical rib stress of 42,000 psi was measured at the backside of the segment. A comparison of the measured and calculated stress distributions at P_c = 1540 psi is given. The comparison between maximum strain levels achieved during this test series and material strength capabilities definitely indicates the potential for further chamber weight reductions.

(U) Based on limit loads, the minimum ultimate factors of safety for various structural components are as follows:

Component	Ultimate Factor of Safety
Baffle Bolts	1.46
Horizontal Titanium Beams	3.76
Vertical Titanium Beams	2.90
Backwall Plate	1.46

As can be seen from the analysis for ultimate factors of safety, the verical and horizontal beam thickness could be optimized but would require a more difficult machine operation.

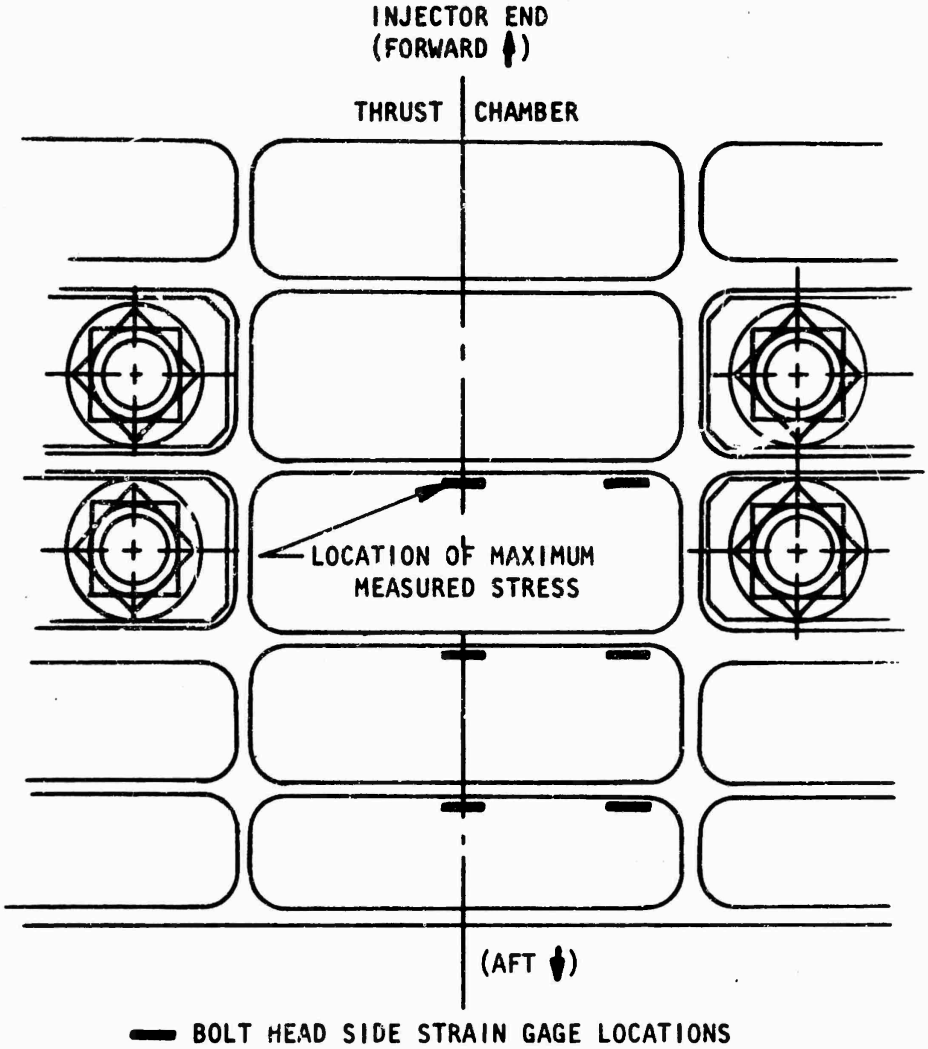

P_c = 1065 PSI	PRESSURE CHAMBER = 1540 PSI	
MAXIMUM MEASURED STRESS, PSI	EXTRAPOLATED STRESS FROM TEST DATA, PSI	CALCULATED STRESS USING MINIMUM DIMENSIONS, PSI
PSI	PSI	PSI
22,300	32,300	32,100

TITANIUM RIBS

CONFIDENTIAL

ULTIMATE TENSILE STRENGTH = 130,000 PSI
TENSILE YIELD STRENGTH = 120,000 PSI

Figure 383.20K Segment Strain Gage Results Horizontal Ribs

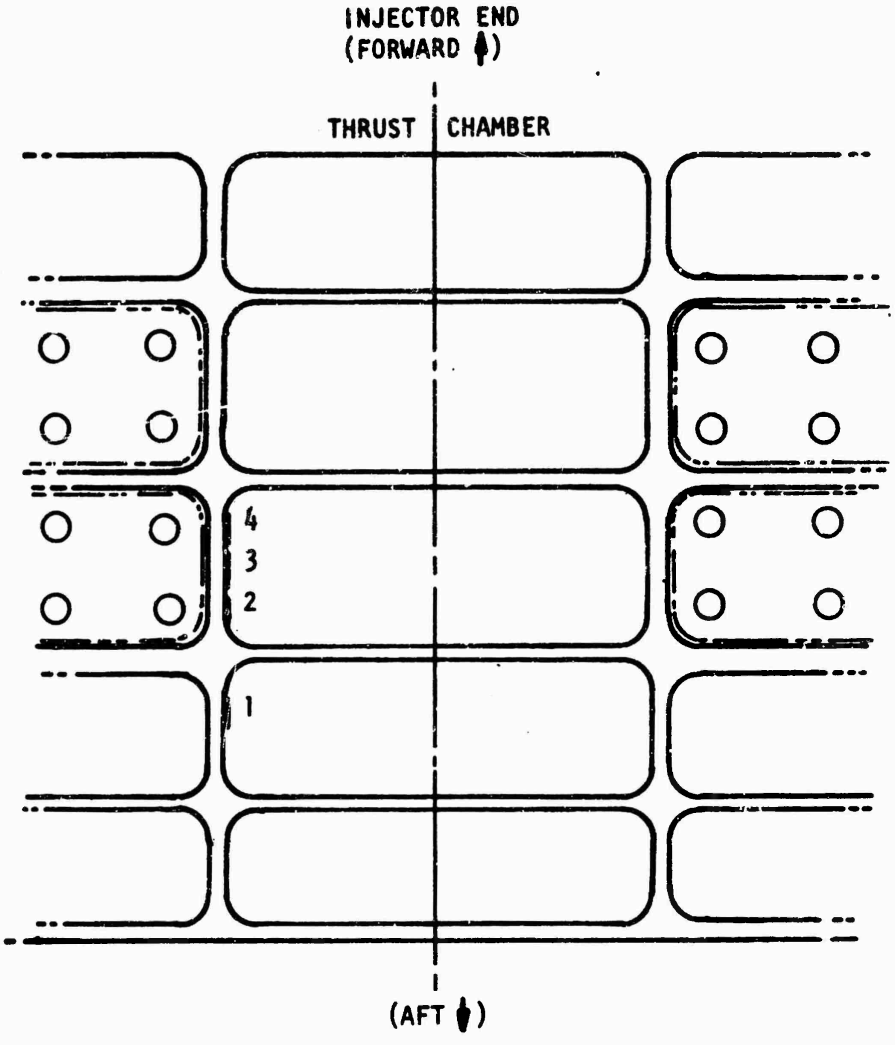

BACKSIDE STRAIN GAGE LOCATIONS

GAGE NO.	PRESSURE CHAMBER = 1540 PSI	
	MAXIMUM MEASURED STRESS, PSI	CALCULATED STRESS USING MINIMUM DIMENSIONS, PSI
1	-14,200	-19,600
2	-35,000	-51,700
3	-42,000	-41,200
4	-37,300	-29,800

TITANIUM RIBS

CONFIDENTIAL

ULTIMATE TENSILE STRENGTH = 130,000 PSI
TENSILE YIELD STRENGTH = 120,000 PSI

Figure 384. 20K Segment Vertical Ribs

(U) The throat gap was monitored throughout the test series by taking measurements with a hall-type gage inserted into the gap. The results are shown in Fig. 385. These measurements indicate that the backup structure showed no signs of plastic yielding and therefore was quite predictable. Even after the hardware was partially disassembled and reassembled, the throat gap returned to its original position. The small variation seen in the last two sets of measurements was shown by posttest inspection to be indicative of separation taking place between the tube bundle and backup structure.

(U) An analysis of the 20K structural segment was conducted to determine the manner in which throat area would change as a function of external loads (chamber pressure). The loads, stresses, and deflections of the 20K segment structure were modeled for solution using the Rocketdyne Space Frame Analysis computer program. The thrust chamber backup structure was depicted as a three-dimensional space grid work of beam-like members and rigid bodies (Fig. 386). Chamber pressure loads were simulated by applying equivalent forces and moments at each intersection of the members (nodal points). Individual members and rigid bodies were assembled into an equivalent structure by utilizing the stiffness method (i.e., nodal equilibrium). The nodal displacements were then computed and individual member reactions determined.

(C) The analytical stress predictions discussed above were shown to be in good agreement with the measured values. The same analysis predicted throat deflections which result in approximately 1-percent throat area increases per 100-psi chamber pressure when nominal assumptions are used. The major portion of the change (90 percent) in area is a direct result of throat expansion due to cantilevered nozzle loads; the small remaining portion of the change in area is due to bending of the horizontal support beams.

(C) It should be noted that this increase in throat area is favorable to performance of a full-scale engine. At full thrust conditions, the Demonstrator

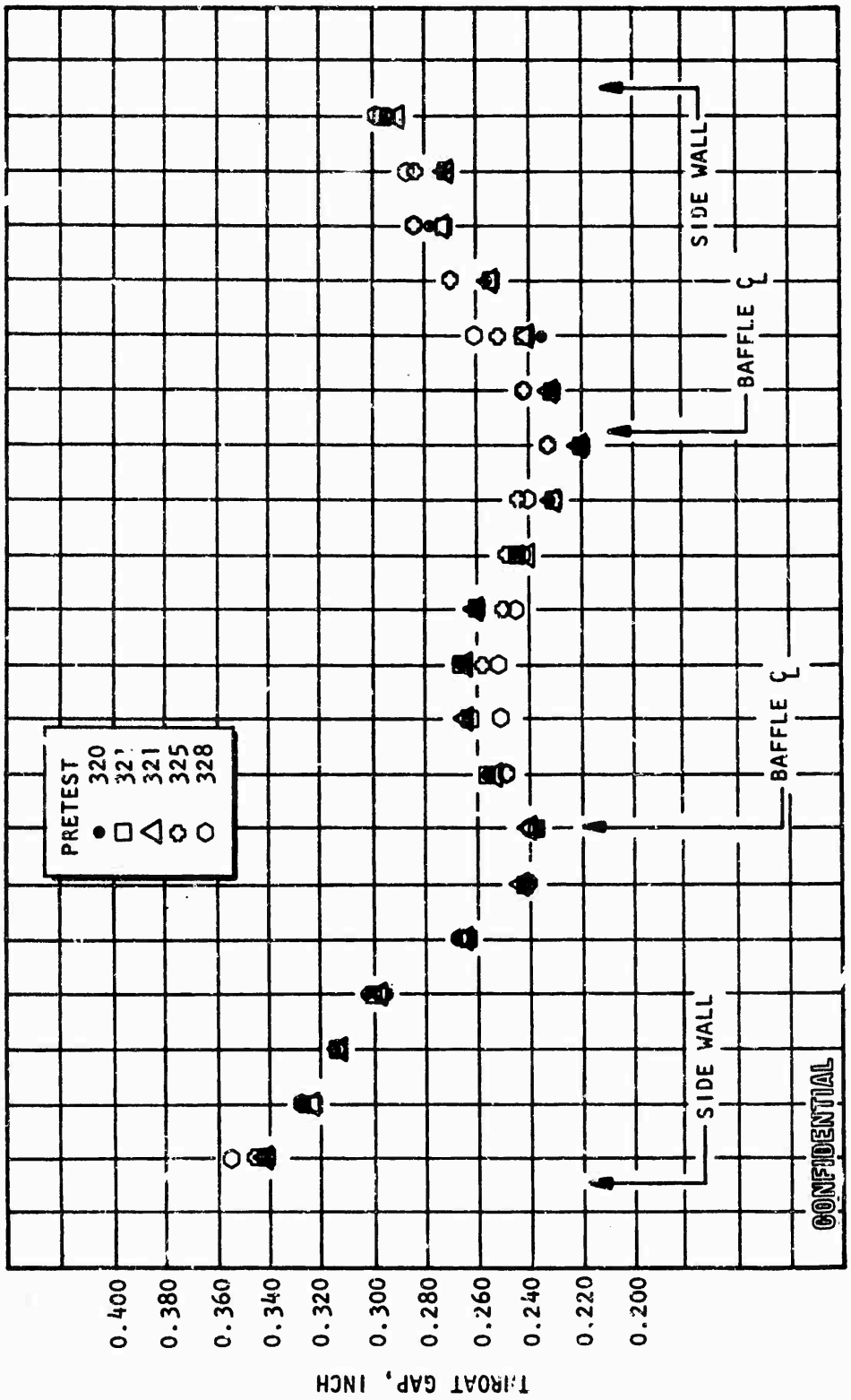

Figure 385. 20K Throat Gap Measurements

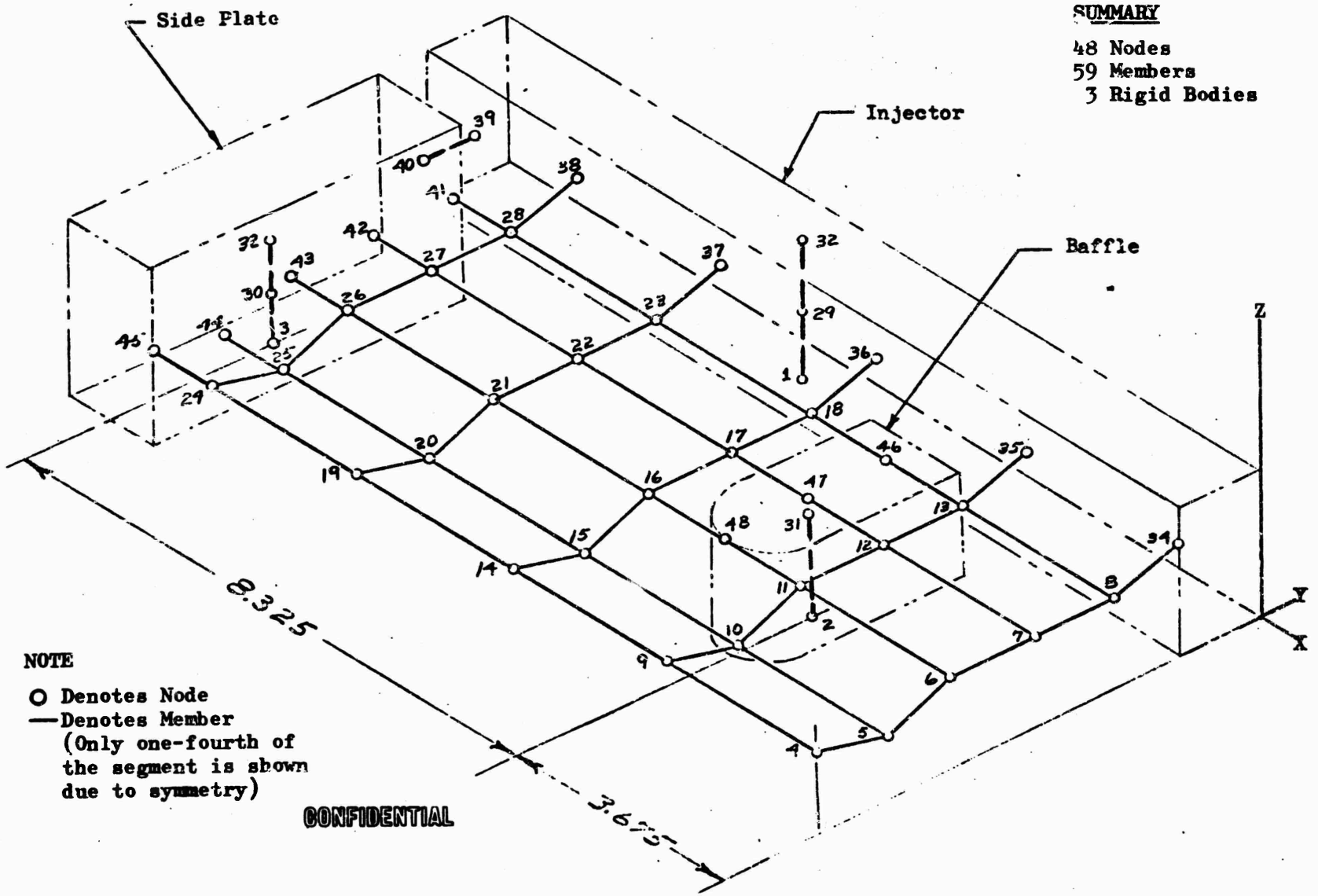

Figure 386. Thrust Chamber Structure Analytical Model

Module would operate at the design area ratio. As the chamber is throttled, throat area would decrease, and the expansion area ratio of the thrust chamber would be increased accordingly. Based on the analysis of the 20K structural segment, the area ratio of the full-scale chamber would be increased approximately 12 percent at the full-throttled condition.

(U) Performance. During the 20K segment test series, performance values were obtained over a wide range of chamber pressures. The performance values shown in Table 93 indicate that a high level of combustion efficiency was achieved throughout the test series. Performance calculations were based on the methods similar to those described in Appendix I.

(C) The tests most indicative of performance levels were 320, 322, 324, 325, 327, and 328. These tests were of sufficient duration for all measurement to be stabilized and accurate performance calculations to be performed. Results from shorter tests are presented for reference only. During these tests, an average combustion efficiency greater than 98 percent was achieved. This combustion efficiency compares faborably with, and may be slightly higher than, both results from previous 2.5K segment tests and recent tests conducted with the 250K full-scale thrust chamber.

(U) The high level of performance achieved during these tests again verifies the validity of segment testing and the ability to scale performance values from the 2.5K to 20K to 250K configurations. Because the 20K segment utilizes baffles, the 20K performance values also provide another important step in substantiating the predicted values for the 250K Demonstrator design. In accordance with previous analytical predictions, the subsonic baffles were found to have no adverse effect on the combustion efficiency achieved by the segment. Instead the baffles may have contributed a turbulence, which promotes mixing and a resultant higher combustion efficiency.

(C)

TABLE 93

20K RESULTS SUMMARY

Test No.	Duration, seconds	Injector Mixture Ratio, (o/f)	$\dot{w}_T$ Injector, lb/sec	Fuel Inlet Temperature, F	Chamber Pressure, psia	η_{c^*}	T_{wg}, F	Q (MR = 6.0) Btu/sec	c* ft/sec
320	2.10	4.32	16.57	-295	655	0.9908	1000	4900	7778
322	2.20	5.49	16.43	-277	655	1.0050	1200	5020	7841
324	2.20	5.93	25.00	-275	935	0.9788	1430	6230	7539
325	2.17	5.87	28.38	-274	1070	0.9954	1560	7070	7695
327	2.30	3.25	30.53	-277	1174	0.9812	1400	6800	8130
328	2.32	2.70	40.56	-275	1539	1.0050	1400	9430	8360

CONFIDENTIAL

(U) Despite the very high performance of this hardware, the usual combustion instability which accompanies high performance was not present in any apparent detrimental form 1600 to 1900 cps oscillation.

(C) The high level of combustion efficiency, as well as stability, was observed over the entire throttled range. Chamber pressure was varied from 600 to 1550 psia and mixture ratios from 2.7 to 6.0.

(U) The fine correlation between flowrates and injector pressure drops (Fig. 387) is indicative of the good measurements obtained on these tests. In addition, heat fluxes correlated well with chamber pressure and mixture ratio (Fig. 388).

(C) Examination of the performance data indicated a slightly larger throat deflection than nominally predicted. This could be explained by deviations between the as-fabricated and as-designed hardware. The estimated throat deflection from the slope of the characteristic velocity (c*) efficiency curve (Fig. 389) was used to determine the throat deflection. This assumption is expected to be a conservative estimate of the throat deflection, since past experience with segments has shown the c* efficiency to increase slightly with chamber pressure.

(C) During the regenerative testing, a modified injector was used which had the fuel film coolant increased from 12.7 to 25.5 percent. This apparently decreased the c* efficiency approximately 2 percent and the total heat flux to the coolant 20 percent (Fig. 389 and 390. This modification was being considered for the 250K chamber to alleviate tube overheating in the upper combustion chamber.

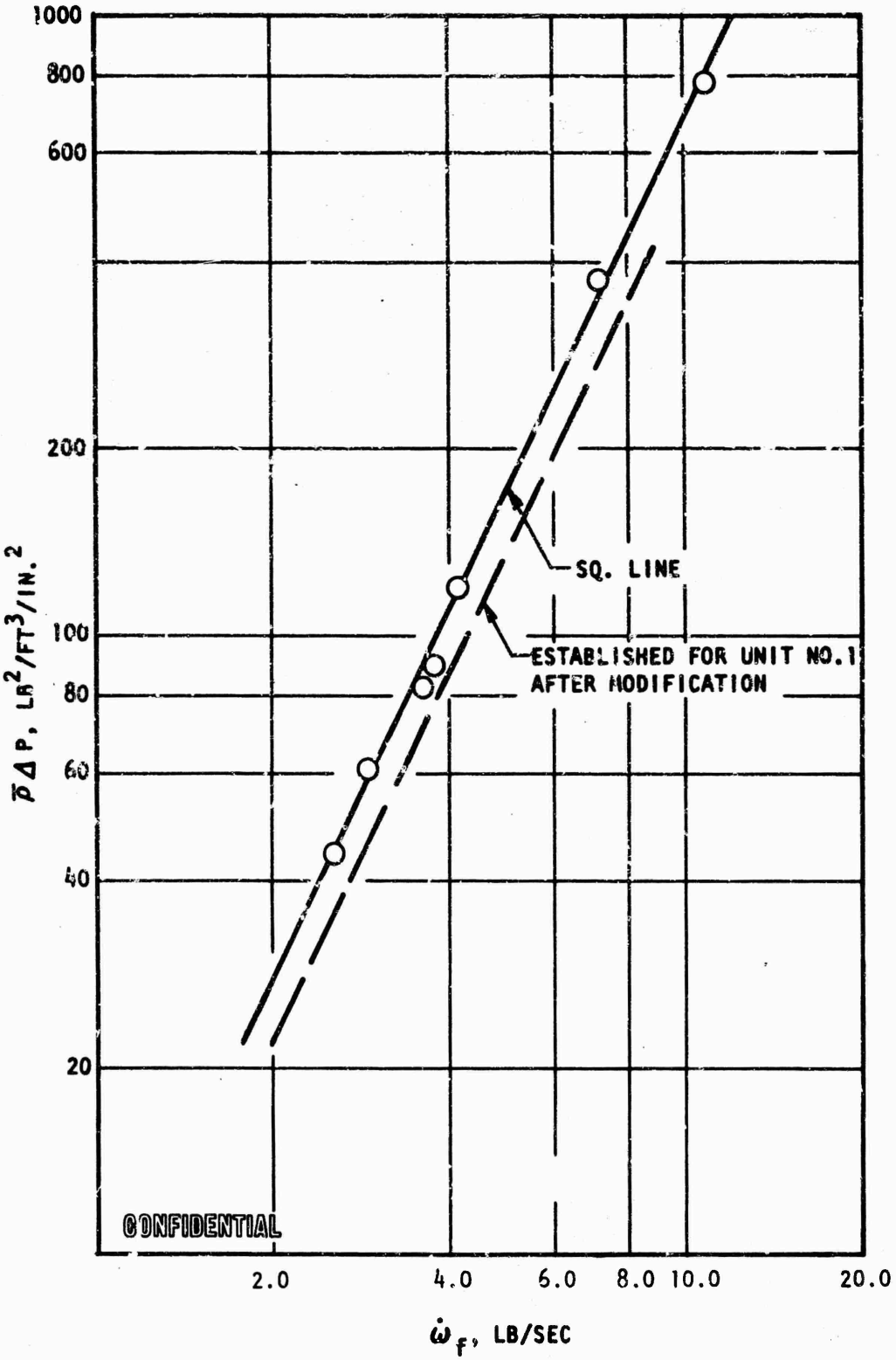

Figure 387. 20K Injector Unit No. 2

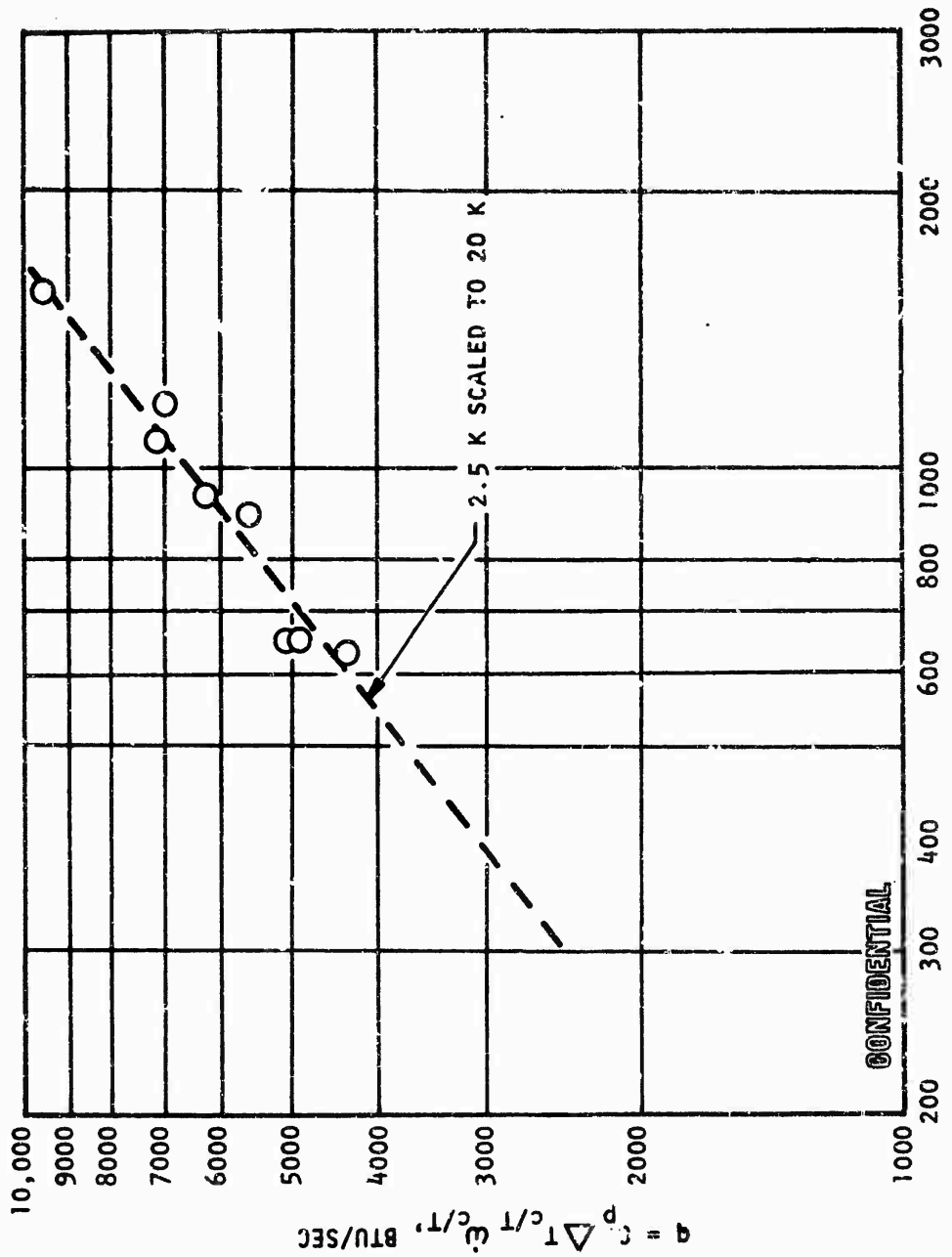

Figure 388. 20K Total Heat Flux to Tubes

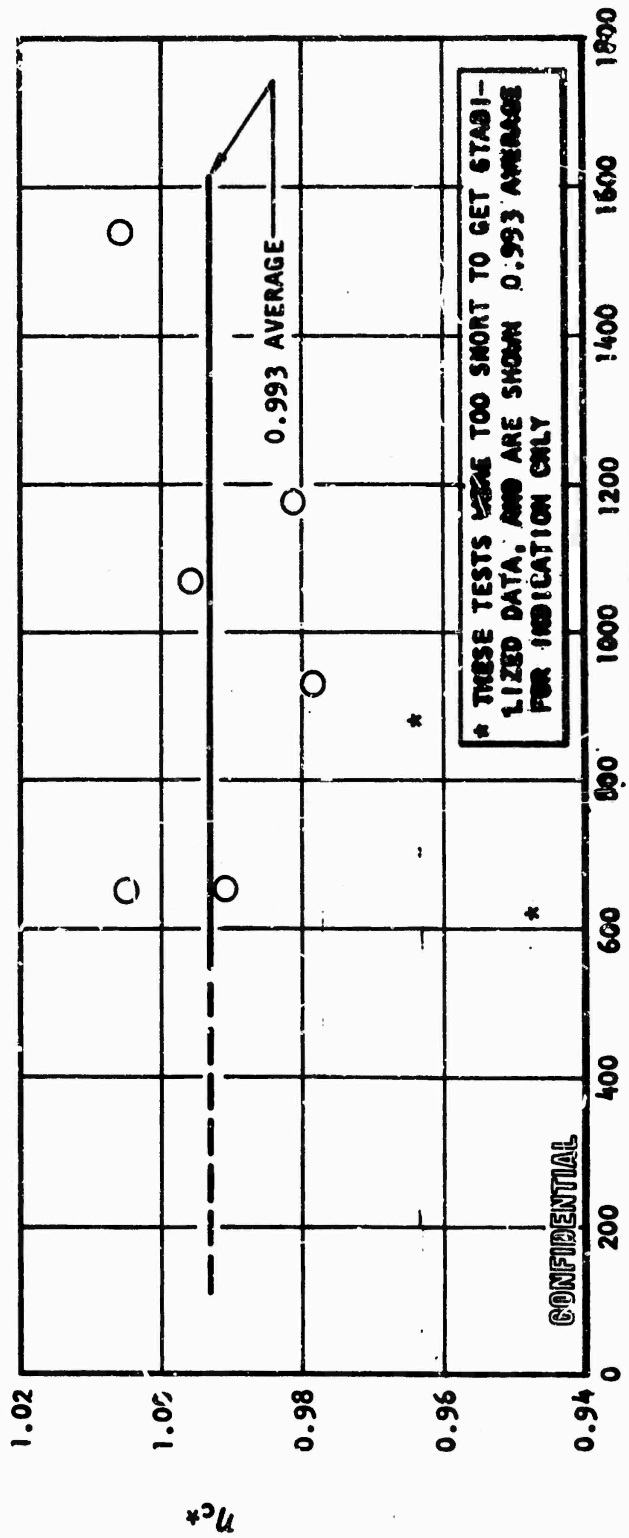

Figure 389. 20K c* Efficiency vs Chamber Pressure

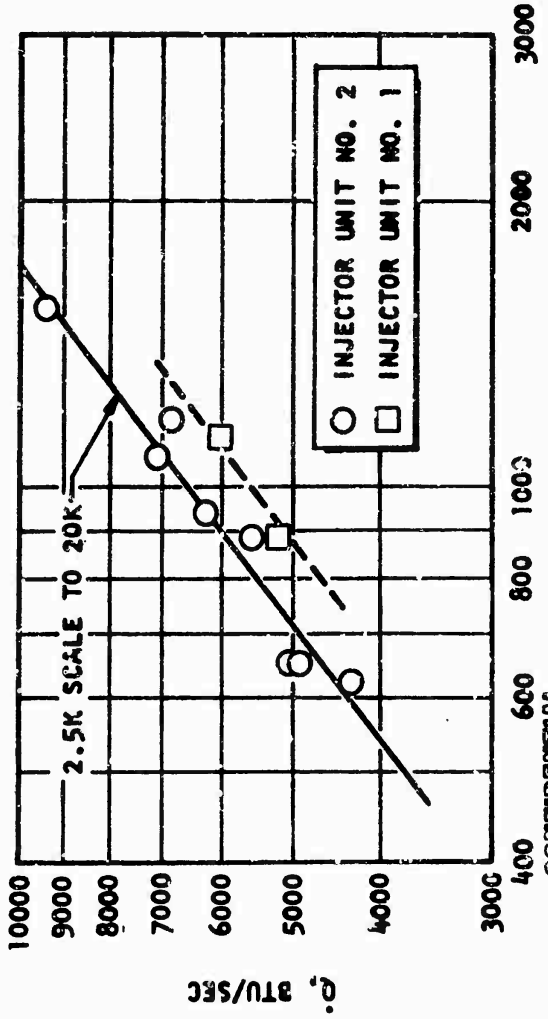

Figure 390. 20K Total Heat Flux

(C) Stability. The high-frequency pressure measurements in the LOX manifold and accelerometers mounted on the injector were analyzed for instability. The pressure measurements showed two predominate frequencies >1600 to 2000 and 1000 to 1300 cps. These same frequencies were evident in the accelerometers. Harmonics of the 1100 and 1600 cps appeared to be present in the accelerometers but not in the LO_2 pressures. It appears that these two frequencies were coupled between the chamber hot gases and the LO_2 fuel injection pressures. However, the coupling mechanism is not yet understood. The observed frequencies and magnitudes of the pressure measurements are shown in Table 94.

(U) Cooling. The cooling circuit on the 20K segment simulates the concept selected for the 250K Demonstrator Module (Fig. 360). The fuel first passes upward through the inner body. At the injector end, the total fuel crosses through the baffle. A portion of the fuel is used to cool the baffle; the remainder is routed through the upper portion of the baffle and recombined with the coolant flow at the inlet to the outer body. This parallel system in the baffle allows for minimizing circuit pressure drops and coolant passage sizes. The outer body is then cooled by a downward pass, from which the coolant is routed back towards the injector to be fed into the combustion chamber. For the 20K segment, an optional dump system is also provided for the fuel after it completes the flow circuit. This allowed greater flexibility in controlling test parameters.

(U) One of the primary objectives of the 20K segment series was to verify the integrity of this coolant circuit and its ability to adequately cool the chamber. Of special interest was the ability to balance flow between baffled compartments and through the parallel flow passages in the baffled structure. In addition, bulk heat transfer measurements of the coolant were taken throughout the test series to compare heat transfer results from the 20K segment to previous measurements taken on the 2.5K solid wall and

TABLE 94

(c) STABILITY SUMMARY, 20K SEGMENT

Test No.	Chamber Pressure, psia	Mixture Ratio (o/f)	Predominant Mainstage Frequency, cps	*Photocon Peak-to-Peak Amplitude	
				psi	Percent of Operating Pressure
318	600	5.0	1600 to 1700	±30	±4.6
319	625	4.3	1650 to 1700	30	4.4
320	615-665	5.0-5.8	1625 to 1700	75	10.8
			1050	120	16.6
321	610	6.0	1600 to 1700	50	7.1
322	655	5.5	1600 to 1650	60	8.5
			1050	100	14.2
323	890	5.2	1800	40	4.2
			1150	100	10.4
324	935	6.0	1800	25	2.4
			1175	120	11.4
325	1065	6.2	1875	40	3.3
			1650	60	4.9
327	1175	3.3	1950	90	6.8
			1225	150	11.4
328	1540	2.8	2050 to 1800	90-60	5.0-3.3
			1275	120	6.7

*Nominal peak-to-peak values during periods of maximum activity. The values are from the oxidizer Photocons unless otherwise noted.

CONFIDENTIAL

tubular configurations. Careful visual inspection of the hardware was made throughout the test series to determine whether there were any indications of local overheating.

(C) Bulk temperature readings from the 20K tests were compared with the 2.5K results by scaling the surface areas of the two segments and adjusting all tests to a mixture ratio of 6. The comparison of the scaled 2.5K test data and the results of the 20K segment are shown in Fig. 388. The results clearly indicate the scalability of the earlier segment data and verify previous extrapolated and analytical predictions for the 20K segment.

(U) Observations of the cooling circuit and baffles during the test series indicated successful operation of the cooling circuit. Pressure drops in the circuit were consistent throughout the test series (Fig. 391). No local overheating existed, and the coolant distribution was satisfactory. The condition of the baffles was excellent, and no adverse effects of the baffle wake on the heat transfer were noted.

(C) In addition to coolant temperature evaluations, two temperature measurements were made on the injector LO_2 strips (Fig. 392). These measurements were taken to evaluate the effect of circulation between the injector and chamber wall. The results (Table 95) from the tests indicate that the temperature near the injector perimeter decreases with increasing chamber pressure. A maximum temperature of 1000 F was experienced at a chamber pressure of 655 psia. Because the last two tests listed were conducted at reduced mixture ratios and lower hydrogen injection temperature, it is not clear whether the former or latter parameter had the predominant effect.

Problem Areas and Solutions

(U) During the calibration blowdowns, pressure was noted in the vent ports provided through the titanium backup structure. The hardware was subsequently

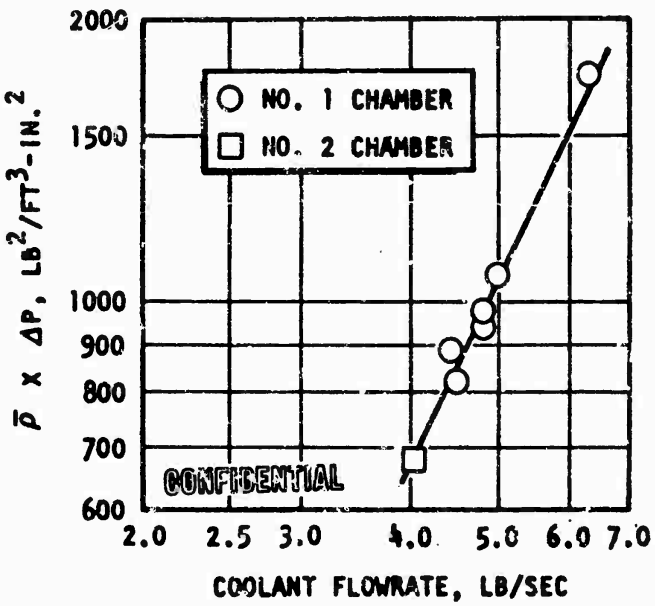

Figure 391. 20K Tube Bundle Total ΔP x $\overline{\rho}$ vs Flowrate

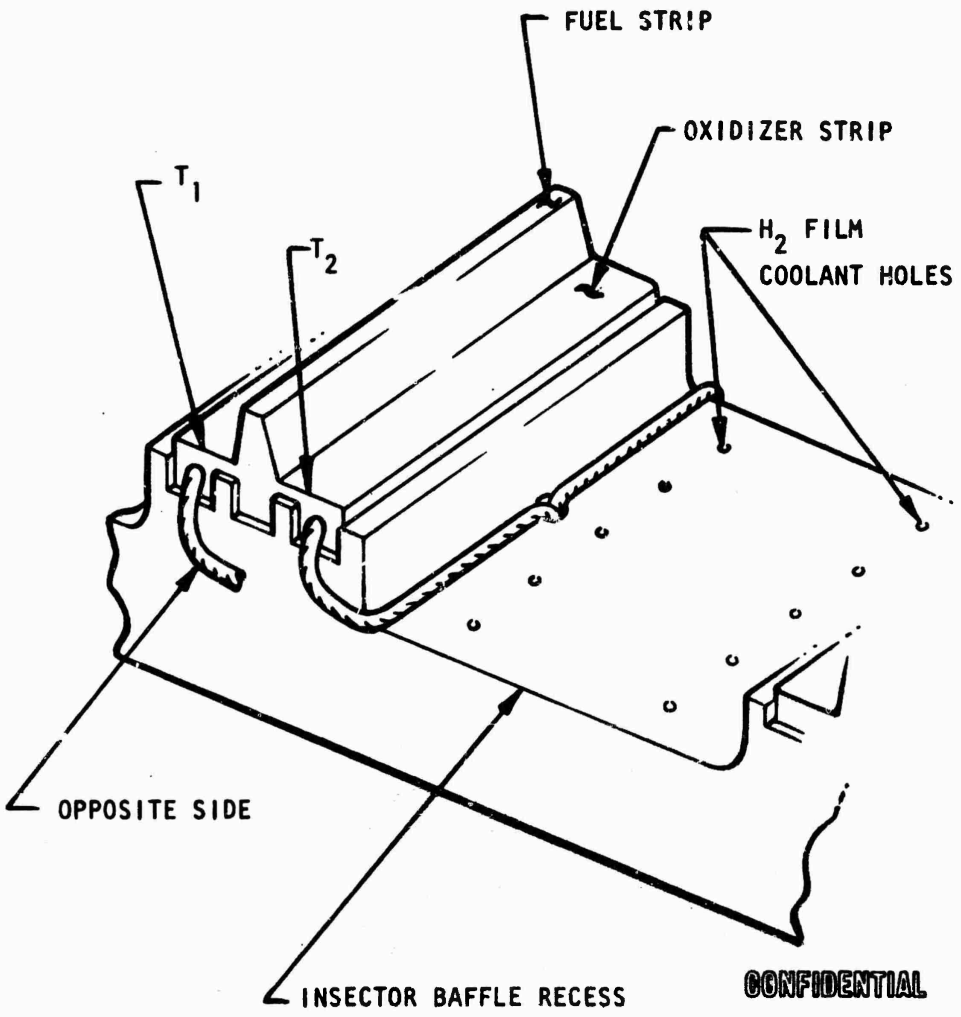

Figure 392. Injector LO_2 Strip Thermocouple Installation

TABLE 95

(C) 20K LO_2 STRIP TEMPERATURE DATA

Test No.	Chamber Pressure, psia	Hydrogen Injection Temperature, F	$Temperature_1$, F	$Temperature_2$, F
322	655	100	1000	300
323	885	50	535	270
324	935	70	670	350
325	1070	87	330	210
327	1174	-283	215	-50
328	1539	-282	345	-50

removed from the test stand and additional vent ports added to prevent excessive pressure buildup between the titanium backup structure and the tube bundle. The next few tests showed the condition to be corrected.

(U) Stainless-steel erosion was noted for several milliseconds during the fifth test. Removal and inspection of the hardware revealed minor erosion between injector and baffle (Fig. 393), one baffle only. The cause is attributed to either a hot-gas leak at a capped-off chamber pressure boss or an excessive volume in the chamber pressure pickup ports of the hardware. The hardware damage was minor and was not repaired. Special inserts were incorporated in the instrumentation ports to decrease the port cavity volume, tubular seals were installed between the baffle and injector to prevent cross flow, and film-coolant holes drilled in the injector (Fig. 392).

(U) Posttest inspection of the hardware showed an almost complete lack of bonding (Fig. 394). It was evident that this was a result of inadequate assembly of the parts to the predetermined position. No check was made following the bonding process to determine the final fitup or effectiveness of the bond. A means of checking the bond effectiveness will have to be devised for future chambers.

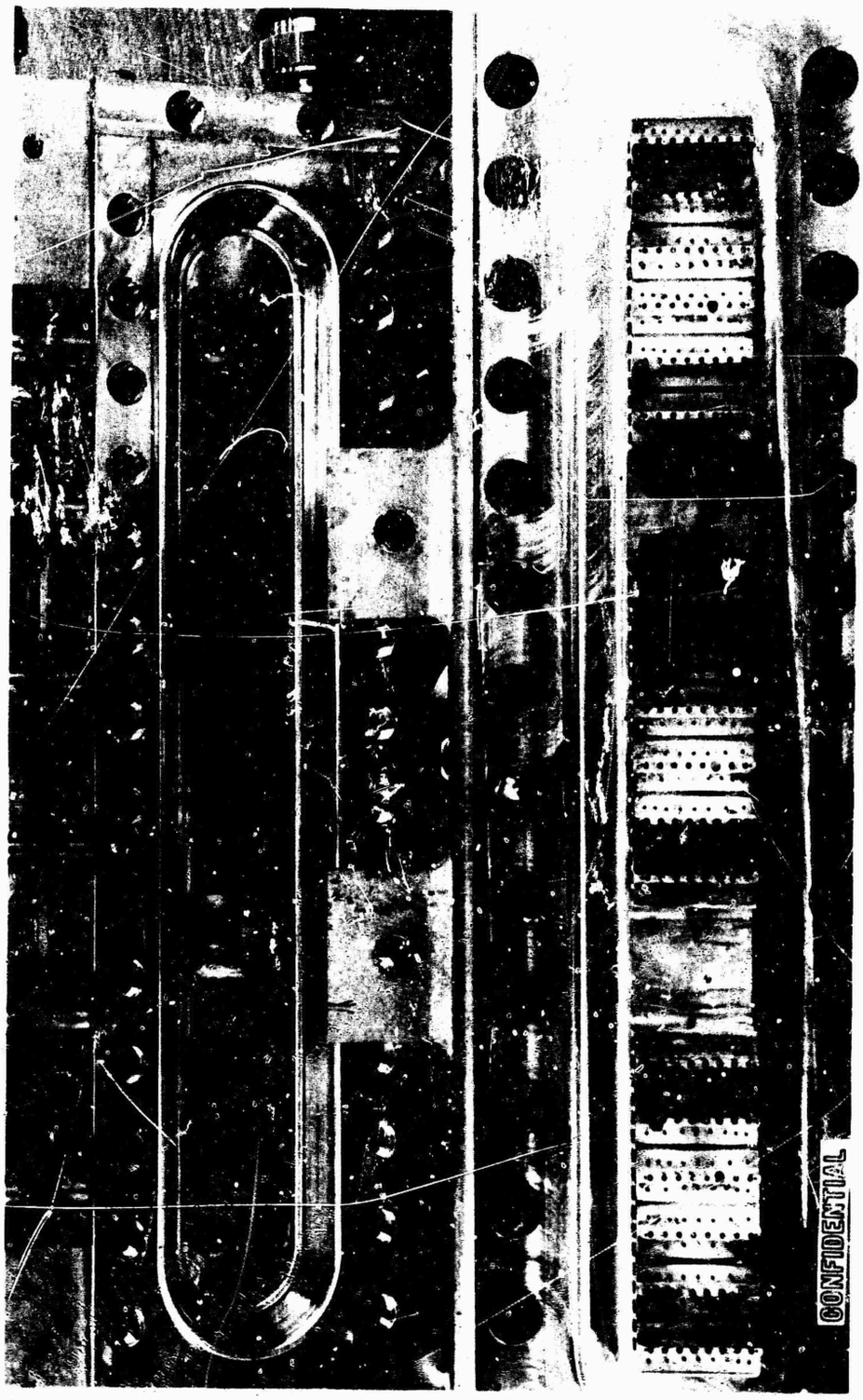

Figure 393. Damage to 20K Injector Baffle Recess Cavity

1XE35-8/18/67-C1G

Figure 394. Posttest View of Adhesive Used in the Structural Segment

APPENDICES

Appendix I 859

Performance Calculation Technique for the ARP Film-Cooled Segment Tests 859

Appendix II 870

Hot-Gas Tapoff Calculations 870

Appendix III 874

Heat Transfer Data Reduction for Water-Cooled Segments 874

Nomenclature 876

Appendix IV 878

Tube-to-Body Cavity Vent Provision 878

Appendix V 881

System Performance Sample Calculations 881

Method of Calculating System Performance 881

Equivalent Flight System 885

Appendix VI 891

Instrumentation Nomenclature 891

Appendix VII 894

Flowrate Calculation Methods 894

Appendix VIII 897

Chamber Start Sequence 897

Oxidizer System 897

Fuel System 898

Ignition System 898

Appendix IX 903

Altitude Compensation 903

APPENDIX I

(U) PERFORMANCE CALCULATION TECHNIQUE FOR THE ADP FILM-COOLED SEGMENT TESTS

(U) The method for calculating the characteristic velocity is obtained from energy balances. A schematic of the film-cooled segment is presented in the following sketch.

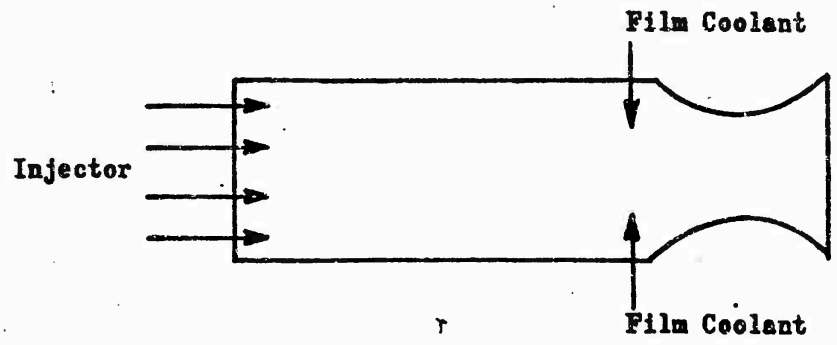

(U) Assuming that no heat is transferred to the chamber walls, and no chemical reaction occurs between the two gases, the energy balance between the injector gases and the film coolant can be written as:

$$\dot{w}_F \, C_{P_F} \, (T_F - T_{F_1}) = \dot{w}_{inj} \, C_{P_{inj}} \, (T_{inj} - T_{inj-1}) \qquad (1)$$

where:

$\dot{w}_F$ = fuel film-coolant flowrate

C_{P_F} = fuel film-coolant heat capacity

T_{F_1} = initial film-coolant temperature

T_F = final film-coolant temperature

$\dot{w}_{inj}$ = propellant flowrate through injector

$C_{P_{inj}}$ = heat capacity of combustion gases at injector end

T_{inj} = adiabatic combustion temperature at injector end mixture ratio

T_{inj-1} = final temperature of injector gases after mixing with film coolant

(U) Defining T_m as the equilibrium temperature of the mixture, T_F and T_{inj-1} can be written in terms of temperature differences, ΔT, from T_m. Thus,

$$T_F = T_m - \Delta T_2 \tag{2}$$

$$T_{inj-1} = T_m + \Delta T_1 \tag{3}$$

Since

$$\Delta T_1 = \Delta T_2 \frac{\dot{w}_F \, C_{P_F}}{\dot{w}_{inj} \, C_{P_{inj}}} \tag{4}$$

substituting into Eq. 1, results in the following equation:

$$\dot{w}_F \, C_{P_F} \, (T_m + \Delta T_2 - T_F) = \dot{w}_{inj} \, C_{P_{inj}} \left(T_{inj} - T_m + \frac{\dot{w}_F \, C_{P_F}}{\dot{w}_{inj} \, C_{P_{inj}}} \Delta T_2 \right) \tag{5}$$

which reduces to

$$\dot{w}_F \, C_{P_F} \, (T_m - T_F) = \dot{w}_{inj} \, C_{P_{inj}} \, (T_{inj} - T_m) \tag{6}$$

or

$$T_{inj} = T_m + \frac{\dot{w}_F \, C_{P_F}}{\dot{w}_{inj} \, C_{P_{inj}}} \, (T_m - T_F) \tag{7}$$

(U) The ideal gas flow equation for constant specific heat ratio, γ, and molecular weight, M, in terms of stagnation pressure and temperature can be written as

$$\dot{w} = PA \sqrt{\frac{\gamma M_g}{RT} (2/\gamma + 1)^{\frac{\gamma + 1}{\gamma - 1}}} \tag{8}$$

Characteristic velocity is given by the equation:

$$c^* = \frac{P_c \, Ag}{\dot{w}} \tag{9}$$

and substituting Eq. 8 into 9, the well-known equation is obtained.

$$c^* = \sqrt{\frac{g\,RT}{M\,\gamma}\left(\frac{\gamma+1}{2}\right)^{\frac{\gamma+1}{\gamma-1}}} \tag{10}$$

For the injector, Eq. 10 can be written as:

$$c^*_{inj} = \sqrt{\frac{g\,RT_{inj}}{M\,\gamma}\left(\frac{\gamma+1}{2}\right)^{\frac{\gamma+1}{\nu-1}}} \tag{11}$$

(U) Combining Eq. 11 and 7 will give η_{c^*} in terms of T_m. Equation 10 can be rewritten for the total flow as:

$$c^*_T = \sqrt{\frac{gRT_T}{\gamma_T M_T}\left(\frac{\gamma_T+1}{2}\right)^{\frac{\gamma+1}{\gamma-1}}} \tag{12}$$

where the subscripts refer to the total flow, T_T can then be written as

$$T_T = c^{*2}_T\,\frac{\gamma_T\,M_T}{RTg}\left(\frac{\gamma_T+1}{2}\right)^{\frac{\gamma+1}{\gamma-1}} \tag{13}$$

(U) If complete mixing has occurred, then $T_m = T_T$. However, for the actual case, T_T is an effective temperature which can be written as:

$$\sqrt{T_T} = X\sqrt{T_{inj-1}} + (1-X)\sqrt{T_F} \tag{14}$$

where X is a weighting fraction because

$$T_m = X\,T_{inj-1} + (1-X)\,T_F \tag{15}$$

(U) Equations 14 and 15 are obtained as follows. Consider the case where the combustion products from the injector and the fuel film coolant have achieved their final temperatures, T_{inj-1} and T_F, respectively. For each of these fluids, we may write a characteristic velocity expression:

$$c_1^* = \frac{P_o A_1 g}{\dot{w}_1} \tag{16}$$

and

$$c_2^* = \frac{P_o A_2 g}{\dot{w}_2} \tag{17}$$

where:

c_1^* = characteristic velocity corresponding to the injector flow

P_o = nozzle throat stagnation pressure

A_1 = aerodynamic throat area occupied by the injector flow

$\dot{w}_1$ = injector flowrate

c_2^* = characteristic velocity corresponding to the film-coolant flow

A_2 = aerodynamic throat area occupied by the film coolant

$\dot{w}_2$ = film coolant flowrate

g = 32.174 lb-ft/lbf-sec^2

Now

$$\dot{w}_1 c_1^* + \dot{w}_2 c_2^* = P_o A_1 g + P_o A_2 g = P_o A g \tag{18}$$

where: A = aerodynamic throat area of the nozzle.

Equation 18 must hold since the injector flow and film-coolant flow are being exhausted through a nozzle of area A under the influence of a pressure P_o.

(U) We rewrite Eq. 18 in the following form

$$\dot{w}_1 c_1^* + \dot{w}_2 c_2^* = \dot{w}_T c_T^* \tag{19}$$

where:

$\dot{w}_T$ = total flowrate through the nozzle

c^*_T = characteristic velocity corresponding to the flowrate $\dot{w}_T$

(U) Dividing Eq. 19 by $\dot{w}_T$ and utilizing the fact that the characteristic velocity is proportional to the square root of the combustion temperature divided by the molecular weight yields

$$X_1 \sqrt{\frac{T_{inj-1}}{M_{inj-1}}} + X_2 \sqrt{\frac{T_F}{M_F}} = \sqrt{\frac{T_T}{M}} \tag{20}$$

where

X_1 = mass fraction of injector flow

X_2 = mass fraction of film-coolant flow

T_T = effective temperature that results from mixing of the two flows

M = effective molecular weight that results from mixing of the two flows

(U) Define an average value for T_{inj-1} and T_F by the following expression

$$\overline{T}_{inj-1} = \frac{T_{inj-1}\, M}{M_{inj-1}} \tag{21}$$

and

$$\overline{T}_F = \frac{T_F\, M}{M_F} \tag{22}$$

then Eq. 20 becomes

$$X_1 \sqrt{\overline{T}_{inj-1}} + (1 - X) \sqrt{\overline{T}_F} = \sqrt{T_T} \tag{23}$$

(U) Using the equilibrium temperature of the mixture, set up a heat balance to obtain

$$(T_m - T_{inj-1})\, C_{P_{inj}}\, \dot{w}_{inj} = (T_F - T_M)\, C_{P_F}\, \dot{w}_F \tag{24}$$

Let

$$T_m = N\, T_{inj-1} + (1 - N)\, T_F \tag{25}$$

where

N = a number less than one that expresses the contribution of T_{inj-1} and T_F to T_m

(U) Substituting Eq. 25 in Eq. 24, it is possible to show that N has the explicit form

$$N = \frac{1}{1 + \dfrac{\dot{w}_F\, C_{P_F}}{\dot{w}_{inj}\, C_{P_{inj}}}} \tag{26}$$

For an ideal gas

$$C_P\, M = \frac{\gamma\, R}{\gamma - 1} \tag{27}$$

where:

R = universal gas constant

γ = specific heat ratio

(U) Since the specific heat ratio for the combustion products is approximately equal to the film-coolant specific heat ratio, the following equation may be written:

$$C_{P_{inj-1}} = M_F\, \frac{C_{P_F}}{M_{inj-1}} \tag{28}$$

Substituting Eq. 28 into Eq. 26 yields

$$N = \frac{\dfrac{\dot{w}_{inj-1}}{M_{inj-1}}}{\dfrac{\dot{w}_{inj-1}}{M_{inj-1}} + \dfrac{\dot{w}_F}{M_F}} = \frac{\left(\dfrac{\dot{w}_{inj-1}}{M_{inj-1}}\right)}{\left(\dfrac{\dot{w}_T}{M}\right)} = \frac{y_{inj-1}}{y_{inj-1} + y_F} \tag{29}$$

where:

M = an effective molecular weight for the mixture of injector gases and film coolant

y_{inj-1} = mole fraction of injector gas

y_F = mole fraction of film coolant

But

$$y_{inj-1} + y_F = 1 \tag{30}$$

by definition of mole fraction, thus

$$N = y_{inj-1} \tag{31}$$

Therefore, by using Eq. 25

$$T_m = y_{inj-1} T_{inj-1} + (1 - y_{inj-1}) T_F \tag{32}$$

(U) It can be seen that T_m is equal to T_T if the final film coolant temperature T_F and the final injector gas temperature, T_{inj-1} are equal. If T_{inj-1} is not equal to T_F, it can be seen from an examination of Eq. 14 and 15 that T_m is greater than T_T. Therefore, substituting T_m for T_T into Eq. 13 will result in a minimum value of T_m. Thus, making the substitution

$$T_m = c^*_T{}^2 \frac{\gamma_T + M_T}{RTg} \left(\frac{\gamma_T + 1}{2}\right)^{\frac{\gamma_T + 1}{1 - \gamma_T}} \tag{33}$$

T_{inj} can be calculated by combining Eq. 33 and 7, which then can be substituted into Eq. 12 to obtain injector characteristic velocity. Then η_{c^*} can be calculated from the definition by the following equation:

$$\eta_{c^*_{inj}} = \frac{c^*_{inj}}{c^*_{inj\ theoretical}} \tag{34}$$

(U) Calculations of $\eta_{c^*\ inj}$ can be simplified by introducing η_{c^*T}, a characteristic velocity efficiency defined by the following equation:

$$\eta_{c^*T} = \frac{c^*_t}{c^*_{E\ theoretical}} \tag{35}$$

where the subscript (E theoretical) refers to the equilibrium value at the mixture ratio (MR) given by

$$MR = \frac{w_o}{w_{H_2\ inj} + w_{H_2\ film}} \tag{36}$$

Therefore, Eq. 35 can be written as

$$\eta_{c^*T} = \sqrt{\frac{T_T\ M_{E\ theo}\ \gamma_{E\ theo}}{T_{E\ theo}\ M_T\ \gamma_T} \left(\frac{\gamma_T + 1}{2}\right)^{\frac{\gamma_T + 1}{\gamma_T - 1}} \left(\frac{\gamma_{E\ theo} + 1}{2}\right)^{\frac{\gamma_{E\ theo} + 1}{1 - \gamma_{E\ theo}}}} \tag{37}$$

with the same assumption as before that $T_T = T_m$, Eq. 19 can be written as

$$T_m = \eta_{c^*T}^2\ T_{E\ theo}\ \frac{M_T\ \gamma_T}{M_{E\ theo}\ \gamma_{E\ theo}} \left(\frac{\gamma_{E\ theo} + 1}{2}\right)^{\frac{\gamma_{E\ theo} + 1}{\gamma_{E\ theo} - 1}} \left(\frac{\gamma_T + 1}{2}\right)^{\frac{\gamma_T + 1}{1 - \gamma_T}} \tag{38}$$

(U) For 10-percent film coolant (the maximum film coolant flowrate during the 2.5K test) added to an injector mixture ratio of 7.0 at 1000-psia chamber pressure, the average molecular weight and specific heat ratio, for no chemical reaction between the film coolant and injector gases differ from that for chemical equilibrium by less than 1/2 percent. Therefore, the γ ratios and M ratios can be ignored, and Eq. 20 can be rewritten as

$$T_m = \eta_{c^*T}^2\ T_{E\ theo} \tag{39}$$

Further simplification of calculations can be made by assuming that the molecular weight and variations caused by combustion inefficiencies can be neglected. Thus, $\eta_{c^* \text{ inj}}$ can be written as:

$$\eta_{c^* \text{ inj}} = \sqrt{\frac{T_{inj}}{T_{inj \text{ theo}}}} \tag{40}$$

(U) It should be pointed out that corrections made to η_{c^*T} were the same as that for no film coolant where the heat losses were greater than that for the film-cooled tests. The value of the correction factor for heat loss, η_{HL} is given by the equation:

$$c^*_T = c^*_T \text{ measured } \eta_{HL}\, \eta \tag{41}$$

where η is the correction factor for all other losses. η_{HL} was calculated to be 1.008 without film coolant and will be less for the film-cooled chamber. However, the anticipated variations in the η_{HL} will only affect c^*_T slightly and can be neglected in Eq. 41.

(U) The technique described above is used in practice as follows. First, calculate the characteristic velocity efficiency using the injector flow and film-coolant flow, i.e.,

$$c^*_T = \frac{P_c A_t g}{\dot{w}_T}\, \eta \tag{42}$$

where

c^*_T = total characteristic velocity

P_c = chamber pressure

A_t = geometric throat area

g = 32.174 lb-ft/lbf-sec^2

$\dot{w}_T$ = sum of injector propellant flow plus film-coolant flow

η = influence coefficient to account for stagnation pressure loss, nozzle throat thermal shrinkage, stagnation pressure loss due to friction, and heat loss to coolant water

Next, it is observed that the adiabatic flame temperature is a unique value for a given chamber pressure and mixture ratio so that the theoretical adiabatic combustion temperature is known and the following expression

may be used to obtain a temperature corresponding to the entire gas mixture

$$T_T = (T_{THEO})_T \, \eta^2_{c^*_T} \tag{43}$$

where

T_T = temperature corresponding to entire gas mixture

$(T_{THEO})_T$ = theoretical temperature corresponding to entire gas mixture

$\eta^2_{c^*_T}$ = characteristic velocity efficiency calculated from the results of Eq. 42

(U) An enthalpy balance between the injector end and nozzle entrance portion of the thrust chamber where the fuel film coolant was injected was made which yielded the following expression

$$T_{inj-1} = \frac{\dot{w}_F \, C_{P_F} \, (T_T - T_F) + \dot{w}_{inj-1} \, C_{P_{inj-1}} \, T_T}{\dot{w}_{inj-1} \, C_{P_{inj-1}}} \tag{44}$$

where

T_{inj-1} = combustion temperature at injector end

$\dot{w}_F$ = fuel film-coolant flowrate

T_F = temperature of film coolant

C_{P_F} = constant pressure heat capacity of film coolant

$\dot{w}_{inj-1}$ = propellant flowrate through injector

$C_{P_{inj-1}}$ = constant pressure heat capacity of combustion products at injector mixture ratio

(U) Finally, since characteristic velocity efficiency is a function of the combustion temperature only for constant molecular weight and specific heat of combustion products, the injector characteristic velocity efficiency is given by

$$\eta_{c^*_{inj}} = \frac{T_{inj} - 1}{(T_{THEO})_{inj}} \tag{45}$$

where

$(T_{THEO})_{inj}$ = Theoretical injector end temperature for the operating chamber pressure and mixture ratio

APPENDIX II

HOT-GAS TAPOFF CALCULATIONS

(U) Since the pressure ratio across the gas tapoff exit orifice was always greater than two, flow through the orifice was sonic and the flowrate could be determined by use of the following expression:

$$\dot{w} = C_D \, P \, A \sqrt{\frac{k\left(\frac{2}{k+1}\right)^{(k+1)/(k-1)} g \, M}{RT}} \qquad (1)$$

where C_D = discharge coefficient (1.0)

P = pressure upstream of orifice (psia)

A = orifice area ($in.^2$)

γ = specific heat ratio

M = molecular weight

R = universal gas constant (1345 ft-lbf/lbm-R)

T = temperature (R)

w_o = gas tapoff oxidizer flowrate (lbm/sec)

w_f = gas tapoff fuel flowrate (lbm/sec)

w = total gas tapoff flowrate (lbm/sec)

MR = gas tapoff mixture ratio

g = dimensional constant (32.2 lbm-ft/lbf-sec^2)

(U) For a fuel-rich gas, the adiabatic combustion temperature is a unique function of the mixture ratio. The relationship between combustion temperature and mixture ratio for the oxygen-hydrogen system is presented in Fig. 395. No difficulty is experienced in using these data over a wide range of tapoff pressures because, at low mixture ratios, combustion temperature is nearly independent of the system pressure. Specific heat ratio was taken from Fig. 395 , and average molecular weight was then obtained from Fig. 396 , for the mixture ratio determined from Fig. 395 , using the measured tapoff temperature. These values were used in Eq. 1 to calculate total tapoff flowrate. This flowrate was decomposed into oxidizer and fuel flowrate by use of the expressions:

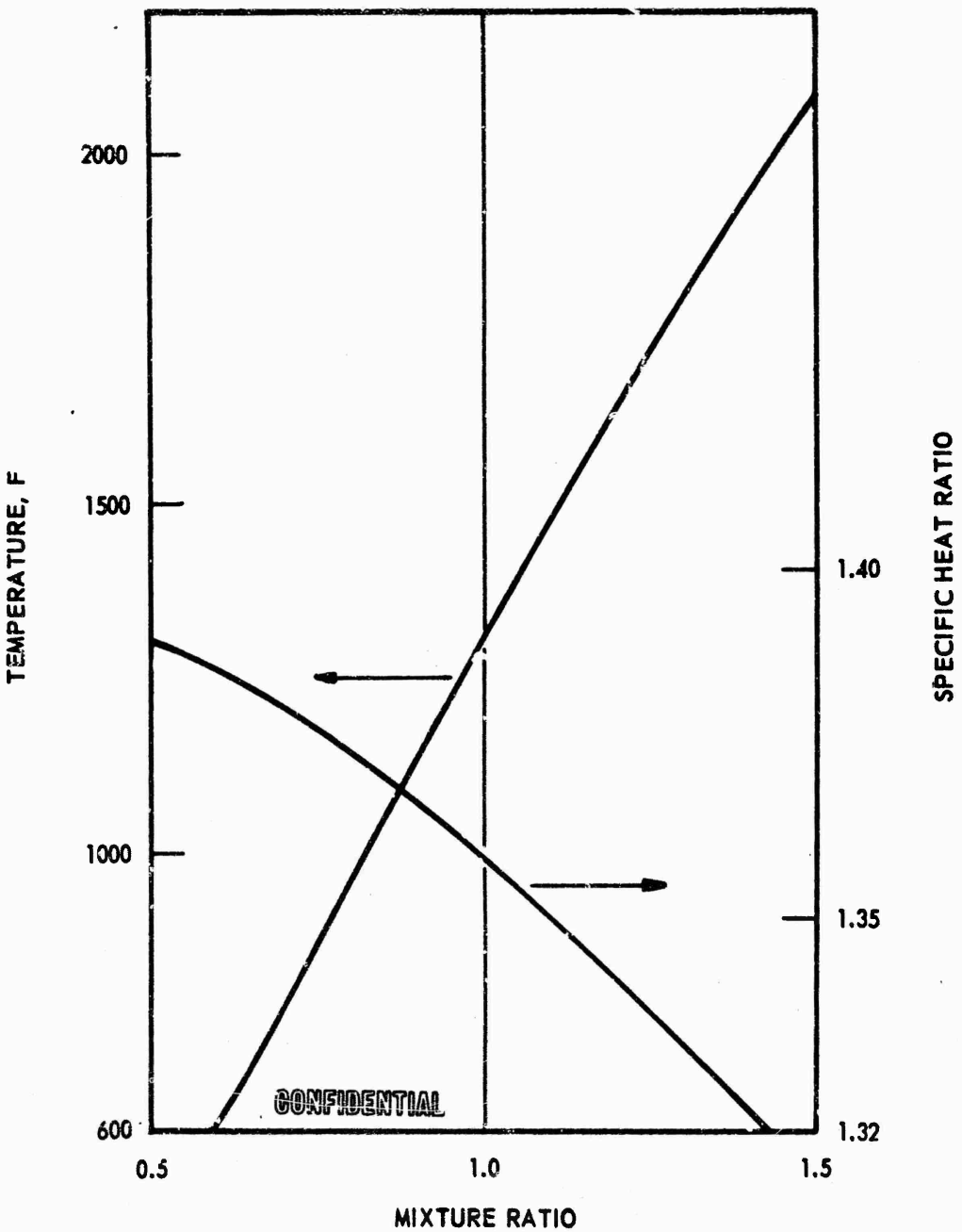

Figure 395. Combustion Temperature for LO_2/LH_2 at a Chamber Pressure of 600 psia

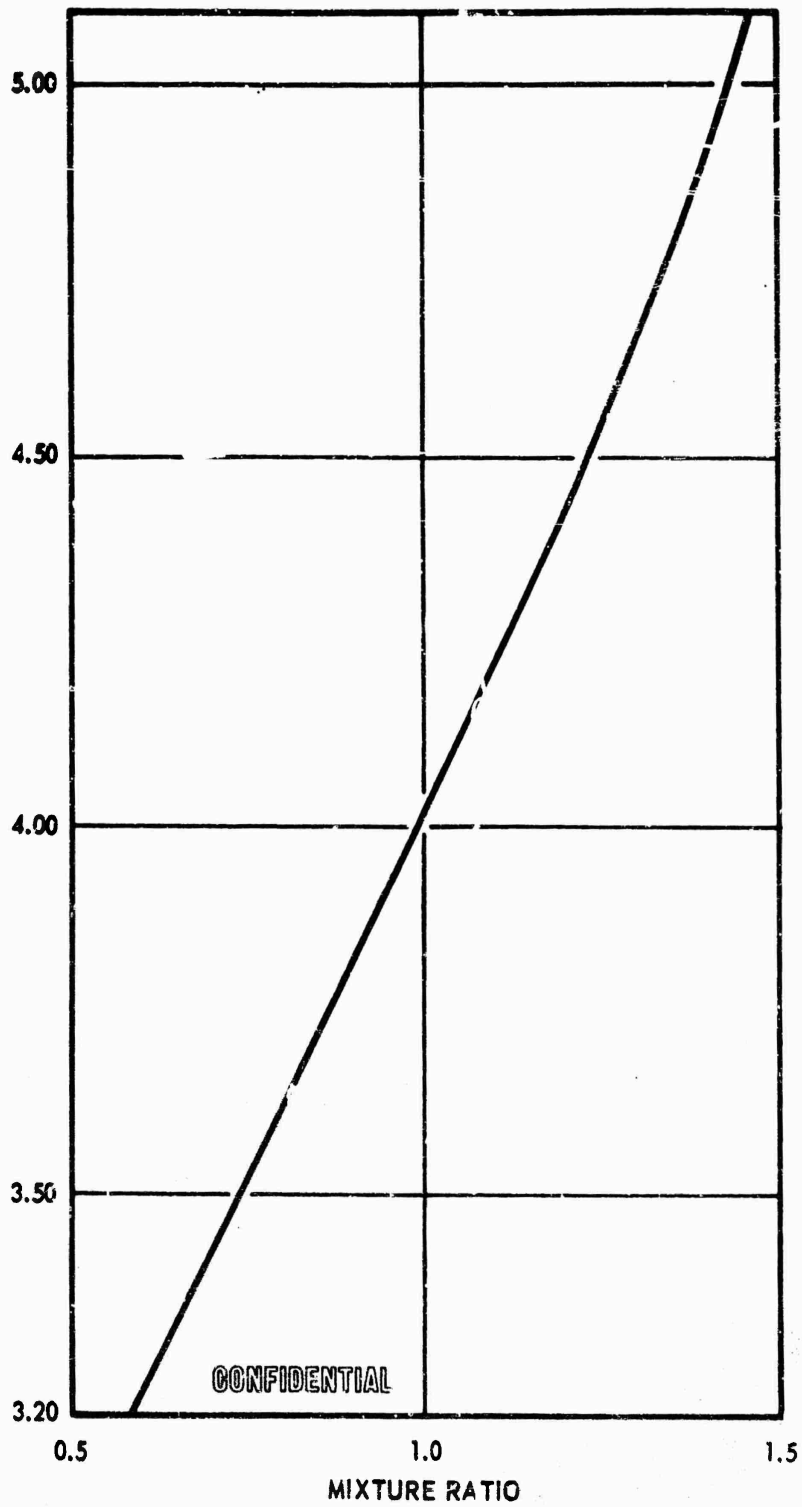

Figure 396. Combustion Products Molecular Weight for LO_2/LH_2 at a Pressure of 600 psia

$$\dot{w}_o = \frac{MR}{MR + 1} \dot{w} \tag{2}$$

and

$$\dot{w}_f = \dot{w} - \dot{w} . \tag{3}$$

APPENDIX III

HEAT TRANSFER DATA REDUCTION FOR WATER-COOLED SEGMENTS

(U) The heat transfer data output includes the water flowrate and overall bulk temperature rise for each transverse water coolant passage. The water flowrates are measured with a turbine flowmeter and the bulk temperature rises are obtained with chromel-alumel thermopiles installed to measure the inlet and outlet temperature difference directly.

(U) The heat transfer rate into each water passage is given in terms of the water flowrate, the water specific heat (C_p = 1 Btu/lbm-F), and the water bulk temperature rise by:

$$q = \dot{w}\, C_p\, \Delta T_B \quad . \tag{1}$$

(U) The average chamber heat flux in the region of the coolant passage is obtained by associating a one-dimensional gas-side heat transfer area with each passage and dividing the heat transfer rate into the passage by the appropriate area:

$$q/A = \frac{\dot{\omega}\, C_p\, \Delta T_B}{A} \tag{2}$$

(U) An average gas-side heat transfer coefficient is obtained for each passage using the relation:

$$h_g = \frac{q/A}{(T_{aw} - T_{wc}) - \frac{x}{k} q/A} \tag{3}$$

(U) The coolant side wall temperature is taken to be 30 F above the saturation temperature of the coolant. The use of this value assumes the coolant side to be in the nucleate boiling regime. The water velocities utilized with this chamber are sometimes high enough, particularly for the low chamber pressure runs, to suppress nucleate boiling. In this case, the assumed coolant side wall temperature will be in error. This simplifying assumption can result in up to 7 percent error in the calculated gas-side film coefficient in the low heat flux regions of the chamber.

(U) The actual combustion temperature is obtained from the ideal combustion temperature corresponding to 100 percent combustion efficiency by:

$$T_c = T_{c\ ideal}\ \eta_C^{*2} \tag{4}$$

(U) The adiabatic wall temperature used in Eq. 3 is obtained from the actual combustion temperature by the relation:

$$T_{aw} = T_c \frac{1 + \sqrt[3]{N_{PR}}\ \frac{\gamma - 1}{2} M_\infty^2}{1 + \frac{\gamma - 1}{2} M_\infty^2} \tag{5}$$

(U) The difference between T_{aw} and T_c is negligible in the combustor where the Mach number is low, and reaches a maximum of about 2 percent near the nozzle exit.

(U) Although the coolant passage geometry is highly two-dimensional, a one-dimensional relation (Eq. 3) will yield correct heat transfer coefficients if the proper value of the wall thickness or "reach" x is used. In reducing these data, the arithmetic average between the maximum and minimum "reaches" for each passage is used in Eq. 3 It is estimated that this introduces up to 3 percent error in the calculated gas-side film coefficient.

(U) During short-duration tests (3 to 5 seconds), the high heat sink capacity of the copper block in the region behind the coolant passages prevents the chamber from entirely reaching steady-state operation. As a result, a slight amount of heat leaks past the coolant passage into the copper backup structure. The amount of leakage depends on the coolant passage spacing and the local heat flux. For the small spacings and high heat transfer rates of the ADP segment, a two-dimensional analysis of the amount of heat leakage should be less than 1 percent in the throat region and less than 3 percent in the lower heat flux regions of the combustion zone.

Local average Stanton numbers:

$$N_{ST} = \frac{h_g}{\rho_\infty V_\infty C_p} \tag{6}$$

and both length and hydraulic diameter Reynolds numbers are computed to provide further correlation of the data. Frozen expansion gas product specific heat and viscostiy values corresponding to ideal

chamber conditions are used. A 3 percent change in the characteristic velocity efficiency results in only a 1 percent change in the combustion product specific heat.

In addition, the heat transfer data correlating parameter

$$N_{ST} \times (N_{PR})^{2/3} \tag{7}$$

is computed. Through the modified Reynold's analogy

$$N_{ST} \times (N_{PR})^{2/3} = C_F/2 \tag{8}$$

for flow over a flat plate, this parameter is equal to the local skin friction coefficient divided by two and, hence, provides a direct indication of local boundary-layer development.

NOMENCLATURE

Symbols	Parameter	Units
A	area	$in.^2$
C_F	skin friction coefficient	—
C_p	specific heat at constant pressure	Btu/lbm-R
M	Mach number	—
N_{PR}	Prandtl number	—
N_{ST}	Staton number	—
T	temperature	R
V	velocity	ft/sec
h_g	gas-side heat transfer coefficient	$Btu/in.^2$-sec-R
k	wall thermal conductivity	$Btu-in./in.^2$-sec-R
q	heat flowrate	Btu/sec
$\dot{w}$	coolant flowrate	lbm/sec
x	wall thickness	inches
γ	specific heat ratio	—
ρ	density	lbm/ft^3
η_{c*}	characteristic velocity efficiency	—

Subscripts

B	bulk
aw	adiabatic wall
c	combustion
wc	wall coolant
∞	flud free-stream conditions

APPENDIX IV

TUBE-TO-BODY CAVITY VENT PROVISION

(U) The inner and outer combustor bodies are provided with tube-to-body cavity vents to relieve pressure buildup caused by fuel leakage into the cavities. Pressure in the body cavities would put the tube-to-body braze joints in tension. Overpressurization would result in the tubes being pushed away from the backup structure.

(U) The vent ports of the inner body were directed overboard to prevent accumulation of fuel within the chamber cavity in the event of fuel leakage into the vent cavity. The outer-body vents were open to atmosphere. Pressures in the inner- and outer-body cavities were monitored to detect fuel leakage.

(U) It was noted that a vacuum was created in the vent cavities during fuel blowdowns and during the fuel lead portion of the first mainstage test. The pressure in the inner-body vent cavity would suddenly rise upon cessation of fuel flow during blowdowns and at transition to mainstage during the first test.

(U) It was determined that a vacuum was being drawn in the cavities by liquefaction of air in the cavity by the very cold hydrogen flowing in the tubes. The vacuum within the cavity drew more air into the cavity. Upon transition to mainstage, or cessation of fuel flow, the liquid air was vaporized at a faster rate than the vent ports were capable of relieving the pressure. The problem was solved by the pre-inerting of the inner-body vent cavity with gaseous hydrogen which could not be liquefied.

(U) The inner-body vents were plumbed into a common manifold (Fig. 397) which was vented to atmosphere through a check valve. The purpose of the

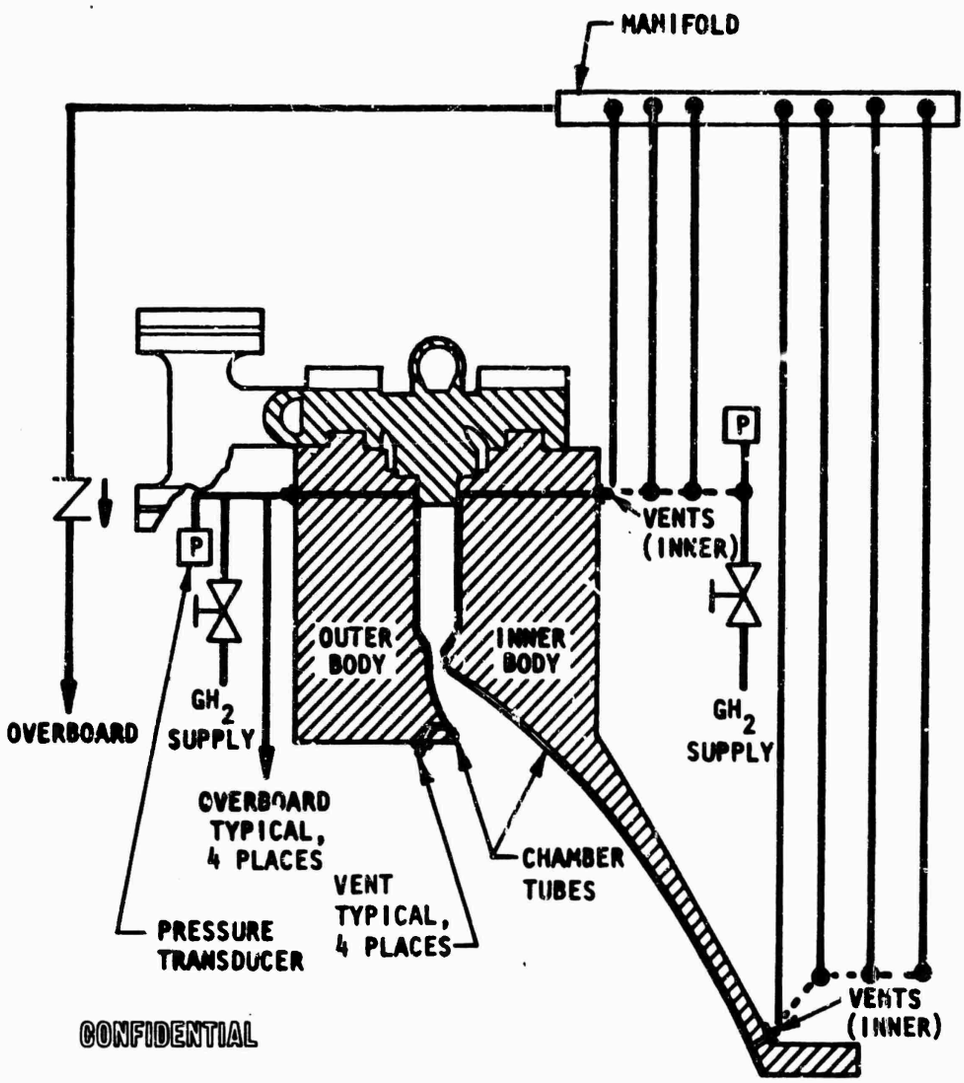

Figure 397. Tube Vent Technique

check valve was to prevent entry of air into the vent cavity because of contraction of the inerting hydrogen in the cavity during fuel lead.

(U) The outer-body vents were plumbed individually overboard. The tube-to-body cavity was inerted with helium supplied by a "K" bottle. The helium purge was continuous throughout the test.

(U) Fuel blowdowns conducted after incorporating the described purging techniques proved that the chamber vent cavity pressure spikes caused by liquefaction of the gas in the cavity had been eliminated.

APPENDIX V

SYSTEM PERFORMANCE SAMPLE CALCULATIONS

(U) Sample calculations for test 023, demonstrating the methods used to calculate system performance and the techniques used to translate the system performance results into an equivalent flight system, are presented.

(C) Flight system data were obtained by adjusting the as-tested system data to account for heat which was lost in the coolant which was dumped overboard through the fuel dump system. Corrections were also made to account for nitrogen dilution of the oxygen. The flight system engine mixture ratio was obtained by assuming that the secondary gases were at a mixture ratio which corresponds to 1960 R gas generator products of combustion. A variable property method of characteristics solution of the nozzle flow field was used to obtain the analytical prediction of primary nozzle geometric efficiency. Primary nozzle drag efficiency was obtained by boundary layer analysis. Primary nozzle kinetics efficiency was obtained by stream tube analysis used in conjunction with experimentally verified chemical combustion rate constants. The specific impulse efficiency was referenced to shifting equilibrium for liquid oxygen and liquid hydrogen at the engine mixture ratio.

METHOD OF CALCULATING SYSTEM PERFORMANCE

(C) Step 1. The aerodynamic throat area (A*) is calculated using measured values of the throat area and analytical values of potential flow and boundary layer discharge coefficients.

$$A^* = (A_t)(C_{d_{pf}})(C_{d_{bl}}) = (87.57)(0.9990)(0.9974) = 87.254 \text{ in.}^2$$

(C) Step 2. Nozzle area ratio (ϵ), base area ratio (ϵ_b), and combustion chamber contraction ratio (ϵ_c) are calculated using the aerodynamic throat area and measured values from the test hardware.

$$\epsilon = (A_e)/(A^*) = (6287.6)/(87.254) = 72.06$$

$$\epsilon_b = (A_b)/(A^*) = (1897\ 8)/(87.254) = 21.75$$

$$\epsilon_c = (A_c)/(A^*) = (590.3)/(87.254) = 6.765$$

(C) Step 3. The nozzle stagnation pressure (P_c) was calculated from measured injection end pressure and a theoretical correction factor.

$$P_c = (P_{ie}^{avg})/(P/P_c) \qquad P/P_c = f(\gamma,\ \epsilon_c) \qquad \gamma = 1.2$$

$$P_c = (608.8)/(1.0048) = 605.9 \text{ psia}$$

(C) Steps 4-8. Primary mixture ratio (MR_p) and primary flowrate ($\dot{w}_p$) account for all propellants at the nozzle throat. Engine mixture ratio (MR_e) and total flowrate ($\dot{w}$) account for all propellant flow. τ is the secondary-to-primary flow ratio.

$$MR_p = \frac{(\dot{w}_{otc})}{(\dot{w}_{f\ tc}) - (\dot{w}_{f\ dump})} = \frac{(185.72)}{(60.58) - (22.91)} = 4.930$$

$$\dot{w}_p = (\dot{w}_o)_{tc} + (\dot{w}_f)_{tc} - (\dot{w}_f)_{dump} = (185.72) + (60.58) - (22.91) = 223.39 \text{ lb/sec}$$

$$MR_e = \frac{(\dot{w}_o)_{tc}}{(\dot{w}_f)_{tc} + (\dot{w}_f)_{gg} - (\dot{w}_f)_{dump}} = \frac{(185.72)}{(60.58) + (1.68) - (22.91)} = 4.720$$

$$\dot{w} = (\dot{w}_p) + (\dot{w}_{f\ gg}) = (223.39) + (1.68) = 225.07 \text{ lb/sec}$$

$$\tau = \frac{(\dot{w}) - (\dot{w}_p)}{(\dot{w}_p)} = \frac{(225.07) - (223.39)}{(223.39)} = 0.007520$$

(C) Step 9. The values given are theoretical shifting equilibrium data for the conditions within the brackets.

$$c^*_{theo}\ (MR_p,\ P_c,\ T^f_{inj}) = 7931 \text{ ft/sec}$$

$$c^*_{theo}\ (MR_e,\ P_c,\ {}^{tank}_{temp}) = 7830 \text{ ft/sec}$$

$$C_{F\ theo}^{vac}\ (MR_p,\ P_c,\ \epsilon,\ T^f_{inj}) = 1.9293$$

$$C_{F\ theo}^{vac}\ (MR_e,\ P_c,\ \epsilon,\ {}^{tank}_{temp}) = 1.9080$$

$$C_{F\ theo}^{opt}\ (MR_p,\ P_c,\ PR,\ T^f_{inj}) = 1.5602$$

$$C_{F\ theo}^{opt}\ (MR_e,\ P_c,\ PR,\ {}^{tank}_{temp}) = 1.5515$$

(C) Steps 10-11. The delivered specific impulse (I_s) of the test hardware is calculated from the measured values of thrust and total flowrate. The specific impulse efficiency (η_{I_s}) is the ratio of delivered specific impulse to ideal specific impulse for liquid oxygen/liquid hydrogen at the engine mixture ratio and the tested pressure ratio.

$$I_s = (F)/(\dot{w}) = (76{,}140)/(225.07) = 338.3\ \frac{lbf}{lbm/sec}$$

$$\eta_{I_s} = \frac{(I_s)\ (g_c)}{\left(c^*_{theo}\left[MR_e,\ P_c,\ {}^{tank}_{temp}\right]\right)\left(C_{F\ theo}^{opt}\left[MR_e,\ P_c,\ PR,\ {}^{tank}_{temp}\right]\right)}$$

$$= \frac{(338.3)(32.174)}{(7830)(1.5515)} = 0.8960$$

(C) Step 12. The primary characteristic velocity (c*) is calculated by two methods. The first method uses the definition of characteristic velocity, and the second uses overall performance reduced by predicted nozzle performance. P_a and P_b are the measured values of ambient and

base pressure, respectively. η_g, η_d, and η_k are the analytical predictions of the primary nozzle geometric, drag, and kinetics efficiencies, respectively. Primary nozzle geometric efficiency is greater than 1.0 because the effects of ambient pressure are not accounted for. The nitrogen dilution correction factor ($\eta_{C_F}^{GN_2}$) is obtained from theoretical thermochemical data for the measured percentage of nitrogen in the liquid oxygen.

$$c^*[P_c] = (P_c)(A^*)(g_c)/(\dot{w}_p) = (605.9)(87.254)(32.174)/(223.39) = 7614 \text{ ft/sec}$$

$$c^*[F] = \frac{\left|(F) + (P_a)(A_e) - (P_b)(A_b)\right| (g_c)}{\left(C_{F\ theo}^{vac}\left[MR_f,\ P_c,\ \epsilon,\ T_{inj}^f\right]\right)\left|(\eta_g)+(\eta_d)+(\eta_k)-2\right| (\dot{w}_p)\left(\eta_{C_F}^{GN_2}\right)}$$

$$= \frac{\left|(76140) + (12.30)(6287.6) - (12.37)(1897.8)\right| (32.174)}{(1.9293)\left|(1.3058) + (0.9683) + (0.9970) - 2\right|(223.39)(0.9976)}$$

$$= 7653 \text{ ft/sec}$$

(C) Steps 13-14. Combustion efficiency (η_{c^*}) and overall nozzle efficiency (C_t) are calculated referenced to both tank and injector inlet conditions.

$$\eta_{c^*}\ [P_c]_p = (c^*[P_c])/\left(c^*_{theo}\left[MR_p,\ P_c,\ T_{inj}^f\right]\right) = (7614)/(7931) = 0.9600$$

$$\eta_{c^*}\ [P_c]_e = (c^*[P_c])/\left(c^*_{theo}\left[MR_e,\ P_c,\ {}^{tank}_{temp}\right]\right) = (7614)/(7830) = 0.9724$$

$$\eta_{c^*}\ [F]_p = (c^*[F])/\left(c^*_{theo}\left[MR_p,\ P_c,\ T_{inj}^f\right]\right) = (7653)/(7931) = 0.9649$$

$$\eta_{c^*}\ [F]_e = (c^*[F])/\left(c^*_{theo}\left[MR_e,\ P_c,\ {}^{tank}_{temp}\right]\right) = (7653)/(7830) = 0.9774$$

$$C_{t_p} = \frac{(F)\ (g_c)}{(c^*[P_c])\ (\dot{w})\left(C_{F\ theo}^{opt}\left[MR_p,\ P_c,\ PR,\ T_{inj}^f\right]\right)} = \frac{(76140)(32.174)}{(7614)(225.07)(1.5602)}$$

$$= 0.9162$$

$$C_{t_e} = \frac{(F)\ (g_c)}{(c^*[P_c])\ (\dot{w})\left(C_{F\ theo}^{opt}\left[MR_e,\ P_c,\ PR,\ {}^{tank}_{temp}\right]\right)} = \frac{(76140)(32.174)}{(7614)(225.07(1.5515)}$$

$$= 0.9213$$

(C) Step 15. The primary nozzle thrust coefficient (C_{Fp}) is calculated by adjusting the measured thrust to vacuum, removing the base thrust contribution, and adjusting back to the tested pressure ratio.

$$C_{F_p} = \frac{\left\{(F) + (P_a)(A_e) - (P_b(A_b)\right\}(g_c)}{(\dot{w}_p)\ (c^*\left[P_c\right])} - \frac{(P_a)\left\{(\epsilon) - (\epsilon_b)\right\}}{(P_c)}$$

$$= \frac{\{(76140) + (12.30)(6287.6) - (12.37)(1897.8)\}(32.174)}{(223.39)(7614)} -$$

$$\frac{(12.30)\{(72.06) - (21.75)\}}{(605.9)} = 1.4378$$

(C) Step 16. The primary intrinsic inviscid thrust coefficient ($C_{F\ p\ int}^{inv}$) is calculated by correcting the primary nozzle thrust coefficient for drag and kinetic losses.

$$(C_{F_p})_{inv}^{int} = (C_{F_p}) - (C_{F\ theo}^{vac}\left[MR_p,\ P_c,\ \epsilon,\ T_{inj}^f\right])$$

$$\{(\eta_d) + (\eta_k) - 2\}\left(\eta_{C_F}^{GN_2}\right) = (1.4378) - (1.9293)$$

$$\{(0.9683) + (0.9970) - 2\}\ (0.9976) = 1.5050$$

(C) Step 17. The primary nozzle velocity coefficient (C_v) is a measure of the nozzle's altitude-compensation capability.

$$C_v = \left(C_{F_p}^{int}{}_{inv}\right)/\left(C_{F\ theo}^{opt}\left[MR_p,\ P_c,\ PR,\ T_{inj}^f\right]\right) = (1.5050)/(1.5602)$$

$$= 0.9646$$

EQUIVALENT FLIGHT SYSTEM

(C) Assumptions

1. No dump cooling
2. Thrust chamber tapoff at 1960 R
3. No nitrogen dilution of the oxidizer

4. Same P_c, P_a, MR_p, P_a, τ, P_b, η_g, η_d, and η_k as the as-tested conditions

(C) Step 1. A fuel flowrate or cooling jacket flowrate is assumed, and the corresponding fuel injection temperature is obtained from theoretical heat transfer calculations.

$$\dot{w}_f' \text{ (assumed)} = 38.3 \text{ lb/sec}$$

$$T_{inj}^{f'} = 640°R$$

(C) Step 2. The base or secondary flow is assumed to be combustion chamber tapoff gases extracted at 1960 R. This assumption results in an engine mixture ratio which corresponded to a flight system. A tapoff mixture ratio (MR_{to}') for 1960 R gases and the assumed fuel injection temperature are obtained from theoretical thermochemical propellant data.

$$MR_{to}' = 0.747$$

(C) Step 3. Engine mixture ratio (MR_e') is calculated using test values of primary mixture ratio and secondary flow ratio.

$$MR_e' = \frac{(MR_p)(1 + MR'_{to}) + (\tau)(MR'_{to})(1 + MR_p)}{(1 + MR'_{to}) + (\tau)(1 + MR_b)}$$

$$= \frac{(4.93)(1 + 0.747) + (0.00752)(0.747)(1 + 4.93)}{(1 + 0.747) + (0.00752)(1 + 4.93)} = 4.826$$

(C) Step 4. Theoretical shifting equilibrium data are tabulated.

$$c^*_{theo}\left[MR_p,\ P_c,\ T_{inj}^{f'}\right] = 7975 \text{ ft/sec}$$

$$c^*_{theo}\left[MR_e',\ P_c,\ \begin{matrix}\text{tank}\\ \text{temp}\end{matrix}\right] = 7810 \text{ ft/sec}$$

$$C_{F\ theo}^{vac}\left[MR_p,\ P_c,\ \epsilon,\ T_{inj}^{f'}\right] = 1.9331$$

$$C_{F\ theo}^{vac}\left[MR_e',\ P_c,\ \epsilon,\ {}^{tank}_{temp}\right] = 1.9140$$

$$C_{F\ theo}^{opt}\left[MR_p,\ P_c,\ PR,\ T_{inj}^{f'}\right] = 1.5614$$

$$C_{F\ theo}^{opt}\left[MR_e',\ P_c,\ PR,\ {}^{tank}_{temp}\right] = 1.5535$$

(C) Steps 5 Through 7. Flight system combustion efficiency is calculated by correcting the test combustion efficiency for nitrogen dilution effects. Flight system characteristic velocity is calculated using the corrected combustion efficiency.

$$\eta_{c^*}[P_c]_p' = (\eta_{c^*}[P_c]_p)/(\eta_{c^*}^{GN_2}) = (0.9600)/(0.9970) = 0.9629$$

$$c^*[P_c]' = (\eta_{c^*}[P_c']_p)\left(c^*_{theo}\left[MR_p,\ P_c,\ T_{inj}^{f'}\right]\right)$$

$$= (0.9629)(7975) = 7679 \text{ ft/sec}$$

$$\eta_{c^*}[P_c]_e' = (c^*[P_c]')/\left(c^*_{theo}\left[MR_e',\ P_c,\ {}^{tank}_{temp}\right]\right)$$

$$= (7679)/(7810) = 0.9832$$

(C) Steps 8 Through 10. Primary flowrate ($\dot{w}_p'$), total flowrate ($\dot{w}'$), and fuel flowrate ($\dot{w}_f'$) are calculated using the computed characteristic velocity and engine mixture ratio and the test value of secondary flow ratio. The fuel flowrate is then compared with the assumed fuel flowrate of step 1. If they are not equal, a further iteration is made.

$$\dot{w}_p' = (P_c)(A^*)(g_c)/(c^*[P_c]') = (605.9)(87.254)(32.174)/(7679)$$

$$= 221.51 \text{ lb/sec}$$

$$\dot{w}' = (\dot{w}_p')(1 + \tau) = (221.51)(1+0.00752) = 223.18 \text{ lb/sec}$$

$$\dot{w}_f' = (\dot{w}')/(1 + MR_e') = (223.18)/(1 + 4.826) = 38.31 \text{ lb/sec}$$

(C) Step 11. Flight system primary thrust is calculated by adjusting the measured thrust for the higher fuel injection temperature.

$$F_p' = \frac{\{(F) + (P_a)(A_e) - (P_b)(A_b)\}\left(C_{F\ \text{theo}}^{\text{vac}}\left[MR_p,\ P_c,\ \epsilon,\ T_{inj}^{f\ '}\right]\right)}{\left(C_{F\ \text{theo}}^{\text{vac}}\left[MR_p,\ P_c,\ \epsilon,\ T_{inj}^{f}\right]\right)\left(\eta_{C_F}^{GN_2}\right)} -$$

$$(P_a)\ \{(A_e) - (A_b)\}$$

$$= \frac{(76140) + (12.30)(6287.6) - (12.37)(1897.8)(1.9331)}{(1.9293)(0.9976)} -$$

$$(12.30)\ \{(6287.6) - (1897.8)\} = 76576\ \text{lbf}$$

(C) Steps 12 Through 14. Primary thrust coefficient (C_{F_p}'), primary inviscid, intrinsic thrust coefficient, and primary nozzle velocity coefficient are calculated in the same manner as the "as-tested" system (see steps 15 through 17 of "as-tested" system).

$$C_{F_p} = \frac{(F_p')(g_c)}{(c^*[P_c]')(w_p')} = \frac{(76576)(32.174)}{(7679)(221.51)} = 1.4484$$

$$C_{F_p}'^{\ \text{int}}_{\text{inv}} = C_{F_p}' - \left(C_{F\ \text{theo}}^{\text{vac}}\left[MR_p,\ P_c,\ \epsilon,\ T_{inj}^{f\ '}\right]\right)\{(\eta_d) + (\eta_k) - 2\}$$

$$= (1.4484) - (1.9331)\ \{(0.9683) + (0.9970) - 2\} = 1.5159$$

$$C_v' = (C_F)_p'^{\ \text{int}}_{\text{inv}} / \left(C_{F\ \text{theo}}^{\text{opt}}\left[MR_p,\ P_c,\ PR,\ T_{inj}^{f'}\right]\right) = (1.5159)/(1.5614)$$

$$= 0.9708$$

(C) Step 15. Total flight system thrust is calculated by summing the calculated primary thrust and the measured base thrust.

$$F' = (F'_p) + (P_b)(A_b) - (P_a)(A_b) = (76576) + (12.37)(1897.8) -$$

$$(12.30)(1897.8) = 76709 \text{ lbf}$$

(C) Steps 16 and 17. The delivered specific impulse (I_s) is calculated from the measured values of thrust and total flowrate. The specific impulse efficiency (η_{I_s}) is the ratio of delivered specific impulse to ideal specific impulse for liquid oxygen/liquid hydrogen at the engine mixture ratio and the tested pressure ratio.

$$I'_s = (F')/(\dot{w}') = (76709)/(233.18) = 343.7 \ \frac{\text{lbf}}{\text{lbm/sec}}$$

$$\eta'_{I_s} = \frac{(I'_s)\ (g_c)}{\left(c^*_{\text{theo}}\left[MR_e,\ P_c,\ \text{tank temp}\right]\right)\left(C_{F\ \text{theo}}^{\text{opt}}\left[MR_e,\ P_c,\ PR,\ \text{tank temp}\right]\right)}$$

$$= \frac{(343.7)(32.174)}{(7810)(1.5535)} = 0.9114$$

(C) Step 18. The overall nozzle efficiencies are calculated.

$$C_{t_p}' = \frac{(F')\ (g_c)}{(c^*[P_c]')(\dot{w}')\left(C_{F\ \text{theo}}^{\text{opt}}\left[MR_p,\ P_c,\ PR,\ T_{\text{inj}}^{f'}\right]\right)}$$

$$= \frac{(76709)(32.174)}{(7679)(223.18)(1.5614)} = 0.9223$$

$$C_{t_e}' = \frac{(F')\,(g_c)}{(c^*\,[P_c]')(\dot{w}')\left(C_{F\ \text{theo}}^{\text{opt}}\left[MR_e,\ P_c,\ PR,\ {}^{\text{tank}}_{\text{temp}}\right]\right)}$$

$$= \frac{(76709)(32.174)}{(7679)(223.18)(1.5535)} = 0.9270$$

APPENDIX VI

INSTRUMENTATION NOMENCLATURE

(U) The Aerospike chamber is divided into zones for instrumentation purposes. These zones are shown in Fig. 398. The zones are numbered consecutively through the chamber, starting with the chamber inlet and progressing along the flow path of the particular media.

(U) Angular direction is defined in degrees clockwise of an index looking from forward to aft down the axial centerline of the chamber. The index is defined as the 12 o'clock position of the chamber when installed on the test stand.

(U) The following is an example of the use of the system:

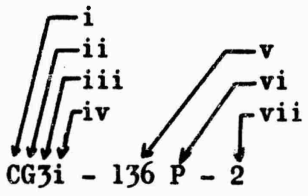

where: i. Component (major component only)

C = thrust chamber
G = gas generator
L = line
I = igniter

ii. Fluid Media Instrumented

O = oxidizer
F = fuel
G = main combustion gas
N = inert gas
T = tapoff gas
I = igniter fluid
Z = other

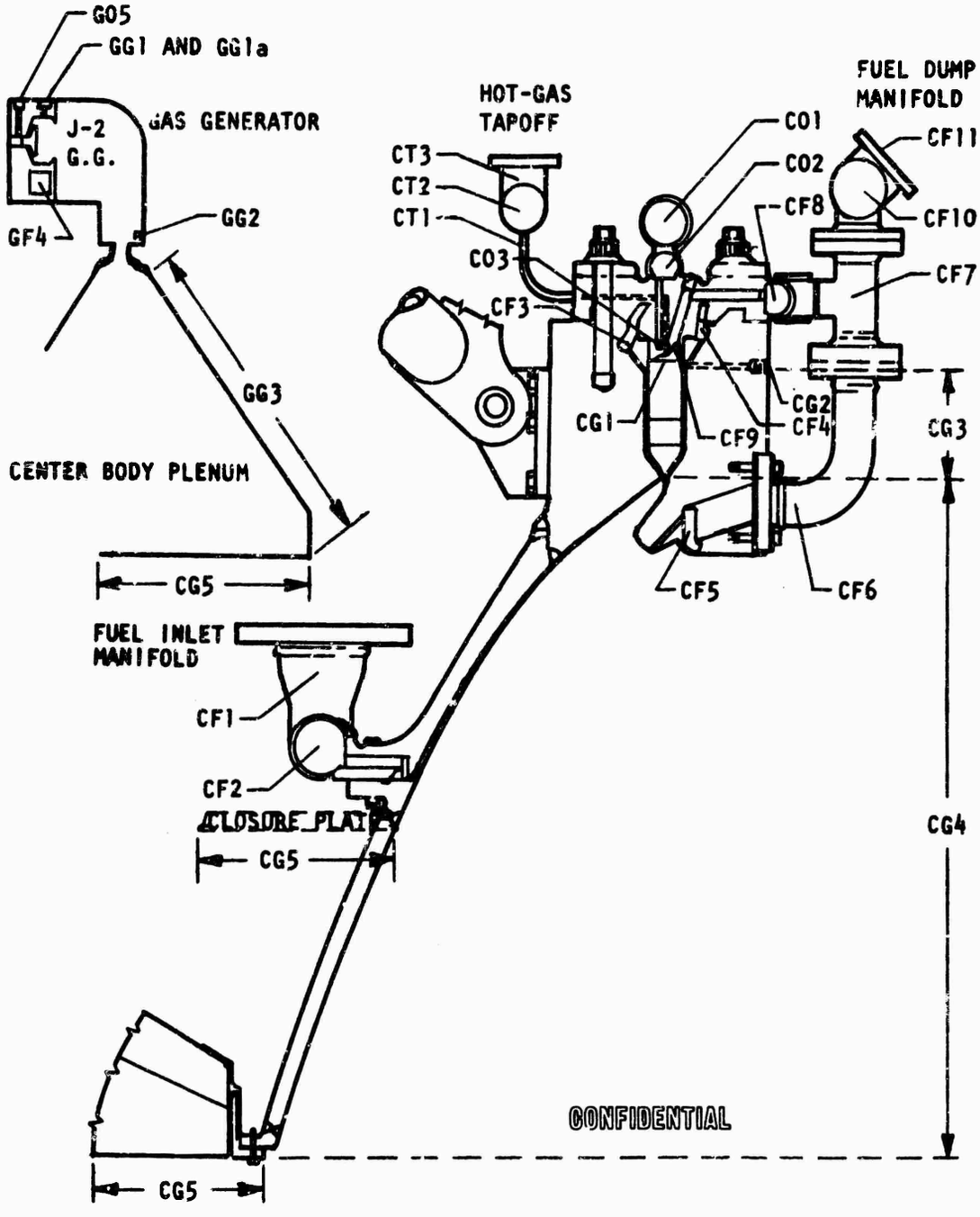

Figure 398. Solid-Wall and Tubular Thrust Chamber Boss Nomenclature

iii. Zone of instrumentation in a given media starting with 1 at the component inlet and assigning subsequent numbers to zones along the path of flow.

iv. Component

This is used only when additional clarification may be required such as on CG3 and CG4 bosses.

i = inner combustor body
0 = outer combustor body

v. Angular location of boss in degrees from 0 degree reference line.

vi. Type of Boss

B = bomb or pulse
P = pressure
T = temperature (resistance bulb or thermocouple)
D = Photocon
C = solid-state flow or pressure transducer
- = purge (no letter designation)
S = seal vent
A = accelerometer

vii. Axial distance in zone or number of path in parallel paths.

In the example, the 2 denotes 2 inches below the injector face.

Combustion gas instrumentation will have the following designation:

CG1 -	Ports in injector face
CG2 -	Injector end ports in chamber wall
CG3 -X	Combustion zone ports other than injector end, where $0 < X < 6$
CG4 -X	Nozzle ports, where X is the axial distance from the injector face
CG5	Baseplate ports
CT1 (and subs)	Tapoff manifold ports

APPENDIX VII

FLOWRATE CALCULATION METHODS

(U) The fuel and oxidizer flow schematic of the ADP tube-wall thrust chamber is shown in Fig. 399. From this figure, it can be seen that the oxidizer-flow system contains a turbine-type flowmeter in series with a cavitating venturi for the measurement of the oxidizer flowrates. The turbine flowmeter is the primary measuring device. The main purpose of the cavitating venturi is to limit the oxidizer flowrate to the steady-state value. Calculations of the flow through a turbine flowmeter are based on industrial standardized techniques. The oxidizer cavitating venturi flowrates can be calculated by:

$$\dot{w} = KA\sqrt{2g\,\rho\,\Delta P}$$

where

A = nozzle throat area, ft^2

ρ = oxidizer density, lbm/ft^3

ΔP = differential pressure between the inlet and vapor pressure of the fluid, lb/ft^2

g = mass conversion factor $\frac{lbm/ft}{lbf/sec^2}$

(U) K is a flow coefficient defined as:

$$K = \frac{C_D}{\left[1 - \left(\frac{A_o}{A_1}\right)^2\right]^{1/2}}$$

where C_D is the nozzle discharge coefficient and A_1 is the nozzle inlet area. Flowrates based on the cavitating venturi were compared to those measured by the turbine flowmeter as a check.

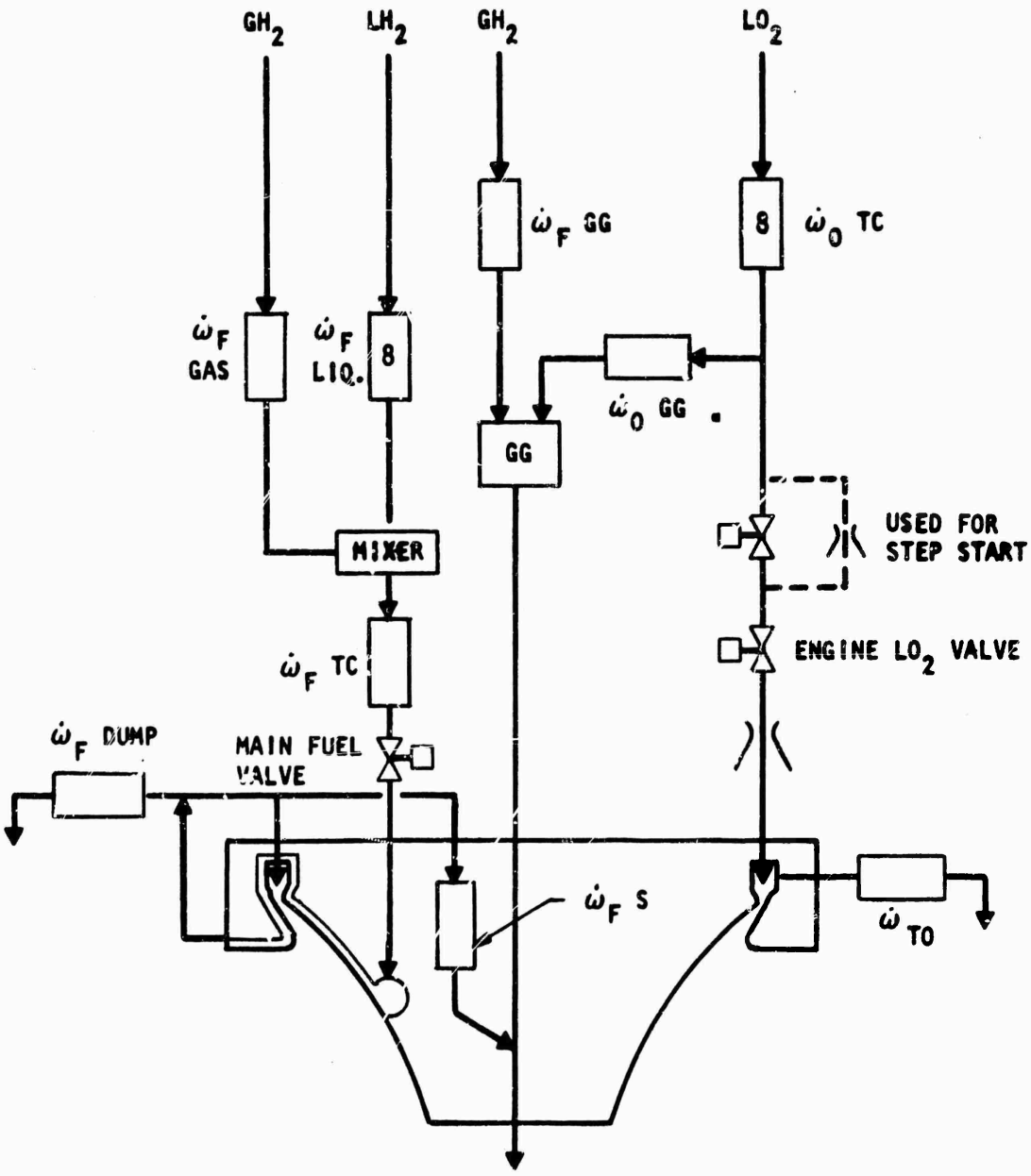

Figure 399. Flow Diagram, Tube-Wall Thrust Chamber

(U) In the fuel system, a combination of liquid turbine type and both subsonic venturis and critical venturis and orifices is employed to evaluate the fuel flowrates. Fuel flow into the hardware is composed of both a liquid and gaseous component. The liquid phase is metered by a flowmeter, and gas phase is metered by a subsonic venturi. Flow into the combustion chamber is obtained by the difference between the total fuel flow and the measured dump flowrate. The dump flowrates are obtained with the use of a sonic nozzle and a sonic orifice. Supplemental gaseous hydrogen is introduced into the base region of the thrust chamber through a sonic venturi. In addition, a sonic nozzle is installed in the main fuel line upstream of the hardware inlet. The main function of this nozzle is to serve as a flow-limiting device; however, it does act as a check on the main fuel flow.

APPENDIX VIII

CHAMBER START SEQUENCE

(U) The detailed chamber start and cutoff sequences for the solid wall and tube wall are shown in Fig. 400 through 403. The start sequence for the No. 2 tube-wall chamber was modified to incorporate a step start to extend the start transient duration. The first stage of oxidizer flowrate is controlled by a cavitating venturi located in parallel with the main oxidizer valve but in series with the main oxidizer cavitating venturi. The first step flowrate was controlled by the first cavitating venturi. The second step was achieved by opening the main facility oxidizer valve to bypass the first venturi.

(U) Purges are locked up on the oxidizer, fuel, ClF_3, and hot-gas tapoff systems which are checked off at transition to mainstage and come "on" automatically at chamber pressure decay.

OXIDIZER SYSTEM

(U) The facility oxidizer system schematic is shown in Fig. 399. A cavitating venturi is located at the oxidizer main valve inlet. The purpose of the venturi is to limit oxidizer flowrate during transition to minimize chamber pressure overshoot.

(U) A dump valve is incorporated into the system to provide a means of emptying the oxidizer ducting between the main valve and the chamber oxidizer manifold. Purges are located at the chamber manifold to expel oxidizer out the dump lines. A test is started with the dump valve closed.

FUEL SYSTEM

(U) The facility fuel system schematic is shown in Fig. 399. A gaseous hydrogen servocontrolled system provides fuel at any predetermined temperature at the chamber inlet. The total fuel flow to the chamber is controlled by means of a sonic venturi located at the chamber inlet. Excess fuel coolant flow is used in the chamber tubes. After making the coolant circuit, the fuel flow is split to the injector and dump systems in parallel paths. Part of the dump fuel is used as secondary base flow fluid.

IGNITION SYSTEM

(U) Chlorine trifluoride is used as the normal hypergol ignition source. Each of the 40 combustion compartments contains one igniter tube. The tube passes through the fuel manifold and terminates at a recessed position behind the face of a fuel strip.

(U) Hypergol is supplied to each igniter tube through a manifold system from one primary charge plenum. A 100-cu in. slug of ClF_3 in the primary plenum is pressurized by GO_2 tapped off of the high-pressure LO_2 line. Figure 403 shows the ignition system schematic.

(U) Ignition is established with main fuel and ClF_3, and is sustained with GO_2 and fuel until introduction of LO_2 into the chamber.

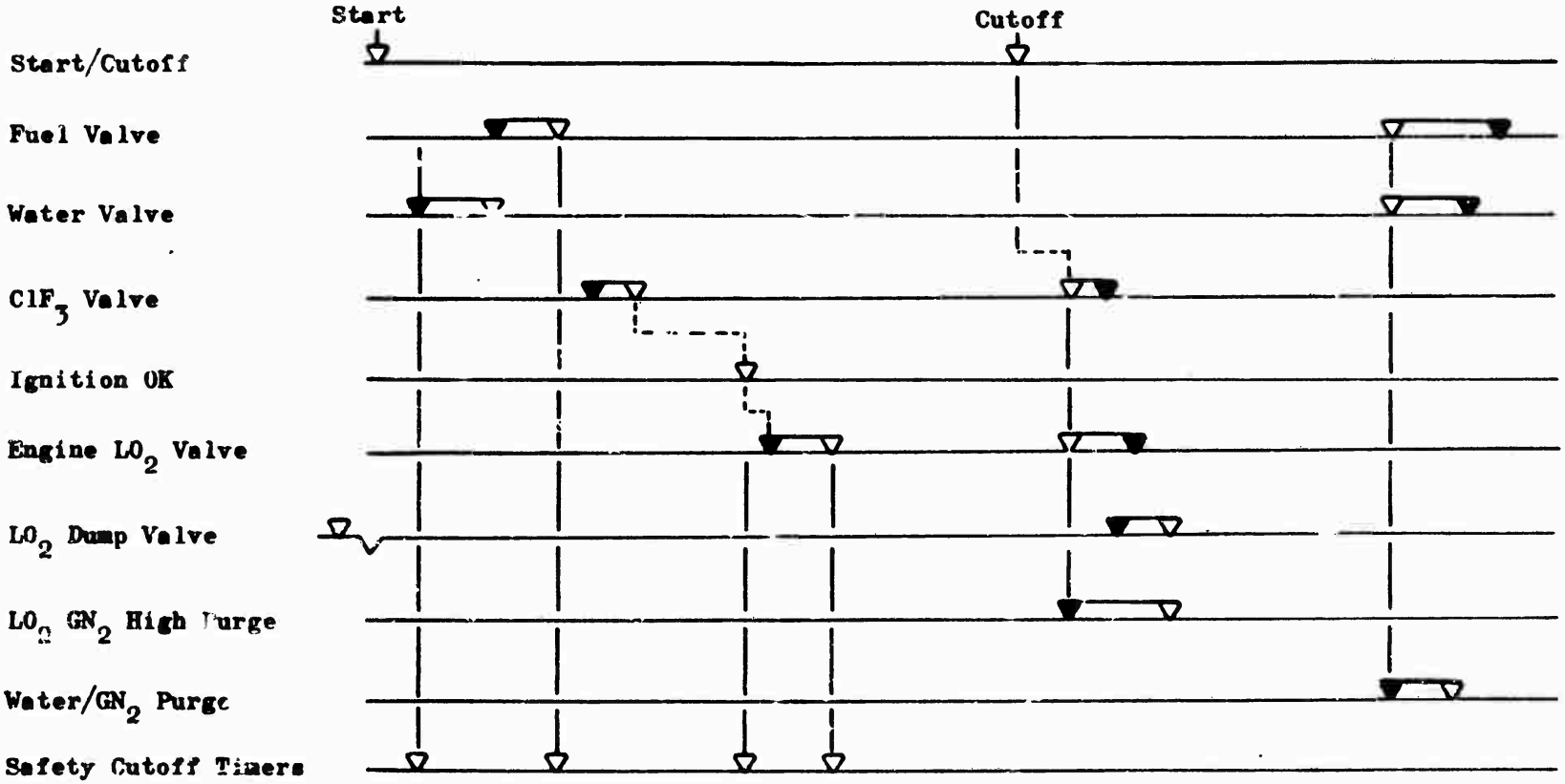

Other purges were: Hypergol System
Hot-gas Manifold
Injector Seal Cavity

Figure 400. Typical Solid-Wall Test Sequence

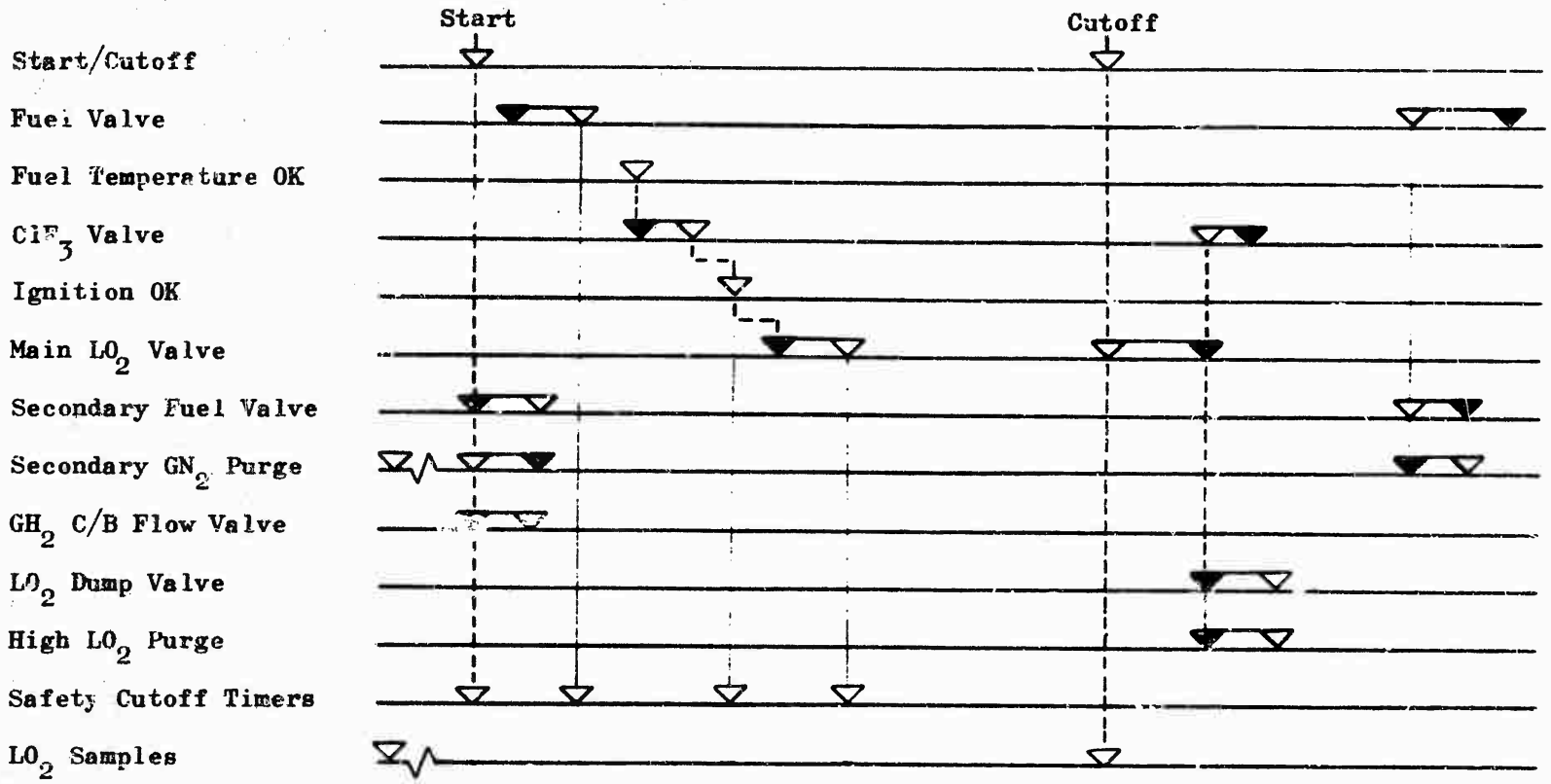

Lockup GN_2 Purges: hot-gas manifold, LO_2 manifold (low level), ClF_3 system, LO_2 dump line

Lockup GH_2 Purge: fuel system

▼ Valve Closed. ▽ Valve Open

Figure 401. 250K Tube-Wall Start and Shutdown Sequence, Test No. 025

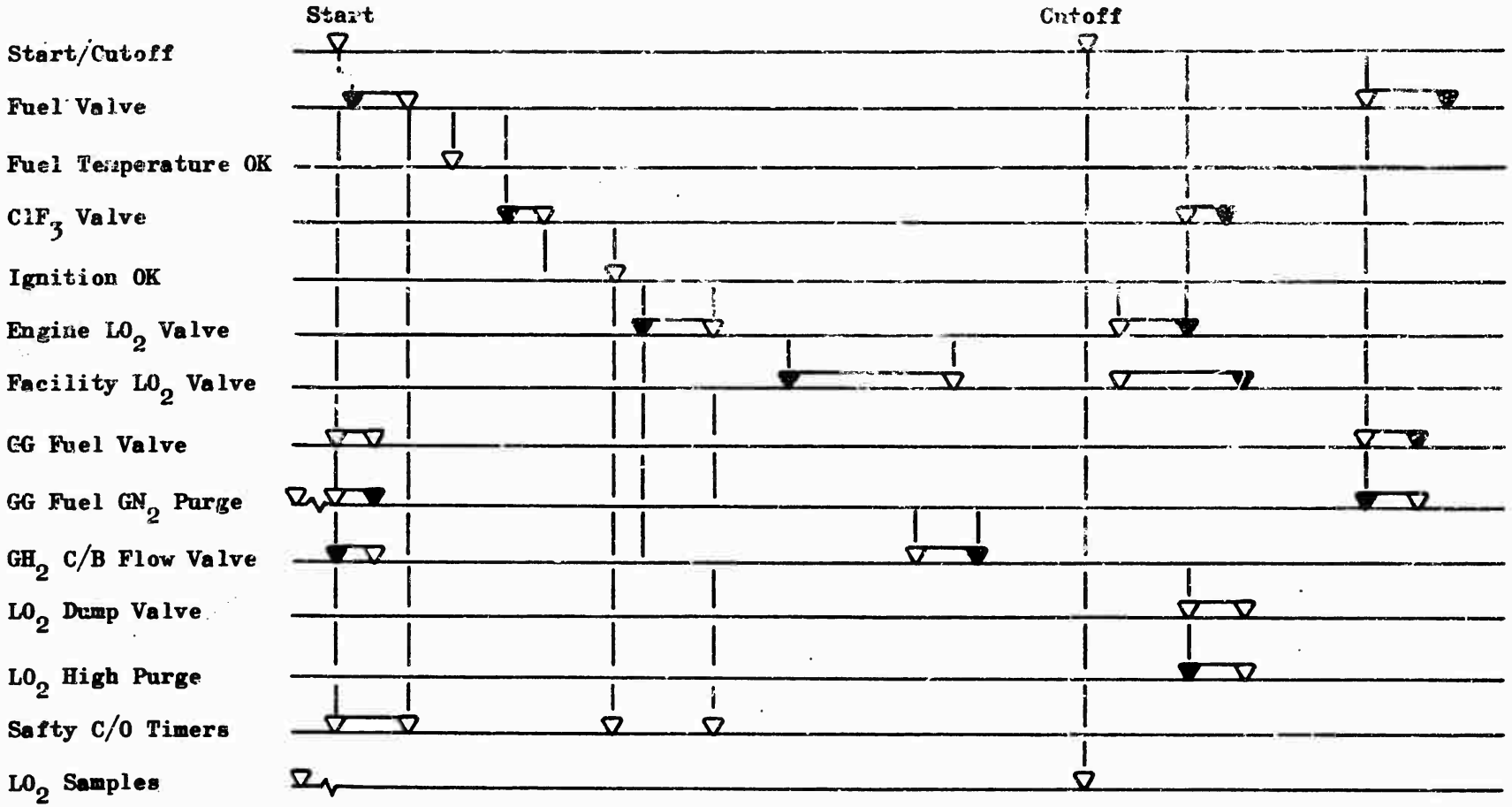

Lockup GN_2 Purges: oxidizer manifold (low flow), ClF_3 main valve, and dump line

Lockup GH_2 Purge: fuel system

▼Valve Closed. ▽Valve Open

Figure 402. 250K Tube-Wall Step Start Sequence

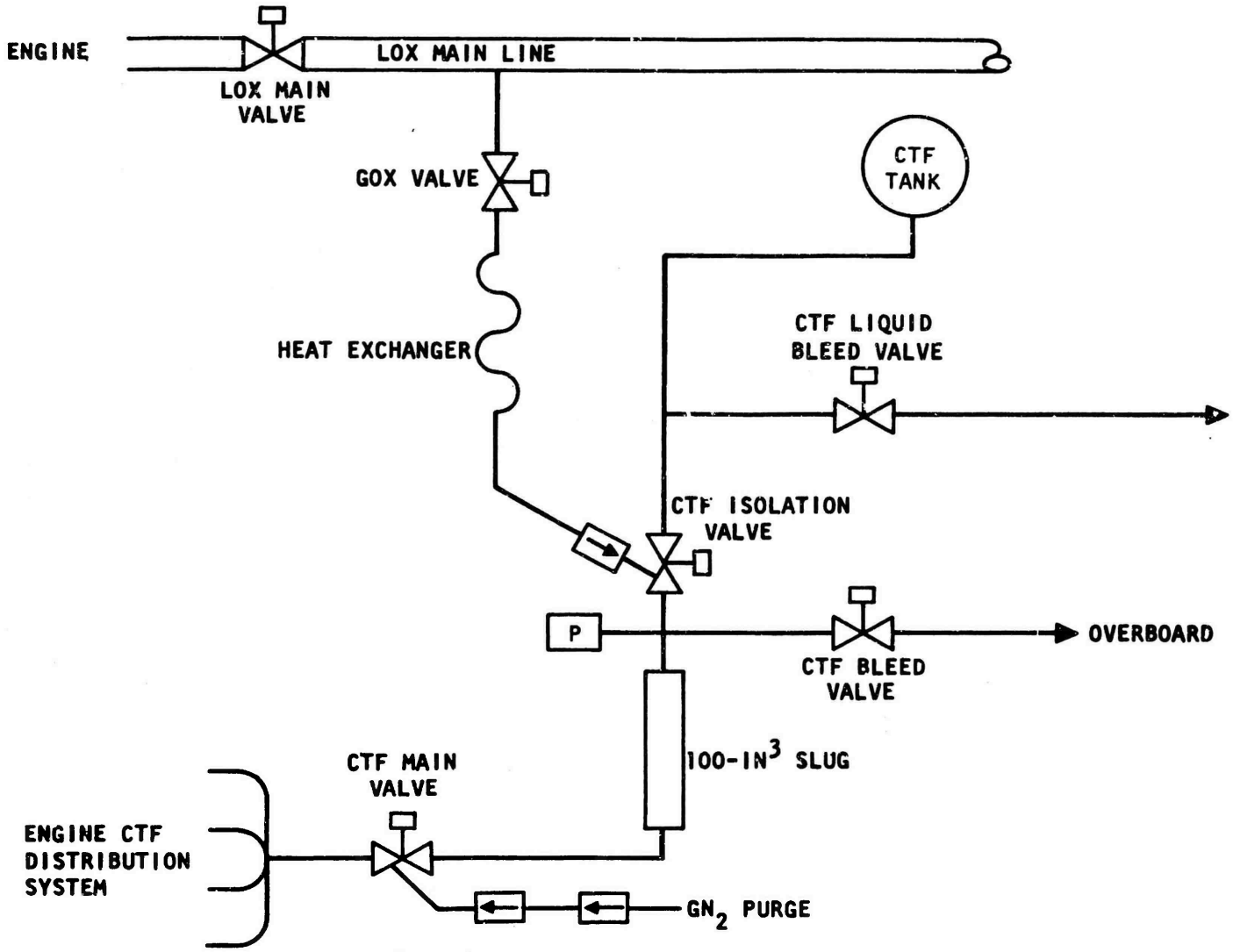

Figure 403. CTF Ignition System Schematic

APPENDIX IX

ALTITUDE COMPENSATION

(U) A major advantage of the aerodynamic spike nozzle concept is its ability to produce near-optimum performance over a wide altitude or pressure ratio range. This ability of the nozzle expansion process to adjust continuously to the prevailing ambient pressure is known as altitude compensation. In the aerodynamic spike nozzle, altitude compensation takes place both on the nozzle wall and in the base region.

(U) The flow model representing the aerodynamic phenomena which govern aerospike nozzle behavior is shown in Fig. 404. During operation at high-pressure ratios (chamber pressure-to-ambient pressure), the characteristics of the primary flow field upstream of the base, shown as region 1 in Fig. 404, are determined only the throat and contour geometry. In region 2, the flow expands around the lower lip of the model and detaches, forming a free shear layer which separates the external flow from a region of subsonic recirculating gases in the base. The inner free-jet boundary is not affected by ambient pressure waves from the outer-jet boundary, and thus is independent of pressure ratio. The flow along the inner-jet boundary and its adjacent shear layer impinges on the centerline where it reattaches and recompresses through a trailing shock. This condition is referred to as closed-wake flow, and the base pressure is constant and higher than ambient so that a positive thrust acting on the base is developed. Ambient pressure effects are not felt on the nozzle contour or base. The basic mechanism governing the base pressure in this regime is flow reattachment.

(U) When a small amount of secondary flow is introduced into the base (at a constant ambient pressure) and the base pressure increases, the inner free-jet boundary of the primary stream still impinges on the centerline; however, the angle of impingement becomes shallower as the

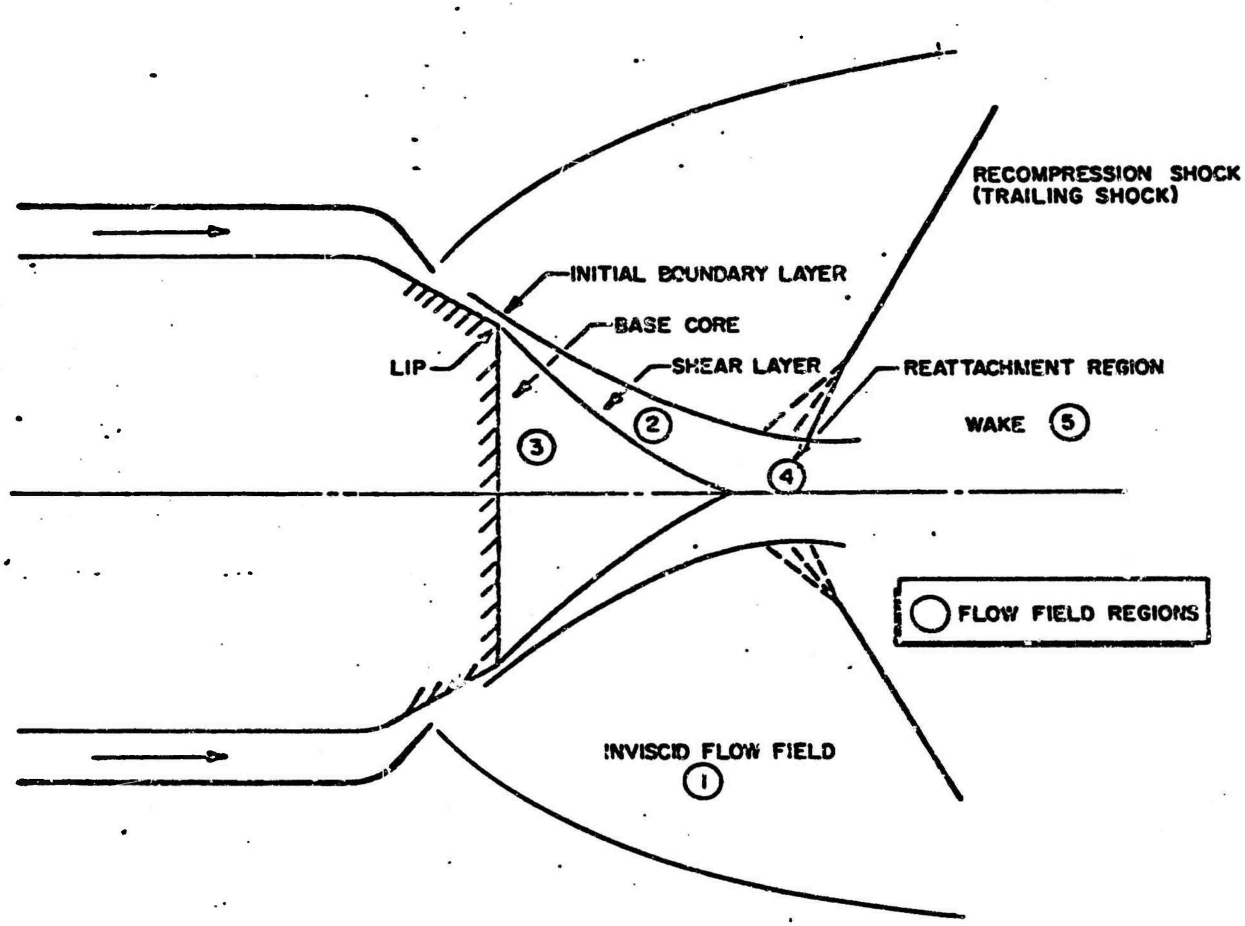

Figure 404. Aerospike Flow Field Model

base pressure increases. Higher base pressures result because the secondary flow modifies the shear layer characteristics, i.e., increases the viscous entrainment region between the primary and secondary flow regions. The modification of the shear layer is accompanied by a change in the flow in the reattachment region (region 4) resulting in increased base pressure

(U) As the pressure ratio decreases, the nature of the flow field changes considerably. The intersection of the envelope shock and the inner free-jet boundary moves upstream toward the reattachment point as the pressure ratio decreases. When the reattachment point is reached, the wake starts to open. When the wake opens, the base pressure no longer remains constant (at a constant secondary flowrate), but increases with increasing ambient pressure (decreasing pressure ratios). Further decreases in pressure ratio will cause the envelope shock to impinge finally on the nozzle contour (Fig. 404), causing recompression of the primary flow. The recompression phenomenon yields increased wall pressures at high ambient pressures, eliminating overexpansion losses common to conventional high-area-ratio nozzles operating at low altitudes. Thus, recompression compensates for the ambient condition, and is largely responsible for the altitude-compensating feature of the aerospike nozzle. The wall pressures due to recompression can be considerably higher than ambient or base pressures. Conventional bell nozzles cannot experience recompression since the primary flow field is internal to the nozzle hardware.

(U) The aerospike nozzle exhibits a performance advantage over a conventional nozzle since the recompression phenomenon results in good low-altitude performance for a high-area-ratio nozzle without compromising design point performance.

REFERENCES

1. Quarterly Progress Reports, Advanced Cryogenic Rocket Engine Program, Aerospike Nozzle Concept: AFRPL-TR-66-138, 242, 348, and TR-67-91, 188, 258, Rocketdyne, a Division of North American Aviation, Inc., Canoga Park, California, Confidential.

2. Applications Study for a High-Performance Cryogenic Aerospike Rocket Engine: AFRPL-TR-67-269 (Revised), Rocketdyne, a Division of North American Rockwell Corporation, Canoga Park, California, November 1967, Confidential.

3. Advanced Cryogenic Rocket Engine Program, Aerospike Nozzle Concept, Materials and Processes Research and Development Report: AFRPL-TR-67-278, Rocketdyne, a Division of North American Rockwell Corporation, Canoga Park, California, November 1967, Confidential.

4. Spenger, H.: "Experimental Investigations of Straight and Curved Diffusers," Mett. Inst. Aerodyn. Zurich (27), 1959, 84 pp.

5. Builder, C. H., W. A. Fey, M. G. Hinton, and R. Krueger: Vehicle Applications Package, 250K, Aerospace Corporation, September 1965.

6. Fey, W. A., M. G. Hinton, and R. Krueger: Vehicle Applications Package, 350K Module, Tor-669(6520-10)-2, Aerospace Corporation, February 1966.

7. Arbit, H. A. and S. D. Clapp: Fluorine-Hydrogen Performance Evaluation, Part I: Analysis, Design, and Demonstration of High-Performance Injectors For the Liquid Fluorine-Gaseous Hydrogen Propellant Combination, RR 66-10, Rocketdyne, a Division of North American Aviation, Inc., April 1966.

8. Beers, Yardley: Introduction to the Theory of Error, Addison-Wesley Publishing Co., Inc., Reading, Massachusetts, 1962.

9. Shapiro, A. H.; The Dynamics and Thermodynamics of Compressible Fluid Flow, Vol. 1, The Ronald Press Co., New York, 1953.

10. Investigation of Cooling Problems at High Chamber Pressures, Final Report: R-6199, Rocketdyne, a Division of North American Aviation, Inc., Canoga Park, California, May 1965, Unclassified.

11. Advanced Engineering Program, Systems and Dynamics Investigation (Aerospike), Final Report: R-7167, Rocketdyne, a Division of North American Aviation, Inc., Canoga Park, California, August 1967, Confidential.

12. Advanced Aerodynamic Spike Configurations, Final Report: AFRPL-TR-246, Rocketdyne, a Division of North American Aviation, Inc., Canoga Park, California, September 1967, Confidential.

13. Advanced Development Program for an Advanced O_2/H_2 Aerospike Engine: R-6360P-2, Rocketdyne, a Division of North American Aviation, Inc., Canoga Park, California, November 1965, Confidential.

Unclassified

Security Classification

DOCUMENT CONTROL DATA - R & D

(Security classification of title, body of abstract and indexing annotation must be entered when the overall report is classified)

1 ORIGINATING ACTIVITY (Corporate author) Rocketdyne, a Division of North American Rockwell Corporation, 6633 Canoga Avenue, Canoga Park, California 91304	2a. REPORT SECURITY CLASSIFICATION Confidential 2b. GROUP 4

3 REPORT TITLE

Advanced Cryogenic Rocket Engine Program, Aerospike Nozzle Concept

4 DESCRIPTIVE NOTES (Type of report and inclusive dates)

Final Report, January 1968

5 AUTHOR(S) (First name, middle initial, last name)

6. REPORT DATE 31 January 1968	7a. TOTAL NO. OF PAGES	7b. NO. OF REFS 13
8a. CONTRACT OR GRANT NO. AF04(611)-11399 b. PROJECT NO. c. d.	9a. ORIGINATOR'S REPORT NUMBER(S) R-7168 9b. OTHER REPORT NO(S) (Any other numbers that may be assigned this report) AFRPL-TR-67-280	

10 DISTRIBUTION STATEMENT "In addition to security requirements which must be met, this document is subject to special export controls and each transmittal to foreign governments or foreign nationals may be made only with prior approval of AFRPL (RPPR/STINFO), Edwards, California 93523."

11 SUPPLEMENTARY NOTES	12 SPONSORING MILITARY ACTIVITY Air Force Rocket Propulsion Laboratory Edwards Air Force Base, California

13 ABSTRACT

Technical results obtained at the completion of the contract effort are described for the Advanced Cryogenic Rocket Engine Program, Aerospike. This program includes analysis and preliminary design of an advanced rocket engine using an aerospike nozzle and experimental evaluation of critical technology related to the aerospike concept. Component and system features, physical arrangements, design parameters and details, operational characteristics, and performance have been established for an optimum demonstrator engine. Studies were made of application of a flight engine to certain vehicles. Experimental injector performance investigations and experimental cooling investigations on segment chambers were conducted, producing the target combustion performance. Various materials were studied for long life of thrust chamber cooling passages and the target life was demonstrated. Full-scale, cooled thrust chambers were fabricated and tested for overall combustor and nozzle performance demonstrations. Injector failure limited these tests, however nozzle and combustor performance were as predicted when not influenced by excess leakage. Structural and cooling evaluations were conducted on a segment embodying essential elements of the Demonstrator chamber design.

DD FORM 1 NOV 65 1473

Unclassified

Security Classification

14 KEY WORDS	LINK A		LINK B		LINK C	
	ROLE	WT	ROLE	WT	ROLE	WT
Aerospike nozzle						
Tapoff cycle						
Combustion efficiency						
Heat transfer						
Thrust chamber structure						
Throat gap						
Tube materials						
Tube fatigue life						
Segment testing						
Parallel turbines						
Transient behavior						